Imperial College
London

Modelling the behaviour of marine composite panels under static and dynamic loading

This thesis is submitted for the degree of Doctor of Philosophy of the University of London

by

Hayley Eve Johnson

Department of Civil and Environmental Engineering
South Kensington Campus
Imperial College London
London SW7 2AZ
U.K.

2007

DECLARATION OF AUTHENTICITY

I confirm that the work presented in this thesis is my own and the work of other persons is appropriately acknowledged within the text.

Declared by:

Hayley Johnson

ABSTRACT

The use of fibre composite materials in more demanding roles is increasing due to the need for increased performance requirements in various applications. The demand for robust numerical modelling techniques to predict the strength and survivability of such structures under static and dynamic loading has thus become more important in the marine and aerospace industry. The following work highlights some of the strengths and deficiencies of popular stress based criteria for 2d and 3d numerical modelling of small and large scale plates and results in the proposal of two delamination modelling techniques and a continuum damage model.

Woven fibre reinforced marine panels were subjected to in-plane loading up to failure to obtain their peak load and post-peak response. Their residual capacity was small and the tests demonstrated amongst other things, the difficulty in controlling the plate boundary conditions, the sensitivity to these boundaries and the imperfection effect on the pre-buckling stiffness. A finite element parametric study using a user-defined-field subroutine was carried out to assess the capability of Hashin's 2d failure criteria in predicting the panel behaviour, which resulted in the modification of Hashin's criterion. Owing to the fact that delamination can be a catastrophic failure mode if left undetected, a resin-rich layer modelling technique was proposed and the performance of Abaqus's new continuum shell was assessed. An empirically derived 2d energy criterion applied at the resin-rich layers provided good predictions of the largest delaminations under dynamic loading. Various stress-based criteria, previously applied with more success under quasi-static loading conditions for delamination, matrix and fibre damage predictions, gave unpredictable and often erroneous results when implemented at the resin-rich layers or woven plies. The contact force, damage size and damage location predictions for dynamic loading were considerably better captured using an in-plane continuum damage based model and a separate transverse damage model to capture the 3d state of stress. Delamination was explicitly modeled with a linear traction separation cohesive zone law at the inter-ply regions. The new, easy to use yet effective material model was implemented in a user material subroutine. It was formulated using strain data from cyclic tests, standard tensile and compressive coupon tests and fracture tests. The transverse degradation of the material properties at the woven plies was observed to be vital in correctly predicting the contact force. This is especially so where larger and thicker plates are concerned and when mesh

density and computational time limitations prevents cohesive mesh discretization of every inter-ply region.

CONTENTS

Abstract..... i

Table of contents..... iii

List of Figures..... ix

List of Tables xx

Acknowledgments..... xxii

Notation..... xxiii

1. Introduction **1**

2. Test specification and data **14**

2.1 Introduction 14
2.2 Resin transfer moulding techniques 14
2.3 Quasi-static material tests 15
2.3.1 In-plane testing 15
2.3.2 Through-thickness testing 16
2.4 Strain rate testing 17
2.5 Fracture testing 18
2.6 Cyclic Testing 18
2.7 In-plane compression testing of large plates 22
2.8 Impact Testing 27
2.8.1 Introduction 27
2.8.2 Small-scale plates 27
2.8.2.1 Photographs of damage 36
2.8.3 Large-scale plates 42
2.8.3.1 Plate size 'Large1' 43
2.8.3.2 Plate size 'Large2' 45
2.9 Reference List 48

3. Numerical simulation of statically loaded panels **49**

3.1 Introduction 49
3.2 Stress Based failure criteria 49
3.3 Selected failure criteria for numerical validation 59
3.4 Method of degrading the material properties 60
3.5 An overview of numerical model specifications 61
3.5.1 Introduction 61
3.5.2 Shell element formulation 61
3.5.3 The Newton-Raphson method 63
3.5.4 The Riks Analysis 65
3.6 Numerical modelling of a transversely loaded E-glass/polyester plate 68
3.6.1 Introduction 68
3.6.2 The finite element model 68
3.6.3 Finite Element Results and Discussion 69

3.6.4 Simple theoretical calculations....70
3.6.5 Matrix and fibre damage predictions....72
3.7 Large-scale testing and numerical modelling of thick composite panels under in-plane compression....74
3.7.1 Introduction....74
3.7.2 Background....75
3.7.3 Damage mechanism....79
3.7.4 The Finite Element model....81
3.7.4.1 Modification of Hashin's compressive matrix damage equation....83
3.7.5 Buckling loads....87
3.7.6 Panel test strains....93
3.7.7 A parametric study in finite element....96
3.7.8 Discussion....102
3.7.8.1 Panel Test 2....103
3.7.8.2 Tests 3, 4 & 5....111
3.7.8.3 Summary of panel behaviour....115
3.7.9 Conclusion....117
3.8 Concluding remarks....118
3.9 Reference List....119

4. Formulation of a continuum damage model....124

4.1 Introduction....124
4.2 Background....125
4.3 Overview of proposed matrix and fibre damage model....129
4.4 Assessment of potential damage regions....130
4.5 In-plane continuum damage fundamentals....132
4.6 Matrix damage initiation....136
4.7 In-plane damage propagation....137
4.7.1 Matrix damage development function....142
4.7.2 Fibre damage development function....145
4.8 Intra-ply transverse damage....146
4.8.1 Initiation of intra-ply transverse damage....146
4.8.2 Propagation of intra-ply transverse damage....147
4.9 Element erosion....148
4.10 Constitutive law for an undamaged 2d orthotropic plate....148

4.11 Constitutive law for a damaged 3d orthotropic plate 149
4.12 Numerical implementation – Impact of small and large-scale plates 154
4.12.1 Introduction 154
4.12.2 Explicit time integration 156
4.12.3 Results and discussion 156
4.12.4 Conclusion 160
4.13 Concluding remarks 161
4.14 Reference List 162

5. Formulation of two delamination modelling techniques 165

5.1 Introduction 165
5.2 Background 166
5.3 Resin-rich layer model 170
5.3.1 Introduction 170
5.3.1 Stress criteria for delamination 171
5.3.2 Energy criterion for delamination 172
5.3.3 In-plane visco-plastic model 174
5.4 Fracture and numerical modelling limitations 180
5.5 The Cohesive Zone model 182
5.5.1 Origin of the Cohesive zone model 182
5.5.2 Function of an eight noded interface element 185
5.5.3 The critical fracture energy value 188
5.5.4 Mesh density 189
5.5.5 A linear coupled traction-separation law 191
5.5.5.1 Implementation method in finite element 195
5.5.6 A non-linear coupled traction-separation law 196
5.5.6.1 Implementation method in finite element 199
5.6 Numerical simulation of plate impacts using cohesive elements 201
5.6.1 Introduction 201
5.6.2 Results and discussion 201
5.6.2.1 Effect of a linear and non-linear cohesive model on a small plate 201
5.6.2.2 Linear model implementation for large plates 205
5.6.2.3 Shear dominated delamination 208
5.6.2.4 Mesh density influence 211
5.6.2.5 Scaling Effects 212
5.6.2.6 Shell element type 213

5.7 Concluding remarks 214
5.8 Reference List 215

6. A numerical study of plate impact using combined damage models 219

6.1. Introduction 219
6.2. 2d damage at the woven plies with resin-rich layers for delamination 220
6.2.1. Shell section definition 220
6.2.2. Transverse shear stiffness 221
6.2.3. Large-scale plate impact 222
6.2.3.1. Transverse shear stiffness influence 223
6.2.3.2. Damage prediction 227
6.2.4. Small-scale plate impact 230
6.2.4.1. Modelling variables 230
6.2.4.2. Transverse stress output 231
6.2.4.3. In-plane and through-thickness mesh density effect on delamination 233
6.2.4.4. Impact energy effect on delamination 235
6.2.4.5. Contact force and out-of-plane displacements for small and large tup impacts 238
6.2.4.6. Implementation of a viscoplastic model at the RR-layers 239
6.2.5. Concluding remarks 240
6.3. 3d Damage at the woven plies with a cohesive zone model for delamination 242
6.3.1. Introduction 242
6.3.2. Small-scale plate impact 242
6.3.2.1. The effect of a delamination model 243
6.3.2.2. Excluding the transverse material degradation at the woven plies 244
6.3.2.3. Strain rate effects 245
6.3.2.4. Modelling half the number of cohesive layers 246
6.3.2.5. Mesh density effects 248
6.3.2.6. Varying the cyclic loading parameters 248
6.3.2.7. Damage propagation criterion – energy versus strain 250
6.3.2.8. The influence of the initiation criterion on the translaminar degradation 251
6.3.2.9. Contact force and displacement results for all the small plate tests 253
6.3.2.10. A quarter plate model and corner damage 259
6.3.2.11. Element erosion 259
6.3.2.12. Energy versus contact force 261
6.3.3. Damage predictions 263

6.3.3.1. Delamination damage 265
6.3.3.2. Stress resolution on matrix and fibre damage predictions 267
6.3.3.3. Effect of impactor diameter on damage prediction 267
6.3.3.4. Displacement-contact force history 269
6.3.4. Large-scale plates 1 271
6.3.4.1. Contact force and displacement results 272
6.3.4.2. Surface strains 275
6.3.4.3. Damage predictions 283
6.3.5. Large-scale plates 2 290
6.3.6. Energy versus contact force for the large plates 292
6.3.7. Concluding remarks 293
6.4. Conclusion 295
6.5. Reference List 296

7. Conclusion and further work 297

7.1 Conclusion 297
7.2 Future work 300

Appendix A 303
Appendix B 304
Appendix C 305
Publications 327

LIST OF FIGURES

Figure 1-1. Holing of the USS Cole in Oct 2000 2

Figure 1-2. Woven strand matt 3

Figure 1-3. Approach to obtaining the residual strength of a naval panel 9

Figure 1-4. Sagging and hogging effect of a naval vessel 10

Figure 2-1. Average strength values at two different strain rates 18

Figure 2-2. Coupon specimen configuration used for cyclic testing – ASTM D638 type III 19

Figure 2-3. Warp-T1 (tens). Strain vs damage. 20

Figure 2-4. Warp-T1 (tens). Damage energy release rate vs damage. 21

Figure 2-5. Warp-T1 (tens).Stress-strain curve. 21

Figure 2-6. Fill-T1 (tens.) Strain vs damage. 21

Figure 2-7. Fill-T2 (tens.) Strain vs damage. 21

Figure 2-8. Warp-T4 (comp.) Strain vs damage. 21

Figure 2-9. Warp-T5 (comp.) Strain vs damage. 21

Figure 2-10. Fill-T5 (comp) Strain vs damage. 21

Figure 2-11. Fill-T6 (comp) Strain vs damage. 21

Figure 2-12. Drawing of rig for in-plane loading of large scale plates (3rd angle projection). 23

Figure 2-13. Photo of panel test 1 24

Figure 2-14. Photo of panel test 2 24

Figure 2-15. Photo of panel test 3 24

Figure 2-16. Out-of-plane displacement along the centre length of the plate, Test 2, at 1200kN. 25

Figure 2-17. Diagram of the 300mm steel block used for tests 3 to 5, (measurements in metres and inches). 25

Figure 2-18. Damage photos of panels 27

Figure 2-19. Photograph of the small plate impact test rig. 28

Figure 2-20. From left to right 0.0127m, 0.0254m and 0.0381m (0.5", 1" and 1.5") diameter impactors 29

Figure 2-21. Contact force-time history for the 12.7mm Tup 29

Figure 2-22. Contact force-time history for the 25.4mm Tup, in lbforce 30

Figure 2-23. Contact force-time history for the 38mm Tup 30

Figure 2-24. Energy vs time for the 12.7mm tup 31

Figure 2-25. Energy-time history for the medium (25.4mm) Tup, in ftlbf 31

Figure 2-26. Energy-time history large (38mm) Tup 32

Figure 2-27. Displacement -time history small (12.7mm) Tup 32

Figure 2-28. Deflection-time history for the medium (25.4mm) in Tup, in inches 33

Figure 2-29. Deflection-time history for large (38mm) Tup 33

Figure 2-30. Test 3S(166J), top. 36

Figure 2-31. Test 3S(166J), bottom. 36

Figure 2-32. Test 5S(193J), top face 37

Figure 2-33. Test 5S195J), bottom face 37

Figure 2-34 Test 6S(196J), Top face 38

Figure 2-35 Test 6S(196J), Top face 38

Figure 2-36 Test 9M(195J), top. 39

Figure 2-37 Test 9(195J), top. 39

Figure 2-38 Test 9M(195J), bottom. 40

Figure 2-39 Test 13L(284J), top. 40

Figure 2-40 Test 13L(284J), top. 41

Figure 2-41 Test 13L(284J), bottom. 41

Figure 2-42. Schematic of large panel impact test fixture 42

Figure 2-43. Large plate impact rig with large1 sized plate positioned in place 43

Figure 2-44. Measurement of damage using discoloured areas. 44

Figure 2-45. Comparison of two different measures of impact force for test 'large2(2)' 46

Figure 2-46. Contact force time history for large plate 2 tests: large2(1) and large2(2) 46

Figure 2-47. Ultrasound C-scan image of large2(2) plate centre 47

Figure 3-1. The Newton Raphson iterative process to find a solution for u1 caused by load P_1 64

Figure 3-2. Pressure-displacement curve from the validation analyses, for no-damage and the Hashin failure model 69

Figure 3-3. Fibre failure shown for a few layers 73

Figure 3-4. Stress along the fibre direction for (a) bottom, tensile face (layer 5) , and (b) top, compressive face (layer 1) 73

Figure 3-5. A highlight of potential cracks and delamination in a schematic of the woven laminate, showing the woven bundles of fibres. 80

Figure 3-6. Damage highlighted on the panel in test 4, compression face 80

Figure 3-7. Layerwise modelling method 81

Figure 3-8. Load-displacement curves for analyses employing different failure criteria 85

Figure 3-9. Load-displacement cuves, demonstrating the importance of modelling damage 86

Figure 3-10. Load-displacement curves, including variations of Hashin's criteria and different boundary conditions. 86

Figure 3-11. Load-displacement curves for the five panel tests 87

Figure 3-12. Loading on a plate element 89

Figure 3-13. In-plane forces on a plate element 90

Figure 3-14. Strain gauge locations for tests 2 to 5. The face in compression has gauges labeled with double letters, shown in brackets 94

Figure 3-15. Panel test 2, 3, 4 & 5 load-strain curves at locations 'a' and 'aa'. 94

Figure 3-16. Panel test 2, 3, 4 & 5 load-strain curves at locations 'c' and 'cc'. 95

Figure 3-17. Load-strain curves for panel test 2 at locations 'a', 'aa', 'e' and 'ee'. 95

Figure 3-18. Average longitudinal strains at all the strain locations for all five panel tests .. 96

Figure 3-19. Horizontal strains at all the strain locations for all five panel tests 96

Figure 3-20. Damage predictions for analysis 'load_S1S2_i2_Hash(bi)'. 98

Figure 3-21. Load-displacement curves, comparison of the two methods of applying Hashin and three panel test results 99

Figure 3-22. Load-displacement curves, demonstrating ensitivity to bc's, using load control FE analyses 100

Figure 3-23. Load-displacement curves, showing sensitivity to residual stiffness, using load and displacement controlled FE analyses 100

Figure 3-24. Load-displacement curves, showing the effect of initial imperfection, using load and displacement FE analyses 101

Figure 3-25. Load-displacement curves, showing sensitivity to material properties, using load and displacement control FE analyses 102

Figure 3-26. Load-displacement curves, showing the most representative FE models of the actual test conditions 103

Figure 3-27. Load-strain curves, for panel test 2 and FE analysis 'Disp_S_1S_2_i2_5%' 104

Figure 3-28. Load-strain curves for the top plate strains for panel test 2 and FE analysis 'Load_S_1S_2_i2_10%' 104

Figure 3-29. Strain positions across the top part of the plate. Location of strain gauge positions *a*, *c* and *e* are highlighted for the compressive side. 105

Figure 3-30. Longitudinal strains, *EE11* at 160kN, across the top of the plate for test 2, at locations shown in Figure 3-29, comparing analyses 'disp_S1S2_i2_5%' and 'load_S1S2_i2_10%' 105

Figure 3-31. Longitudinal strains, *EE11* at 420kN, across the plate for test 2, at locations shown in Figure 3-29, comparing analyses 'disp_S1S2_i2_5%' and 'load_S1S2_i2_10%' 105

Figure 3-32. Longitudinal strains at the top gauge locations at a 160kN load: test 2 and FE 107

Figure 3-33. Longitudinal strains at the top gauge locations at a 440kN load: test 2 and FE. 107

Figure 3-34. Longitudinal strains at the top gauge locations at a 1000kN load: test 2 and FE. 107

Figure 3-35. Horizontal strains at the top gauge locations at a 160kN load: test 2 and FE. 108

Figure 3-36. Horizontal strains at the top gauge locations at a 440kN load: test 2 and FE. 108

Figure 3-37. Horizontal strains at the top gauge locations at a 440kN load: test 2 and FE. 108

Figure 3-38. Vertical strains at the centre gauge locations at a 160kN load: test 2 and FE. 109

Figure 3-39. Vertical strains at the centre gauge locations at a 440kN load: test 2 and FE. 109

Figure 3-40. Vertical strains at the centre gauge locations at a 1000kN load: test 2 and FE. 109

Figure 3-41. Horizontal strains at the centre gauge locations at a 160kN load: test 2 and FE. 110

Figure 3-42. Horizontal strains at the centre gauge locations at a 440kN load: test 2 and FE. 110

Figure 3-43. Horizontal strains at the centre gauge locations at a 1000kN load: test 2 and FE. 110

Figure 3-44. Load-displacement curves, examples of sensitivity to bc's, initial imperfection and material properties 112

Figure 3-45. FE analyses most closely resembling panel tests 2 and 3 113

Figure 3-46. Strain comparisons between FE analyses 'Disp_S_1S_2_i2_5%' and 'Load_S_1S_2_i2_10%' and panel test 3 at gauge locations 'a' and 'c' 113

Figure 3-47. Panel test 4 – showing final failure pattern 114

Figure 3-48. Load_ E_1E_2_i2_10% FE results for the top ply (tensile face) at the end of the analysis, showing (a) matrix cracking, (b) fibre failure, (c) o.o.p displacement 116

Figure 3-49. Disp_E_1C_2_i_5% FE results for the top ply (tensile face) at the end of the analysis, showing (a) matrix failure, (b) fibre failure, (c) o.o.p displacement 116

Figure 3-50. Load-strain curves, longitudinal centre panel strains from tests 1 to 4, and FE analyses Disp_S_1S_2_i2_10% and Load_S_1S_2_i2_10% 117

Figure 4-1. Three dimensional stress acting on a schematic of the laminate 130

Figure 4-2. Close up of fibre bundle showing fibre-matrix interface cracking 131

Figure 4-3. Matrix cracking in the woven composite 132

Figure 4-4. Nominal stress versus effective stress 133

Figure 4-5. Fictitious stress-strain response 135

Figure 4-6. Crack formation from in-plane stresses and the respective damage parameter assigned to each mode 138

Figure 4-7. Damage parameter d as a function of F, where F and d vary for tension and compression. 141

Figure 4-8. Modulus reduction as a function of d, for a given in-plane direction. 141

Figure 4-9. Function of damage energy release rate versus damage. 144

Figure 4-10. Transverse fracture and the respective damage variables assigned to these modes 147

Figure 4-11. C3D8R brick element in Abaqus 155

Figure 4-12. Standard mesh used for the small plate analyses 156

Figure 4-13. Contact force for small plate, Test 9M(195J): test and FE results 157

Figure 4-14. Test and FE results for Large1(A), (a) contact force and (b) Max. o.o.p displacement. 157

Figure 4-15. Contact force-time history, for large1(C/D): test and FE results. 158

Figure 4-16. Max. o.o.p disp. for large1(C/D): test and FE results 158

Figure 4-17. Force-displacement plot for large1(D), test and FE 159

Figure 4-18. In-plane modulus E_{11} contours, in Pascal, for the small plate, test 9M(195J). 160

Figure 4-19. In-plane modulus E_{22} contours (in Pascal), for large1(C/D) 160

Figure 5-1. Composite layering through the thickness of the elements. 172

Figure 5-2. One integration point per resin-rich layer element. 173

Figure 5-3. The relationship between the plastic strain and effective stress can be fitted with a power law. 175

Figure 5-4. Crack process zone 184

Figure 5-5. Stable crack propagation 184

Figure 5-6. Cohesive fracture regions associated with a example of a traction-separation curve 185

Figure 5-7. Fracture/delamination modes I, II and III 185

Figure 5-8. Global and local interface element coordinates 186

Figure 5-9. Resultant displacements 186

Figure 5-10. Cohesive zone length for a single crack tip 189

Figure 5-11. Cohesive length relative to the element size in a FE mesh. 190

Figure 5-12. Mixed-mode linear traction-separation 193

Figure 5-13. Plan view of the mixed mode behaviour dictated by the fracture energy criterion for damage propagation 194

Figure 5-14. Linear mixed-mode traction and displacement. 196

Figure 5-15. Parabolic coupled traction-separation law 198

Figure 5-16. Linear unloading and re-loading paths, parabolic traction-separation law 199

Figure 5-17. (a) Test and FE contact force-time history and (b) delamination prediction for small plate test 9M(195J)_co8 using the linear cohesive model. 202

Figure 5-18. Non-linear cohesive model test and FE (a) Contact force-time history, (b) delamination, for test 9M(195J)_co8. 203

Figure 5-19. Maximum o.o.p-time history using the non-linear cohesive model, displacement, test and finite element results, small plate test 9M(195J)_co8. 203

Figure 5-20. Mixed-mode initiation and failure displacements, in metres, using the linear cohesive model 204

Figure 5-21. Test versus finite element results using the linear cohesive zone model (a) Max. o.o.p displacement-time history, (b) contact force-time history, (c) delamination predictions, plate large1 test A 205

Figure 5-22. Test versus finite element results with a cohesive only model, (a) Max. o.o.p displacement-time history, (c) contact force-time history, for large plate 1, test 'large1(B)'. 206

Figure 5-23. Contact force-time history using a linear cohesive zone model for tests large2(1) and large2(2) and FE prediction, ... 207

Figure 5-24. Contact force-time history using a linear cohesive zone model for large2(2) and FE no delamination versus delamination predictions 207

Figure 5-25. Delamination prediction for large2 tests 208

Figure 5-26. Status of cohesive elements at 4msecs, (a) failed cohesive elements shown in black, (b) Cohesive elements experiencing normal transverse tension, shown in black, for test9_co8_p2t2. 209

Figure 5-27. (a) Elements influenced largely by the transverse shear displacement, shown for LE13 only (b) Elements highly influenced by the tensile normal displacement, in m, shown for a few elements in Figure 5-27 (b), test9_co8_p2t2. The transverse shear and normal displacements have dotted lines and solid lines respectively. 210

Figure 5-28. Cohesive displacements-time histories for (a) large1(B), top elements, (b) test 9M(195J)_co8, top elements, (c) large1(B), bottom elements, (d) test 9M(195J)_co8, bottom elements. The transverse shear and normal displacements have dotted lines and solid lines respectively. 211

Figure 5-29. Mesh density effect on delamination, test large1(B) 212

Figure 5-30. Effect of continuum shell elements and solid elements , (a) contact force-time history and (b) max. o.o.p displacement, for large panel 'large2(2)' 214

Figure 6-1. Out-of-plane disp. at the panel centre using Abaqus/Explicit and maximum stress criterion 2, test large2 224

Figure 6-2. Contact force-time history, showing the effect of the transverse shear stiffness, using stress criterion 2 for delamination and S4R in Abaqus/Expli., test large2. 225

Figure 6-3. Effect of transverse shear stiffness with shell element type, using stress criterion 2, (a) contact force, (b) max. o.o.p displacement, test large2. 225

Figure 6-4. Contact force-time history, showing the effect of transverse shear stiffness, using energy criterion for delamination and SC8R, Abaqus/Explicit, test large2. 226

Figure 6-5. Out-of-plane displacement-time history, for the bottom-centre node using energy for delamination and larger shear stiffness value, test large2. 226

Figure 6-6. Contact force-time history for the implicit and explicit analyses using S4R elements and transverse stiffness 5.22E7, test large2. 227

Figure 6-7. Damage predictions using Hashin's 2D criteria for large2, (a) matrix damage and (b) fibre damage using Abaqus/Standard and S4R elements and (c) matrix damage and (d) fibre damage using Abaqus/Explicit and SC8R elements 228

Figure 6-8. C-Scan of large2 plate impact. The variation in colours shows the extent of delamination through the layers. (Damage area in inches, only central portion of plate shown)..... 229

Figure 6-9. Delamination through the thickness using Explicit analysis, SC8R elements and energy criterion, analysis for test large2 229

Figure 6-10. Delamination prediction at the bottom of the plate in Abaqus/Explicit for large2 using (a) the energy criterion and SC8R (b) stress criterion 1 and S4R. 229

Figure 6-11 Contact force-time history for variations in mesh density, test 9M(195J). 231

Figure 6-12. The average normal transverse stress vs time, SSAVG6 for FE analyses modelling damage, test 9M(195J)..... 232

Figure 6-13. Delamination results for test 9M(195J), (a) bottom face, test and (b) top face, test, and FE predictions for the bottom face using analyses (c) coarse2 (34x44x2 elements), (d) fine2 (56x72x2 elements) and (e) fine9 (56x72x9 elements) a quarter-plate model..... 233

Figure 6-14. Delamination damage through the thickness for FE analysis 'fine9', test 9M(195J)..... 234

Figure 6-15. Delamination damage through the thickness for FE analysis 'fine2', test 9M(195J)..... 234

Figure 6-16. Delamination damage for test 13L(284J), shown to scale. (a) top face, test, (b) top face, FE, (c) bottom face, test, (d) bottom face, FE..... 237

Figure 6-17. Delamination damage for (a) test 13L(284J) cross-section, (b) FE prediction237

Figure 6-18. Matrix cracking predictions using 2d Hashin, for the bottom, middle and top layers, (a) test 1S(91J), (b)test 13(284J). 238

Figure 6-19. Cross-section of the plate, test 2S(140J), showing delamination. 238

Figure 6-20. Max. o.o.p disp.-time history for tests 1S(91J), 2S(140J) and 13L(284J), test and FE. 239

Figure 6-21. Contact force-time history for tests 1S(91J), 2S(140J) and 13L(284J), test and FE. 239

Figure 6-22. (a)Max. o.o.p disp. and (b) contact force-time histories, for RR-layer and energy for failure FE analyses with and without strain rate sensitivity, test 9M(195J). 240

Figure 6-23. Contact force-time history, comparing a damage model exclusive of delamination with a no-damage and full damage model, test 9M(195J), mesh p1t1..... 244

Figure 6-24. Contact force-time history, comparing a no-damage model with a 2d and 3d damage model at the woven plies, test 9M(195J), mesh p1t1..... 244

Figure 6-25. Contact force-time history, comparing a 2d and 3d damage model at woven plies, test 7M(247J)..... 245

Figure 6-26. Delamination predictions for test 9M(195J), analysis 'co4_ p2t2' 245

Figure 6-27. Delamination predictions for test 9M(195J), analysis 'Co4_p2t2_2d' 245

Figure 6-28. Contact force-time history for a 2d damage model at the woven plies, comparing 4 and 8 cohesive layers, test 9M(195J) 246

Figure 6-29. Contact force-time history for a 4 and 8 cohesive layer model, test 10M(217J). 247

Figure 6-30. Contact force-time history for a 4 and 8 cohesive layer model, test 11L(211J). 247

Figure 6-31. Contact force-time history for a 4 and 8 cohesive layer model, test 13L(284J), ... 247

Figure 6-32. Contact force-time history for a 4 and 8 cohesive layer model, test 15L(496J). 247

Figure 6-33. Contact force-time history for variations in contact definitions, test 9M(195J), mesh p1t1. 248

Figure 6-34. Contact force-time history for variations in mesh density using a small sliding analysis test 9M(195J) 249

Figure 6-35. Contact force-time history for variations in mesh density using a finite sliding analysis test 9M(195J) 249

Figure 6-36. Contact force-time history for variations in the plate and tup mesh density, 4 cohesive layer model, test 10M(217J) 249

Figure 6-37. Contact force-time history for variations in plate and tup mesh, 4 cohesive layer model, test 13L(284J). 250

Figure 6-38. Contact force-time history, the effect of differentiating tensile and compressive cyclic loading parameters, test 9M(195J), mesh p1t1. 250

Figure 6-39. Damage vs the potential function and the effect of increasing d_{II}. 251

Figure 6-40. Contact force-time history, comparing the strain versus the energy approach for in-plane damage propagation, for test 9M(195J), mesh p1t1 251

Figure 6-41. Contact force-time history for variation of the transverse damage initiation criteria, test 9(195J), mesh p1t1. 252

Figure 6-42. Degradation contours of the transverse modulus E_{33} in Pa, using analysis (a) Co4 and (b) Co4_TT2, for test 9M(195J), mesh p1t1 252

Figure 6-43. Delamination, test 9M(195J), 'co4_TT2' (mesh p1t1) 253

Figure 6-44. Contact force-time history and maximum o.o.p displacement predictions for the small tup impacts 255

Figure 6-45. Contact force-time history and maximum o.o.p displacement predictions for the medium tup impacts 257

Figure 6-46. Contact force-time history and maximum o.o.p displacement predictions for the large tup impacts 258

Figure 6-47. Showing damage at one corner of symmetry, for E_{33} contours test 22M(228J), in Pa. 259

Figure 6-48. Full plate RR-layer model shown in half, showing section normal transverse stress SSAVG6 in Pa, using SC8R elements, test 9M(195J). 259

Figure 6-49. Damage with element erosion for test 6S(190J), co8_p2t2. Shown with the in-plane modulus E_{11} contours. 260

Figure 6-50. Contact force-energy relationship for the small tup tests 262

Figure 6-51. Contact force-energy relationship for the medium tup tests 262

Figure 6-52. Contact force-energy relationship for the large tup tests 263

Figure 6-53. Delamination area versus impact energy for the small plate impact tests. 'Bot' and 'top' refer to the maximum delamination measured in the top and bottom half of the plates respectfully. 264

Figure 6-54. Damage results for test 9M(195J), (a) 1/5 from top of plate, (b) 1/5 from bottom of plate 266

Figure 6-55. Degradation contours of modulus E_{11} in Pa, (a) test 9M(195J), co4_ p1t1, (b) test 9M(195J), co8_p2t2. 267

Figure 6-56. Normal transverse damage shown with E_{33} contours in Pa, co8_p2t2 type analyses, (a) test 10M(217J), (b) test 13L(211J) 268

Figure 6-57. Delamination predicted using (a) 4 cohesive layers and (b) 8 cohesive layers, for test 15L(495J) 269

Figure 6-58. Contact force-disp. results for a few of the medium sized tup impact tests ... 270

Figure 6-59. FE results, test 20M(180J), (a) Start of in-plane damage, (b) start of delamination damage (initiating at the bottom layers) 270

Figure 6-60. Modulus E_{11} (in Pa) vs time (in secs) for a few elements at the bottom centre of the plate shown in Figure 6-61 270

Figure 6-61. Elements selected at the bottom-centre of the plate for analysis 271

Figure 6-62. strain in the impact site at time 3.5E-3 approximately at 'peak 3' 271

Figure 6-63. Modulus E_{11} (in Pa), vs time (in secs), for all the elements through-the thickness in the immediate impact site 271

Figure 6-64. Test A, (a) o.o.p displacement-time, (b) contact force-time histories 273

Figure 6-65. Test B, (a) max. o.o.p displacement-time (b) contact force-time histories 274

Figure 6-66. Test C and D, (a) max. o.o.p displacement-time, (b) contact force-time histories 275

Figure 6-67. Gauge locations on the (a) top (impact) face of the plates with corresponding (b) bottom face gauge locations 276

Figure 6-68. (a) to (r) Predicted and measured strains for test A, at gauge locations 1 to 18. 279

Figure 6-69. (a) to (r) Predicted and measured strains for test B, at gauge locations 1 to 18. 281

Figure 6-70. (a) to (r) Predicted and measured strains for tests C & D, at gauge locations 1 to 18. 283

Figure 6-71. (a) to (d) Damage for test A – predicted and experimental 286

Figure 6-72. Damage for test B – predicted and experimental 287

Figure 6-73. Experimental and predicted damage – test C/D 288

Figure 6-74. Finite element E_{11} and E_{22} modulus contours in Pa, for test C/D. 289

Figure 6-75. Holes along a large1 plate edge used to attach the plates to the test fixture.... 290

Figure 6-76. Contact force-time history for large2(2) and FE with 9 cohesive layers..... 291

Figure 6-77. Delamination and E_{12} contours in Pa, for large2. 292

Figure 6-78. Relationship between kinetic energy and contact force for the large plates.... 292

LIST OF TABLES

Table 2-1. Moduli for the 24oz/yd^2 WR E-glass/Derakane 8084 vinyl-ester, in GPa..... 16

Table 2-2. Poisson's ratios for the WR E-glass/Derakane 8084 vinyl-ester..... 16

Table 2-3. Average material properties for the 24oz/yd^2 WR E-glass/Derakane 8084 vinyl-ester, in MPa. 16

Table 2-4. Properties for the vinyl-ester resin..... 16

Table 2-5. Failure strain for the 24oz/yd^2 WR E-glass/Derakane 8084 vinyl-ester, in microstrain. 16

Table 2-6. Through-thickness tensile and compressive strengths and moduli taken from 5 panels fabricated from quasi-statically loaded E-glass and Dow Derakane 510A samples, SCRIMP manufactured. 17

Table 2-7. Mode I critical fracture energy test values for WR E-glass/Derakane 8084 vinyl-ester. 18

Table 2-8. Specified coupon dimensions. 19

Table 2-9. Summary of cyclic test data..... 20

Table 2-10. Plate sizes tested 27

Table 2-11. Small plate tests, small 'S' (12.7mm) tup, in order of impact energy 34

Table 2-12. Small plate tests, medium 'M' (25.4mm) tup, in order of impact energy. 35

Table 2-13. Small plate impact tests, large 'L' (38mm) tup, in order of impact energy..... 35

Table 2-14. Large1 plate, impact mass and energy..... 44

Table 2-15. Damage measurements for large1 sized plates tests A to D. 45

Table 2-16. Measured out-of-plane displacement at the plate centre for tests A to D. 45

Table 3-1. In-plane property degradation dependency on the failure mode 61

Table 3-2. Test and FE results for Shenoi's work..... 69

Table 3-3. Maximum plate deflection results 71

Table 3-4. Labels describing the damage mode, for Figure 3-6. 79

Table 3-5. Critical buckling loads from the tests..... 87

Table 3-6. FE and theoretical critical buckling loads 88

Table 3-7. Key to FE analysis labels..... 97

Table 4-1. Critical strain and damage parameters used in the in-plane damage model..... 146

Table 5-1. Parameters for the parabolic (non-linear) cohesive law 198

Table 6-1. Peak contact force and o.o.p disp. using various delamination criteria in Abaqus /Implicit and Explicit , where 'R' is RR-layer thickness, test large2..... 224

Table 6-2. Summary of main test and FE results for test 9M(195J) 235

Table 6-3. Delamination test results for test 1S(91J), 2S(140J), 9M(195J) and 13L(284J) and FE damage predictions..... 236

Table 6-4. Mesh densities studied..... 243

Table 6-5. Small tup (12.7mm dia.) test damage measurements against FE delamination results, using a co8_p2t2 mesh. Tests are in order of increasing impact energy. 264

Table 6-6. Medium tup (24.5mm dia.) test damage measurements against FE delamination results, using a co8_p2t2 mesh. Tests are in order of increasing impact energy. 265

Table 6-7. Large tup (38mm dia.) test damage measurements against FE delamination results, using a co8_p2t2 mesh. Tests are in order of increasing impact energy. 265

Table 6-8. Summary of 42x30x0.75in plate test and FE results 272

Table 6-9. Summary of the max. o.o.p disp. from the tests and FE predictions 273

Table 6-10. Delamination areas measured for tests A, B, C and D 289

ACKNOWLEDGEMENTS

The work presented in this thesis was sponsored by the Office of Naval Research, Office of Naval Research Global and the Health and Safety Executive of the United Kingdom and was supervised by Dr Louca, all of whom I would like to thank for the opportunity to carry out this work.

I would also like to show my gratitude to the US Naval Academy and Prof. Sarah Mouring who supervised much of the testing carried out in the US. Also, Ron Millward and Alan Roberts from the Civil and Environmental Engineering Department at Imperial College, for their skill in constructing the test equipment and sorting out the instrumentation for the structural tests.

Thank-you to the students and members of staff in the Structures Section of the Civil and Environmental Engineering Department of Imperial College, for their friendliness and interesting discussions.

Last but not least, I would like to thank Matt and my mum, without both of whom I would not have been able to continue with the PhD.

NOTATION

Upper case Roman letters

A	Total area
A_d	Damaged area
A_{ij}	Shear-extension coupling coefficients
$\bar{A}$	Undamaged area
B	Plastic strain rate parameter
B_{ij}	Bending-extension coupling coefficients
C_c	A parameter dependent on boundary conditions, from E.Greene's buckling load expression
C_{x1}	Product of the stiffness matrix and inverse section stiffness
C_{x2}	Product of the stiffness matrix and inverse section stiffness
C_{ij}	Stiffness matrix
C^{ep}	Elastic-plastic stiffness matrix
D_{ij}	Laminate bending stiffness coefficients
E_c	Cohesive element modulus for isotropic element properties
E_d	Energy density
E_{fa}	Flexural modulus in in-plane 'a' direction, from E. Greene buckling load expression
E_{fb}	Flexural modulus in in-plane 'b' direction, from E. Greene's Buckling load expression
E_{ij}	Undamaged moduli (i,j=1,2,3)
E_{ij}^d	Damaged moduli (i,j=1,2,3)
E_{ini}	Initial modulus
F_{mi}	Damage development function for matrix failure in in-plane

	direction 11 or 22 (i=1,2)
F_{fi}	The damage development fucntion for fibre failure in in-plane direction 11 or 22 (i=1,2)
F_{ij}	Interactive failure criteria, general tensor
E_{fin}	Final modulus
F_I	Potential function threshold for matrix damage
F_{II}	Potential function threshold for start of fibre damage
F_{III}	Potential function threshold for full rupture/material failure
F_m	The damage potential for matrix failure
F_{ts}	Shear force vector
FVi	Field variable (i=1,2,3)
F_4	Potential function for normal transverse damage (33 direction)
F_5	Potential function for transverse shear damage on 13 plane
F_6	Potential function for transverse shear damage on 23 plane
G_{ij}	Shear modulus on the ij plane (i,j=1,2,3)
G_{IC}	Mode I critical fracture energy
G_{IIC}	Mode II critical fracture energy
H	Function of stiffness and the Raleigh wave function
H^p	Rate dependent plastic modulus
J_2	Stress invariant
K	Strain to failure in local 11 direction
K_c	Cohesive element penalty stiffness
K_{IC}	Mode I critical fracture toughness
K_{12}	'Directional interaction' coefficient, Gotsis et al.
L	Strain to failure in local 22 direction
L_c	Cohesive length
L_e	Characteristic element length
L_1, L_2	In-plane element dimensions
M_{xx}	Moment per unit width of a plate
M_e	Mass of resin-rich layer for an element of thickness R
M_i	Bending moment for planes i=1,2
M_{12}	Shear bending moment
N	Element shape function
N_{ij}	In-plane forces, (i,j=1,2)
P	Load

$\overline{Q}_{ij}$	Transformed stiffness matrix constants (i.e. For global direction)
R	Thickness of resin-rich layer
SDVi	State dependent variables (i=1,2,...n)
S	Local in-plane shear strain to failure
S	Compliance matrix
S	Surface
S_{ij}	Materials strength in the ij direction (i,j=1,2,3)
S_{ij}	Deviatoric stress component
S_T	Material strength, transverse shear (13 or 23) direction
S_{12}	Material strength, in-plane shear (12) direction
$\overline{\mathbf{S}}$	Compliance matrix for undamaged material
T	Normal transverse (through-thickness) strain to failure
T	Cohesive element traction vector
T_c	Thickness of the cohesive element
T_i^{max}	Maximum individual mode traction (i=n,t,s*)
U	Transverse shear strain to failure, in 13 direction
U_{bot}	Cohesive element bottom node displacements
u_m^f	Mixed mode displacement at failure, linear traction-separation law
u_m^0	Mixed mode displacement at delamination initiation, linear traction-separation law
U_{top}	Cohesive element top node displacements
U_i^f	The critical displacement for failure for the individual mode fracture (i=n,t,s)
U_i^0	The critical displacement for failure for the individual mode fracture (i=n,t,s)
V	Transverse shear strain to failure in 23 direction
V_x	Transverse shear force per unit width of the plate
V_e	Volume of resin equal to one element of thickness R
X_C	Material strength, in-plane 11 direction, compression
X_T	Material strength, in-plane 11 direction, tension
$\mathbf{X_R^C}$	Resin strength in compression, in-plane 11 and 22 directions
$\mathbf{X_R^T}$	Resin strength in tension, in-plane 11 and 22 directions
Y_C	Material strength, in-plane 22 direction, compression
Y_i	Damage energy release rate variables

Y_{max}	Maximum attained damage energy release rate
Y_T	Material strength, in-plane 22 direction, tension
Y_0	Damage energy release rate at start of matrix damage
Y'	Energy released due to damage
Z_C	Material strength, transverse 33 direction, compression
Z_T	Material strength, transverse 33 direction, tension

Lower case Roman letters

a	Plate width
b	Damping coefficient
b	Plate length
C_d	Current dilatational wave speed
$d\varepsilon$	Increment in strain
d_{sat}	Matrix damage saturation value
d_I	Damage threshold for matrix damage initiation
d_{II}	Damage threshold for fibre damage initiation
d_{III}	Damage threshold at fibre rupture/material failure
d_1	Damage variable in the 11direction
d_2	Damage variable in the 22 direction
d_3	Damage variable in the shear 12 plane
d_4	Damage variable in the normal transverse 33 direction
d_5	Damage variable in the transverse shear 13 plane
d_6	Damage variable in the transverse shear 23 plane
k	Initial material stiffness
k_{g0}	Geometric stiffness at base state
k_t	Tangent stiffness
k_N	Non-linear stiffness function
h_c	A parameter obtained from a chart, from E.Greene's buckling load expression
m	The number of half waves in the x direction
n	Multiple factor used in expression for length of cohesive zone
n	The number of half waves in the y direction
p_0	Pressure, initial applied
w	Out-of-plane deflection
p_b	Bulk viscosity pressure
r_{ij}	Denotes the damage variables assigned to a specific Poisson's ratio, (ij=1,2,3)

t	Current time
u	Displacement
u_{bot}	Shear displacements for cohesive element bottom nodes
u_i	Cohesive element relative nodal displacement (i=n,t,s where n=normal, t=shear 13, s=shear 23 planes)
u_{top}	Shear displacements for cohesive element top nodes
U_{tr}	
u_0	Initial displacement
v	Impact velocity
v_{bot}	Normal displacements for cohesive element bottom nodes
v_{top}	Normal displacements for cohesive element top nodes
x	Distance along the width of plate
y	Distance along the length of of the plate
z	Distance from shell reference surface
$\overline{z}$	Shell reference surface

Lower case Greek letters

α	Non-linear shear term in Chang-Chang failure criteria
α	Variable controlling influence of hydrostatic stress
β	State variable controlling the extent of the effect of the hydrostatic stresses
γ	Power indice in general expression for interactive failure criterion
ε_d	'Damage strain', i.e. Unrecoverable/inelastic
ε_e	Elastic /recoverable strain
ε_f	Strain at the start of fibre damage, from cyclic tests
ε_{ij}	Strain component (ij=11,22,12,33,13,23)
ε_{ij}^0	Strain component at the plate centre, for planes ij (ij=11, 22, 12)
ε_0	Strain at the start of matrix damage, from cyclic tests
$\overline{\varepsilon}^p$	Effective plastic strain
$\dot{\overline{\varepsilon}}^p$	Effective plastic strain rate
$\dot{\varepsilon}_{vol}$	Volumetric strain rate
λ	Eigenvalue
λ	Mixed-mode displacement parameter in non-linear cohesive zone model

λ_u	Mixed-mode displacement parameter at the start of unloading
λ_0	Mixed-mode displacement parameter at the start of delamination
μ_{fab}, μ_{fba}	Poisson's ratios with the primary stress across the length 'a' and width 'b' of the panel respectively, from E.Greene's buckling load expression
ν_{ij}	Poisson's ratio in the ij plane (i,j=1,2,3)
ρ	Density
ρ_c	Cohesive element density
$\tilde{\rho}_c$	Cohesive element density per unit element area
σ	Stress tensor
σ_c	Yield stress
σ_{kk}	Hydrostatic stress components (k=1,2,3)
σ_{max} , τ_{max}	Normal interfacial strength
$\bar{\sigma}$	Effective stress
τ	Previous time
τ	Cohesive element mixed mode tractions
τ_{max}	The critical normal surface traction
$\bar{\tau}$	Linear shear behaviour term in Chang-Chang's failure criterion
ψ	Factor relating mode I and mode II critical fracture energies

Abbreviations

FE	Finite element
Max.	Maximum
o.o.p disp.	Out-of-plane displacement
vs	Versus

* n = transverse (through-thickness) normal direction; t = transverse shear 13 direction; s = transverse shear 23 direction

CHAPTER 1

Introduction

There is compelling evidence that ships are the new weapons of choice for certain terrorist groups. Recent terrorist activity has shown the vulnerability of marine structures to such events as the suicide attack masterminded on the guided missile destroyer *USS Cole* in October 2000 of the cost of Yemen, as well as an identical attempt nine months earlier, on the destroyer The *USS Sullivans*, which failed when the suicide boat overloaded with explosives was sunk. A French crude oil carrier off the coast of Yemen was also attacked by terrorists in 2002. Terrorists claimed responsibility for the sinking of a superferry travelling between Manila and the central Philippines in February 2004. In August 2005 a rocket attack targeted US naval vessels docked in the Red Sea port of Aqaba in Jordan and the attempted assault on offshore installations off the coast of Iraq. There is evidence that experts specializing in naval demolition sabotage have developed a four-pronged strategy to attack Western shipping targets:

- Ramming vulnerable vessels at sea
- Blowing up medium-sized vessels at ports
- Attacking vulnerable, large cargo ships such as supertankers from the air by using explosive-laden small aircraft
- Underwater attacks by divers or suicide demolition teams, using limpet mines.



Figure 1-1. Holing of the USS Cole in Oct 2000

In addition, non-terrorist accidents such as ship collisions are not uncommon and these forms of impact damage can cause significant repercussions. Several world-wide oil-tanker disasters have resulted from impact, including the *UK Liberian-registered Sea Empress* hitting rocks near Milford Haven in Wales, spilling 72,000 tonnes of oil and *Exxon Valdez* oil tanker which hit a reef in the Gulf of Alaska and spilled an 11 to 50,000 m^3 to 150,000 m^3 of crude oil.

The need for increased operational performance and reduced costs has driven the development of composite materials for naval structures. Improvements to naval vessels, in particular warships and submarines, are sought in areas such as operational range, stability, manoeuvrability, stealth, payload and resistance to explosive shock. There is a need to reduce production, maintenance and fuel costs that add greatly to cost. These are all areas where composite application can make improvements. Much of the interest in composite research within the marine industry can be accredited to the success with composites application in the aerospace industry. However naval composites are different in constitution, cost, and scale.

The ultimate importance of weight saving in the aerospace industry demands the use of elite composite materials, namely Kevlar and carbon fibres and epoxy resins. In the marine industry on the other hand, the most commonly used composite components are polyester and vinyl-ester resin and E-glass fibres in the form of chopped strand mat, woven rovings (WR), see Figure 1-2, or unidirectional fibres. Woven roving reinforcements consist of bundles of continuous strands in a plain weave pattern with more material in the direction of the warp. The main advantages of fibre-glass reinforced plastics compared to other fibres, is the low cost and excellent chemical resistance to salt water and engine fuels. Compared to the stiffer carbon fibre, glass fibres perform better under impact. For higher performance marine constructions, vinyl-ester resins are preferred over polyesters due to their greater

water resistance, higher heat-distortion temperature and superior mechanical properties. Designing with composites is to a great extent dependent on the manufacturing method and the raw materials to be used.

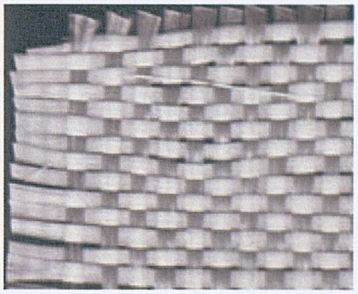


Figure 1-2. Woven strand matt

Vaccum assisted resin transfer processes are one method of obtaining a better consolidated composite; reducing the void content and increasing the fibre content over traditional resin transfer moulding (RTM) methods hand lay-ups. See Chapter 7. The Derakane 510A reinforced with 24oz woven roving (510A/WR) is a composite resin that the US Navy has great interest in. The resin is a modified vinyl ester with added Bromine to reduce its flammability and offering the greatest fire retardancy out of all the present day vinyl-esters. Dow Derakane 510A can be cured under room temperature which makes this composite appealing for the fabrication of large structures. Compared to the 510A, the other familiar resin used in marine composites is the Dow Derakane 8084, which provides increased toughness and chemical resistance over other vinyl-esters. A study was conducted [1] on the dynamic tensile properties of various composite systems including 24oz woven rovings with the above two resins. The 510A/WR showed more strain rate sensitivity than the 8084/WR. However there were differences in fibre volume fractions as two different manufacturing processes were used, thus making it difficult to effectively conclude on this matter.

To date, large patrol boats, hovercraft, mine countermeasure vessels and corvettes have been built completely out of composite materials. Owing to the vast improvements in composite design and fabrication, there are currently a few all-composite naval ships up to 80-90m in length (the longest being amongst corvettes) but they are not common. Many other naval applications are being proposed and a large volume of research is currently being undertaken. Feasibility studies with submarine structures have also been carried out. A submarine of small dimensions (20m long x 2.5m wide) has been designed for the US Navy to undertake covert operations. The submarines are built with a steel pressure hull and covered with an external composite structure. Other examples of composites in current naval

applications are the superstructures, bulkheads, decks, advanced mast systems, propulsion shafts and rudders. The US Navy is considering using composite materials in their next-generation corvettes, studies have been carried out [2] on the feasibility of building warships up to 85m long and 1200tonnes displacement using composite instead of steel. It is envisaged that from about the year 2020 all mid-sized war ships such as frigates (120-160m long) will be constructed from composites [3].

As composites are being more widely used in both new naval structures and for the strengthening of existing structural assemblies, a better understanding of their damage tolerance and overall performance to such extreme loading is urgently needed as this will become an essential feature in the design process of new blast and impact resistant construction and strengthening techniques.

In composite design, the performance of the structural component can be determined through the residual properties that are considered important to the design application. The aerospace industry has an established procedure for dealing with impacts and all parts need to be designed as damage tolerant. This has put into place inspection levels and limit loads. The CAI (compression after impact) is considered a critical design measure. More specifically, certain damage thresholds have been put in place such as assumptions of damage type and size and service life [4-6]. The naval industry also has stringent performance measurements on composite naval structures as well as steel naval structures. In addition to the requirements imposed on commercial ship structures, Naval structures are required to resist highly dynamic loads during combat situations, due to weapons impact, or to air or underwater explosions. The developments made in the understanding of the damage mechanisms from impact, blast and UNDEX loads on the structural response of composite ship and submarine structures, have resulted in some structural design aimed to alleviate the effects of this type of loading. With regards to composite design in the US navy, one of the requirements is that the structure must survive an impact from a 680kg (1500lbs) load travelling at 10 knots (5m/s) i.e. 8500J, a much harsher demand on the material compared to the 133J kinetic energy imposed in aircraft design. Currently there is still a lack of data relating to the survivability of naval composite structures to such dynamic loading [7] and there is no one specific failure criterion to determine failure of a plate under impact damage.

Early work has been reported by Smith [8, 9] on the effects of an underwater explosion on large scale glass reinforced plastic (GRP) panels (3m by 3m) typical of those used for minesweeper vessels. Failure modes in the form of extensive delamination and stiffener

debonding were reported. The effects of underwater explosions on small scale GRP panels for use in marine vessels was extensively studied by Mouritz [10-13] who made the intuitive finding that increasing the peak overpressure resulted in increased levels of damage. Below a peak overpressure of 8 MPa damage was noted as resin cracking only and the flexural properties remained unchanged. Above this value, delamination, fibre failure and buckling occurred which resulted in a significant reduction in flexural strength and stiffness. Also, a number of tests were conducted on superstructure components of naval vessels in order to assess their vulnerability to air blast loading [14, 15]. Critchfield et [14] reported two tests on a stiffened GRP panel subjected to air blast loading. No damage was reported in the first test and the panel was tested again at a higher pressure which resulted in intermittent delamination along the bottom of the tapered stiffeners.

It was observed by Mouritz [12] that the damage arising to GRP's from underwater shock tests is not dissimilar to that observed in the four-point bend test. Mouritz used simply supported boundary conditions for the panels in both tests and the bending test applied a uniform load. This generated similar bending stresses but the strain rate difference remained. Subsequent to Mouritz's work, Boh et al [16] carried out a study on progressive damage prediction of a woven roving E-glass/vinyl ester laminated beam subjected to transverse shear.

The security restrictions involved with underwater explosion (UNDEX) data, have impeded the current work from analysing composite panels under this type of loading. Instead, impact tests have been carried using large diameter, large mass, low velocity impactors, in an attempt to emulate the type and location of damage experienced in naval composites. Impact testing has been identified as an effective means of modelling an underwater blast on a composite material. A recent study conducted by James O'Daniel, et al [17] evaluated how precision impact tests could be effectively used to model the response of a composite material to an underwater blast. Data is very scarce on impact of large composite plates and in particular relating to contact force time history, which according to Zhou and Greaves [18], is one way of revealing the dominant damage mechanisms is through examination of the peaks.

There exist non-destructive ways of measuring damage, including visual inspection with a bright light, ultrasound methods, X-radiography, X-ray computed tomography, laser holography and acoustic emission technology. For in-service damage, visual inspection with a bright light, information on the limited available test data and common sense is used to

decide whether a component should be repaired or replaced. However, *predicting* damage and the survivability of a structure is an area still undergoing much development. A better understanding is required particularly with respect to the residual strength and stiffness, which is vital in establishing the possibility of progressive collapse occurring.

There are several approaches to modelling damage in composites and choosing the appropriate one depends on several factors including: the scale of the laminate in question, the loading type (dynamic/static, uni-axial multi-axial), the complexity of the ply lay-up, the extent of material data available on the laminate and the detail of failure prediction required [19, 20]. Some common methods of modelling damage in brittle materials are categorised as shown below:

- Failure criteria – stress or strain based criteria for elastic, brittle materials, using a once only property degradation rule on failure.
- Fracture mechanics - Linear or non-linear elastic fracture mechanics for micro-scale modelling of individual cracks in brittle materials.
- Damage mechanics on a mesoscale or macro-scale– Used to predict the behaviour of the material in the presence of damage that initiates at some level of stress or strain and generally increases with increase in load up to macroscopic crack initiation or failure. The damage evolution is based on experimental observations of the response of the damage material through gradual degradation of the material properties. Damage may be considered as consisting of surface discontinuities (microcracks) and volume discontinuities (microvoids).

The failure of composites has been thoroughly researched from the micro-mechanical through to the macro-mechanical scales. From the micromechanical point of view, failure mechanisms are fully dependent on the constituent phases; the matrix and the reinforcement, and the type of loading, generating an assortment of failure processes. Although a micromechanics approach is accurate in the prediction of critical points and the exact point of failure initiation, they only provide an approximation to global failure of a multi-layered laminate. Thus a macro-mechanical model becomes more reliable and therefore necessary when it comes to modelling failure on a structural scale. Despite this, the global limiting factor with regards to modelling very large structures in any detail, more so with decrease in model scale and complexity, lies in the computational specification (e.g. CPU and RAM).

Stress based failure criteria, although limited, have been widely used to model either mixed or individual failure modes, many of which were evaluated by Padhi et al [21]. Delamination

models, using some of these developed criteria, were implemented by Hou [22] for low velocity impact on unidirectional composites. Zhou et al [18] on the other hand, applied stress-based criteria for initiation and fracture mechanics for propagation. Fracture mechanics has been adopted by a number of researchers to predict damage propagation. However this approach has been limited to small scale models relying predominantly on crack growth data from static tests. The progressive degradation of composite performance from multiple fine cracks, is a phenomenon that is likely to be observed in practice, can be modelled using damage mechanics, although limited work has been carried out on impact and damage scaling of composites.

A range of failure theories have been proposed, many of which are often used by the composite structural designer. These can be classified into three groups, *non-interactive or limit theories* (maximum stress, maximum strain); *interactive theories*; and *partially interactive or failure mode based theories.* A given theory is only as good as the experimental data used to develop it and is only really of value if it can be applied with relative convenience. Also, very often it is difficult to know which theory to use, given that all of them look competent and appropriate, coming with a large collection of reliable experimental data.

A recently coordinated study [23-27], known as the 'World-wide failure exercise', compared the accuracy of 12 leading theories for predicting failure in composite laminates against 14 test cases. The participants were asked to predict the behaviour without prior knowledge of the experimental results which all involved static loads. A large scatter in the predictions of 200-300% was found amongst the theories, even for unidirectional lamina, and a key point was the lack of robustness for predicting final strength of multidirectional laminates. However, with regards to failure of unidirectional lamina, the best agreement with experimental results was obtained with the Tsai-Wu theory and Puck and Schürmann's theory. Nevertheless, it became apparent that better modelling approaches were very much in demand. This applies to dynamic modelling also.

Model development for dynamic applications is a growing area but has been addressed less in comparison. To this day, there are no established composite models for predicting the behaviour and damage formation of composite plates under a dynamic or static load. Furthermore, there is has been no validation work of thick *large*-scale woven roving composite plates using existing plane stress damage criteria. Data is also lacking on the in-

plane strength of such panels and the sensitivity of finite element analyses to modelling their behaviour.

One of the drawbacks with composites is the lack of robust damage models applicable to large composite structures capable of reliably predicting damage growth and ultimate failure loads. This is particularly so in the prediction of internal damage such as delamination which can occur when composites are subjected to impact or explosive loads. Damage modelling has been studied extensively more so on the micro scale than the macro scale, and recently with increase in focus on the nano scale. The advances made in damage modelling on a meso and macro scale have been attributed largely to the aerospace industry and little work has been carried out to validate their techniques on marine structures. The class of composites, scale of structures and the nature of the loading is very different to that experienced in the aerospace industry.

The damage caused by low velocity impact is more typical to naval structures. The damage is often hidden and for thicker plates the effect of the transverse stresses are significant in promoting delamination. Thus it is important to develop an understanding of the strength after damage of such plates in order to predict their life expectancy if they are damaged in service. This requires knowledge of the intact strength of the panels for comparison purposes and data on both the intact and post-damage strength of naval panels is rare. The behaviour of naval panels under in-plane loading and the sensitivity of finite element analyses to the various loading conditions, material properties and imperfection size are in real need of investigation.

Commercial FE codes are currently implemented to model impact of composite plates but most still lack effective constitutive models for laminates experiencing damage, especially for large-scale configurations. The majority of these models were developed for static loading or plane stress conditions. Currently there are no established failure criteria to effectively model damage or determine full failure of composite structures under a dynamic load. Moreover, there is very little validation work of large-scale, thick composite plates under such loading. Experimental data is also scarce on naval composites relating in particular to the contact force history of plates under dynamic loading. The latter according to some, is one way of assessing the main damage mechanisms. Some of the naval composites in most demand for evaluation are the woven roving E-glass/vinyl-esters. The current work aims to address some of these shortcomings and help to fill some of the deficiency in the data.

The bulk of the current project has been funded by the Office of Naval Research (ONR) from the USA as part of their programme on improving the understanding of the behaviour of fibre reinforced composite materials subjected to shock loading. The major focus of the ONR is on the establishment of physically based models for deformation and failure. The scale of the structures involved means they are also ideal candidates for consideration in offshore applications. Developments in damage modelling have not been as robust in composite materials as they are in modelling damage of metal structures due to their more complex damage modes and make up, exhibiting anisotropic and non-homogeneous behaviour. Composites are also more sensitive to the manufacturing process and in many cases are very dependent on the skill of the designer.

The current work is part of a wider study to establish the residual strength of the panels under in-plane compression loading. The type of loading that would be experienced by the composite panels in between the bulkheads of large and long ships, see Figure 1-4, under hogging or sagging loading conditions depending on how much weight the ship is carrying the weight distribution. There are three stages to the work: 1. To obtain the intact strength of a panel; 2. To incur damage in the panel using a shock load; 3. To obtain the residual strength after shock loading. In this study, stages 1 and 2 are here completed both experimentally and numerically.

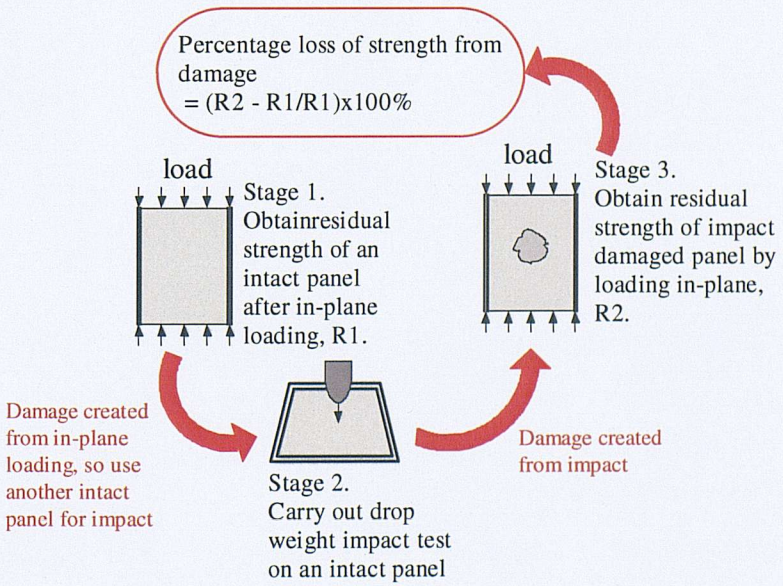


Figure 1-3. Approach to obtaining the residual strength of a naval panel

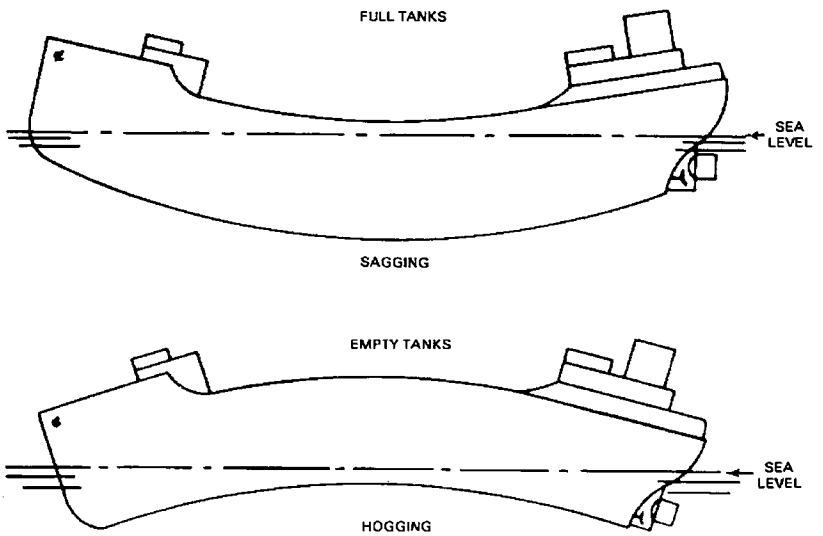


Figure 1-4. Sagging and hogging effect of a naval vessel

The methodology undertaken involves a combination of testing and the development of finite element models on a macro scale to validate against the experimental data. Several methods of modelling damage, new and existing, are examined for WR E-glass/vinyl-ester plates using the finite element packages Abaqus/Implicit and Abaqus/Explicit versions 6.4 and 6.5. Attention is placed on repeatability, computational cost and ease of application.

The plates were manufactured using the Computer Assisted Resin Transfer Moulding Technique (CARTM) to ensure maximum fibre-matrix consolidation. A range of testing was performed for the present work, including in-plane loading of large plates, designed and carried out by the author at ICL (Imperial College London); impact loading of large-scale plates, carried out by S. Mouring (of the USNA) at the USNA, and small-scale plates by L.A. Louca (of ICL) also at the USNA. Large scale plates were impact tested to minimize the effect of the boundary conditions on the response. However, the cost of testing at this scale is expensive, as more manpower is involved in setting up each test. More testing was carried out with small scale plates owing to reduced costs. The small scale specimens were fairly simple to set up and a more extensive range of parameters were studied. The numerical modelling was performed using non-linear finite element computer packages Abaqus/Standard and Abaqus/Explicit, where a number of user subroutines were developed to describe the constitutive behaviour of the materials and the failure modes observed such as matrix cracking, fibre failure and delamination.

The thesis is divided into eight chapters, of which the first is this introduction. The bulk of the experimental work and experimental data can be found in Chapter 2. Broadly speaking, chapter 3 examines the quasi-static in-plane loading of large-scale plates, both

experimentally and numerically. In addition to validating several failure criteria, the chapter also presents a study of the sensitivity of the finite element model to various parameter variations. Chapter 4 proposes a damage model applied at the woven plies, to gradually degrade the through-thickness properties in addition to the in-plane properties as a function of the level of matrix and fibre damage prediction. A few analyses are carried out for validation. Chapter 5 describes two methods of modelling delamination and one of the models is tested. Chapter 6 amalgamates the models proposed in Chapters 4 and 5 and examines the robustness of these models. The work is concluded in Chapter 7.

Reference List

1. Greenfield RJ, Dynamic tensile properties of woven glass fabric composites, University of Delaware, 1997.

2. Nguyen LB, Critchfield MO. Feasibility study and fabrication demonstration of FRP hull structures for naval surface combatants.Dunfermline, Scotland, Advances in Marine Structures III, 1997.

3. Mouritz AP, Gellert E, Burchill P, Challis K. Review of advanced composite structures for naval ships and submarines. Composite Structures 2001; 53(1):21-41.

4. Shenoi RA, Wellicome JF. Composite Materials in Maritime Structures - Vol. 1 : Fundamental Aspects, Cambridge University Press, 1993: 351.

5. Shenoi RA, Wellicome JF. Composite Materials in Maritime Structures - Vol. 2 : Practical Considerations, Cambridge University Press, 1993: 306.

6. Shenoi RA. Key Considerations in the Structural Design of FRP Ships and Boats. Proc of SERC/IMechE Expert Conference on failure of Composite Structures - Mechanisms and Criteria for the Prediction of Performance, St Albans, Herts, 23 Sep 1991, SERC/IMechE Failure of Composite Structures, 1991.

7. Zinoviev PA, Smerdov AA. Ultimate properties of unidirectional fiber composites. Composites Science and Technology 1999; 59(5):625-34.

8. Smith CS. Design of marine structures in composite materials, London: Elsevier Science, 1990: 180-267.

9. Smith CS. Structural design of longitudinally corrugated ship hulls. Proc of Int. Conf. at ARE, Dunfermline, 20 May 1986, Advances in Marine Structures, 1986.

10. Mouritz AP, Saunders DS, Buckley S. The damage and failure of GRP laminates by underwater explosion shock loading. Composites 1994; 25(6):431-37.

11. Mouritz AP. The damage to stitched GRP laminates by underwater explosion shock loading. Composites Science and Technology 1995; 55(4):365-74.

12. Mouritz AP. The effect of underwater explosion shock loading on the flexural properties of GRP laminates. International Journal of Impact Engineering 1996; 18(2):129-39.

13. Mouritz AP. The effect of processing on the underwater explosion shock behaviour of GRP laminates. Journal of Composite Materials 1995; 29(18):2488-503.

14. Critchfield MO, Morgan SL, Potter PC. GRP deckhouse developments for naval ships. In: Advances in Marine Structures. Elsevier Applied Science, 1991.

15. Smith CS, Murphy P. Response of hybrid GRP/steel superstructures to blast loading - Theory and Experiment. In: Advances in Marine Structures. Elsevier Applied Science, 1991.

16. Boh JW, Louca LA, Choo YS, Mouring SE. Damage modelling of SCRIMP woven roving laminated beams subjected to transverse shear. Composites Part B: Engineering 2005; 36(5):427-38.

17. O'Daniel JL, Koudela KL, Krauthammer T. Numerical simulation and validation of distributed impact events. International Journal of Impact Engineering 2005; 31(8):1013-38.

18. Zhou G, Greaves LJ. Damage resistance and tolerance of thick laminated woven roving GFRP plates subjected to low-velocity impact. In: Reid SR, Zhou G (eds.), Impact Behaviour of Fibre-reinforced Composite Materials and Structures. Woodhead Publishing Ltd, 2000: 133-183.

19. Beaumont PWR, Dimant HR, Shercliff HR. Failure processes in composite materials: getting physical. Journal of Materials Science 2006; 41(20):6526-46.

20. Talreja R. Multi-scale modeling in damage mechanics of composite materials. Journal of Composite Materials 2006; 41(20):6800-12.

21. Padhi GS, Shenoi RA, Moy SSJ, Hawkins GL. Progressive failure and ultimate collapse of laminated composite plates in bending. Composite Structures 1997; 40(3-4):277-91.

22. Hou JP, Petrinic N, Ruiz C. A delamination criterion for laminated composites under low-velocity impact. Composites Science and Technology 2001; 61(14):2069-74.

23. Hinton MJ, Kaddour AS, Soden PD. Evaluation of failure prediction in composite laminates: background to 'part C' of the exercise. Composites Science and Technology 2004; 64(3-4):321-27.

24. Hinton MJ, Kaddour AS, Soden PD. A further assessment of the predictive capabilities of current failure theories for composite laminates: comparison with experimental evidence. Composites Science and Technology 2004; 64(3-4):549-88.

25. Hinton MJ, Kaddour AS, Soden PD. Evaluation of failure prediction in composite laminates: background to 'part B' of the exercise. Composites Science and Technology 2002; 62(12-13):1481-88.

26. Hinton MJ, Kaddour AS, Soden PD. A comparison of the predictive capabilities of current failure theories for composite laminates, judged against experimental evidence. Composites Science and Technology 2002; 62(12-13):1725-97.

27. Hinton MJ, Soden PD. Predicting failure in composite laminates: The background to the exercise. Composites Science and Technology 1998; 58(7):1001-10.

CHAPTER 2

Test specifications and data

2.1 Introduction

Various tests were carried out on a 24oz woven roving E-glass/vinyl-ester composite manufactured using a vacuum assisted resin transfer moulding technique. Not all the tests were carried out using the same resin system. Where indicated, the matrix comprised either of the Dow Derakane 510A or Dow Derakane 8084 resin. Similarly, the manufacturing technique may be different. The various techniques are described below.

All the tests, except the in-plane loading of the composite panels, were carried out either by the USNA (US Naval Academy) or at the NSWCCD (Naval Surface Warfare Center Carderock Division). The in-plane panel testing was designed and carried out by the author.

2.2 Resin transfer moulding techniques

There are various composite manufacturing techniques available nowadays that have stemmed from RTM (resin transfer moulding). VARTM is a closed-mold pressure injection system which allows for faster gel and cure times as compared to contact molded parts. The process uses polyester matrix materials systems association with cold-molding.

VARTM stands for 'vacuum assisted resin transfer moulding' technique. It is a slower but more precise method of consolidating composite laminates than other typical RTM processes. It has been developed over half a century up the present day SCRIMP^{TM} version patented by Seamann's Composites in 1990. It is an automated technique for producing high quality composite sections. The reinforcing material is in fabric form for a woven composite. These are cut to size and placed in the mould. The mould is vacuum-sealed using a flexible cover and a vacuum pump feeds the resin (with catalyst) into the mould. Once the required

amount of resin is introduced, the laminate is kept under vacuum until it has cured. The vacuum seal is subsequently removed and the panel machined to size as necessary.

More recently, the CARTM™ process 'Computer Assisted Resin Transfer Moulding Technique' was patented by General Composites and allows precise temperature, flow rate and pressure control of the moulding process. Fibre volume fractions of 55-65% are typically achieved with high quality surface finish. The production cycles are short and the method improves over other methods because the molds are cheaper to make, the parts produced are of higher quality, minimal waste is produced and the time to infiltrate the preform is reduced. Hollow tubes with moveable portions provide Channels which Assist in Resin Transfer Molding of composites (CARTM).The CARTM process uses reusable silicone bags, reusable seals, a reusable "spacer system" and vacuum to infuse preforms with resin. The CARTM™ process uses an inner and outer silicone bag and reusable perimeter seals to allow a vacuum to be drawn on the perform. There are two sets of seal because there are two bags — one on either side of a "spacer system." Typically, the spacer system consists of thin plastic sheet having a network of channels. The "spacer system" is the key to the CARTM™ process. It allows temporary channels to form on the surface of the preform during infusion. The first step in the CARTM™ process is to load the preform into the mold. Next, the first "inner" silicone bag is placed over the preform. and a vacuum is drawn on the preform causing the inner bag to compress the preform. Next, the spacer system is placed over the inner bag and the outer bag is placed over the spacer system (i.e. the spacer system is sandwiched in between both silicone bags). A vacuum is applied on the spacer system thereby causing the outer bag to conform to the mold. Resin is introduced under the inner bag causing the inner bag to compress onto the channels in the spacer system and therefore creating temporary resin flow pathways on the surface of the preform and assisting the flow of resin throughout the perform. When the infusion is complete, the outer silicone bag is removed. When the vacuum is released on the outer bag, the temporary channels collapse and the inner bag presses uniformly on the preform. The resin is allowed to cure and then the part is ready to be removed from the mould.

2.3 Quasi-static material tests

2.3.1 In-plane testing

The following ASTM standards were used to perform the in-plane tests on a 24oz/yd^2 WR E-glass/Derakane 8084 vinyl ester composite, manufactured using the CARTM process. These tests were carried out at the Cincinnati Testing Laboratories, report No. 0083-6557 & 6558 as requested by the Department of Naval Architecture and Ocean Engineering, USNA.

- Tensile Test per ASTM D638 - machined
- Compression Test per ASTM D6641 - machined
- Shear Test per ASTM D4255 - machined

The average results are shown in Table 2-1 to Table 2-3.

E_{11T}	E_{11C}	E_{22T}	E_{11C}	E_{12}	E_{13}	E_{23}	E_{33}
24.139	23.37	24.139	23.37	8.273	3.586	3.586	16.89

Table 2-1. Moduli for the 24oz/yd^2 WR E-glass/Derakane 8084 vinyl-ester, in GPa.

v_{12}	V_{13}	V_{23}
0.14	0.16	0.16

Table 2-2. Poisson's ratios for the WR E-glass/Derakane 8084 vinyl-ester

$S11_T$ (warp)	$S22_T$ (weft)	$S11_c$=$S22_c$	S13	S23	$S33_T$	$S33_T$
330.328	298.6	329.6	51.6	51.6	30.55	570

Table 2-3. Average material properties for the 24oz/yd^2 WR E-glass/Derakane 8084 vinyl-ester, in MPa.

E	S_R^T	S_R^C	v_{12}
3.5 GPa	75.84 MPa	110 MPa	0.32

Table 2-4. Properties for the vinyl-ester resin

Average for ε_{11T} and ε_{22T}	Average for ε_{11C} and ε_{11C}
4780	2070

Table 2-5. Failure strain for the 24oz/yd^2 WR E-glass/Derakane 8084 vinyl-ester, in microstrain.

2.3.2 Through-thickness testing

These tests were carried out by the NSWCCD, report NSWCCD-65-TR-1998/16. Table 2-6 shows the strength and stiffness values for specimens from five different Derakane 510A batches. There are currently no published standards for out-of-plane tensile or compression test methods relating to composites. The material properties were thus generated following MIL-HDBK-17 guidelines and a spool shaped specimen and a CTL-modified ASTM C-297 test procedure was used. Out-of-plane shear testing for carried out following ASTM D5379. Six specimens were selected for testing from each of five panels for a total of 30 specimens.

This composite had typical fibre volume fractions (FVF) of between 50 and 55%, and although this is not very high, the material was better consolidated through the SCRIMP process than a similar hand lay-up composite which was testing under higher strain rates (see 'Strain rate testing' section).

As the impact testing may see strain rates of over $100s^{-1}$ and based on what we know about the effects of increasing the strain rate, the through-thickness modulus used in the FE analyses is taken as the largest value from the available tests and that is the compressive value from the quasi-static tests for the SCRIMP material in Table 2-6.

Material	**Average ultimate strength ($10^6 N/m^2$)**	**Average modulus of Elasticity ($10^9 N/m^2$)**
Resin Batch 1 Panel #1 FVF=52.3%	Tens.: 35.43 STD = 2.4	Tens.:10.27
	Comp.: 541.55 STD = 21.11	Comp.:12.44
Resin Batch 2 Panel #2 FVF=53.9%	Tens.: 33.95 STD = 2.97	Tens.:12.08
	Comp.:563.78 STD = 28.19	Comp.:14.08
Resin Batch 3 Panel #3 FVF=51.8%	Tens.: 21.36 STD = 2.59	Tens.: 11.17
	Comp.: 547.41 STD = 36.67	Comp.:13.62
Resin Batch 4 Panel #4 FVF=53.8%	Tens.: 39.66 STD = 2.06	Tens.: 11.08
	Comp.: 547.18 STD =9.18	Comp.: 14.46
Resin Batch 5 Panel #5 FVF=55.3%	Tens.: 22.17 STD = 1.9	Tens.: 12.66
	Comp.: 591.71 STD = 12.47	Comp.: 17.65

Table 2-6. Through-thickness tensile and compressive strengths and moduli taken from 5 panels fabricated from quasi-statically loaded E-glass and Dow Derakane 510A samples, SCRIMP manufactured.

2.4 Strain rate testing

Strain rate tests were carried out by the NSWCCD 652, report No. CASP-03-017. Strain rate tests on vinyl-ester composites have indicated an increase in modulus and strength values over those from quasi-static tests, [1] Strain rate tests in the warp and fill directions of a SCRIMP manufactured glass/vinyl-ester 510A WR were carried out for strain rates ranging from 0.1 to 5/s. However, the moduli results did show divergence and thus were determined as inconclusive. The ultimate strength results were more promising, seeing an increase in value of 59 to 82% from static to dynamic at 5/s.

The only available through-thickness strain rate data is for compression loading in the normal direction. A hand lay-up glass/ Derakane 8084 composite sample obtained from a half-scale Corvette was subjected to strain rates of $0.001s^{-1}$ and $100s^{-1}$, see Figure 2-1 . The composite was poorly consolidated, giving results that are smaller than what was obtained under quasi-static loading for a very similar resin, a Derakane 510A (see Table 2-6).

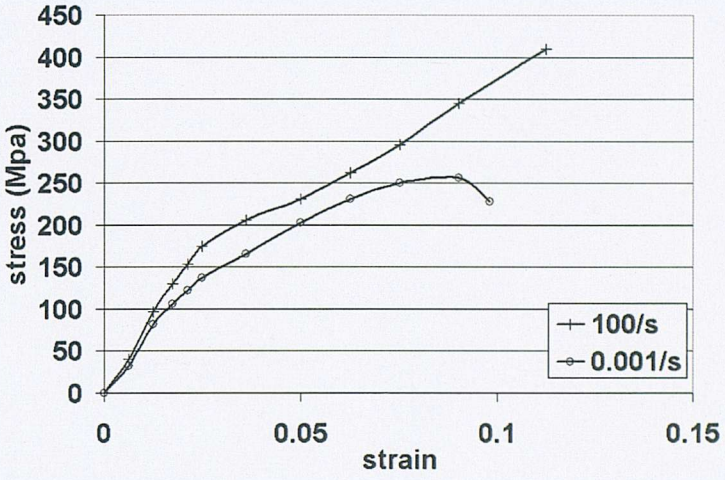


Figure 2-1. Average strength values at two different strain rates

2.5 Fracture testing

Fracture tests were carried out by the NSWCCD, report No. CASP-02-019. The mode I fracture test results for the WR E-glass/Derakane 8084 are shown in Table 2-7, manufactured using the SCRIMP process.

Crack initiation	Crack propagation
Min value: $596J/m^2$ (3.4in-lb/in^2) Max value: $806J/m^2$ (4.6in-lb/in^2)	Min value: $1665J/m^2$ (9.05in-lb/in^2) Max value: $1928J/m^2$ (11in-lb/in^2)

Table 2-7. Mode I critical fracture energy test values for WR E-glass/Derakane 8084 vinyl-ester.

2.6 Cyclic Testing

The composite evaluated in this study was fabricated at the NSWCCD using a proprietary 24 ounce woven roving E-glass/ Derakane 8084 vinyl-ester coupon manufactured using the CARTM method. Cyclic tests were requested by the USNA and were conducted at the Cincinnati Testing Laboratories, report N0. 0083-7601. Cyclic tests were performed on

twelve coupons; three in the fill and three in the weft directions, in tension: coupons Warp-T1,T2, T3 and Fill-T1,T2,T3, and in compression: coupons Warp-T3,T4,T5 and Fill-T3,T4-T5).

The cyclic tests were performed with test coupons of ASTM D638 type III specification, as shown in Figure 2-2. The actual measured dimensions varied very slightly between specimens compared to the specified values, detailed in Table 2-8. The average gauge thickness for all the coupons was 0.7097in and the average minimum gauge width was 0.7551in. A summary of the cyclic test results is shown in Table 2-9. Some of the tests provided unreliable results and these are shown in the dark grey font.

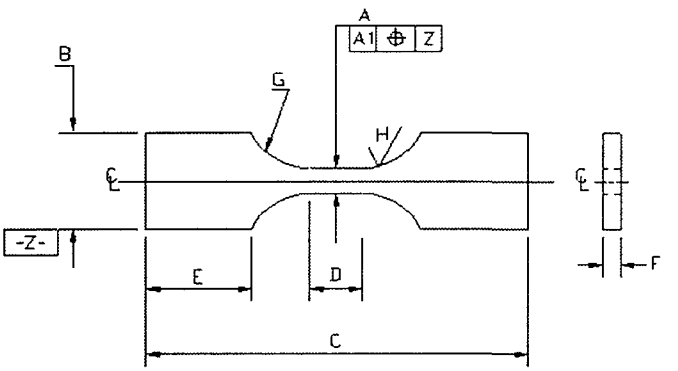


Figure 2-2. Coupon specimen configuration used for cyclic testing – ASTM D638 type III

	Specified
A	.750 ± .020
A1	.002
B	1.130-1.380
C	9.70 Min.
D	2.25 ± .020
F	Thickness(AVG.)
G	3.00 ± .040

Table 2-8. Specified coupon dimensions.

The cyclic loading program for tension and compression was exactly the same other than the direction of strain. The loading frequency was carried out at 0.5Hz in triangular waveform under strain control. The strain was applied from 0% to 0.5% ($5(10^{-3})$ strain), and then in increments of 0.25%. Five loading cycles were carried out at every new increment of strain. A summary of the test results is detailed in Table 2-9. A selection of strain-damage plots are highlighted in the table and shown in Figure 2-3 to Figure 2-11. The five load and un-load cycles taking place at the first strain increment is highlighted in Figure 2-3 for coupon test 'Warp-T1'. The relationship between damage and energy release rate is plotted in Figure 2-4 and Figure 2-5 shows the strain versus stress for this test. Three of the tests in compression produced unreliable results, those relating to coupons Fill-T5, Fill-T6 in particular, and Fill-T4 seen in Figure 2-10.

The actual termination of the cyclic tests took place before a strain of 2.5% was reached, when audible pops were heard and the mean strain shifted causing a shift in the mean load in the direction of loading. It is difficult to know with certainty the exact point at which fibre cracking initiated however a reasonable approximation was taken as the termination of the

cyclic tests, based on this information. It provides an average tensile and compressive strain value of 0.019 compared to William's [2] of 0.016 for the stiffer CFRP composite he tested.

	Max N^0 of cycles	Maximum stress at last cycle (MPa)	Maximum strain at last cycle (strain)	Initial modulus (GPa)	Final damaged modulus (GPa)	Maximum damage (stiffness lost)
Tension						
Warp-T1	38	485.04	0.0248	28.78	23.86	0.17
Warp-T2	40	511.97	0.02245	28.05	22.85	0.19
Warp-T3	36	457.83	0.02024	27.98	23.67	0.15
Fill-T1	36	371.82	0.02158	23.72	18.29	0.23
Fill-T2	31	315.75	0.01853	23.53	17.95	0.24
Fill-T3	36	393.07	0.02237	24.09	18.75	0.22
Compression						
Warp-T4	21	412.32	-0.01490	28.60	27.99	0.05
Warp-T5	25	382.91	-0.01503	27.69	27.07	0.02
Warp-T6	24	385.20	-0.01502	27.96	27.41	0.02
Fill-T4	32	400.09	-0.01896	24.78	24.10	0.03
Fill-T5	32	356.99	-0.01504	26.08	25.73	0.01
Fill-T6	25	338.9	-0.01508	25.27	24.36	0.04

Table 2-9. Summary of cyclic test data.

The data for specimen Warp-T1 was used in the damage model, see Figure 2-3 to Figure 2-5.

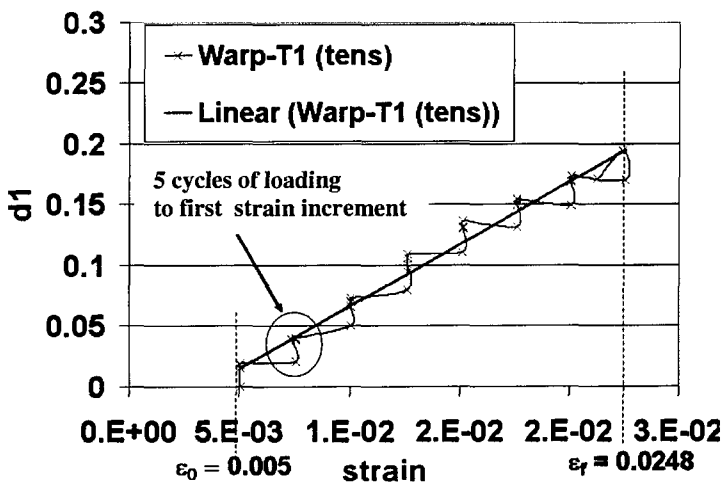


Figure 2-3. Warp-T1 (tens). Strain vs damage.

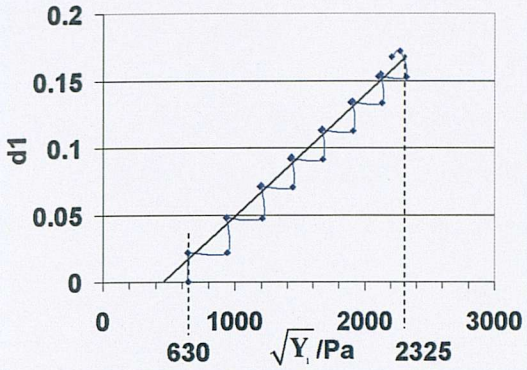


Figure 2-4. Warp-T1 (tens). Damage energy release rate vs damage.

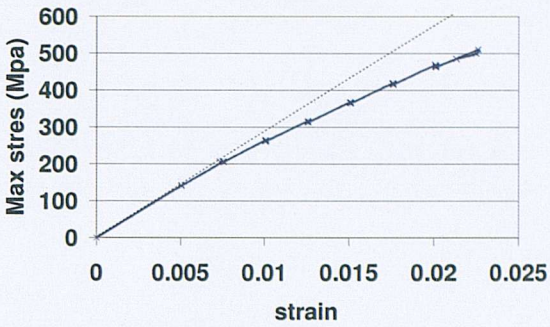


Figure 2-5. Warp-T1 (tens).Stress-strain curve.

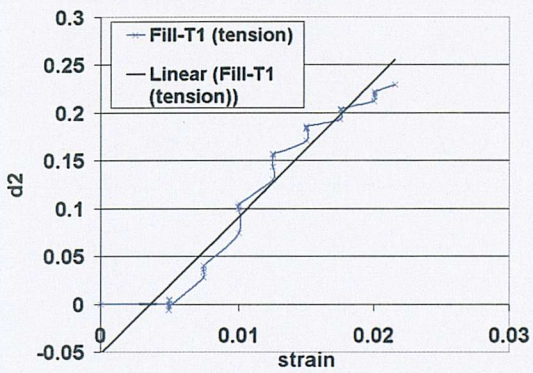


Figure 2-6. Fill-T1 (tens.) Strain vs damage.

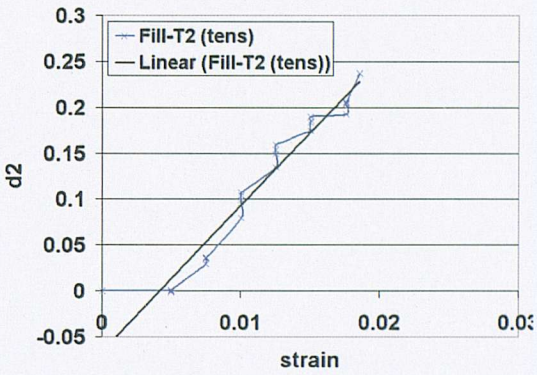


Figure 2-7. Fill-T2 (tens.) Strain vs damage.

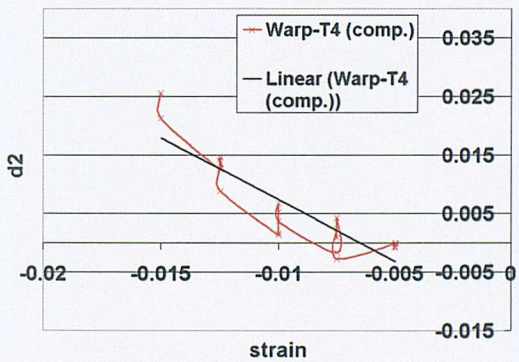


Figure 2-8. Warp-T4 (comp.) Strain vs damage.

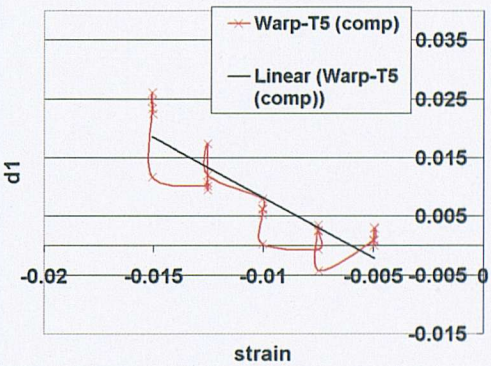


Figure 2-9. Warp-T5 (comp.) Strain vs damage.

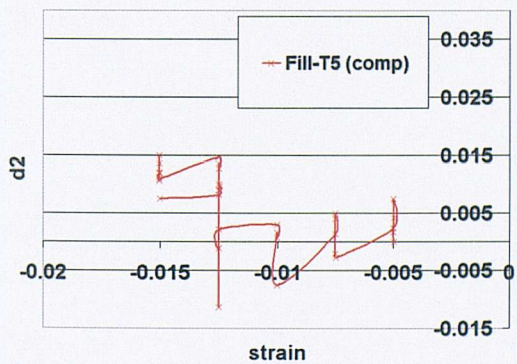


Figure 2-10. Fill-T5 (comp) Strain vs damage.

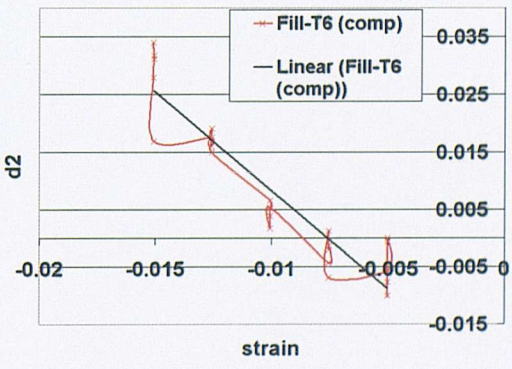


Figure 2-11. Fill-T6 (comp) Strain vs damage.

2.7 In-plane compression testing of large plates

Panels of size 1.219x0.914x0.019m made from WR E-glass/Dow Derakane 8084 were manufactured using the CARTM process and tested under in-plane compression. Five panels were tested in total. The author designed the tests, the supporting frame and carried out the tests.

A test rig was designed and constructed so that the bottom edge of the panels had pinned supports (using a lubricated steel roller) and the top and sides are also simply supported. The two ends of each panel were potted inside their fixtures using Araldyte resin. For the first two panel tests, the load was applied directly on to the 100mm high top fixture and out-of-plane (o.o.p) rotation was permitted at the bearings located above the load cells. These actuator bearings were subsequently removed for panel tests 3 to 5 and were replaced with a full-length lubricated mild steel roller configuration at the top of the panel similar to that used for the bottom edge, as shown in

Figure 2-12. As expected, given the aspect ratio of the panel and the designated experimental boundary conditions, all the panels buckled into one half wave-lengths. For simplicity, the plots of o.o.p deflections are restricted to the panel centre, displacement 'U3'.

Prior to obtaining full material properties, approximations were made for the load carrying capacity of the panel. For the first panel test a 1000kN Instron load cell was applied to the centre of the top panel edge, see Figure 2-13, but the strength of the panel was under-estimated and the maximum load of 10000kN was not sufficient. The plate in this first test was unloaded and examined with a bright light for any signs of damage. The panel had not suffered any damage thus the same panel was subsequently re-tested using 2 x1000kN load cells, as seen in Figure 2-14. The centre of the load cells were situated 102 mm (4 ins) from either edge of the top of the plate, a limit imposed by the over-all diameter of the actuators. Loading was carried out under displacement control using 0.25mm increments up to the buckling load after which increments of 0.1mm were used. The plate in test 2 failed at the two top corners. During the displacement controlled loading, the load measured by both load cells was almost equal but as loading progressed and the plate entered the post-buckling phase the two loads began to significantly deviate. The result was an uneven spread of the load, which was reflected in the strain gauge readings. As expected, the longitudinal strains started off in compression and the horizontal strains in tension. However, tension began to develop on the upper-central region of the compression face of the panel resulting from a

change in inflection in the top region compared to the remaining larger lower part of the panel. The out-of-plane deflection taken along the centre line of the panel at 1200KN demonstrates this, see Figure 2-16. Damage propagated from the two top corners along the top edge, as shown in Figure 2-18(a) and (b) for both sides of the panel.

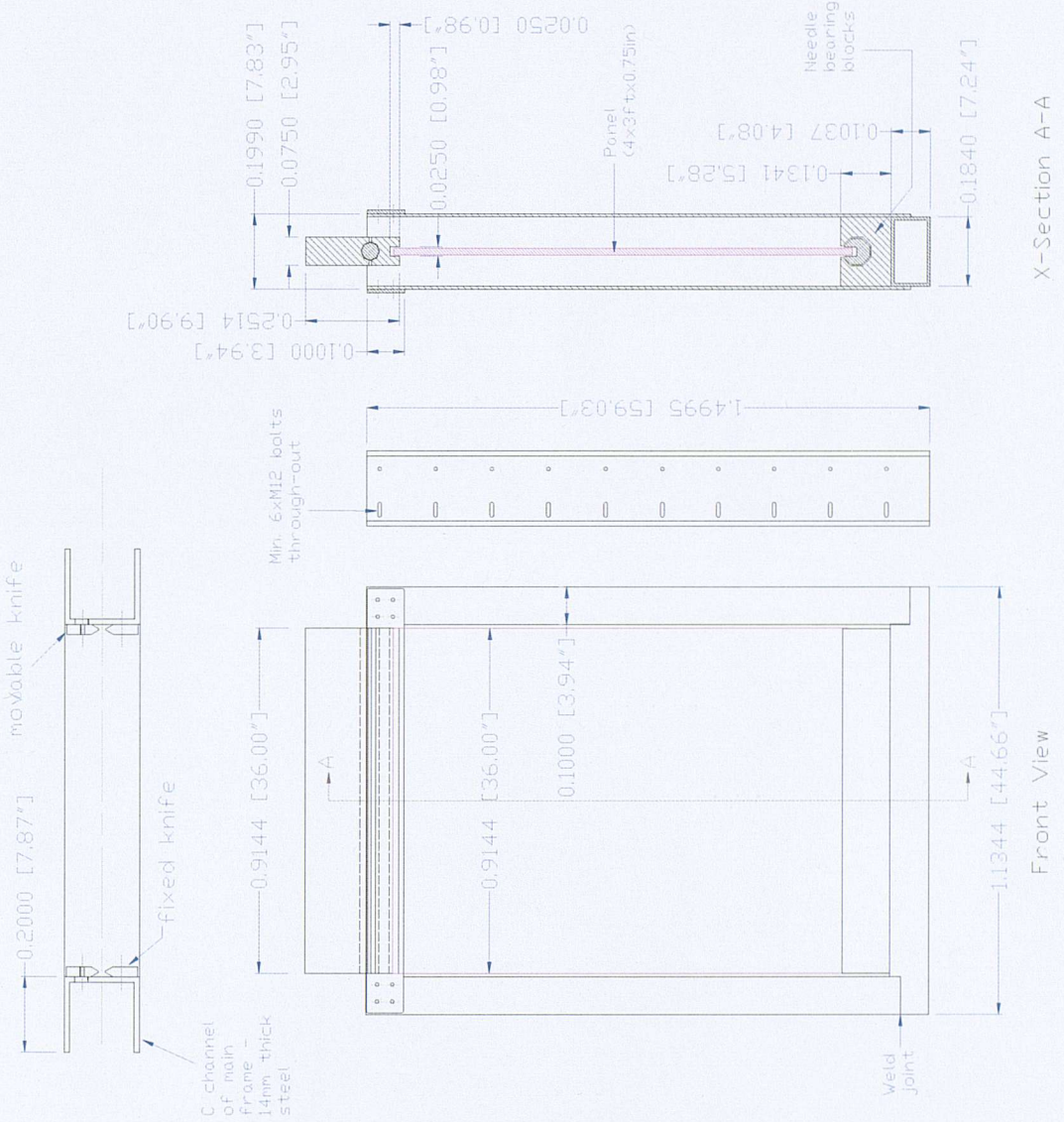


Figure 2-12. Drawing of rig for in-plane loading of large scale plates (3rd angle projection).

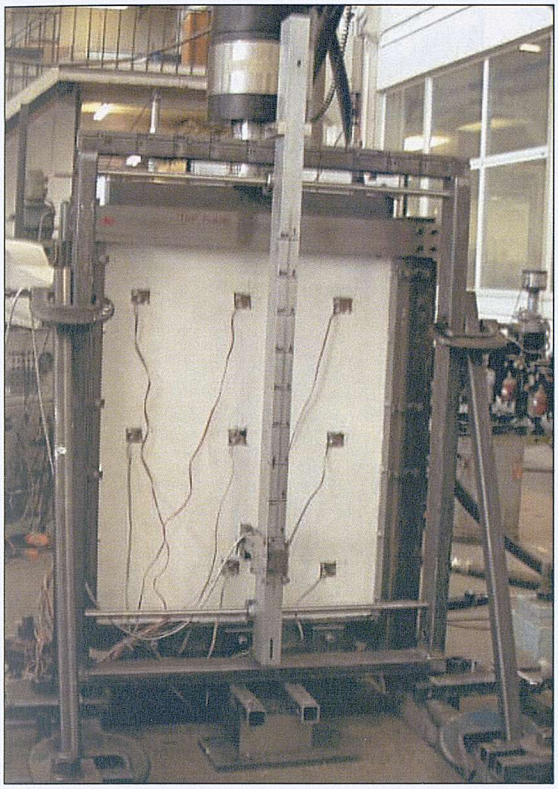


Figure 2-13. Photo of panel test 1

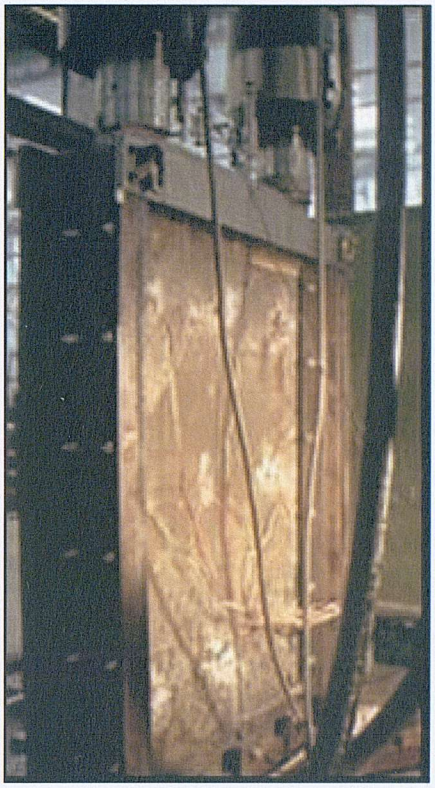


Figure 2-14. Photo of panel test 2

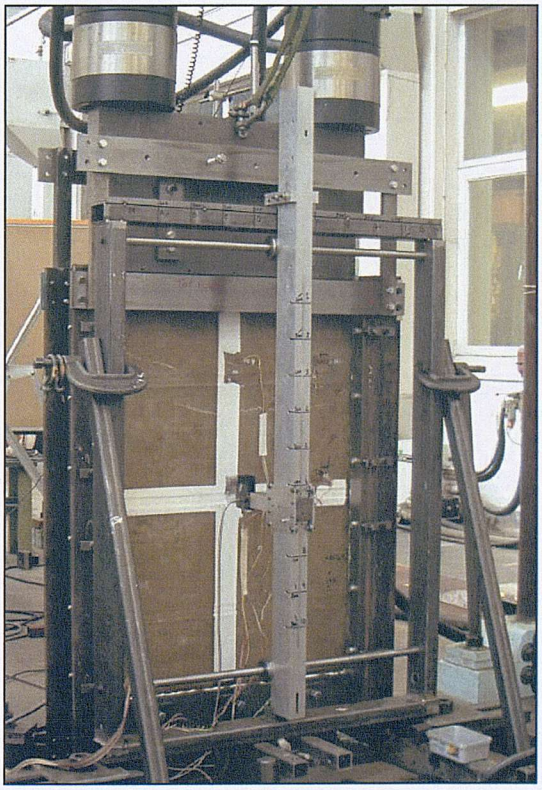


Figure 2-15. Photo of panel test 3

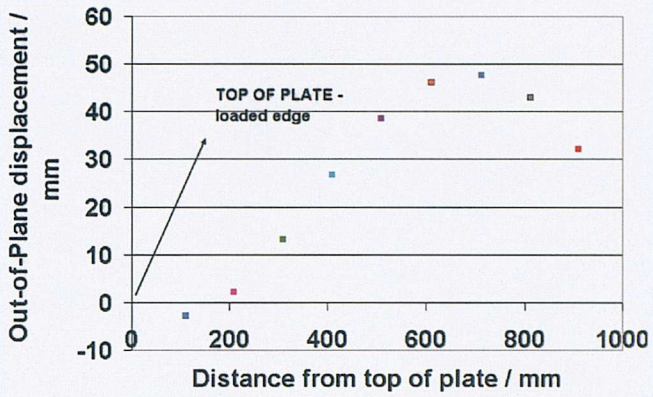


Figure 2-16. Out-of-plane displacement along the centre length of the plate, Test 2, at 1200kN.

A third panel test was carried out, shown in Figure 2-15, which aimed to eliminate the apparent uneven load distribution found in the panel of test 2. This was done by inserting a 300-mm high steel block in between the loading cells and the bearing at the top of the plate, depicted in Figure 2-17. The failure on the previous panels had been largely localised at the two top corners which was attributed to the uneven load. Test 3 developed matrix cracking, delamination and fibre failure, which emanated from the top corners, attempting to propagate in a diagonal fashion, see Figure 2-18(c) and (d). The stiffer curve results from a sticking top-roller bearing which possibly caused premature failure and prevented further loading to obtain the panel's residual capacity. Better loading was achieved with test 4, providing more widespread damage, as shown in Figure 2-18 (e) and (f). Test 5 followed a similar, less symmetrical pattern, see Figure 2-18 (g), (h).

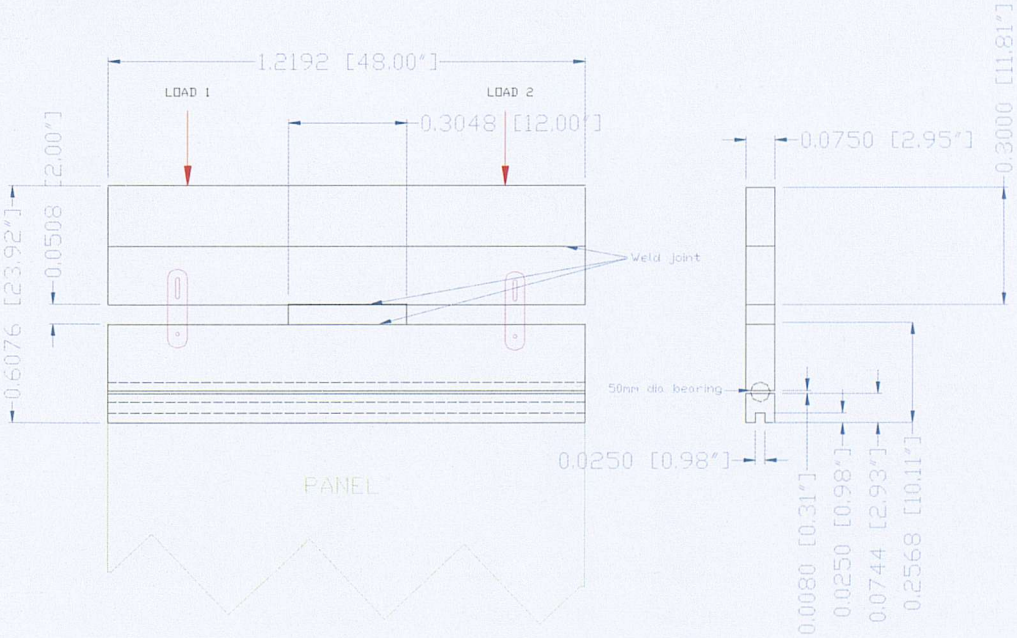
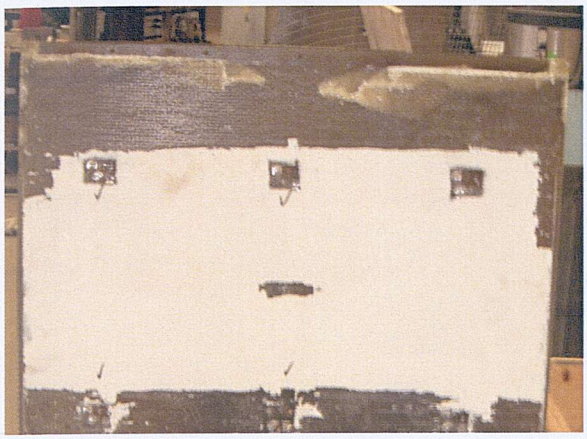


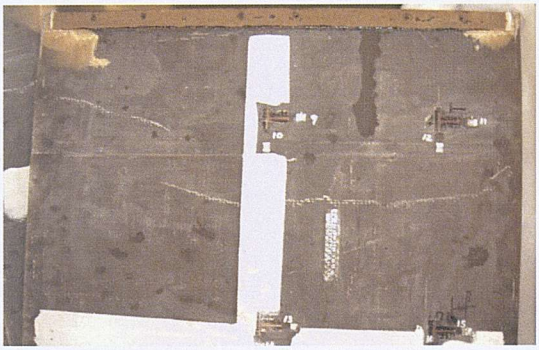
Figure 2-17. Diagram of the 300mm steel block used for tests 3 to 5, (measurements in metres and inches).



(a) Test 2, rough side in tension



(b) Test 2, smooth side in compression



(c) Test 3, rough side in compression



(d) Test 3, smooth side in tension



(c) Test 4, rough side in compression, top-left hand corner



(d) Test 4, rough side, top-right hand corner



(f) Test 5, rough side in compression



(g) Test 5, smooth side in tension

Figure 2-18. Damage photos of panels

Gauges were positioned on both sides of all the panels, vertically (parallel to the longest sides of the panel) and orthogonal to these. The panels were gauged with FLA-30-11 general purpose gauges.

2.8 Impact Testing

2.8.1 Introduction

Three different plate sizes were impact tested with hemispherical steel impactors (tups). The plates were made from WR E-glass/Dow Derakane 8084 manufactured using the CARTM process. An impact velocity of 4.6m/s was used in all of the tests, except for some of the small plate tests. There are 3 plate sizes in question, detailed below in Table 2-10:

Plate	Tests	Size /metres	Number of woven plies
Small plate	Tests 1-16, test 20, 21 and 22.	0.2286x0.1778x0.006	8
Large plate 1	Large1, Test A, B and C	1.07315x0.76835x0.019	29
Large plate 2	Large2	1.27x1.27x0.0381	58

Table 2-10. Plate sizes tested

2.8.2 Small-scale plates

GFRP plates of size 0.2286x0.1778x0.00635m (9x7x0.25in) were tested using an Instron-Dynatup Model 9250HV (High Velocity) Impact Test Instrument with Impulse Control and

Data System shown in Figure 2-19. These tests were carried out by L.A.Louca of ICL at the USNA. Three tup diameters were used to impact the panels: a 25.4mm (1inch) and a 38mm (1.5inch) hemispherical tup, see Figure 2-20. These were dropped under gravity to impact at a velocity of 4.6m/s. A photodiode was used to determine the velocity of the impactor just before impact. The high speed video was taken using an Olympus I Speed mounted on a tripod and recording took place at 1000 frames per second out of a possible 33000 frames per second. The panel was also illuminated by high-powered work lights in order for effective visualization of the target area. Recording initiated just before the impactor was dropped so that the impact and the post-impact results could be captured. The o.o.p displacement was measured by double integration of the load/time curves obtained from the load cell.

The panels were fabricated at the NSWCCDusing a proprietary 24 ounce woven roving glass/vinyl-ester manufactured with a vacuum assisted resin transfer moulding (VARTM) process. Woven roving reinforcements consist of bundles of continuous strands in a plain weave pattern with more material in the direction of the warp.

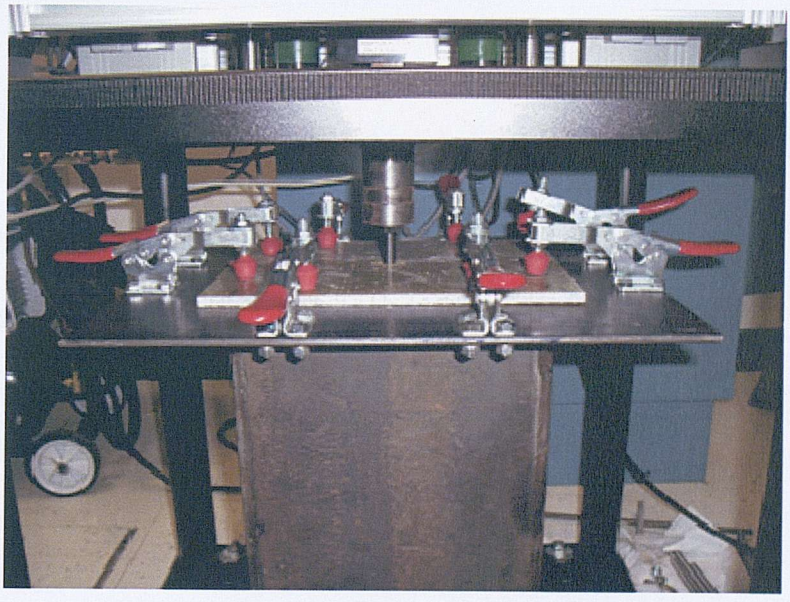


Figure 2-19. Photograph of the small plate impact test rig.

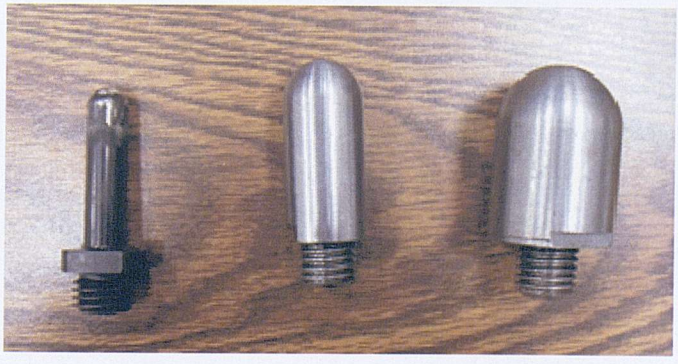


Figure 2-20. From left to right 0.0127m, 0.0254m and 0.0381m (0.5", 1" and 1.5") diameter impactors

Several of the tests were repeated for the medium tup impacts to assure validity of results. All test repetitions showed consistency with the originals except for test 7 and the repeat of this test labeled test 7-R, which gave dissimilar results. Contact force-time plots are shown for the small, medium and large tup impacts in Figure 2-21, Figure 2-22 and Figure 2-23. Energy-time plots in Figure 2-24, Figure 2-25 and Figure 2-26; and maximum out-of-plane displacement-time plots in Figure 2-27, Figure 2-28 and Figure 2-29. The tests have a sequential numerical numbering in order of impact energy.

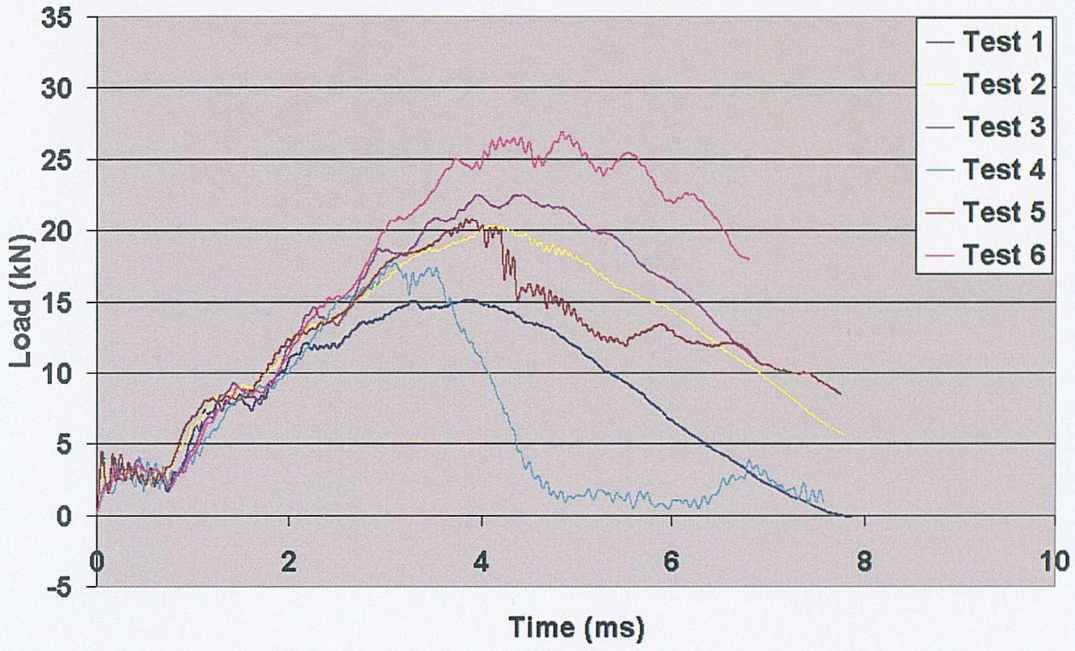


Figure 2-21. Contact force-time history for the small sized (12.7mm) tup

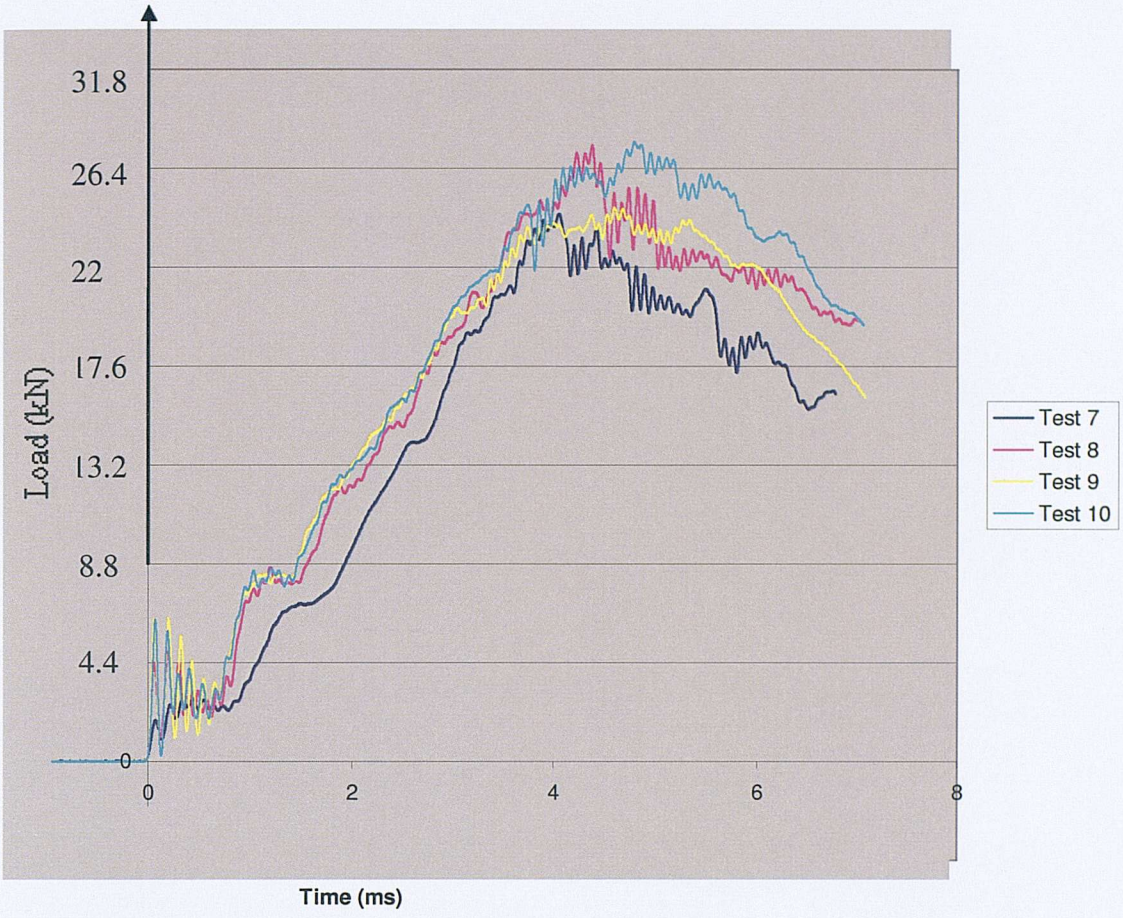


Figure 2-22. Contact force-time history for the medium sized (25.4mm) tup.

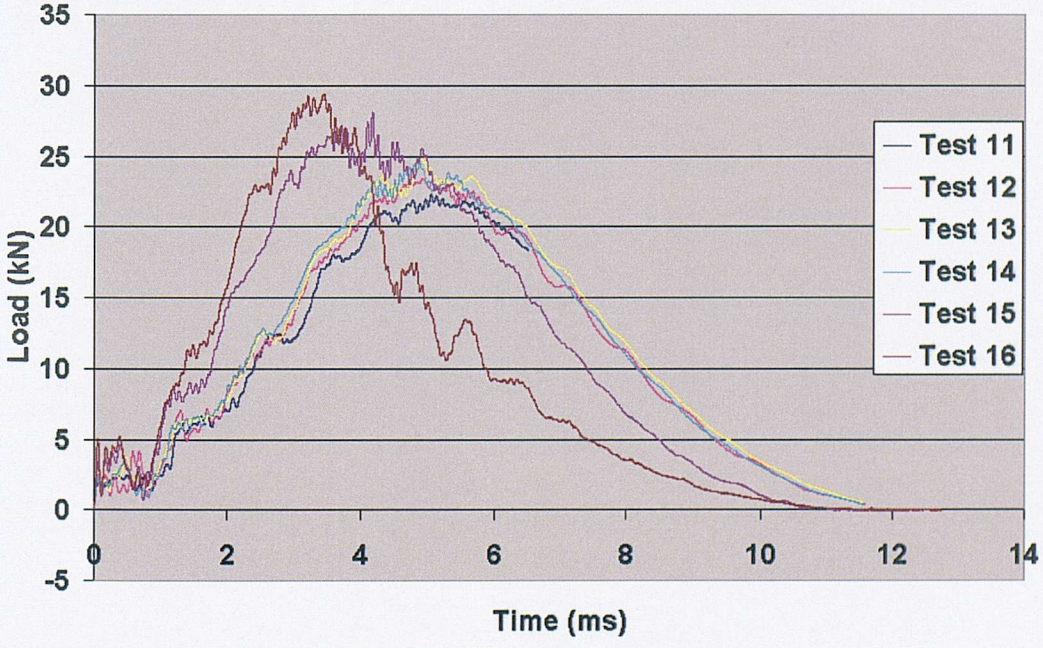


Figure 2-23. Contact force-time history for the large sized (38mm) tup

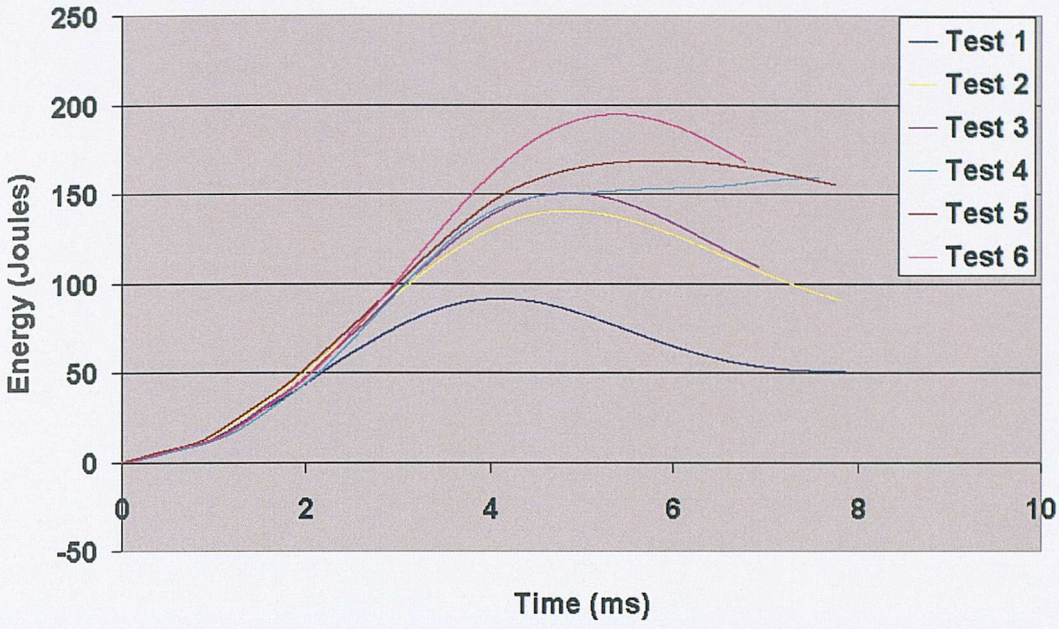


Figure 2-24. Energy-time history for the small sized (12.7mm) tup

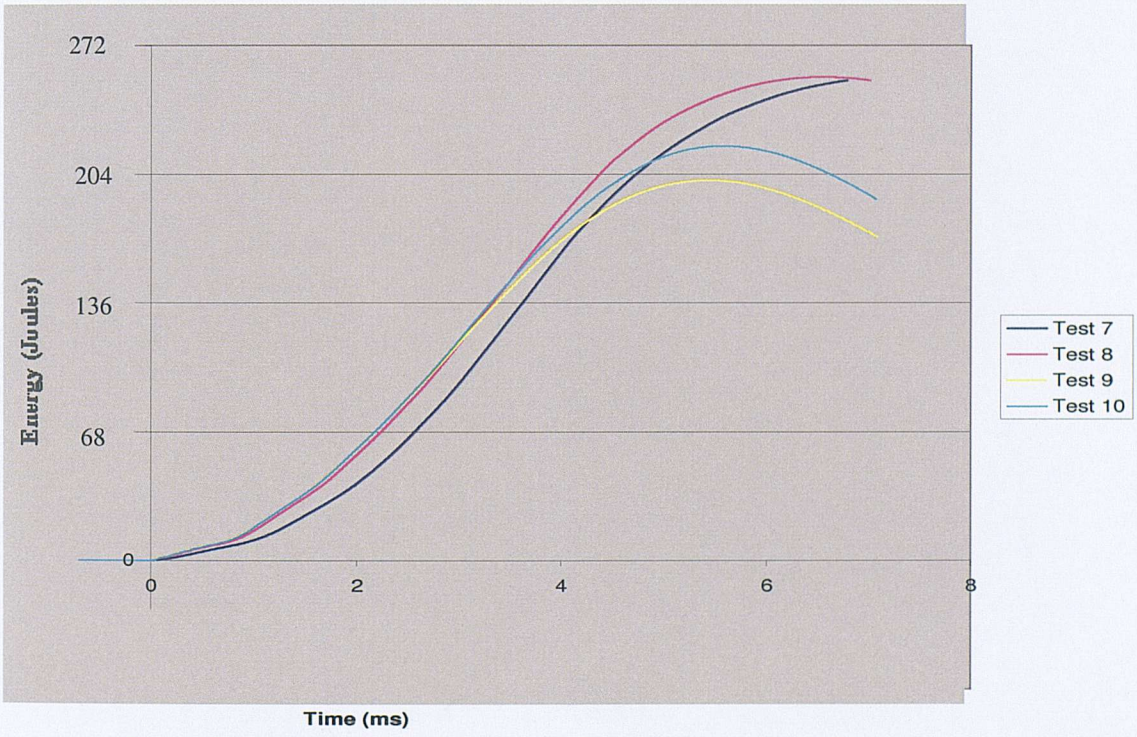


Figure 2-25. Energy-time history for the medium sized (24.5mm) tup

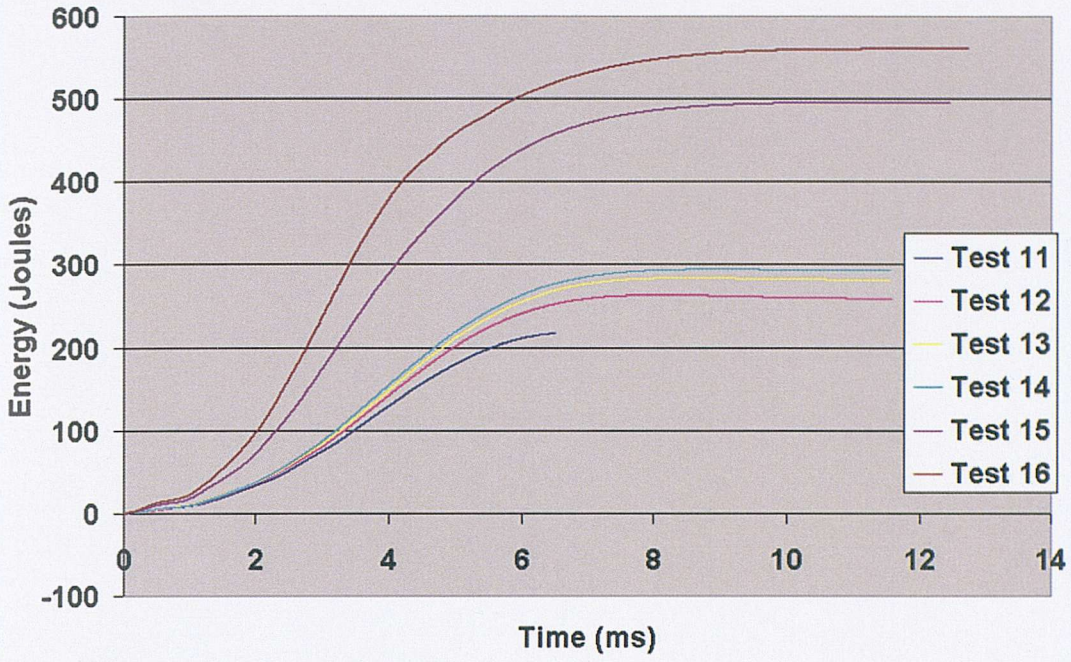


Figure 2-26. Energy-time history for the large (38mm) tup

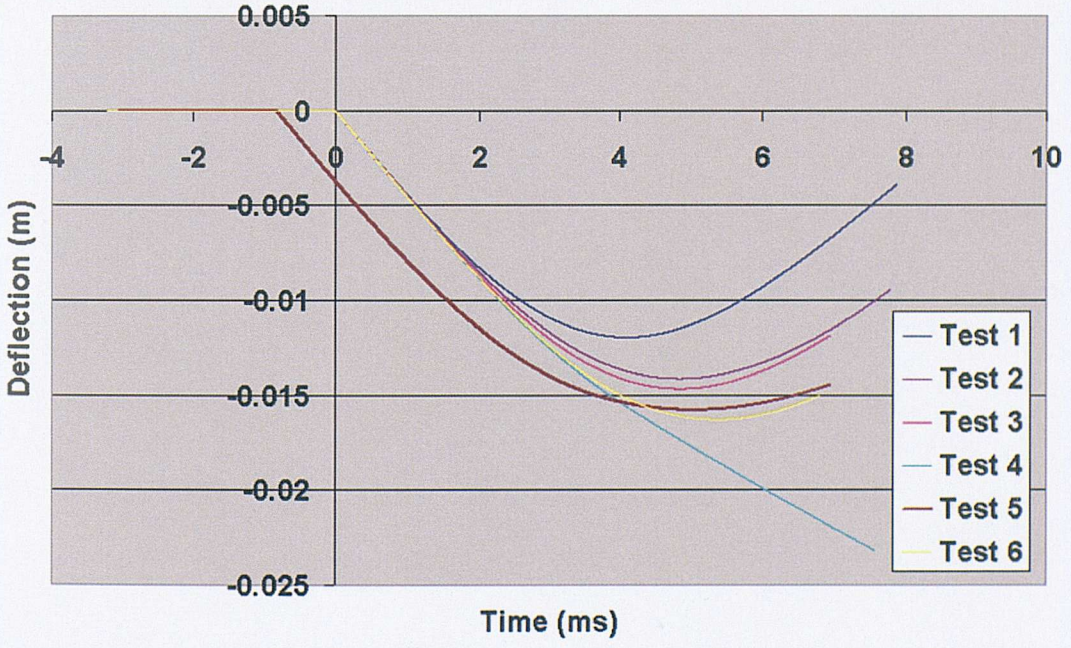


Figure 2-27. Deflection-time history small sized (12.7mm) tup

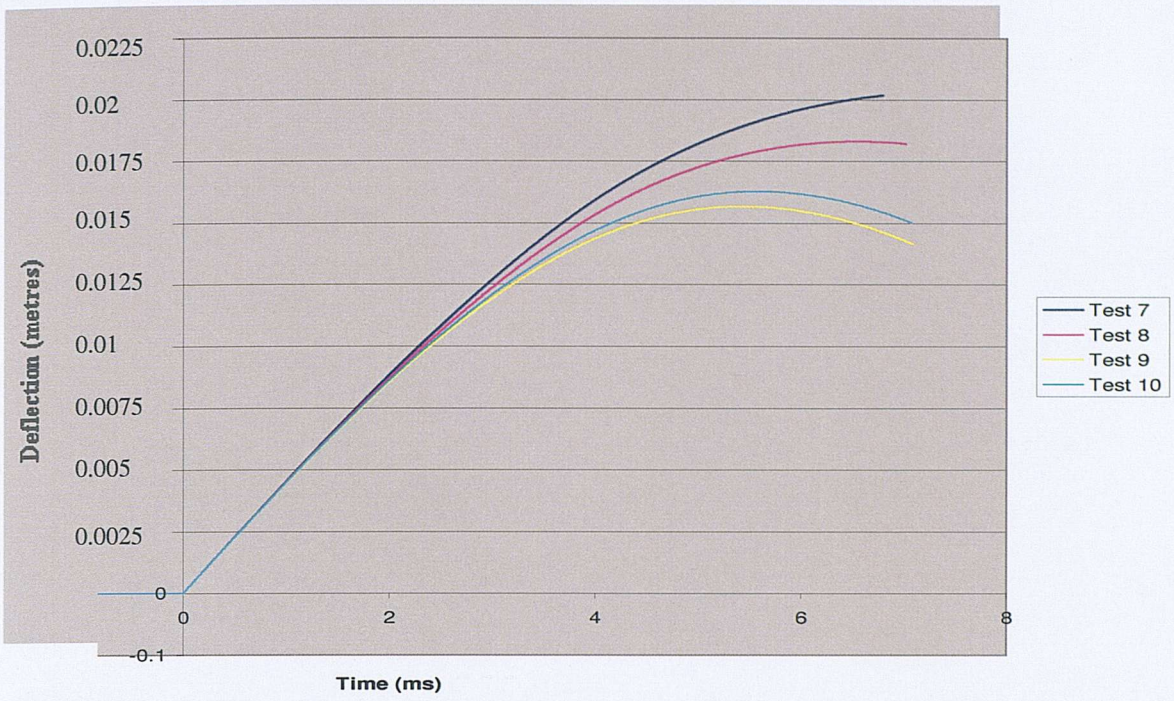


Figure 2-28. Deflection-time history for the medium sized (24.5mm) tup. (NOTE: plate deflection was in the same direction as the other tups but shown as positive on this plot).

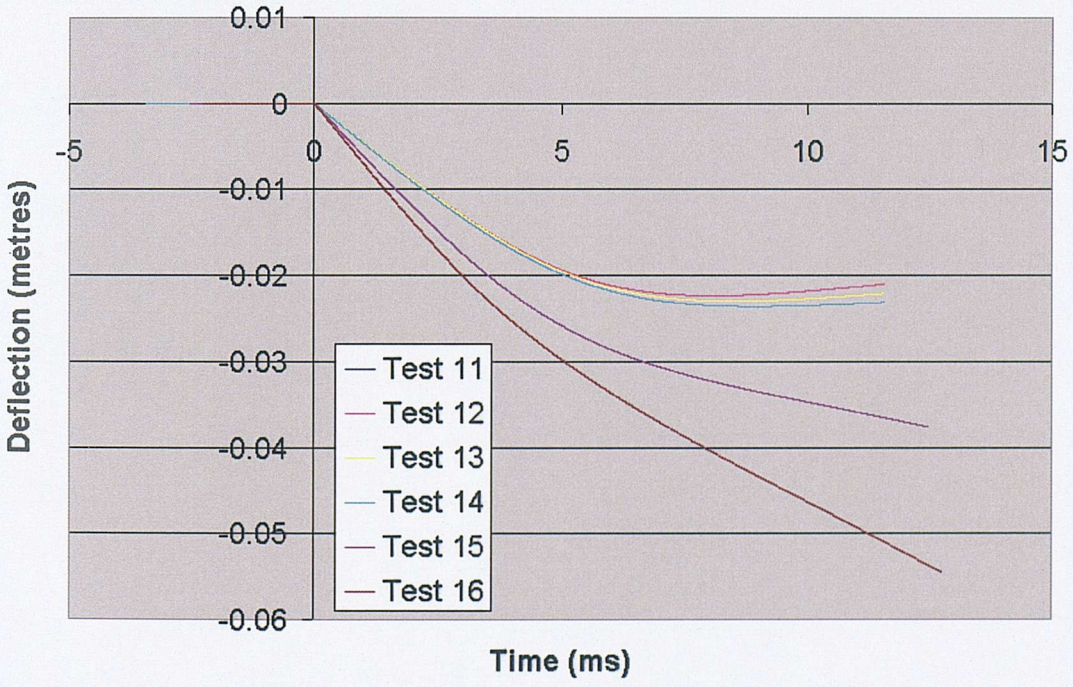


Figure 2-29. Deflection-time history for large sized (38mm) tup

Test	Tup velocity / ms^{-1} (ft/s)	Mass/ kg (lb)	Contact Force/ kN (lbf)	δ / m (in)	Approximate Damage Size (Top)/ m (in)	Approximate Damage Size (Bottom)/ m (in)	Energy Level / J (ft lbf)
1	4.59 (15.08)	8.55 (18.86)	15.15 (3406)	0.0119 (0.470)	0.0381 x 0.0254 (1.5 x1)	0.0381 x 0.0381 (1.5 x 1.5)	**91.52 (67.5)**
2	4.572 (15)	13.33 (29.39)	20.35 (4574)	0.0141 (0.557)	0.03175 x 0.0254 (1.25 x 1)	0.0381 x 0.0381 (1.5 x 1.5)	**140.57 (103.68)**
3	4.58114 (15.03)	15.87 (34.98)	20.77 (4670)	0.0158 (0.622) (Partial Penetration)	0.03175 x 0.0254 (1.25 x 1)	0.0381 x 0.0381 (1.5 x 1.5)	**165.82 (122.3)**
4[+]	4.584 (15.04)	18.37 (40.5)	17.73 (3985)	Penetration	0.03175 x 0.0254 (1.25 x 1)	0.0381 x 0.0381 (1.5 x 1.5)	193 (142.3)
5	4.615 (15.14)	18.37 (40.5)	22.52 (5062)	Penetration	0.0381 x 0.0254 (1.5 x1)	0.0381 x 0.0508 (1.5 x 2)	195.6 (143.8)
6	4.594 (15.07)	18.62 (41.05)	26.98 (6066)	Penetration	0.0381 x 0.0254 (1.5 x1)	0.0381 x 0.0381 (1.5 x 1.5)	196 (144.6)

[+] **Dubious impact result**

Table 2-11. Small plate tests, small 'S' (12.7mm) tup, in order of impact energy

Test	Tup velocity / ms^{-1} (ft/s)	Mass/ kg (lb)	Contact Force/ kN (lbf)	δ / m (in)	Approximate Damage Size (Top)/ m (in)	Approximate Damage Size (Bottom)/ m (in)	Energy Level / J (ft lbf)
20-1805	4.56 (14.96)	17.47 (38.36)	25.72 (5783)	0.01532 (0.603)			**180.74 (133.3)**
9	4.593 (15.07)	18.70 (41.23)	24.93 (5604)	0.0159 (0.627)	0.03175 x 0.0254 (1.25 x 1)	0.0381 x 0.03175 (1.5 x 1.25)	**195.51 (144.2)**
21	4.56 (14.96)	19.04 (41.98)	27.16 (6105)	0.01643 (0.635)			**197.80 (145.89)**
10	4.59638 (15.08)	20.34 (44.84)	27.86 (6263)	0.0165 (0.651)	0.0381 x 0.03175 (1.5 x 1.25)	0.0381 x 0.03175 (1.5 x 1.25)	**217.41 (160.35)**
22	4.56 (14.96)	21.99 (48.47)	28.2 (6330)	0.01732 (0.682)			**228.38 (168.442)**
7[+]	4.59943 (15.09)	23.69 (52.23)	24.64 (5538)	0.0205 (0.807) (Partial Penetration	0.0381 x 0.0381 (1.5 x 1.5)	0.0508 x 0.0381 (2 x 1.5)	**247.59 (182.61)**
7_R	4.59638 (15.08)	23.69 (52.23)	27.74 (6237)	0.0186 (0.733) (Partial Penetration)	0.03175 x 0.0381 (1.25 x 1.5)	0.04445 x 0.04445 (1.75 x 1.75)	**247.59 (182.61)**
23	4.56 (14.96)	25.99 (57.2)	27.8 (6240)	0.01935 (0.762)			**269.93 (199.0)**

[+] **Dubious impact result**

Table 2-12. Small plate tests, medium 'M' (25.4mm) tup, in order of impact energy.

Test	Tup velocity / ms-1 (ft/s)	Mass/ kg (lb)	Contact Force/ kN (lbf)	δ / m (in)	Approximate Damage Size (Top)/ m (in)	Approximate Damage Size (Bottom)/ m (in)	**Energy Level / J (ft lbf)**
11 (281)	4.60553 (15.11)	20.26 (44.66)	22.28 (5009)	0.0206 (0.81)	0.04445 x 0.0381 (1.75 x 1.5)	0.0381 x 0.0381 (1.5 x 1.5)	**211.71 (156.15)**
12 (282)	4.60553 (15.11)	24.32 (53.61)	23.43 (5268)	0.0223 (0.88)	0.04445 x 0.0381 (1.75 x 1.5)	0.0381 x 0.0381 (1.5 x 1.5)	**263.41 (194.28)**
13 (283)	4.60858 (15.12)	26.19 (57.73)	24.86 (5588)	0.0229 (0.9)	0.05715 x 0.03175 (2.25 x 1.25)	0.0381 x 0.0381 (1.5 x 1.5)	**284.05 (209.5)**
14 (284)	4.69087 (15.39)	26.19 (57.73)	24.57 (552)	0.0236 (0.93)	0.0381 x 0.0381 (1.5 x 1.5)	0.04445 x 0.0381 (1.75 x 1.5)	**294.16 (216.96)**
15 (285)	6.2088 (20.37)	26.19 (57.73)	28.13 (6324)	0.0376 (1.48)	0.03175 x 0.03175 (2.5 x 1.25)	0.05715 x 0.04445 (2.25 x 1.75)	**495.85 (365.72)**
16 (286)	7.13 (23.39)	26.19 (57.73)	29.40 (6609)	0.0546 (2.15)	0.06985 x 0.0508 (2.75 x 2)	0.03175 x 0.03175 (2.5 x 2.5)	**664.9325 (490.43)**

Table 2-13. Small plate impact tests, large 'L' (38mm) tup, in order of impact energy.

2.8.2.1 Photographs of damage

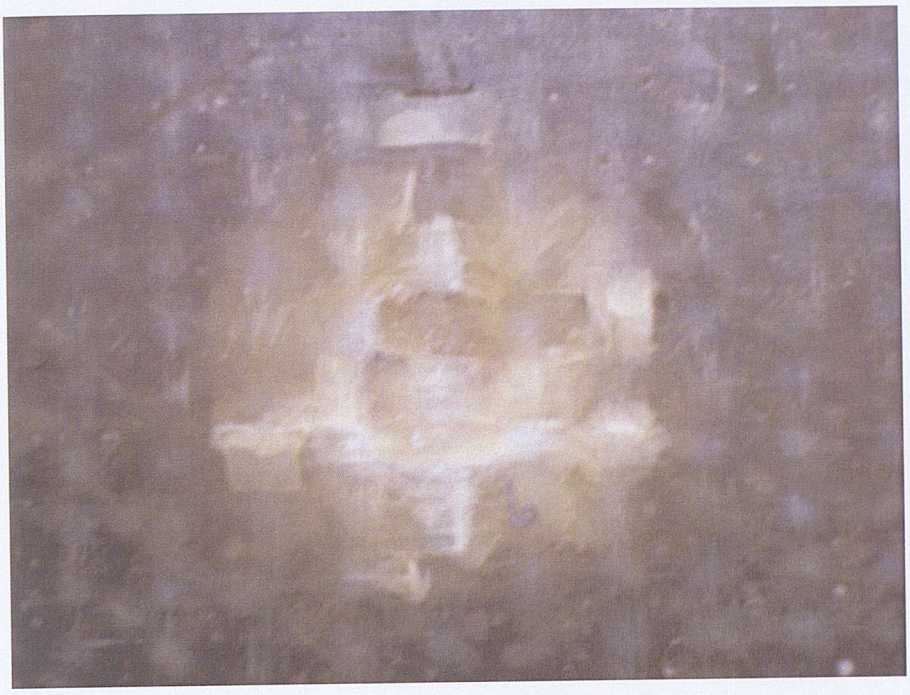


Figure 2-30. Test 3S(166J), top.



Figure 2-31. Test 3S(166J), bottom.

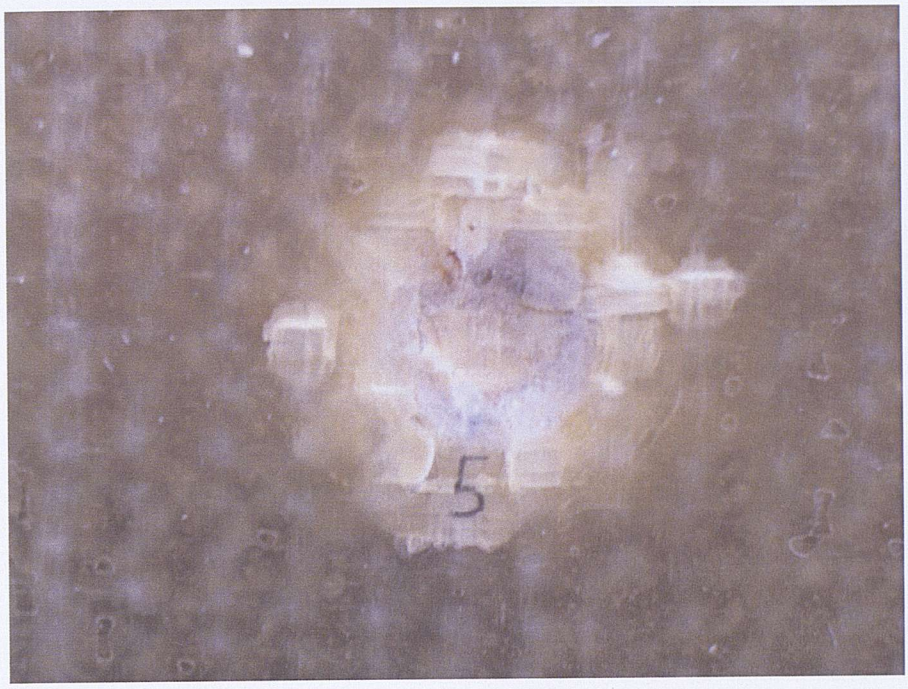


Figure 2-32. Test 5S(193J), top face



Figure 2-33. Test 5S195J), bottom face



Figure 2-34 Test 6S(196J), Top face

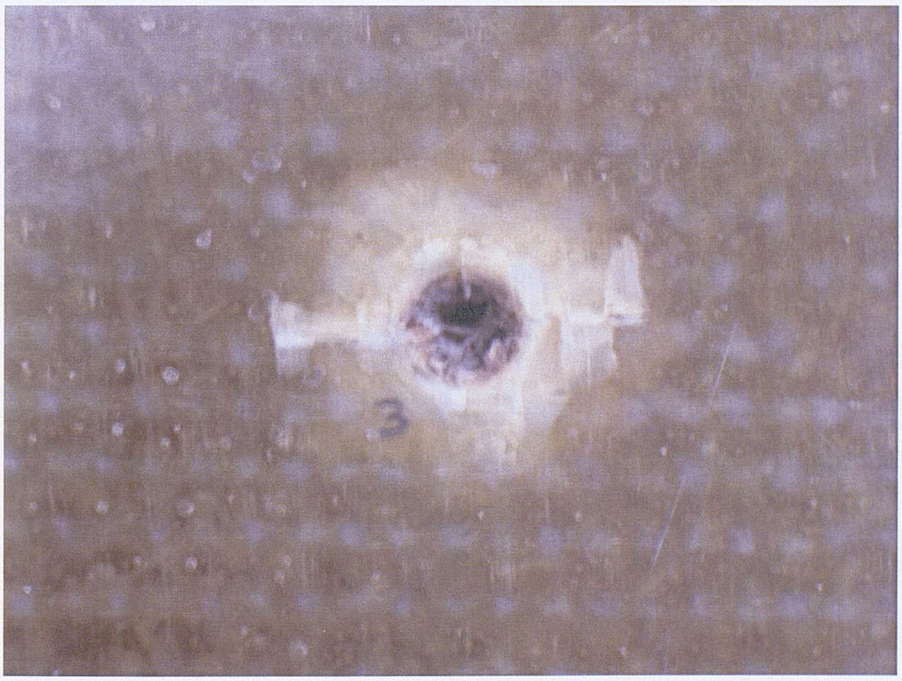


Figure 2-35 Test 6S(196J), Top face

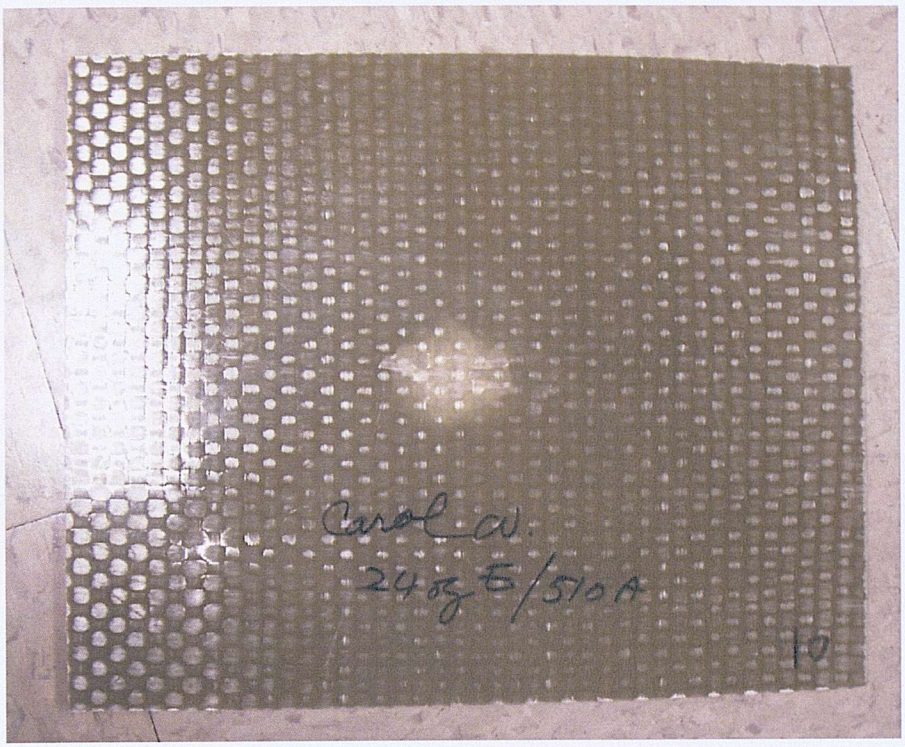


Figure 2-36 Test 9M(195J), top.

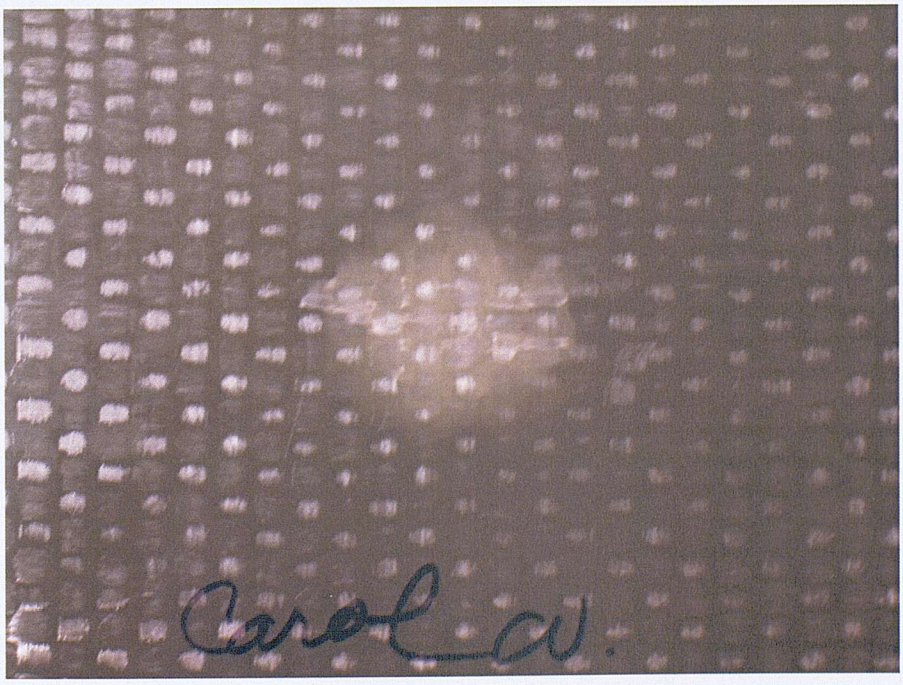


Figure 2-37 Test 9(195J), top.

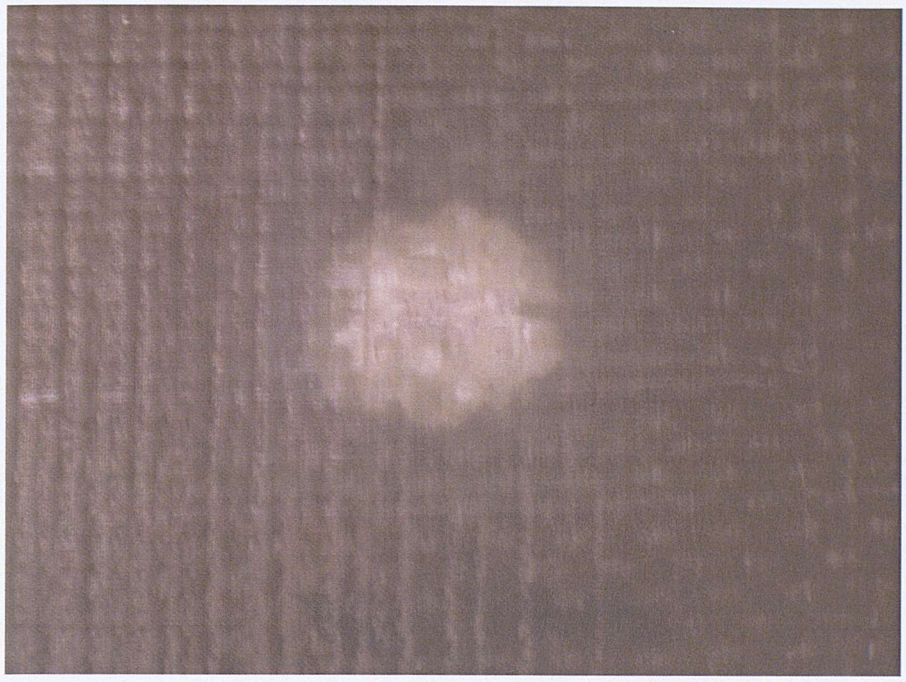


Figure 2-38 Test 9M(195J), bottom.

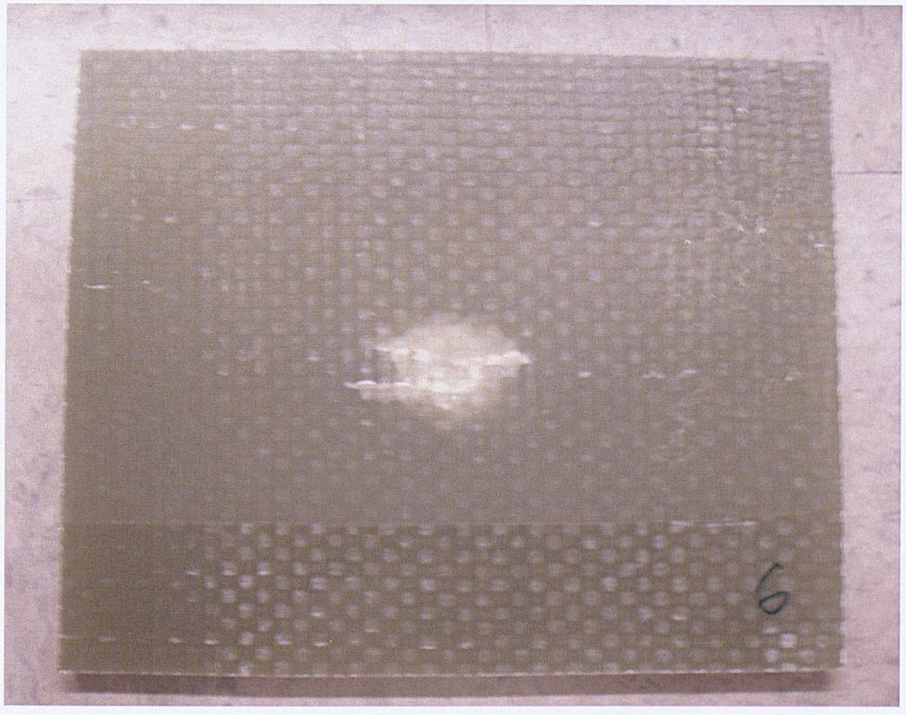


Figure 2-39 Test 13L(284J), top.

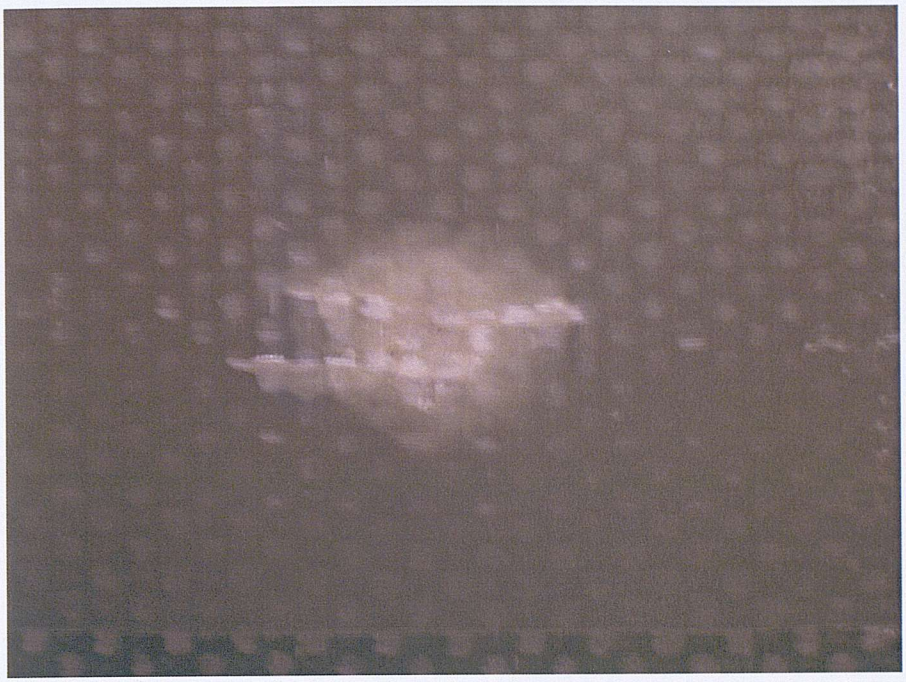


Figure 2-40 Test 13L(284J), top.

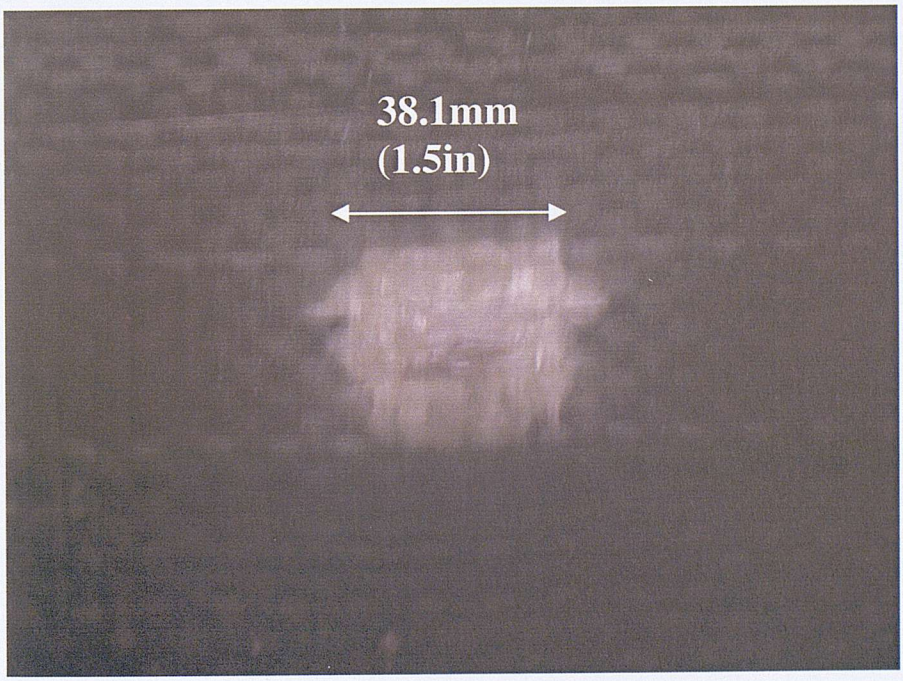


Figure 2-41 Test 13L(284J), bottom.

2.8.3 Large-scale plates

Two difference sized large-scale plates were subjected to low velocity impact using 0.203m (8in) diameter hemispherical tups, impacting the plate surface at a velocity of 4.6m/s.

Following smaller impact trials the tup diameter 203.2mm (8in) and the tup velocity 4.6 ms^{-1} (15ft/s). The tup mass varied for the four large plate tests carried out, as referenced in the following sections.

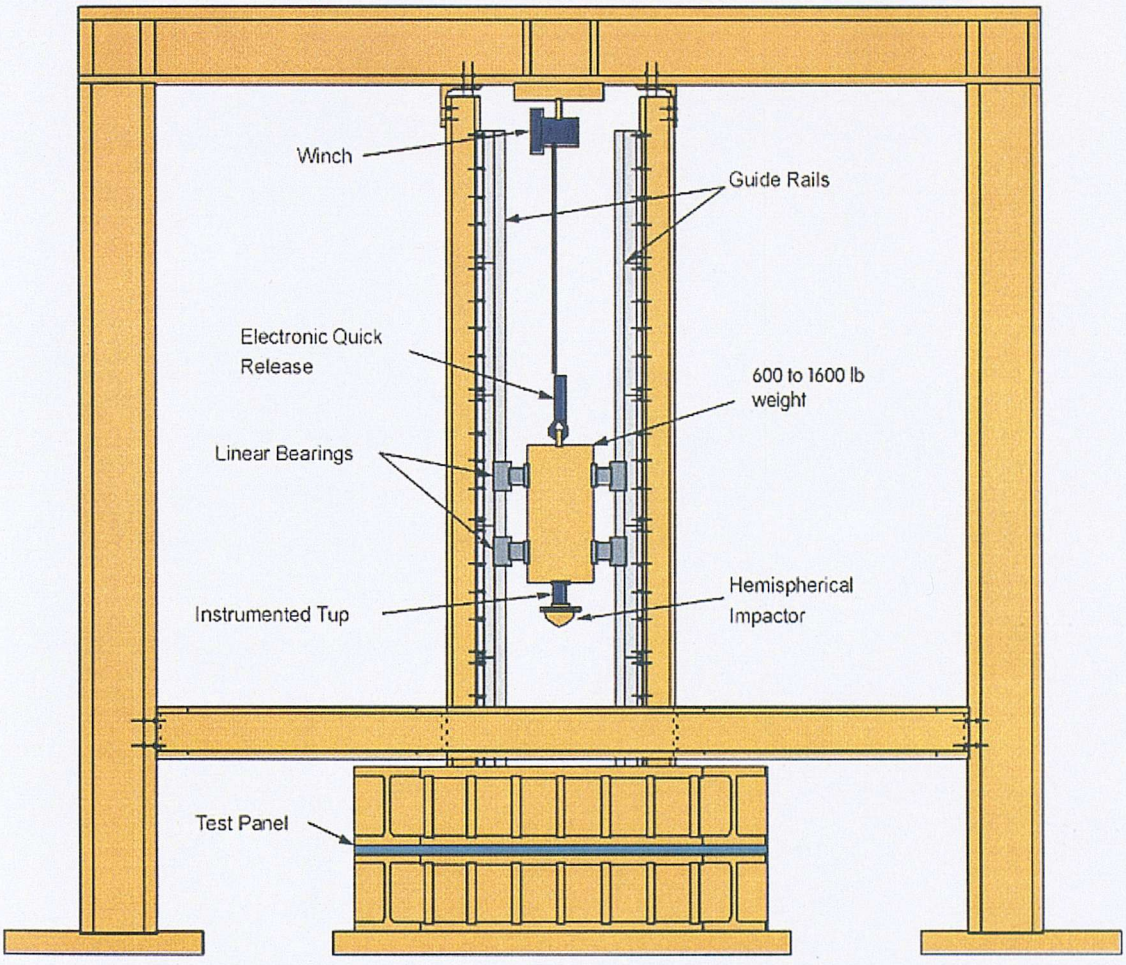


Figure 2-42. Schematic of large panel impact test fixture



Figure 2-43. Large plate impact rig with large1 sized plate positioned in place

2.8.3.1 Plate size 'Large1'

Four plates of sizes 1.07315x0.76835x0.019m were tested impacted using a 0.203m (8in) diameter tup and an impact velocity of 4.6ms^{-1}. Test D was a repeat of test C using a new panel. These tests were carried out by the USNA.

A few test details are summarized in bullet points below:

- Displacement sensors (laser) were located underneath the test panels such that sensor #1 measured displacement at the point of impact and sensor #2 measured displacement 0.25m (10 ins) away along the centerline along the long direction of the test panel.
- The strain gages were installed into a single-active Wheatstone Bridge.
- The test height for all three tests was 1.2954m (51.0in). This distance is measured from the impact surface of the 'tup' force sensor to the top face of the test panel.
- During impact on the third test panel (the first panel at 681.6kg – test C), the accelerometer mount separated from the weight sled. It was reattached for the fourth test (test D).
- The velocity sensor had a gap of 4.06mm (0.16in)

Plate test	Tup mass in kg (lbf)	Impact energy in J (ft lbf)
A	338.4 (746)	3580 (2640)
B	453.6 (1000)	4799 (3540)
C & D	681.7 (1503)	7212 (5319)

Table 2-14. Large1 plate, impact mass and energy

The damage incurred by the plates was measured by visual inspection. For each face, the 'top face' and 'bottom face', two delamination measurements were taken; recording the length 'l' and width 'w' of the discoloured area in the direction of the respective length (longest side) and width of the plate, see Figure 2-44. The generally larger 'darker' discolouration ('D') and the smaller 'lighter' discolouration ('L') was measured for each plate surface, detailed in Table 2-15. The darker discolouration appeared further away from the plate surface and the lighter discolouration was nearer the plate surface. Table 2-15 presents the damage measurements.

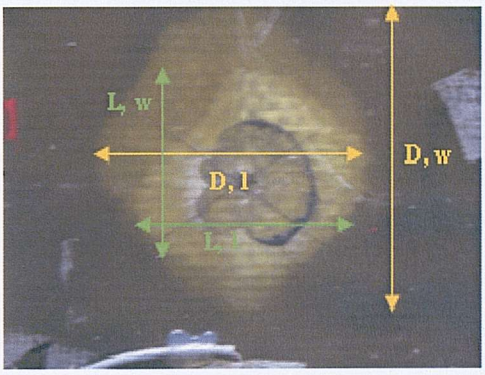


Figure 2-44. Measurement of damage using discoloured areas.

Generally speaking, the discoloured areas can be directly related to delaminated regions. This method of measuring the delamination can only be approximate as the exact location of the delaminated plies cannot be obtained in this way. As only an educated guess can provide, we can speculate that the 'lighter discolouration' lies in the quarter of the plate nearer the surface inspected and the 'darker discolouration' lies nearer the plate centre.

All three plates suffered fibre spall at the bottom of the plate. The out-of-plane displacements have thus been calculated in two ways; the first to include the fibre spall and the second exclusive of the fibre spall. These results, together with peak contact force readings, are presented in Table 2-16. The full contact force time histories are discussed in Chapter 6 together with photographs of the incurred damage.

TEST		Top Part (smooth)				Bottom Part (rough)			
		Lighter discoloration (lxw) in mm's (in)		Darker discoloration (l x w) In mm (in)		Lighter discoloration (l x w) In mm (in)		Darker discoloration (l x w) In mm (in)	
		l	w	l	w	l	w	l	w
Test A	Plate 2, 746#, Test 1	124 (4.874)	117 (4.61)	151 (5.954)	166 (6.534)	68.7 (2.706)	90 (3.547)	143 (5.623)	192 (7.57)
Test B	Plate 3, 1000#, Test 2	147 (5.787)	131 (5.161)	152 (6)	165 (6.51)	73.5 (2.895)	132 (5.178)	142 (5.602)	186 (7.337)
Test C	Plate 1, 1503#, Test 3	250 (9.847)	146 (5.735)	215 (8.477)	174 (6.833)	121.6 (4.789)	143 (5.635)	152 (6)	184 (7.247)
Test D	Plate 4, 1503#, Test 4	206 (8.125)	144 (5.667)	164 (6.454)	170 (6.699)	110 (4.319)	112 (4.424)	147 (5.802)	145 (5.709)

NOTE: l = length of plate (longest side), w=width of plate

Table 2-15. Damage measurements for large1 sized plates tests A to D.

Plate Description	CFN from test in kN (lbs)	Total o.o.p disp. in mm (in) LASER DISP	Depth of damage in mm (in) MOUND	o.o.p minus depth of damage NET DISP in mm (in)
'Test A' (Plate 2, 746#, Test 1)	296 (66543)	44.9 (1.767)	7.94 (0.313)	36.9 (1.455)
'Test B' (Plate 3, 1000#, Test 2)	339.8 (76394)	56.9 (2.243)	11.1 (0.438)	45.8 (1.805)
'Test C' (Plate 1, 1503#, Test 3)	382.0 (85878)	73.9 (2.912)	28.6 (1.125)	45.4 (1.787)
'Test D' (Plate 4, 1503#, Test 4)	387.2 (87057)	66.9 (2.636)	25.4 (1)	41.5 (1.636)

Table 2-16. Measured out-of-plane displacement at the plate centre for tests A to D.

2.8.3.2 Plate size 'Large2'

This plate size was the largest tested, measuring 1.524x1.524x0.038m (5x5ftx1.5ins). The panel was made from a VARTM manufactured 50oz/yd^2 WR E-glass/ BFG 281/C055 vinyl-ester resin and has 58 woven plies. The impact tests were carried out by the NSWCCD, report No. NSWCCD-TR-65-2003/24. The plate edges were clamped, enclosing a border width of 0.1524 m, leaving an effective plate size of 1.3716x1.3716 m (4.5x4.5ft). The tup mass was chosen as 453kg (1000lbs). Two identical tests were conducted on two separate plates of the same specification, labeled as 'large2(1)' and 'large2(2)'. In the tests, the force of the impact was measured in two ways, by measuring the force directly using an

instrumented tup and by integration of the acceleration of the weight box. Both force results were very close, seen in Figure 2-45 for large2(2). The contact force for both the tests is shown in Figure 2-46 using the tup force data. The contact force for both tests was almost identical for the first 6msecs, and there after the peak contact force appears at different times.

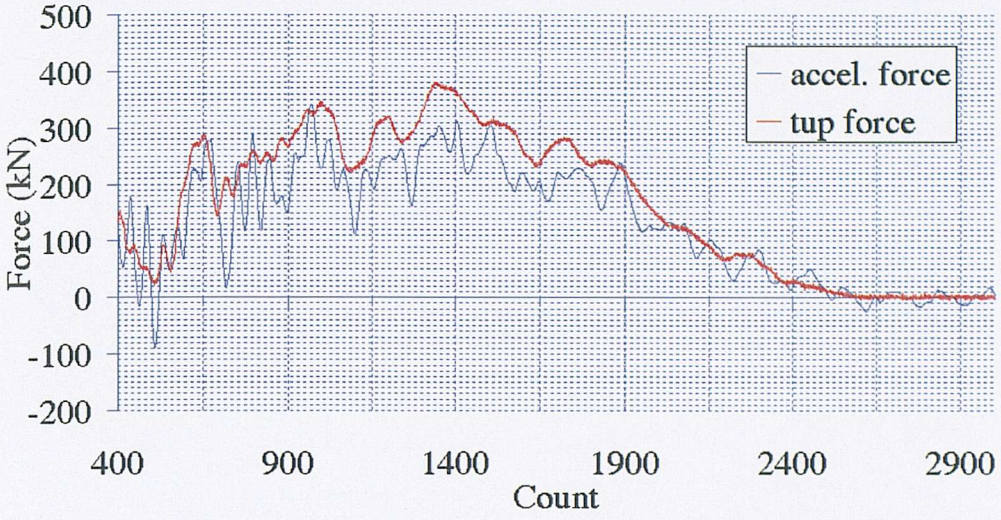


Figure 2-45. Comparison of two different measures of impact force for test 'large2(2)'

Ultrasound C-Scan of the large2(2) plate was carried out to record the extend of damage through the thickness at the ply level, see Figure 2-47, also presented in Chapter 6.

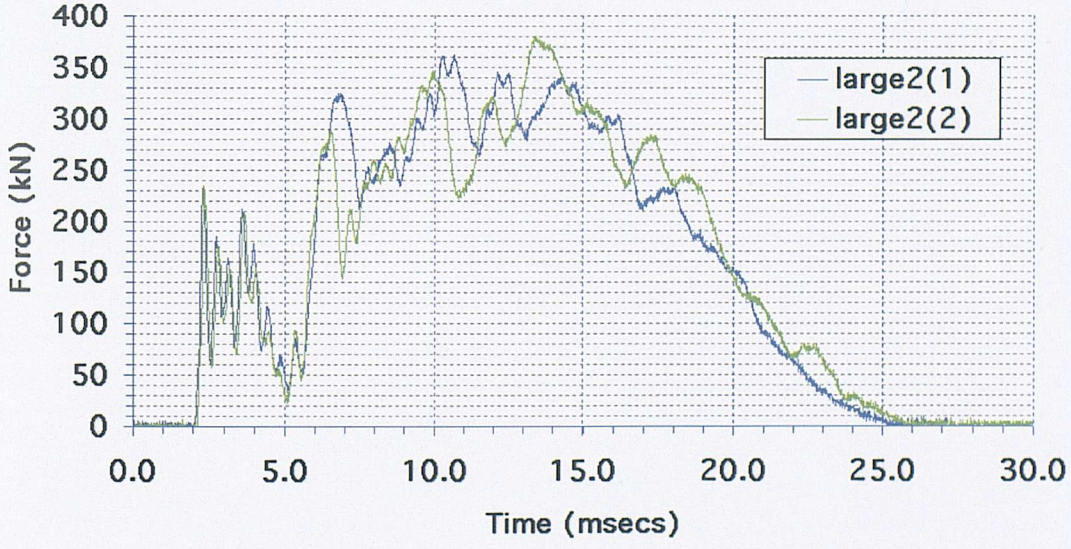


Figure 2-46. Contact force time history for large plate 2 tests: large2(1) and large2(2).

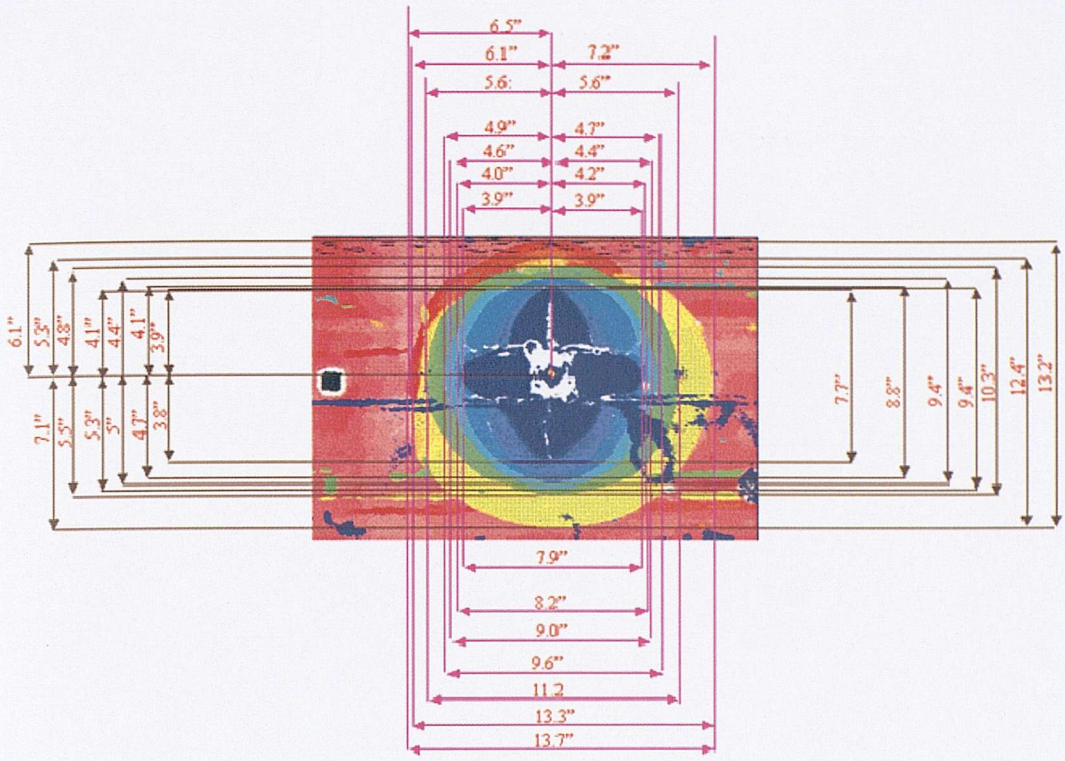


Figure 2-47. Ultrasound C-scan image of large2(2) plate centre

2.9 Reference List

1. Greenfield RJ, Dynamic tensile properties of woven glass fabric composites, University of Delaware, 1997.

2. Williams KV, Vaziri R, Poursartip A. A physically based continuum damage mechanics model for thin laminated composite structures. International Journal of Solids and Structures 2003; 40(9):2267-300.

CHAPTER 3

Numerical simulation of statically loaded panels

3.1 Introduction

This chapter begins by discussing a range of the most recognised stress-based failure criteria for composites and applies a few of the original theories to 2d finite element (FE) plate models in two different studies. The first study is a small validation exercise of previous experimental and FE work carried out by Padhi et al [1]. It involves the transverse loading of angle-ply composite plates and damage modelling using two different failure criteria. The resistance of marine composite plates to in-plane loading is an area that has received some attention in the past [2, 3], although the vast majority of testing was not carried out to failure. Also advances in manufacturing methods results in more elite composite panels, many of which have not been tested. This prompted the larger second study, designed and carried out by the present author. It involves analysing the behaviour of large scale woven composite plates under in-plane loading and attempts to model this using a finite element model and various failure criteria, with a focus on Hashin's 2d failure criterion. A FE parametric study is also carried out to see the sensitivity to several variables.

3.2 Stress Based failure criteria

Stressed based failure criteria are used to determine the load levels a structure can withstand before damage or complete failure is incurred. All popular failure criteria rely on only a handful of basic tests (such as uniaxial tensile and/or compression strength), even though most machine parts and structural members are typically subjected to multi-axial loading. This deficiency in testing is usually motivated by cost, since complete multi-axial failure testing requires extensive, complicated, and expensive tests. As a result some of the earliest failure models use simple maximum stress and strain criteria to define material failure. The 'maximum stress criterion' is also known as the normal stress criterion, Coulomb, or

Rankine criterion, is often used to predict the failure of brittle materials. This criterion states that failure occurs when the maximum (normal) principal stress reaches either the *uniaxial* tension strength or the *uniaxial* compression strength. The Mohr Theory of Failure, also known as the Coulomb-Mohr criterion is based on Mohr's Circle. Mohr's theory is often to predict the failure of brittle materials and is applied to cases of 2D stress. Mohr's theory suggests that failure occurs when Mohr's Circle at a point in the body exceeds the envelope created by the two Mohr's circles for uniaxial tensile strength and uniaxial compression strength. These simple criteria work best where the loading conditions and material system is relatively simple. However, multiaxial stresses must be considered with 2d or 3d members such as plates, shells or other elements subjected to combined loading.

The anisotropic nature of composite materials has driven the development of various failure theories, commonly known as Interactive failure theories. These are basically developed from theories formulated in the 1950's to describe yielding of metals, which are updated to account for material anisotropy and the tensile or compressive dependent strength characteristics observed in FRP's. These were amongst the first to be implemented in computer programmes as they can be easily represented in an effective algorithm form. The formulation of failure envelopes (curve-fitting) such as Von Mises, are often used in what are classed as *phenomenological models.* A phenomenological criterion applies to the phenomenon of failure only and cannot be used to predict the failure mechanism itself. It is expressed by a mathematical expression that describes an open or closed 'strength surface'. Phenomenological models are not derived from physical theories of failure where microscopic processes that cause failure are embraced within the model. Instead, in phenomenological theories, the causes of failure are neglected and gross macroscopic effects are only considered. Those applicable to composites include Tsai-Hill [4]; Tsai-Wu [5], Hoffman [6], Puppo-Evensen [7] and Hart-Smith [8, 9] used to define first ply failure. On the other hand, physically based failure criteria, define specific modes of failure, each mode being described by a unique equation within the theory. For composites, the criteria will differentiate between matrix cracking and fibre breakage, and some also include fibre-matrix shearing, and further differentiate between compressive and tensile loading and brittle and ductile matrix failure modes. Therefore physically based failure criteria provides not only predictions of strength, strain to failure and so on, but also the mode of failure and sometimes the direction of the fracture plane. Some of the most well known and commonly used failure theories are Hashin's failure criteria [10] for unidirectional fibre composites and Chang and Chang [11]. More recently Puck [12] developed a failure criterion for matrix compression failure based on the Mohr-Coulomb criterion which is the most common failure

criterion encountered in geotechnical engineering. The Mohr-Coulomb criterion describes a linear relationship between normal and shear stresses (or maximum and minimum principal stresses) at failure and requires the knowledge of the angle of friction associated with the fracture plane of maximum shear stresses.

1. Max stress and strain
2. Interactive failure theories – failure based on interaction of stresses
3. Phenomenological failure criteria (non-empirical. Based on previous criteria)
4. Physically based failure criteria

Most simulations tools have codes which usually include simple stiffness degradation laws or 'reduction' factors. Codes like ABAQUS, ADINA, NASTRAN, ANSYS, LUSAS and DIANA, treat the component elastically and apply a scalar damage factor, normally a first ply failure criterion, based on maximum stress or strain values. Since the present work, Abaqus/Standard version 6.6 have incorporated an energy based damage model which has not been validated here.

Interactive failure criteria can be described with a polynomial, generally of quadratic form and the parameters for the equation are obtained by running unixial or biaxial tests. The mathematical formulation of these criteria is similar to that of polynomial tensorial criteria, both of which introduce coefficients and parameters to improve the correlation with experimental data. The general form taken by these type of criteria is shown in Equation (3-1) but more specific to a quadratic relationship is that the following general Equation (3-2):

$$(F_i\sigma_i)^{\alpha} + (F_{ij}\sigma_i\sigma_j)^{\beta} + (F_{ijk}\sigma_i\sigma_j\sigma_k)^{\gamma} + \ldots \geq 1 \tag{3-1}$$

$$F_{ij}\sigma_{ij} + F_i\sigma_i \geq 1 \tag{3-2}$$

For plane stress, quadratic polynomial equations include that of Tsai-Hill [4] Equation (3-3) which is an extension of the Von-Mises yield criterion for metals but applied to orthotropic materials. Failure is deemed to occur when the criterion is equal to or greater than one. The Tsai-Hill criterion has been previously used for modelling damage initiation of woven composite plates under low velocity impact, [13].

Hoffman's equation, Equation (3-4), is the same as Tsai-Hill but allows for differences in the compressive and tensile moduli by the addition of linear terms to the equation. The advantage of this method is that a single failure criterion is used in all four quadrants (unlike Tsai-Hill's). Also, it allows the interaction between the various failure modes and is a very simple failure model to use. The Hoffman criterion has shown good correlation with experimental data with glass/graphite and boron/epoxy laminates.

Tsai-Wu [5], Equation (3-5), improves on Tsai-Hill's failure criterion. This is a phenomenological criterion with its derivation being based on linking experimental constants rather than on a physical interpretation of material behaviour. This criterion is also represented by smooth continuous curves in each quadrant. The authors introduce an increased number of terms than the previous criteria and use first and second order strength tensors. The property F_{12} is obtained from bi-axial tests made on the lamina material, see Equations (3-5). It is involved in the interaction term of the failure function (of stresses σ_{11} and σ_{22}) but has shown to have a very small contribution. A modification to Tsai-Wu's criterion has been previously applied with some success to woven composites in the form of a loaded DCB (Double Cantilever Beam) specimen [14].

$$\frac{\sigma_{11}^2}{X^2}-\frac{\sigma_{11}.\sigma_{12}}{X^2}+\frac{\sigma_{22}^2}{Y^2}+\frac{\sigma_{12}^2}{S_t^2}\geq 1 \qquad (3\text{-}3)$$

Tsai-Hill's failure

$$-\frac{\sigma_{11}^2}{X_C X_T}+\frac{\sigma_{11}\sigma_{22}}{X_C X_T}-\frac{\sigma_{22}^2}{Y_C Y_T}+\frac{X_C+X_T}{X_C X_T}\sigma_{11}+\frac{Y_C+Y_T}{Y_C Y_T}\sigma_{22}+\frac{\tau_{12}^2}{S_{12}^2}\geq 1 \qquad (3\text{-}4)$$

Hoffman failure

$$F=F_{11}\sigma_{11}^2+F_{22}\sigma_{22}^2+F_{66}\sigma_{12}^2+F_1\sigma_{11}+F_2\sigma_{22}+2F_{12}\sigma_{11}\sigma_{22}\geq 1$$

$$F_{11}=-\frac{1}{X_T X_C},F_{22}=-\frac{1}{Y_T Y_C},F_{66}=\frac{1}{S_{12}^2},F_1=\frac{1}{X_T}+\frac{1}{X_C},F_2=\frac{1}{Y_T}+\frac{1}{Y_C} \qquad (3\text{-}5)$$

$$F_{12}=\frac{1}{2Y_T^2}\left[1-Y_T\left(F_1+F_2\right)-Y_T^2\left(F_{11}+F_{22}\right)\right]$$

Tsai-Wu's failure

For three dimensional quadratic stress interaction for transversely isotropic laminates exists the Hashin-Rotem criteria [15] for tensile failure of the matrix and fibre failure modes which was further modified by Hashin [10] to include compression failure. The criteria give an

elliptical relationship between axial and shear strengths. Hashin's equations started off with a set of invariants of coordinate transformation about the axis of transverse isotropy, which for a unidirectional composite is along the fibre direction. With transverse isotropy, symmetry is about an axis that is normal to a plane of isotropy. This transverse plane has infinite planes of symmetry and therefore within this plane the material properties are same in all directions. The way Hashin's criteria were developed is different to the interactive theories such as Tsai-Wu, which is made up of all possible combinations of stresses up to quadratic terms. In contrast to Hashin's failure theory, the number of individual strength properties is not obvious. Tsai-Wu's theory may predict no failure in one coordinate system under a given set of stresses but predict failure in another coordinate system under the same stresses. Hashin overcomes this problem by writing the failure criterion in terms of stress invariants. Hashin's criteria for both 2d and 3d stress is shown with Equations (3-6) to (3-12). Hashin's 2d equations have been previously applied to woven composites under quasi-static in-plane loading, with more success than the Hoffman criterion [16].

$$\left(\frac{\sigma_{11}}{X_T}\right)^2+\left(\frac{\sigma_{12}^2+\sigma_{13}^2}{S_{12}^2}\right)\geq 1 \tag{3-6}$$

3d Hashin - Fibre tension failure

$$\left(\frac{\sigma_{11}}{X_T}\right)^2+\left(\frac{\sigma_{12}}{S_{12}}\right)^2\geq 1 \tag{3-7}$$

2d Hashin - Fibre tension failure

$$\frac{\sigma_{11C}}{X_C}\geq 1 \tag{3-8}$$

3d and 2d Hashin - fibre compression failure

$$\left(\frac{\sigma_{22}+\sigma_{33}}{Y_T}\right)^2+\left(\frac{\sigma_{23}^2-\sigma_{22}\sigma_{33}}{S_T^2}\right)+\left(\frac{\sigma_{13}^2\sigma_{12}^2}{S_{12}}\right)\geq 1 \tag{3-9}$$

3d Hashin - matrix tension failure

$$\left(\frac{\sigma_{22}}{Y_T}\right)^2+\left(\frac{\sigma_{12}}{S_{12}}\right)^2\geq 1 \tag{3-10}$$

2d Hashin - matrix tension failure

$$\left(\frac{\sigma_{22}+\sigma_{33}}{2S_T}\right)^2+\left[\left(\frac{Y_C}{2S_T}\right)^2-1\right]\cdot\left(\frac{\sigma_{22}+\sigma_{33}}{Y_C}\right)+\frac{\sigma_{23}^2-\sigma_{22}\sigma_{33}}{S_T^2}+\left(\frac{\sigma_{12}^2+\sigma_{13}^2}{S_{12}^2}\right)\geq 1 \tag{3-11}$$

3d Hashin - matrix compression failure

$$\frac{\sigma_{22}}{Y_C}\left[\left(\frac{Y_C}{2S_{12}}\right)^2-1\right]+\left(\frac{\sigma_{22}}{2S_{12}}\right)^2+\left(\frac{\sigma_{12}}{S_{12}}\right)^2\geq 1 \tag{3-12}$$

2d Hashin - matrix compression failure

Chang-Chang is similar to Hashin's equations except the non-linear relationship between the in-plane shear stress and strain is incorporated in a parameter 'α' that is determined experimentally from: $\gamma_{12}=\frac{\sigma_{12}}{G_{12}}+\alpha\sigma_{12}^3$. The mathematical model for the nonlinear shear response was originally developed by Hahn and Tsai [17] and the value can range from approximately $2.44\times10^{-8}\,MPa^{-3}$ for a unidirectional graphite/epoxy laminate with $[(+45/-45)_6]_S$ plies [18] to $3.05x10^{-6}MPa^{-3}$ for cross plies woven roving GRFP [19]. The shear parameter represents the non-linearity of the relative movement of the stiff fibres within the ductile matrix and has the effect of decreasing the shear term in the failure criterion. Chang-Chang's criterion, shown with Equations (3-13) to (3-16) reduces to the Hashin-Rotem equation for linear shear behaviour, i.e. when $\alpha=0$.

$$\bar{\tau}=\frac{\frac{\sigma_{12}^2}{2G_{12}}+\frac{3}{4}\alpha\sigma_{12}^4}{\frac{S_c^2}{2G_{12}}+\frac{3}{4}\alpha S_c^4} \tag{3-13}$$

Chang-Chang – non-linear shear parameter

$$\left(\frac{\sigma_{11}}{X_T}\right)^2+\bar{\tau}\geq 1 \tag{3-14}$$

Chang-Chang - fibre tension failure. Fibre failure.

$$\left(\frac{\sigma_{11}}{X_C}\right)^2+\bar{\tau}\geq 1 \tag{3-15}$$

Chang-Chang - fibre compression failure. Fibre/matrix shear-out.

$$\left(\frac{\sigma_{22}}{Y_T}\right)^2+\bar{\tau}\geq 1 \tag{3-16}$$

Chang-Chang - matrix tension failure

$$\left(\frac{\sigma_{22}}{2S_c}\right)^2+\left(\left(\frac{Y_c}{2S_c}\right)^2-1\right)\frac{\sigma_{22}}{Y_c}+\bar{\tau}\geq 1 \tag{3-17}$$

Chang-Chang - matrix compression failure

C. T. Sun [20] compared various failure theories were with experiment for six different composite material systems and various loading conditions. These included uniaxial (normal and shear) loading, off-axis loading and biaxial (normal and shear) loading. It was reconfirmed that there is little difference between the theories. Most of these theories were very similar in the first (tension-tension) quadrant, as previously found and the biggest differences occurred under combined transverse compression and shear. In this case predictions of the Tsai-Wu interactive theory were in better agreement with experimental results than other theories.

In 1991 Hinton [21-23] carried out a world-wide failure exercise to establish the most current failure theories for continuous fibre reinforced polymeric composites, to compare the capabilities of the theories in the study against each other and against quasi-static experimental data. Some of the participants included Zinoviev [24] who applied a structural-phenomenological approach to failure for multi-layered laminates using plane-stress maximum stress criteria and obtaining reasonable comparison with experiment. Their failure surface is rectangular and the model remains elastic up to the materials ultimate stress and thus complete failure. The model assumes that the properties of the reinforcing fibres practically do not change at deformation and any changes to the material properties stem from the formation of cracks in the matrix. The model does consider geometric non-linearity, where reinforcing angles (such as in angle-ply laminates) change with deformation of the composite as a consequence of shear strains. Unstable deformation is also modelled (where the strains increase with practically no increase in the load).

There are two main parts to the failure analysis of laminated composites which are the first is the prediction of lam*ina* failure and the second is the stress analysis of the lam*inate* with the lamina stiffness reduction incorporated. In progressive damage modelling the stresses in the laminate are calculated using classical laminate theory. Stress loading takes place incrementally, to assure a state of elasticity. On reaching an initial state of damage, the stresses are re-distributed by decreasing the load on the damaged area and transferring extra load on the neighbouring non-damaged areas. For each new mode of damage, a new stress calculation is required. After every damage mechanism, the properties of the material are changed by reducing the relevant moduli and or Poisson's ratios to zero in the individual failed layers. For example, for matrix cracking in a layer, the transverse modulus and Poisson's ratio are reduced to zero.

More recent work by *Liu*-Tsai [25] involved the development of criteria for selective material property degradation in response to matrix cracking. A quadratic failure criterion is used to find the first ply failure (lowest ratio of strength amongst all the plies). The transverse strain of this failed ply is used to check if micro-cracking (under tension only) has taken place If micro-cracking has occurred, the ply is *degraded* and the *matrix* modulus is reduced by a factor determined using a micromechanics approach. Catastrophic failure is defined by fibre failure. This progressive damage analysis takes place until the laminate reaches its ultimate strength, after which the load is reduced as additional plies fail. This method is clearly different to other physically based failure criteria such as Hashin and Chang-Chang where individual layer stiffness is not gradually reduced with damage but annulled at the onset of failure of a given mode. Despite the damage in Chang-Chang's model being progressive (layer by layer), the ability for a damaged layer to resist additional load before complete failure is not addressed. However, due to the empirical nature of the failure criteria models, the criteria is only as worthy as the data available. This criterion was presented for Hinton and Soden's failure exercise in 1998 and 2002. It was found that the selective degradation scheme works well in most cases but has problems in certain loading conditions. It was found that eliminating the selection gives better comparison with the experimental data provided.

Puck and Schürman [12] considered progressive failure analysis by applying gradual degradation of the plies with increasing load until fibre fracture in one ply provoked ultimate laminate failure. Through fracture mechanics on a meso-scale, they were able to determine the fracture angle of inter-fibre cracks leading to ultimate failure. Puck-Schürman applied classical laminate theory to analyse the stresses and strains of single plies but modified it to include non-linear terms. The non-linearity was accounted for between the stresses and strains in in-plane shear (as previously implemented by Chang-Chang and then Hahn and Tsai) and also between the orthogonal in-plane stresses and strains (i.e. σ_2 ,ε_2) for compressive σ_2. In addition, Puck-Schürman included this orthogonal in-plane compressive stress effect on the non-linearity of τ_{21},γ_{21} which leads to a shallower τ_{21},γ_{21} curve than τ_{21} applied alone, normally ignored in other models. Neglecting this stress interaction results in a level of crack initiation which is higher than in reality.

An expression for strain along the fibres of a uni-directional laminate can be written in terms of fibre stress and strain and the addition of another term describing a magnified effect due to the Poisson's effect of the transverse stress in the fibre direction. Puck-Schürman found that on the basis that unidirectional layers behave in a very brittle manner, Mohr-Coulomb's

criterion for brittle materials was applied to matrix compression failure. This is a better approach when dealing with shear fracture than a yield criterion like Hill's. The angle of fracture was found in uni-directional composites by determining the maximum stressed plane. A fracture curve was produced for orthogonal in-plane tensile stress and in-plane shear stress loading with fracture cracks developing on a plane running parallel with the fibres. Three modes of cracking were distinguished under the two aforementioned global stresses. Residual stresses were also given consideration in their equations.

Sun and Tao [26] considered progressive laminate failure and material non-linearity using a one parameter plasticity model developed by Sun and Chen [27] reduced for plane stress assuming that the fibre direction is elastic until failure. The Hashin-Rotem criterion was applied to detect failure initiation of the matrix and the fibres, differentiating between compression and tension by maximum stress values only. Progressive damage modelling until full failure was achieved using a shear-lag model.

Moy et al [28] applied a simplified version of Hashin's criterion to include longitudinal, transverse and shear stresses for thin unidirectional and *plain weave* composite panels. A macro-analysis was applied which incorporated the results of a foregoing micro-structural analysis. A micro-analysis of a repeating unit element (RUE) of a woven composite was performed which showed stress concentrations in the fibres and pure resin regions creating different potential areas of failure initiation than in the unidirectional panels. However, on a macroscopic scale these stress concentrations had little effect on the over all transverse and shear strengths. Progressive damage modelling was carried out in a similar fashion to Chang-Chang where depending on the damage mode, the relevant mechanical properties of the ply are brought to a negligible value and stresses are redistributed to surrounding regions. Comparison of simulation and experiment was favourable showing a good degree of accuracy from the model predictions.

The work by *Gotsis et al* [29] formed part of the by Hinton and Soden failure exercise part B in 2002. Two computer codes were used and compared on a range of multi-directional laminates: ICAN and CODSTRAN. ICAN detects damage initiation using a MDE (Modified Distortion Energy) failure criterion. This resembles previous quadratic failure criteria except for an additional 'directional interaction' coefficient which is very sensitive to biaxial stress.

$$F=1-\left[\left(\frac{\sigma_{11}}{S_{11}}\right)^2+\left(\frac{\sigma_{22}}{S_{22}}\right)^2-K_{12}\left(\frac{\sigma_{11}}{S_{11}}\right)\left(\frac{\sigma_{22}}{S_{22}}\right)+\left(\frac{\sigma_{12}}{S_{12}}\right)^2\right] \tag{3-18}$$

Where $K_{12}=\dfrac{(1+4\nu_{12}-\nu_{13})E_{22}+(1-\nu_{23})E_{11}}{\sqrt{E_{11}E_{22}(2+\nu_{12}+\nu_{13})(2+\nu_{21}+\nu_{23})}}$

The maximum stress limits used in the equation are calculated by ICAN based on the constituent fibre and matrix strengths and *micromechanics* equations but the MDE failure equation, in which they are inserted, is on a macro (ply by ply) scale. The second computer code is CODSTRAN which also works using the MDE criterion, but in addition applies maximum stress criterion which presides over the MDE when its conditions are met and then assigns damage. Even if F in the MDE equation is not equal to zero (denoting complete failure) damage can still be assigned by ICAN when any of the individual stresses exceeds its maximum stress. For example, when σ_{11} reaches its maximum value, both matrix and fibre failure are deemed active. The fourteen different unidirectional and multidirectional laminae assessed using both these computer codes and compared with experimental results, show best correlation between theory with CODSTRAN. Failure by compression, however, was not as well predicted by either code and laminate predictions were somewhat underestimated. The main shortfall of their model was attributed to several factors, including the neglect of a residual stiffness matrix after property degradation.

Failure of a laminate is more complicated than what can be addressed with a simple a 2-D analysis, as encountered with many failure criteria. There are other effects such as non-linear behaviour (such as stress non-linearity examined by Puck and Schurman, above) and 3-D failure modes such as delamination and free-edge stresses. Transverse stresses, particularly transverse shear stresses can be quite large near the edge of a laminate and may participate in the failure of laminates. Large interlaminar shear stresses can also produce matrix cracks at free edges potentially the initiation of edge delamination, [30]. However, according to Sun-Tao [31] including these latter effects in model analysis is prohibitive.

Hou et al [32] modified Chang-Chang's failure criteria putting $\alpha=0$ and Brewer-Lagace's for delamination and implemented these modified failure criteria into their material models. Chang-Chang's matrix cracking equation does not include the contribution of the shear stress σ_{23} which is a major contributory stress for shear matrix cracking and σ_{13} for fibre failure. For the case of through-thickness tensile stress, a shear term is added. For fibre failure, the shear stress σ_{13} is also included in an additional term, attributed to having an

equal effect as the action of σ_{12}. The matrix crushing criterion was not changed. They also included the tensile transverse normal stress in the criterion for delamination which had at the time been excluded in DYNA3D. According to Hou et al the compressive transverse normal stress actually suppresses delamination, validated for impact loading conditions.

The effectiveness of a failure theory when it comes to failure prediction of laminates under uniaxial loading depends on whether the damage mode is fibre or matrix dominated. For matrix dominated angle-ply laminates, predictions with the various interactive theories can be quite mixed as also the comparison with experimental results. Failure in these laminates is governed by the lamina normal stress σ_2 and the in-plane shear stress τ_{12}. Depending on the lamina angles and whether the stress is in compression or in tension, some theories work better than others. When it comes to biaxial loading of angle-ply laminates it becomes more difficult to define which damage mode is the most influential in the failure process, as this is dependent on the biaxiality.

Ultimate failure of fibre dominated laminates is relatively well predicted with theories based on the maximum stress criterion, a partly interactive approach (Puck et al. [12]), or a totally interactive criterion (Tsai-Wu), if first fibre failure is used as the definition of ultimate ply failure. Distinctions must be made between compressive or tensile transverse in-plane stresses (σ_2) for matrix dominated failure. For σ_2 in tension maximum stress theories agree better with experimental results, whereas interactive theories under-predict the strength. The reverse is true when σ_2 is in compression. As of yet, the range and accuracy of application of each failure theory has not been determined because of the limited experimental data, especially in relation to first ply failure and loading of laminates under biaxial compression or compression and shear [33]. Thus the requirement is still there to test these failure theories for a range of conditions in order to conclude on their applicability.

3.3 Selected failure criteria for numerical validation

The criteria selected for investigation in this section are applied to transverse loading of angle ply laminates and in-plane loading of a woven ply laminated and have been limited to a few of the classical, most implemented theories of maximum stress, Tsai-Wu, Hashin and Chang-Chang. These criteria, however, were essentially intended for unidirectional laminates. The woven laminate makes it difficult to apply some of the more recently developed criteria which are largely targeted at angle-ply composites rather than woven

composites. Prior to carrying out any additional specific material tests on the woven laminate that may be required with a more complex model, it is important to validate simpler models suited to simple uni-axial loading conditions and then compare their performance with more complex loading conditions. In addition to the above failure criteria, an additional more conservative approach for first ply failure [34] is also tested, shown in Equation (3-19) for plane stress.

$$\sum_{i=1}^{2}\sum_{i=1}^{2}\left(\frac{\sigma_{ij}}{S_{ij}}\right)^2 \geq 1 \qquad (3\text{-}19)$$

Where S_{ij} is the strength of the material in the direction ij

3.4 Method of degrading the material properties

For the criteria selected, a one-off degradation rule is applied, leaving a residual stiffness factor of 5-10% (i.e. reducing the moduli down to either 5% or 10% of their intact value). This percentage residual was chosen as a result of in-house testing at DSTL suggesting 5-10% and previous work [35] supporting 10%. Iannucci [36] also justifies this residual by approximating the residual strength of the composite to the strength of the resin, which is only 16.5MPa in tension, compared to the composite strength properties as shown in Table 2-3 of Chapter 2. The effect of the fibre presence will add to the strength but this is dependent on the fibre orientation angle which is not readily quantifiable. In addition to the above, a residual stiffness also helps to avoid numerical problems. Table 3-1 shows the residual factors applied to the in-plane properties of the laminate for the various combined failure modes. Field variables (FV's), FV1, FV2 and FV3 are representative of the failure modes, as shown below. Field variables act as flags to events. They can be a value of '0', representing an inactive state, or a value of '1' for active which in the current work flags the onset of a particular failure mode. Field variables are assigned these 'on' and 'off' states based on the numerical values of the state dependent variables (SDV's). SDV's, as the name suggests, vary with a function and in this case the function is a failure criterion. For example, the value calculated at every increment in the FE analysis for matrix damage in compression is stored as 'SDV1'. This variable gets fed into the next increment as an old variable ready to be updated. The SDV's are updated every increment and are normally used to decide what status to give the FV's. For example, when SDV1 = 1 then FV changes status from '0' to '1', flagging matrix failure.

FV1: MATRIX COMPRESSION/TENSION FAILURE

FV2: FIBRE/MATRIX SHEAR FAILURE

FV3: MATERIAL DAMAGE (SHEAR NONLINEARITY) – applicable to Chang-Chang only.

	Field variable				Percentage of property retained (in-plane)			
FAILURE MODE	FV1	FV2	FV3		E_1	E_2	v_{12}	G_{12}
NO FAILURE	0	0	0	----->	100%	100%	100%	100%
MATRIX CRUSHING	1	0	0	----->	100%	5-10%	0	100%
MATRIX CRACKING	0	1	0	----->	100%	5-10%	0	5-10%
FIBRE FAILURE	0	0	1	----->	5-10%	5-10%	0	5-10%

Table 3-1. In-plane property degradation dependency on the failure mode

3.5 An overview of numerical model specifications

3.5.1 Introduction

The selected failure criteria were implemented in Abaqus/Standard within a User Defined Field subroutine (USDFLD) written in Fortran. The USDFLD allows state dependent variables and user defined fields to describe the failure criteria, omitting the need to write the constitutive equations. The finite element analyses were carried out for small-scale multidirectional lay-up composite plates and large-scale woven composite plates subjected to simple loading conditions. All the simulations use thick shell elements of type S4R. Two different types of numerical techniques available in Abaqus/Standard were applied to solve the non-linear equilibrium equations: Newton Raphson method and Riks method, both of which are briefly described in following sections.

3.5.2 Shell element formulation

The S4R element is has a finite-strain formulation which assumes finite membrane strains and arbitrary large rotations are permitted and are suitable for large strain analyses. These elements are based on first-order transverse shear flexible theory in which the transverse shear strain is assumed to be constant through the thickness. The transverse shear stress is calculated through the thickness of the shell, for the case of unidirectional bending and assuming linear elastic response. They include the change in shell thickness in their formulation by specifying Poisson's ratio for the section. Thickness change is calculated by

enforcing plane-stress condition and using the Poisson's ratio to allow the thickness to change as a function of membrane strains only. The elements have 3 displacement and 3 rotational degrees of freedom are the structural plate is discretized with shell elements by defining the geometry at the reference surface of the shell.

Abaqus assumes only bending and shear in the x-direction and that the shell section directions are the principal bending direction. Unless the shell is not symmetric about the mid-surface, it is assumed that bending about one principal direction does not require a restraining moment about the other direction. If the plate is not symmetric, then the transverse shear stiffness approximations made are therefore less accurate.

Therefore, assuming moments are only taken in the x-direction, the equilibrium within the section in this direction is that shown in Equation (3-20) i.e. transverse shear stresses are produced as a result of the bending stresses.

$$\frac{\partial \sigma_{xx}}{\partial x} + \frac{\partial \tau_{xz}}{\partial z} = 0 \tag{3-20}$$

Another expression, taking the moment equilibrium about the y axis gives Equation (3-21). Where V_x is the transverse shear force per unit width of the plate and M_{xx} is the moment per unit width of the plate.

$$V_x + \frac{\partial M_{xx}}{\partial x} = 0 \tag{3-21}$$

Abaqus uses the inplane properties of the plate to calculate the stress in the x direction. It is a function of the stiffness matrix components and the inverse of the section stiffness matrix components and of the bending moment in the x direction. i.e. Equation (3-22), where z is the distance from the reference surface $\overline{z}$.

$$\sigma_{xx} = \left(C_{x1} - (z - \overline{z})C_{x2}\right)M_{xx} \tag{3-22}$$

Where C_{x1} and C_{x2} are matrix products of the stiffness matrix and inverse section stiffness matrix.

Differentiating w.r.to x gives:

$$\frac{\partial \sigma_{xx}}{\partial x} = \left(C_{x1} - (z - \overline{z})C_{x2}\right)\frac{\partial M_{xx}}{\partial x} \tag{3-23}$$

This is then put into (A) and $\frac{\partial M_{xx}}{\partial x}$ is replaced with V_x from Equation (3-21) to give:

$$\therefore \frac{\partial \tau_{xz}}{\partial z} = \left(C_{x1} - (z - \overline{z})C_{x2}\right)V_x \tag{3-24}$$

A variation of the transverse shear stress through the thickness of the plate.

The transverse shear stress for one layer (if composite) can then be calculated. The transverse shear stiffness is then calculated by matching the shear strain energy of each individual layer with that of the whole section. The continuum transverse shear stiffness used for each layer must be that obtained from the input file.

3.5.3 The Newton-Raphson method

The Newton-Raphson method is a numerical technique for solving the non-linear equilibrium equations. Considering a material point with one degree of freedom, such as a displacement, where k_0 is the initial material stiffness (a constant). For a non-linear problem, we can say that the material stiffness k changes with changes to displacement. This can be represented by the following expression that considers the non-linear variable part of the stiffness K_N (a function of displacement u), separately from the constant stiffness term k_0. Both added together gives the tangent stiffness k_t.

$$k_t = k_0 + k \tag{3-25}$$

Therefore for an applied load P a simple expression relating the stiffness and the displacement is:

$$P = Ku = (k_0 + k_N)u \tag{3-26}$$

Calculating the first iteration

1. For this example, assume to start from a state of equilibrium where the displacement u_0 is known for an applied load P_0, such as from a linear material behavior. A further load is going to be applied, for which the corresponding displacement is required.

2. Apply the new load P_1 and find a better displacement approximation u_a.

The load can be described as a truncated Taylor series about the first displacement u_0. As load P is also a function of displacement u, then:

$$P = f(u_0) + \left(\frac{dP}{du}\right)_0 \Delta u \tag{3-27}$$

Then expanding dP/du separately gives Equation (3-28):

$$\frac{dP}{du} = \frac{d}{du}\left(k_0 u + k_N u\right) = k_0 + \frac{d}{du} k_N u = k_t \tag{3-28}$$

Equation (3-28) shows the tangent stiffness being a function of the constant stiffness k_0 and the non-linear stiffness function k_N. For this first iteration, u would be equal to u_0 thus giving the following two Equations (3-29) and (3-30):

$$P_1 = f(u_0) + (k_0 + k_{N0})\Delta u_a \tag{3-29}$$

$$P_1 = f(u_0) + k_{t0}\Delta u_a \tag{3-30}$$

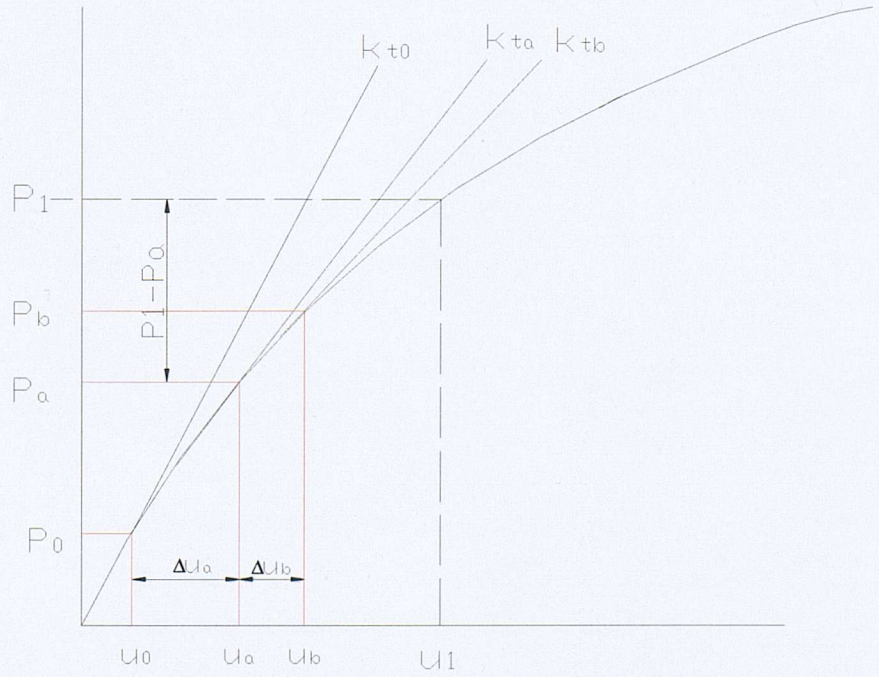


Figure 3-1. The Newton Raphson iterative process to find a solution for u1 caused by load P_1

The load imbalance is the difference between the applied load P_l and the force in the material when it is stretched (in this example) by u_0. Dividing by the value of the tangent stiffness at the old displacement u_0 gives the new displacement estimate Δu_a.

$$\frac{P_l - P_o}{k_{t0}} = \Delta u_a \tag{3-31}$$

Calculating the second iteration

Further iterations are performed until the most accurate displacement is obtained for the given load applied. For this second iteration the next tangent stiffness k_{ta} needs to be calculated at the previously found displacement $u_a = u_0 + \Delta u_a$. This is obtained using equation (3-28). Then applying the truncated Taylor series expansion about u_a to obtain Δu_b.

$$P_l = f(u_a) + (k_0 + k_{Na})\Delta u_b \tag{3-32}$$

$$P_l = P_a + k_{ta}\Delta u_b \tag{3-33}$$

This procedure is similarly applied for further iterations until u_l is obtained.

3.5.4 The Riks Analysis

The Newton Raphson method is often not robust enough for very non-linear problems, such as snap-back behaviour or when load-displacement response shows a negative stiffness. The Riks method is a variant of the Newton method. A Riks analysis has two quantities that it can serve as a measure of the solution progress:

1. Arc length along the static equilibrium path in load-displacement space
2. Load proportionality factor (LPF)

In a Riks analysis the displacement and the current load magnitude are both unknown quantities, unlike in most static FE analyses where the displacement of the structure is calculated in response to a known load. The Riks analysis cannot use 'time' to obtain a solution but uses the arc length along the static equilibrium path. The load magnitudes depend on a single scalar value which is the LPF. In each increment of the solution, the LPF is determined as part of the solution. When an increment converges it means that the solution

has been found for a load state that has been uniformly scaled by the LPF. The LPF provides direct indication as to the load magnitude at each increment. This information is very useful, for example for finding when 'snap through' may occur and how the load is changing in a post-buckling analysis. The LPF may not be a monotonically increasing value for an unstable model therefore it cannot be used directly for plotting 'load/displacement' curves.

$$P_{total} = P_0 + \lambda(P_{ref} - P_0) \tag{3-34}$$

3.5.5 An eigenvalue buckling analysis based on linear elastic theory

A buckling analysis is used to find critical load at which a structure becomes elastically unstable. This analysis is properly termed `bifurcation buckling.' The buckling problem is formulated as an eigenvalue problem. This involves finding the loads for the following stiffness matrix singularity:

$$Ku = 0 \tag{3-35}$$

A buckling mode is the actual shape the structure (in this case a plate) buckles into. The shape can be described with *eigenvectors* i.e. the deformation vectors **u**. The buckling mode shapes (eigenvectors) are normalized and do not represent an actual displacement value for the deformation and the largest component is 1.0. Thus, the stresses should only be interpreted as a relative distribution of stresses.

If the buckling analysis follows a previous analysis, the geometric stiffness at the base state, K_{g0}, is included in the buckling analysis, unless geometric non-linearity is not selected. If the buckling step is the first step in the analysis, then the stiffness matrix is the tangent elastic stiffness K_t, and K_{g0} is equal to zero, see Equation (3-36). In this last case, the eigenvalue problem for a particular eigenmode 'i' can be expressed as Equation (3-37).

$$\left(k_t + k_{g0}\right)u = 0 \tag{3-36}$$

$$\lambda_i k_t u_i = 0 \tag{3-37}$$

The first assumption of classical stability is that the structure remains linear until buckling. The second assumption is that the non-linear stiffness matrix, depends linearly on the displacements and similarly it depends linearly on the loads, P, see Equation (3-38).

$$k_N(\lambda P) = \lambda k_N(P) \tag{3-38}$$

The eigenvalue λ can be extracted using two methods in Abaqus/Standard and for the extraction of less than 20 eigenmodes the subspace iteration eigenvalue solver is more than adequate.

Any load applied in the eigenvalue analysis is known as a 'live' load, P and its magnitude is not important. A static perturbation analysis is first carried out to obtain the incremental stresses $\Delta\sigma$ corresponding to the applied load P. Following this, the eigenvalue extraction part of the analysis takes place. The critical load, P_c, for a particular buckling mode can be obtained by multiplying the extracted eigenvalue with the incremental loading pattern.

$$P_c = \lambda_i P \tag{3-39}$$

3.5.6 A non-linear buckling analysis

In real-life, structural imperfections and nonlinearities prevent most real-world structures from reaching their eigenvalue predicted buckling strength, in other words it over-predicts the expected buckling loads. Therefore the eigenvalue method is not recommended for accurate, realistic buckling prediction analyses.

A non-linear analysis can be carried out to see the buckle and post-buckle behaviour of a plate. A non-linear buckling analysis is more accurate than an eigenvalue analysis because it employs non-linear, large-deflection static analysis to predict buckling loads. If the loading on the structure is perfectly in-plane (membrane or axial stresses only), the out-of-plane deflections necessary to initiate buckling will not develop, and the analysis will be unable to predict the buckling behavior. To overcome this problem and thus to begin the buckling response, it is necessary to apply a small out-of-plane perturbation, such as through the application of a marginally off-axis load or a small temporary force or a specified displacement. One of the best ways of doing this is by carrying out a preliminary eigenvalue buckling analysis of the plate structure to predict the buckling mode shape. The structure in the eigenvalue analysis should be of the same shape and size as in the non-linear analysis. It

is then possible to choose appropriate locations for applying imperfections (perturbations) to promote the desired buckling response. The chosen imperfection should match the location and size of the imperfection in the real structure. In the present case, three imperfection sizes were tested: 0.5mm, 1mm and 2mm at the centre of the plate for mode I buckling. The sensitivity to these imperfections is discussed later in this chapter.

In the non-linear analysis the applied load is gradually increased until a load level is found whereby the structure becomes unstable (where a very small increase in the load will suddenly cause very large deflections). This analysis can be extended into the post-buckled range by activating the Riks arc-length method. This feature, as explained above, is used to trace the load-deflection curve through regions of 'snap-through' and 'snap-back' response.

3.6 Numerical modelling of a transversely loaded E-glass/polyester plate

3.6.1 Introduction

This section serves to validate finite element work and test data carried out by Shenoi et al [37, 38] on transversely loaded E-glass/polyester plates. Abaqus/Standard was used to study the non-linear behaviour, first ply failure and ultimate failure of various sized laminates with clamped edge conditions.

Shenoi et al modelled three different plate dimensions of the same lay-up, 0/45/90/-45/0, and thickness 3.43mm, however for the present verification model only the square plate of 0.6x0.6m was analysed for comparison.

3.6.2 The finite element model

The composite plate was modelled using 400S4R thick shell elements, using one element through the thickness. The in-plane material properties used are shown below, where X and Y denote the strength in the fibre and orthogonal to the fibre direction and the subscripts 'T' and 'C' stand for tensile and compressive values.

E_{11} = 23.6GPa; E_{22} = 10.0GPa ; E_{12}=1.0GPa; v_{12}=0.23; X_T =735MPa; X_c = 600MPa; Y_T =45MPa; Y_c=100MPa; SC= 45MPa.

Two non-linear analyses were carried out. The first neglected damage development and the other applies Tsai-Wu and Hashin's damage criteria to depict onset of material failure using the USDFLD subroutine.

The load is applied incrementally in Shenoi et al's analyses and the Newton-Raphson method used to solve the non-linear equilibrium equations.

3.6.3 Finite Element Results and Discussion

The predictions made by Shenoi et al and those obtained from the present validation work include maximum out-of-plane displacement (o.o.p), to be found at the plate centre, and the pressure at first ply failure and ultimate failure, shown in Table 3-2. The results are shown for the Tsai-Wu and Hashin models and are compared to the test results which were obtained by Shenoi et al. The pressure-displacement curves produced by the validation analyses for a no-damage model and a model using Hashin's failure criteria are shown in Figure 3-2.

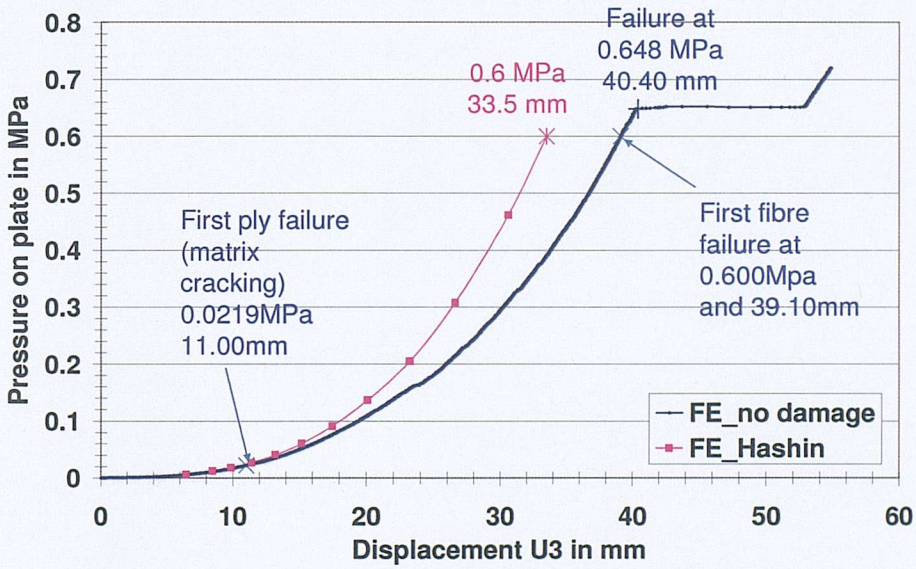


Figure 3-2. Pressure-displacement curve from the validation analyses, for no-damage and the Hashin failure model

Model	Maximum o.o.p deflection / mm	Pressure at first ply failure (matrix) /MPa	Pressure at ultimate failure (fibre) / MPa
Shenoi, test	*41.7*	*0.035*	*0.605*
Shenoi, Tsai-Wu	*40.9*	*0.0221*	*0.610*
FE validation Using Tsai-Wu	34.15	0.0255	0.602
Shenoi, Hashin	*41.0*	*0.0218 Bottom layer*	*0.6*
FE validation Using 2d Hashin	40.4	0.0219 Bottom layer.	0.648

Table 3-2. Test and FE results for Shenoi's work.

3.6.4 Simple theoretical calculations

Simple theoretical calculations for the maximum deflection were carried out for comparison with the finite element results modelling damage and no damage and the results are shown in Table 3-3. The maximum (undamaged) deflection was calculated using three different equations. The first assumes small deflection theory of isotropic plates, applicable to thick plates. The second is based on large deflection theory (and isotropy again) for thin plates where the load is supported largely by membrane action. The third is applying the small plate deflection theory for especially orthotropic laminated plates.

1. Treating plate as isotropic and applying small deflection theory:

$$w = -0.00140\frac{p_0 a^4}{D} \quad \text{for clamped boundaries} \tag{3-40}$$

$$\text{Where} \quad D = \frac{Et^3}{12(1-\nu^2)}, \; p_0 \text{ is the pressure and E is the isotropic modulus} \tag{3-41}$$

2. Treating plate as a membrane and applying large deflection theory:

$$w = 0.802\left(\frac{a}{2}\right)\sqrt[3]{\frac{p_0\left(\frac{a}{2}\right)}{Et}} \tag{3-42}$$

Where 'a' is the plate length and 't' is the thickness.

3. Treating the plate as orthotropic. The stiffness coefficients for the entire laminate (D_{ij}) are calculated from the summation of the transformed individual ply properties:

$$D_{ij} = \frac{1}{3}\sum_{k=1}^{N}(\overline{Q}_{ij})(z_k^3 - z_{k-1}^3) \tag{3-43}$$

The bending stiffness coefficients D_{ij} and the bending strength values are sensitive to the changes in the relative position of various layers, namely the laminate stacking sequence, even when the number and type of layers remains unchanged. This is in contrast to the in-plane behavior of laminates, which is, to a first approximation, insensitive to the laminate stacking sequence. Therefore, bending and buckling computations should always be checked using the correct bending stiffness matrix computed for the actual laminate stacking sequence being used. The transformed stiffness properties from the local principal to global

principal directions were calculated for the following coefficients: Q_{11}, Q_{12}, Q_{22}, Q_{66}. The transformation equation, for example for the fibre (11) direction is as follows:

$$\overline{Q}_{11} = Q_{11}\cos^4\theta + 2(Q_{12} + 2Q_{66})\sin^2\theta\cos^2\theta + Q_{22}\sin^4\theta \tag{3-44}$$

The maximum central transverse displacement equation for a especially orthotropic laminated plate was applied, Equation (3-45).

$$w = \frac{16P_0}{\pi^4}\sum_{m=1,3,5..}^{\infty}\sum_{n=1,3,5..}^{\infty}\left[\frac{\frac{1}{mn}\sin\frac{m\pi x}{a}\sin\frac{n\pi y}{b}}{D_{11}\left(\frac{m}{a}\right)^4 + 2(D_{12}+2D_{66})\left(\frac{m}{a}\right)^2\left(\frac{n}{b}\right)^2 + D_{22}\left(\frac{n}{b}\right)^4}\right] \tag{3-45}$$

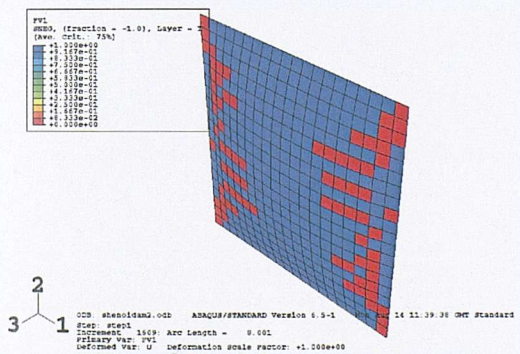
The displacement value given by the small deflection theory for isotropic plates is understandably larger than the other calculations as non-linear geometry and the effect of membrane action in supporting the load are not considered. This calculation was carried out to demonstrate how important it is to use the correct equation. In small deflection theory, the deflections are small (less than the thickness of the plate) and the middle plane of the plate does not stretch during bending and remains a neutral surface, analogous to the neutral axis of a beam. The load is fully resisted by bending and twisting of the plate and the effect of shearing forces is ignored. Plane sections rotate during bending so that they stay normal to the neutral surface and do not distort. In this way, the stresses and strains remain proportional to the neutral axis. Membrane action is most pronounced for thinner plates undergoing large deflections and the plate in question has a width-to-thickness ratio of 173 – thus largest deflection theory gives better results, which accounts for large deflections and membrane action. For deflections that are greater than the plate thickness, resembling the current case, a non-linear analysis will predict the stiffness of the plate and deflection with more accuracy than a linear analysis will. The FE model incorporating damage provides geometrical non-linearity and in addition allows failure to occur, providing results that are in very close proximity to the test.

Model	**Maximum o.o.p deflection / mm**
Shenoi test	42
Shenoi FE, no damage model	33
FE Validation, no damage model	33.5
Large deflection theory	31.67
Small deflection theory, isotropic, E=E11	1350
Theory - composite	64.6

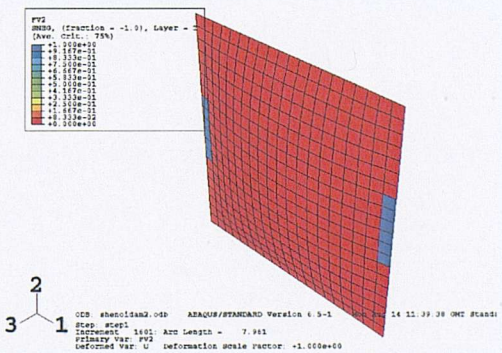
Table 3-3. Maximum plate deflection results

3.6.5 Matrix and fibre damage predictions

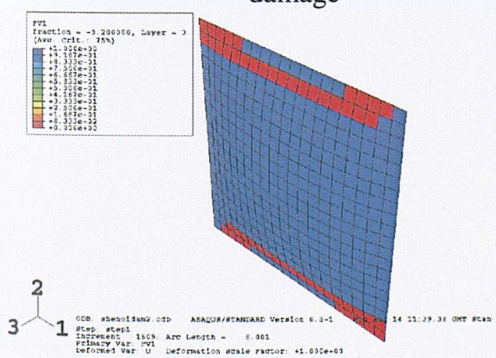
The results for the validation analysis with damage compare favourably with Shenoi et al's FE results. The point of ultimate failure obtained with the models, including Shenoi et al's, correlates well with Shenoi et al's test results although first ply failure is predicted at a lower pressure than in reality. The point of first matrix failure in the validation model took place at 0.0219MPa, compared to first ply failure at 0.6MPa. Matrix damage initiated close to the edges of the plate in the direction of the fibres for the 0° and 90° layers whereas for the 45° layers failure initiated from the corners. The failure pattern can be seen in Abaqus for each composite layer within the shell element by requesting element output of the field variables (FV) and state-dependent variable (SDV) for the relevant integration points (1,3,5,7,9 13,15, where 1 is the top, pressure loaded surface of the shell. The default number of integration points through the shell using Simpson's rule is 3. It is found that matrix cracking covers the majority of the plate at the point of full failure when fibre failure initiates at the edges perpendicular to the fibres of layers 1 (top 0° layer) and 5 (bottom 0° layer). After this point, further fibre failure occurs, affecting the inner layers of the plate as the out-of-plane displacement increases significantly under a negligible increase in load. Damage is shown by the blue colouring of Figure 3-3.



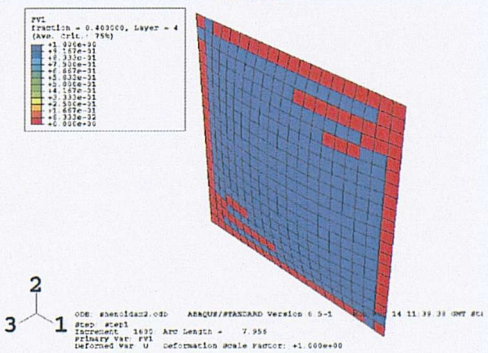
(a) Top, layer 1, 'compressive face' - matrix damage



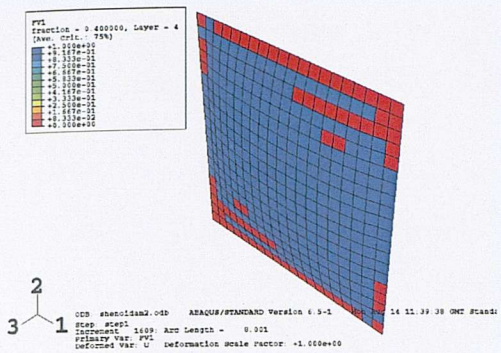
(b) top, layer 1, 'compressive face' - fibre failure



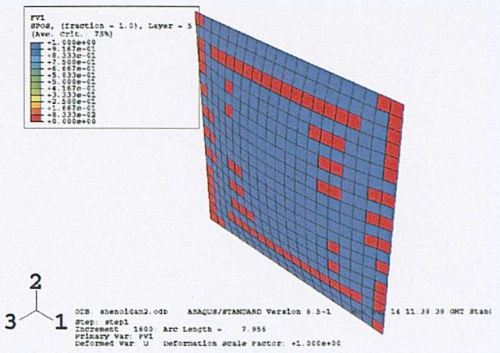
(c) Layer 2 - matrix damage



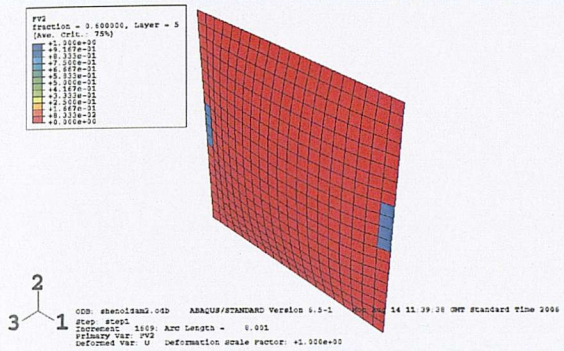
(d) Layer 3 - matrix damage



(e) Layer 4 – matrix damage



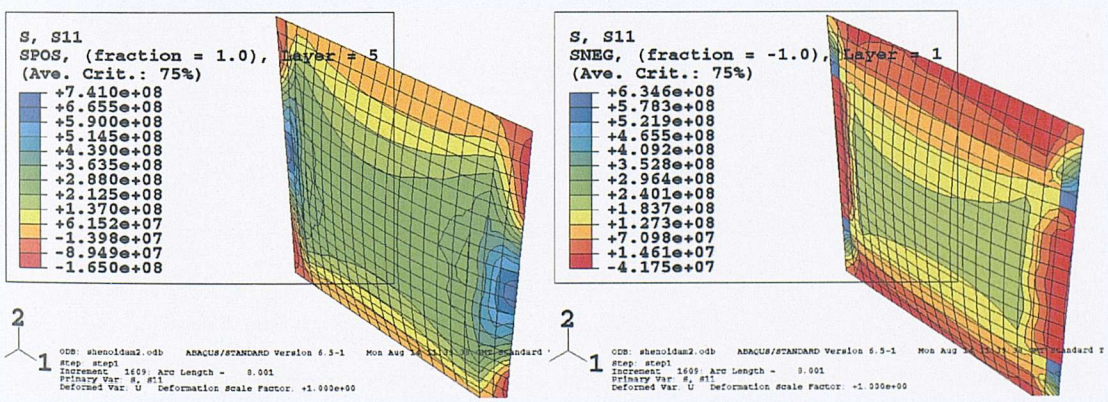
(f) Bottom, layer 5, 'tensile face' - matrix damage



(g) Bottom, layer 5, 'tensile face' - fibre damage

Figure 3-3. Fibre failure shown for a few layers

Figure 3-4 demonstrates how the bottom 0° ply (layer 5) is mostly in tension at the point of failure. The sides perpendicular to the 11 fibre direction have the highest tensile longitudinal (σ_{11}) stress, thus the reason why the elements in Figure 3-3 failed first from fibre failure under tensile loading, shown in blue. The top 0° ply (layer 1) has the same sides in compression, thus suffering compressive fibre failure instead.



(a) (b)

Figure 3-4. Stress along the fibre direction for (a) bottom, tensile face (layer 5) , and (b) top, compressive face (layer 1), in Pascal.

3.7 Large-scale testing and numerical modelling of thick composite panels under in-plane compression

3.7.1 Introduction

This study aimed to find the strength to failure of large woven composite panels and compare the results with finite element analyses. It formed part of a larger project which is concerned with modelling the residual strength of these panels after having incurred damage from a shock load. The tests performed were able to demonstrate the renowned sensitivity of panels to boundary conditions, which is also reflected in a parametric study carried out in Abaqus/Standard 6.4. Different stress-based failure criteria were implemented via a user-defined field (USFLD) subroutine to test their effectiveness.

The panels under investigation were un-stiffened, solid rectangular panels of dimensions 1.219mx0.9144mx0.019m (4ft x 3ft x 0.75 in) which were tested under in-plane compression under displacement control, see Section 2-6 of Chapter 2. These large panels are representative of typical naval applications such as in mine countermeasure vessels where longitudinal and transverse stiffened panels would be adopted. It is important to test a large enough panel as the shock loading tends to cause damage in the form of delamination which can be extensive and have a severe effect on the residual capacity of the panel [39]. A panel wide enough to contain a large delaminated area is required.

The panels were made from WR E-glass/Dow Derakane 8084 vinyl-ester composite, manufactured by an advanced vacuum assisted resin transfer moulding technique called 'CARTM' (Channel Assisted Resin Transfer Moulding). The panels comprised of 29 woven plies and the stronger orthogonal warp direction is parallel to the longest sides of the panels. The composite had a 70% fibre volume fraction and a low void volume fraction resulting from a superior consolidation of the fibres and matrix produced by the CARTM process. A rig was custom-built to apply a vertical load across the shortest length. A parametric study was carried out to examine the sensitivity of the FE models to changes in boundary conditions, loading type (load or displacement control); boundary conditions; material properties; residual stiffness and initial imperfection. The analyses in this study also used Hashin's 2d stress criteria to model matrix and fibre damage. A suitable mesh size was used in the FE analyses based on a short study involving three different mesh densities. The medium coarse in-plane mesh of 31x42 elements and one shell element through the thickness was applied.

3.7.2 Background

Delamination is a principal damage mode caused by a shock load and it is sometimes difficult to detect when the material is in service. The reduction of the material's stiffness and strength caused by delamination damage is most prominent under in-plane loading; that is when a load is applied parallel to the delaminated layers [40]. Subjecting a composite panel to in-plane loading allows deformation, damage propagation and residual strength of the panel to be evaluated.

The first work of its kind in the field of axial compression testing of composite plates was carried out by Hoff, Boley and Coan in 1948 [41], Ashton and Love, Kicher and Mandell, Willey, Verchery, Chailleuz, Hans and Verchery [3], and later on Banks and Harvey [42] and Marshall and Banks [43].

Hoff et al [44] proposed the first technique for in-plane compression testing of fibreglass panels to apply a uniform displacement along the loaded edges and simply supported flexural boundary conditions along all edges. They verified the influence of geometrical imperfections in significantly reducing the load-carrying capacity of the structure.

Kicher and Mandell [45] tested square graphite FRP plates to validate the use of classical buckling theories and the effects of membrane-bending coupling. Plates with simple/simple and simple/free boundary conditions were tested under uniform load control. The loaded edges were simply supported using wedge shaped bearings and a v-shaped piston controlled with a springs acted upon the top of the edge fixture and a soft loading-head was used. The springs had the same axial stiffness as the plate. The unloaded edge supports used rollers. The out-of-plane deflections were measured with an electrical micrometer and the Southwell method was used to obtain the critical load from the load-displacement curves. The results correlated well with the analytical methods.

Banks and Harvey in 1978 [42] and Marshall and Banks also in 1978 [43] studied the buckling and post-buckling of reinforced plastics using a rig similar to Hoff et al, aiming to validate some of their theoretical studies [46]. They used adjustable knife edges for the simple support unloaded edge conditions and used roller bearings for the loaded edges. The loaded edges were potted in polyester resin. A 900kN Timius Oken test machine was used and displacement controlled loading was applied. Two 90° rosette strain gauges were placed along the horizontal centre line on either side of the plate. The test results correlated

reasonably well with the analytical predictions. It was observed that the presence of imperfections had a significant effect in reducing the load carrying capacity of the plates.

With specific regards to the field of naval composites, a large volume of interesting work put together in 1990 can be found by Smith C.S. [47] who examined the design and testing of composite marine structures and provides formulas for naval design with structural composites.

More recently, in 1997, Bao et al [48] carried out a review of analytical solutions for bending and buckling of flat rectangular orthotropic thin plates with a combination of various simple supported and clamped boundary conditions. The analytical solutions were compared with Abaqus/Standard finite element analyses which were carried out using S4R shell elements for range of plate aspect ratios and thicknesses under in-plane compression. The analytical solutions are only valid up to a certain plate thickness which was verified with the FE solutions.

The influence of delamination length in composite plates and its location along the thickness on the critical buckling load was examined by Gaudenzi in 1997 [49]. Laminates with and without pre-existing delamination were subjected to in-plane loading and a parametric study was performed. The plates were modelled using 2d finite elements and an algorithm was implemented to control the contact constraints with the introduction of a contact element. However, the model's capability was limited to assuming that the delamination does not propagate.

It is important to understand the post-buckling behaviour of composite plates in order to recognise their design limits and although a moderate amount of literature has been produced in this area for solid plates, sandwich plates and reinforced plates, it is still an area under much research. Some early work in this field includes that by Chia and Prabhakara [50] examined the post-buckling response of unidirectional orthotropic plates made of graphite, glass and boron fibres in epoxy resin. They applied simply supported boundary conditions on all four edges and compared the behaviour of the composite plate to that of an isotropic plate. They found that the isotropic plates could support a higher load and for the same load, the composite plates produced greater deflections. Under these larger deflections, any small increase in stress triggered common failure mechanisms such as delamination. Much work was conducted at TELAC in MIT from 1978 onwards. Finch [51], Jensen [52], Jensen and Lagace [53], Lagace, Jensen and Finch [54], Minguet [55, 56] and Minguet, Dugundji and

Lagace [57, 58], produced extensive experimental and theoretical work on the buckling and post-buckling behaviour of flat, symmetrical and unsymmetrical laminated composite panels.

Also in the 1980's, Starnes and Rouse [59] carried out an experimental study to see the buckling and post-buckling effect of flat orthotropic rectangular 24 ply graphite/epoxy plates and amongst other things examined the effect impact damage carried out under velocities of 44 to 95ms^{-1} using a 12.7mm diameter aluminium sphere. A 1.33MN capacity hydraulic testing machine was used to in-plane compress plates of 0.508m in length and ranging from 0.076m to 0.241m wide. The thickest plate had a width-to-thickness ratio of 24. The loaded edges of the plates were clamped and the unloaded edges were simply supported by knife-edge restraints. Out-of-plane deflections were viewed using the Moiré-fringe method and strain gauges were placed back-to-back; one along the centreline near the point of maximum o.o.p displacement and another near the edge. Some of the initially un-damaged specimens supported up to 5 times their buckling load. It was found that the plates with higher initial buckling strains reach a lower failure load than those with smaller initial buckling strains. An interesting point was made regarding impact damage and residual strength. It was found that impact damage near a plate edge reduces the post-buckling strength more than impact damage in the plate centre.

The buckling and post-buckling response of anisotropic graphite-epoxy panels was studied both experimentally and using numerical simulations by Noor et al in 1989 [60]. Amongst other finding and as referenced in previous published work, they found that initiation of failure (categorised by the onset of delamination) in the post-buckling regime occurs at or close to positions of nodal lines.

In relation to woven plates manufactured using the SCRIMP process (see Section 2.2 of Chapter 2), Moy and Shenoi [38] subjected 34 thin rectangular woven plates to a transverse load using water pressure. The tests were carried out to see the effects of lay-up, method of manufacture and panel shape of the strength and stiffness. The plates had aspect ratios of 1, 1.5 and 2 for a fixed width of 0.6m, and a thickness ratio of 200. Initial damage was resin cracking, identified by the noise emitted during loading. The resin in the cracked regions had lost its initial sheen and at higher loads large cracks were observed to form across individual fibre bundles. The direction of the bulk of the cracks (longitudinal, transverse or at 45°) varied with aspect ratio. For an aspect ratio of 2, cracks only appeared parallel to the long edges. Up to aspect ratios of 1.5, cracks appeared in both directions. Strain distribution was

recorded across the plates along the centre lines. It was found that curves of non-dimentionalised load-deflection parameters could be produced to relate the effect of aspect ratio for each of the 4 lay-up configurations, however the study needed to be broadened to thicker plates to include the greater influence of bending stiffness. The tests showed that for the vast majority of the panels, failure along an edge, resulting in complete breakage of the panel. The failure mechanism was from combined tension, bending and transverse shear. Interestingly enough and perhaps an indication of scaling issues. it was found that the material strengths found from coupon tests were not appropriate for predicting panel failure. It was found that the method of manufacture played an insignificant role on the strength and stiffness. In terms of reinforcement, it was found that the more evenly distributed reinforcement and the more of it the greater the strength and stiffness.

More recently and more specific to naval composites and 24oz WR E-glass/Dow Derakane 8084 vinyl-ester, is work carried out by Roberts et al on solid and sandwich un-stiffened orthotropic panels of dimensions 1.9mx0.9mx0.0019m made using the VARTM process [61, 62]. The plates were potted using aluminium filled particular potting compound and the fixtures where clamped to create fully fixed end conditions. The unloaded edges were simply supported. Strain gauges were placed at along the centre lines. Abaqus/Standard and S4R elements were used to model a plate with clamped/simply supported edge conditions, giving good buckling load predictions compared to the test. Prior to this, a FE and analytical study was performed to see the effect of various boundary conditions, plate aspect ratios and plate thicknesses, on buckling [63].

The effect of varying the boundary conditions on the unloaded edges of composite plates subjected to buckling loads has been taken approached by Chai and Khong [64] using a semi-numerical approach called the finite strip method. This technique can deal with uniform in-plane compression to pure in-plane bending for different boundary conditions along the unloaded edge. In later work, bending-twisting of the plate was addressed using multi-term trigonometric series functions to obtain the displacement function [65].

Even more recently Singer et al [3] discussed a number of world-wide experimental methods in buckling of thin-walled structures. The test methods described for composite panels mostly assume clamped conditions for the top and bottom edges and maximum composite panel size of 250mmx500mm.

Research relating to the effects of imperfection size is less common. Experimental

observation was carried out by Suh et al 2003 [66] on impact-damaged stiffened stitched and unstitched woven graphite/epoxy 3mm thick composite panels. Abaqus/standard using S8R shell elements was used to predict the buckling and failure strength of the panels under displacement control for simply supported boundary conditions and for various damage regions. The initial imperfection was introduced from a buckle analysis with 5 possible mode shapes. An imperfection size of 0.005m was assigned for mode I and 0.001m for the other four mode shapes. The damaged region resulting from the impact, was obtained from x-ray photos of the tested panel. These regions were assigned substantially lower material properties in the FE model. The in-plane material properties were obtained from coupon tests and the shear moduli were calculated from a micromechanics model.

3.7.3 Damage mechanism

The three main modes of damage; matrix cracking, delamination and fibre failure was created in the panels and are pin-pointed in Figure 3-6, shown for the compression face of the panel in test 4. The compressive face is regarded as the face which carries the largest compressive in-plane stresses, the tensile face sees the largest in-plane tensile stresses. The damage labels are explained in Table 3-4.

Label	Damage
1	Fibre breakage from horizontal stress, σ_{22}
2	Delamination along the fibre cause by matrix cracking from the horizontal stress, σ_{22}
3	Delamination spread
4	Fibre breakage from longitudinal stress, σ_{11}

Table 3-4. Labels describing the damage mode, for Figure 3-6.

Transverse cracks created in the resin-rich regions between the woven plies from stresses σ_{11} and σ_{22} , can create in-plane cracks along the higher stressed fibre-matrix boundary leading to delaminations, see Figure 3-5. Such delaminations were created along the length of the fibres in several locations on the plates, shown with label 2 in Figure 3-6.

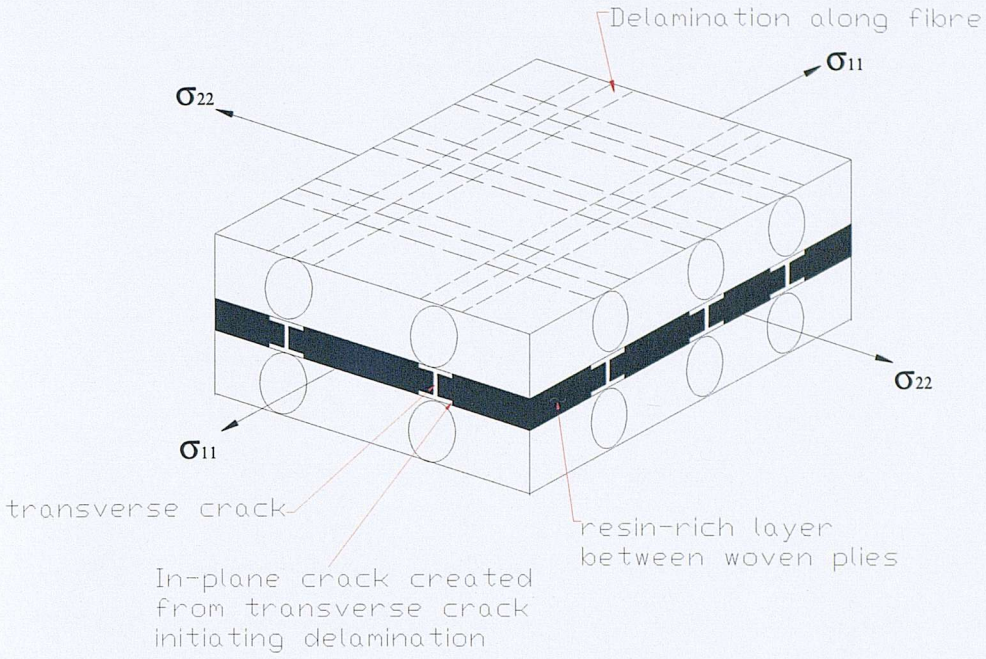


Figure 3-5. A highlight of potential cracks and delamination in a schematic of the woven laminate, showing the woven bundles of fibres.

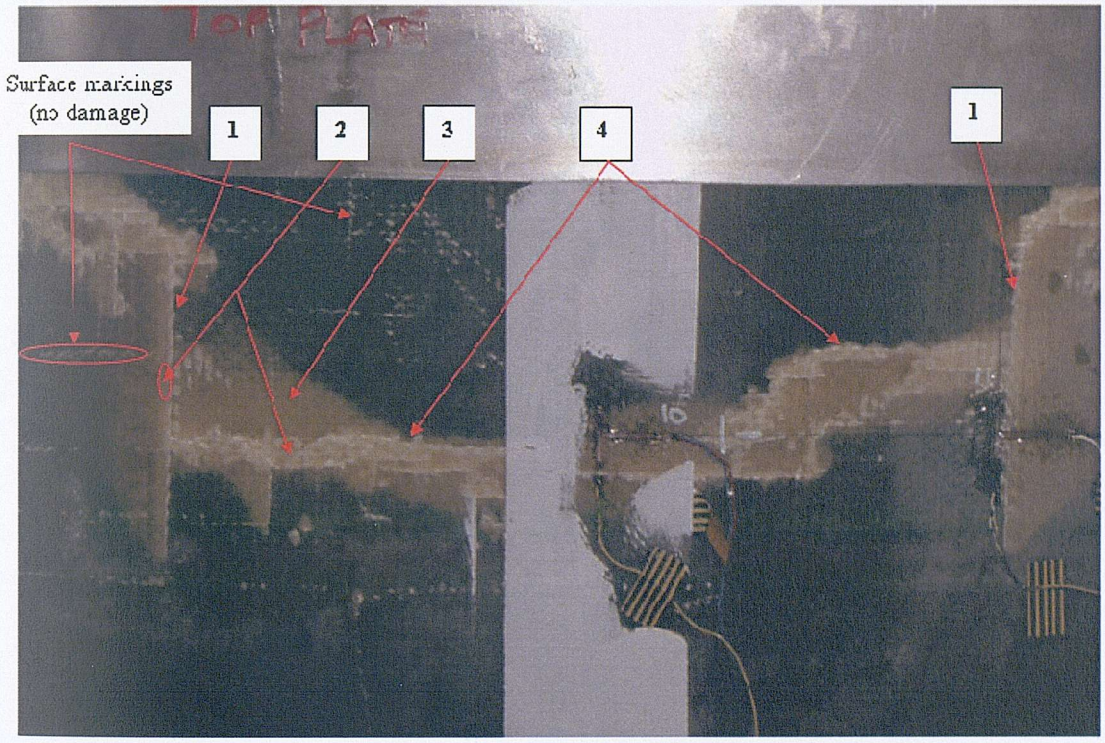


Figure 3-6. Damage highlighted on the panel in test 4, compression face

3.7.4 The Finite Element model

Finite element analyses were carried out using the commercial finite element code Abaqus/Standard. The panel was modelled with S4R thick-shell elements using one shell element through the panel thickness.



Figure 3-7. Layerwise modelling method

The orthotropic woven composite layers were stacked within the shell in a 'layerwise' fashion, each layer having three integration points. Due to the especially non-linear behaviour of the buckling event, a Riks analysis was performed to effectively trace the non-linear equilibrium path of the buckling process. Half of the FE analyses were carried out using displacement control of the top edge, representative of the actual test conditions and the other half were performed under incremental load control thereby allowing displacement variation in the loading direction.

Material characterisation tests were carried out following ASTM test procedures and the average properties used in the analyses are found in Tables 2-1 and 2-2 of Chapter 2. There is some scatter in the modulus results for the weft and the fill directions; the weft being marginally stronger than the fill. However, for lack of knowledge as to the weft or fill directions in the panels, a single average value of all the in-plane fibre-direction moduli for both directions was implemented.

A number of FE analyses were carried out to interpret the behaviour of the panel tests. The FE analyses 'Load_S_1S_2_i2_10%' (load controlled) and 'Disp_S_1S_2_i2_10%' (displacement controlled) were modelled with all four sides simply supported, average material properties, an initial central imperfection of 2mm, and 10% retention of material properties on failure (90% degradation). Although the tests were carried out under displacement control, there were times when the load had to be adjusted due to a load in-balance between one load cell and the other. Thus it was considered important to see the effect of load control analysis on the failure of the panel. The simply supported boundary conditions for the top edge of the panel and pinned bottom edge were chosen to represent the test conditions. The imperfection size is the distance the plate centre deviates from complete flatness. A 2mm imperfection

size (a 0.002 scaling factor for mode I from the initial perturbation analysis) at the plate centre was used as an initial estimate based on approximate measurements of one of panels prior to testing. A 10% residual of all material properties was retained on fibre failure at each element integration point. Other FE analyses have been carried out with changes to these modelling conditions, described under Section 3.7.7.

Hashin's 2D failure criteria was used to model fibre and matrix damage [10] using the user defined subroutine USFLD coded in Fortran. Material characterisation tests were carried out following ASTM test procedures and the average properties used in the majority of the FE analyses are found in Table 1. Hashin was chosen after some preliminary analyses carried out to test this and other criteria, namely: maximum-stress, a simple quadratic stress criterion, Equation (3-19), Tsai-Wu, Equation (3-5), and Chang-Chang, Equations (3-13) to (3-17), see Figure 3-8. This figure also shows the experimental results for plate tests 2 and 3 described in Section 2-6 of Chapter 2 and also shown in Figure 3-11.

The boundary conditions used for these analyses were pinned at the top and bottom edges and simply-supported at the sides. Chang-Chang's equations produced a significantly different result from Hashin's due to the shear term in the fibre compression failure equation, not present in Hashin's equations. The figure also shows some of the fibre damage and matrix damage predictions. Modelling no damage leads to the un-realistically large load-displacement curve, as seen in Figure 3-9.

Hashin's failure criteria were applied in two ways. Given the fact that the criteria were developed for unidirectional laminae, the fibre damage is dependent on the principal stress along the fibre direction 'σ_{11}'. This suggests that in the case of the woven laminate, the fibre failure criterion should be applied to both the orthogonal in-plane fibre directions of the laminate. The same reasoning cannot as easily be applied to the matrix damage criterion because this relies on a substantially weaker matrix-dominated material direction, orthogonal to the principal fibre direction, which the woven laminate does not have. However, the criteria were applied separately to each orthogonal direction and failure of either mode was determined as:

$$F_m = \max\left[F_{m1}, F_{m2}\right] \geq 1 \tag{3-46}$$

$$F_f = \max\left[F_{f1}, F_{f2}\right] \geq 1 \tag{3-47}$$

Where F_{mi}, F_{fi} are the values of the failure functions for matrix and fibre failure in the two orthogonal inplane directions i=1,2.

The second method of implementing Hashin's matrix and fibre failure criteria was as intended for a unidirectional composite; taking the fibre direction in the longitudinal direction of the plate and the transverse presumed 'matrix-dominated' direction orthogonal to this, along the width of the plate.

$$F_m = F_{m2} \geq 1 \tag{3-48}$$

$$F_f = F_{f1} \geq 1 \tag{3-49}$$

This second method can be more readily applied to the given problem because the loading is unidirectional and is fibre dominated.

3.7.4.1 Modification of Hashin's compressive matrix damage equation

Although Hashin's two criteria proved to be the most effective at modelling the in-plane compression of the composite panels, the load-displacement curves are not the correct shape during the damage phase. It was found that they predicted too much drop in load once damage initiated – regardless of the boundary conditions, material properties, residual load or initial imperfection. Figure 3-10 highlights this fact with predictions using Hashin's full equations and three different boundary conditions: simply supported (S1S2), no rotation at the top edge (C1S2) and equal rotation for all points along the top edge (E1S2). Instead, it was found that excluding the separate shear term in the equation to give Equation (3-50) gives a load/displacement curve that does not droop towards the peak load, thus producing a good correlation with experiment, see 'Hashin_S1S2' plot.

$$\frac{\sigma_{22}}{Y_C}\left[\left(\frac{Y_C}{2S_{12}}\right)^2 - 1\right] + \left(\frac{\sigma_{22}}{2S_{12}}\right)^2 \geq 1 \tag{3-50}$$

2d Hashin matrix compression formulation modified

In contrast, removing the shear term from the equation for fibre damage (in tension) made negligible difference to the damage prediction and load/displacement curve, as highlighted with a circle on the graph. It is interesting to note that in Yamada and Sun's [67]failure

criteria applied to the fibre direction, the shear term is included for both the compressive and tensile modes, whereas in contrast, Hashin includes this only for tension and Camanho and Lambert [68] only for compression. Hashin expressed σ_{11} and σ_{12} as being mutually weakening and thus proposed a convex locus for these two stresses. However for a more drastic approximation, a maximums stress criterion was also suggested. For compressive fibre failure, Hashin expressed the uncertainty of the axial stresses on the weakening or strengthening effect of the fibre direction compressive strength. Thus, Hashin presented the fibre compressive failure criterion in the simple maximum stress form. In the case of a woven composite under in-plane loading, this latter point justifies the removal of the shear parameter in Hashin's matrix damage equation for a compressive load, since the woven composite has fibres in the two orthogonal directions. This proposed modified expression gives better results.

$$\sum_{i=1}^{2}\sum_{i=1}^{2}\left(\frac{\sigma_{ij}}{S_{ij}}\right)^2 \geq 1 \tag{3-51}$$

Where S_{ij} is the strength of the material in the direction ij

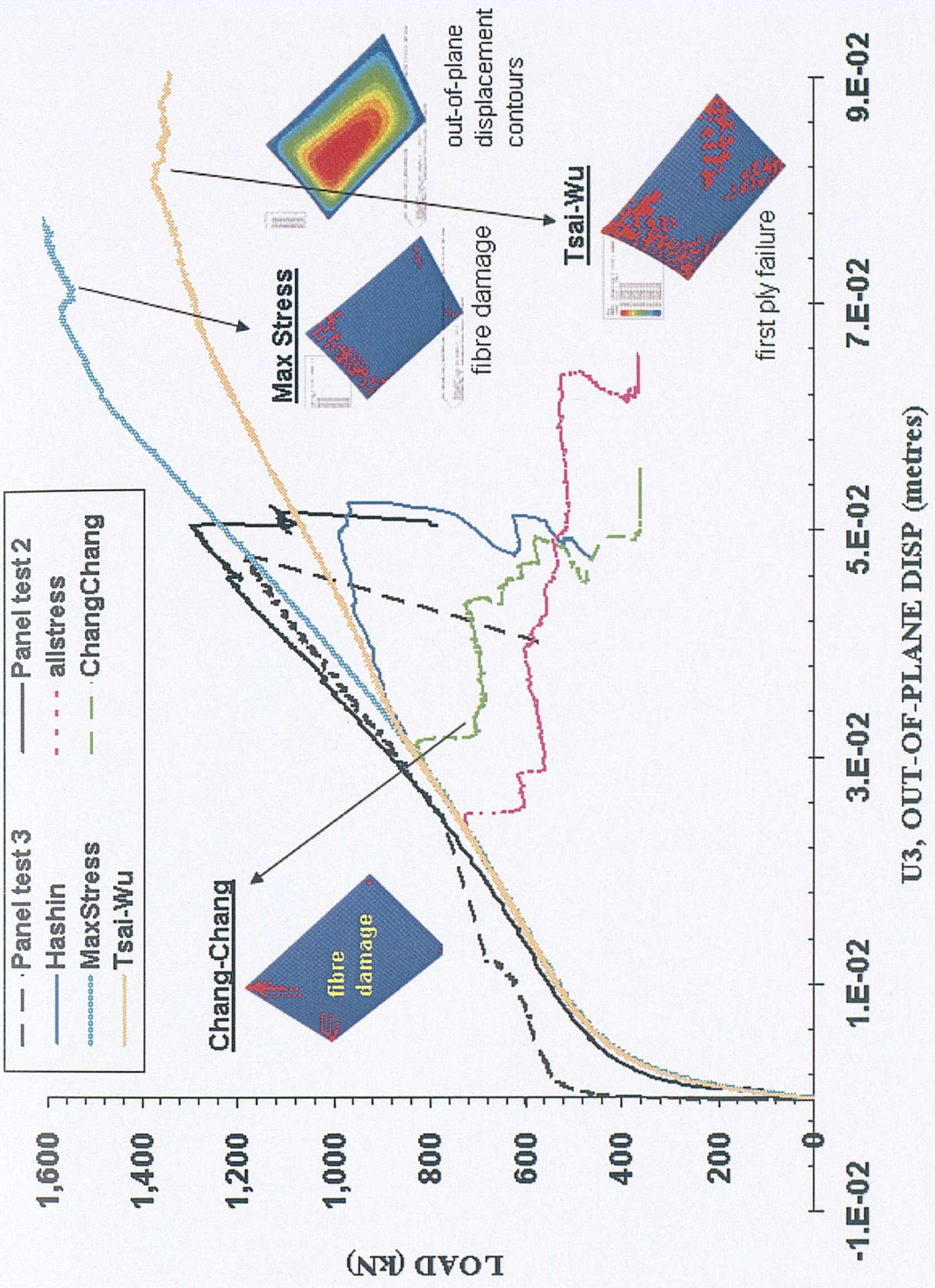


Figure 3-8. Load-displacement curves for analyses employing different failure criteria

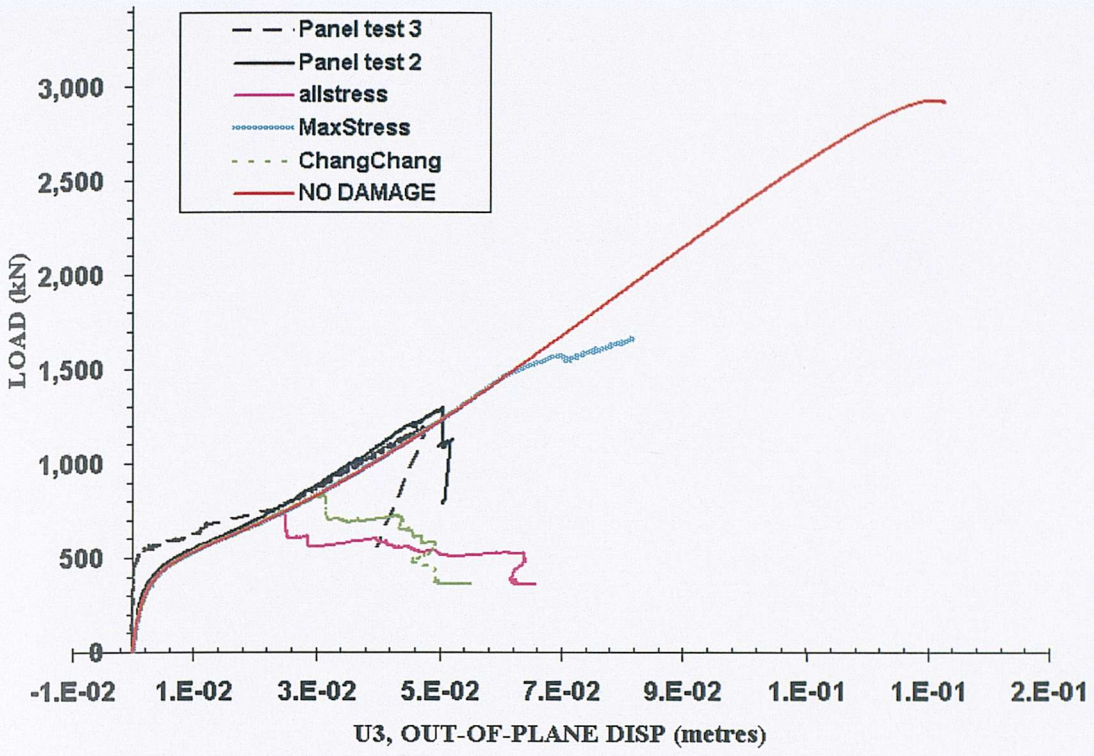


Figure 3-9. Load-displacement cuves, demonstrating the importance of modelling damage

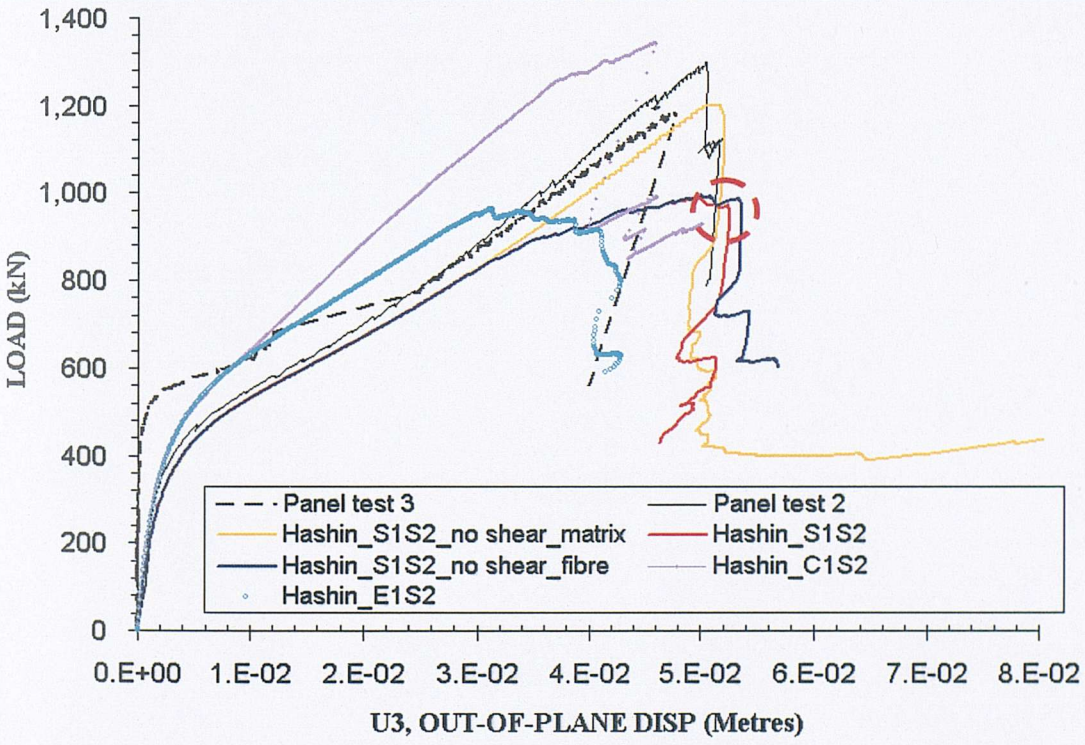


Figure 3-10. Load-displacement curves, including variations of Hashin's criteria and different boundary conditions.

Based on the above, the ensuing analyses, unless otherwise specified, apply this modified version of Hashin's 2d criteria, i.e. the implementation of Equations (3-7), (3-8), (3-10) and (3-50).

3.7.5 Buckling loads

The load-displacement plots for the five panel tests are shown in Figure 3-11.

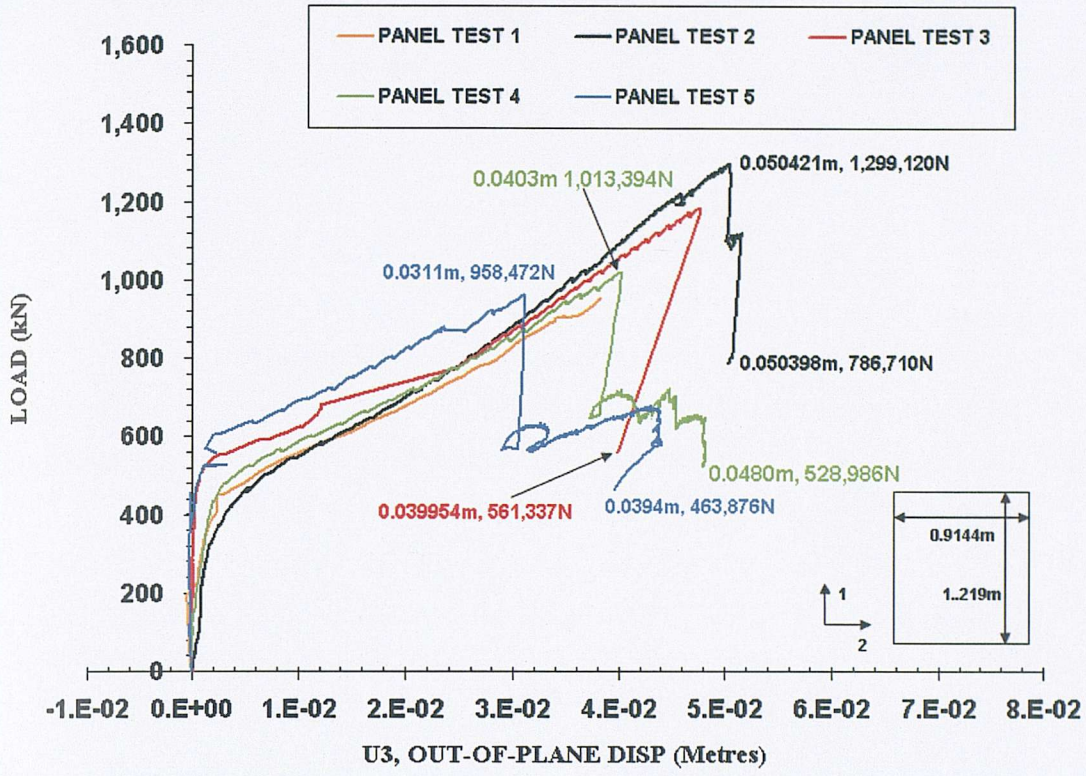


Figure 3-11. Load-displacement curves for the five panel tests

The experimental buckling loads were calculated by taking the tangent of the pre-buckle and post-buckle curves and taking the load reading where the two lines meet. The values are checked with those taken using a similar approach from stress-strain curves, some of which are shown later. The buckling loads for the five tests show a scatter of up to 25%. If the average of the test buckle loads is calculated and compared to the FE result in Table 3-5, the difference between the two values is only 3%.

Test number	Buckle load /kN
Test 1	440
Test 2	440
Test 3	540
Test 4	460
Test 5	580
FE [1]	474

[1] From analyses: Load_S_1S_2_i2_10% and Disp_S_1S_2_i2_10%

Table 3-5. Critical buckling loads from the tests

FE – simply supported.[1]	FE – equal rotation constraint.[2]	FE – clamped top & bottom.[3]	Theory: simply supported.[4]	Analytical: simply supported.[5]
474.52 kN	681.1 kN	747.2 kN	370.4 kN	441.9 kN

[1.] From analyses: Load_S_1S_2_i2_10% and Disp_S_1S_2_i2_10%

[2.] From analyses: Load_E_1E_2_i2_10% and Disp_E_1E_2_i2_10%

[3.] From analyses: Load_C_1C_2_i2_10% and Disp_C_1C_2_i2_10%

[4.] Equation (3-57)

[5.] E.Greene, equation (3-61)

Table 3-6. FE and theoretical critical buckling loads

Exact analytical solutions for obtaining the critical buckling load are limited to a few loading combinations and boundary conditions. Therefore most buckling problems are solved using approximate methods such as Rayleigh-Ritz, Galerkin, finite difference and the finite element methods. The finite element method is increasingly one of the most common methods used to calculate the buckling and also post-buckling behaviour of structures. The buckling solution for laminated composite plates used to calculate the theoretical buckling load in Table 3-6 will be briefly explained here. The Kirchoff hypothesis is assumed which does not include transverse shear deformations. Studies have shown that the buckling stress predictions are smaller in thicker plates when the shear deformation is included than when classical laminate theory is assumed. The total strains are given by Equation (3-52), where ε^o are the membrane (stretching) strains and k are the strains due to bending alone.

$$\begin{bmatrix} \varepsilon_1 \\ \varepsilon_2 \\ \varepsilon_{12} \end{bmatrix} = \begin{bmatrix} \varepsilon_1^o \\ \varepsilon_2^o \\ \gamma_{12}^o \end{bmatrix} + z \begin{bmatrix} k_1 \\ k_2 \\ k_{12} \end{bmatrix} \tag{3-52}$$

The in-plane forces are related to the mid-plane strains as shown in Equation (3-53) and the out-of-plane moments are related to the curvature changes of the plate as shown in Equation (3-54). The coefficients A_{ij}, B_{ij} and D_{ij} are stiffness coefficients with subscript numbering in accordance with plane stress conditions. Because the WR laminate in the current work has the same fibre orientation at the same distance above as below the mi-plane, (in face through-out the whole laminate) it can be termed 'symmetric'. This means that the B_{ij} coefficients relating to bending-extension coupling can be removed from the force and moment matrices. Similarly, so can A_{26}, A_{26}, which relate to shear-extension coupling and D_{16} and D_{26} which are for bend-twist coupling. Labelling the laminate thickness as 't' and the distance from the mid-thickness of the layer to the mid-plane of the laminate as 'z',

Equations (3-55) show how the coefficients are derived. The D_{ij} coefficients were also defined earlier in Section 3.6.4.

$$\begin{bmatrix} N_1 \\ N_2 \\ N_{12} \end{bmatrix} = \begin{bmatrix} A_{11} & A_{12} & A_{16} & B_{11} & B_{12} & B_{16} \\ A_{12} & A_{22} & A_{26} & B_{12} & B_{22} & B_{26} \\ A_{16} & A_{26} & A_{66} & B_{16} & B_{26} & B_{66} \end{bmatrix} \begin{Bmatrix} \varepsilon_1^o \\ \varepsilon_2^o \\ \gamma_{12}^o \end{Bmatrix} \tag{3-53}$$

$$\begin{bmatrix} M_1 \\ M_2 \\ M_{12} \end{bmatrix} = \begin{bmatrix} B_{11} & B_{12} & B_{16} & D_{11} & D_{12} & D_{16} \\ B_{12} & B_{22} & B_{26} & D_{12} & D_{22} & D_{26} \\ B_{16} & B_{26} & B_{66} & D_{16} & D_{26} & D_{66} \end{bmatrix} \begin{Bmatrix} k_1 \\ k_2 \\ k_{12} \end{Bmatrix} \tag{3-54}$$

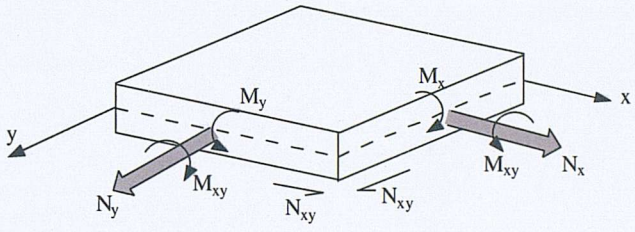


Figure 3-12. Loading on a plate element

$$A_{ij} = \sum_{-t/2}^{t/2} \bar{Q}_{ij} dz, \quad B_{ij} = \sum_{-t/2}^{t/2} \bar{Q}_{ij} z dz, \quad D_{ij} = \sum_{-t/2}^{t/2} \bar{Q}_{ij} z^2 dz \tag{3-55}$$

A plate buckles when the in-plane compressive load is large enough to cause the plate to become unstable and bend into a wavy configuration. Bi-furcation buckling is a mathematical concept. The initally flat configuration of the plate is sometimes called the *membrane pre-buckled state*. Under this state, the plane can only undergo extension, compression or shear. As the load in first applied, the plate shortens in the load direction but remains flat and only at a critical load does the plate become unstable and buckle and thereafter an out-of-plane displacement is produced. In reality, imperfections in real materials causes the plate to bend initially before the buckle load and produce an out-of-plane deflection. Only after the buckle load does the plate stiffness reduce although the plate can still support a higher load.

The simplest form of buckling is to apply an in-plane compressive load to simply supported edges and allowing the unloaded edges to have no support. This closely resembles an Euler column. With this plate configuration, once a critical load is reached, the plate is unable to

support any more load. This is unlike the behaviour of a plate with it's unloaded edges prevented from moving out-of-plane, causing the centre of the plate to bulge while the sides remain vertical. In this case, buckling loads are usually much lower than the loads required to create damage in the plate.

The derivation of the following equation can be obtained in numerous structural references and is thus unnecessary to include in the current text. Analysis of plate buckling under in-plane loading involves the solution of an eigenvalue problem. The critical buckling load can be determined from the stationary value of the total potential energy of the plate. The energy is the sum of internal energy (produced by bending alone) and potential energy from the applied load. Consider a unit element of size $\delta x \delta y$ of a thin plate and call the in-plane forces N_x, N_y, and N_{xy} acting per unit width of the plate, for the respective normal and shear direction, see Figure 3-13. Taking 'w' as the out-of-plane displacement, the contribution of the loads to the equilibrium of the element in the z-direction can be expressed as shown in the RHS of Equation (3-56).

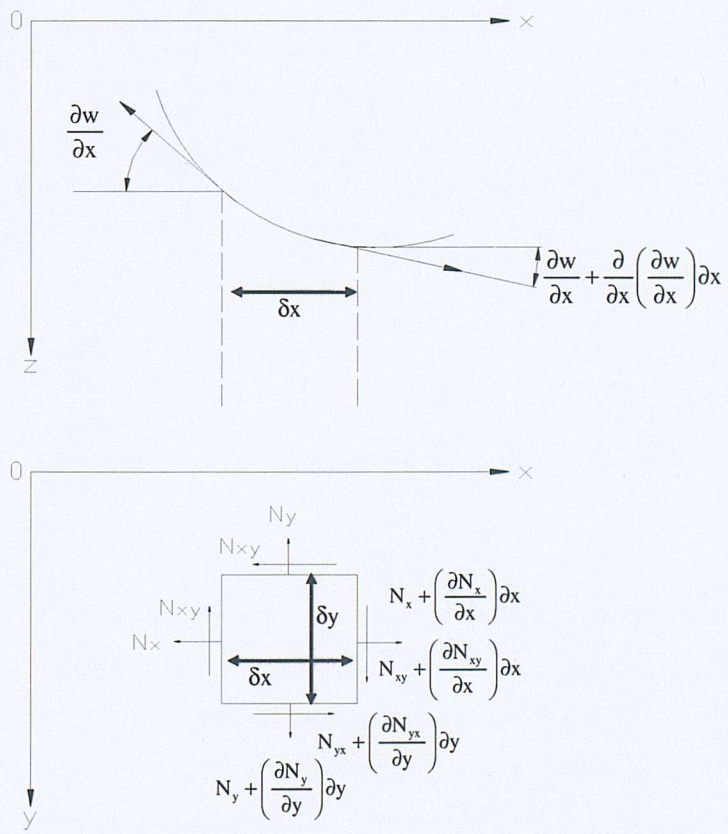


Figure 3-13. In-plane forces on a plate element

The equilibrium equation for the bending moment contributions of a symmetrical orthotropic plate is shown on the LHS of Equation (3-56).

$$D_{11}\frac{\partial^4 w}{\partial x^4}+D_{22}\frac{\partial^4 w}{\partial y^4}4D_{16}\frac{\partial^4 w}{\partial x^3\partial y}+2(D_{12}+2D_{66})\frac{\partial^4 w}{\partial x^2\partial y^2}+4D_{25}\frac{\partial^4 w}{\partial x\partial y^3}$$
$$=N_x\frac{\partial^2 w}{\partial x^2}+N_y\frac{\partial^2 w}{\partial y^2}+2N_{xy}\frac{\partial^2 w}{\partial x\partial y} \quad (3\text{-}56)$$

Navier (1820) proposed the Fourier series for the deflection of w, which is a function of the plate size and also a function of 'm' and 'n', representing the number of half waves in the x and y directions respectively. Solving for the boundary conditions for a simply supported plate, the critical buckling stress for loading in the x-direction only can be shown in Equation (3-57), putting n=1 and m=1.

Studies to examine the relationship between the plate aspect ratio, loading stress and the buckle mode (the number of half wavelengths the plate buckles under), has lead to plots of the non-dimensional buckling stress parameter $\frac{k_x}{\pi^2}$, against the aspect ratio. This parameter is shown in Equation (3-58).

$$\sigma_x=\frac{\pi^2}{tb^2}\left(D_{11}\left(\frac{a}{b}\right)^2 m^2+2(D_{11}+2D_{66})n^2+D_{22}\left(\frac{a}{b}\right)^2\frac{n^4}{m^2}\right) \quad (3\text{-}57)$$

$$\frac{k_x}{\pi^2}=-\frac{\sigma_x tb^2}{\pi^2 D_{22}} \quad (3\text{-}58)$$

The critical buckling load is obtained by multiplying Equation (3-57) by the plate thickness, 't'.

The stiffness coefficients D_{ij} for the orthotropic plate described in Equations (3-55), have been calculated as shown in Equations (3-59). The stiffness matrix constants for the orthotropic plate, Q_{ij}, can be written in terms of the engineering constants, see Equations (3-60). The 'transformed' stiffness matrix constants in Equation (3-55) have not required transformation into a global coordinate system of the plate where the x and y axes are orthogonal to the sides of the plate, because all the layers have the same layout, with fibres in both orthogonal directions. Thus, in this case $\overline{Q}_{ij}=Q_{ij}$ and Equation (3-44) used earlier is not required.

$$D_{11}=\frac{Q_{11}t^3}{12}, D_{22}=\frac{Q_{22}t^3}{12}, D_{12}=\frac{Q_{12}t^3}{12}, \quad D_{66}=\frac{Q_{66}t^3}{12} \tag{3-59}$$

$$Q_{11}=\frac{E_1}{1-v_{12}v_{21}}, \quad Q_{22}=\frac{E_2}{1-v_{12}v_{21}}, \quad Q_{12}=\frac{v_{12}E_{12}}{1-v_{12}v_{21}}, \quad Q_{66}=G_{12} \tag{3-60}$$

Each woven layer is orthotropic and neglecting any small variations in the normal and orthogonal in-plane directions makes it possible to put $D_{11}=D_{22}$. This gives a mode 1 buckling load of 370.4kN .

The assumptions related to plate bending and buckling of plates is as follows:

- In-plane displacement 'u' and 'v' and out-of-plane displacement 'w' are small compared to the plate thickness. This generally indicates small-deflection theory.
- The in-plane stresses (in x-y plane) dominate the behaviour of the plate. The transverse stresses are taken as zero for a state of plane-stress. This assumption also becomes increasingly unreasonable as the plate width-to-thickness decreases.
- Transverse shear and normal strains are taken as negligible as part of the Kirchoff hypothesis. This results in plane sections remaining plane after bending (i.e. non-deformable normals to the middle surface).
- The in-plane strains are small compared to unity (small-strain theory) and are linear function of the transverse z coordinate.
- Negligible rotatory inertia terms.

The main restrictions of plate theory are:

- Applicability only to thin plates, i.e. where the thickness is very small compared to the length and width.
- With regards to composite plates, the stiffness of each layer must be calculated in relation to the plate axes.
- The plate is linear-elastic.
- The plate is of constant thickness.

Another expression used for calculating the buckling load of composite panels was proposed by Eric Greene [69] whose work uniquely addresses the naval industry. The expression takes into account the orthotropy of a laminate and is used to obtain the analytical solution in Table 3-6 shown in Equation (3-61).

$$N_{xCR} = \left(h_c - \frac{C_c\left(E_{fb}\mu_{fab} + 2G_{ba}\left(1-\mu_{fba}\mu_{fab}\right)\right)}{\sqrt{E_{fa}E_{fb}}} \right) \times \frac{\sqrt{E_{fa}E_{fb}}}{1-\mu_{fba}\mu_{fab}} \left(\frac{t^3}{b}\right)$$

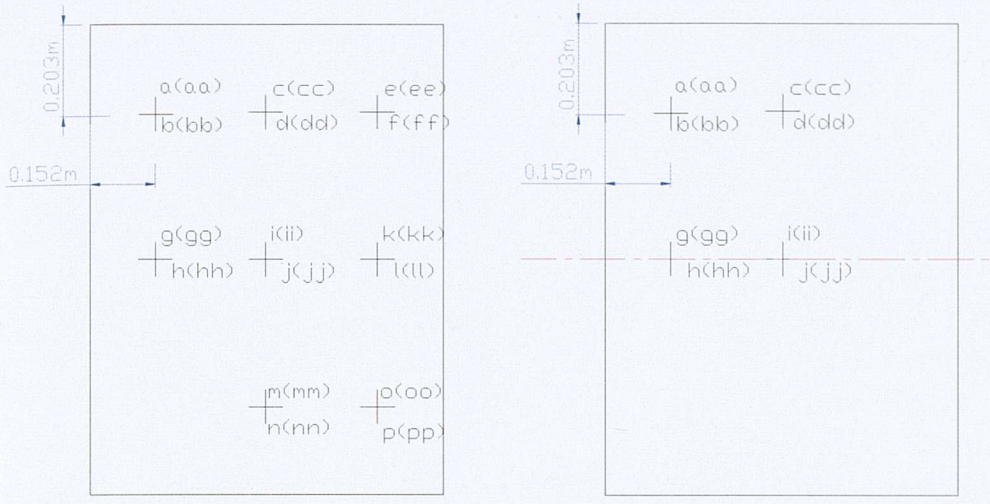
$$\text{where } h_c = h_c(bc's, r) \text{ for which } r = \frac{a}{b}\left(\frac{E_{fb}}{E_{fa}}\right)^{\frac{1}{2}} \qquad (3\text{-}61)$$

E_{fa} and E_{fb} are flexural moduli in the two in-plane principal directions; μ_{fab}, μ_{fba} are Poisson's ratios with the primary stress across the length 'a' and width 'b' of the panel respectively; t is the thickness of the laminate; h_c is a parameter obtained from a chart [69], which is a function of edge stiffener factor 'r' and the boundary conditions; C_c is a parameter which is dependent on the boundary conditions; and G_{ba} is the in-plane shear modulus. For all edges simply supported: h_c= 1.7 and C_c= $\pi^2/6$ and for loaded edges clamped and sides simply supported: h_c= 2.58 and C_c= $\pi^2/6$.

The buckle load calculated with this expression compares particularly well with the results for tests 1, 2 and 4 and only 7% under-estimated compared to the FE prediction.

3.7.6 Panel test strains

Strain gauges were positioned across the whole of the plate at 8 horizontal and vertical locations on both sides for test 2, as shown in Figure 3-14(a). For tests 3 to 5 strain gauges were located only on the top quarter of the plate on both sides, shown in Figure 3-14(b). The gauges are labelled alphabetically, with single alphabet labelling for the compressive face and double labelling on the tensile face as shown. Each panel had one side significantly rougher than the other and possessed two 20mm wide ridges attributable to the location of the infusion channels used in the CARTM process. Panels with lower failure loads are associated with lower strains, seen in Figure 3-15 and Figure 3-16 for gauge locations a, c, aa and cc, and smaller o.o.p displacements as can be seen in Figure 3-11. The gauge readings at locations 'e', 'ee' and 'a', 'aa' for test 2 are plotted in Figure 3-17 to show the difference in strain between these two top corner locations, particularly noticeable on the tensile side. This asymmetry is discussed later.



(a) Test 2 (b) Tests 3,4 & 5

Figure 3-14. Strain gauge locations for tests 2 to 5. The face in compression has gauges labeled with double letters, shown in brackets.

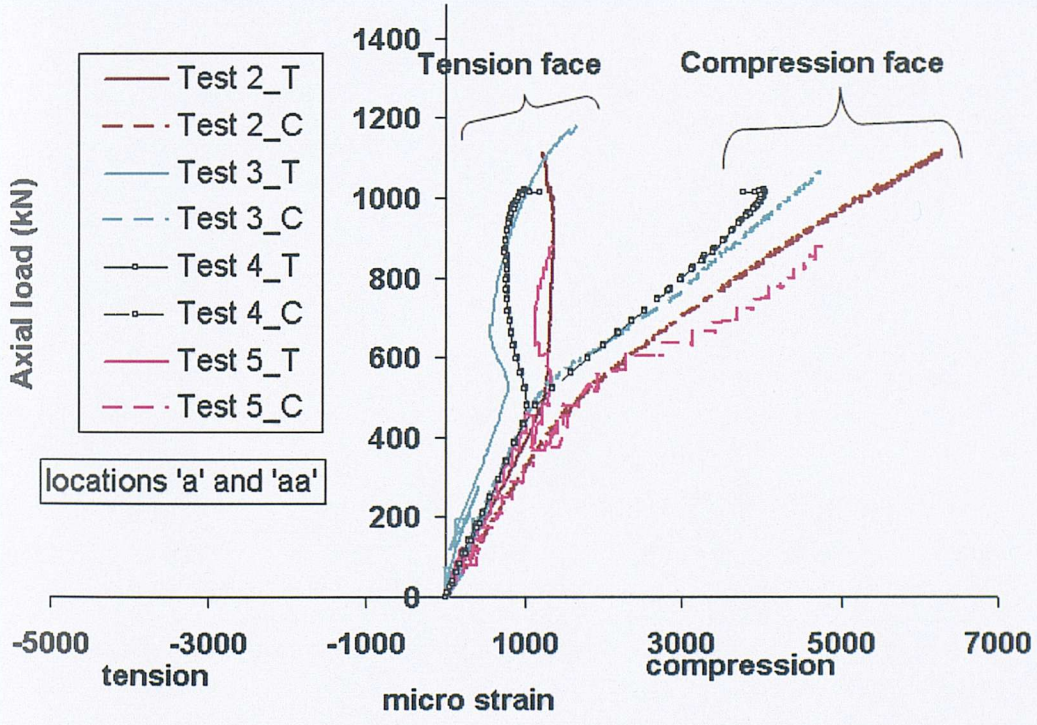


Figure 3-15. Panel test 2, 3, 4 & 5 load-strain curves at locations 'a' and 'aa'.

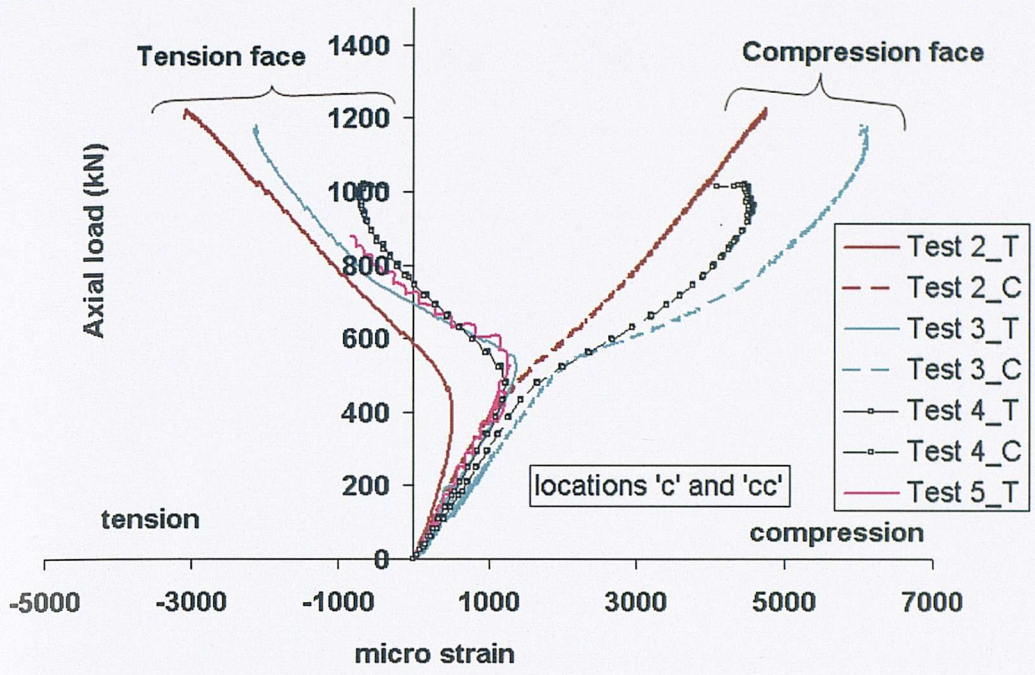


Figure 3-16. Panel test 2, 3, 4 & 5 load-strain curves at locations 'c' and 'cc'.

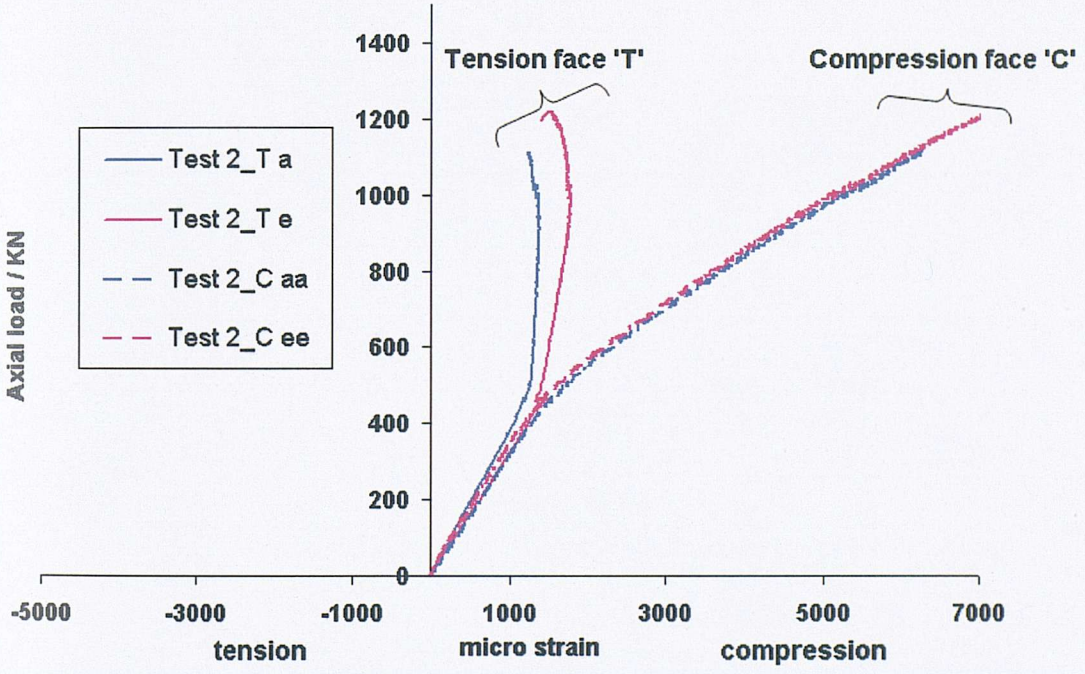


Figure 3-17. Load-strain curves for panel test 2 at locations 'a', 'aa', 'e' and 'ee'.

The strain readings at each strain location for each panel have been averaged and plotted against each other. Figure 3-18 shows a plot of the average longitudinal strains and Figure 3-19 of the average horizontal strains. The greatest variation in strains amongst all the plates appears to be in the top region of the plate. The largest strains were obtained for panel test 2.

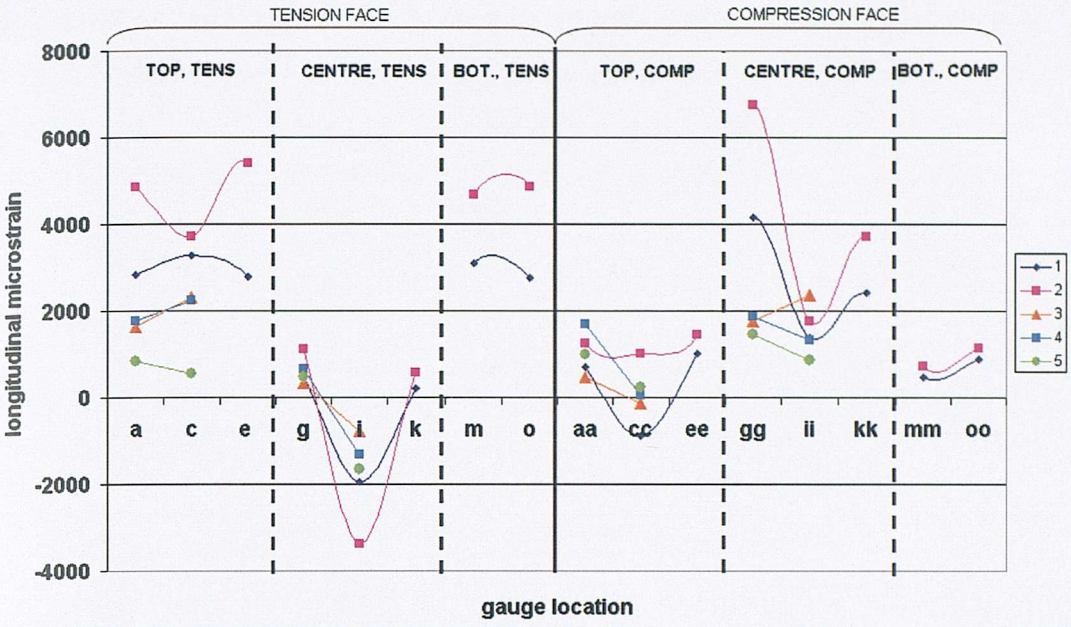


Figure 3-18. Average longitudinal strains at all the strain locations for all five panel tests

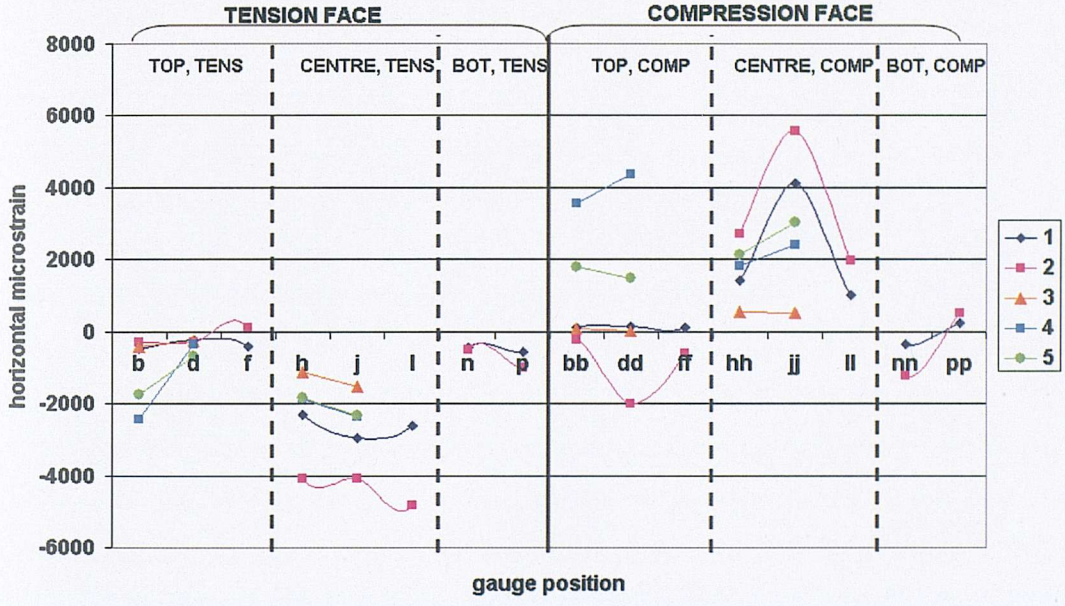


Figure 3-19. Horizontal strains at all the strain locations for all five panel tests

3.7.7 A parametric study in finite element

A parametric study in Abaqus/Implicit was carried out to examine several variables. All but one analysis was modelled with average material properties and vertical sides were simply supported in all the models but the effect of changing the top and bottom edge boundary conditions was examined. The key to an analysis name can be found in Table 3-7. For example, the analysis labelled 'Disp_C_1C_2_i2_10%' was modelled using average material properties, simply supported vertical sides, top and bottom edges clamped, a central

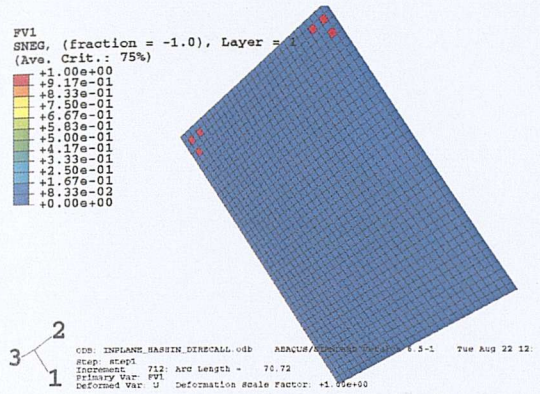
imperfection of 2mm and 10% of the material properties were retained after material point failure. The equal rotation constraint is applied using multiple point constraints, which constrains the degree of freedom of certain nodes relative to others using a linear equation. In this case, the nodes along the plate edge are limited to rotate only as much as a node next to the corner node.

Loading type	
Load	Loading of the top edge applied under load control
Disp	Loading of the top edge applied under displacement control
Boundary conditions for top and bottom edges	
S_1	Simply supported top edge
S_2	Simply supported bottom edge
C_1	Clamped top edge
C_2	Clamped bottom edge
E_1	Constant rotation constraint top edge
E_2	Constant rotation constraint bottom edge
Other analyses conditions	
i2, i1, i0.5	Central panel imperfection of either 2mm, 1mm or 0.5mm
5%, 10%	Percentage of properties retained after damage, either 5% or 10%
Min/Max	Minimum/maximum properties applied, obtained from the range of coupon test results.

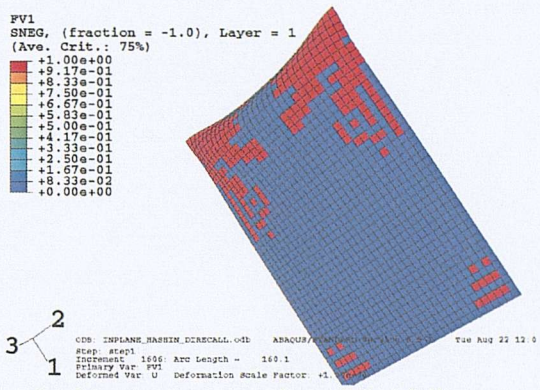
Table 3-7. Key to FE analysis labels

Implementation of Hashin's criteria: It was found that applying the matrix damage criterion to the woven material in both orthogonal directions, 'method 1', produces earlier matrix damage and fibre damage that initiates across the plate, as shown in Figure 3-20(a) and (c). In contrast fibre damage in the panel tests always initiated near the corners and propagated in an angle towards the vertical centre-line of the plate. After failure, the plates continue to deform mainly in the top quarter of the plate as an increased level and rate of matrix and fibre damage develops, as shown in red with Figure 3-20(b) and (d). This damage cannot be compared with any experimental results because in the tests once the load dropped to a residual value it was unsafe to carry on loading. The initiation of matrix and fibre failure for an analysis using method 1, 'load_S1S2_i2_Hash(bi)', is shown in Figure 3-21, with the respective labels 'M' and 'F'. The peak load is more conservative with this method of implementation than if method 2 is applied. However, method 2 which applies Hashin as though the panel material were unidirectional, provides better damage predictions and a better load-displacement shape and for this reason this method of application is used in the foregoing analyses. Generally, even though method 2 provides an upper bound peak load, larger than that obtained for panel tests 4 and 5, the shape of the load-displacement curve is very similar to all the tests, more so than with method 1. The negligible change in panel

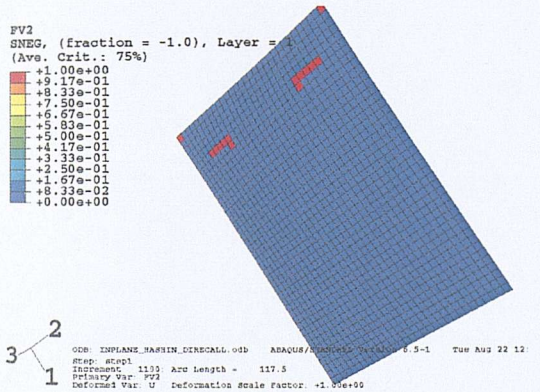
stiffness in the tests is a consequence of fast damage development in the later stages of loading and then failure from the sudden onset of fibre fracture. This is contrary to the more gradual prediction with method 1, which is largely dominated by in-plane cracking caused by the longitudinal σ_{11} stress and early fibre failure in both orthogonal directions, thus creating a significant change in stiffness prior to failure.



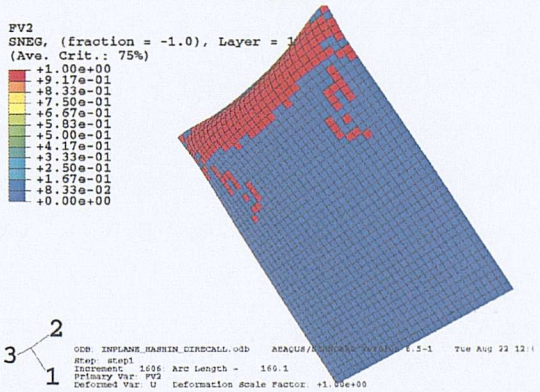
(a) Start of matrix damage at 812kN



(b) Matrix damage after global failure at 416kN



(c) Start of fibre failure, at 920kN



(d) Fibre damage after global failure at 416kN

Figure 3-20. Damage predictions for analysis 'load_S1S2_i2_Hash(bi)' shown in blue.

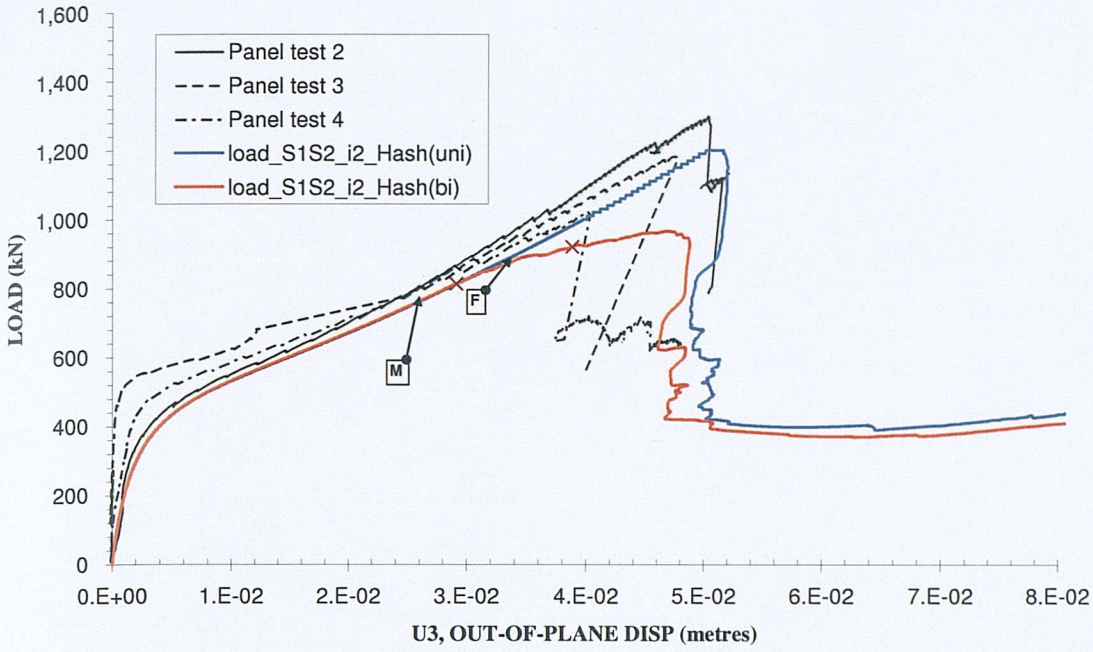


Figure 3-21. Load-displacement curves, comparison of the two methods of applying Hashin and three panel test results

It could be surmised from the above results that Hashin's criteria must be applied with the intention they were developed for. The criteria were developed using uni-directional laminates which have a weaker matrix dominated direction and this shows when they are applied to woven laminates. Checking for matrix damage in the two in-plane orthogonal directions of a woven laminate will predict early matrix damage. This is likely because the fibre presence in the orthogonal '22' direction will have an effect on the ease of formation and location of cracks compared to a uni-directional laminate, even if the Y_T and Y_c strength properties in the failure criteria are equal to those of X_T and Xc respectively. The location of the cracks will not necessarily be the same for a woven roving and a uni-directional laminate.

Boundary conditions: The sensitivity to boundary conditions in the FE analyses is the same for both load and displacement control analyses. Figure 3-22 shows the effect of reducing the mobility of the top and bottom horizontal plate edges. The analyses shown were all carried out under load control with a 2mm central imperfection and 10% residual stiffness. Preventing rotation of the edges by assigning clamped conditions, 'C1C2' for both edges produces the greatest pre- and post-buckling stiffness. Clamping the top edge in 'C1S2' reduces the fold that is created at the top of the plate more so than clamping the bottom edge and thus reduces the damage development concentration in the top half of the plate, thus producing a higher residual strength.

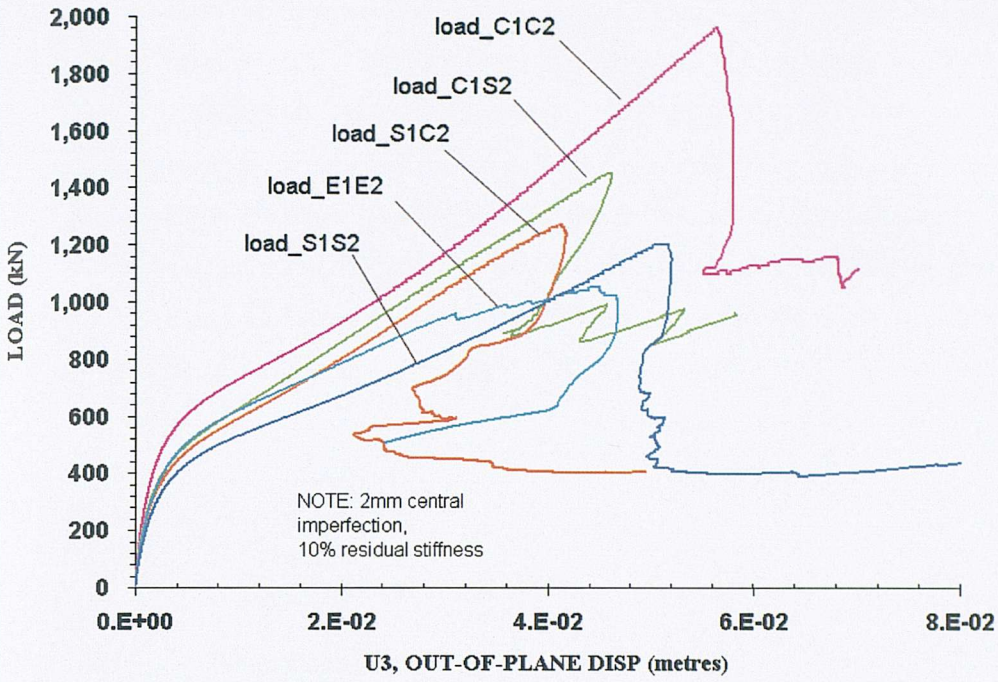


Figure 3-22. Load-displacement curves, demonstrating ensitivity to bc's, using load control FE analyses

Residual stiffness: On failure of a particular mode, from either tensile or compressive failure, the effect of increasing the residual of each modulus from 5% to 10% has a significant effect on the residual strength of the panel. This is shown in Figure 3-23 for a displacement controlled analysis, the same effect is also experienced with a load controlled analysis. The residual capacity of the plate is measured just after the plate has suffered global failure, when a significant drop in load is seen for a minor change in deflection. Thus the red lines shown in Figure 3-23 are indicative of the residual loads for the two analyses.

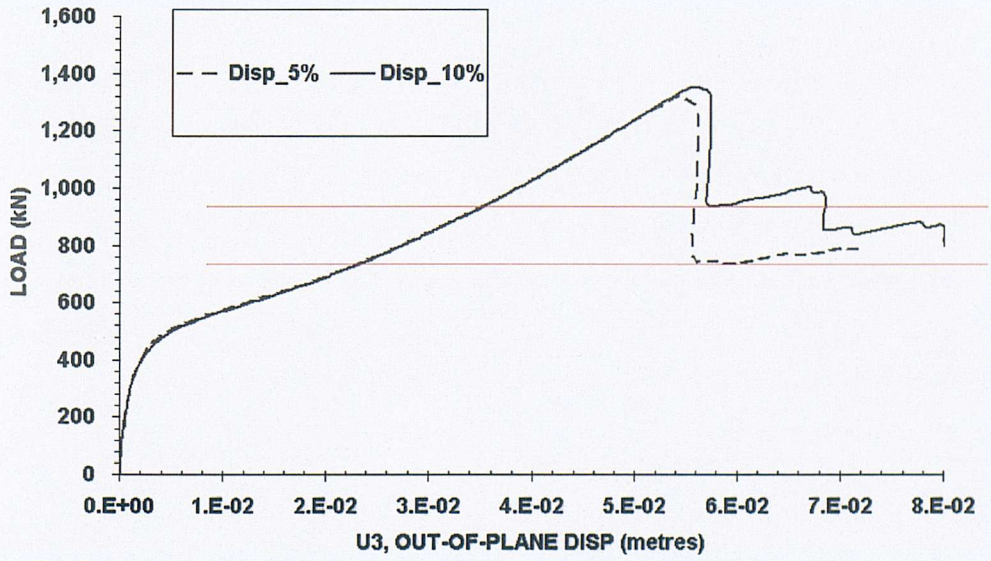


Figure 3-23. Load-displacement curves, showing sensitivity to residual stiffness, using load and displacement controlled FE analyses

Initial imperfection: The increase in initial imperfection at the centre of the plate for mode I from 0.5mm to 2mm is shown with a reduction in pre-buckling stiffness, seen in Figure 3-24, although the immediate post-buckling stiffness is actually increased. Despite this latter trend, for the same type of loading the peak strength is negligibly affected between the different imperfection analyses. The figure also demonstrates how for the same residual stiffness (10%) the peak strength and particularly the residual strength of the displacement controlled analysis is considerably higher. The residual load is more than twice the 420kN value obtained with the load controlled analysis.

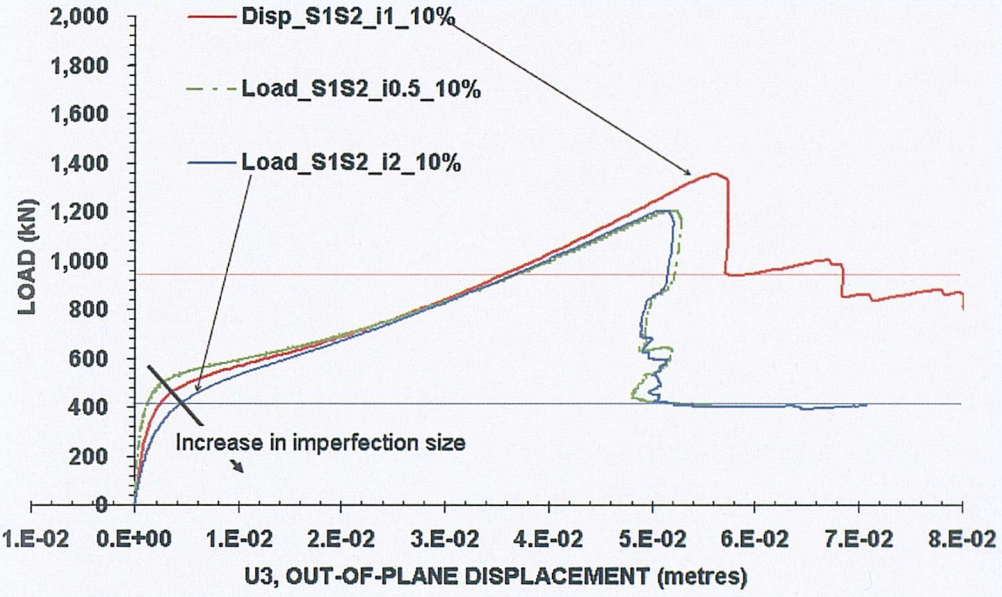


Figure 3-24. Load-displacement curves, showing the effect of initial imperfection, using load and displacement FE analyses

Material properties: Material properties obtained from a batch of coupon tests showed a 20% scatter. A load controlled analysis with a 2% imperfection and a displacement controlled analysis with a 1% imperfection were carried out using maximum and minimum material properties from the range. Both models implemented a 10% residual stiffness. The variation in material properties has a slight effect on the buckling load but little effect on the post-buckling stiffness, as shown in Figure 3-23. The peak stress is marginally increased when the maximum properties are implemented, however the residual strength is negligibly affected.

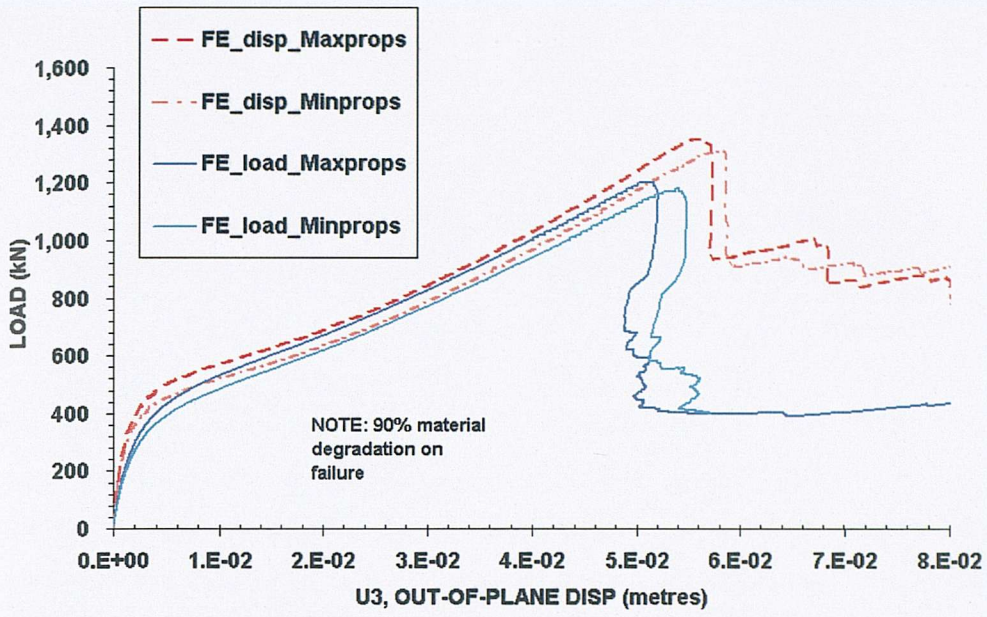


Figure 3-25. Load-displacement curves, showing sensitivity to material properties, using load and displacement control FE analyses

3.7.8 Discussion

This section aims to obtain the closest agreement to the behaviour of the tested plates using one or more finite element analyses. In order to do this properly, the test conditions have been identified with the accuracy they deserve by noting any irregularities with the help of a relatively wide a range of measurements/readings. The mesh size for all the analyses was chosen based on a no-damage model and the sensitivity of the damage predictions to the mesh size is something to be further looked into. However, some studies are carried out for the impact analyses in Chapter 6.

All the tests to varying degrees resembled the load controlled FE analyses, 'Load_S_1S_2_i2_10%' and 'Disp_S_1S_2_i2_5%' in Figure 3-26, which assumed no rotational constraints. The test conditions are not ideal however they are closer to the intended conditions than any others. This is demonstrated by comparison with a number of other analyses on the same load-displacement plot with test conditions which may initially be mistaken as resembling the true test conditions. Panel tests 2 to 5 are discussed separately in more detail, in the following sections. The panel in test 1 was only loaded past its buckling load only.

3.7.8.1 Panel Test 2

Panel test 2 gave the larger displacement and strain plots out of all the tests with failure occurring along the top edge whilst the rest of the panel appeared to be undamaged. The rotation along the top edge appeared to be constrained in the last 400kN before the peak load, but the buckling load was the lowest obtained out of all the tests, as shown in Table 3-5.

The strains along the top of the panel in test 2 at locations 'a', 'c' and 'e', are similar in magnitude to those of the Disp_S_1S_2_i2_5% analysis, which appears in the load-displacement history of Figure 3-26. The strains more so resemble the displacement controlled analysis than Load_S_1S_2_i2_10%, see Figure 3-27 compared to Figure 3-28. Generally the strains are under-predicted with the load controlled analysis and over-predicted with the displacement controlled analysis.

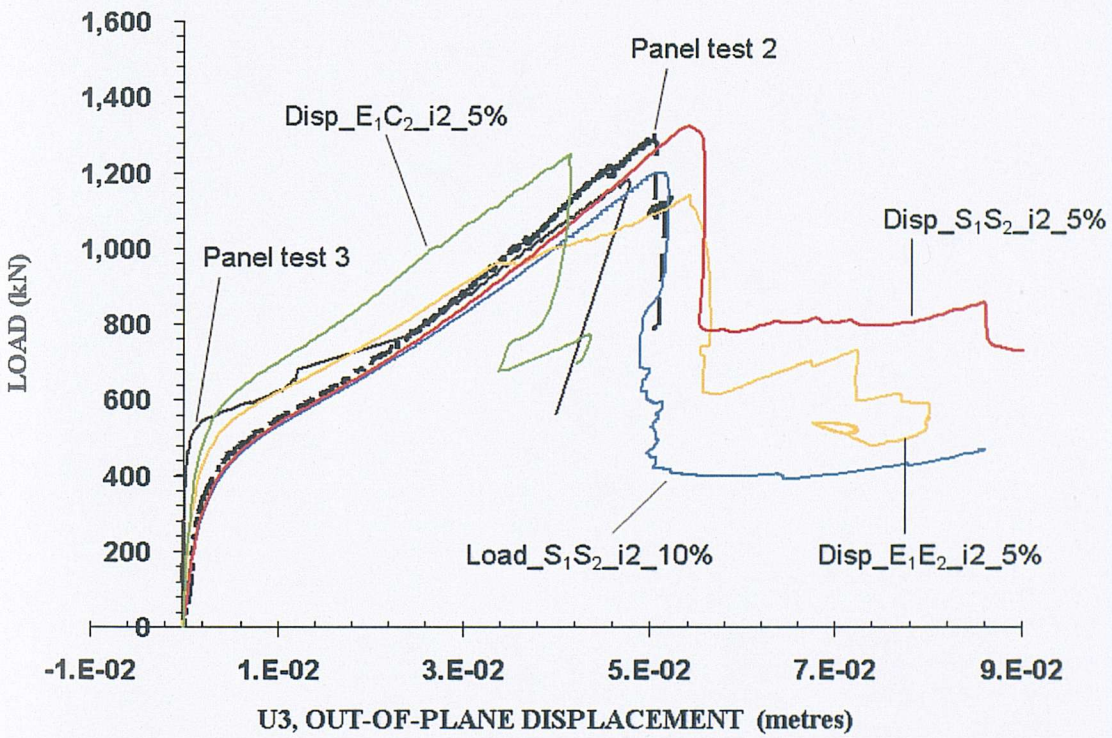


Figure 3-26. Load-displacement curves, showing the most representative FE models of the actual test conditions

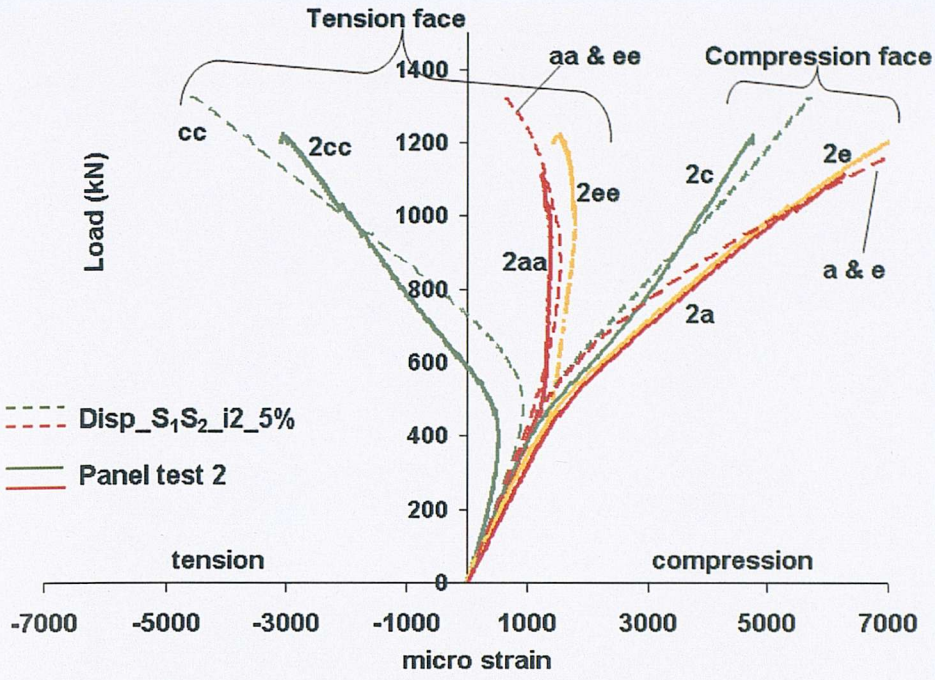


Figure 3-27. Load-strain curves, for panel test 2 and FE analysis 'Disp_S_1S_2_i2_5%' strains at locations a, c and e.

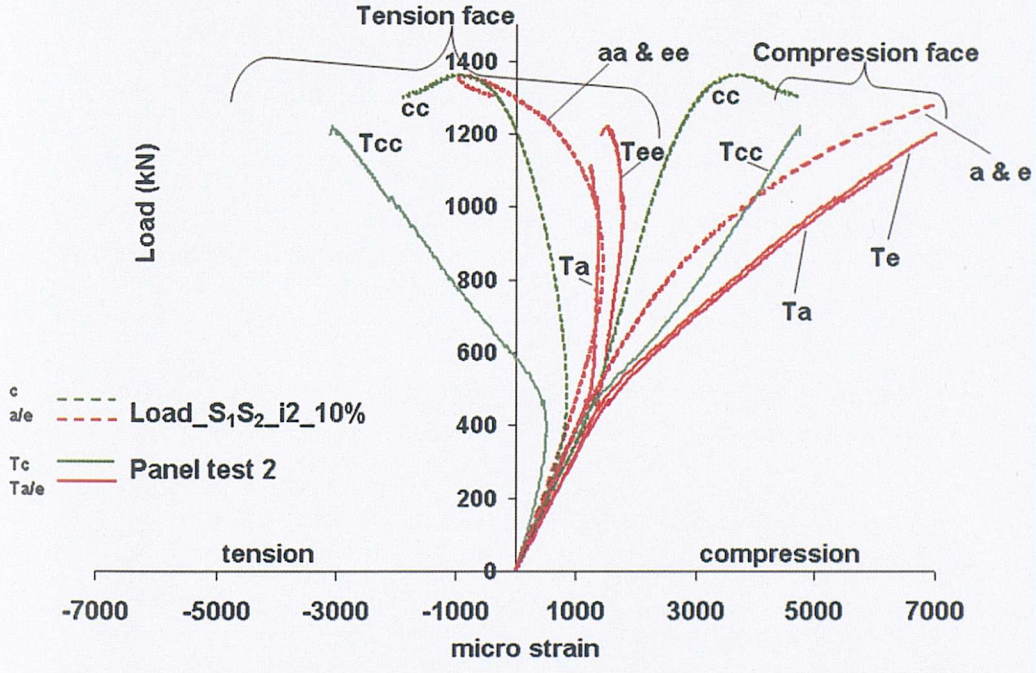


Figure 3-28. Load-strain curves for the top plate strains for panel test 2 and FE analysis 'Load_S_1S_2_i2_10%'

The longitudinal strains at the top of the plate for the displacement and load controlled FE analysis behave differently. Plotting the strain values at the marked locations in Figure 3-29 at a small load of 160kN and at the test buckle load of 440kN, shows that the strains near the

centre line are always larger than those near the corners in a load controlled analysis and the reverse is true with the displacement controlled one.

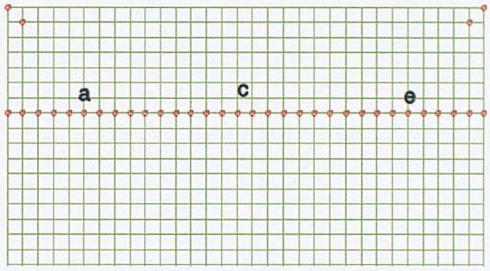


Figure 3-29. Strain positions across the top part of the plate. Location of strain gauge positions *a*, *c* and *e* are highlighted for the compressive side.

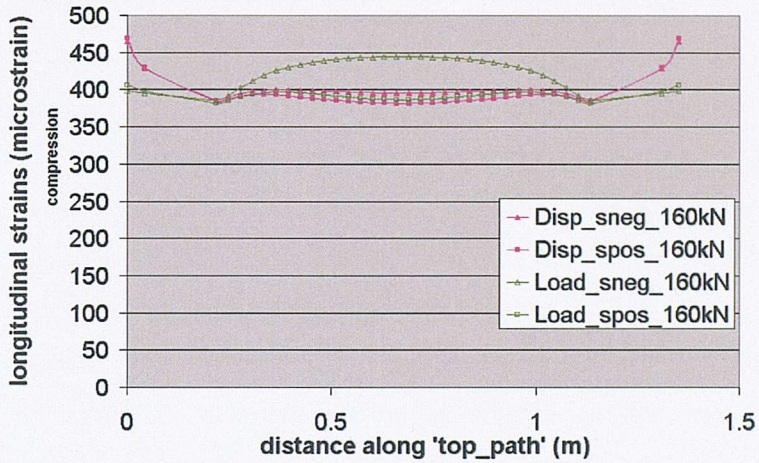


Figure 3-30. Longitudinal strains, *EE11* at 160kN, across the top of the plate for test 2, at locations shown in Figure 3-29, comparing analyses 'disp_S1S2_i2_5%' and 'load_S1S2_i2_10%'

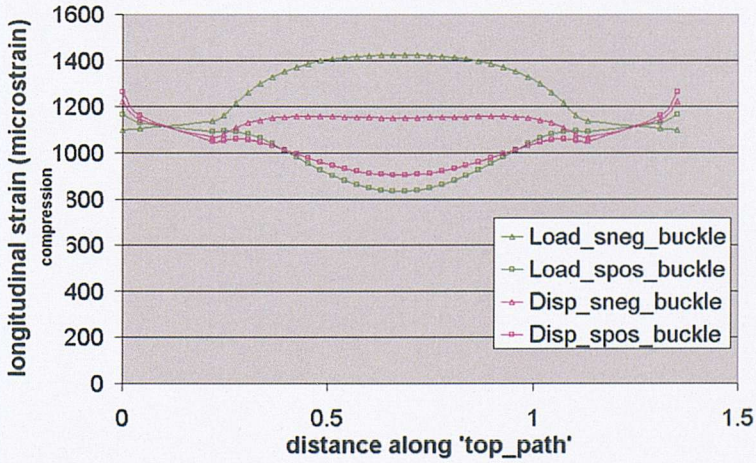


Figure 3-31. Longitudinal strains, *EE11* at 420kN, across the plate for test 2, at locations shown in Figure 3-29, comparing analyses 'disp_S1S2_i2_5%' and 'load_S1S2_i2_10%'

For Test 2, the maximum compressive strain at 'cc' is smaller than that at locations 'a' or 'e', contrary to the other tests where the maximum strain at 'c' is larger than at 'a', resembling more the load controlled analysis. During the early loading stage of tests 2 to 5 it was found that under the displacement controlled loading one of the corners was being subjected to an increasing higher load than the other. This could be mistaken for asymmetry in panel stiffness, however there are other more likely reasons for this, such as a combination of the following: load cell positioning was not precisely the same distance from the edge of both plates; the platen they were pushing on to was not perfectly aligned; one half of the top edge of the plate was better embedded in the resin within the block than the other;.

The strains at the top and centre locations of the plate in test 2 are plotted against those from the FE analyses Disp_S_1S_2_i2_5% and Load_S1S2_i2_10%. The strains at 'a', 'e', 'aa' and 'ee' i.e. the four locations nearest the top corners, are not symmetrical and this is evident from the start of loading for both the vertical and horizontal strains. Figure 3-32 to Figure 3-37 show these strains at loads of 160kN, 440kN and 1000kN. This strain in-balance near the corners is an indication of poor load distribution. The protruding, predominantly 'tensile' face of the plate was identified in the test and as the FE simulations confirm how under the simply supported loading conditions this face should experience smaller compressive strains than the compressive face. However, the figures indicate that the top, tensile face of the plate, experiences larger compressive longitudinal strains than the compressive face. The reverse is true at the gauge locations across the centre of the plate, see Figure 3-38 to Figure 3-43. This odd strain behaviour at the top of the plate is a reflection of a potentially misaligned load. The poor load distribution, although manifested primarily through the top gauge readings, is also reflected in the centre located gauge readings, see Figure 3-38 to Figure 3-40, but as these strain gauges were further from the loaded edge, they correlate far better with the FE analyses. The problem is not as obvious with the horizontal readings in Figure 3-41 to Figure 3-43.

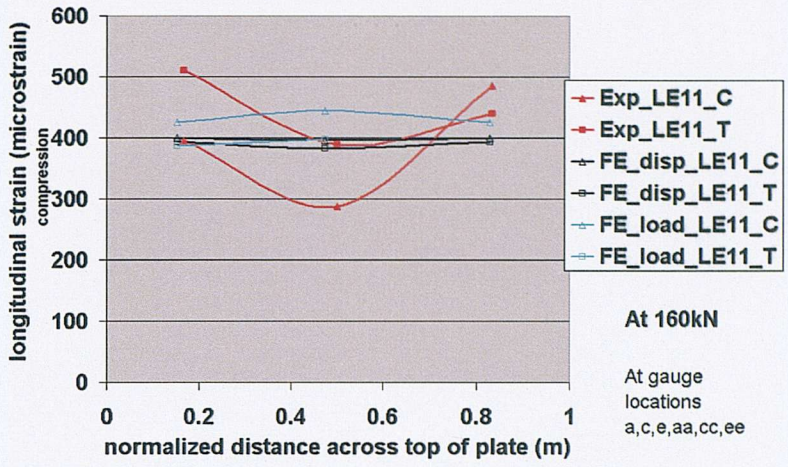


Figure 3-32. Longitudinal strains at the top gauge locations at a 160kN load: test 2 and FE

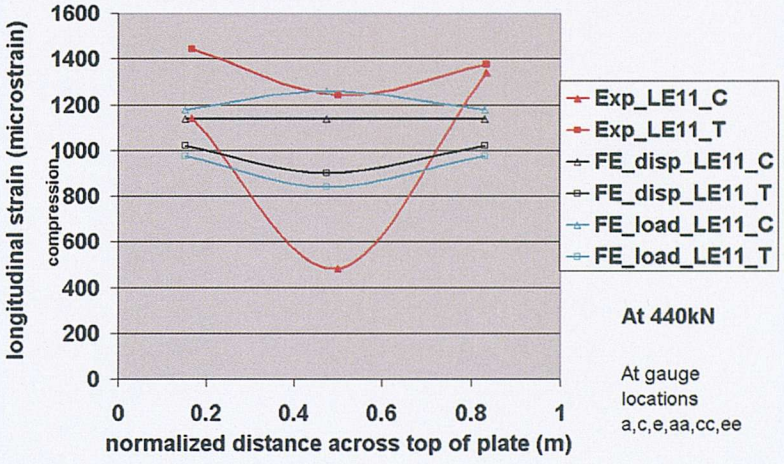


Figure 3-33. Longitudinal strains at the top gauge locations at a 440kN load: test 2 and FE.

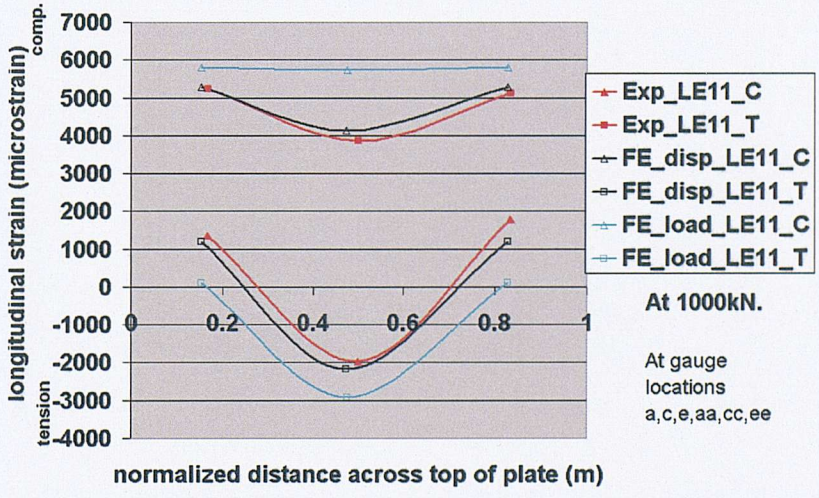


Figure 3-34. Longitudinal strains at the top gauge locations at a 1000kN load: test 2 and FE.

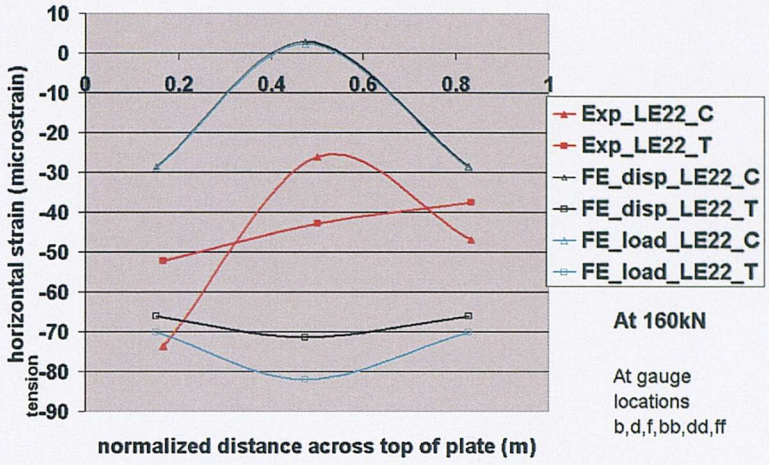


Figure 3-35. Horizontal strains at the top gauge locations at a 160kN load: test 2 and FE.

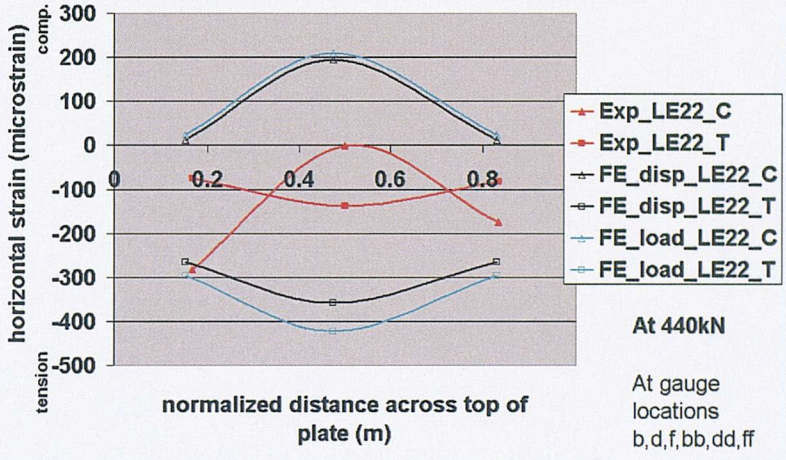


Figure 3-36. Horizontal strains at the top gauge locations at a 440kN load: test 2 and FE.

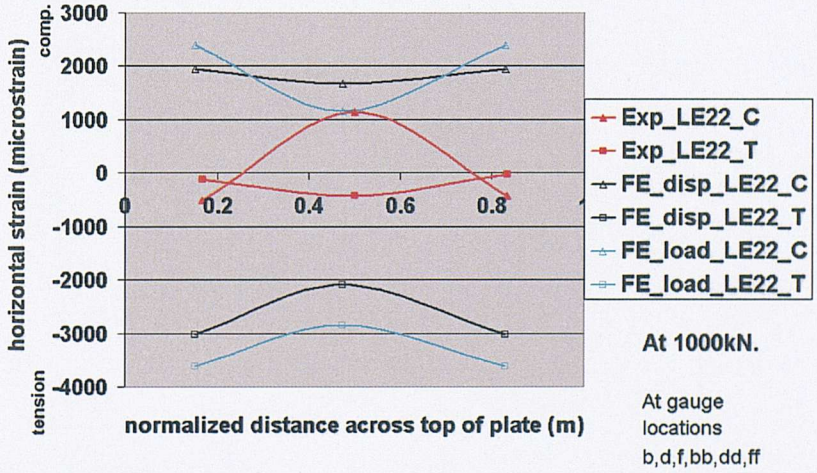


Figure 3-37. Horizontal strains at the top gauge locations at a 440kN load: test 2 and FE.

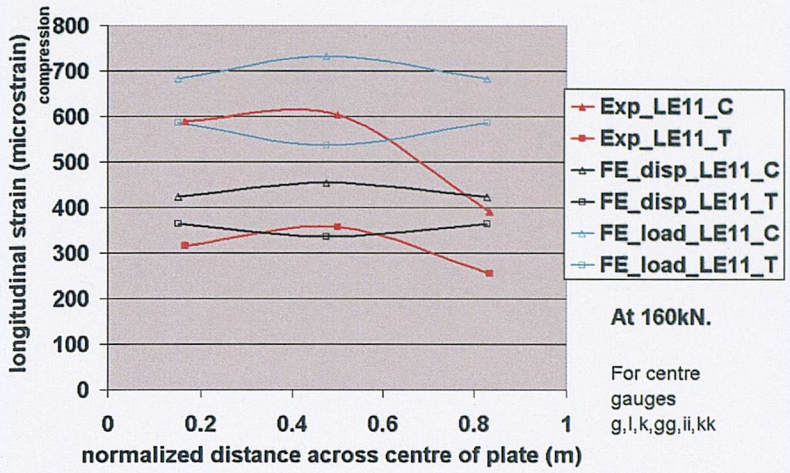


Figure 3-38. Vertical strains at the centre gauge locations at a 160kN load: test 2 and FE.

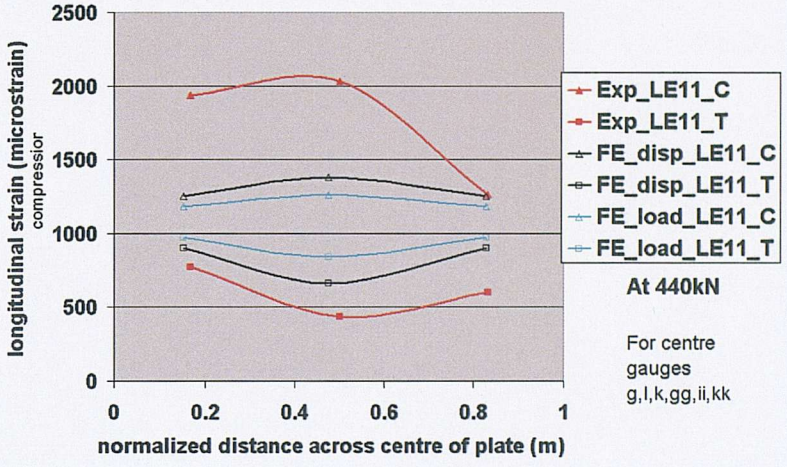


Figure 3-39. Vertical strains at the centre gauge locations at a 440kN load: test 2 and FE.

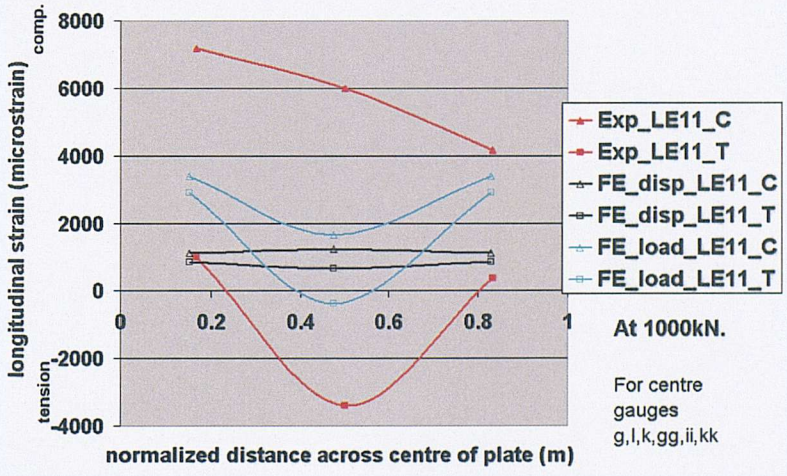


Figure 3-40. Vertical strains at the centre gauge locations at a 1000kN load: test 2 and FE.

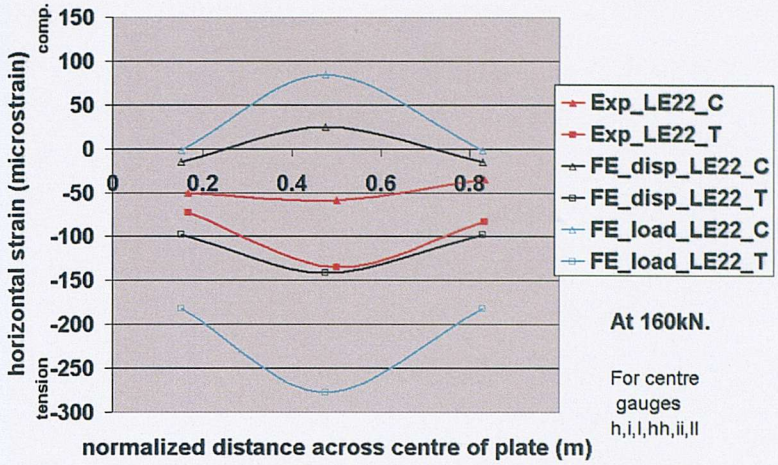


Figure 3-41. Horizontal strains at the centre gauge locations at a 160kN load: test 2 and FE.

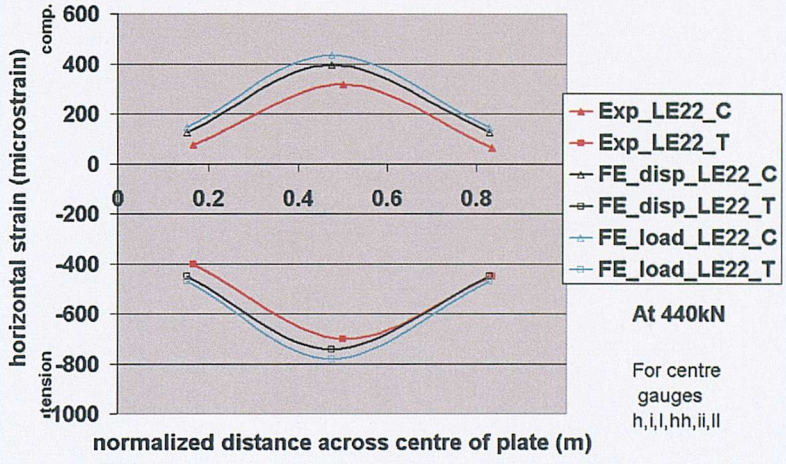


Figure 3-42. Horizontal strains at the centre gauge locations at a 440kN load: test 2 and FE.

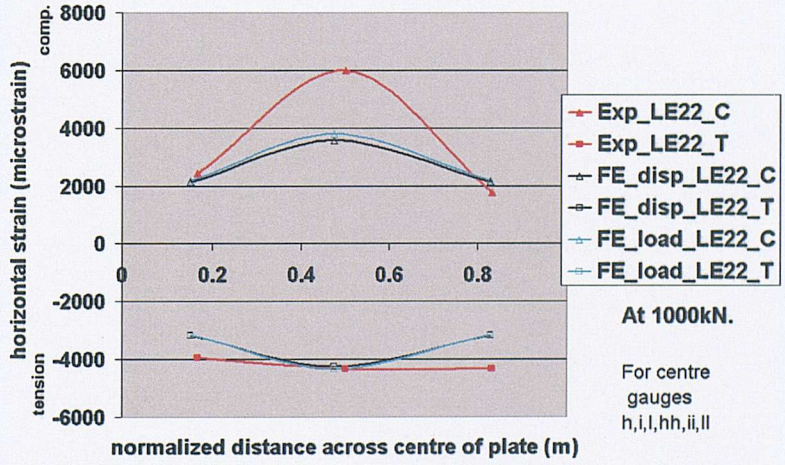


Figure 3-43. Horizontal strains at the centre gauge locations at a 1000kN load: test 2 and FE.

Another reflection of poor stress distribution is in the damage incurred to the panel, which was localized in the two top corners. The damage initiated at the corners and propagated from each of these corners and along the top edge. The damage started off as cracking and delamination followed by fibre failure. The first cracking *noise* began around the buckling load (either at the load or just after). No matrix or delamination damage could be seen at this stage although but damage to the top two corners is unknown. A width of approximately 40mm of both sides of the plate was supported by knife edges and although the two top corners were not potted in resin inside the top section, the corners were masked by the knife edges and any local damage in this area could not be seen. The onset of *visual* matrix cracking occurred at a load of approximately 800kN for test 2, seen clearly starting off at the two top corners following an audible cracking sound and visible whitening. This matrix damage gradually grew together with delamination along the top edge. Fibre damage generally came as a continuation of matrix and delamination damage as this propagated along although more was created at higher loads of 1000kN. There was no matrix or fibre damage visible along the location of the strain gauges for this plate test. This is reflected in the strain gauge readings at a load of 100kN. The average failure strain of the composite in the warp and weft directions is 4780μs in tension and 2070μs in compression. The tensile strains do not exceed the strain for tensile failure but the compressive do. However, the mode of failure under compression is different to tension and in particular the behaviour of a small coupon specimen in compression will be different to an entire plate under compression. It is also likely that local fibre kinking was being picked up of the fibre bundles alleviating any serious matrix crushing.

3.7.8.2 Tests 3, 4 & 5

For subsequent panel tests, a 300mm high steel block was introduced between the load cell and the top fixture in an attempt to further improve the load distribution across the panel and remove the localized damage to the top edge. The panel in test 3 failed at nearly an identical load as that predicted by the 'Load_S_1S_2_i2_10%' FE analysis in Figure 3-26 but at a slightly lower central o.o.p deflection. During the buckling stage the panel was very stiff, giving the second highest buckling load out of the five tests. This panel appeared to be flatter than all the other panels, demonstrated after the first 300kN or so of loading through a very noticeable change in direction of the central o.o.p displacement, as shown earlier in Figure 3-11. This panel failed at the top corners, with cracking and delamination initiating at a load just above 750kN at one corner attempting to propagate in a direction that was approximately 45° from the top edge. The damage to the other corner propagated along part of the top edge similar to that in panel test 2. The compressive strain at gauge locations 'a'

and 'c' shown in Figure 3-44 exceeds the compressive strain to failure of the composite, more so at the top centre gauge 'c' where fibre damage is clearly being picked up, as shown in the photograph of Figure 3-47.

The high stiffness at the start appears to resemble the FE analysis for clamped top and bottom edges with a 1mm central imperfection, disp_C1C2_i1_10%, or the more flexible disp_C1S2_i1_10%, shown in Figure 3-44, however the tested panel was not as stiff in the post-buckling region and its buckling load was smaller than this FE analysis. Its behaviour is clearly much closer to the analysis Load_S_1S_2_i0.5_10% with a 0.5mm imperfection size, illustrating that the initial stiffness of the panel in test 3 was likely to be dominated by the initial imperfection and not the boundary conditions. Figure 3-26 shows the effect an initial imperfection of Figure 3-45 shows the analyses most closely resembling panel tests 2 and 3 and the significant effect the initial imperfection has on the buckling stiffness. The post-buckling curve of Load_S_1S_2_i0.5_10% is the same as that of Load_S_1S_2_i2_10%, demonstrating that the initial imperfection has only an effect on the pre-buckling stiffness. The strains at the top of the panel in test 3, seen Figure 3-46, are actually closer in behaviour to those of Disp_S_1S_2_i2_5% and Load_S_1S_2_i2_10% analyses, although smaller in magnitude. The strains for Load_S_1S_2_i0.5_10% are very similar to Load_S_1S_2_i2_10%, but are omitted from the graph for clarity.

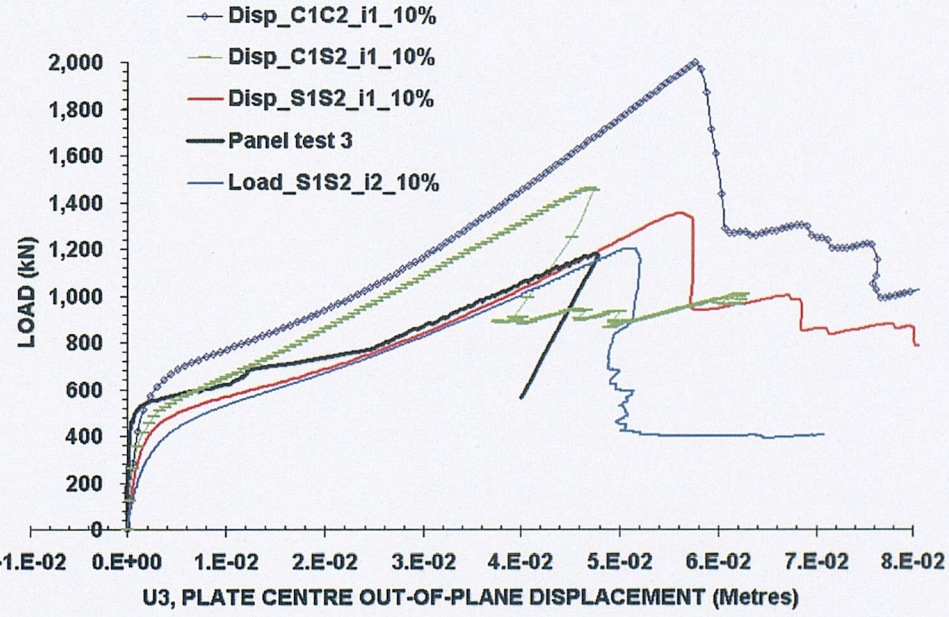


Figure 3-44. Load-displacement curves, examples of sensitivity to bc's, initial imperfection and material properties

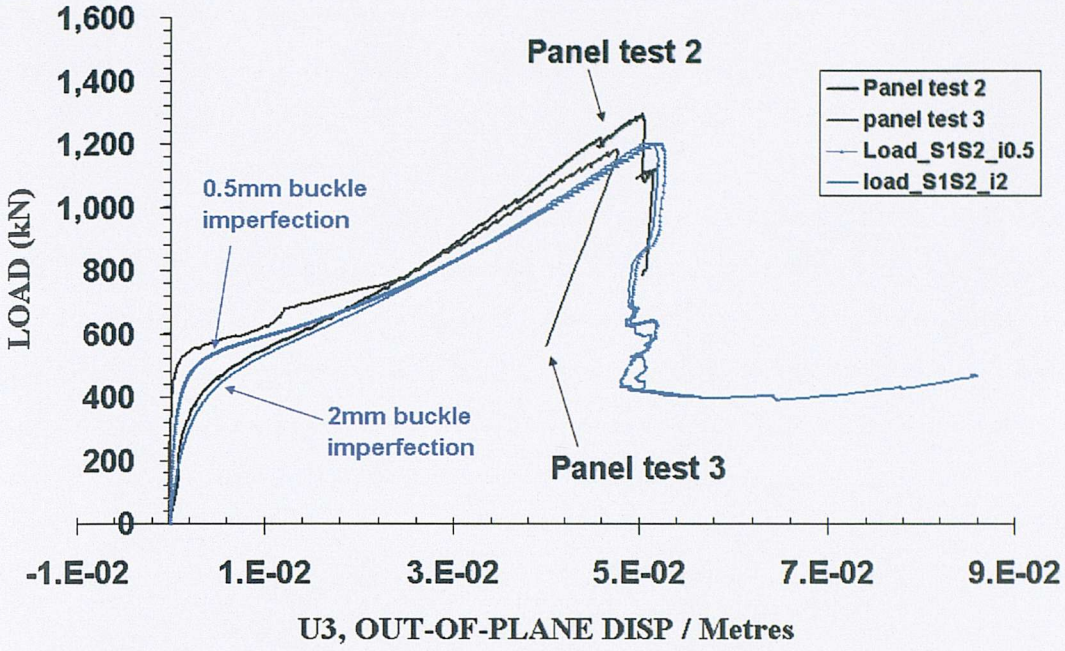


Figure 3-45. FE analyses most closely resembling panel tests 2 and 3

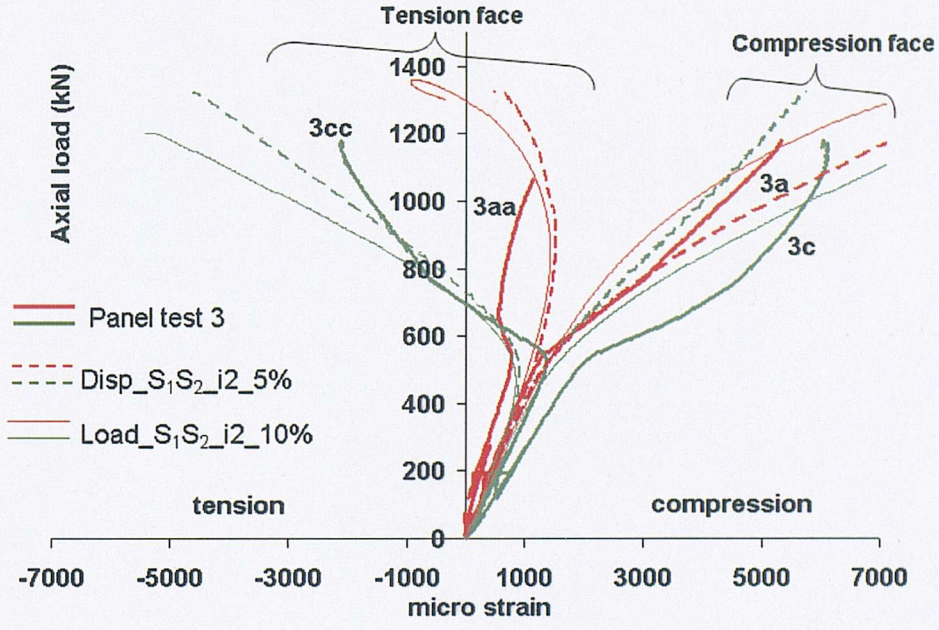


Figure 3-46. Strain comparisons between FE analyses 'Disp_S_1S_2_i2_5%' and 'Load_S_1S_2_i2_10%' and panel test 3 at gauge locations 'a' and 'c'

The panel in test 4 failed at a load of 1018kN, nearly 200kN less than that the highest attained in test 2. For test 4, rubber strips were inserted between the knife edges and the panel and the knife edges were moved inwards by a total of 20mm to alleviate any rotation constraint at the corners, aiming to reduce any high stress concentrations contributing to the non-uniform and localized failure pattern seen in tests 2 and 3. Examination of the damage,

again exclusively incurred at the top of the panel, as seen in Figure 3-47, still suggests the higher stress localization at the top is probably caused by inconsistent or unsymmetrical boundary conditions. This is partly reflected in two FE analyses:- The failure pattern closely resembles that generated by the 'Load_E_1E_2_i2_10%' analysis as illustrated in Figure 3-48 but also the displacement controlled 'Disp_S_1C_2_i1_5%' analysis in Figure 3-49 which models a lack of rotation of the bottom roller and models a smaller initial imperfection of 1mm, see Figure 3-26. The top and bottom roller of the panel in test 4 stopped rotating a couple of loading increments prior to failure, which caused the entire 300mm steel block to rotate off axis by a couple of degrees. What was a seemingly premature failure of this panel could therefore be largely attributed to this incident.

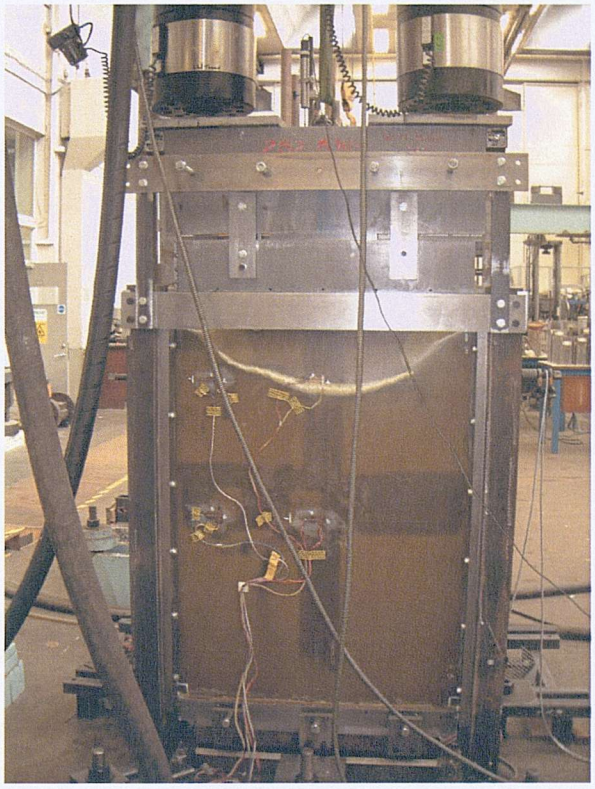


Figure 3-47. Panel test 4 – showing final failure pattern

The panel in test 5 had the corners chamfered by 40mm to further reduce the stress concentrations at these corners, still considered a concern at this stage. The panel in test 5 behaved similarly to that of test 4 but failed at the lowest load of approximately 950kN. Deviation from purely axial loading could have been highly influential in these last two panel tests. This effect may have been attributed to either a small misalignment of the loading block during the test setup (having a cumulative effect with loading), or more likely during the post-buckling regime, when the rollers were sometimes found to stick intermittently. This was able to cause some rotation of the 300mm steel block, creating a

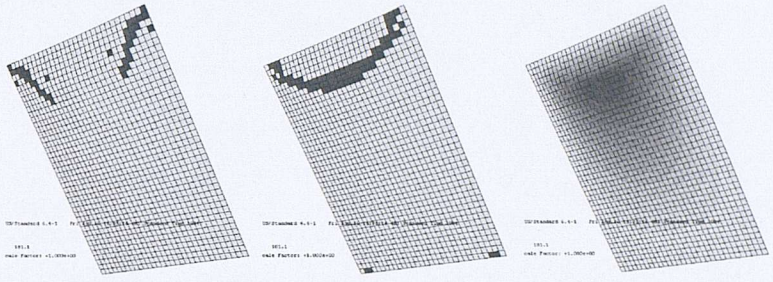
larger moment across the top-half of the panel and hence premature failure. The strains at the top of panel test 5 in Figure 4 follow a similar trend to panel tests 3 and 4 with the top-centre strains at 'c' being larger than those nearer the corners at 'a'. This trend again appears to reflect a resemblance towards the load-controlled analyses generated by Abaqus.

3.7.8.3 Summary of panel behaviour

The FE analysis Disp_E_1E_2_i1_10% models uniform in-plane deflection and rotation along the top edge to reflect the idealized test conditions. In all the tests, the panels buckled into a half wave length in both directions giving the maximum o.o.p deflection at the centre of the panel. However, this changed as the peak load was approached, and the maximum o.o.p displacement started to migrate towards the top of the panels. The Load_S_1S_2_i2_10% analysis, having no rotation constraint, exaggerates this behaviour with the creation of a prominent 'fold' at the top edge and giving rise to higher strains in the top third of the panel. The matrix cracking, delamination and fibre failure patterns in all the panels either formed or almost formed the damage pattern simulated with the Load_E_1E_2_i2_10% and Disp_E_1C_2_i1_5% analyses shown in Figure 3-48 and Figure 3-49. However, the o.o.p displacement bears a closer resemblance to that of Load_S_1S_2_i2_10%. Judging by the test results and stiffness effects caused by dissimilar imperfections between panels, the panels are probably being supported as intended during the buckling stages. However subsequently, during the early post-buckling stages with increase in load, one of the rollers appears to stick intermittently which can lead to out-of-plane movement of the 300mm loading block and consequently sudden premature failure. Some movement within the resin may also be occurring during these stages causing the stiffness of the curve in the post-buckling regime to fall slightly. The test may therefore be providing imperfect boundary conditions in comparison to the ideal FE models. The panel in test 2 resisted a higher load probably because the rotation at the top of the plate was taking place at the roller bearings within the load cells and not at the less sophisticated full length roller used in tests 3 to 5. In summary, the behaviour of the panels resembles one or more of the following FE analyses, independent of the initial imperfection: Load_S_1S_2_i2_10%, Load_E_1E_2_i2_10%, Disp_E_1E_2_i2_5% and Disp_E_1C_2_i2_5%, see Figure 3-26.

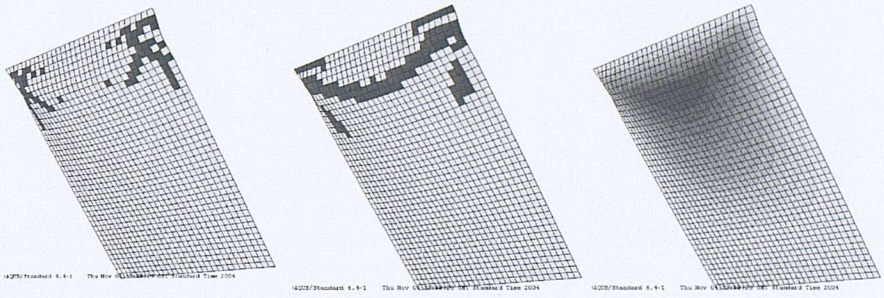
The residual strength and peak loads of the panels is also more closely predicted with the load than the displacement controlled analyses, and largely more conservative. The main difference between the FE load controlled analyses compared to the displacement controlled analyses is in the poorer stress distribution and thus the lower peak load. The even load

distribution that would have been achieved with a perfect displacement controlled analysis was not obtained. Although it is likely that the boundary conditions were not perfectly consistent, the shape of the displacement/load graphs are still of closer resemblance to the FE analyses with simply supported boundary conditions than the simply supported conditions with rotational control (E_1E_2).



(a) (b) (c)

Figure 3-48. Load_ E_1E_2_i2_10% FE results for the top ply (tensile face) at the end of the analysis, showing (a) matrix cracking, (b) fibre failure, (c) o.o.p displacement



(a) (b) (c)

Figure 3-49. Disp_E_1C_2_i_5% FE results for the top ply (tensile face) at the end of the analysis, showing (a) matrix failure, (b) fibre failure, (c) o.o.p displacement

Imperfections have been shown to significantly affect the stiffness of the panel up to the buckling load. The longitudinal strains measured at the panel centre reflect the movement of the tensile face from an initial state of compression during the pre-buckling stages to a state of tension thereafter. The reverse can be said about the compression face, as see in Figure 3-50 showing tests 1 to 4 against results for Disp_S1S2_i2_10% and Load_S1S2_i2_10% analyses. This reinforces the uncertainty of the panels to deflect in one direction or another. The initial compressive strains seen on the tension face are larger than the initial tensile strains on the compression face which is explainable because the loading is in compression.

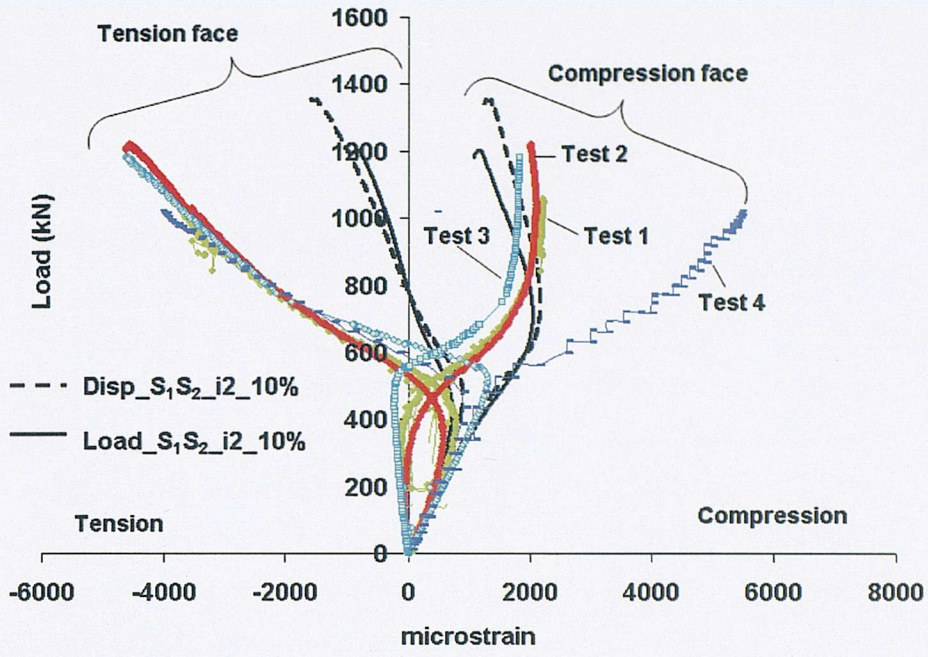


Figure 3-50. Load-strain curves, longitudinal centre panel strains from tests 1 to 4, and FE analyses Disp_S_1S_2_i2_10% and Load_S_1S_2_i2_10%

3.7.9 Conclusion

It is evident from the five panel tests that the load was largely more distributed across the top half of the panels and consequently not generating any visible damage on the bottom half. This was possibly due to the slight difference in stiffness at the top of the rig compared to the bottom and the load distribution on the top edge. The in-plane domination of such a compression test suggests that the non-linear FE analyses, using the simple 2D Hashin stress-based criteria without the shear term in the expression for matrix damage, can effectively model the panel's response for an orthotropic material. The study has highlighted the sensitivity of the FE analyses to different variables and the sensitivity of the test procedure. Symmetry of the applied load, friction at the boundaries, boundary conditions and differences in panel initial imperfections have shown to contribute greatly to pre-buckling and post-buckling stiffness and maximum load carrying capacity. There is no individual FE model discussed above that can fully replicate the panel tests unless the precise test conditions can be pin-pointed or the perfect test conditions can be created for new panel tests. However, the load-deflection curve of the panels bear more resemblance to a load controlled analysis with simply supported boundary conditions and a 10% residual of properties on ply failure. Generally speaking, the FE analyses provide good representations of the behaviour of the tested panels. The panel tests have been valuable and have provided

an indication of the behaviour and strength of a woven composite panel, for which little data has been previously reported in the public domain.

3.8 Concluding remarks

Several stressed based criteria have been implemented in finite element models and validated against experimental results. It was found that behaviour of an angle-ply composite plate subjected to transverse loading was relatively well approximated with 2d Hashin and Tsai-Wu failure criteria; these criteria being applied relative to the local material orientation. With respect to woven composites, the criteria put on trial were not always as reliable, even though the applied load was in-plane and unidirectional. Maximum stress criteria over-estimated the strength of the panels whereas generally the reverse was obtained with the interactive criteria. Nonetheless, good results were produced with Hashin's 2d phenomenological based criteria when the shear term for matrix crushing was excluded. The inclusion of this shear term has a significantly affect on the last portion of the post-buckling response and thus the peak stress of the load-deflection curve. To properly assess the applicability of Hashin's criteria, it is important to test it for dynamic loading conditions and this is addressed in Chapter 6. The in-plane compression testing of large-scale woven ply panels carried out re-confirmed the known sensitivity of plates to boundary conditions, out-of-plane imperfections and also load distribution. A parametric study through finite element also concluded on this, with the largest over-all effect on the pre- and post-buckling behaviour being attributable to the boundary conditions.

3.9 Reference List

1. Padhi GS, Shenoi RA, Moy SSJ, Hawkins GL. Progressive failure and ultimate collapse of laminated composite plates in bending. Composite Structures 1997; 40(3-4):277-91.

2. Smith CS, Murphy P. Advances in Marine Structures - 2, Elsevier Applied Science, 1991.

3. Singer J, Arbocz J, Weller T. Buckling Experiments, Experimental Methods in Buckling of Thin-Walled Structures, New York: John Wiley &Sons Inc, 2002.

4. Tsai SW. Strength Theories of Filamentary Structures. In: RT Schwartz and HS Schwartz (ed.), Fundamental Aspects of Fibre Reinforced Plastic Composites. New York: Wiley, 1968: 3-11.

5. Tsai SW, Wu EM. General Theory of Strength for Anisotropic Materials. Journal of Composite Materials 1971; 5(Jan):58.

6. Hoffman O. The brittle strength of orthotropic materials. Journal of Composite Materials 1967; 1:200-6.

7. Puppo AH, Evensen HA. Interlaminar shear in laminated composites under generalized plane stress. Journal of Composite Materials 1970; 4:204.

8. Hart-Smith LJ. Predictions of the original and truncated maximum-strain failure models for certain fibrous composite laminates. Composites Science and Technology 1998; 58(7):1151-78.

9. Hart-Smith LJ. Predictions of a generalized maximum-shear-stress failure criterion for certain fibrous composite laminates. Composites Science and Technology 1998; 58(7):1179-208.

10. Hashin Z. Failure criteria for unidirectional fiber composites. Journal of applied mechanics 1980; 47(2):329-34.

11. Chang FK, Chang KY. A Progressive Damage Model for Laminated Composites Containing Stress-Concentrations. Journal of Composite Materials 1987; 21(9):834-55.

12. Puck A, Schürmann H. Failure analysis of FRP laminates by means of physically based phenomenological models. Composites Science and Technology 2002; 62(12-13):1633-62.

13. Naik NK, Sekher YC, Meduri S. Damage in woven-fabric composites subjected to low-velocity impact. Composites Science and Technology 2000; 60(5):731-44.

14. Zou Z, Reid SR, Li S, Soden PD. Application of a delamination model to laminated composite structures. Composite Structures 2002; 56(4):375-89.

15. Rotem A, Hashin Z. Failure Modes of Angle Ply Laminates. Journal of Composite Materials 1975; 9(APR):191-206.

16. Icten BM, Karakuzu R. Progressive failure analysis of pin-loaded carbon-epoxy woven composite plates. Composites Science and Technology 2002; 62(9):1259-71.

17. Hahn HT, Tsai SW. Nonlinear Elastic Behavior of Unidirectional Composite Laminae. Journal of Composite Materials 1973; 7(JAN):102-18.

18. Chang FK, Lessard LB. Damage Tolerance of Laminated Composites Containing An Open Hole and Subjected to Compressive Loadings .1. Analysis. Journal of Composite Materials 1991; 25(1):2-43.

19. Viita-aho TE, Jones RD, Al-Hassani STS, Wahoono AR. A DYNA3D Analysis Composite Panels Subjected to Blast Loading. Proc of DYNA3D User Group Conference, UMIST, Manchester, 1992, 1-14.

20. Sun CT. Strength analysis of unidirectional composites and laminates. In: Kelly A., Zweben C. (eds.), Comprehensive Composite Materials. Oxford: Elsevier Science Ltd, 2000.

21. Hinton MJ, Soden PD. Predicting failure in composite laminates: The background to the exercise. Composites Science and Technology 1998; 58(7):1001-10.

22. Hinton MJ, Kaddour AS, Soden PD. Evaluation of failure prediction in composite laminates: background to 'part B' of the exercise. Composites Science and Technology 2002; 62(12-13):1481-8.

23. Hinton MJ, Kaddour AS, Soden PD. A comparison of the predictive capabilities of current failure theories for composite laminates, judged against experimental evidence. Composites Science and Technology 2002; 62(12-13):1725-97.

24. Zinoviev PA, Grigoriev SV, Lebedeva OV, Tairova LP. The strength of multilayered composites under a plane-stress state. Composites Science and Technology 1998; 58(7):1209-23.

25. Liu KS, Tsai SW. A progressive quadratic failure criterion for a laminate. Composites Science and Technology 1998; 58(7):1023-32.

26. Sun CT, Tao J. Prediction of failure envelopes and stress/strain behaviour of composite laminates. Composites Science and Technology 1998; 58(7):1125-36.

27. Sun CT, Chen JL. A Simple Flow Rule for Characterizing Nonlinear Behavior of Fiber Composites. Journal of Composite Materials 1989; 23(10):1009-20.

28. Moy SSJ, Shenoi RA, Allen HG, Feng ZN, Pahdi GS. Progressive damage analysis of GRP panels under extreme transverse pressure loading.La Jolla California, 17 May 1998, Advances in Composite Materials and Mechanics, 1999, 24-33.

29. Gotsis PK, Chamis CC, Minnetyan L. Application of progressive fracture analysis for predicting failure envelopes and stress-strain behaviors of composite laminates: a comparison with experimental results. Composites Science and Technology 2002; 62(12-13):1545-59.

30. Matthew FL, Davies GAO, Hitchings D, Soutis C. Analytical and numerical modelling. In: Cambridge: Woodhead Publishing Ltd, 2000: 158-73.

31. Sun CT, Tao J, Kaddour AS. The prediction of failure envelopes and stress/strain behavior of composite laminates: comparison with experimental results. Composites Science and Technology 2002; 62(12-13):1673-82.

32. Hou JP, Petrinic N, Ruiz C, Hallett SR. Prediction of impact damage in composite plates. Composites Science and Technology 2000; 60(2):273-81.

33. Daniel I. Failure of composite materials. Proc of 16th European Conference on Fracture, Alexandroupolis Greece, Jun 2006.

34. Shlkolniv VM, Louca L.A., personal communication.

35. Boh JW, Louca LA, Choo YS, Mouring SE. Damage modelling of SCRIMP woven roving laminated beams subjected to transverse shear. Composites Part B: Engineering 2005; 36(5):427-38.

36. Iannucci L, Willows ML. An energy based damage mechanics approach to modelling impact onto woven composite materials - Part I: Numerical models. Composites Part A-Applied Science and Manufacturing 2006; 37(11):2041-56.

37. Padhi GS, Shenoi RA, Moy SSJ, Hawkins GL. Progressive failure and ultimate collapse of laminated composite plates in bending. Composite Structures 1997; 40(3-4):277-91.

38. Moy SSJ, Shenoi RA, Allen HG. Strength and stiffness of fibre reinforced plastic plates.Institution of Civil Engineers, 1996, 116:204-220.

39. Hoff NJ, Boley BA, Coan JM.The Society for Experimental Stress Analysis, 1948, 5:14-24.

40. Chen H, Sun X. Residual compressive strength of laminated plates with delamination. Composite Structures 1999; 47(1-4):711-7.

41. Hoff NJ, Boley BA, Coan JM.The Society for Experimental Stress Analysis, 1948, 5:14-24.

42. Banks WM, Harvey JM. Stability problems in engineering structures and components. In: Richards T.H., Stanley P. (eds.), London: Applied Science Publishers, 1978.

43. Marshall IH, Banks WM. Stability problems in engineering structures and components, Richards T.H., Stanley P. (eds.), London: Applied Science Publishers, 1978.

44. Hoff NJ, Boley BA, Coan JM.The Society for Experimental Stress Analysis, 1948, 5:14-24.

45. Kicher TP, Mandell JF. An Experimental Study of the Buckling of Anisotropic Plates. Proc of 10th ASME/AIAA Structures, New Orleans, LA, Structural Dynamics and Materials Conference, 1969.

46. Banks WM. The post buckling behaviour of composite panels. Proc of International Conference of Composite Structures, Geneva, 1975.

47. Smith CS. Design of marine structures in composite materials, London: Elsevier Science, 1990: 180-267.

48. Bao G, Jiang W, Roberts JC. Analytic and finite element solutions for bending and buckling of orthotropic rectangular plates. International Journal of Solids and Structures 1997; 34(14):1797-822.

49. Gaudenzi P, Perugini P, Spadaccia F. Post-buckling analysis of a delaminated composite plate under compression. Composite Structures 1997; 40(3-4):231-8.

50. Chia CY, Prabhakara MK. Postbuckling behavior of unsymmetrically layered anisotropic rectangular plates. Journal of applied mechanics 1974; 155-62.

51. Finch DC. The Buckling of Symmetric and Unsymmetric Composite Plates with Various Boundary Conditions. Report 84-03, Massachusetts Institute of Technology, 1984, TELAC.

52. Jensen DW. Buckling and Postbuckling Behavior of Unbalanced and Unsymmetric Laminated Graphite/Epoxy Plates. Report 86-03, Massachusetts Institute of Technology, 1986, TELAC.

53. Jensen DW, Lagace PA. Influence of Mechanical Couplings on the Buckling and Postbuckling of Anisotropic Plates. Aiaa Journal 1988; 26(10):1269-77.

54. Lagace PA, Jensen DW, Finch DC. Buckling of unsymmetric composite laminates. Composite Structures 1986; 5(2):101-23.

55. Minguet P. Reference Manual for PostBS, Postbuckling Analysis Program for Laminated Rectangular Plates. Report 87-18, Massachusetts Institute of Technology, 1987, TELAC.

56. Minguet P. Buckling of Graphite/Epoxy Sandwich Plates. Report 86-16, Massachusetts Institute of Technology, 1986, TELAC.

57. Minguet P, Dugundji J, Lagace PA. Buckling and Failure of Sandwich Plates with Graphite-Epoxy Faces and Various Cores. Journal of Aircraft 1988; 25(4):372-9.

58. Minguet P, Dugundji J, Lagace PA. Buckling and Failure of Sandwich Plates with Graphite-Epoxy Faces and Various Cores. Journal of Aircraft 1988; 25(4):372-9.

59. Starnes JH, Rouse M. Postbuckling and failure of selected flat rectangular graphite-epoxy plates loaded in compression. Proc of Structural Dynamics and Materials Conference, Atlanta USA, 6 Apr 1981, AIAA/ASME/ASCE/AHS 22nd Structures, 1981.

60. Noor AK, Starnes JH, Waters WA. Numerical and experimental simulations of the postbuckling response of laminated anisotropic panels. Proc of Structural Dynamics and Materials Conference, Longbeach California USA, AIAA/ASME/ASCE/AHS/ASC 32nd Structures, 2 Apr 1990, 848-861.

61. Roberts JC, Bao G, White GJ. Experimental, numerical and analytical results for bending and buckling of rectangular orthotropic plates. Composite Structures 1998; 43(4):289-99.

62. Roberts JC, Bao G, White GJ. Experimental, numerical and analytical results for bending and buckling of rectangular orthotropic plates. Composite Structures 1998; 43(4):289-99.

63. Roberts JC and Bao G. Design equations for fiber reinforced plastic (FRP) ship hulls. Report TEO-97-088, John Hopkins University, Applied Physics Laboratory, Laurel, MD, 1997.

64. Chai GB, Khong PW. The Effect of Varying the Support Conditions on the Buckling of Laminated Composite Plates. Composite Structures 1993; 24(2):99-106.

65. Chai GB. Buckling of Generally Laminated Composite Plates with Various Edge Support Conditions. Composite Structures 1994; 29(3):299-310.

66. Suh SS, Han NL, Yang JM, Hahn HT. Compression behavior of stitched stiffened panel with a clearly visible stiffener impact damage. Composite Structures 2003; 62(2):213-21.

67. Yamada SE, Sun CT. Analysis of laminate strength and its distribution. Journal of Composite Materials 1978; 12(Jul):275-84.

68. Camanho PP, Lambert M. A design methodology for mechanically fastened joints in laminated composite materials. Composites Science and Technology 2006; (in Press).

69. Greene E. Marine Composites, Annapolis: Eric Greene Associates, 1999: 123-33.

CHAPTER 4

Formulation of a continuum damage model

4.1 Introduction

Commercial FE codes currently exist to model impact of composite plates but most still lack effective constitutive models for laminates experiencing damage. The following work aims to present a simple yet effective method of modelling progressive damage in composite plates under impact based on the fundamentals of Continuum Damage Mechanics (CDM) and Ladeveze's work [1]. The chapter begins with a review of some of the work carried out in the field of CDM and impact and an introduction to damage mechanics. The damage model proposed is divided into damage initiation and damage propagation. Damage propagation covers in-plane damage in the form of matrix and fibre cracking and through-thickness (transverse) *intra*-ply damage which is omitted in other models. This requires the implementation of three dimensional solid elements (continuum elements). The combined choice of damage initiation and propagation criteria is also unique to this model. Full scale impact tests are used to validate the model by comparing the damage incurred and contact force/time histories. A description of the impact tests and the results is given in Section 2.8 Chapter 2.

Stress or strain based criteria have been the most common tools to model failure on a macro-scale but in a basic way, degrading the properties once only to a residual value once failure is determined, as discussed in Section 3.4 of Chapter 3. Currently however, CDM is becoming increasingly popular and has yet to be introduced in many finite element packages for composite modelling. The resulting shortcoming has prompted the current work aimed at introducing an effective damage model into Abaqus/Explicit via a user material subroutine that can be used to assess impact damage of composite laminates with the knowledge of standard material tensile and compressive tests and simple cyclic test data. Damage (particularly cracking and delamination) is found to occur more readily under cyclic loading

than under quasi-static loading, [2]. Cyclic loading tests are often carried out to reproduce the effects caused by a dynamic load.

The finite element model is intended to fulfill two objectives:

- To obtain a visual idea of the scale and mode of damage in the composite and its location at ply level.
- To allow further assessment of the damage inflicted on the laminate through the examination of other variables mainly the contact force and out-of-plane displacement.

4.2 Background

Damage mechanics is used to predict the behaviour of a material which has suffered damage initiation as a result of an initial stress state and then damage propagation with increase in stress. Damage accumulation causes changes in the material stiffness which is one of the major contributions to material non-linearity in composites. In damage mechanics, a micro-mechanical process such as matrix cracking, can be represented on a macro-level by regarding this damage as being spread over a given volume of material. With reference to damage of composites, Ladeveze [1, 3] and Chaboche [4] produced some of the earlier works in this area. In the latter paper Chaboche gives a good description of the general concepts of damage mechanics.

To this date work in the field of CDM is continuously seeking to find the most suitable model to predict the extent of matrix cracking, delamination and fibre damage in composite materials subjected to damaging loads and the effect of this damage on the material properties. The main limitations of these models arise from the testing procedures; it is often difficult to generate suitable experimental data.

The damage progression of a composite under load can be split into several levels of damage. For example: the start of matrix cracking, the propagation of matrix cracking, the onset of fibre cracking and full failure. Tests can be carried out to establish the point of matrix damage initiation and the change in properties during crack propagation. The initiation of damage in composite materials is the point at which the stresses or strains in the material are large enough to incur some permanent damage in the form of matrix cracking. Much of the initial damage is caused by in-plane stresses creating transverse cracks. Talreja

[5] examined transverse cracking and the effect on the stiffness on glass/epoxy and graphite/epoxy laminated composites. An analytical method was developed for predicting the crack density and also the reduction in elastic moduli from crack initiation up to crack saturation. Changes to the composites' longitudinal elastic moduli were characterized using continuum damage principles developed by the author. Talreja included the effect of certain constraints on the development of matrix cracking, namely the degree of constraint of the plies adjacent to the *cracking plies/off-axis plies* (those plies most likely to damage first). The analytical response of $(0,90)_s$ coupons, amongst others, undergoing tension-tension cycles, were compared to experimental work giving good results. The residual stiffness at matrix saturation using this analytical method was also compared to that obtained using the ply discount method. The ply discount method is a mathematical approach [6] using linear elastic laminate plate theory to calculate the stresses and strains in each ply of the degraded laminate. Talreja found that this method can either under or over-predicts the residual stiffness at different stages of matrix damage, depending on the composite lay up. According to Williams et al [7] however, the ply-discount approach is adequate enough to find the residual strength at matrix saturation, with errors of five to ten percent and believe that the various other analytical approaches available to predict the stiffness lost from damage can be a little over convoluted.

Various constitutive models have been proposed by various authors for woven composites. Matzenmiller et al [8] developed an anisotropic damage mechanics model to model the several damage modes; fibre rupture, fibre buckling and kinking and matrix cracking under transverse tension and shearing and compression and shearing. The model was tested against experimental data of uniaxial tension, compression and simple shear. Kollegal et al [9] used an in-plane damage mechanics model for woven composites. An in-house parametric finite element mesh generator was implemented in Abaqus/Standard to automatically mesh unit cells of a plain weave composite epoxy composite. The elements used were 10 to 20 noded solid elements. The composite plate model was built up of many of these unit cells having specific boundary conditions. A user material subroutine called a UMAT was used to write the constitutive behavior of the composite. The results were tested for tensile loading and in-plane shear loading. Similarly Lua et al [10] used a hybrid and discrete CDM for modeling the dynamic failure of woven marine composite structures. However the model has its limitations, in that only small scales can be analysed, thus requiring a large number of elements.

Zako et al [11] used a damage mechanics approach to model a woven composites in the form of heterogenous 3-dimensional coupon subjected to a tensile load. The resin and the fibres were macroscopically modelled as isotropic and anisotropic homogenous bodies respectfully. The matrix was arranged as interlayer plies without fibres. Damage parameters were applied to represent each of four modes of damage which included matrix cracking under transverse and in-plane shear stresses in the weft direction and similarly in the warp direction. After damage initiation with a stress based failure criterion, the in-plane and transverse properties were reduced according to the damage configuration. These damage configurations were based on calculations of stress to strength ratios for the different modes of failure.

Odegard et al [12] developed an elastic-plastic hardening model for woven fabric composites. The model was treated as having a separate damaging elastic phase and a non-damaging elastic-plastic phase. This model was based on the assumption for woven-fabric composites the elastic strain increment is much smaller than the plastic strain increment when loaded to relatively large strains, therefore when plasticity begins elastic damage ceases. Odegard et al tested their model using torsional tube specimens subjected to biaxial loading.

Of particular interest in the field of damage mechanics and impact modelling of woven composites is Iannucci's and Dechaene's work. Iannucci et al [13] used a stress-based energy dissipation approach to model damage propagation in woven CFRP subjected to impact. A stress threshold was used to determine damage initiation. Strain rate sensitivity was modelled using a damage lag approach, incorporated in the explicit dynamic finite element code Dyna3d, with the rate of damage modelled as an increasing function of stress and of existing damage. This model predicts matrix cracking and fibre fracture in the warp and weft (in-plane) directions and has been implemented for shell elements. This was extended for solid elements in work by Dechaene et al [14] and results were compared with composite beam and plate impact experiments. The model was later further validated and a parametric study were carried out by Iannucci [15].

More relevant to the damage incurred to naval composites under dynamic loads is that by Zhou and Greaves [16] who carried out low velocity impact tests on polyester and phenolic GFRP composites, producing high incident kinetic energy with the use of large masses. Impact velocities varied between 2 and 8m/s using one flat-nosed impactor of diameter 20mm. Various incident KE's were tested using masses of 6kg up to 105kg on thick

laminates of up to 500mm in diameter. Impact KE, delamination area and depth of surface indent have previously been used as measures of damage but have shown their limitations. Delaminations severely reduce the residual strength of laminates, but the use of absorbed energy rather than delamination area was suggested by the authors as a more suitable measure of damage. According to Zhou and Greaves, the use of impact force thresholds is a more recent measure of the dominant damage mechanisms and can be compared directly to the static ones (such as for rate analysis).

Mouritz [17] examined the damaged to stitched and non-stitched woven E-glass/vinyl-ester composites under underwater shock loading. Specimens were taken from the shock tested laminates and examined using SEM to view the damage formation. For the non-stiched laminates, the back surface of the laminate showed a large amount of cracking and the cracks showed to propagate in a direction normal to the back surface, through the resin-rich layers between the glass plies. Cracking of both the matrix and glass fibres was observed. In another paper, Mouritz et al [18] highlight the weakness of GRP laminates in the translaminar direction and therefore to impact resistance. Impact of the laminates results in cracking of the matrix and the fibres together with delamination, acting to severely degrade the composites' properties, having a particularly detrimental effect on the inter-laminar shear and flexural strength.

Interesting work on damage formation and impact damage on structural design was carried out Sierakowski [19]. Sierakowski highlighted the effect of the boundary conditions on the type of damage formation and its location. A low velocity impacted plate that is freely supported would typically see internal delamination damage and back-face cracking than a more supported plate undergoing less bending. Such a plate would instead experience more damage on the impact surface. The plate length-thickness ratio and stiffness also plays a part in the damage formation.

Davies et al [20] subjected thick polyester GFRP laminates to low velocity impact using 8kg to 18kg for their flat nosed impactor on 10 to 25mm diameter laminates. They developed damage force (impact force) and incident kinetic energy maps and used this to pinpoint damage initiation. An increase in damage size was detected with increase in incident kinetic energy (IKE). The most dominant failure modes were delamination and fibre shear-out. They also concluded that the impact response and energy absorption are dependent on the laminate geometries.

More recently and again specific to naval composites, Lemmen et al [21] proposed a damage mechanics based model for composite ship structures under dynamic loading. The damage initiation criterion was based on Hashin's equations [22]. The model is tested for the quasi-static loading of a T-joint panel and compared with experiment.
Williams [7] used a simple plane-stress continuum damage mechanics (CDM) approach on a macroscale by making assumptions about the type of damage and it's influence over the macroscale properties (i.e. the moduli). Williams' used analytical and experimental work to predict several model parameters, such as the size of matrix damage at matrix saturation and the uniaxial strains at which matrix damage initiation, fibre damage initiation and final failure occurs. A bi-linear damage model was developed which shows damage development as a result of pure matrix damage, followed by a combined matrix and fibre damage phase until final failure. Reference is made to Talreja's work amongst others.

Pickett [23] developed a plane stress damage mechanics model for impact modelling of unidirectional composites based on Ladevèze's work, resulting in its implementation into the explicit FE code PAM-CRASH^{TM}. This model is similar to Williams' and Johnson's [24, 25] and has been since used by Fouinneteau et al [26] as a basis for an improved non-linear damage model in shear for application to braided composites. Quantification of the fibre angles during loading was used to characterize the shear damage by using optical methods in the form of digital image correlation (DIC) rather than the less reliable conventional strain gauges.

The quest for better models and testing techniques for fracture problems in tough structural composites is well captured by Cox et al [27]. The literature focuses on the approaches used for structural composites, on a meso and macro-scale. Interestingly they reconfirm the fact that the greatest motivation for replacing experimental tests by virtual experiments (simulations) is driven by the aerospace industry. They also highlight the fact that three-dimensional finite elements should be used to effectively model the three-dimensional damage progression.

4.3 Overview of proposed matrix and fibre damage model

The damage mechanics based model in this work can be divided into three parts: damage initiation, matrix damage only and combined matrix and fibre damage propagation until full

failure. In the present study, three separate functions are tested to predict damage initiation, amongst them Hashin's 3d failure criterion.

The propagation of in-plane matrix damage is modelled using a maximum strain criterion, based on the strain for matrix damage initiation and the strain at the start of fibre damage. In-plane fibre damage propagation based on a maximum strain criterion that initiates once the function for matrix damage development is equal to unity. The translaminar (through-thickness) intra-ply damage propagation is treated separately with a maximum stress criterion for the normal transverse direction and for each of the two transverse shear directions.

4.4 Assessment of potential damage regions

Damage in woven composites under a three dimensional state of stress, see Figure 4-1, is quite complex and it is difficult to define precise modes of failure. As with other composite lay-ups, damage can be in the form of matrix cracking, delamination and fibre failure, however due to the weaving nature of the plies, not all the crack formations will be exactly orientated along a principle in-plane or transverse plane. Despite this, taking away the real-life manufacturing imperfections and structural changes during deformation and damage formation, we can identify some modes of damage:

- Fibre-matrix interface micro-cracking
- Intra-yarn transverse cracking
- Inter-ply transverse cracking
- Inter-yarn in-plane cracking
- Delamination
- Fibre fracture

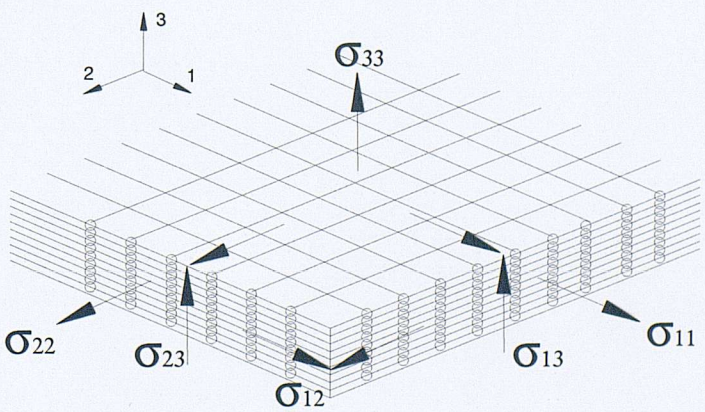


Figure 4-1. Three dimensional stress acting on a schematic of the laminate

Localised stresses at the fibre-matrix interface, see Figure 4-2, cause micro-cracking at these locations, resulting from a complex state of stress. Intra-bundle cracks can run across a yarn (fibre bundle), through the matrix that surrounds the individual fibres, see Figure 4-3. These cracks may be created transversely, in-plane or at an angle. The transverse crack development will be mainly dominated by the in-plane stresses but those at other angles, including in-plane cracks, will be influenced to varying degrees by the transverse shear and normal stresses. Similarly, the inter-ply transverse cracks can appear on the planes perpendicular to the normal in-plane stresses, created not only from these stresses but also by in-plane shear (as shown with Figure 3-5 in Chapter 3). It is thought that delamination is triggered by these transverse inter-ply cracks when they reach the matrix-fibre interface which creates high-stress concentrations. In-plane and transverse stresses can also cause inter-yarn in-plane cracking which can cause localized delamination between fibre bundles [28, 29]. In-plane spacing between yarns has been shown to significantly influence the mechanical behaviour of woven composites, relating in particular to the in-plane moduli [29]. This can increase the potential for inter-yarn delamination.

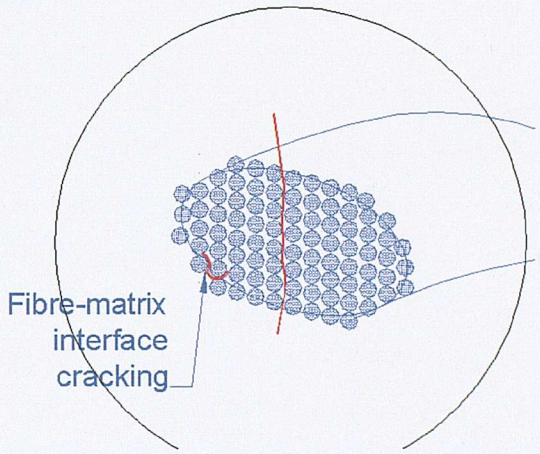


Figure 4-2. Close up of fibre bundle showing fibre-matrix interface cracking

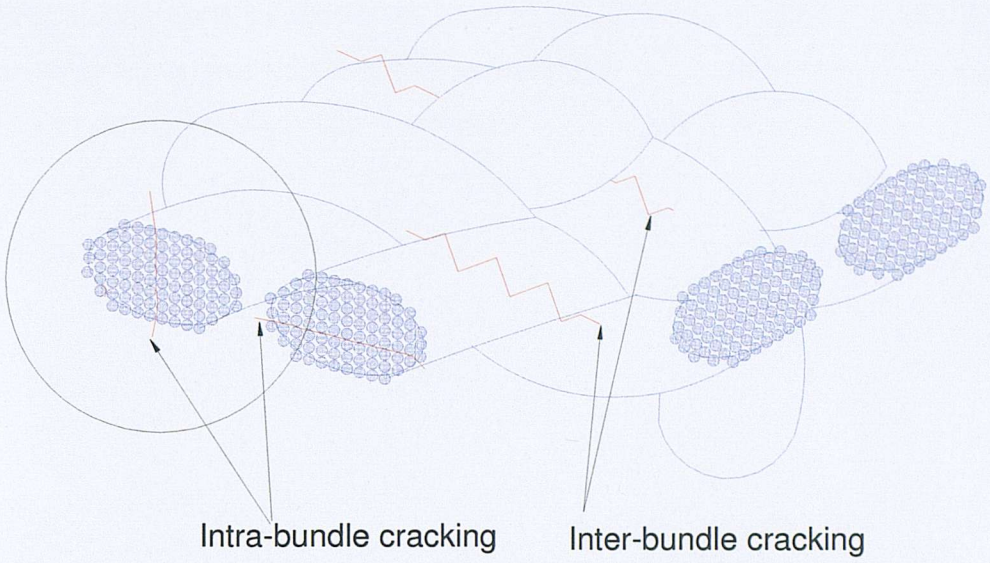


Figure 4-3. Matrix cracking in the woven composite

4.5 In-plane continuum damage fundamentals

Once damage has initiated, the material degrades and the elastic properties of the virgin material diminish, something that must be accounted for in the constitutive equations of the material model. Damage generally increases with increase in stress up to failure. Tests can be carried out to relate energy for damage to the number of cracks incurred over a given volume of the material. The energy per unit volume, i.e. energy density, absorbed by the material is a function of the material's elastic properties and the material stresses. The mean value of the energy density for a damaged material, represented with equation (4-1) [26] for plane-stress conditions, will therefore be different to that for an intact material, where ε_e represents the elastic strain. The degradation of the material properties can be achieved by introducing damage parameters, '**d**', and equation (4-1) is therefore a function of these damage parameters, the mean stresses and the virgin material moduli at each material point of interest. The degradation of each material property will depend on the particular state of stress and each damage parameter will therefore be a function of that stress. For example, d_1 represents damage in the principle 1 direction.

$$E_d = \frac{1}{2}\bar{\sigma}\varepsilon_e = \frac{1}{2}\left[\frac{\sigma_{11}^{\ 2}}{E_1^0(1-d_1)} - 2\frac{v_{12}^0}{E_1^0}\sigma_{11}\sigma_{22} + \frac{\sigma_{22}^{\ 2}}{E_2^0(1-d_2)} + \frac{\sigma_{12}^{\ 2}}{G_{12}^0(1-d_3)}\right] \tag{4-1}$$

Once damage has been created, the stress can described as the *effective stress,* $\bar{\sigma}$, which is the stress acting over the effective undamaged area, 'A'. Consider a specimen with damage (cracks and voids) pulled under a tension force 'F', see Figure 4-4(a).

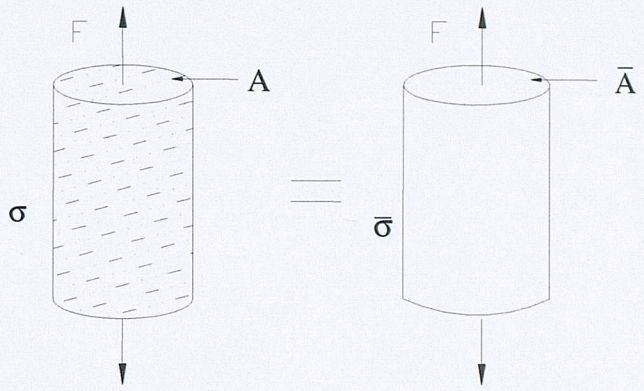


Figure 4-4. Nominal stress versus effective stress

The force F divided by the nominal total area 'A' is equal to the *nominal stress,* σ, as shown above, see also equation (4-2). If the same force is applied over an undamaged area $\bar{A}$; the total area minus the damage area, the resulting stress is the effective stress $\bar{\sigma}$. Shown schematically, $\bar{A}$ is the equivalent of Figure 4-4(a) minus the voids and cracks to give Figure 4-4(b). The damage created can be expressed as the damaged area over the total (damaged and undamaged area), see equation (4-3). Using equations (4-2) and (4-3), the equivalent stress can be written in terms of the damage parameter 'd' as shown with equation (4-4) .

$$F = \sigma A = \bar{\sigma}\bar{A} \tag{4-2}$$

$$d = \frac{A - \bar{A}}{A} = \frac{A_d}{A} \tag{4-3}$$

$$\bar{\sigma}_{ij} = \frac{\sigma_{ij}}{(1-d)} \tag{4-4}$$

The ability to create damage can be expressed in terms of *thermodynamic forces* or *damage energy release rates*, more specifically defined as the change in energy density with damage.

These energy variables are derivatives of equation (4-1) with respect to each individual damage variable, see equations (4-5) to (4-7). The in-plane damage variables are denoted by d_1, d_2, d_3 and these are responsible for the damage to the in-plane directions 11, 22, and 12 respectively, where E_{ij}^0 are the undamaged moduli.

$$Y_1 = \left.\frac{\partial E_d}{\partial d_1}\right|_{\tilde{\sigma},d_1,d_2:\text{cnst}} = \frac{\sigma_{11}^2}{2E_{11}^0(1-d_1)^2} \tag{4-5}$$

$$Y_2 = \left.\frac{\partial E_d}{\partial d_2}\right|_{\tilde{\sigma},d_1,d_2:\text{cnst}} = \frac{\sigma_{22}^2}{2E_{22}^0(1-d_2)^2} \tag{4-6}$$

$$Y_3 = \left.\frac{\partial E_d}{\partial d_3}\right|_{\tilde{\sigma},d_1,d_2:\text{cnst}} = \frac{\sigma_{12}^2}{2E_{12}^0(1-d_3)^2} \tag{4-7}$$

The evolution of damage in each material direction is represented with damage parameters that can be expressed in terms of one or more damage energy release rate variables, Y_i. For example, matrix cracking in one of the in-plane fibre directions, may be attributed to loading not only in this material direction but from in-plane shear stress also; as the type of damage produced is similar between normal in-plane tension and in-plane shear. Therefore in theory, a combination of stresses could be responsible for the damage incurred in each one of the material directions, and the damage parameter could, for a plane stress model, be a function of all of three energy density release rates, as shown with equations (4-8). This is in effect used to model coupling of different damage modes but in the proposed model coupling is not addressed.

$$d_1 = f_1(Y_1, Y_2, Y_3) \quad d_2 = f_2(Y_1, Y_2, Y_3), \quad d_3 = f_3(Y_1, Y_2, Y_3) \tag{4-8}$$

When a structural engineering material demonstrates non-linear deformation beyond a given limit stress (e.g. yield point for metals) and is loaded beyond this stress, permanent strain is often observed after unloading in shear. This was observed by Johnson [30] who implemented an elastic-plastic model to model these inelastic shear effects and validated the impact response of a E-glass fabric/epoxy composite plate. With fibre-reinforced (FRP) composites the permanent strain is often caused by the effects of damage and for prolonged loading also creep. The inelastic deformation from damage is caused by crack openings,

delamination and fibre failure, which is different to the actual plastic flow of the constitutive materials seen with plasticity. The composite material is brittle enough to exclude plastic flow in this definition of permanent strain. The proposed model, however, does not model any permanent strains and assumes a fictitious stress-strain response, where all the damage strain is recoverable, see Figure 4-5, where the initial modulus is E_{ini}, which gets degraded down to the final value at unloading, E_{fin}. In this model, the cracks created are closed again on unloading, and the damaged strain ε_d is not modelled as permanent and thus recoverable. So, even though the damage is created and the strains are recovered, the material has not healed.

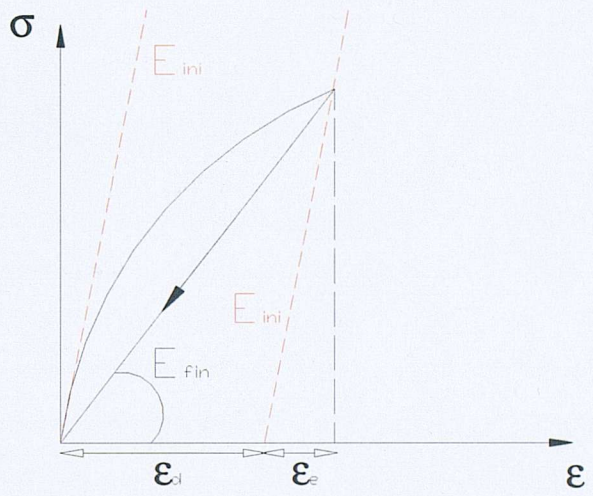


Figure 4-5. Fictitious stress-strain response

There are several assumptions associated with the proposed damage model, some of which are highlighted here:

i. The term 'damage' is generally referred to as the proportion of damaged material and although a material cross-section may be 80% saturated with cracks, the loss in stiffness may not be necessarily equal to 80% of the original stiffness. In this model, the *damage* term means the same as *stiffness reduction*. The stiffness reduction occurs as a result of the volume of numerous cracks within a unit volume of the material. In the FE analysis this is represented by the stiffness at a material point. This assumption implies that the crack size must be very small in relation to the volume associated with the material point, thus the cracks are not individually modelled but considered to be 'smeared' over the element volume. The amount of damage can be expressed through the damage parameter d.

ii. In this model, the *damage* term means the same as *stiffness reduction*.

iii. Keeping with the first and second laws of thermodynamics, the damage is irreversible and therefore the damage function is monotonically increasing, with the form:

$$d(t) = \max_{\tau \le t} \{d(\tau)\} \tag{4-9}$$

Where τ is the previous time and t is the current time, this condition states that the damage in the current time is dependent on the maximum attained damage during the loading history up to the current time.

iv. The material is elastic damaging and therefore the strains comprise of elastic strains and damage strains only.

*v.*Damage growth does not always lead to full failure of a material point or indeed a ply.

vi. Damage can only develop once the damage initiation function is activated to allow this.

4.6 Matrix damage initiation

Damage initiation is the point at which the stresses are large enough to initiate fracture mechanisms in the composite but more specifically related to cracking of the matrix before the reinforcing constituent. Treating the ply level as an orthotropic continuum, it is possible to postulate stress or strain based criteria that relate to specific fracture mechanisms or a more global criterion relating to 'in-plane damage' initiation or even more broadly if the stress is strongly three-dimensional as 'global' damage initiation i.e. when a crack is created in any direction in the material and is followed by damage propagation in any direction.

Various criteria have here been tested to predict the initiation of global damage. In addition, a separate in-plane criterion and translaminar criterion for damage initiation is also evaluated.

The first criterion to predict transverse matrix cracking (and thus in-plane damage initiation) is Hashin's 3D criterion [22] for matrix cracking which makes use of two equations; one when the transverse σ_{22} stress is compressive and the other for when it is tensile. The fact that the failure envelopes were designed for unidirectional laminae is manifested when the criteria are used on an orthotropic laminate, predicting a damage pattern that is always rectangular in shape. In the current work this is amended by replacing the orthogonal stress σ_{22} with an average of both the normal in-plane stresses. The FE analysis results are not shown in this chapter but a similar problem was experienced with the analyses in Figures 6-18 of Chapter 6. The results were not satisfactory with this formulation, since the tensile (bottom) side of the plate was always first to damage and continuing to do so predominantly more than the top of the plate. Hashin's formulation appeared to be inadequate for this

problem as damage initiation is predicted very late on in the analyses and is then followed by over-extensive areas of damage initiation.

The third criterion tested here for damage initiation has been successfully used for impact analyses of composite plates. It is an effective strain criterion suggested by Williams et al [7], shown in equation (4-10) which here includes the through-thickness strain component so that it can be used for 3d predictions.

- Equivalent strain function, a 3d version of that used by S K Williams.

$$F_i = \sqrt{\left(\frac{\varepsilon_{11}}{K}\right)^2 - \left(\frac{\varepsilon_{11}}{K}\right)\left(\frac{\varepsilon_{22}}{L}\right) + \left(\frac{\varepsilon_{22}}{L}\right)^2 + \left(\frac{\gamma_{12}}{S}\right)^2 + \left(\frac{\gamma_{23}}{T}\right)^2 + \left(\frac{\gamma_{31}}{U}\right)^2 + \left(\frac{\varepsilon_{33}}{V}\right)^2} \geq 1 \qquad (4\text{-}10)$$

Where K, L, S, T ,U and V are the strains to failure of the ply in the local in-plane 11-direction, the in-plane 22-direction, the in-plane shear (12) direction, the transverse normal 33-direciton and the two transverse shear directions 13 and 23 respectively, using standard tensile and compressive tests.

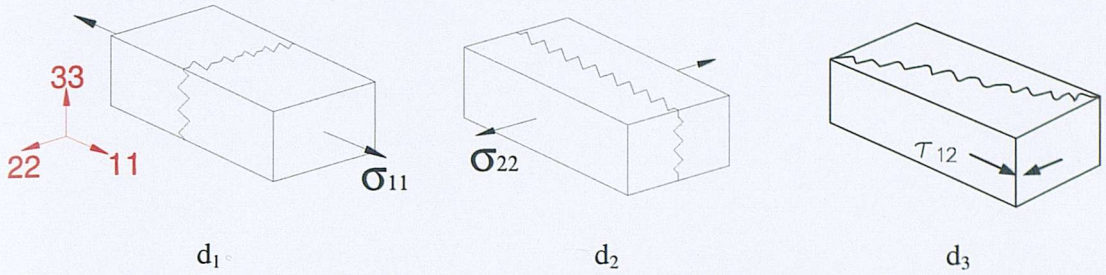
An alternative approach to damage initiation is to apply a separate stress criterion for out-of-plane damage initiation and use equation (4-10) to predict in-plane damage only without the transverse normal strain component. This approach is described later in Section 4.8.

4.7 In-plane damage propagation

Once damage has initiated under a given state of stress or strain, any increase in this loading will propagate the damage. In the present work, the normal in-plane damage propagation modes are uncoupled. The influence of the in-plane shear failure mode on the two fibre directions is also excluded. The former influence has the least consequence. A damaging stress σ_{11} creates transverse cracks on the '1' plane but their orientation is parallel to the orthogonal '2' direction and the effect of these cracks on the damage in the '2' direction can, on the over-all scale, be considered small. Therefore the only effect the normal in-plane directions have on each other is from Poisson's effect.

The three damage parameters are assumed to cover damage created in the form of transverse matrix cracks in the inter-yarn, intra-yarn and inter-ply region. Based on a continuum

approach, the damage modes can be simplified as shown in Figure 4-6: where damage in the normal '1' direction is a function of the normal stress σ_{11}, and damage in the normal '2' direction is a function of the stress σ_{22}.



d_1 d_2 d_3

Figure 4-6. Crack formation from in-plane stresses and the respective damage parameter assigned to each mode

Although cracks in the two orthogonal planes can also be created by the in-plane shear stress, here the shear damage variable d_3, which controls shear damage only, is not obtained directly from cyclic shear tests but is calculated as a function of the normal in-plane damage modes. The evolution of damage described with equations (4-8) can thereby be reduced to equations (4-11).

$$d_1 = f_1(Y_1) \quad d_2 = f_2(Y_2), \quad d_3 = f_3(Y_1, Y_2) \tag{4-11}$$

In the current model d_1, d_2, d_3 are responsible for both matrix and fibre damage.

A test that produces stable crack growth is required to characterize the effect of damage propagation in composites. Unnotched coupon tensile tests used in the past produce unstable crack growth soon after the start of any damage but cyclic or fatigue loading is one method of getting stable crack growth by developing the damage very slowly. Work by Talreja as discussed earlier, and other authors demonstrate that changes in moduli seen in fatigue testing of coupons can be used to quantify the damage incurred.

Inelastic (permanent) strains are caused by inelastic damage to the material (such as matrix cracking). GFRP plastics are generally strain-rate sensitive, however to reduce the testing complexity that would be involved with coupled strain rate and cyclic testing [13], the elastic constants are assumed to be independent of the strain rate of the material.

Work by Poursartip showed for CFRP that matrix and delamination damage produced a degradation of material stiffness that was linear with damage density [31]. A similar phenomenon is seen with GFRP work [5]. We would expect the rate of stiffness degradation for matrix and fibre damage to be different thus each damage parameter is assumed to have a

bilinear relationship with the stiffness lost. Previous work [2, 32, 33] shows that matrix damage occurs first followed by combined matrix and fibre damage until full failure. The in-plane CDM model can thus be regarded as consisting of four stages of material response:

1. Undamaged elastic stage
2. Damaging stage 1 – matrix dominated
3. Damaging stage 2 – fibre and matrix dominated
4. Failed

In-plane damage propagation can be described with a bilinear model. The value of each variable at each moment in time during the loading phase depends on a step function F. It is made up of the damage development functions F_{ini} F_m and F_f as shown in equation (4-12). The function for damage initiation i.e. the start of damaging stage 1, is F_{ini}, described above with equation (4-10) Thus when matrix damage is predicted then $F_i = 1$ and $F = 1 = F_I$.

The function that predicts the start of damaging stage 2 is F_m. When fibre damage initiates F_m=1 then $F = 2 = F_{II}$, see equations (4-13). The function that predicts full failure is F_f. When F_f =1 then F=3=F_{III}. The relationship between F and d is shown in Figure 4-7.

$$F = F_i + F_m + F_f$$
Step function (4-12)

$$d = \begin{cases} 0 & = d_m & \Leftarrow 0 < F \le F_I \\ \dfrac{F - F_I}{F_{II} - F_I} d_{II} = F d_{II} & = d_m & \Leftarrow F_I < F \le F_{II} \\ d_{II} + (1 - d_{II})(F - 2) & = d_m + d_f & \Leftarrow F_{II} < F \le F_{III} \\ 1 & = d_m + d_f & \Leftarrow F > F_{III} \end{cases} \quad (4\text{-}13)$$

The orthotropic nature of the WR composite requires that the in-plane moduli are reduced using individual functions. The damage variables for matrix and fibre damage responsible for degrading each of the 11 (warp), 22 (weft) and 12 (shear) directions are denoted by d_1, d_2, d_3 respectively. The variables d_1 and d_2 are applied to the warp and weft directions respectfully. They comprise of damage variables d_{im} and d_{if} representative of damage phase

1 and phase 2 respectfully, see equations (4-14). The matrix damage parameter is in the range of $d_I < d < d_{II}$, and the damage function for matrix damage F_m is in the range of $F_I < F_m < F_{II}$.

$$\begin{aligned} d_1 &= d_{1m} + d_{1f} \\ d_2 &= d_{2m} + d_{2f} \end{aligned} \tag{4-14}$$

The damage parameters can be further split into 'tension' and 'compression', in other words: d_{1T}, d_{2T} and d_{1C}, d_{2C} respectfully. The individual original intact moduli, E_{ij}^0 in tension and compression are therefore degraded as shown with equations (4-15). The stiffness *loss* is thus given by $E_{ij}^0 d_i$. An schematic of the relationship between d and E is shown in (4-8).

$$\begin{aligned} E_{11T} &= E_{11T}^0 (1 - d_{1T}) \\ E_{11C} &= E_{11C}^0 (1 - d_{1C}) \\ E_{22T} &= E_{22T}^0 (1 - d_{2T}) \\ E_{22C} &= E_{22C}^0 (1 - d_{2C}) \end{aligned} \tag{4-15}$$

The tensile and compressive moduli are only available for one of the orthogonal in-plane directions, therefore in the present work it is approximated that the composite is transversely orthotropic and therefore E_{22}=E_{11}.

The in-plane shear damage parameter d_3, can be given directly using William's damage coupling criterion shown in equation (4-16), omitting the need to carry out cyclic shear tests.

$$d_3 = \sqrt{d_1^2 + d_2^2 - d_1 d_2} \tag{4-16}$$

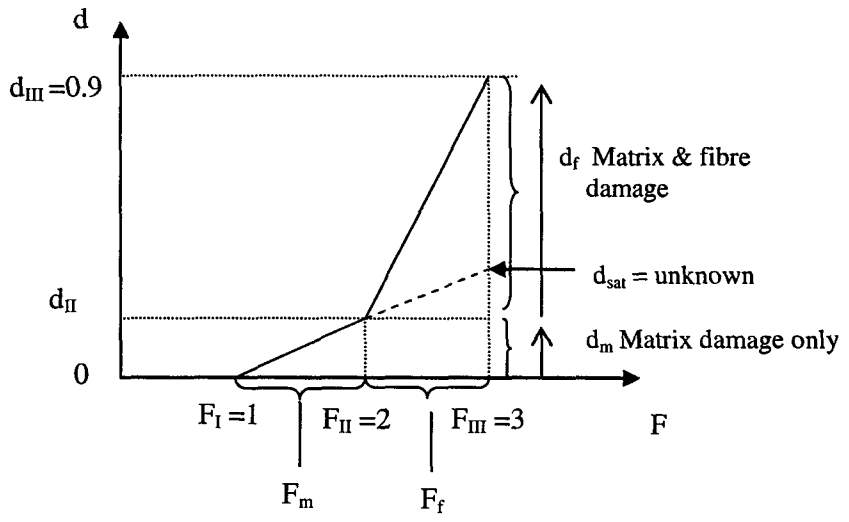


Figure 4-7. Damage parameter d as a function of F, where F and d vary for tension and compression.

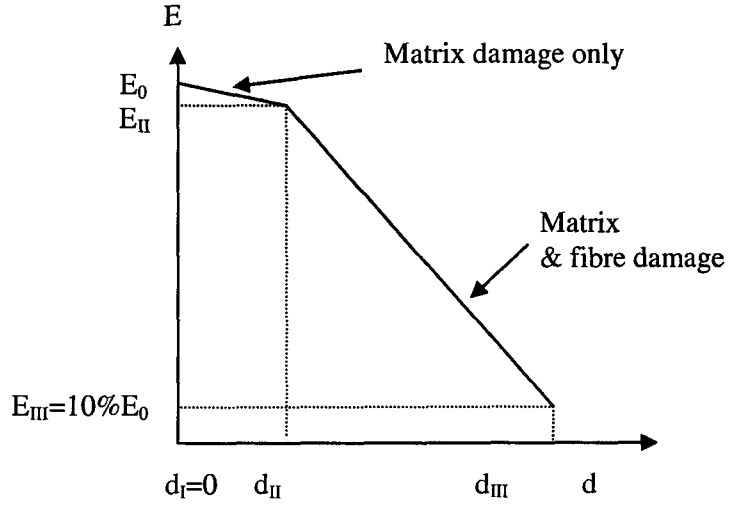


Figure 4-8. Modulus reduction as a function of d, for a given in-plane direction.

Ideally, in order to have two variables: one representing the damaged area and another representing the reduction in stiffness up to failure requires the extraction of the matrix damage saturation value $d_{sat(i)}$ [32] for transverse cracks, where i=1,2 represents the in-plane 11 and 22 directions. This value relates to the point when the area is saturated with matrix cracks and any other damage incurred is in the form of fibre failure. The area saturated with cracks can be measured and related to the degradation in stiffness. The stiffness at the point of matrix saturation can be used to obtain the rate of matrix damage i.e. the slope between $d_{I(i)}$ and $d_{II(i)}$ in The matrix saturation parameter is given by equation (4-17) where A_{net} is the

cross-sectional area of the remaining load bearing material and A_{total} is the total cross-sectional area. This parameter would be used to obtain $d_{II(i)}$ and $E_{II(i)}$ using the more involved expression in equation (4-18), where $R_{sat(i)}$ and $E_{sat(i)}$ is the reduction in stiffness and the stiffness at the point of matrix saturation respectfully.

The $d_{sat(i)}$ parameter was not obtained for the current material model therefore the term 'damage' is directly referred to as the percentage of stiffness loss and the $d_{II(i)}$ parameter was thus more simply obtained. The tangent of the stress-strain curve was derived for the last load cycle before fibre damage, thus providing the degraded modulus $E_{II(i)}$ for each of the two orthogonal in-plane directions, i.e. $E_{II1)}$ and $E_{m(2)}$. The stiffness during damage phase 1 $E_{II(i)}$ can therefore be directly related to the damage variable $d_{II(i)}$ using equation (4-19).

$$d_{sat} = 1 - \frac{A_{net}}{A_{total}} \tag{4-17}$$

$$E_{II(i)} = 1 - (1 - R_{sat(i)})\frac{d_{II(i)}}{d_{sat(i)}} \tag{4-18}$$

$$\text{where } d_{II(i)} = d_{sat(i)}\left(\frac{F_{(i)} - F_{I(i)}}{F_{III(i)} - F_{I(i)}}\right) \text{ and } R_{sat(i)} = \frac{E_{sat(i)}}{E_i^0}$$

$$d_{II(i)} = \frac{E_i^0 - E_{II(i)}}{E_i^0} \tag{4-19}$$

4.7.1 Matrix damage development function

Here we test two damage development functions for phase 1 damage: one based on the energy density of the material, equation (4-20) and the other based on the strain, equation (4-21).

$$F_{mi} = f(Y_i) \tag{4-20}$$

$$F_{mi} = f(\varepsilon_{ii}) \tag{4-21}$$

Damage progression is only possible if the damage forces are larger than those obtained throughout the previous loading history. This is best expressed in terms of the maximum attained value, as exemplified with equation (4-22) for the energy based function, where 't' is any time during the loading history up to the current time 'T'.

$$F_{mi}(T) = \max\{Y_i(t)\}, \tag{4-22}$$

The parameters for both functions are obtained experimentally from cyclic tests on the woven laminate coupons.

Energy function

The dissipated energy function is calculated for the warp and weft directions for tension and compression, as shown with equation (4-23).

$$F_{miT} = f(Y_{iT}),\ F_{miC} = f(Y_{iC}) \quad \text{where i=1,2 (no summation of i)} \tag{4-23}$$

The general function is a linear function of the damage forces, given with equation (4-24). The maximum attained damage force, $Y_{max} = \sqrt{Y_{max}} = \frac{\bar{\sigma}}{\sqrt{2E}}$, is calculated during the FE analysis and inserted into (4-24). Various cyclic tests were carried out along each of the warp and weft directions, as explained in Chapter 2, half under compression loading and the other half under tensile loading. For a given test the square root of the energy is plotted against the damage variable, as shown schematically with Figure 4-9, which represents damage stage 1 in Figure 4-7. The energy values were obtained by taking the area under the stress-strain curve for the last cycle of the set of 5 before the next increment in strain. The parameter $\sqrt{Y_0}$ coincides with the start of matrix damage and $\sqrt{Y_0} + \sqrt{Y'}$ the start of fibre damage (start of phase 2 damage). However, the damage initiation function of equation (4-10) still dictates the start of matrix damage and $\sqrt{Y_0}$ only acts to define the damage gradient of damage stage 1.

The damage variable is calculated by the gradient of the stress-strain curve at that point and the original intact modulus, using expression (4-25).

$$F_m = \frac{\frac{\bar{\sigma}}{\sqrt{2E}} - \sqrt{Y_0}}{\sqrt{Y'}} \tag{4-24}$$

$$d_{mi} = \frac{E_i^0 - E_i}{E_i^0} \tag{4-25}$$

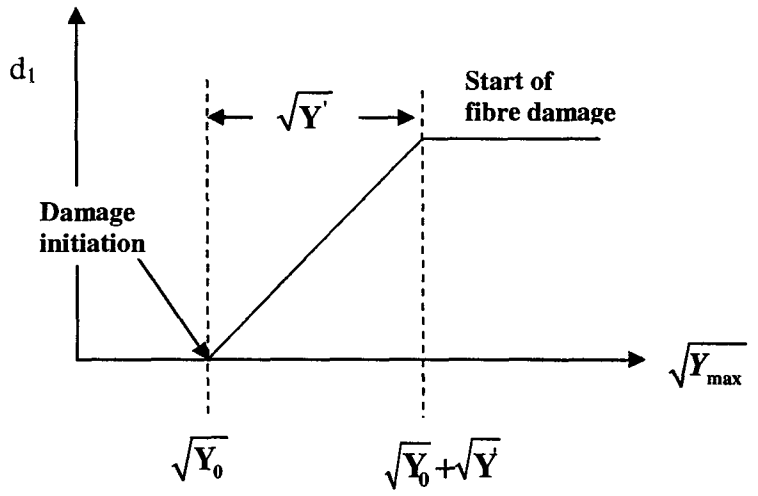


Figure 4-9. Function of damage energy release rate versus damage.

Strain function

The second function tested to predict matrix damage development is one of strain. Equations (4-26) represent the damage functions for damaging phase 1 for the warp and weft in tension and compression.

$$F_{miT} = f(\varepsilon_{iiT}),\ F_{miC} = f(\varepsilon_{iiC}) \quad \text{where i=1,2 (no summation of i)} \tag{4-26}$$

This general function is linear in strain and is given by equation (4-27); where ε_0 is the strain at which matrix damage initiates, ε is the actual instantaneous strain calculated in the analysis and ε_f is the strain at which fibre damage initiates. The strain thresholds used in these damage development functions were obtained from tensile cyclic tests in the warp and weft directions, for tension and compression, as shown below, also discussed earlier in Section 2.6 of Chapter 2.

ε_{f1T} = strain at the start of fibre damage in the warp direction under a tensile load.
ε_{f2T} = strain at the start of fibre damage in the weft direction under a tensile load.
ε_{f1C} = strain at the start of fibre damage in the warp direction under a compressive load
ε_{f2C} = strain at the start of fibre damage in the weft direction under a compressive load.

$$F_m = \frac{\varepsilon_f(\varepsilon - \varepsilon_0)}{\varepsilon(\varepsilon_f - \varepsilon_0)} \tag{4-27}$$

The formulation of equation (4-27) suggests that damage cannot initiate until ε_0 has been reached. This strain is dictated by the damage initiation function. Therefore the strain in the warp and weft directions, ε_{01} and ε_{02}, when $F_{ini}=1$ are recorded during the FE analysis and used in the above expression. Hence their values are not fixed.

The damage variable d_{mi} is obtained in the same way as described above, with equation (4-25).

4.7.2 Fibre damage development function

Fibre damage takes place when the scalar potential function for fibre failure, F_f, lies in the range $F_{II} < F_f < F_{III}$ and the damage variable is in the region $d_{II} < d < d_{III}$. The function is strain based and should be applied separately to the warp and weft direction in tension and compression, as shown with equations (4-28).

$$F_{fiT} = f(\varepsilon_{iiT}),\ F_{fiC} = f(\varepsilon_{iiC}) \quad \text{where i=1,2 (no summation of i)} \tag{4-28}$$

The potential function is based on the strain to failure of the fibre, ε_{max}, as shown with equation (4-29).

$$F_f = \frac{\varepsilon_{11}}{\varepsilon_{max}} \tag{4-29}$$

The strain at rupture, parameter ε_{max}, is not easy to estimate analytically and requires test data. As one would expect, the strain to failure of the undamaged composite material is found to be lower than that of the damaged material in the softening zone, as shown by Kongshavn and Poursartip [34] and their work on carbon fibre/epoxy systems. This work involved growing damage in a stable manner using a compact tension specimen then carrying out tensile tests to failure using material from the damaged portion of the specimen, demonstrating rupture strains of 3-4%. Tensile tests to failure for the undamaged material on the other hand, gave rupture strains of about 1.5%. Williams et al used a strain to rupture value of 0.04 in their model, although there is no indication of where this value came from, reference is made to the significance of Kongshavn and Poursartip's experimental work. Thus, due to lack of experimental data for fibre failure for the woven E-glass/vinyl ester in the present work, we use the strain value of 0.04 to depict full fibre failure and therefore full material failure in the warp and weft directions, for tension and compression. In other words

the strains in expressions (4-28) are assigned the same values: $\varepsilon_{11T} = \varepsilon_{11C} = \varepsilon_{22T} = \varepsilon_{22C} = \varepsilon = 0.04$. In reality this strain may be larger for this woven roving.

The parameters ε_f, d_{II} and ε_{max} used for the FE analyses are shown below in Table 4-1. The table shows the average values of ε_f and d_{II} obtained from the set of coupon tests in each of the warp and weft directions for tensile and compressive loading.

Cyclic testing	ε_f (average)	ε_{max}	d_{II} (average)
Warp, tensile	0.0225	0.04 (Williams)	0.17
Warp, compressive	-0.015	-0.04	0.035
Weft, tensile	0.0208	0.04	0.23
Weft, compressive	-0.015	-0.04	0.027

Table 4-1. Critical strain and damage parameters used in the in-plane damage model.

4.8 Intra-ply transverse damage

4.8.1 Initiation of intra-ply transverse damage

Three different criteria are tested to predict the initiation of in-plane cracks caused by the transverse stresses at the woven ply.

- Global damage initiation prediction

Using the equivalent strain criterion, equation (4-10), used globally for damage anywhere in the material.

- Separate transverse intra-ply damage initiation criteria
  - Maximum stress criteria, applied to each transverse direction individually.
  - Quadratic criterion of the transverse stresses.

The first approach is to use the equivalent strain criterion as a global damage initiation criterion. The second approach is to apply a separate out-of-plane stress criterion to predict intra-laminar transverse damage and use the equivalent strain criterion separately to predict in-plane damage initiation. The first out-of-plane criterion is one of simple maximum stress, equations (4-30), after which the modulus is simply reduced once only down to its residual value, thus requiring no damage propagation criterion. The second criterion is a quadratic stress function, equation (4-31), the same as Brewer and Legace delamination criterion [35]. This was chosen because it requires readily available strength data and it is also more conservative than using the single maximum stress criterion.

$$\left(\frac{\sigma_{33}}{Z_T}\right) \geq 1, \left(\frac{\sigma_{23}}{S_{23}}\right) \geq 1, \left(\frac{\sigma_{13}}{S_{31}}\right) \geq 1 \tag{4-30}$$

$$\left(\frac{\sigma_{33}}{Z_T}\right)^2 + \left(\frac{\sigma_{23}}{S_{23}}\right)^2 + \left(\frac{\sigma_{13}}{S_{31}}\right)^2 \geq 1 \tag{4-31}$$

4.8.2 Propagation of intra-ply transverse damage

The translaminar properties are reduced due to the formation of in-plane and transverse shear cracks inside the fibre bundles but a more serious contribution of these stresses is inter-ply separation, i.e. delamination, and ply-shear out [16]. In the present work delamination is separately modelled using a cohesive zone model in Section 5.6 of Chapter 5. With thicker plates not every ply in the FE model can be analysed for delamination thus transverse damage modelling at the solid layers is important in addition to delamination modelling. The modes of damage resulting from these stresses are represented with the damage variables d_4, d_5 and d_6, as shown with the crude schematic in (4-10).

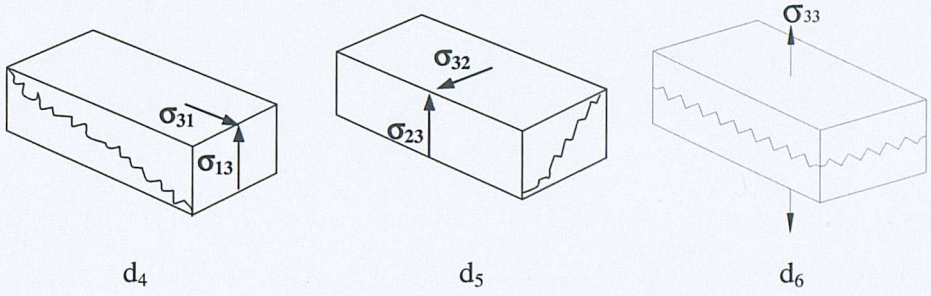


Figure 4-10. Transverse fracture and the respective damage variables assigned to these modes

Unless specified, damage initiation in the transverse direction is defined with either the global equivalent strain criterion, equation (4-10) or a separate stress criterion specific to the transverse direction only; equations (4-30) or (4-31). The moduli of the solid elements are gradually reduced to 10% of their original value using maximum stress criteria, equations (4-32) unless equation (4-30) is used for damage initiation, in which case the propagation criterion for the transverse direction is ignored and the moduli are degraded once to the residual value. The Macauley brackets used in the equations are denoted by $\langle x \rangle_+ = \frac{1}{2}(x + |x|)$ and $\langle x \rangle_- = \frac{1}{2}(x - |x|)$. Degradation is carried out using the damage variables in equations (4-33). The difference between the compressive and tensile behaviour of the material is incorporated using the relevant ultimate stress values from standard transverse compressive and tensile tests.

$$F_3 = \frac{\langle \sigma_{33} \rangle_+}{\sigma_{33T}^{max}} + \frac{\langle \sigma_{33} \rangle_-}{\sigma_{33C}^{max}}, \quad F_4 = \frac{\sigma_{13}}{\sigma_{13}^{max}}, \quad F_5 = \frac{\sigma_{23}}{\sigma_{23}^{max}} \tag{4-32}$$

$$d_4 = 0.9F_4 \quad d_5 = 0.9F_5, \quad d_6 = 0.9F_6 \tag{4-33}$$

The transverse moduli are thus degraded as shown with equations (4-34).

$$\begin{aligned} E_{13} &= E_{13}^0(1-d_4) \\ E_{23} &= E_{23}^0(1-d_5) \\ E_{33T} &= E_{33T}^0(1-d_{6T}) \\ E_{33C} &= E_{33C}^0(1-d_{6C}) \end{aligned} \tag{4-34}$$

4.9 Element erosion

Some impacts may cause the tup to partially or fully penetrate the plate. Under these circumstances it would be reasonable to delete elements that have fully failed by all modes of failure. This concept is however limited by the mesh density. If the mesh density is too coarse, the deformation of the plate may not be modelled as accurately and sudden deletion of a large element may result in unrealistic damage behaviour. In any case, the capability for element erosion is examined and the following criterion is put to the test:

$$F_{1f} + F_{2f} + F_3 + F_4 + F_5 = 5 \tag{4-35}$$

Where F_{1f} and F_{2f} are the potential functions for fibre failure and F_3, F_4 and F_5 for transverse damage.

4.10 Constitutive law for an undamaged 2d orthotropic plate

The in-plane orthotropic nature of the composite can be described with the stress-strain relationship in equation (4-36), where Q_{ij} is the reduced stiffness matrix.

$$\begin{aligned} Q_{11} &= E_{11}/\left(1-v_{12}^2\right) \\ Q_{22} &= E_{22}/\left(1-v_{12}^2\right) \end{aligned} \tag{4-36}$$

$$\begin{Bmatrix}\sigma_{11}\\ \sigma_{22}\\ \sigma_{12}\end{Bmatrix}=\begin{bmatrix}Q_{11} & Q_{12} & 0\\ Q_{12} & Q_{22} & 0\\ 0 & 0 & Q_{33}\end{bmatrix}\begin{Bmatrix}\varepsilon_{11}\\ \varepsilon_{22}\\ \varepsilon_{12}\end{Bmatrix} \qquad Q_{12}=v_{12}E_{22}/\left(1-v_{12}^2\right)$$

4.11 Constitutive law for a damaged 3d orthotropic plate

The stress acting over the effective undamaged area of the damaged material is the effective stress, equation (4-37), where D is the damage matrix, equation (4-38), and σ is the nominal stress (stress acting over the original, undamaged area).

$$\bar{\sigma}=\sigma\mathbf{D} \tag{4-37}$$

$$D=\frac{1}{1-d} \tag{4-38}$$

The stiffness matrix in the expression for σ, equation (4-39), is shown in equation (4-40) for an orthotropic material.

$$\sigma_{ij}=C_{ijkl}\varepsilon_{kl} \tag{4-39}$$

$$\{C\}=\begin{bmatrix}C_{11} & C_{12} & C_{13} & 0 & 0 & 0\\ C_{12} & C_{22} & C_{23} & 0 & 0 & 0\\ C_{13} & C_{23} & C_{33} & 0 & 0 & 0\\ 0 & 0 & 0 & C_{44} & 0 & 0\\ 0 & 0 & 0 & 0 & C_{55} & 0\\ 0 & 0 & 0 & 0 & 0 & C_{66}\end{bmatrix} \tag{4-40}$$

The stiffness matrix for the damaged material can be obtained by inversing the compliance matrix, see equation (4-41).

$$\mathbf{C}=\mathbf{S}^{-1} \tag{4-41}$$

The strain created in the in-plane fibre direction 11 for a damaging material is created by the effective stress $\bar{\sigma}_{11}$ and the Poisson's effect from the other two normal effective stresses

Damage of the Poisson's ratios can be expressed as a function of the damage variables ($\mathbf{d}$ = d_1, d_2, d_3, d_4, d_5, d_6). Thus the strain in the fibre direction 11 from Poisson's effect can be written as shown in equation (4-42), where '$r_{ij}(\mathbf{d})$' are the Poisson's ratios degradation

factors. They are functions of the damage variables assigned to a specific Poisson's ratio. The functions assigned to r_{ij} are discussed further on.

$$\varepsilon_{11} = \frac{1}{E_{11}}\bar{\sigma}_{11} - \frac{r_{21}(\mathbf{d})\nu_{21}}{E_{11}}\bar{\sigma}_{22} - \frac{r_{31}(\mathbf{d})\nu_{31}}{E_{11}}\bar{\sigma}_{33} \tag{4-42}$$

The postulate of strain equivalence states that the strain created by a stress σ applied to a damaged material is equivalent to the strain created by a stress $\bar{\sigma}$ to an undamaged material. See equation (4-43) where $\bar{S}$ represents the compliance matrix for the damaged material, σ is the nominal stress, is S the compliance matrix for the undamaged material.

$$\boldsymbol{\varepsilon} = \bar{\mathbf{S}}\boldsymbol{\sigma} = \mathbf{S}\bar{\boldsymbol{\sigma}} \tag{4-43}$$

Therefore the strain can be given as:

$$\begin{Bmatrix} \varepsilon_{11} \\ \varepsilon_{22} \\ \varepsilon_{33} \\ \varepsilon_{23} \\ \varepsilon_{13} \\ \varepsilon_{12} \end{Bmatrix} = \begin{bmatrix} \frac{1}{(1-d_1)E_{11}} & \frac{-r_{21}\nu_{21}}{(1-d_2)E_{22}} & \frac{-r_{31}\nu_{31}}{(1-d_3)E_{33}} & 0 & 0 & 0 \\ \frac{-r_{12}\nu_{12}}{(1-d_1)E_{11}} & \frac{1}{(1-d_2)E_{22}} & \frac{-r_{32}\nu_{32}}{(1-d_3)E_{33}} & 0 & 0 & 0 \\ \frac{-r_{13}\nu_{13}}{(1-d_1)E_{11}} & \frac{-r_{23}\nu_{23}}{(1-d_2)E_{22}} & \frac{1}{(1-d_3)E_{33}} & 0 & 0 & 0 \\ 0 & 0 & 0 & \frac{1}{(1-d_4)E_{11}} & 0 & 0 \\ 0 & 0 & 0 & 0 & \frac{1}{(1-d_5)E_{11}} & 0 \\ 0 & 0 & 0 & 0 & 0 & \frac{1}{(1-d_6)E_{12}} \end{bmatrix} \begin{Bmatrix} \sigma_{11} \\ \sigma_{22} \\ \sigma_{33} \\ \sigma_{23} \\ \sigma_{13} \\ \sigma_{12} \end{Bmatrix} \tag{4-44}$$

Work carried out by various authors including Highsmith and Reifsnider and Law's et al showed that cracks parallel to the fibre direction do not have an effect on the stiffness in that direction. The same can be said about Poisson's effect. Poisson's effects from the orthogonal direction, ν_{21}, for example, is affected by the damage in the 22 direction and not from cracks in the 11 direction. The symmetry of the compliance tensor applies to both the damaged and undamaged material, thus the following relationship applies, where the superscript 'd' refers to the damaged variable:

$$\frac{\upsilon_{12}}{E_{11}} = \frac{\upsilon_{21}}{E_{22}}$$
$$\frac{\nu_{12}^{d}}{E_{11}^{d}} = \frac{\nu_{21}^{d}}{E_{22}^{d}} \tag{4-45}$$

$$\frac{r_{12}\upsilon_{12}}{(1-d_1)E_{11}} = \frac{r_{21}\upsilon_{21}}{(1-d_2)E_{22}} \tag{4-46}$$

Based on equation (4-45) and (4-46), the relationship in equation (4-47) also holds true.

$$\frac{r_{12}}{(1-d_1)} = \frac{r_{21}}{(1-d_2)} \tag{4-47}$$

One simple formulation for r_{12} and r_{21} could be $(1-d_1)$ and $(1-d_2)$ respectfully. This could be an approximation for the current material as an actual value for the degradation is unknown. However, evidence on Poisson's ratio reduction with damage in cross-ply composites [36] shows a maximum degradation of almost 50%. In the current work, due to lack of data on Poisson's reduction in woven composites, this degradation factor is used. The Poisson's ratio degradation factors, written in terms of the orthogonal in-plane damage variables, can thus be given directly as: $(1-0.556d_1)$ and $(1-0.556d_2)$. Noting that $0.556d_{III} = 0.5$. The Poisson's ratios degradation factors are therefore simple functions of the damage variables as shown in equations (4-48).

$$r_{12} = (1-0.556d_1),\ r_{21} = (1-0.556d_2)$$
$$r_{13} = (1-0.556d_1),\ r_{31} = (1-0.556d_6),\ r_{23} = (1-0.556d_2),\ r_{32} = (1-0.556d_6) \tag{4-48}$$

The moduli in the warp and weft directions are assigned the same values, shown in Tables 2-1 and 2-2 of Chapter 2. Thus the following relationships hold true between the in-plane minor and major Poisson's ratios, see equations (4-49).

$$E_1 = E_2$$
$$\text{as } \frac{\nu_{ij}}{E_i} = \frac{\nu_{ji}}{E_j} \quad \therefore \nu_{12} = \nu_{21} \tag{4-49}$$

There is no experimental data on the intact through-thickness Poisson's ratios ν_{13} or ν_{23}. Therefore these properties were assigned the values for the WR E-glass/vinyl-ester properties used by Bahei-El-Din et al [37].

Based on all of the above, the stiffness matrix can be given as in equation (4-50).

$$\begin{Bmatrix}\sigma_{11}\\ \sigma_{22}\\ \sigma_{33}\\ \sigma_{23}\\ \sigma_{13}\\ \sigma_{12}\end{Bmatrix}=\begin{bmatrix}\frac{(1-r_{23}r_{32}\nu_{23}\nu_{32})(1-d_1)E_1}{\Delta} & \frac{(r_{21}\nu_{21}+r_{31}r_{23}\nu_{31}\nu_{23})(1-d_1)E_1}{\Delta} & \frac{(r_{31}\nu_{31}+r_{21}r_{32}\nu_{21}\nu_{32})(1-d_1)E_1}{\Delta} & 0 & 0 & 0\\ \frac{(r_{12}\nu_{12}+r_{32}r_{13}\nu_{32}\nu_{13})(1-d_2)E_2}{\Delta} & \frac{(1-r_{13}r_{31}\nu_{13}\nu_{31})(1-d_2)E_2}{\Delta} & \frac{(r_{32}\nu_{32}+r_{12}r_{31}\nu_{12}\nu_{31})(1-d_2)E_2}{\Delta} & 0 & 0 & 0\\ \frac{(r_{13}\nu_{13}+r_{12}r_{23}\nu_{12}\nu_{23})(1-d_3)E_3}{\Delta} & \frac{(r_{23}\nu_{23}+r_{21}r_{13}\nu_{21}\nu_{13})(1-d_3)E_3}{\Delta} & \frac{(1-r_{12}r_{21}\nu_{12}\nu_{21})(1-d_3)E_3}{\Delta} & 0 & 0 & 0\\ 0 & 0 & 0 & (1-d_4)G_{23} & 0 & 0\\ 0 & 0 & 0 & 0 & (1-d_5)G_{31} & 0\\ 0 & 0 & 0 & 0 & 0 & (1-d_6)G_{12}\end{bmatrix}\begin{Bmatrix}\varepsilon_{11}\\ \varepsilon_{22}\\ \varepsilon_{33}\\ \varepsilon_{23}\\ \varepsilon_{13}\\ \varepsilon_{12}\end{Bmatrix} \quad (4\text{-}50)$$

$$\Delta=1-r_{12}r_{21}\nu_{12}\nu_{21}-r_{13}r_{31}\nu_{13}\nu_{31}-r_{23}r_{32}\nu_{23}\nu_{32}-2r_{21}r_{13}r_{32}\nu_{21}\nu_{13}\nu_{32}$$

Implementing the constitutive material behaviour in a finite element package such as Abaqus can be done via a user material subroutine. When Abaqus/Explicit is used, the subroutine, which is coded in Fortran, is called a VUMAT. The stresses in the VUMAT are updated incrementally as shown in equation (4-51) and the incremental stress as in equation (4-52), where C_{ijkl} is the undamaged or damaged stiffness matrix.

$$\sigma_{ij}^{new} = \sigma_{ij}^{old} + \Delta\sigma_{ij} \tag{4-51}$$

$$\Delta\sigma_{ij} = C_{ijkl}\Delta\varepsilon_{kl} \tag{4-52}$$

In Abaqus/Explicit, a small amount of damping is implemented by default in the form of 'bulk viscosity, to reduce high frequency oscillations. This method of damping is associated with volumetric straining and in Explicit, the default is a linear relationship. A bulk viscosity pressure is generated based on the equation:

$$P_{bv} = b\rho C_d L_e \dot{\varepsilon}_{vol}$$

Where b is the damping coefficient, by default equal to 0.06; ρ is the material density; C_d is the current dilatational wave speed; L_e is the characteristic element length and $\dot{\varepsilon}_{vol}$ is the volumetric strain rate.

4.12 Numerical implementation – Impact of small and large-scale plates

4.12.1 Introduction

In this section the proposed damage model is validated for small and large scale woven-ply composite plates under low velocity impact in Abaqus/Explicit. Small composite plates of 0.2286x0.1778x0.00638m^3 (9x7x0.25in^3) were tested under impact, with 'small' 12.7mm, 'medium' 25.4mm and 'large' 38mm diameter tups of various masses, as detailed in Section 2.8 of Chapter 2. The test name labels provide information on the size of the impactor and the impact energy. The letters following the test number (which for the medium tup impact tests is not sequential), 'S', 'M' or 'L', stand for small, medium and large impactor diameter. All the small plates in the ensuing analyses are modelled with simply supported boundary conditions, i.e. if u(x) and v(y) are the displacements along the plate edges and w(z) in the

o.o.p direction, then $(w)_{x=0}=0$ and $\left(\frac{\partial^2 w}{\partial x^2}\right)_{x=0}=0$ along the edge x=0 and similarly along the edge y=0. The large-scale plates ($1.07315x0.76835x0.019m^3$), large1, were impacted with a 203mm tup diameter. Their boundary conditions were $(w)_{x=0}=(u)_{x=0}=(v)_{x=0}=0$ and $\left(\frac{\partial^2 w}{\partial x^2}\right)_{x=0}=0$. Only one of the small and two of the large1 were considered for numerical validation in this section. Eight solid elements were used through the thickness for the small plate and five for the large plate.

Abaqus/Explicit has no USFLD subroutine available to define failure criteria. It is therefore necessary to implement a User Material subroutine (VUMAT), which requires the definition of the composite's constitutive behaviour. Seeing that the loading is dynamic, the ensuing analyses were applied in Abaqus/explicit, largely to reduce the modelling time.

The following FE analyses applied the global strain criterion, equation (4-10) for global damage initiation, and equation (4-27) for the propagation of in-plane matrix damage. The transverse material properties were degraded as per Section 4.8. The plates were meshed with solid elements (continuum elements) of type C3D8R, which are linear, have 8 nodes and are of reduced integration, as shown with Figure 4-11, and also have hourglass control. The integration point of the C3D8R element can be found at the centre of the element.

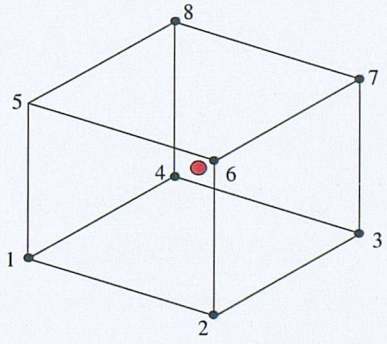


Figure 4-11. C3D8R brick element in Abaqus

A small and three large plate tests are validated here: test 9M(195J) ('M' indicating medium sized tup and 195J the impact energy), and large1 tests A, C and D. The small plate was modelled with five solid elements through the thickness, therefore one element representing 1.8 plies. To reduce the computational cost, the large plate was also modelled with 8 C3D8R elements through the thickness, even though the plate had in reality of 29 plies. This solid element stacking is consistent with part of the work in Chapter 6. The largest plate element size was 3.2mm long for the small plate, see Figure 4-12, and 5mm for the large plate.

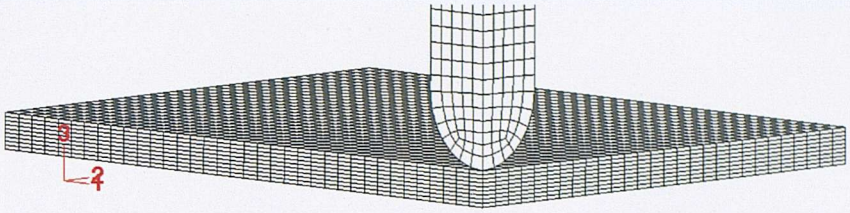


Figure 4-12. Standard mesh used for the small plate analyses

Cyclic tests were carried out to obtain the model parameters where performed on the same WR composite used for the plates in these impact tests. The material properties applied were an average of those obtained from standard coupon tests, summarized in Section 2.3 of Chapter 2.

4.12.2 Explicit time integration

The analyses were carried out in Abaqus/Explicit because the impact event is dynamic with relatively short dynamic response times (at least compared to a quasi-static case). The largest difference between the implicit and explicit integration schemes is the way in which the nodal accelerations is calculated. In implicit these are calculated by solving a set of linear equations using an iterative solution method (see Section 3.5.3 of Chapter 3). In Explicit there is no global tangent stiffness matrix and no iterations or tolerances are required. The explicit integration technique, using the central difference operator, is conditionally stable, which means there is a stability limit for the time increment based on the time it takes for an elastic wave to cross the shortest element dimension in the model. In implicit the size of the time increment is dictated by the accuracy of the solution; each time increment requires a number of iterations to reach equilibrium based on the prescribed tolerances. Even though explicit integration is carried out using many small increments an implicit analysis with many iterations is comparably much less efficient and as a result the running times can be quite long, particularly where subroutines are involved. The disk space and memory usage for the same simulation is also much larger than with an explicit analysis.

4.12.3 Results and discussion

The 3d damage model has the effect of reducing the contact force and increasing the maximum o.o.p. displacement compared to a no-damage model. The contact force for the small plate, test 9M(195J), is shown in Figure 4-13. The contact force is visibly reduced from using a no-damage model, 'No damage solid 5', to applying the 3d damage at the woven plies, 'solid 5'. The o.o.p displacement is as expected, slightly larger for the damage

model because moduli are reduced thus responsible for the larger elastic strains. A viscoplastic (hardening) model would help reduce the size of the elastic strains and although an isotropic viscoplastic model is implemented later in Chapter 5 at the resin-rich layers, the current work has not considered a similar model for the woven plies.

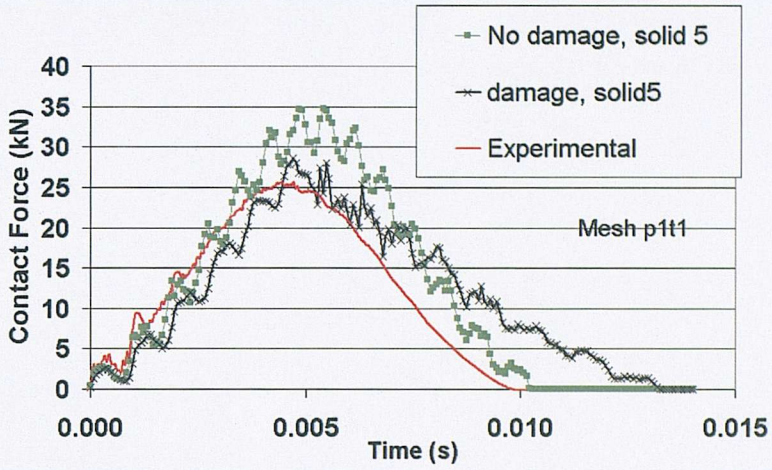
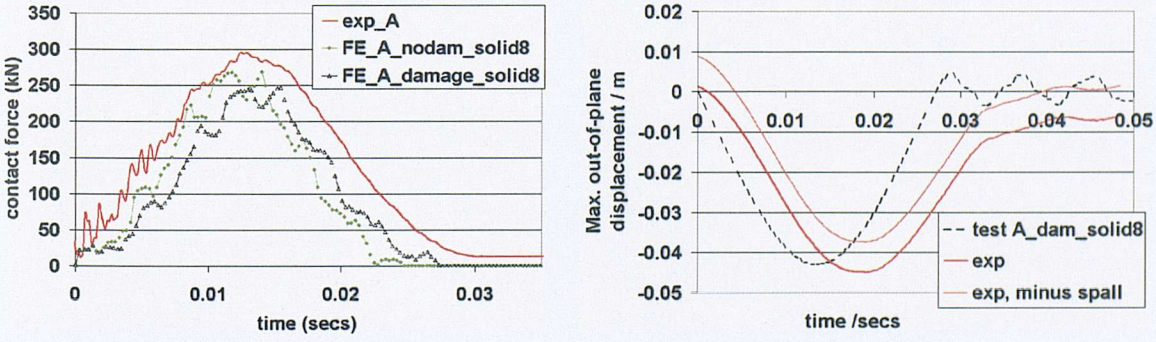


Figure 4-13. Contact force for small plate, Test 9M(195J): test and FE results

Whereas the contact force is improved for the small plate analysis, the same is not true with test large1(A). In fact, the no-damage model was already under predicting the contact force compared to the test, and in the analysis the plate appears to be quite flexible see Figure 4-14(a) and (b), even relative to the spall-inclusive displacement. Spalling is where the fibres at the bottom of the plate break and fan out because of the high tensile stresses. Fibre spall cannot be modelled with the current model and the spall must be subtracted from the test o.o.p displacement measurements. Under-prediction of contact force is not as prominent with the higher energy impact test large1(B), with the no-damage model providing a peak contact force of similar magnitude to the test not lower. Increasing the impact energy even further, as with tests C and D, results in an analysis that benefits from the damage mod el.



(a) (b)

Figure 4-14. Test and FE results for Large1(A), (a) contact force and (b) Max. o.o.p displacement.

Two identical tests were carried out for the large plate 'large1', tests C and D. The peak contact force prediction with the damage model is reduced for the large plate although not significantly, see Figure 4-15. The maximum o.o.p displacements for tests C and D are different and the spall at the bottom of the plate makes a considerable difference to the maximum o.o.p displacement, as evident in Figure 4-16. The maximum o.o.p displacement prediction is again conservative when compared against the test results which exclude the fibre spall.

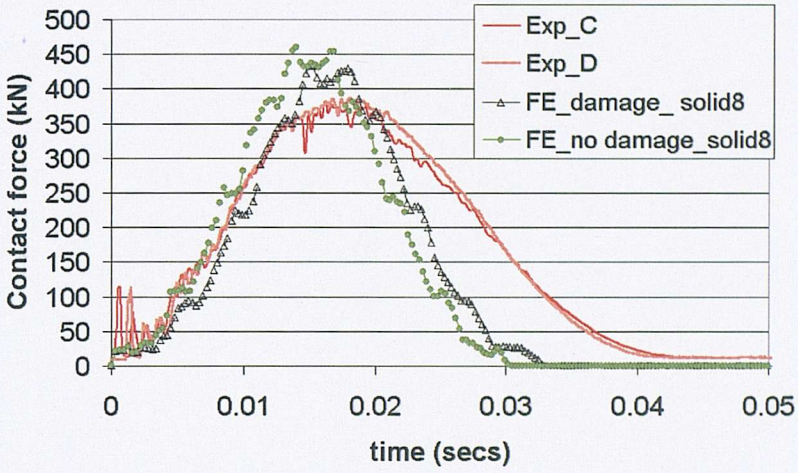


Figure 4-15. Contact force-time history, for large1(C/D): test and FE results.

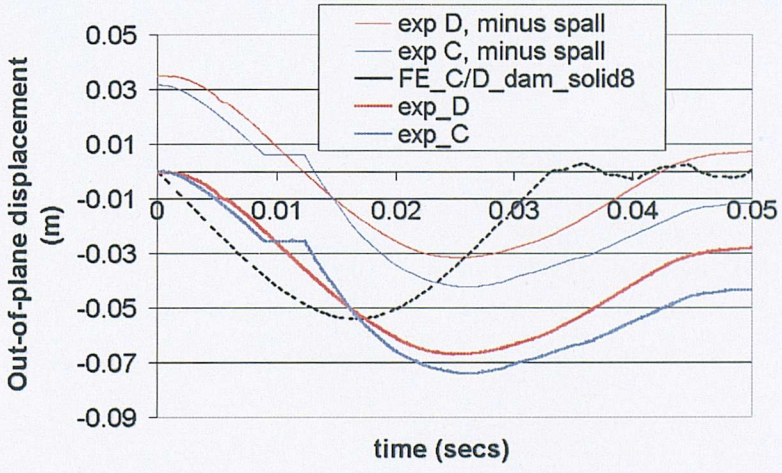


Figure 4-16. Max. o.o.p disp. for large1(C/D): test and FE results

Plotting the contact force against the displacement at the bottom-centre of the plate for test D shows a substantial amount of irreversible energy, given by the area inside the 'looped' curve, as shown in Figure 4-16. In the work by Sutherland et al [38, 39], found that 65% of the incident energy is absorbed irreversibly during the tests for the very short response of thick WR E-glass laminate subjected to low velocity impact, even though no significant damage had occurred. However, when delamination occurs, an increase to 80% is observed

and similarly with fibre damage. Hence excluding damage, other energy absorption mechanisms are believed to be dominant until fibre damage takes place, for example visco-elastic effects and friction. Based on this finding, the FE analysis modelling damage should show some unrecoverable energy loss, although not as extensive as that obtained with the test. However, the analysis shows no signs of irreversible energy loss resulting from damage, despite the reduction in moduli during damage progression and the reduction in contact force compared to a no-damage analysis. This deficiency is likely as a result of two reasons: firstly the model is elastic and therefore all cracks are assumed to close up again (leaving zero permanent deformation) and secondly due to the lack of strain rate modelling.

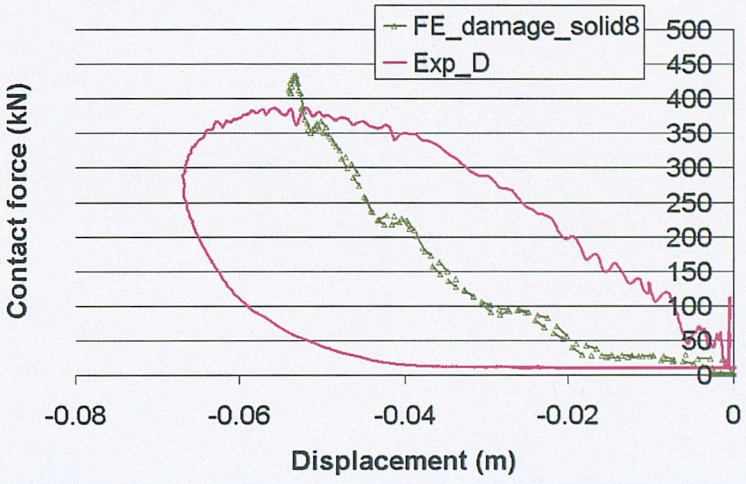


Figure 4-17. Force-displacement plot for large1(D), test and FE

The in-plane damage prediction for the small plate is shown with the contours of moduli in one of the principle fibre directions, see Figure 4-18. The contours in red represent significant fibre damage at the bottom of the plate. Similarly, the damage observed for large1(C/D) is demonstrated in Figure 4-19 with the E_{22} modulus contours. Although the damage predictions only cover matrix and fibre cracking, the damage areas recorded in the test are also inclusive of delamination. The damage in the test was measured as the areas showing colour change. Although these measurements are approximate and include all modes of damage, the vast proportion of the areas included delamination damage. It is possible however, than outside these discoloured areas exists small amounts of matrix cracking also. We can postulate that where delamination is found transverse matrix cracking also exists, based on the assumption that transverse cracks initiate delamination, only a few papers suggest otherwise [40]. Work on cross-ply laminates [41] indicates that when the material reaches a state of transverse matrix crack saturation it is normally followed by delamination.. Both Figure 4-18 and Figure 4-19 point out the damage measured in the test with dotted lines. The region is smaller than the largest damage contour predictions, the

outer-part of which represents a small amount of matrix cracking only. Based on the above assumptions, we can surmise that the FE model gives a good over-all prediction of the damage size inflicted from impact.

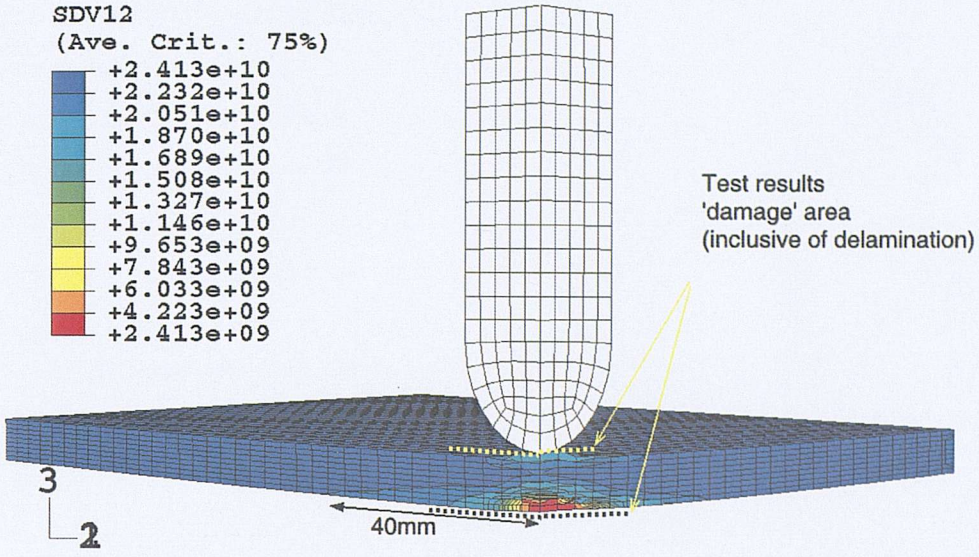


Figure 4-18. In-plane modulus E_{11} contours, in Pascal, for the small plate, test 9M(195J)

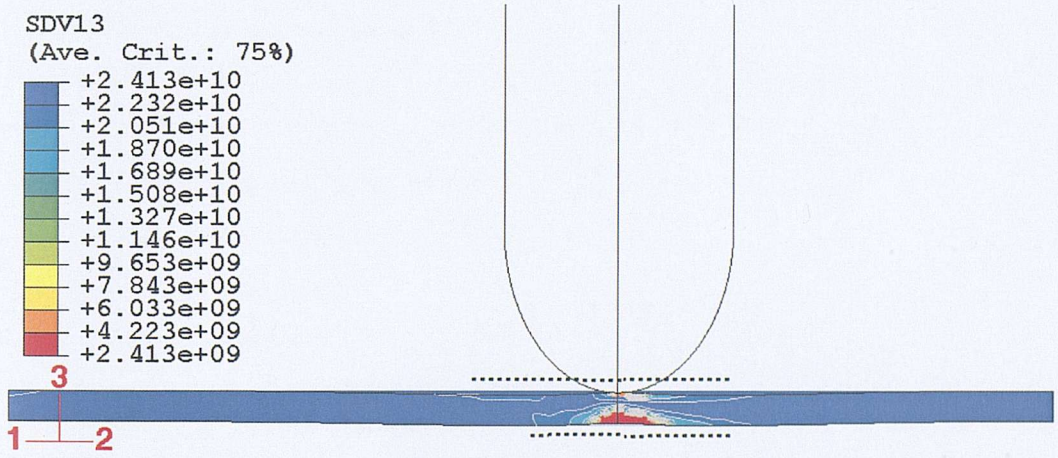


Figure 4-19. In-plane modulus E_{22} contours (in Pascal), for large1(C/D)

4.12.4 Conclusion

The proposed damage model was implemented in an Explicit impact analysis and reduces the contact force predictions over a no-damage model. It also has the effect of over-predicting the maximum o.o.p displacement compared to experiment. It is interesting to note that contact force is under-predicted with a no-damage model when applied to the large scale plate low impact energy test. Only when the energy for impact is large enough, does the analysis then benefit from the damage model. Consequently there must be other modelling

issues such strain rate effects, element choice and contact issues; the latter being briefly discussed later in Chapter 5. Although user experience can provide a relatively good estimation of an adequate mesh size, problems will undoubtedly be encountered with very large scale models where the stress and strain resolution is too coarse. A small mesh-sensitivity study is performed in Chapter 6.

The model parameters are fairly simple to obtain, relying largely on simple cyclic tests with the exception of the ultimate strain to failure for a damaged material, which is more difficult to derive. Although the matrix and fibre damage predictions are believed to be a good estimation of the actual damage inflicted, further validation is required with C-Scan and SEM tests. So far only one of the proposed damage initiation functions and the strain criterion for damage propagation has been put to the test and the remaining criteria are validated in Chapter 6.

4.13 Concluding remarks

A simple damage model was presented based on damage mechanics principles, relying on standard test data and simple cyclic tests. The model was successfully validated against two different plate scales. The model gradually degrades both the in-plane and through-thickness material properties but there is no coupling between failure modes. It offers a simple way of determining the extent of matrix and fibre damage with the accuracy that a macro-model of this size deserves. The proposed model is however limited in its capability and does not include strain rate sensitivity, scale-independence nor does it explicitly model fibre spalling. Furthermore, the finite element analyses would benefit from a delamination model to primarily determine the size of the largest delamination followed by its location. Delamination is dealt with in Chapter 5 and in Chapter 6 a delamination model is implemented in conjunction with the present damage model.

4.14 Reference List

1. Ladeveze P, LeDantec E. Damage modelling of the elementary ply for laminated composites. Composites Science and Technology 1992; 43(3):257-67.

2. Wharmby AW, Ellyin F, Wolodko JD. Observations on damage development in fibre reinforced polymer laminates under cyclic loading. International Journal of Fatigue 2003; 25(5):437-46.

3. Ladeveze P, Allix O, Daudeville L. Mesomodeling of damage for laminate composites. Application to delamination. IUTAM Symposium 1991; 607-22.

4. Chaboche JL. Continuum Damage Mechanics. I. General Concepts. Journal of applied mechanics 1988; 55:59-64.

5. Talreja R. Transverse Cracking and Stiffness Reduction in Composite Laminates. Journal of Composite Materials 1985; 19:355-75.

6. Sun CT, Tao JX. Prediction of failure envelopes and stress/strain behaviour of composite laminates. Composites Science and Technology 1998; 58(7):1125-36.

7. Williams KV, Vaziri R, Poursartip A. A physically based continuum damage mechanics model for thin laminated composite structures. International Journal of Solids and Structures 2003; 40(9):2267-300.

8. Matzenmiller A, Lubliner J, Taylor RL. A constitutive model for anisotropic damage in fiber-composites. Mechanics of Materials 1995; 20(2):125-52.

9. Kollegal M. Progressive failure analysis of plain weaves using damage mechanics based constitutive laws. International journal of damage mechanics 2001; 10(4):301-23.

10. Lua J, Williams G, Sankar J. Multi-scale dynamic failure prediction tool for marine composite structures. Journal of Materials Science 2006; 41(20):6673-92.

11. Zako M, Uetsuji Y, Kurashiki T. Finite element analysis of damaged woven fabric composite materials. Composites Science and Technology 2003; 63(3-4):507-16.

12. Odegard G, Searles K, Kumosa M. A continuum elastic-plastic model for woven-fabric/polymer-matrix composite materials under biaxial stresses. Composites Science and Technology 2001; 61(16):2501-10.

13. Iannucci L, Dechaene R, Willows M, Degrieck J. A failure model for the analysis of thin woven glass composite structures under impact loadings. Computers & Structures 2001; 79(8):785-99.

14. Dechaene R. A constitutive model for glass fibre fabric composites under impact. Journal of Composite Materials 2002; 36(8):983-1004.

15. Iannucci L. Progressive failure modelling of woven carbon composite under impact. International Journal of Impact Engineering 2006; 32(6):1013-43.

16. Zhou G, Greaves LJ. Damage resistance and tolerance of thick laminated woven roving GFRP plates subjected to low-velocity impact. In: Reid SR, Zhou G (eds.), Impact Behaviour of Fibre-reinforced Composite Materials and Structures. Woodhead Publishing Ltd, 2000: 133-83.

17. Mouritz AP. The damage to stitched GRP laminates by underwater explosion shock loading. Composites Science and Technology 1995; 55(4):365-74.

18. Mouritz AP, Gallagher J, Goodwin AA. Flexural strength and interlaminar shear strength of stitched GRP laminates following repeated impacts. Composites Science and Technology 1997; 57(5):509-22.

19. Sierakowski RL. Impact damage - tolerant composite structural design. In: Reid SR, Zhou G (eds.), Impact Behaviour of Fibre-reinforced Composite Materials and Structures. Woodhead Publishing Ltd, 2000: 106-28.

20. Davies GAO, Hitchings D, Zhou G. Impact damage and residual strengths of woven fabric glass/polyester laminates. Composites Part A: Applied Science and Manufacturing 1996; 27(12):1147-56.

21. Lemmen P, Meijer G-J, Rasmussen EA. Dynamic behavior of composite ship structures (DYCOSS) failure prediction tool. 2006.

22. Hashin Z. Failure criteria for unidirectional fiber composites. Journal of applied mechanics 1980; 47(2):329-34.

23. Pickett AK, Fouinneteau MRC. Material characterisation and calibration of a meso-mechanical damage model for braid reinforced composites. Composites Part A-Applied Science and Manufacturing 2006; 37(2):368-77.

24. Johnson AF, Pickett AK, Rozycki P. Computational methods for predicting impact damage in composite structures. Composites Science and Technology 2001; 61(15):2183-92.

25. Johnson AF, Holzapfel M. Influence of delamination on impact damage in composite structures. Composites Science and Technology 2006; 66(6):807-15.

26. Fouinneteau MRC, Pickett AK. Shear mechanism modelling of heavy tow braided composites using a meso-mechanical damage model. Composites Part A: Applied Science and Manufacturing 2007; (in press).

27. Cox B, Yang QD. In quest of virtual tests for structural composites. Science 2006; 314(5802):1102-7.

28. Sihn S, Iarve EV, Roy AK. Three-dimensional stress analysis of textile composites: Part I. Numerical analysis. International Journal of Solids and Structures 2004; 41(5-6):1377-93.

29. Huang ZM. The mechanical properties of composites reinforced with woven and braided fabrics. Composites Science and Technology 2000; 60(4):479-98.

30. Johnson AF. Modelling fabric reinforced composites under impact loads. Composites Part A-Applied Science and Manufacturing 2001; 32(9):1197-206.

31. Poursartip A, Ashby MF, Beaumont PWR. The Fatigue Damage Mechanics of A Carbon-Fiber Composite Laminate .1. Development of the Model. Composites Science and Technology 1986; 25(3):193-218.

32. Talreja R. Transverse cracking and stiffness reduction in composite laminates. Journal of Composite Materials 1985; 19:355-75.

33. Asp LE, Berglund LA, Talreja R. Prediction of matrix-initiated transverse failure in polymer composites. Composites Science and Technology 1996; 56(9):1089-97.

34. Kongshavn I, Poursartip A. Experimental investigation of a strain-softening approach to predicting failure in notched fibre-reinforced composite laminates. Composites Science and Technology 1999; 59(1):29-40.

35. Brewer JC, Legace PA. Quadratic stress criterion for initiation of delamination. Journal of Composite Materials 1988; 22(12):1141-55.

36. Surgeon M, Vanswijgenhoven E, Wevers M, Van der Biest O. Transverse cracking and Poisson's ratio reduction in cross-ply carbon fibre-reinforced polymers. Journal of Materials Science 1999; 34(22):5513-7.

37. Bahei-El-Din YA, Zikry MA. Impact-induced deformation fields in 2D and 3D woven composites. Composites Science and Technology 2003; 63(7):923-42.

38. Sutherland LS, Guedes Soares C. Impact characterisation of low fibre-volume glass reinforced polyester circular laminated plates. International Journal of Impact Engineering 2005; 31(1):1-23.

39. Sutherland LS, Guedes Soares C. Impact behaviour of typical marine composite laminates. Composites Part B: Engineering 2006; 37(2-3):89-100.

40. Diaz A, Caron JF. Interface plasticity and delamination onset prediction. Mechanics of Materials 2006; 38(7):648-63.

41. Highsmith AL, Reifnsider KL, . Stiffness Reduction Mechanisms in Composite Laminates. In: Reifnsider KL (ed.), Damage in Composite Materials. American Society of Testing and Materials, 1982: 103-17.

CHAPTER 5

Formulation of two delamination modelling techniques

5.1 Introduction

Delamination is a major damage mode in polymer composite plates, specially under transverse loading. Consequently it would be of great benefit to be able to predict the size and location of at least the largest delamination in structural composite plates subjected to potential dynamic loads. Experimental data is scarce on composites, relating particularly to contact force history, which according to Zhou and Greaves [1] is one way of revealing the dominant damage mechanisms, namely delamination and fibre failure. Thus, the contact force is one of the principle variables to be examined.

In this chapter two cohesive zone models are validated for small and large-scale impact tests of thick plates, which for the latter case had not been previously carried out. The first is a linear model with high penalty stiffness and a linear softening law. The second model is based on a parabolic function of the damage and is implemented in a user defined subroutine (VUMAT) in Abaqus/Explicit. Normal and shear transverse (inter-laminar) stresses acting in a lamina have proven to have a dominant effect on delamination and are more abundant in thicker plates. Both laws assume coupling of the shear and normal tractions resulting from mode I and mode II loading. Once a critical mixed mode stress has been reached, damage can develop and for both laws unloading and re-load occurs linearly. The cohesive laws are tested on three different plate sizes. Continuum elements are used in the analyses which are more accurate in the calculation of the crack displacements (inter-ply displacements) [2] over the shell elements.

5.2 Background

There are two types of delamination: free-edge delamination (created at the free edges due to Poisson's ratio mismatch) and local delamination. Local delamination is caused by high stresses at the fibre-matrix interface ('ply interface') creating cracks parallel to the plane of the lamina which then extend along the interface. These in-plane cracks are first triggered by transverse matrix cracks reaching the ply interface. Crack movement through the composite thickness can be described as follows:

1. A crack propagates transversely through the matrix and is stopped by the fibre.
2. As the load on composite is increased, the matrix and the fibres at the crack tip deform differently.
3. Large stresses build up at the fibre, causing local Poisson contraction.
4. The addition of tensile stress ahead of the crack tip (normal to the interface) initiates fibre/matrix debonding.
5. Differences in the fibre/matrix moduli results in shear stresses at the interface causing extension of the debonding along the fibre on both sides of the crack plane.
6. As a result, further opening of the crack occurs beyond the fibre.

Impact loading is one method of inducing a three-dimensional state of stress. Impact loading will cause a plate to bend and thus produce transverse shear stresses. In addition, compressive normal transverse stresses are created during the compressive phase whereas these develop into tensile stresses as the impactor moves away. It is thought that the normal compressive stress hinders two plies from coming apart, whereas the tensile normal stress helps to pull them apart. Unfortunately, classical laminate theory takes no account for the inter-laminar stresses σ_z , τ_{xz}, τ_{zy} which exist largely on the surfaces of adjacent layers and which contribute to delamination and matrix cracking. CLT considers only the stresses in the plane of the laminate. This theory also ignores free-edges as in-plane stresses are considered constant, implying that the plate is infinitely long and wide. Cross-ply laminates have free-edge effects due to the mismatch in Poisson's ratio, and these can occur up to one or two plate thicknesses from the edge. The stresses responsible for this are the transverse shear stresses. Inter-laminar stacking sequence therefore plays an important part in the magnitude of these stresses. There have been many developments of the classical analysis in this area reported by authors like Pipes and Pagano [3] and Whitney [4]. Many numerical techniques and approximations have been developed for comparison with the classical solutions with

some success. These have been tested for certain lay-ups and loading conditions and are not yet considered as global solutions.

Some of the simplest and earliest methods of modelling delamination has been to use stress based criteria. Chang and Chang (1987, for example, proposed a matrix cracking failure criterion which was later modified by Hahn and Tsai for non-linear behaviour and further by Hou et al (2000) [5]. The inter-ply regions where delaminations take place are in effect resin-rich regions. Although the use of RR-layers is still a relatively new and under-practiced technique, literature suggests that a maximum transverse shear strain criterion has been previously applied at the RR-layers to model delamination, [6]. Other work includes that by Boh et al [7] who applied a maximum stress criterion at these layers in modelling the response of woven composite beams subjected to transverse shear loading. Following this work, Johnson et al [8] validated this and a further two criteria for small and larger plates under impact. This RR-layer technique provides moderately good results but does not model the physical separation and ensuing contact condition of the delaminated layers. Also, these resin-rich layers are only as effective as the designated failure criteria.

Delamination is now more commonly modelled with cohesive elements. Cohesive theories of fracture are phenomenological continuum theories and are based on atomic forces, equivalent to Griffith's energy approach in classical fracture mechanics, provided the integral of the cohesive forces is equal to the fracture energy. Cohesive theories are able to describe the separation across cohesive surfaces using a cohesive law and define the deformation of the bulk using a constitutive law. The origins of work for cohesive theories are from authors such as Dugdale (1960) [9], Barrenblatt (1962) [10], Willis (1967) and Rice (1968) [11] (the latter two based on Griffith's theory). Cohesive theories of fracture are able to address certain issues that are difficult to address within classical fracture mechanics, such as dynamic effects and crack tip velocity; overloads and complex crack paths. Three dimensional cohesive modelling in finite element analysis often use zero-thickness interface elements embedded between the lamina. The 'stress/strain' variables for the interface elements are then the tractions and the relative displacements between the structural components at the interface. Normally a small thickness is included where composite modelling is concerned, to effectively represent the resin-rich region.

The cohesive zone model is becoming an increasingly popular method and has been largely tested for relatively simple static and dynamic loading events. The use of cohesive zone models in non-composite related fields has greatly expanded such as in the application to

thin films and metals [12, 13]. With regards to polymer composite plates, cohesive elements using traction-separation laws are being increasingly used and work in this area includes that by Espinosa [14], Chen [15], Scheider [16], Camanho [17] and Turon [18]. A range of cohesive laws have been proposed, of linear and non-linear formulation, and have been mostly assessed for static loading conditions. Camanho et al [17, 19-22] used linear and non-linear models for quasi-static loading of DCB specimens and sub-structures including open-hole specimens loaded in multi-axial tension; double-shear lap joints bolted and loaded in tension; and skin-stiffner sub-components loaded in tension. Most dynamic analyses have been modelled using linear cohesive laws. The cohesive zone models are dependent on the energy data from small coupon fracture tests and have so far been limited to modelling only a few delaminating layers in structures that have thus far been relatively small in size.

Other energy methods have been experimented by Ruiz [23] and Mines et al [24] who examined the differences in energy density dissipation between specimens for a number of specimen sizes that were subjected to impact up to perforation. Tang et al [25] took an engineering approach for the residual analysis of impacted laminated composites and used a bending strain energy density expression for delamination prediction but its implementation is limited to a computer code that was specially developed based on their model features.

Low velocity impact damage and residual strength of woven fabric glass/polyester laminates was also carried out by Davies and Hitchings [26] who related the impact force and incident kinetic energy to identify damage initiation. The plates were 100 to 500mm (3.94 to 19.68in) long and up to 25mm (0.984in) thick. Damage-force maps were developed from the experiments and proved to be successful with carbon composite plates of different sizes. A simple mode II fracture analysis was used to model a single circular delamination in an isotropic material, with the assumption that the woven fabric is not too far from isotropic. Kuboki at al [27] carried out impact tests on glass/polyester specimens to search for the relationship between the delamination resistance and the impact resistance. Delamination resistance was characterized using static mode I and mode II delamination tests. Their study highlighted the problems currently existing in the relationship between the delamination resistance of GFRP and its impact resistance. Hou et al [28] describe an improved stress-based delamination criterion for laminated composite structures and verified with low velocity impact tests on plates 140x85x2.6mm^3 (5.51x3.35x0.1in^3) The failure criteria were implemented in LS-DYNA3D using one solid element through the thickness and taking into consideration the out-of-plane stresses for damage initiation. The influence of matrix cracking and fibre failure on delamination was modelled by reducing the interlaminar shear

strength. Reis and Freitas [29] determined through experiment the limit loading capacity and damage growth mechanisms of impacted composite laminates when subjected to compression after impact (CAI) loading. They concluded that the residual strength is influenced by the delaminated area which is a function of the impact energy.
Espinosa carried out dynamic explicit FE analyses for modelling the impact of a PMMA impactor plate onto a woven polyester/glass sample plate (although other variations were also examined) and evaluated against experimental results. The deformation of the material was modelled using an anisotropic plasticity model. Espinosa did not have all the required parameter information for each model and kept the τ_{max} value to 50MPa for all models.

More recently and again more specific to naval composites, Lemmen et al [30] proposed a damage mechanics based model for composite ship structures under dynamic loading. Debonding of composite plies modelled with a linear cohesive model, using damage initiation criterion based on Hashin's work [31]. Beyond the point of crack initiation, a traction separation law with coupled inter-laminar mode I and mode II displacements is applied whereby the inter-laminar stiffness is gradually degraded to zero. After complete ply separation i.e. delamination, subsequent contact between the two ply surfaces are modelled as inpenetrable and a rate dependent Coloumb friction is applied. The model is tested for the quasi-static loading of a T-joint panel and compared with experiment.

A review on delamination predictive methods [6] discusses damage and fracture mechanics approaches applied to low velocity impact events on aircraft composites. They conclude that additional development of these techniques is required before any one technique can be described as a definitive delamination model.

Significant evidence suggests that woven-fabric/polymer composites demonstrate a substantial amount of inelastic behaviour, which often occurs during the initial loading stages of the material, however some of the load paths create more non-linearity than others. Johnson & Simon [32] modelled the elastic and inelastic behaviour of 0.25x0.25m^2 glass fabric/epoxy plates using damage mechanics and a plastic potential function that is a function of the in-plane shear stress only. Other authors have also made the assumption that the fibre direction behaves largely in an elastic manner [33] unlike the resin dominated directions.

Despite this, tests on some woven composites have shown that the strength and elastic modulus in the fibre directions is sensitive to strain rate, as concluded by Khan et al [34, 35]

who carried out tests on WR E-glass/Derakane 8084 vinyl ester composites, mainly used in naval applications, for strain rates of 10^{-3} to $10s^{-1}$. They also found that the strength in the through-thickness direction did increase whereas the modulus change was insignificant. Strain rate modelling is thus important when it comes to obtaining the stresses and strains. However, depending on the delamination model employed, the significance of the strain rate on the delamination prediction may vary.

Strain rate tests in the warp and fill directions of a SCRIMP manufactured glass/vinyl-ester 510A WR were carried out for strain rates ranging from 0.1 to 5/s, [36]. However, the moduli results did show divergence and thus were determined as inconclusive. The ultimate strength results were more promising, seeing an increase in value of 59 to 82% from static to dynamic at 5/s. The only through-thickness strain rate data available was carried out under compression on a hand lay-up glass/ Derakane 8084 composite sample obtained from a half-scale Corvette, subjected to strain rates of $0.001s^{-1}$ and $100s^{-1}$. The composite was poorly consolidated, giving results that are smaller than what was obtained under quasi-static loading for a very similar resin, a Derakane 510A. The compression and tension results for this composite are shown in Figure 2-1 Chapter 2.

Lesar [37] also carried out strain rate tests on vinyl-ester composites have indicated an increase in modulus and strength values over those from quasi-static tests,

5.3 Resin-rich layer model

5.3.1 Introduction

Resin rich layers (RR-layers) are a way of describing the resin-rich region that is naturally present in between every ply in composite materials and it is at these locations that delaminations are most likely to occur.

Reis and Freitas [29] determined through experiment the limit loading capacity and damage growth mechanisms of impacted composite laminates when subjected to compression after impact (CAI) loading. They concluded that the residual strength is influenced by the delaminated area which is a function of the impact energy. Delamination is a very prominent failure mode for shock damaged composites and should ideally be modelled using full scale test data to minimize any scaling uncertainties. For low velocity impacts the delamination and matrix damage area has been shown to be proportional to the impact energy, [38].

For the proposed model, the RR-layers and the woven plies are modelled an elastic materials that are also elastic damaging. The composite woven plies are orthotropic, and Hashin's 2D failure criteria are applied at these layers to model matrix and fibre failure. When failure is predicted, the relevant material properties are degraded to 90% of their original value. The majority of the analyses are carried out in Abaqus/Explicit, requiring a user material subroutine to define the material's constitutive behaviour. The transverse shear stiffness and the through-thickness modulus and Poisson's ratio are only made available in the input file and cannot be modified during the analysis. Delamination damage is modelled with RR-layers. The RR-layers are modelled as a fraction of the woven ply thickness, typically 5%, reducing the woven layer thickness accordingly to keep the overall laminate thickness constant. One standard thick shell element or one or more continuum shell elements can be used through the thickness and the RR-layers are sub-modelled within the element, see Figure 5-1.

5.3.1 Stress criteria for delamination

The first stress failure criterion at the RR-layers applies a simple in-plane stress criterion, 'stress criterion 1', shown in equations (5-1), with the definition that failure occurs when RRL1 + RRL2 ≥ 1. At this point, all the properties of the resin are degraded to nearly zero, leaving a small residual value for the sake of numerical stability. The Macauley brackets used in the equations are denoted by $\langle x \rangle_+ = \frac{1}{2}(x + |x|)$ and $\langle x \rangle_- = \frac{1}{2}(x - |x|)$.

A variation of stress criterion 1 is 'stress criterion 2', indicating failure when the largest of either RRL1 or RRL2 is equal or greater than one. The maximum strength values of the resin used in the equations are also reduced to half their value if either matrix or fibre failure is detected first using Hashin's 2D failure criteria, shown with equations (7), (8), (10) and (12) in Chapter 3. The strength of the resin in tension and compression is denoted by S_R^C for tension and S_R^C for compression. The resin properties are shown in Table 2.4 of Chapter 2.

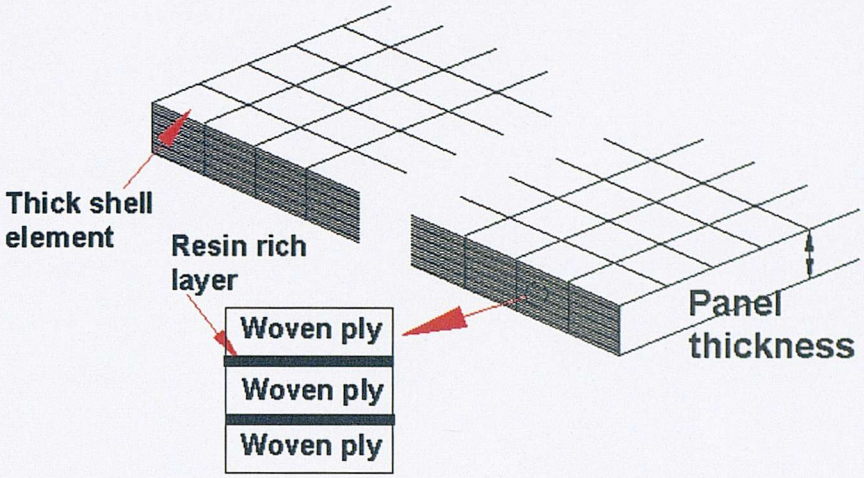


Figure 5-1. Composite layering through the thickness of the elements.

$$RRL1 = \left(\frac{\langle \sigma_{11} \rangle_+}{S_R^T} \right)^2 + \left(\frac{\langle \sigma_{11} \rangle_-}{S_R^C} \right)^2$$
$$RRL2 = \left(\frac{\langle \sigma_{22} \rangle_+}{S_R^T} \right)^2 + \left(\frac{\langle \sigma_{22} \rangle_-}{S_R^C} \right)^2 \qquad (5\text{-}1)$$

Stress criterion 1:

$RRL1 + RRL2 \geq 1 \Rightarrow E_{ij} \equiv 0$ at RR-layer integration point

Stress criterion 2:

$RRL1$ or $RRL2 \geq 1 \Rightarrow E_{ij} \equiv 0$ at RR-layer integration point

5.3.2 Energy criterion for delamination

The third failure criterion applied at the RR-layers is one of simple internal energy. The internal energy at the RR-layer material integration point is calculated at the end of every time increment. When the a critical energy value is reached, the material properties are degraded to almost zero. Two energy density values are compared: the average mode I critical energy density value, G_{IC}, obtained from typical Mode I fracture tests, see equation (5-2), and an energy density criterion from full impact tests. M_e is the mass of the resin layer for one element width and length, ρ is the density of the resin, R is the thickness of the RR-layer, $L_1 x L_2$ is the area of a shell element. This energy is representative of the fracture mechanisms within the element.

$$E_{frac} = \frac{L_1 L_2 G_{IC}}{M_e} = \frac{L_1 L_2 G_{IC}}{\rho L_1 L_2 R} = \frac{G_{IC}}{\rho R} \tag{5-2}$$

The internal energy per unit mass is calculated at every RR-layer integration point using equation (5-3), see Figure 5-2. When using shell elements, the transverse stresses are not fed into the subroutine therefore only in-plane stresses are used in this equation. This energy value is updated at the end of every time increment and is compared with the critical energy for failure. V_e is the volume of the resin layer for one element width and length.

$$E_{int} = \frac{1}{\rho V_e} \int_{V_e} \tfrac{1}{2}\{\varepsilon\}^T [E]\{\varepsilon\} \partial V = \frac{1}{2\rho}[\sigma]\{\varepsilon\} \tag{5-3}$$

The energy values from the critical fracture tests on the WR E-glass/Derakane 8084 vinyl-ester is shown in Table 2-1 Chapter 2, calculated using equation (5-2), where 'R' is the thickness of the RR-layer.

The energy value for failure from the impact tests has been obtained from a simple expression, equation (5-4), for the total energy absorbed during impact.

$$E = \int_{t_0}^{t_f} P v \partial t \tag{5-4}$$

Where P and v are the instantaneous load and velocity respectively, t_0 is the time of initial impact, taken as zero, and t_f is the time at which contact with the plate is lost. Because the instantaneous velocity can only be measured at the beginning and at the end of the impact, the *apparent energy* can be used instead, as shown with equation (5-5).

$$E_a = v_0 \int_0^{t_f} P \partial t \tag{5-5}$$

This energy for failure is then divided by the mass of the plate to give an energy value that compares with the internal energy calculated at each integration point.

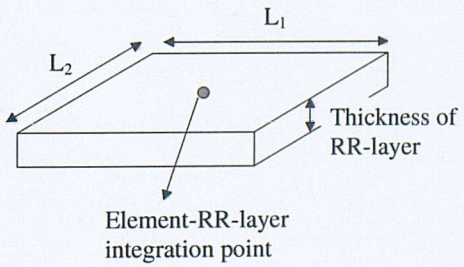


Figure 5-2. One integration point per resin-rich layer element.

In these impact tests, the contact force is known from experiment and is used in the apparent energy equation. Where the contact force and time to impact are unknown, an independent energy formulation is required. The ideal is to obtain a critical energy value based on the level of internal energy of the plate that results in fracture: an energy value that is not obtained from small scale (coupon) fracture test but from large-scale dynamic tests. For both RR-layer models, the resin properties at the integration points are degraded to nearly zero when the failure criteria are met. A small residual is retained for numerical stability.

Ideally, to eliminate mesh sensitivity of fracture in the numerical analyses would require enforcing a constant mesh resolution over the damage zone. The energy would be calculated for a constant volumetric region that decreases with increase in specimen scale once the relationships are established from experiments between the scale of the specimen and the energy absorbed by the specimen [38]. Unfortunately, Abaqus' VUMAT does not provide element number information into the subroutine and the subroutine is run for every increment at every integration point, for which their locations are also unknown.

5.3.3 In-plane visco-plastic model

Strain-rate sensitive materials exhibit a discrete effective stress and plastic strain curve for different applied strain rates, shown as an example in Figure 5-3. In this case the 'plasticity' is related to permanent matrix and fibre damage. The following proposed visco-plastic model uses a function developed by Sun [39] that collapses a range of these strain rate plots onto once curve which was developed around experimental data.

An expression for the plastic strains is required that is both a function of stress and strain rate. Equation (5-6) is Sun's power-law relationship between the effective stress and the effective plastic strains at a given strain rate. Here, the parameter 'B' is a function of the plastic strain rate.

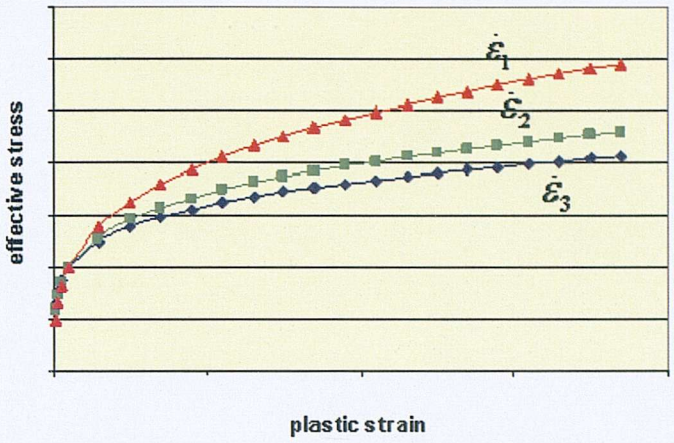


Figure 5-3. The relationship between the plastic strain and effective stress can be fitted with a power law.

$$\bar{\varepsilon}^p = B\bar{\sigma}^\beta = Q\left(\dot{\bar{\varepsilon}}^p\right)^m \bar{\sigma}^\beta \tag{5-6}$$

The plastic flow potential generally assumed to have the same shape as the yield surface. This approximation closely approximates experimental observations, and can also be justified from dislocation based theories of plasticity. A flow law derived from the yield surface is known as an *associated plastic flow law*, which is the case in the current proposal. In view of the fact that polymers are sensitive to the hydrostatic stress component, [40] the plastic potential function is taken as a function of the actual stresses. The plastic potential function is based on the Drucker-Prager yield criterion, as shown with equation (5-7), where β is a state variable which controls the extent of the effect of the hydrostatic stresses, σ_{kk}, but is not rate dependent, and σ_c is the 'yield' stress or yield locus which changes with the strain rate. The second invariant of the stress tensor for a three-dimensional material model is given by equation (5-8), where S_{ij} are the

$$f = \sqrt{J_2} + \alpha\sigma_{kk} - \sigma_c(\dot{\lambda}) \tag{5-7}$$

$$J_2 = \tfrac{1}{2}S_{ij}S_{ij} = \tfrac{1}{2}(S_{11}^2 + S_{22}^2 + S_{33}^2 + 2S_{12}^2 + 2S_{23}^2 + 2S_{31}^2) \tag{5-8}$$

The idea is to apply the viscoplastic model at the resin-rich layers embedded within continuum shell elements which have a similar constitutive behaviour to standard thick shells. Therefore the 3D representation of the plastic potential function is reduced to plane stress, as shown with equation (5-9).

$$J_2 = \tfrac{1}{2}(S_{11}^2 + S_{22}^2 + 2S_{12}^2) \tag{5-9}$$

The easiest way to model strain hardening is to make the yield surface increase in size, but remain the same shape, as a result of plastic straining. This requires defining an appropriate relationship between the 'yield stress' (the size of the yield locus) and the plastic strain. To get a suitable scalar measure of plastic strain, the principle of accumulated plastic work can be applied, $W = \int \sigma_{ij} d\varepsilon_{ij}^p$, or the accumulated plastic strain magnitude $\lambda = \int \sqrt{\tfrac{2}{3} d\varepsilon_{ij}^p d\varepsilon_{ij}^p}$ (the factor of 2/3 is introduced so that $\lambda = \varepsilon$ under a uniaxial strain ε). The last expression excludes the hydrostatic stress component. A plastic function 'H_P' can be derived by curve fitting a uniaxial tension test. Different curves will be produced for different loading rates and what is required is a function that tells us the plastic strain increment with stress increment above the 'yield' stress for any loading rate. The *magnitude* of the plastic strain is completely determined by the hardening behavior of the solid. This is because during continued plastic flow, the stress must be on the yield surface at all times. Since the radius of the yield surface is related to the magnitude of the plastic strain increment through an appropriate hardening law, this means the plastic strain magnitude must be related to the stress increment. The relationship that most closely resembles this behaviour is that described by the flow rule in equation (5-10).

$$\dot{\varepsilon}_{ij}^p = \dot{\lambda} \frac{\partial f}{\partial \sigma_{ij}} \tag{5-10}$$

If $d\lambda = \sqrt{\tfrac{2}{3} d\varepsilon_{ij}^p d\varepsilon_{ij}^p}$ denotes the magnitude of the plastic strain increment (exclusive of hydrostatic stress) and let $f(\sigma_{ij}, \lambda) = 0$ denote the yield criterion for a particular strain rate, then, the condition that the solid is at yield during plastic straining can be given as the differential of the yield function with respect to the stress and the plastic strain, as $\frac{\partial f}{\partial \sigma_{ij}} d\sigma_{ij} + \frac{\partial f}{\partial \lambda} d\lambda = 0$. Then re-arranging gives $d\lambda = \frac{1}{H} \frac{\partial f}{\partial \sigma_{ij}} d\sigma_{ij}$, where H is equal to $-\frac{\partial f}{\partial \lambda}$, the slope of the stress-plastic strain curve under uni-axial loading. This curve is later shown as function of strain rate also.

To include the hydrostatic stress influence in the plastic flow expression, the approach outlined in Goldberg's work [40] is proposed. The proportionality factor, λ, can be obtained by squaring the stress derivative in equation (5-11) and then putting into the flow rule and re-arranging to give equation (5-12). The variable α controls the influence of the hydrostatic stress.

$$\frac{df}{d\sigma_{ij}} = \frac{d\left(\sqrt{J_2} + \alpha\sigma_{kk}\right)}{d\sigma_{ij}} = \frac{S_{ij}}{2\sqrt{J_2}} + \alpha\delta_{ij} \tag{5-11}$$

$$\dot{\lambda} = \frac{\sqrt{2\dot{\varepsilon}_{ij}^{p}\dot{\varepsilon}_{ij}^{p}}}{\sqrt{1+6\alpha^2}} \tag{5-12}$$

Another expression for λ can be obtained using the principal of the equivalence of the inelastic work rate, equation (5-13), and the effective stress definition, equation (5-14), giving equation (5-15). The denominator of equation (5-12) is equal to around 1.13 when α is a third and equal to one when alpha is zero. The latter can be reduced to equation (5-15), which can also be re-written as equation (5-16) by introducing the viscoplastic modulus. The rate dependent plastic modulus, H^p, is equal to the rate of effective stress divided by the effective strain rate, as shown with equation (5-17).

$$\dot{W}^p = \bar{\sigma}\dot{\bar{\varepsilon}}^p = \sigma_{ij}\dot{\varepsilon}_{ij}{}^p = \sigma_{ij}\dot{\lambda}\frac{df}{d\sigma_{ij}}$$

$$\bar{\sigma}\dot{\bar{\varepsilon}}^p = \sigma_{ij}\dot{\lambda}\left(\frac{S_{ij}}{2\sqrt{J_2}} + \alpha\delta_{ij}\right) \tag{5-13}$$

$$\bar{\sigma} = \sqrt{3}f = \sqrt{3J_2} + \sqrt{3}\alpha\sigma_{kk} \tag{5-14}$$

$$\dot{\lambda} = \sqrt{3}\dot{\bar{\varepsilon}}^p \tag{5-15}$$

$$\dot{\lambda} = \sqrt{3}\frac{\dot{\bar{\sigma}}}{H^p} \tag{5-16}$$

$$H^p = \frac{\dot{\bar{\sigma}}}{\dot{\bar{\varepsilon}}^p} = \frac{d\bar{\sigma}}{d\bar{\varepsilon}^p} \tag{5-17}$$

Inserting equation (5-12) into (5-15) gives the expression for the effective plastic strain, shown with equation (5-18). Putting equations (5-11) and (5-16) into (5-10), give the expression for the flow rule as shown in equation (5-19).

$$\dot{\bar{\varepsilon}} = \frac{\sqrt{\frac{2}{3}\varepsilon_{ij}^{p}\varepsilon_{ij}^{p}}}{\sqrt{1+6\alpha^{2}}} \tag{5-18}$$

$$\dot{\varepsilon}_{ij}^{p} = \sqrt{3}\frac{\dot{\bar{\sigma}}}{H^{p}}\left(\frac{S_{ij}}{2\sqrt{J_2}} + \alpha\delta_{ij}\right) \tag{5-19}$$

The viscoplastic modulus is defined with equation (5-20); where the effective plastic strain rate is given by the time differential of equation (5-6) is put into the relationship shown in equation (5-17),

$$H^{p} = \frac{1}{\beta Q\left(\bar{\varepsilon}^{p}\right)^{m}\bar{\sigma}^{\beta-1}} \tag{5-20}$$

Replacing the effective stress rate in equation (5-19) with the time derivative of equation (5-14) gives the complete equation for the plastic strain rate, equation (5-21). This equation can be split into terms with each effective stress ($\dot{S}_{11}, \dot{S}_{22}$.. etc) making up a value within a one column matrix, as shown with two of the A_{ij} coefficients in Appendix A, equations A.2. equation (5-21) is given in matrix form in Appendix C, equation C.1 and equation C.2.

$$\dot{\varepsilon}_{ij}^{p} = \frac{1}{H^{p}}\left(\frac{S_{ij}}{2\sqrt{J_2}} + \alpha\delta_{ij}\right)\left(\frac{\sqrt{3}}{\sqrt{2J_2}}\left(\dot{S}_{11}S_{11} + \dot{S}_{22}S_{22} + 2\dot{S}_{12}S_{12}\right) + \sqrt{3}\alpha\dot{\sigma}_{kk}\right) \tag{5-21}$$

The total strain rate is equal to the compliance matrix, s, multiplied by the stress rate, equations (5-22). The stress rate can split into the hydrostatic and the deviatoric stress terms, equations (5-23). The elastic compliance matrix is shown in Appendix A, equation A.1 to A.3 and equation A.4 shows the full expression for $\dot{\boldsymbol{\varepsilon}}$.

$$\begin{Bmatrix} \dot{\varepsilon}_{11} \\ \dot{\varepsilon}_{22} \\ \dot{\varepsilon}_{12} \end{Bmatrix} = \left[s_e + s_p \right] \begin{Bmatrix} \dot{\sigma}_{11} \\ \dot{\sigma}_{22} \\ \dot{\sigma}_{12} \end{Bmatrix} \tag{5-22}$$

$$\begin{aligned} \dot{\varepsilon} &= \dot{\sigma}(s^e + s^p) = (\tfrac{1}{3}\dot{\sigma}_{kk} + \dot{S})(s^e + s^p) \\ \dot{\varepsilon} &= \tfrac{1}{3}\dot{\sigma}_{kk}(s^e + s^p) + \dot{S}(s^e + s^p) \end{aligned} \tag{5-23}$$

In the user material subroutine, the VUMAT, the in-plane stresses have to be updated after every increment, defined as the stress from the previous increment, σ_{ij}^{old}, plus the increment in stress, $\Delta\sigma_{ij}$, produced in the current increment, see equation (5-24).

$$\sigma^{new} = \sigma^{old} + d\sigma \tag{5-24}$$

The incremental stress-strain relation for an elastic work-hardening material is shown with equation (5-25).

$$d\sigma = C^e d\varepsilon^e = C^e(d\varepsilon - d\varepsilon^p) \tag{5-25}$$

Inserting the flow rule gives the expression for the stress increment as equation (5-26).

$$d\sigma = C^e\left(d\varepsilon - \frac{\partial f}{\partial \sigma} d\lambda \right) \tag{5-26}$$

The new stress can be thus defined as equation (5-27), where the increment in total strain, $d\varepsilon$, is provided by Abaqus into the subroutine at the start of the increment. Here the constitutive relationship is shown in terms of the elastic-viscoplastic modulus C^{ep} and the total strain increment. C^{ep} is a function of the elastic and plastic moduli and the total strain rate i.e. the sum of the elastic and plastic strain rates and can be expressed as equation (5-28).

$$\sigma^{new} = \sigma^{old} + d\varepsilon C^{ep} \tag{5-27}$$

$$C^{ep} = [C] - [C]\left(\frac{\partial f}{\partial \sigma}\frac{\partial \lambda}{\partial \varepsilon}\right) \tag{5-28}$$

Although this viscoplastic model is two dimensional, the transverse shear stresses are marginally affected by the stresses in the principal in-plane x-direction, as detailed in the Abaqus Theory manual and summarized in Section 3.5.2 Chapter 3.

The constants used for equation (5-6) in the viscoplastic model were those obtained from strain rate tests. Through-thickness uni-axial tensile and compressive strain rate tests were carried out at $0.001s^{-1}$ and $100s^{-1}$ using cylindrical specimens. The material was obtained from an all-composite ¼ scale Corvette hull – the same vinyl-ester/glass composite used for the 5x5ft panel except for some of the hull was fabricated from a combination of hand lay-up and VARTM techniques, see Section 7.4 of Chapter 2.

5.4 Fracture and numerical modelling limitations

There are various ways of modelling fracture and the general debonding of two surfaces in Abaqus/Implicit and Abaqus/Explicit. Most of the fracture criteria are available in Abaqus/Standard and largely for quasi-static analyses. Fracture analyses can be generalised under three categories:

- Predicting onset of fracture using contour integral methods, such as the J-integral and C-integral for individual cracks, in Abaqus/Standard, or continuum methods in Abaqus/Explicit.
- Predicting the propagation of fracture along pre-determined fracture surfaces, only available in Abaqus/Standard.
- Separation of two surfaces in shell elements, using line spring elements. The stiffness of these springs cannot be gradually degraded and the force and displacement output is that in the direction of the spring. Available in Abaqus/Explicit and Abaqus/Standard.

Two different criteria may be used to detect *crack initiation* in Abaqus/Standard using the contour integral method. A simple Rankine criterion states that a crack forms when the maximum principal tensile stress exceeds the tensile strength of the brittle material. The other method applies Hilleborg's (1976) fracture energy proposal [41]. Hilleborg defines the energy required to open a unit area of crack in Mode I as a material parameter, using brittle

fracture concepts. With this approach the brittle behaviour is characterized by a stress-displacement response rather than a stress-strain response. Crack detection is based purely on Mode I fracture, however subsequent cracked behaviour includes both Mode I and Mode II behaviour. For homogeneous, isotropic elastic materials the direction of cracking initiation can be calculated using one of three criteria, including the maximum tangential stress criterion and the maximum energy release rate criterion.

Crack propagation along predetermined surfaces can be simulated using the *DEBOND and *FRACTURE CRITERION options together in Abaqus/Standard. The former requires that the user define two distinct initially partially bonded contact surfaces between which the crack will propagate. The fracture criteria available include maximums stress, COD (crack opening displacement) and crack length. Cracking is irrecoverable meaning that once a crack has occurred at a point it remains throughout the rest of the calculation. However, crack closing and reopening may take place along the directions of the crack surface normals. The model neglects any permanent strain associated with cracking and so the cracks can close completely when the stress across them becomes compressive.

The standard crack propagation facility is limited to small models and modelling the dynamic crack initiation in a larger structure requires a different approach. There is a smeared crack model for modelling discontinuous brittle behaviour in concrete in Abaqus/Explicit. This method does not track individual macro-cracks; instead it assumes a continuum of microcracks orientated depending upon the number and size of the stress components at a material point. The term 'crack' therefore implies the direction in which cracking has been predicted at a material point. The first crack can be detected using the Rankine criterion or the critical fracture energy, based purely on Mode I behaviour. The plane of the first crack is assumed to be perpendicular to the principal tensile stress. Ensuing crack propagation is determined by the normal and shear state of stress. Further cracks can develop at the same material point, with crack faces orthogonal to the original crack and perpendicular to the principal stress direction. Hence for a three dimensional model only 3 cracks can form at any one material point. The post-failure behaviour of the material is a softening stress-strain response. The model is limited in that it can only be used with a linear-elastic material and the there is no coupling behaviour between the shear and normal stress induced cracks. Also, this model is not adequate to model delamination because the crack path can be discontinous and cracks can appear anywhere in the material. Also, it cannot be used in conjunction with a user-defined material subroutine

Hitchings (1) believes that the onset of delamination and propagation is best predicted using the strain energy release rate (rather than stress). One way of implementing this for the discrete opening of macro-cracks or delaminations at composite ply interfaces is by using cohesive elements to model these interfaces whose behaviour is defined with a cohesive zone model, described next.

5.5 The Cohesive Zone model

5.5.1 Origin of the Cohesive zone model

Cohesive zone models were developed from fracture mechanics principles. A fracture mechanics approach to crack propagation and delamination is commonly applied as an energy-based failure criterion and is ideal for micro-modelling. The assumption is that a critical energy value at a crack will cause its propagation to a longer crack length. Under quasi-static conditions, the crack is deemed to propagate in a stable manner and does not accelerate under a given load. In unstable conditions the energy/work provided is greater than that required to propagate the crack at a constant velocity. Numerically, using finite element computer packages, this may be done element by element with the splitting of nodes at an interface.

The concept of fracture energy was first proposed by Griffith who considered the cracked body as an equilibrium problem. If the crack to specimen size ratio (i.e. namely the a/W ratio) is fairly constant, then the postulation is that the crack size increases with increase in specimen size. Based on this assumption a simple stress ratio can be derived, assuming linear elastic fracture mechanics (LEFM). Griffith [42] introduced the relationship between the loss in elastic energy during crack propagation and the creation of new surfaces; relating the stress to create a crack with the surface energy and crack length: $\sigma^2 = \frac{2\gamma E}{\pi a}$. Griffith's work was based on microcracks with an elliptical shape of initial length 'a' and stress singularities at both tips. The importance of friction between crack surfaces was dealt with by Irwin who developed Griffith's crack initiation theory for any crack and also proposed a crack propagation criterion by determination of the strain energy release rate G. For mode I this becomes equation (5-29), where G_{IC} is the critical fracture energy.

$$\sigma = \sqrt{\frac{EG_{IC}}{\pi a}} \tag{5-29}$$

If the strain energy release rate G is greater than or equal to the critical value G_{IC}, then the crack propagates. LEFM (linear elastic fracture mechanics) predicts infinite stress at the crack front at a sharp tip region, which cannot be true for a real material. There must be a region where non-linear material behaviour exists. In this region, energy dissipative mechanisms such as elasto-plastic behaviour or microcracking occur and it is called the FPF (fracture process zone). Thus the J-integral was developed by Rice [11] for non-linear elastic and elastic-plastic materials and if applied to linear elastic problems is equal to the energy release rate. This integral is path-independent as a crack within a body could potentially propagate in any direction. The J-integral is the integral of a line of the local stress-strain field around a crack tip and represents the strain energy release rate of non-linear elastic materials.

Work always has to be done to propagate a crack. The load on a cracked body can be increased until a critical state is reached resulting in crack extension. During the consequent crack propagation:

i. The strain energy of the system changes
ii. External work may be done by the loading forces in moving the loaded points
iii. KE may be generated by the inertia of the faces of the crack moving apart if the crack velocity is very fast.

In elastic fracture mechanics, if all the energy contributions are balanced out, it is found that energy is lost due to crack extension and this is called *fracture work.* Sometimes, the work of fracture is simply calculated as the area under the traction-displacement (force-displacement) curve after the load has fallen to zero and the specimen has broken.

Barenblatt [10] and Dugdale [9] proposed a new concept to the traditional fracture mechanics by introducing cohesive forces near the crack ends. The CZM (cohesive zone model) represents the relation between the normal **crack** opening and the normal traction. The length of the cohesive zone is defined as the distance from the crack tip to the point where the maximum cohesive traction is reached. The crack tip is relating to the real crack, when the opening displacement is maximum u_{fail}, see Figure 5-4, and the maximum traction T_{max} occurs when the opening displacement is equal to u_{crit}. A typical stable propagating crack is shown in Figure 5-5. The enclosed areas labeled E_i are the fracture energy values calculated from the increase in crack length e,g. from A_1 to A_2, the applied load and the crack opening displacement. If E_1, E_2 and E_3 are fairly similar, we can state that the average

fracture energy for the material is fairly constant, resulting from a fairly constant crack velocity so the crack propagation can be deemed stable.

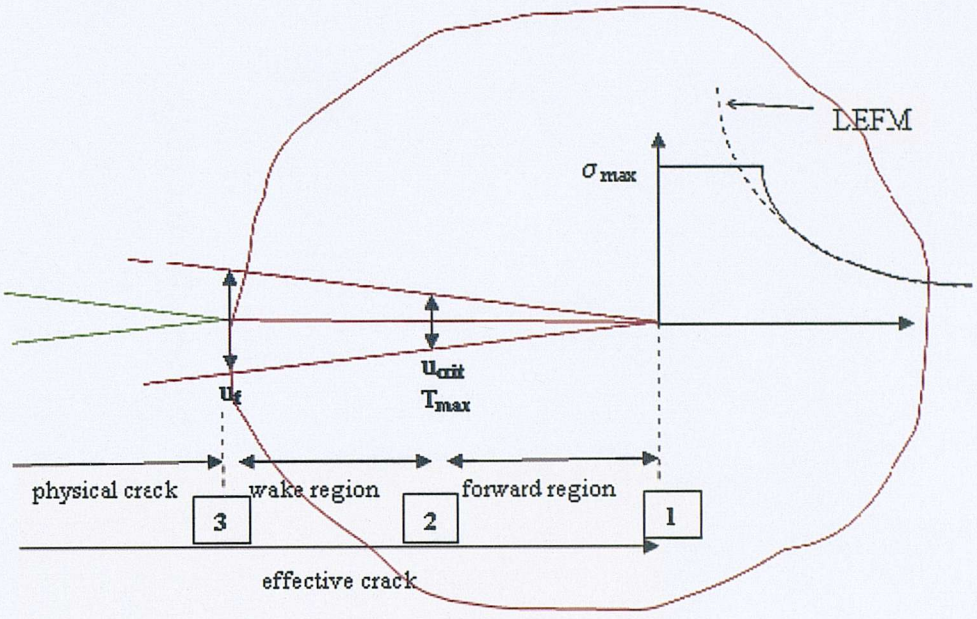


Figure 5-4. Crack process zone

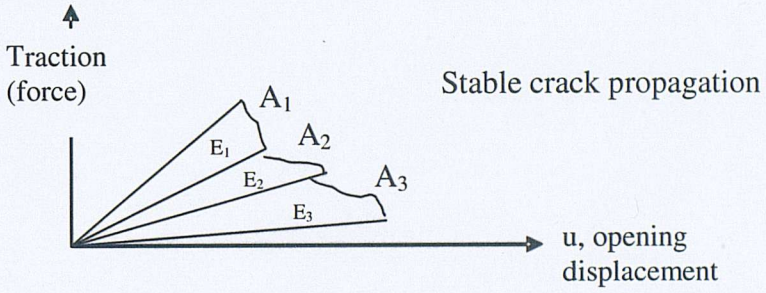


Figure 5-5. Stable crack propagation

The cohesive zone associated with this type of model is a region that is larger than that the crack tip problem. Figure 5-6 shows an example of a non-linear traction separation curve, where u_{max} is the maximum displacement of the crack faces before the crack starts to propagate and is the location of the 'cohesive crack tip'. The build up in elastic energy up to this point is related to the 'forward' crack region, shown in Figure 5-4. The maximum physical crack face displacement at crack failure is measured in the 'wake' region In fact, the maximum. The process zone in a CZM can be defined as the region within the separating surfaces where the tractions are non-zero. The CZM in effect resembles similar behaviour to that shown in Figure 5-5, except each traction-separation curve, such as the one in Figure 5-6, represents one large crack opening. When the peak traction force is reached, the two crack faces start to fail. This is the 'wake region' when microvoids, small hairline cracks and

plasticity occurs. This damage builds up until no more load can be supported when the traction forces go to zero and the crack is fully formed.

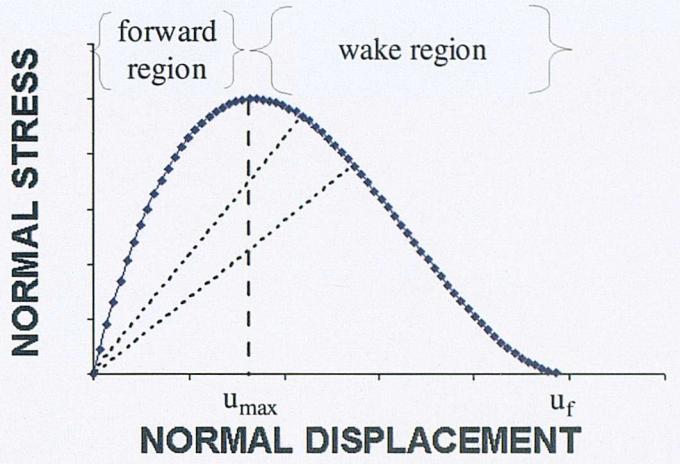


Figure 5-6. Cohesive fracture regions associated with a example of a traction-separation curve

If we consider the three principle planes of the material, delamination can occur under one or more modes of loading on these planes. Mode I refers to ply separation resulting from a normal transverse load; mode II from a transverse shear load and mode III is the scissor mode as shown in Figure 5-7.

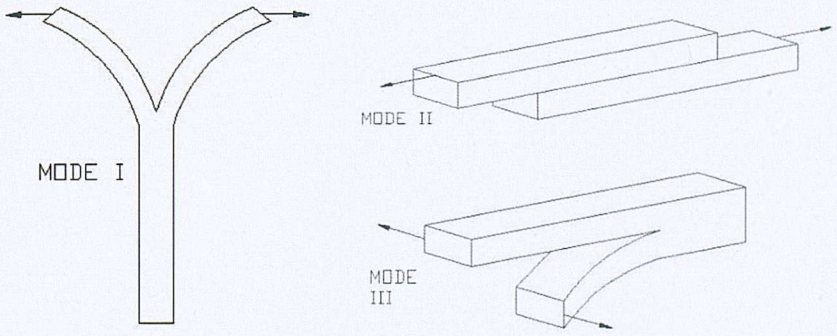


Figure 5-7. Fracture/delamination modes I, II and III.

5.5.2 Function of an eight noded interface element

A typical Abaqus cohesive element considered in the present work is eight nodded and has four integration points, as shown in Figure 5-8.

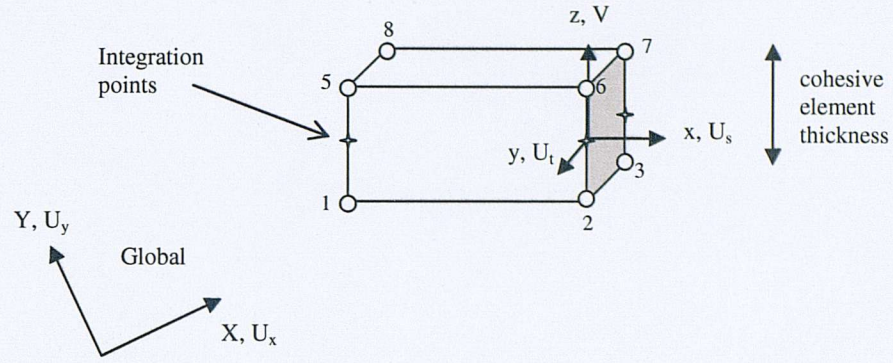


Figure 5-8. Global and local interface element coordinates

The displacements are given for each of the four interface element nodes - where nodes 1, 2, 3 and 4 are connected to the bottom neighbouring elements and nodes 5, 6, 7 and 8 are connected to the top neighbouring elements. Each node has three degrees of freedom – one normal and two tangential. These local displacements are converted to relative top-bottom nodal displacements for the three local directions. Consider the local interface element directions as 'tangential' for the local 'x' and 'y' and 'normal' for the local 'z'. These *relative* displacements of nodes 1 and 5, 2 and 6, 3 and 7 and 4 and 8, are considered to act at the mid-plane of each pair of cohesive element nodes. In two dimensions this can be seen more clearly as shown in Figure 5-9. The relative displacements and tractions are the cohesive element's 'strain' and 'stress' respectively.

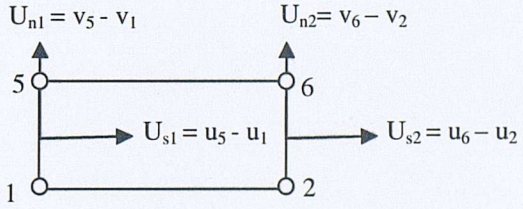


Figure 5-9. Resultant displacements

The relative displacements, in the normal and one of the tangential directions, corresponding to fracture modes I and II respectively, are shown by the difference between the top and bottom element node displacements at the element centre, U_{top} and U_{bot}, see equation (5-30). These are obtained from the extrapolated nodal displacements; the normal displacements v_{top} and v_{bot} for the nodes in the top and bottom faces of the cohesive element respectively, and the shear displacement u_{top} and u_{bot}, for a 2d case.

$$\varepsilon = \begin{Bmatrix} \varepsilon_I \\ \varepsilon_{IIs} \end{Bmatrix} = U_{top} - U_{bot} = \begin{Bmatrix} U_{n1} \\ U_{n2} \\ U_{n3} \\ U_{n4} \\ U_{s1} \\ U_{s2} \\ U_{s3} \\ U_{s4} \end{Bmatrix} = \begin{Bmatrix} v_{top} \\ u_{top} \end{Bmatrix} - \begin{Bmatrix} v_{bot} \\ u_{bot} \end{Bmatrix} = \begin{Bmatrix} v_5 \\ v_6 \\ v_7 \\ v_8 \\ u_5 \\ u_6 \\ u_7 \\ u_8 \end{Bmatrix} - \begin{Bmatrix} v_1 \\ v_2 \\ v_3 \\ v_4 \\ u_1 \\ u_2 \\ u_3 \\ u_4 \end{Bmatrix} \tag{5-30}$$

The forces acting on the element nodes are calculated from the interface element surface tractions τ_n and τ_t specified with the cohesive zone law at the integration points using the relative displacements. The nodal forces are obtained by calculating the virtual work using the surface tractions and shape function N, as shown in equation (5-32), where F_{ts} is the shear force vector, **T** are the tractions and *S* is the surface related to the shear and normal directions. The matrix **N** represents the shape function.

$$F = \begin{bmatrix} F_n \\ F_{ts} \end{bmatrix} = \int_S N^T T dS \tag{5-31}$$

These F_n and F_{ts} forces obtained from these tractions are then applied to both nodes 1, 2, 3 and 4 and in opposing direction for nodes 5,6,7 and 8 of the interface elements.

The interface elements are normally modelled as having a very small, finite thickness and are thus allocated a high initial stiffness. The thinner the layer, the higher the initial penalty stiffness, 'K_c', given by the following relationship, where 'E_c' is the cohesive element material modulus and 'T_c' is the thickness of the cohesive element:

$$K_c = \frac{E_c}{T_c} \tag{5-32}$$

The density is given per unit area of the cohesive element, $\tilde{\rho}_c$. The stable time increment in an explicit analysis is given by the time taken for a stress wave to travel the shortest element dimension. Where cohesive elements are involved, this is the thickness of the cohesive element and is given by equation (5-33).

$$\Delta t = T_c \sqrt{\frac{\rho_c}{E_c}} = \sqrt{\frac{\tilde{\rho}_c}{K_c}} \tag{5-33}$$

5.5.3 The critical fracture energy value

The dynamic nature of shock-wave loading is ultimately responsible for dynamic fracture. There are two main problem types in dynamic fracture and the present work is concerned with dynamically growing interlaminar cracks. These are cracks having tip speeds typically higher than 20% of the material Rayleigh wave speed. They can be classified as 'steady state dynamic' (constant but fast crack speeds) or 'transient dynamic' (high speeds and accelerations) [43].

Material rate sensitivity effects become important in dynamic fracture and the strain rate has an influence over the mode I and mode II fracture in GFRP woven composites [44]. Ideally, if the fracture is of a dynamic and brittle nature then the *dynamic* initiation fracture toughness should ideally be applied as opposed the quasi-static one. Fracture toughness has been recognised by some as a relevant material property and is a function of the loading rate experienced near the crack tip. Sun and Han [45] and Rosakis et al [46] have commented on the need to review the subject of dynamic fracture with further work required on the important Mode I dynamic fracture with regards to delamination.

Unlike in quasi-static fracture, where the critical fracture energy G_{IC} (for Mode I) is proportional to the fracture toughness (also known as the stress intensity factor) K_I and the stiffness, E, in dynamic fracture the relation between K_I and G_{IC} also becomes dependent on the crack propagation speed. Dynamic fracture theories predict the Rayleigh surface wave speed (C_R) to be the limiting speed for mode-I (opening) cracks propagating dynamically along prescribed, low toughness paths in isotropic, linear elastic materials subjected to remote loading. The energy release rate is thought to be almost constant up to a given percentage of the Raleigh surface/shear wave speed after which it becomes a function of K_I and the wave speed, in the form $(¼)HK_{IC}^2=G_{IC}$, where H is a function of stiffness and the Raleigh wave function.

$$\frac{1}{E}K_{IC}^2 = G_{IC} \tag{5-34}$$

Studies also show that critical fracture energy changes with crack length up to a critical fracture energy value, after which propagation continues without a load increase. Mouritz (2001) [47] carried out mode I fracture tests on stitched and un-stitched vinyl-ester composites, showing a fairly constant fracture toughness value with delamination crack length after G_{IC} was reached (and relatively stable propagation for the un-stitched).

In the present work, access to mode I fracture tests were available for the woven E-glass/Derakane vinyl-ester composite for quasi-static loading conditions only. Critical energy values for crack initiation and crack propagation were obtained and for conservative measures, the lower figure was used in delamination criteria described in a later section.

5.5.4 Mesh density

The length of the cohesive zone is important in order to select an appropriate mesh size. Figure 5-10 shows this more simply for a single crack tip (such as for a DCB specimen). In the models concerned in this study, the cracks will have two tips, as shown with Figure 5-11. The length of the plastic zone in front of the crack has been approximated for ductile materials by various researchers. All the expressions for to estimate the length of this cohesive zone, L_c, have the same form and only differ in a multiple factor 'n', see equation (5-35), where σ_{max} is the interfacial strength. Irwin considered the crack tip zone as the region where the Von Mises stress is greater than the tensile yield stress and proposed $n=1/\pi$, which is the same as equation (5-29) with the length of the cohesive zone equal to half crack length '*a*'. Dugdale idealised the plastic region ahead of a mode I crack as being a narrow strip, putting $n= \pi/8$. Based on this work, Barenblatt produced an equivalent approximation of the plastic yield zone for brittle materials whereas Rice's formulation resulted as a function of the crack velocity. Hilleborg was the first to develop the FE interface cracking model for delamination in concrete, who proposed the relationship shown in equation (5-35) with n equal to 1.

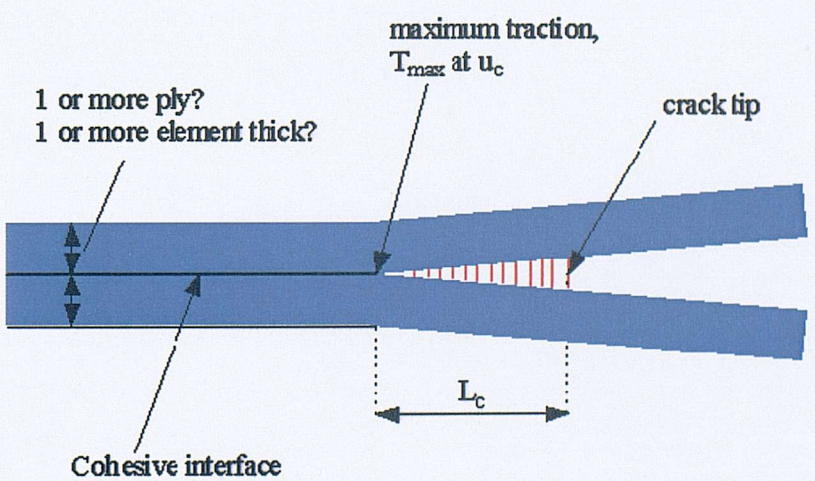


Figure 5-10. Cohesive zone length for a single crack tip

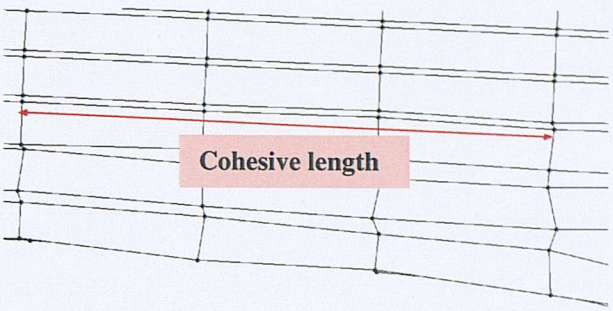


Figure 5-11. Cohesive length relative to the element size in a FE mesh.

$$L_c = \frac{nE_cG_c}{\sigma_{max}^2} \tag{5-35}$$

In an FE analysis, the cohesive zone must be discretised with a certain number of elements. The element length can be simply defined as shown in equation (5-36), where N is the number of elements. The exact number of elements required is still being debated. Some researchers have proposed more than 10 elements, others 2 to 5 [18], whereas Camanho and Davila [21] believe 3 elements is adequate enough, based on a parametric study on a DCB specimen.

$$L_e = \frac{L_c}{N} \tag{5-36}$$

Based on Hilleborg's expression and the material properties for the woven roving vinyl-ester composite, and mode I and mode II fracture tests, see Section 2.5 Chapter 2, L_c is calculated as 9.7mm. The structures considered in the present study are big compared to a DCB specimen, and more than 3 elements within the cohesive zone would be unwise in terms of numerical running times, even in Explicit. Therefore based on this number, the element length applied is no larger than 3.2mm.

It is clear that the structure size and element length size is important when it comes to producing a reliable cohesive model. For materials with large interfacial stiffness or small critical fracture energy values the length of the cohesive zone becomes impracticably small for the implementation of a cohesive model in structures larger than the size of a typical fracture specimen. However, based on work by Alfano and Crisfield [48], it was found that moderate changes to maximum interfacial strength do not have a critical influence on the delamination results, although they will affect local stress contours around the crack tip. In

fact, based on equation (5-35), reducing the value of the interfacial strength permits the increase of the element length. Thus the maximum traction force may be to a certain degree tailored to meet the mesh size requirements.

The above postulations on mesh size do not include size effect on the fracture parameters. Fracture processes do not scale with length, as failure processes at the micro-level involve characteristic lengths that do not scale with specimen size [49]. However there must be a characteristic material dimension (length scale) associated with a given fracture energy consumed by the fracture process. Markeset and Hilleborg [50] proposed a method of predicting the cohesive damage zone and found that the energy per unit area after the peak cohesive stress increases with increase in specimen length for specimens of slenderness ratio (length divided by width) less than 2.5. Fracture energy is traditionally considered a fixed material property, however not only can it vary with crack propagation, as described earlier, but also with scale. As shown by Frantziskonis [51], fracture energy increases with specimen size, as opposed to the nominal strength which decreases with size. The traditional fracture energy value applied is in fact an average value of the microstructural effect and not a local one. The current work is limited to applying the fracture energy from standard coupon tests.

5.5.5 A linear coupled traction-separation law

A linear cohesive zone model is proposed to model delamination in between the woven plies. Out of the various cohesive zone models available in Abaqus [52], a traction-separation response is chosen for all the analyses to follow. Here, a mixed mode damage initiation criterion is applied which means that the loading in the translaminar normal and shear directions (mode I and modes II), will have an influence over each other. This implies that damage will most likely initiate at a stress that is smaller than the maximum stress for failure for the individual mode.

The maximum attained value during the loading history of equivalent mixed mode displacement, $\bar{u}_m$, is used to detect the damage at the interface. The initiation of delamination damage is determined when a maximum nominal stress criterion, as shown in equation (5-37), is equal to one. This occurs at mixed mode stress values of $\tau_i = \langle \tau_i^{max} \rangle$, where i=n,s,t, represents the normal '33' direction and the transverse shear '13' and '23' directions. T_i^{max} is the maximum stress for the pure modes (i.e. when no other mode is acting). The Macaulay brackets are an indication of positive stresses only (i.e. only relevant

to the normal stress τ_n). In other words, when the criterion is equal to one under mixed mode loading, the stresses τ_i at that point in time are said to be equal to τ_i^{max}.

$$\left(\frac{\langle \tau_n^{max} \rangle}{T_n^{max}}\right)^2 + \left(\frac{\tau_s^{max}}{T_s^{max}}\right)^2 + \left(\frac{\tau_t^{max}}{T_t^{max}}\right)^2 = 1 \tag{5-37}$$

The stiffness of the material in the normal and shear directions is then later reduced based on the propagation criterion.

The quadratic stress criterion can be re-written in terms of the displacements, equation (5-38) by substituting the maximum stresses with the product of the penalty stiffness and initiation strain.

$$\left(\frac{\langle u_n^0 \rangle}{U_n^0}\right)^2 + \left(\frac{u_s^0}{U_s^0}\right)^2 + \left(\frac{u_t^0}{U_t^0}\right)^2 = 1 \tag{5-38}$$

U_i^0 are the critical pure mode displacements and u_i^0 are the mixed mode displacements, where i=n,t,s. The mixed-mode transverse shear displacements can be expressed as shown in equation (5-39). For simplicity also $U_{ts}^0 = U_t^0 = U_s^0$, as properties for only one of shear directions is available in the present work.

$$u_{ts} = \sqrt{u_t^2 + u_s^2} \tag{5-39}$$

The evolution of delamination damage can be expressed in terms of a single damage variable, d, which is a function of the effective mixed-mode displacement values at delamination initiation, u_m^0, and at full failure, u_m^f. Once damage has initiated the cohesive elements are non-healing. The parameter u_m^0 can be obtained from the initiation criterion and u_m^f from the damage propagation criterion.

The displacement u_m^0 is obtained by using equation (5-38) and the relationships shown in equations (5-40), (5-41), and (5-42), so that u_m^0 is written only in terms of the pure mode displacements and the mixed mode ratio, as shown with equation (5-43).

$$\lambda = \frac{u_{ts}}{u_n} = \tan\theta \tag{5-40}$$

$$\cos\theta = \frac{1}{\sqrt{1+\lambda^2}} \tag{5-41}$$

$$\left(u_{ts}^0\right)^2 = \left(u_m^0\right)^2 - \left(u_m^0 \cos\theta\right)^2 \tag{5-42}$$

$$u_m^0 = \frac{U_n^0 U_{ts}^0 \sqrt{1+\lambda^2}}{(U_{ts}^0)^2 + (\lambda U_n^0)^2} \quad \text{whilst } u_n > 0 \tag{5-43}$$

$$u_m^0 = u_{ts}^0 \quad \text{whilst } u_n < 0$$

It is assumed that the mode I stress does not contribute towards delamination damage when this stress is compressive and therefore under this loading mode I behavior is excluded from the equation.

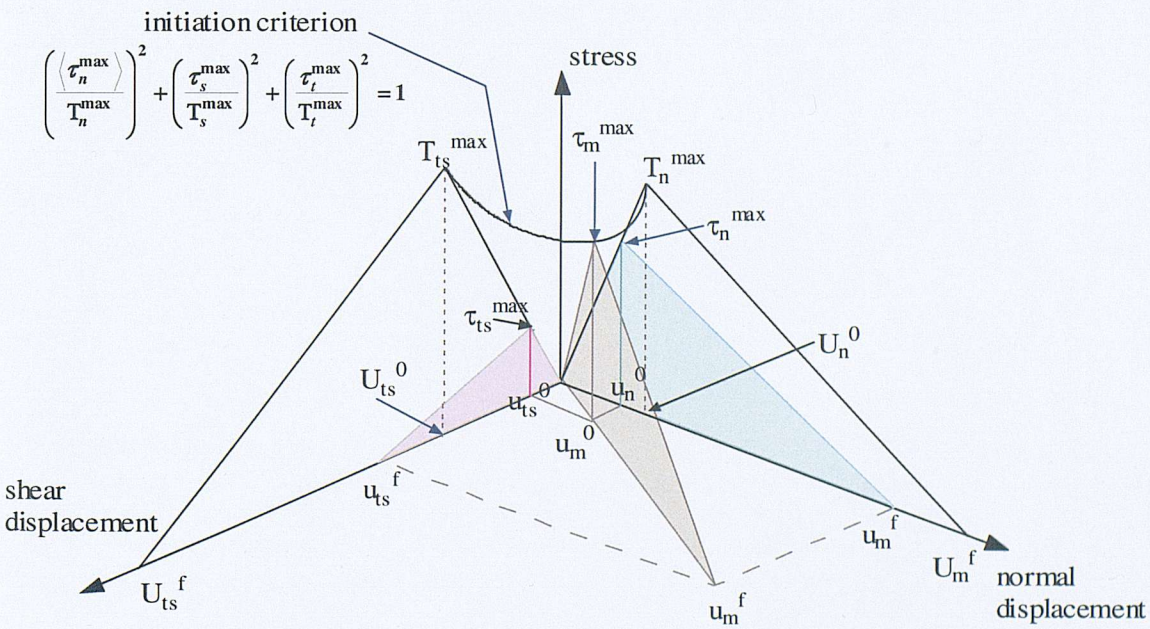


Figure 5-12. Mixed-mode linear traction-separation

The delamination damage evolution criterion used here is one based on fracture energy, shown by equation (5-44), where G_{IC}, and G_{IItC}, G_{IIsC} are the critical (pure mode) fracture

energies for the normal and transverse shear directions respectively and G_n, G_t and G_s are the mixed mode fracture energies. For simplicity, $G_{IIC}=G_{IItC}=G_{IIsC}$. An inbuilt model is available in Abaqus and the softening behavior can be either linear or exponential. For validation of a simpler model, a linear case was chosen and implemented in a user material subroutine (VUMAT). The power indice defines the shape of the failure locus and is typically equal to one or two. There is still discrepancy as to which power indice should be used or if indeed the power law criterion is adequate for certain composites or not. Opinions are varied as highlighted with work by Goyal et al [53] and Camanho et al [21]. According to Camanho there is no reliable mixed mode loading criteria for delamination propagation that involves mode III because of the lack of adequate mixed-mode tests that include mode III activity.

$$f(G)=\left(\frac{G_n}{G_{IC}}\right)^{\alpha}+\left(\frac{G_t}{G_{IItC}}\right)^{\alpha}+\left(\frac{G_s}{G_{IIsC}}\right)^{\alpha}, \quad \alpha=2 \tag{5-44}$$

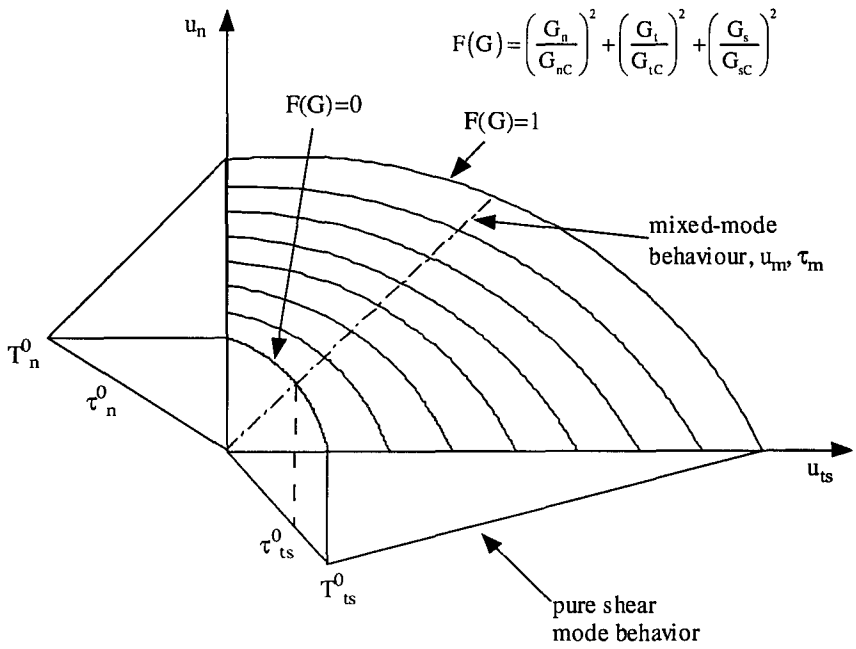


Figure 5-13. Plan view of the mixed mode behaviour dictated by the fracture energy criterion for damage propagation

The effective mixed mode displacement at failure, u_m^f, also shown in plan view in Figure 5-13, can be obtained from equation (5-44) by replacing the mixed mode fracture energies with the effective mixed mode displacement values and the critical fracture energies. This is done by writing the mode II fracture energy, G_{II}, in terms of mode I using relationship (5-45) (analogous to equation (5-40)) and then replacing the G_I variables with equation (5-46). The

mixed mode displacements in the expression for G_I are re-written in terms of the effective mixed mode displacements using equations (5-41) and (5-42).

$$\gamma = \frac{G_{II}}{G_I} \tag{5-45}$$

$$G_I = \int_0^{u_n^f} \tau_n du_n = \tfrac{1}{2}\tau_n^{max} u_n^f = \tfrac{1}{2}\left(K_n u_n^0\right) u_n^f \tag{5-46}$$

The effective mixed mode displacement at failure is thus given by equation (5-47).

$$u_m^f = \begin{cases} \left[\left(\frac{1}{G_{IC}}\right)^2 + \left(\frac{\gamma}{G_{IIC}}\right)^2\right]^{1/2} \frac{2\left(1+\gamma^2\right)}{K u_m^0} & \Leftarrow u_n > 0 \\ \sqrt{\left(U_n^f\right)^2 + \left(U_s^f\right)^2} \end{cases} \tag{5-47}$$

5.5.5.1 Implementation method in finite element

The traction-separation law was defined in a VUMAT user material subroutine for the cohesive element. In order to implement the cohesive law, it is necessary to express the tractions as stresses in the following incremental form shown with equations (5-48), where T_i^{old} are the tractions from the previous time increment.

$$\begin{aligned} T_n &= T_n^{old} + dT_n \\ T_t &= T_t^{old} + dT_t \\ T_s &= T_s^{old} + dT_s \end{aligned} \tag{5-48}$$

To obtain an expression for dT_n, the damage parameter d is required, which can be stated as a function of the maximum attained mixed mode interface displacement value up to the current time, u_m^{max}, and the mixed mode damage initiation and failure parameters, as shown in Figure 5-14 and with equation (5-43), (5-47) and (5-49).

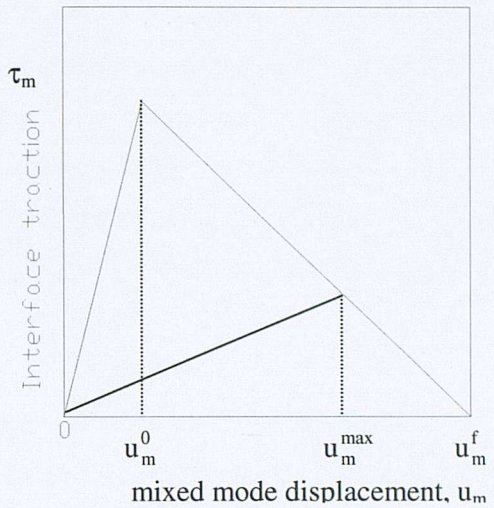


Figure 5-14. Linear mixed-mode traction and displacement.

$$d = \frac{u_m^f (u_m^{max} - u_m^0)}{u_m^{max} (u_m^f - u_m^0)} \tag{5-49}$$

The mixed mode displacement is calculated using the total normal and shear strains, $u_i = u_n, u_t$ and u_s, which feed into the subroutine, shown with equation (5-49).

$$\left.\begin{aligned} u_i &= u_i^{old} + du_i \\ u_m &= \sqrt{u_n^2 + u_t^2 + u_s^2} \end{aligned}\right\} i = n,t,s \tag{5-50}$$

The damage is taken as the maximum attained, described with equation (5-51), to prevent material 'healing', where 'τ' is the time at which point d attained its maximum, which can be any time up to the current time 't'. The increment in stress can thus be obtained as equation (5-52).

$$d(t) = \max_{\tau \le t} \{d(\tau)\} \tag{5-51}$$

$$\left.d\sigma_i = (1-d)K_c du_i\right\} i = n,t,s \tag{5-52}$$

5.5.6 A non-linear coupled traction-separation law

The proposed non-linear cohesive law describes a parabolic relationship between the tractions and the mixed-mode displacement λ, based on Needleman's work [54]. The Greek

letter lambda has been used instead of u_m (used in the linear model) because unlike the linear model, the mixed-mode displacement parameter in the non-linear model is expressed as a normalized displacement value. The cohesive zone model has been since implemented largely for quasi-static problems [12] however Espinosa [55] is one of a few authors who has applied it to impact analyses of small GFRP plates (subjected to impact velocities of over $85ms^{-1}$). In the current work, it is implemented for a larger and thicker plate subjected to a low impact velocity.

As the mixed-mode normal and shear tractions increase so does the mixed mode parameter λ. When λ is equal to λ_0, the maximum interface tractions are attained after which any further increase (or decrease) in λ results in reduction of the traction forces. When λ reaches 1, this signifies that the respective mixed-mode displacements have attained their mixed mode failure values and thus the interface fails, at which point the tractions have been brought down to zero. To fully define the cohesive law, the knowledge of the following experimental quantities is required:

- U_n^f, U_{ts}^f, the critical displacement for failure for the individual mode I and II fracture.
- $\tau_{max} = T_n^{max}$, the critical normal surface traction.
- G_{Ic} and G_{IIc}, the pure mode I and mode II critical strain energy release rates.

The value of the element surface tractions at any given time depends upon the value of λ, which is defined in equation (5-53), where the mixed-mode shear displacement u_{ts} is that of equation (5-39) and the critical pure shear mode displacement is the same for both shear planes and equal to U_t^f. Figure 5-15 shows the curve of mixed mode normal and shear tractions τ_n and τ_{ts} versus λ. The pure normal (mode I) mode of loading is represented with the dashed line for which the area under the curve is equal to the critical energy release rate G_{Ic}.

$$\lambda = \sqrt{\left(\frac{u_n}{U_n^f}\right) + \left(\frac{u_{ts}}{U_t^f}\right)} \qquad (5\text{-}53)$$

Mixed-mode displacement parameter

The mixed mode tractions, energy release rates and pure mode tractions are defined in Table 5-1. The coupled shear tractions are represented with τ_{ts}. The components of this traction into the two shear directions, 't' and 's' are shown in equations (5-61). Loading takes place

along the curve. Unloading before the maximum traction force is reached, i.e. when $\lambda=\lambda_0$, follows the parabolic curve. However, once damage has initiated, the cohesive elements are non-healing, and any unloading and re-loading takes place linearly and elastically, see Figure 5-16. The mixed-mode traction and displacement after which point unloading takes place is $\tau(\lambda_u)$ and λ_u respectively.

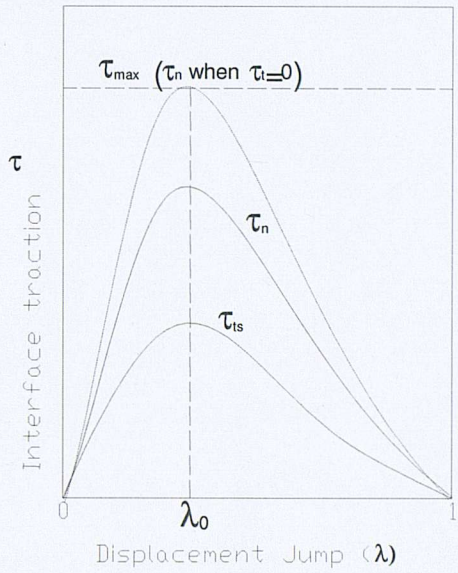


Figure 5-15. Parabolic coupled traction-separation law

Parameters	Cohesive law		
$\tau(\lambda)$	$\frac{27}{4}\tau_{max}\left(1-2\lambda+\lambda^2\right)$		(5-54)
τ_n	**Loading**	$\frac{u_n}{U_n^f}\tau(\lambda)$ $0\le\lambda\le 1$	(5-55)
	Unloading	$\frac{u_n}{U_n^f}\tau(\lambda_u)\frac{\lambda}{\lambda_u}$ $0\le\lambda\le\lambda_u$	(5-56)
τ_{ts}	**Loading**	$\psi\frac{u_{ts}}{U_t^f}\tau(\lambda)$ $0\le\lambda\le 1$	(5-57)
	Unloading	$\psi\frac{u_t}{U_t^f}\tau(\lambda_u)\frac{\lambda}{\lambda_u}$ $0\le\lambda\le\lambda_u$	(5-58)
G_{Ic}		$\frac{27}{48}\tau_{max}U_n^f$	(5-59)
G_{IIc}		ψG_{IC}	(5-60)
Max. traction for pure mode I		τ_{max}	
Max. traction for pure mode II		$\psi\tau_{max}$	

Table 5-1. Parameters for the parabolic (non-linear) cohesive law

$$\tau_t = \frac{u_t}{u_{ts}}\tau_{ts} = \psi\frac{u_t}{U_t^f}\tau(\lambda)$$
$$\tau_s = \frac{u_s}{u_{ts}}\tau_{ts} = \psi\frac{u_s}{U_t^f}\tau(\lambda) \qquad (5\text{-}61)$$

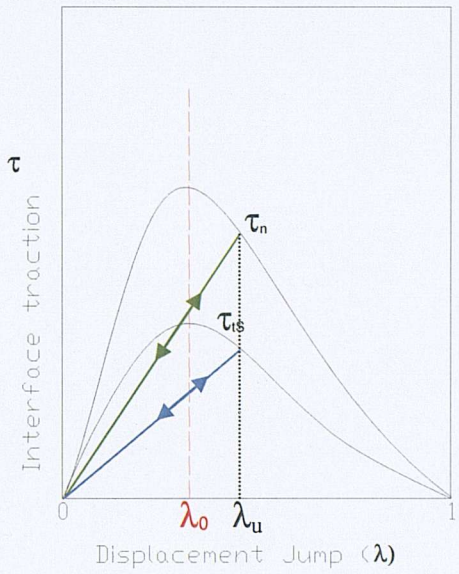


Figure 5-16. Linear unloading and re-loading paths, parabolic traction-separation law.

5.5.6.1 Implementation method in finite element

In order to implement the non-linear cohesive law, it is necessary to express the tractions in the following incremental form, shown with equations (5-48). To reduce unnecessary writing in the following explanations, only one of the shear tractions is described and because of the orthotropic nature of the woven composite concerned, the other shear is analogous. Each traction is a function of the displacement in the direction of the traction and of the mixed-mode displacement parameter, as we can see with equations (5-55) and (5-57) which are of the form of equations (5-62).

$$\tau_n = \tau_n\left(u_n, \lambda(u_n, u_s, u_t)\right)$$
$$\tau_t = \tau_t\left(u_t, \lambda(u_n, u_s, u_t)\right) \qquad (5\text{-}62)$$

The increment in tractions must be obtained by partial derivatives, as shown with equations (5-63).

$$d\tau_n = \frac{\partial \tau_n}{\partial u_n} du_n + \frac{\partial \tau_n}{\partial u_t} du_t + \frac{\partial \tau_n}{\partial u_s} du_s$$
$$d\tau_t = \frac{\partial \tau_t}{\partial u_t} du_t + \frac{\partial \tau_t}{\partial u_s} du_s + \frac{\partial \tau_t}{\partial u_n} du_n \quad (5\text{-}63)$$

The derivative of the normal traction with respect to the normal displacement and shear displacement u_t is shown with equations (5-64) and (5-65) respectively. Similarly, the derivative of one of the shear tractions, T_t, with respect to the shear displacement and normal displacement is shown with equations (5-65) and (5-66) respectively.

$$\frac{\partial \tau_n(u_n,u_s,u_t)}{\partial u_n} = \frac{\partial \tau_n(u_n,\lambda)}{\partial u_n} + \frac{\partial \tau_n(u_n,\lambda)}{\partial \lambda}\frac{\partial \lambda}{\partial u_n} \quad (5\text{-}64)$$

$$\frac{\partial T_n(u_n,u_s,u_t)}{\partial u_t} = \cancelto{0}{\frac{\partial \tau_n(u_n,\lambda)}{\partial u_{ts}}}\frac{\partial u_{ts}}{\partial u_t} + \frac{\partial \tau_n(u_n,\lambda)}{\partial \lambda}\frac{\partial \lambda}{\partial u_{ts}}\frac{\partial u_{ts}}{\partial u_t} \quad (5\text{-}65)$$

$$\begin{aligned}\frac{\partial \tau_t(u_n,u_s,u_t)}{\partial u_t} &= \frac{\partial}{\partial u_t}\frac{u_t}{u_{ts}}\tau_{ts} \\ &= \frac{\partial \tau_{ts}}{\partial u_t}\frac{u_t}{u_{ts}} + \frac{\partial}{\partial u_t}\left\{\frac{u_t}{u_{ts}}\right\}\tau_{ts} \\ &= \left(\frac{\partial \tau_{ts}(u_{tr},\lambda)}{\partial u_{tr}}\frac{u_{tr}}{u_t} + \frac{\partial \tau_{ts}(u_{tr},\lambda)}{\partial \lambda}\frac{\partial \lambda}{\partial u_{tr}}\frac{u_{tr}}{u_t}\right)\frac{u_t}{u_{ts}} + \left(u_{ts} - \frac{u_t}{u_{ts}}u_t\right)\frac{\tau_{ts}}{u_{ts}^2}\end{aligned} \quad (5\text{-}66)$$

$$\frac{\partial \tau_t(u_n,u_s,u_t)}{\partial u_n} = \cancelto{0}{\frac{\partial \tau_t(u_t,\lambda)}{\partial u_n}} + \frac{\partial \tau_t(u_t,\lambda)}{\partial \lambda}\frac{\partial \lambda}{\partial u_n} \quad (5\text{-}67)$$

The unloading conditions are dealt with similarly, with $\tau(\lambda_u)$ and λ_u being invariants during the unloading phase. The constituents of the above derivative equations are detailed in Table B.1 of Appendix B.

5.6 Numerical simulation of plate impacts using cohesive elements

5.6.1 Introduction

In this section, the effect of including a delamination model only is implemented in Abaqus/Explicit for three different plate sizes and impact energies but the same impact velocity, as detailed in Table 7-6 of Chapter 2. The material at the woven is modelled as orthotropic and damage at the woven plies is not included. A VUMAT, user material subroutine, was used to apply the linear elastic woven ply material model at the solid elements and to define the cohesive element behaviour. The contact force and maximum o.o.p. displacement predictions are plotted against the test results. Solid elements were used in all the models in order to permit a fair comparison with full 3d damage models later discussed in Chapter 6. The smallest plate has few plies and this permits modelling a cohesive layer in between each ply unlike the two larger plates which have 29 and 50 plies and modelling every ply would require a very fine mesh.

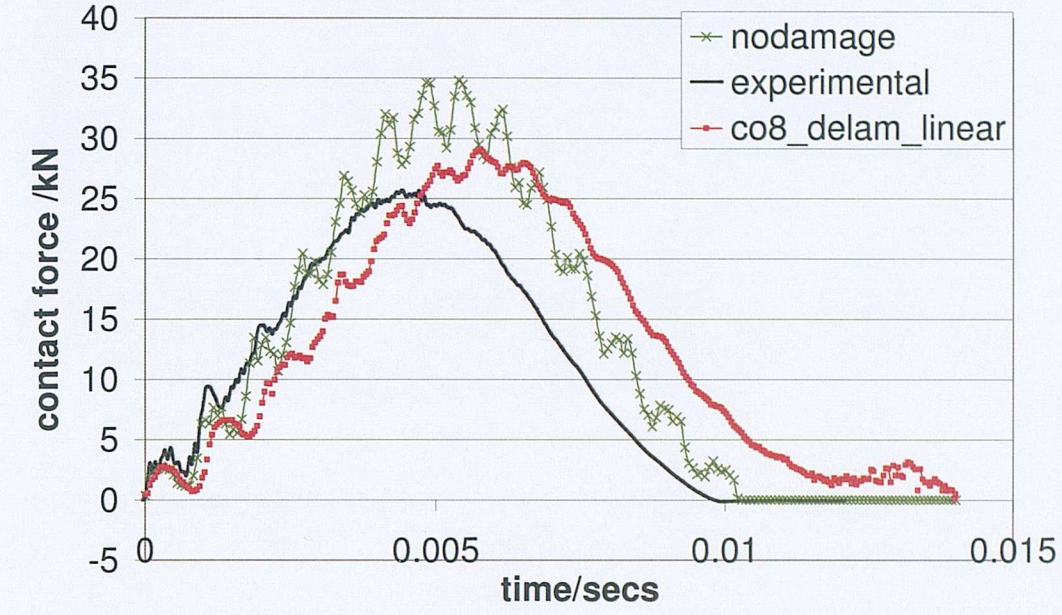
5.6.2 Results and discussion

5.6.2.1 Effect of a linear and non-linear cohesive model on a small plate

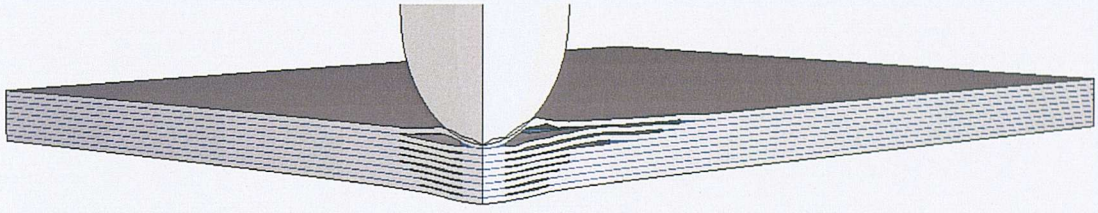
A significant difference was found between the impact simulations using the linear and the non-linear cohesive zone models. The small plate impact test 9M(195J), with an impact energy of 195.5J, Table 7-8 in Chapter 2, was validated for two different delamination models. The stiffer linear model produced a contact force-time history as shown in Figure 5-17(a); an improvement over the no-damage model, where 'co8' refers to a model with 8 cohesive layers. Although the location of the largest delaminations are not accurate, the sizes are moderately conservative, see Figure 5-17(b). The visible fold in the top ply is an occurrence that will be seen for other analyses in the subsequent work and is no reflection of the material model. Instead it is an effect of the contact definition in the Abaqus input file. General contact was assumed and the delamination of the top layer appears to 'stick' to tup before the tup finally looses contact. This is evident with the slight increase in contact force recorded towards the end of the impact event, seen in the contact force-time history in Figure 5-17(a).

In contrast to the linear cohesive zone model, the parabolic delamination model is overly conservative, evident through the significantly smaller contact force compared to the test, see Figure 5-18(a), caused by excessive delamination, Figure 5-18(b). This consequently

results in larger flexibility of the plate as seen Figure 5-19, showing the maximum o.o.p displacement for the two analyses.

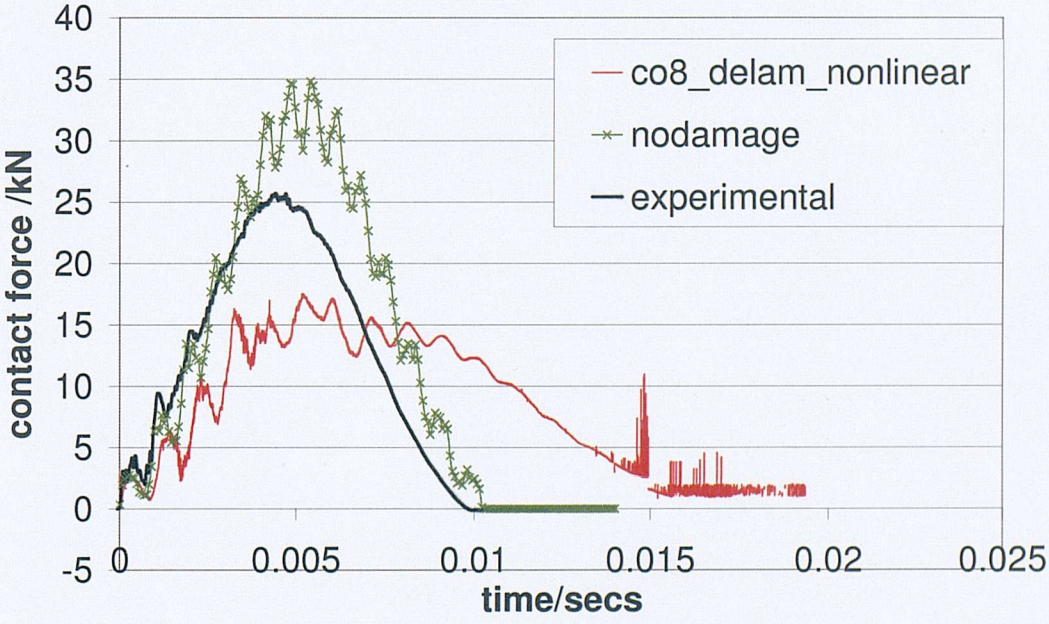


(a)

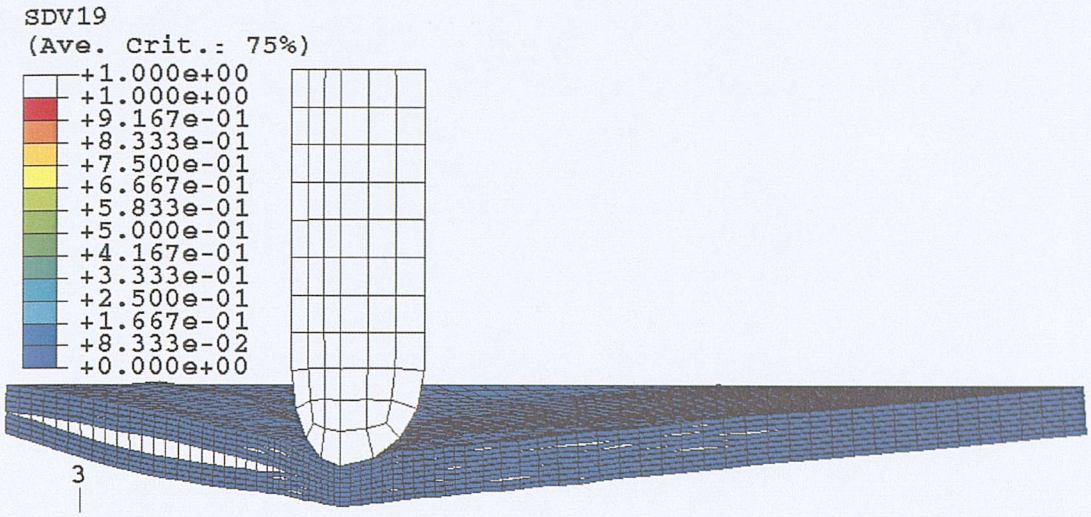


(b)

Figure 5-17. (a) Test and FE contact force-time history and (b) delamination prediction for small plate test 9M(195J)_co8 using the linear cohesive model.



(a)



(b)

Figure 5-18. Non-linear cohesive model test and FE (a) Contact force-time history, (b) delamination, for test 9M(195J)_co8.

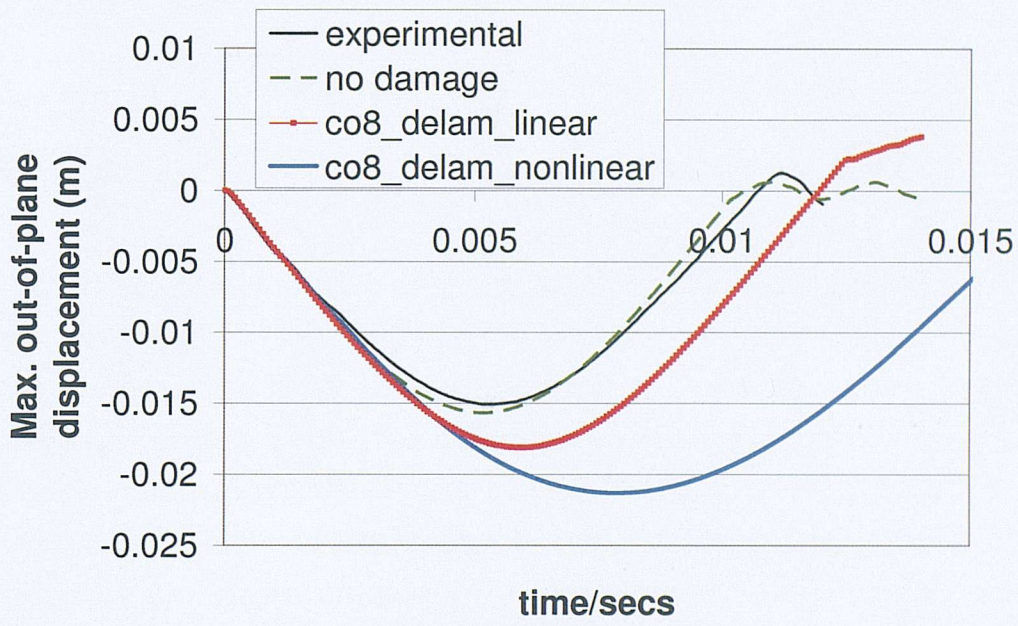


Figure 5-19. Maximum o.o.p-time history using the non-linear cohesive model, displacement, test and finite element results, small plate test 9M(195J)_co8.

The nonlinear model predicts a large amount of delamination, largely shear dominated. These results are unsurprising as the initial tangent stiffness, before the onset of stiffness degradation, is substantially lower than with the linear model. The mixed-mode displacement parameter λ_0 at which degradation begins is equal to a third of the maximum parameter value at failure (equal to 1). This ratio is much larger compared to that for the linear model, with a typical mixed-mode damage initiation value u_m^0 of $1.2(10^{-6})$ and a mixed-mode failure value u_m^f ranging from $6.3(10^{-5})$ to $2.5(10^{-5})$: giving a ratio of 1/20. For

the linear model, Figure 5-20 shows U_m^0 in the dashed line and u_m^f in the solid line, calculated throughout the analysis for one of the elements in the impact site.

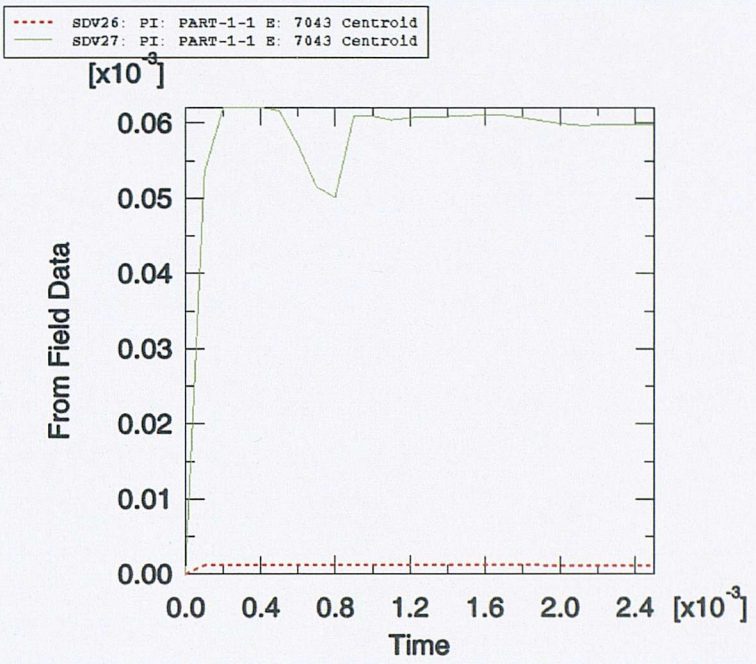


Figure 5-20. Mixed-mode initiation and failure displacements, in metres, using the linear cohesive model.

The CZM should combine the effects of the various elastic and plastic processes occurring in the process zone region. There should in theory be a link between the fracture processes and the shape and size of the CZM. Earlier the CZM was described as having a *forward* and a *wake* region. Compared to the linear model, the non-linear model has in proportion a forward region that is bigger than the wake. Although the energy absorbed from the fracture process is the same in both models (the area under the CZ curve), the size of the wake and forward region (the cohesive zone length) is different. A large forward region represents a larger plastic zone at the crack tip. In Espinosa's work, the attenuation of the free surface velocity and the peak stress values are in good correlation with experiment. However, the size of the delaminations are unknown. Also, his work involved high velocity impact using impactor *plates* not an impactor of smaller surface than the test plate. Moreover, Espinosa included a viscoplastic model, which would have the effect of reducing the interlaminar displacement and thus the over-all delamination size. Lastly, Espinosa tested two other cohesive models of linear form and concluded that they provided better results.

5.6.2.2 Linear model implementation for large plates

Large panels tests of size 1.07315x0.76835x0.019m^3, 'large1', were tested under impact, see Section 7.8.3.1 Chapter 2. Plate tests A and B were modelled using the linear traction separation law because of the poor results obtained with the non-linear model in the previous small plate simulation. The maximum out-of-plane displacement at the bottom-centre of the plate, the contact force and the delamination predictions are shown in Figure 5-21 and Figure 5-22. The displacements correlate relatively well with those of the tests measured without the fibre spall, which was quite pronounced in all of them. The contact force is marginally reduced over a no-damage model, however for test A the no-damage model under predicts the test contact force, pointing towards another factor of influence. As will become evident a little later on, the contact force is also affected by the element type. As the impact energies increase, shown for test B, the under-predictions diminish. The maximum delamination areas are predicted towards the top of the plate whereas in the experiment they are marginally larger in the bottom half. The size of the delaminations are also under-predicted by up to 19%.

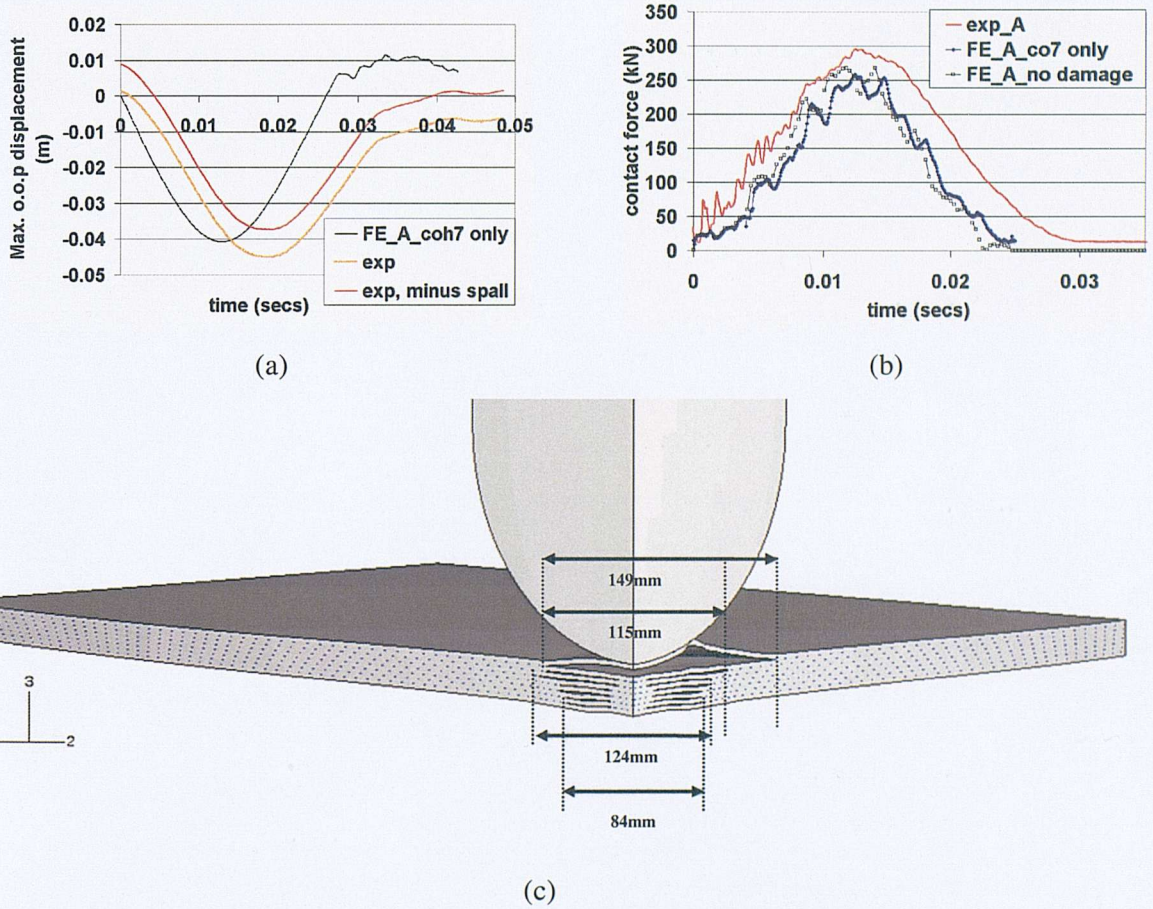


Figure 5-21. Test versus finite element results using the linear cohesive zone model (a) Max. o.o.p displacement-time history, (b) contact force-time history, (c) delamination predictions, plate large1 test A.

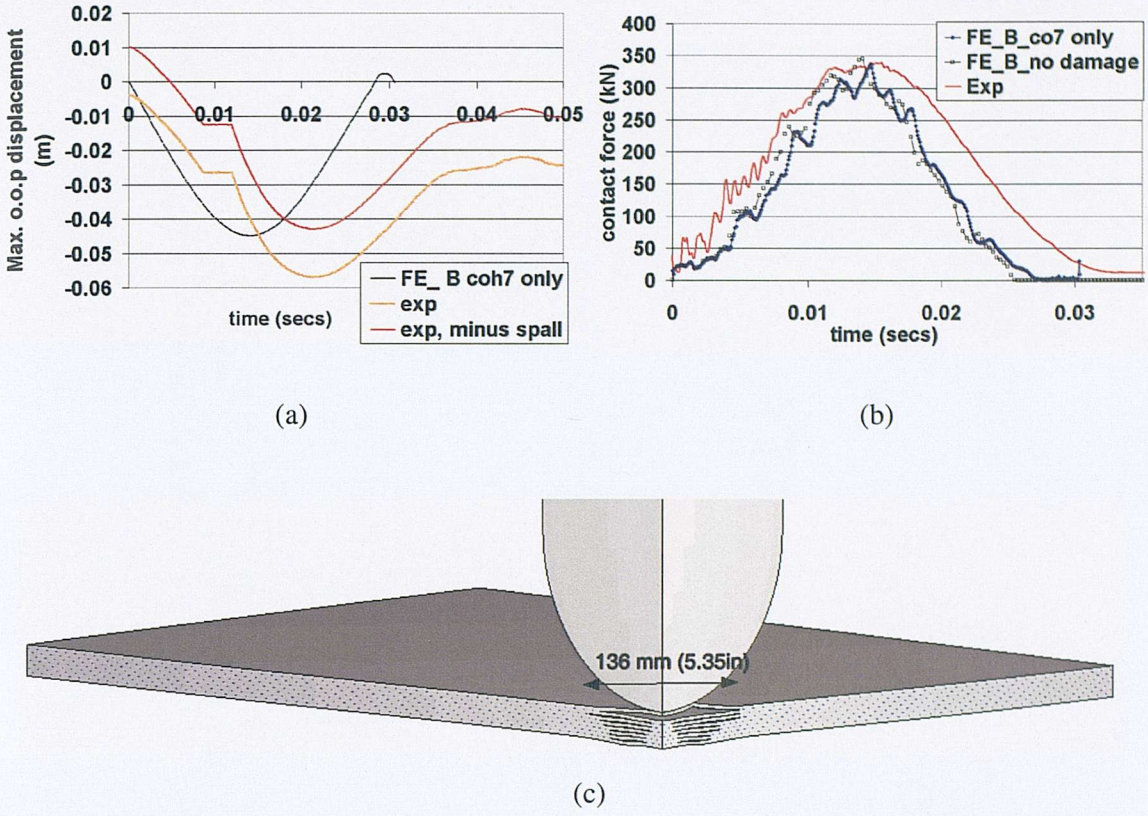


Figure 5-22. Test versus finite element results with a cohesive only model, (a) Max. o.o.p displacement-time history, (c) contact force-time history, for large plate 1, test 'large1(B)'.

The largest and thickest of the plates examined are of size 1.37x1.37x0.0381, 'large2', having the smallest width-to-thickness ratio. Although these plates were manufactured with a denser weave and resin system, 50oz/yd^2 WR E-glass/ BFG 281/C055 vinyl-ester, the material properties for the 24oz/yd^2 WR E-glass/8084 Derakane vinyl-ester were applied. Two tests were carried out, shown in Figure 5-23. The cohesive model gave a peak contact force of a similar magnitude to test large2(2) (large plate 2, test 2). The frequency content is improved over the no-damage model, see Figure 5-24, however the delamination prediction of 156mm is small compared to the largest C-scanned damage area of 347mm in diameter, see Figure 5-25. The sudden drop in contact force seen at 5msecs coincides with the start of matrix cracking and delamination.

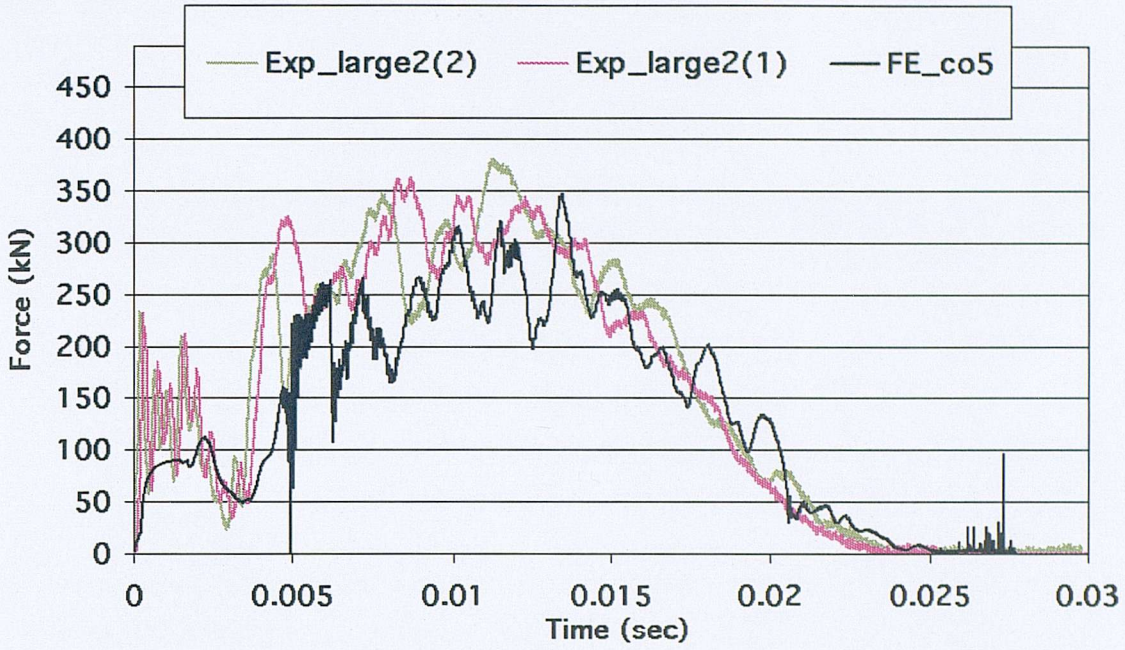


Figure 5-23. Contact force-time history using a linear cohesive zone model for tests large2(1) and large2(2) and FE prediction,

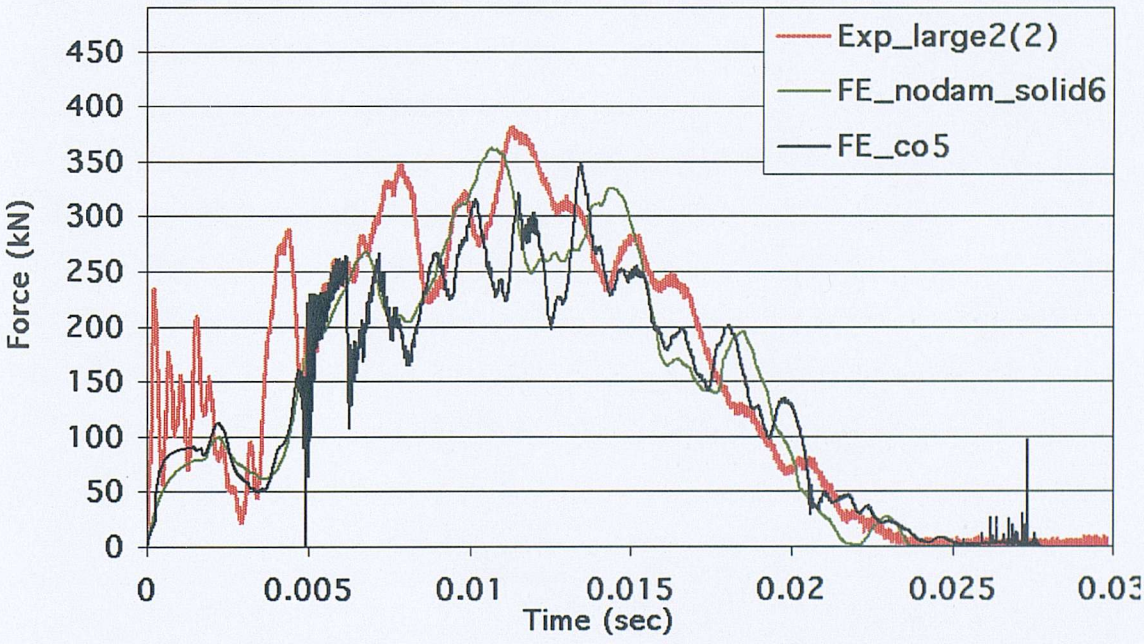
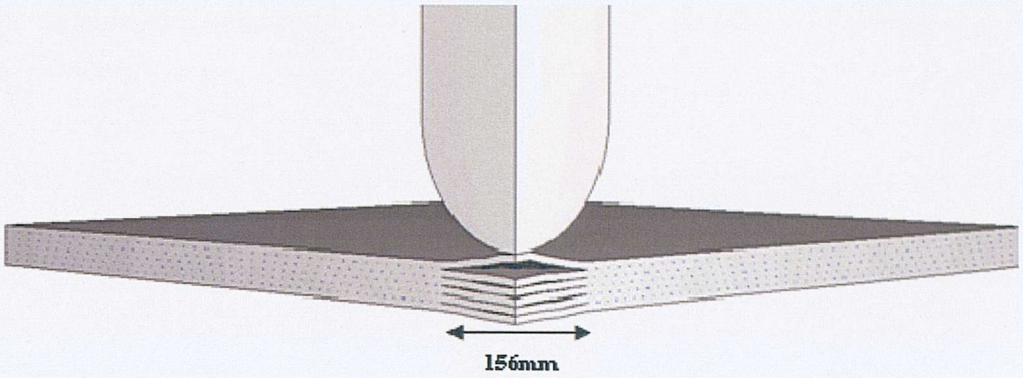


Figure 5-24. Contact force-time history using a linear cohesive zone model for large2(2) and FE no delamination versus delamination predictions



(c)

Figure 5-25. Delamination prediction for large2 tests

The impact energy for large1(B) and large2(2) is almost the same and the peak contact force is only about 20kN higher for the largest plate. The contact time is shorter by about 5msecs which is a result of the difference in plate thickness and boundary conditions. This is manifested with the 10mm larger maximum o.o.p displacement obtained with large1(B). Although these variables are relatively well captured in the analyses, the delamination for large2(2) is the most under-predicted. In reality this plate received a larger maximum delamination damage area than for large1(B) (a maximum of 335mm diameter compared to 186mm for large1(B)). However, the damage for large1(B) was recorded with the naked eye in contrast to the C-scan derived large2(2) damage measurements. The plate in large1(B) did however suffer more fibre damage, prevalent at the top and bottom faces. This is consistent with the fact that large2(2) plate was clamped and even though the plate is thicker than for large1(B), some of the load could also be taken through membrane action. In contrast, the plate in large1(B) had to rely on bending thus the large compressive and tensile stresses responsible for fibre rupture.

5.6.2.3 Shear dominated delamination

Mesh density, discussed later, has an influence the location of the largest delaminated regions. The cohesive elements are largely more influenced by the transverse shear displacements than the transverse normal displacements. However where localized bending occurs, as in the case of the small plate impacts using the 25.4mm and 12.7mm diameter tups (where the impact area is smaller relative to the plate dimensions than with the larger plates), an increased influence of the tensile normal transverse displacements (u_3) is observed in the FE analyses. Figure 5-26(a) shows the failed cohesive elements at 4msecs of impact time (note that the maximum contact force for this FE model is attained at 5.6msecs). Those

elements experiencing tensile u_3 are highlighted in Figure 2 (b). The elements nearer the plate centre fail largely from shear with little influence from the tensile u_3 (outputted as LE33), see Figure 5-27(a). However those elements furthest away, are more affected by the tensile u_3, see Figure 5-27(b), increasing in influence during the end of the compressive phase. Again, the elements chosen are highlighted in Figure 5-26(b). The cohesive elements at the interface nearest the top of the plate do experience any significant tensile u_3 influence even during the tensile phase of the impact event i.e. when the tup moves away. This can be seen with Figure 5-28(a) and (b) for large1(B) and test A, where the dotted lines represent the transverse shear displacement (outputted as LE13). The length of the interface selected for the displacement/time histories spans the width of the tup in question for that particular test. The cohesive elements nearest the bottom face of the plate experience in contrast, an increased influence of the normal displacements a little earlier on in the analysis, see Figure 5-28(c) and (d). It is important to also note that influence of the transverse shear displacement components at the outer-most interfaces will reduce with increase in the number of interface layers, reaching a threshold value when the full number of layers is modelled, as with test 9M(195J)_co8. Stacked solid elements do not provide a smooth parabolic shear stress distribution through the thickness. Instead, the distribution is be stepped and the transverse shear stress are non-zero at the surface.

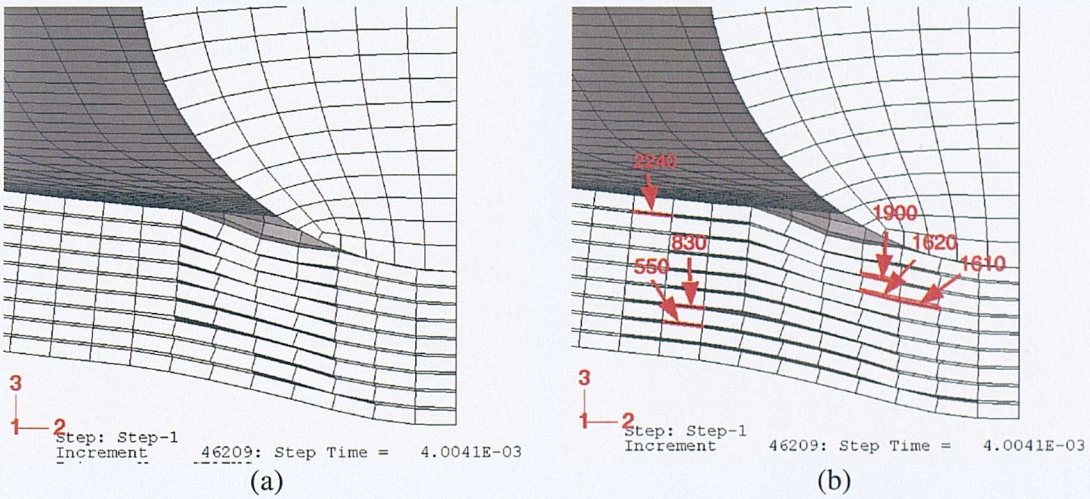
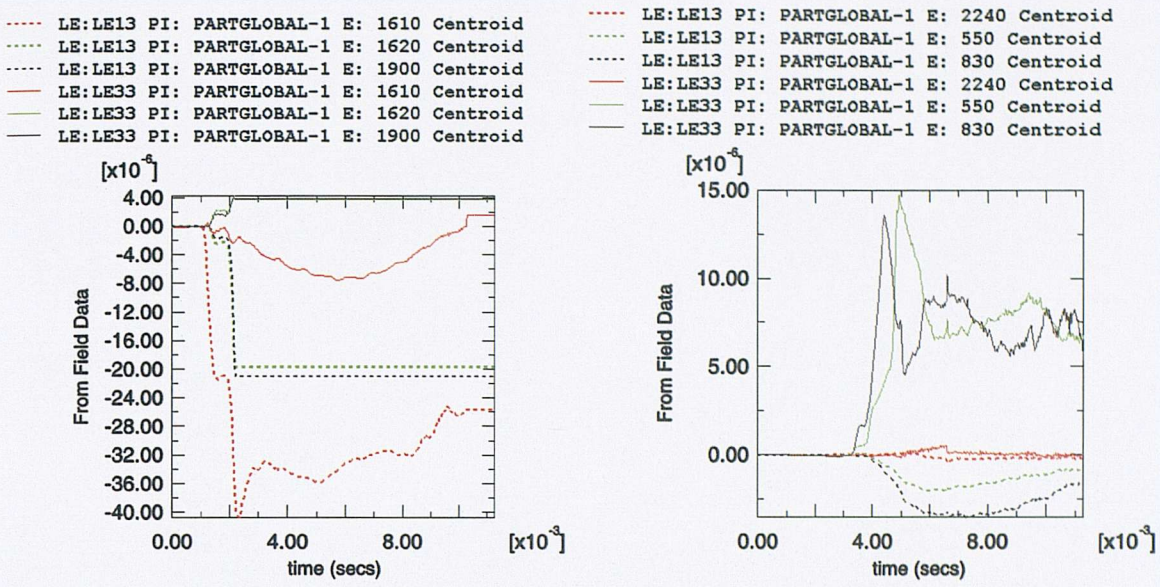
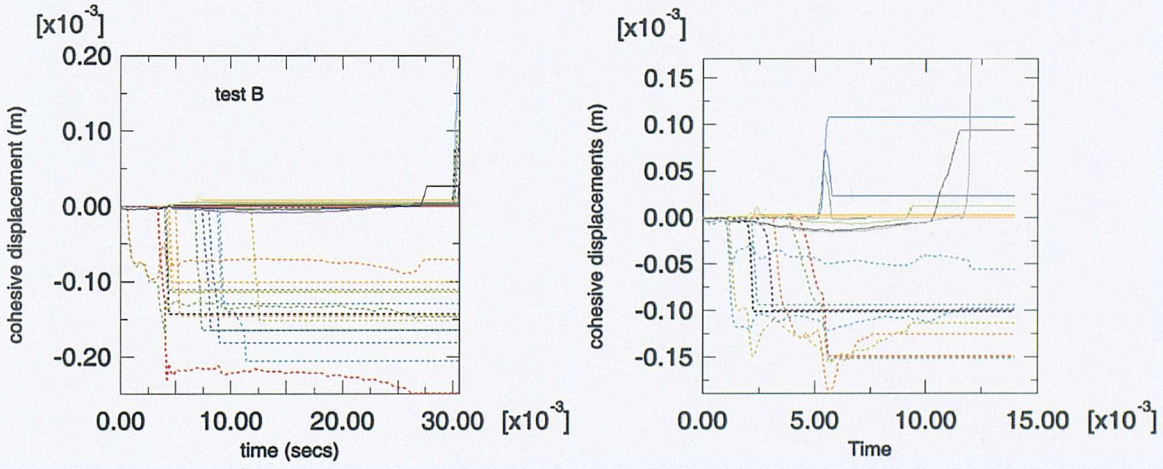


Figure 5-26. Status of cohesive elements at 4msecs, (a) failed cohesive elements shown in black, (b) Cohesive elements experiencing normal transverse tension, shown in black, for test9_co8_p2t2.



(a) (b)

Figure 5-27. (a) Elements influenced largely by the transverse shear displacement, shown for LE13 only (b) Elements highly influenced by the tensile normal displacement, in m, shown for a few elements in Figure 5-27 (b), test9_co8_p2t2. The transverse shear and normal displacements have dotted lines and solid lines respectively.



(a) (b)

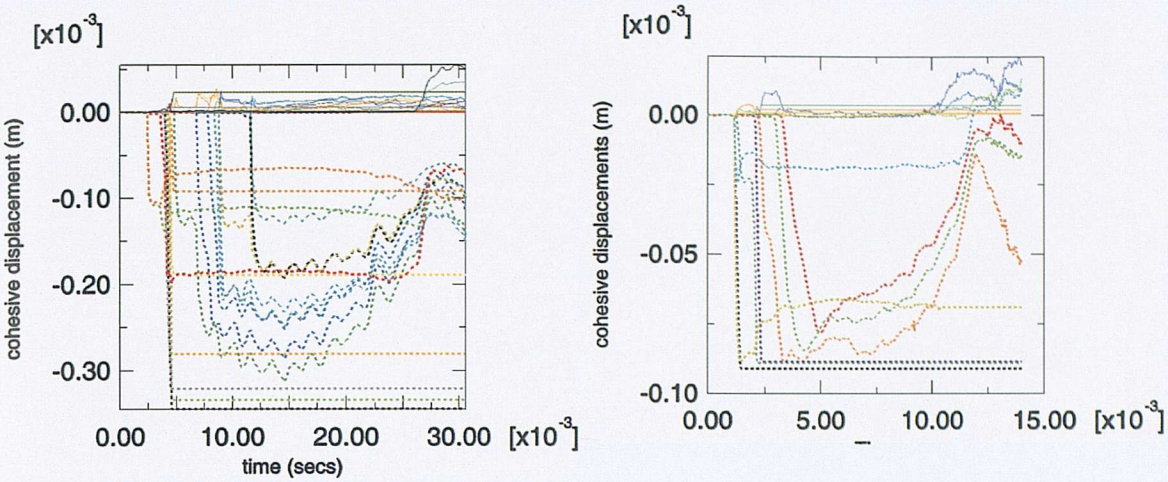
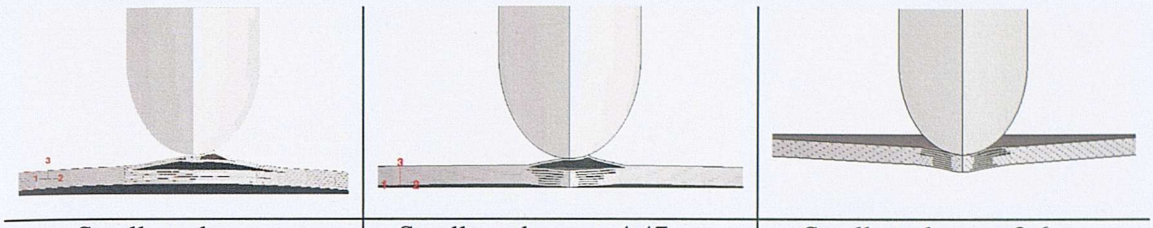


Figure 5-28. Cohesive displacements-time histories for (a) large1(B), top elements, (b) test 9M(195J)_co8, top elements, (c) large1(B), bottom elements, (d) test 9M(195J)_co8, bottom elements. The transverse shear and normal displacements have dotted lines and solid lines respectively.

5.6.2.4 Mesh density influence

It is evident that applying a sufficiently fine mesh (both plate and impactor) is important to effectively represent the shape of the plate during deformation which influences the contact event and as a result the delamination prediction.

The most significant limitation of finite element methods is that the accuracy of the obtained solution is usually a function of the mesh resolution. Any regions of highly concentrated stress, such as around loading points, must be carefully analyzed with the use of a sufficiently refined mesh. The meshes used here were chosen to minimize the mesh influence without resulting in long computational times. The present analyses take typically 2 to 8 days to complete, depending on the plate size. As one of many examples, Figure 5-29 shows this for different element sizes in the impact zone as the tup is moving away. The last picture of Figure 5-29 was taken at 0.0246secs compared to the others at 0.03secs, to show that full delamination had occurred at this point. The other figures give the false impression that the top layer is being 'pulled open' by the tup in the latter stages when in fact it had already delaminated. The delamination size and its location changes with mesh density and starts to level off after a certain mesh that can be approximated to the value calculated above using equation (5-36).



Smallest element: 10.67mm.	Smallest element: 4.47mm.	Smallest element:2.6mm.

Figure 5-29. Mesh density effect on delamination, test large1(B)

A cohesive zone model benefits from a fine cohesive mesh however, keeping the same mesh *density* with increase in model scale may result in unrealistically large stresses and strain outputs. If on the other hand, the same mesh resolution is maintained regardless of the scale, the increase in element size may affect the accuracy of the delamination model.

The present work shows that an increase in element size has the effect of creating larger delaminations. This is clearly a geometric and contact issue: a coarse mesh affects the contact which has a knock-on effect on the delamination. Moreover it has a direct effect on delamination with respect to cohesive zone length. If a coarse mesh is thus used with larger plates, the predicted delamination size may however, not be as unrealistically large as expected, since it has been found that delamination increases with specimen size more so than that predicted with fracture mechanics [56, 57].

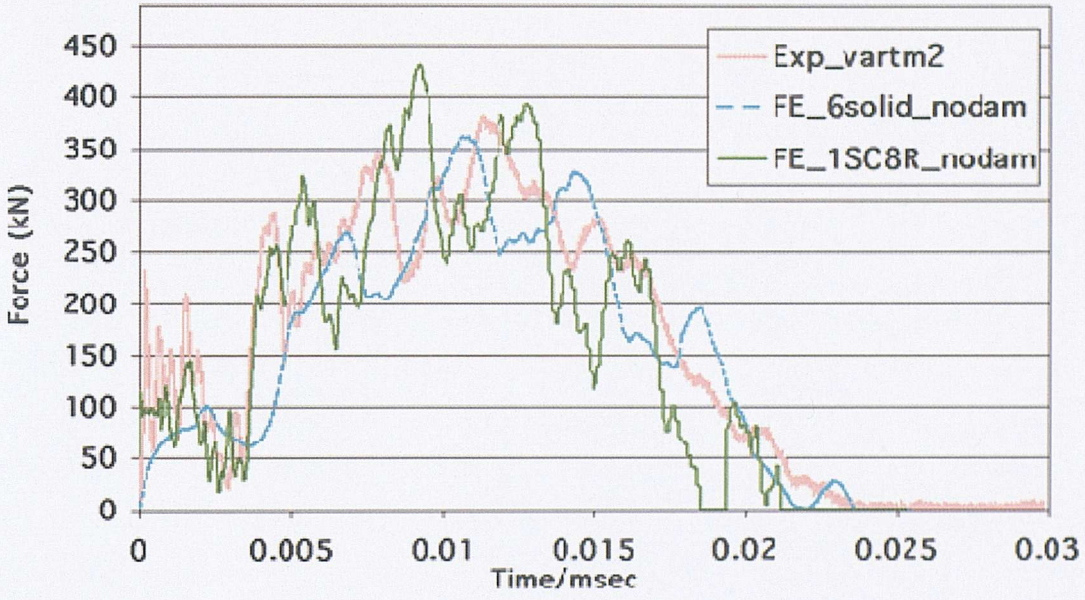
5.6.2.5 Scaling Effects

Scaling effects regarding the cohesive zone material parameters may be of some influence in the models, the extent of which is unknown for this particular scale. The energy for fracture specified by G_C is calculated using small material specimens and size effects play a part in the value of the critical energy for fracture. The test specimens used to calculate this critical value are considered large enough to examine this energy on a macro-scale, as on a micro-scale the displacements are to do with molecular or granular separation which is of no purpose for an engineer. However, there are infinite macro-scales and the energy used to open up a small, specimen surface area cannot be directly considered for a significantly larger piece (particularly of a different shape). Furthermore, G_c is known to be strain rate dependent [58]. The limitation of a cohesive zone model is that it assumes that both the critical crack opening displacement and the ultimate strength of the interface are independent of the structural size, which experiments show is not true [59, 60]. These topics are too

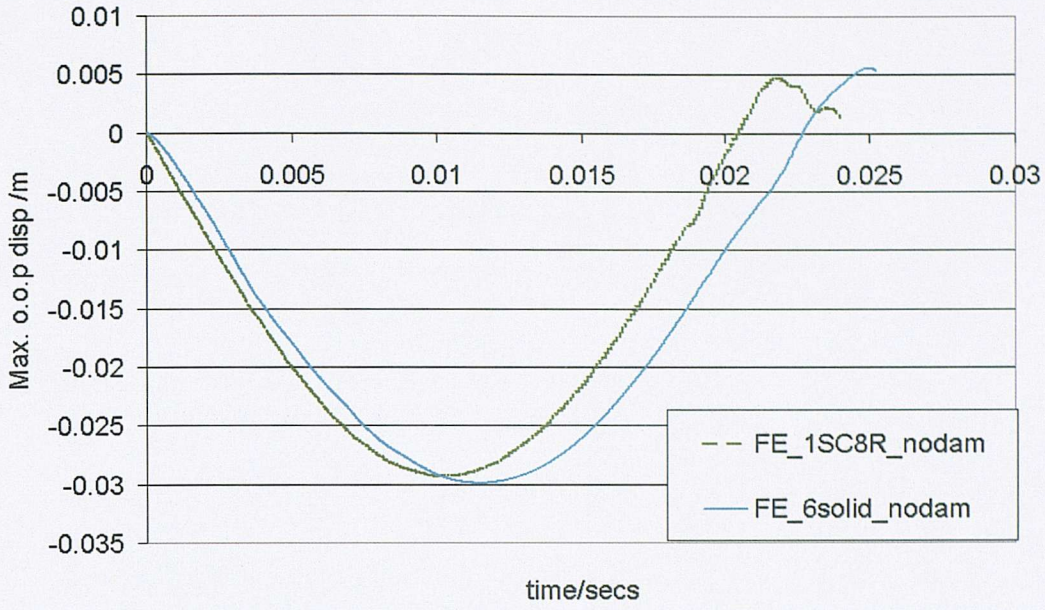
extensive to deal with in the current work and are thus presented as an area for future consideration.

5.6.2.6 Shell element type

The use of either shell or solid elements was proven to make a difference for a no-damage model, as we can see with the large2(2) simulation using 1 SC8R element and 6 solid C3D8R elements through the thickness, See Figure 5-30(a) and (b). Even though the contact force is higher with the continuum elements, this can vary with transverse shear stiffness for the section, later discussed in Chapter 6. The frequency content and shape of the curve is better modelled with one continuum shell through the thickness than with 6 solid elements, particularly during the first three-quarters of the analysis.



(a)



(b)

Figure 5-30. Effect of continuum shell elements and solid elements , (a) contact force-time history and (b) max. o.o.p displacement, for large panel 'large2(2)'

5.7 Concluding remarks

The implementation of damage in the form of a stand-alone cohesive zone model, appears to be limited in its prediction of the size and location of the delaminations. The largest delaminations are under-predicted particularly at the bottom-half of the plates and more-so with the largest plate considered. Although the mesh density for the all the analyses was chosen to minimize any effect on the contact force, it is likely that the delamination parameters need adjusting to cater for scale effect. It is also found that the transverse shear displacements at the interface are generally larger in magnitude and of more influence than the tensile transverse normal displacements. The fact that no other damage was modelled at the woven plies (i.e. matrix and fibre damage) will also have an influence, as later observed in Chapter 6. The contact force is marginally reduced compared to a no-damage model but this does not always improve the comparison with the test results, particularly where larger plates are concerned. If anything, it provides more conservative contact force predictions.

5.8 Reference List

1. Zhou G, Greaves LJ. Damage resistance and tolerance of thick laminated woven roving GFRP plates subjected to low-velocity impact. In: Reid SR, Zhou G (eds.), Impact Behaviour of Fibre-reinforced Composite Materials and Structures. Woodhead Publishing Ltd, 2000: 133-83.

2. Cox B, Yang QD. In quest of virtual tests for structural composites. Science 2006; 314(5802):1102-7.

3. Pagano NJ, Pipes RB. Some Observations on Interlaminar Strength of Composite Laminates. International Journal of Mechanical Sciences 1973; 15(8):679-88.

4. Whitney JM, Browning CE. Free-Edge Delamination of Tensile Coupons. Journal of Composite Materials 1972; 6(APR):300-&.

5. Ladeveze P, LeDantec E. Damage modelling of the elementary ply for laminated composites. Composites Science and Technology 1992; 43(3):257-67.

6. Elder DJ, Thomson RS, Nguyen MQ, Scott ML. Review of delamination predictive methods for low speed impact of composite laminates. Composite Structures 2004; 66(1-4):677-83.

7. Boh JW, Louca LA, Choo YS, Mouring SE. Damage modelling of SCRIMP woven roving laminated beams subjected to transverse shear. Composites Part B: Engineering 2005; 36(5):427-38.

8. Johnson HE, Louca LA, Mouring SE. Current research into modelling of shock damage to large scale composite panels. Journal of Materials Science, Special Edition 2006; 41(20):6655-72.

9. Dugdale DS. Yielding of steel sheets containing slits. Journal of the Mechanics and Physics of Solids 1960; 8(2):100-4.

10. Barenblatt GI. Mathematical theory of equilibrium cracks. Advances in Applied Mechanics 1962; 55-125.

11. Rice JR. Path independent integral and approximate analysis of strain concentration by notches and cracks. Proc of ASME Meeting APM-31, 1968, 8-.

12. Hutchinson JW, Suo Z. Mixed-Mode Cracking in Layered Materials. Advances in Applied Mechanics, Vol 29 1992; 29:63-191.

13. Tvergaard V. Effect of fibre debonding in a whisker-reinforced metal. Materials Science and Engineering A 1990; 125(2):203-13.

14. Espinosa HD, Dwivedi S, Lu H-C. Modeling impact induced delamination of woven fiber reinforced composites with contact/cohesive laws. Computer Methods in Applied Mechanics and Engineering 2000; 183(3-4):259-90.

15. Chen WH, Chang CM, Yeh JT. An Incremental Relaxation Finite-Element Analysis of Viscoelastic Problems with Contact and Friction. Computer Methods in Applied Mechanics and Engineering 1993; 109(3-4):315-29.

16. Scheider I. Cohesive Model for Crack Propagation Analyses of Structures with Elastic-Plastic Material Behavior: Foundations and Implementation, 2001, GKSS Research Center, Geesthacht, Dept. WMS.

17. Camanho PP. Numerical simulation of mixed-mode progressive delamination in composite materials. Journal of Composite Materials 2003; 37(16):1415-38.

18. Turon A, Davila CG, Camanho PP, and Costa J. An Engineering Solution for using Coarse Meshes in the Simulation of Delamination With Cohesive Zone Models. Report NASA/TM-2005-213547, 2005, NASA.

19. Camanho PP, Matthews FL. A progressive damage model for mechanically fastened joints in composite laminates. Journal of Composite Materials 1999; 33(24):2248-80.

20. Camanho PP, Matthews FL. Delamination onset prediction in mechanically fastened joints in composite laminates. Journal of Composite Materials 1999; 33(10):906-27.

21. Camanho PP and Davila C.G. Mixed-Mode decohesion finite elements for the simulation of delamination in composite materials. Report NASA / TM-2002-211737, 2002.

22. Camanho PP, Davila CG, and Ampur DR. Numerical simulation of delamination growth in composite materials. Report NASA /TP - 2001 - 211041, 2006, Hampton, Virginia, Langley Research Center.

23. Ruiz C. Scaling in penetration and perforation mechanics. Proc of Size Effects in Fracture, Farnborough, Inst Mech Engng, 1996, 11-17.

24. Mines RAW, Roach AM, Jones N, and Cantwell. Impact and residual properties of composite laminates subjected to secondary blast damage, 2006, Impact Research Centre, The University of Liverpool.

25. Tang X, Shen Z, Chen P, and Gaedke M. Methodology for residual strength of damaged laminated composites. Report AIAA-97-1220, 1997.

26. Davies GAO, Hitchings D, Zhou G. Impact damage and residual strengths of woven fabric glass/polyester laminates. Composites Part A: Applied Science and Manufacturing 1996; 27(12):1147-56.

27. Kuboki T, Jar PYB, Forest TW. Influence of interlaminar fracture toughness on impact resistance of glass fibre reinforced polymers. Composites Science and Technology 2003; 63(7):943-53.

28. Hou JP, Petrinic N, Ruiz C. A delamination criterions for laminated composites under low-velocity impact. Composites Science and Technology 2001; 61(14):2069-74.

29. Reis L, de Freitas M. Damage growth analysis of low velocity impacted composite panels. Composite Structures 1997; 38(1-4):509-15.

30. Lemmen P, Meijer G-J, Rasmussen EA. Dynamic behavior of composite ship structures (DYCOSS) failure prediction tool. 2006.

31. Hashin Z. Failure criteria for unidirectional fiber composites. Journal of applied mechanics 1980; 47(2):329-34.

32. Johnson AF. Modelling fabric reinforced composites under impact loads. Composites Part A-Applied Science and Manufacturing 2001; 32(9):1197-206.

33. Sun CT. Modelling high strain rate response and failure in polymeric composites. Proc of The 2nd Int. Conf. On Struc. Stability and Dynamics, Singapore, 2002.

34. Khan MZS, Simpson G. Mechanical properties of a glass reinforced plastic naval composite material under increasing compressive strain rates. Materials Letters 2000; 45(3-4):167-74.

35. Shah Khan MZ, Simpson G, Gellert EP. Resistance of glass-fibre reinforced polymer composites to increasing compressive strain rates and loading rates. Composites Part A: Applied Science and Manufacturing 2000; 31(1):57-67.

36. Greenfield RJ, Dynamic tensile properties of woven glass fabric composites, University of Delaware, 1997.

37. Lesar DE. Composite Sail Advanced Project Report, Plan for sensitivity analyses of rate-dependent composite material properties in composite advanced sail structure. Report NSWCCD 652, 2003, NSWCCD.

38. Rajbhandari SP, Scott ML, Thomson RS, Hachenbeg D. An approach to Modelling and predicting impact damage in composite structures. Proc of ICAS 2002 Congress, 2002.

39. Sun CT, Chen JL. A Simple Flow Rule for Characterizing Nonlinear Behavior of Fiber Composites. Journal of Composite Materials 1989; 23(10):1009-20.

40. Goldberg RK, Stouffer DC. Strain rate dependent analysis of a polymer matrix composite utilizing a micromechanics approach. Journal of Composite Materials 2002; 36(7):773-93.

41. Hillerborg A, Modeer M, Petersson P-E. Analysis of crack formation and crack growth in concrete by means of fracture mechanics and finite elements. Cement and Concrete Research 1976; 6(6):773-81.

42. Griffith AA. The phenomenon of rupture and flow in solids. Phil.Trans.Royal Society 1921; A221:163-98.

43. Rosakis AJ, Ravichandran G. Dynamic failure mechanics. International Journal of Solids and Structures 2000; 37(1-2):331-48.

44. Szekrenyes A. Overview on the Experimental Investigations of the Fracture Toughness in Composite Materials. Hungarian Electronic Journal of Sciences 2002; MET-020507-A.

45. Sierakowski RL. Impact damage - tolerant composite structural design. In: Reid SR, Zhou G (eds.), Impact Behaviour of Fibre-reinforced Composite Materials and Structures. Woodhead Publishing Ltd, 2000: 106-28.

46. Hart-Smith LJ. Predictions of a generalized maximum-shear-stress failure criterion for certain fibrous composite laminates. Composites Science and Technology 1998; 58(7):1179-208.

47. Mouritz AP, Baini C, Herszberg I. Mode I interlaminar fracture toughness properties of advanced textile fibreglass composites. Composites Part A-Applied Science and Manufacturing 1999; 30(7):859-70.

48. Alfano G, Crisfield MA. Finite element interface models for the delamination analysis of laminated composites: Mechanical and computational issues. International Journal for Numerical Methods in Engineering 2001; 50(7):1701-36.

49. Jones RM. Mechanics of Composite Materials, Taylor and Francis, 1998.

50. Markeset G, Hillerborg A. Softening of concrete in compression -- Localization and size effects. Cement and Concrete Research 1995; 25(4):702-8.

51. Frantziskonis GN, Konstantinidis AA, Aifantis EC. Scale-dependent constitutive relations and the role of scale on nominal properties. European Journal of Mechanics A-Solids 2001; 20(6):925-36.

52. Abaqus Users Reference Manual, Versions 6.4 and 6.5. 2005.

53. Goyal VK, Johnson ER, Davila CG, and Jaunky N. An irreversible constitutive law for modelling the delamination process using interface elements. Report NASA/CR-2002-211758, ICASE Report No. 2002-25, 2002, NASA.

54. Needleman A. A Continuum Model for Void Nucleation by Inclusion Debonding. Journal of Applied Mechanics-Transactions of the Asme 1987; 54(3):525-31.

55. Espinosa HD, Dwivedi S, Lu H-C. Modeling impact induced delamination of woven fiber reinforced composites with contact/cohesive laws. Computer Methods in Applied Mechanics and Engineering 2000; 183(3-4):259-90.

56. Nettles AT, Douglas MJ, and Estes EE. Scaling Effects in Carbon/Epoxy Laminates under Transverse Quasi-Static Loading. Report NASA/TM-1999-209-103, 1999, Langley Research Centre, Virginia, NASA.

57. Swanson SR. Scaling of Impact Damage in Fiber Composites from Laboratory Specimens to Structures. Composite Structures 1993; 25(1-4):249-55.

58. Nettles AT, Douglas MJ, and Estes EE. Scaling Effects in Carbon/Epoxy Laminates under Transverse Quasi-Static Loading. Report NASA/TM-1999-209-103, 1999, Langley Research Centre, Virginia, NASA.

59. Carpinteri A, Chiaia B, Cornetti P. A scale-invariant cohesive crack model for quasi-brittle materials. Engineering Fracture Mechanics 2002; 69(2):207-17.

60. Carpinteri A, Cornetti P, Barpi F, Valente S. Cohesive crack model description of ductile to brittle size-scale transition: dimensional analysis vs. renormalization group theory. Engineering Fracture Mechanics 2003; 70(14):1809-39.

CHAPTER 6.

A numerical study of plate impact using combined damage models

6.1. Introduction

The modelling of matrix and fibre damage has until now been tested separately to delamination damage, prompting the need for an amalgamated model. Two different models are validated in this chapter for both small and large scale plates under impact.

The emphasis of the first model was to adopt a simple approach to delamination modelling and matrix and fibre damage prediction for shell elements. An energy criterion for failure, described in Section 5.3.3 of Chapter 5, is applied at the resin-rich layers (RR-layers) which are modelled in between every ply.

Thick plates are largely more affected by transverse stresses than slender plates and it is therefore favourable to consider damage on a three-dimensional level. For this reason the second model includes through-thickness damage modelling, necessitating the use of solid elements as opposed to shell elements. The model applies a 3d damage criterion at the woven plies described in Section 4.3 onwards of chapter 4 and delamination is dealt with using a traction-separation law at the cohesive layers, see Section 5.5.5 of Chapter 5. The effect of some of the modelling parameters, including the number of cohesive layers and the transverse shear stiffness is briefly discussed.

6.2. 2d damage at the woven plies with resin-rich layers for delamination

Shell elements were used for all the following analyses. These elements are sub-layered with alternating layers of woven plies and resin-rich regions, both materials modelled as elastic damaging. Hashin's 2D stress-based failure criteria is applied at every woven-layer integration point and a once-only 90% material property degradation is used, as detailed in Table 3.1 of Chapter 3. The RR-layers are degraded more so, retaining only a 1% stiffness.

Abaqus' standard thick shells, type S4R, were used for two analyses however the relatively new SC8R continuum shell elements were used in the remaining majority of the models to assess their performance. The S4R shells have four nodes and six degrees of freedom per node, with reduced integration and large strain formulation. The S4R and SC8R are categorised as 'general purpose conventional shell elements'. They allow transverse shear deformation. They apply thick shell theory if the shell increases past 1/15 of a characteristic length of the shell surface (e.g. for a dynamic analysis, the wavelength of a significant natural mode). As the shell thickness decreases the transverse shear deformation also decreases and the element becomes more like a Kirchoff shell (i.e. when the shell normal is constraint to remain orthogonal to the shell reference surface). As covered in Section 3.5.3 of Chapter 3, the S4R shell elements as well as the SC8R elements model the change in shell thickness and enforce plane-stress conditions, however the continuum shell elements have 8 nodes and discretise a three-dimensional body giving them advantages over the conventional shells by modelling the through-thickness response of the shell more accurately. The transverse stresses are calculated by Abaqus for continuum shells, making them an attractive choice for thick plate simulations. However for both element types, using a VUMAT requires the user to provide the transverse shear stiffness as part of the shell section definition in the Abaqus input file.

The sensitivity of some of the FE results to two modelling variables is examined; mesh density and the number of continuum shell elements through the thickness.

6.2.1. Shell section definition

There are two ways of defining the shell section in Abaqus; using either 'shell general section' or 'shell integrated section' (the latter being simply defined as 'shell section'). When the material is linear and the composite comprises of just one material, the most economic definition is that of 'shell general section'. Both analysis types accept a layered

shell definition comprising of one or more layering materials. However, where numerical integration through the shell section is required during an Abaqus/Explicit analysis to output the stresses strains and other variables at the section integration points, the 'shell integrated section' must be used over the 'shell general section'. This is not the case in Abaqus/Standard unless the section properties (section stiffness coefficients) are specified directly at the beginning of the analysis in the input file. By doing this the stresses and strains cannot be calculated at the integration points during the analysis: therefore only section moments, forces and strains are available for output. If the material properties are assigned individually to each composite layer, then output at the integration points is available in Abaqus/Standard. Still, any dependence on temperature or other field variables such as those related to user defined field or user material subroutines (USFLD or UMAT/VUMAT), automatically exempts the application of 'general shell section' in both Abaqus/Standard and Abaqus/Explicit.

6.2.2. Transverse shear stiffness

The transverse shear stiffness is normally calculated from the shear stiffness matrix coefficients or engineering constants defined in the material definition. It is calculated by matching the shear energy for the shell with that of a 3d solid in pure bending about one axis, using a parabolic variation of the transverse shear stress through the shell thickness, again as described in Section 3.5.3 of Chapter 3. However, when using a user material subroutine, the shear modulus is not available during the pre-processing stage of the analysis. Therefore the transverse shear stiffness must be provided earlier on under the 'shell section' definition, and can be approximated as follows.

The transverse stiffness to be given for the 13 and 23 shear planes are K_{11}^{ts} and K_{22}^{ts} respectively. The following calculations are based on a homogenous shell made of a linear, orthotropic elastic material, where the strong material direction is along the local 1 direction:

$$K_{11}^{ts} = \frac{5}{6} G_{13} t, \quad K_{22}^{ts} = \frac{5}{6} G_{23} t, \quad K_{12}^{ts} = 0 \tag{6-1}$$

The number 5/6 is the shear correction coefficient, which also results from the matching of the shear energy/bending for an isotropic plate and 't' is the plate thickness.

The $K_{\alpha\beta}^{ts}$ values are then multiplied by another dimensionless factor, f_p, which is used to prevent the shear stiffness from becoming too large in thin shells:

$$\bar{K}_{\alpha\beta}^{ts} = f_p K_{\alpha\beta}^{ts} \tag{6-2}$$

$$f_p = 1 \Big/ \left(1 + 2.5E^{-4} \frac{A}{t^2} \right) \tag{6-3}$$

Where 'A' is the surface area of the element.

It must be noted, that because the transverse shear stiffness is only calculated or provided as in this case, once at the beginning of the analysis, any changes to the transverse shear stiffness (or indeed the normal transverse stiffness) during the analysis cannot be made. This is why the transverse properties of a material modelled with shells cannot be degraded and only two dimensional degradation models can be applied.

The calculation of the transverse shear stiffness for a homogenous shell section can only be improved upon if the composite layering through the thickness is taken into consideration. A simple and efficient way of calculating the transverse shear stiffness for a composite layered shell is by running a general shell section analysis in Abaqus/Standard, without a subroutine, and outputting a 'preprint' of the model definition data, which includes calculations made by Abaqus.

6.2.3. Large-scale plate impact

Two types of failure criteria are put to the test at the RR-layers: stress criteria 1 and 2 and the simple energy criterion, defined in Equations 5-1 of Chapter 5, for the analysis of test 'large2'. Matrix and fibre damage is predicted using Hashin's 2d criteria, as detailed in Equation 3-7, 3-8, 3-10, 3-12 of chapter 3. The plate size analysed is large2.

Abaqus/Standard was used for two of the analyses using standard thick shell elements, type S4R', and a USFLD subroutine, to test the validity of stress criteria 1 and 2. The dynamic nature of the problem makes the explicit FE method the preferred choice however, (briefly addressed in Section 4.11.2 Chapter 4, particularly where faster impact speeds are involved. This requires running Abaqus/Explicit with a VUMAT subroutine, as described in Chapter 4.

The FE simulation results for the large panel are presented for a single mesh density of 44x44 elements (each element length is 31mm) for a full plate model, and one element through the thickness. This panel is sub-layered with 58 composite orthotropic (woven) plies and 57 RR-layers. Each woven layer was assigned 3 integration points and each RR-layer 1 integration point.

6.2.3.1. Transverse shear stiffness influence

The Abaqus/Standard and Abaqus/Explicit contact force, maximum o.o.p displacement and contact force results are shown in Table 6-1. The explicit analysis was run four times to see the effect of the transverse shear stiffness value for an S4R and SC8R element model. The first value used, 5.23E7, was calculated for a homogenous shell, using Equations (6-1) and the second, 1.33E8, was obtained from an Abaqus/Standard 'shell general section' analysis for the composite layered shell.

The energy for delamination used in analyses 7 and 8, using the energy criterion for delamination, was 340J/M. The energy value from standard mode I fracture tests was used for one of the analyses using fracture data from Table 7.3 of Chapter 7, calculated as 12560J/M. This large value resulted in zero delamination prediction, thus generating results very similar to the analyses using stress criterion 2, discussed hereafter.

Out of the explicit analyses, the highest contact force predictions are obtained with the S4R elements: compare analyses 3 with 5 and 4 with 6. The differences in contact force between the two element types for the same transverse shear stiffness value is likely to result from the superior contact behaviour of the SC8R as the o.o.p displacement is negligibly affected by the element type. This is demonstrated in Figure 6-1 using stress criterion 2 which also shows the larger flexibility predicted with the Abaqus/Standard over the Abaqus/Explicit analysis.

Neither of the two stress criteria have any effect on the contact force or out-of-plane displacements, mainly because the damage predicted is so small, see analyses 2 and 5. The presence of more damage and thus some influence over these variables is achieved with the energy criterion for delamination, see analyses 3 and 7.

The larger transverse shear stiffness value, calculated from a Standard analysis creates as expected, a stiffer plate and a higher frequency output, see Figure 6-2 (shown for S4R element analyses). The larger contact force output for the S4R element model is also

demonstrated in Figure 6-3(a) using analyses 3 to 6, which shows the relationship between the transverse shear stiffness and the contact force for the two shell element types. The o.o.p displacement, also sensitive to the transverse shear stiffness, behaves similarly, Figure 6-3(b).

	Delamination criterion	Max. out-of-plane displacement (m)	Max. contact force (kN)
Abaqus/Implicit			
1	Maximum stress criterion 2, S4R	0.035	265
Abaqus/Explicit			
2	Max. stress criterion 1, S4R, TS5E7*	0.0332	389
3	Max. stress criterion 2, SC8R, TS5E7*	0.0332	373
4	Max. stress criterion 2, SC8R, TS1E8**	0.0313	382.6
5	Max. stress criterion 2, S4R, TS5E7*	0.0333	389
6	Max. stress criterion 2, S4R, TS1E8**	0.0319	406
7	Energy criterion from full-scale impact tests, SC8R, TS5E7*	0.0306	362
8	Energy criterion from full-scale impact tests, SC8R, TS1E8**	0.0299	379
TEST		**0.0287**	**380**

* Calculated for a homogenous shell section, $K_{11}^{ts} = K_{22}^{ts} = 5.23E7$

** From Abaqus/Standard 'shell general section' analysis, $K_{11}^{ts} = K_{22}^{ts} = 1.13E8$

Table 6-1. Peak contact force and o.o.p disp. using various delamination criteria in Abaqus /Implicit and Explicit , where 'R' is RR-layer thickness, test large2.

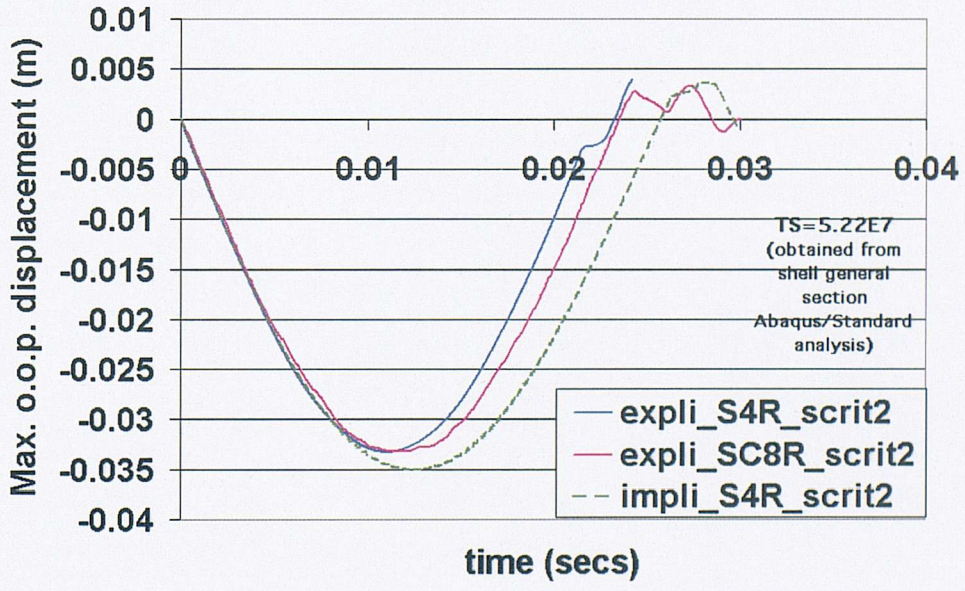


Figure 6-1. Out-of-plane disp. at the panel centre using Abaqus/Explicit and maximum stress criterion 2, test large2.

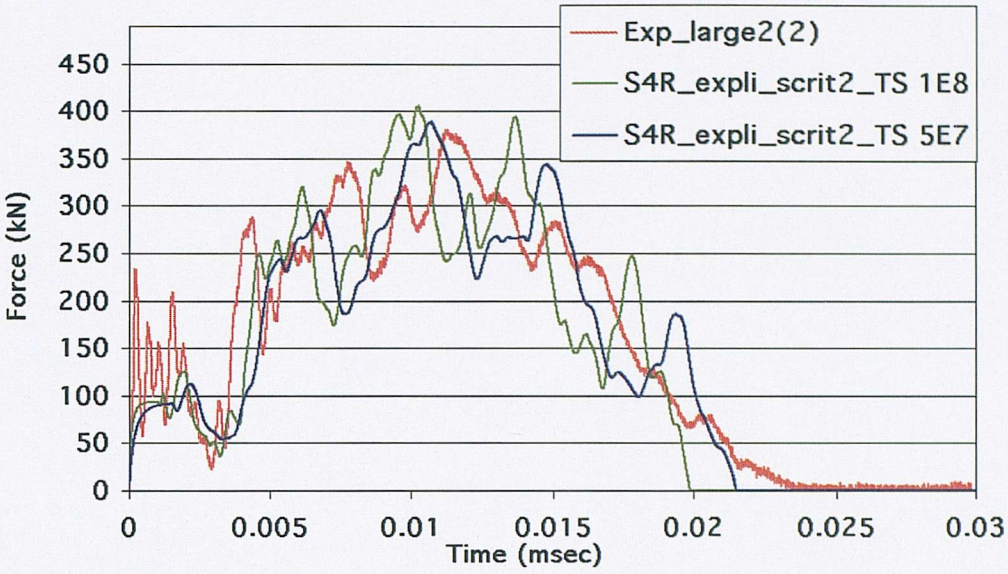


Figure 6-2. Contact force-time history, showing the effect of the transverse shear stiffness, using stress criterion 2 for delamination and S4R in Abaqus/Expli., test large2.

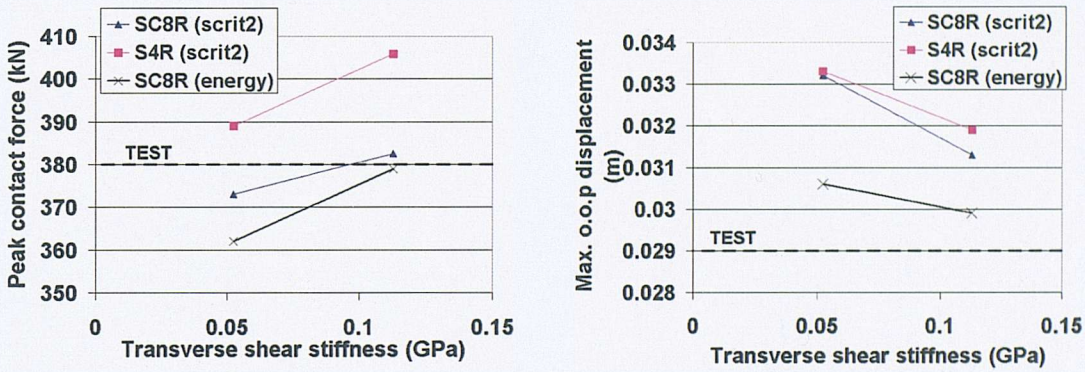


Figure 6-3. Effect of transverse shear stiffness with shell element type, using stress criterion 2, (a) contact force, (b) max. o.o.p displacement, test large2.

The maximum tup force and o.o.p displacement in the test calculated using the accelerometer is almost identical to that obtained by the Explicit analysis using the energy for delamination from the impact tests and the higher transverse shear stiffness, see Figure 6-3, Figure 6-4 and Figure 6-5. The accuracy of the result is surprising considering the numerical analysis does not physically model the separation of the delaminated layers and only in-plane material degradation was applied. The frequency content of the contact force is picked up relatively well and gives some confidence that the panel behaviour is being captured in a qualitative manner. However, the total contact time is better derived with the lower transverse shear stiffness and for a more conservative approach it is advisable to use the homogenous shell value.

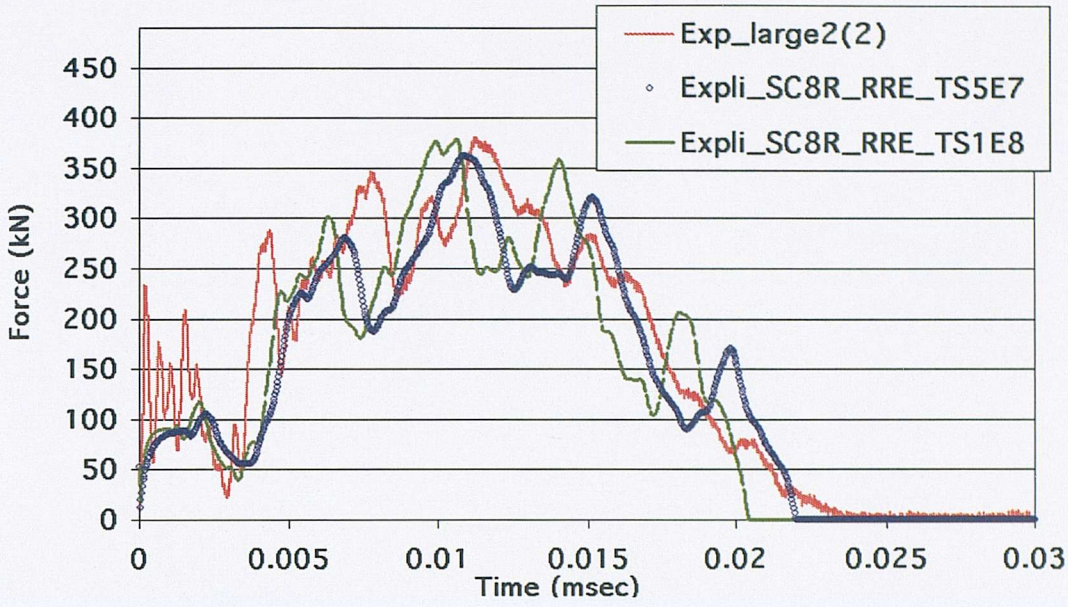


Figure 6-4. Contact force-time history, showing the effect of transverse shear stiffness, using energy criterion for delamination and SC8R, Abaqus/Explicit, test large2.

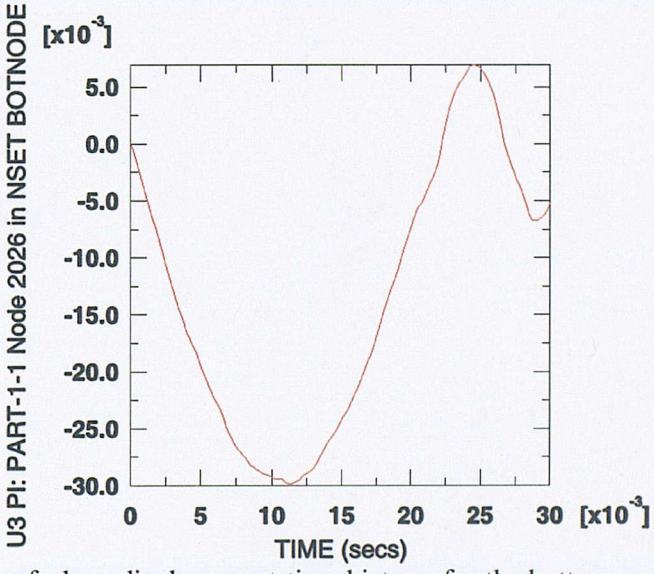


Figure 6-5. Out-of-plane displacement-time history, for the bottom-centre node using energy for delamination and larger shear stiffness value, test large2.

The contact force was substantially under-predicted with the implicit analysis as the wave propagation is clearly not being adequately captured, see Figure 6-6 (using the smaller transverse stiffness value).

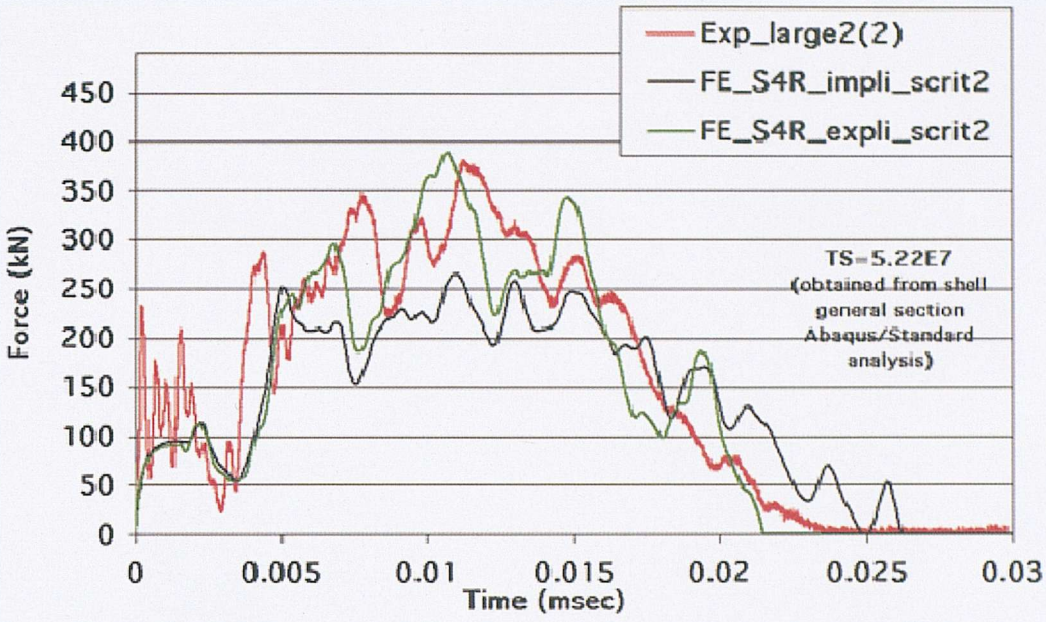


Figure 6-6. Contact force-time history for the implicit and explicit analyses using S4R elements and transverse stiffness 5.22E7, test large2.

6.2.3.2. Damage prediction

Matrix and fibre damage predictions using Hashin's 2d criteria have been recorded at five locations: at the external plies, a quarter distance into the section and mid-section. More matrix and fibre damage was predicted on the bottom half of the plate, more so on the first ply (other side of the impact face). Generally speaking the pattern predicted is that of maximum matrix/fibre damage area nearest the top and bottom surfaces decreasing in size towards the centre.

Abaqus/Standard simulations give a larger matrix and fibre damage area compared to the Explicit analyses; an average of $0.31 \times 0.31 m^2$ compared to $0.18 \times 0.18 m^2$, see Figure 6-7. The shape of the damage is also dissimilar, attributed to the differences in the two shell elements. The rectangular shape is generated with the continuum shell largely due to the better contact obtained between the tup and the plate. Conversely, the ordinary shells produce a damage pattern which is in the shape of a cross. With all simulations, the maximum matrix damage and fibre damage size falls within the size of the largest delamination area measured in the test, Figure 6-8, and the matrix damage may possibly be somewhat under-predicted.

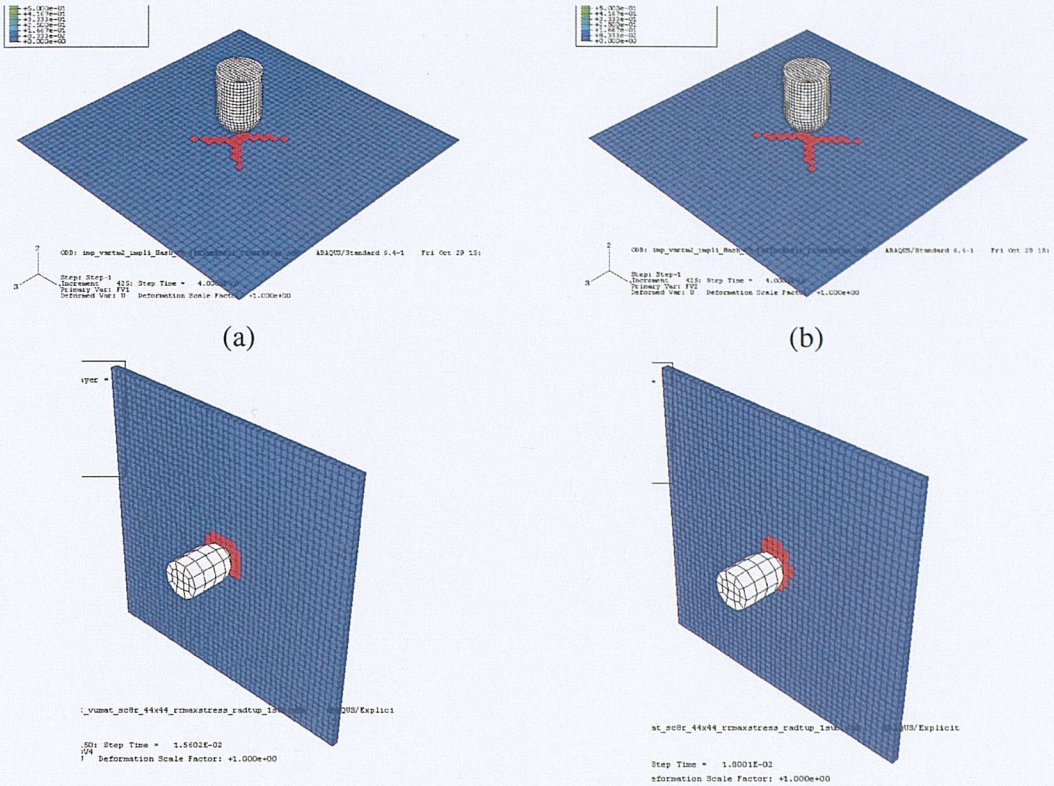


Figure 6-7. Damage predictions using Hashin's 2D criteria for large2, (a) matrix damage and (b) fibre damage using Abaqus/Standard and S4R elements and (c) matrix damage and (d) fibre damage using Abaqus/Explicit and SC8R elements.

Delamination damage follows a similar, less symmetrical pattern using the energy criterion, with maximum delamination predicted near the bottom face of the panel, see Figure 6-9. Better delamination prediction is obtained compared to using either of the maximum stress criteria, see Figure 6-10. In contrast, the tests show delamination all the way through the thickness, more so near the centre of the plate followed by layers near the outer faces. The maximum bending stresses (responsible for matrix cracking/crushing and an initiator of delamination) together with the normal transverse stresses would have been largely responsible for the delamination found nearer the surfaces. The transverse shear stresses although strongly influential throughout the thickness, are the most responsible for the delamination in the central region of the plate where they are highest. Unfortunately, the transverse stresses were not involved in the presently assessed criteria for delamination and furthermore they cannot be fed into any subroutine in Abaqus where shell elements are concerned. Consequently, the predicted delamination strongly reflects the in-plane dominance.

The *maximum* area of delamination given by the Explicit analysis using the energy criterion, compares very closely to that obtained from the test results. Figure 6-8 shows the

delamination through the thickness from a C-scan for one of the full-scale impact tests and Figure 6-10 (i) shows the delamination area at the bottom RR-layer for the FE analysis. The extent of delamination area obtained near the centre layer is shown with the yellow colouring (the largest shaded area). The maximum delamination is under predicted using the stress based criteria, see Figure 6-10 (ii).

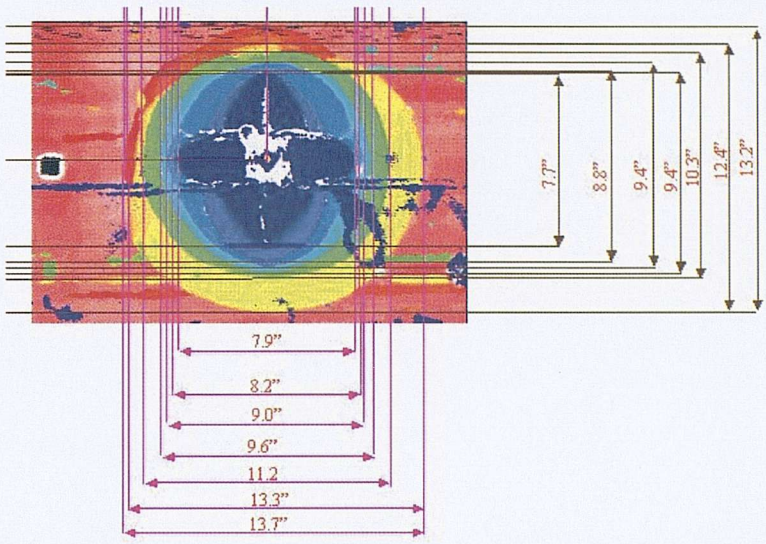


Figure 6-8. C-Scan of large2 plate impact. The variation in colours shows the extent of delamination through the layers. (Damage area in inches, only central portion of plate shown).

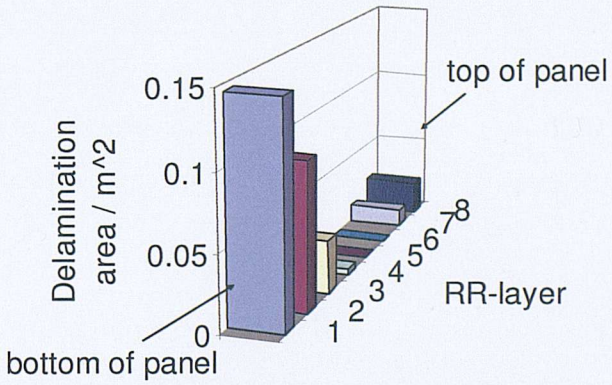
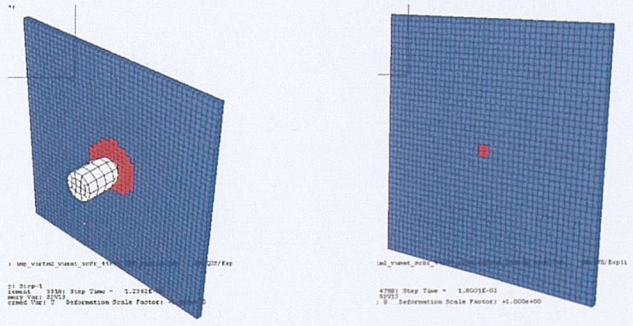


Figure 6-9. Delamination through the thickness using Explicit analysis, SC8R elements and energy criterion, analysis for test large2



(a) (b)

Figure 6-10. Delamination prediction at the bottom of the plate in Abaqus/Explicit for large2 using (a) the energy criterion and SC8R (b) stress criterion 1 and S4R.

6.2.4. Small-scale plate impact

A few of the small plate tests detailed in Section 7.8.2 of Chapter 7 were compared to FE results with SC8R elements in Abaqus/Explicit using a VUMAT. The SC8R were chosen over the S4R following the more conservative contact force predictions for the larger plate using the SC8R shells. The laminate has 9 woven plies and is modelled as an orthotropic material.

The impact velocity is practically the same for the four tests examined, a value of $4.6ms^{-1}$. The critical energy for failure criterion, Equation 5-4 in Chapter 5 obtained from the impact tests is applied to the RR-layers and Hashin's 2d stress based failure criteria is used at the woven plies. A transverse shear stiffness of $1.8975E7Nm^{-1}$ was applied for conservative measures.

6.2.4.1. Modelling variables

In this section, all of the following FE analyses were carried out to see the effect of different variables on an FE model of the 195J impact Test 9M(195J) (25.4mm diameter, 18.7kg tup). Two modelling variables were examined: the mesh density and the number of elements through the thickness. The model 'coarse2' had a mesh of 34x44x2 elements; analysis 'Fine2' had 56x72x2 elements and analysis 'Fine9' had 56x72x9 elements (9 elements through the thickness as opposed to 2 with the others). Due to the larger number of elements, analysis 'Fine9' was carried out using symmetrical boundary conditions on a quarter plate model.

The surface mesh density had negligible effect on the out-of-plane displacement but the number of elements stacked through the thickness from 2 to 9 does reduce the magnitude of this displacement by about 0.5mm. The contact force from these analyses is also shown in Figure 6-11, showing insignificant differences between them.

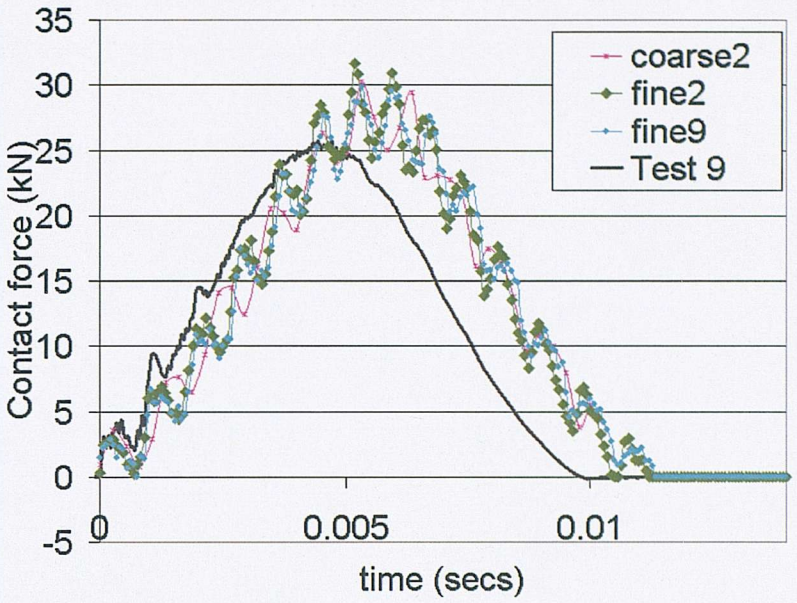


Figure 6-11 Contact force-time history for variations in mesh density, test 9M(195J).

6.2.4.2. Transverse stress output

The average section normal transverse stress, SSAVG6, can be outputted across the plate for any of the elements. SSAVG6 is largely affected by the mesh density, particularly by the number of elements through the thickness. The variation of SSAVG6 was examined at a location that is a distance of approximately 16mm from the centre of the plate along the length. This location was chosen as it is close to the impact site yet it is not affected by some of the irregularities experience at the contact area between the tup and the plate. Every woven ply and RR-layer had three section points but the SSAVG6 was outputted at the single integration point at the centre of each element.

Increasing the number of elements through the thickness provides a sharper stress output, as each stress is calculated from the strains at the element centre: the more elements the less deviation of the average values from the maximum or minimum across the section. Figure 6-12 demonstrates how larger and more detailed normal transverse stresses are averaged with 9 elements through the thickness compared to 2 elements through the thickness. The 'B' in the legend script refers to the element at the bottom of the plate and 'T' the element at the top of the plate. With analysis fine9 there were 7 elements also in between. The analyses showed that the tensile normal transverse stresses develop on the underside of the plate and the compressive stresses develop on the top side of the plate. The model with 9 through-thickness elements estimated that the positive tensile stresses were larger than the negative compressive stresses, whereas the same model with only 2 through-thickness elements

estimated the reverse, although this difference is small. Moreover, the stresses provided by analysis fine9 were of an order of magnitude of up to 50 times larger than those from fine2.

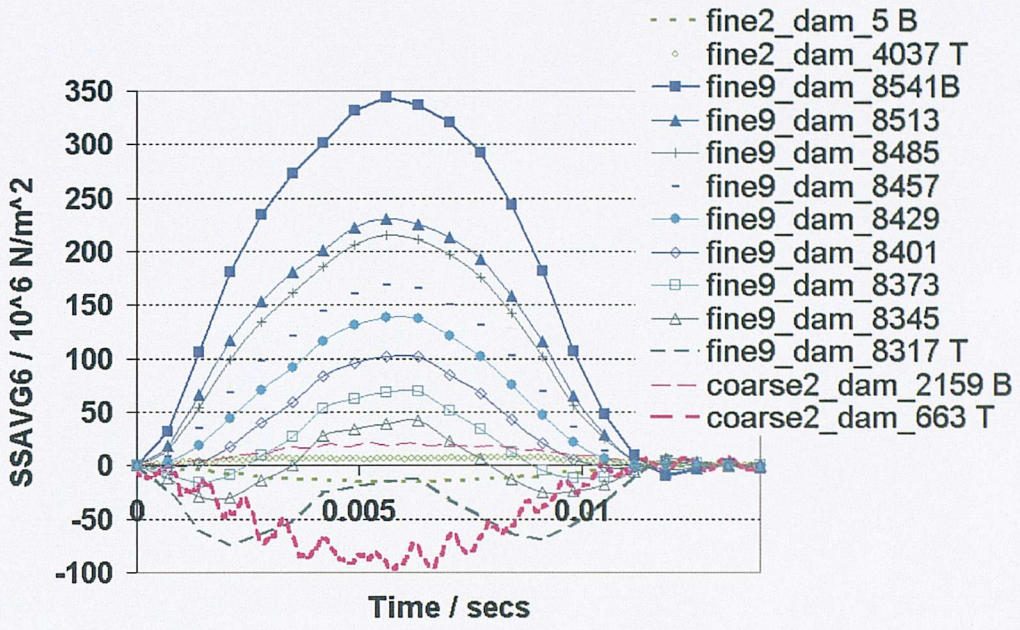


Figure 6-12. The average normal transverse stress vs time, SSAVG6 for FE analyses modelling damage, test 9M(195J)

The element with the maximum tensile normal transverse stress value for analysis fine9 was at the bottom of the plate where delamination was very pronounced in both the FE simulations and the tests. The high tensile stresses act to pull the plies apart significantly and can cause the broken fibres to spall.

Based on the tensile and compressive through-thickness test data, the analysis with 9 through-thickness elements is probably a better approximation of the SSAVG6. We know from experiment that delamination in and around the impact site occurred throughout the plate thickness more so near the lower surface. The largest delaminated area visually inspected from the lower surface in test 9M(195J) was measured as 0.0381x0.03175mm (1.5 x 1.25in), see Figure 6-13(a), and the cross-section photo shows prominent delamination of the bottom layer. Thus delamination also occurred at location A on this bottom face and would have been initiated by transverse matrix cracks in the adjacent ply resulting from the large bending stresses and developed largely due to the high normal tensile stresses. The maximum SSAVG6 value obtained from analysis fine9 is $350(10^6)N/m^2$, which exceeds the 21 to 40kN quasi-static through-thickness tensile strength values and most likely that also any dynamic values measured in future tests. Thus these predicted tensile SSAVG6 stand-alone values would indicate almost certain delamination at this location.

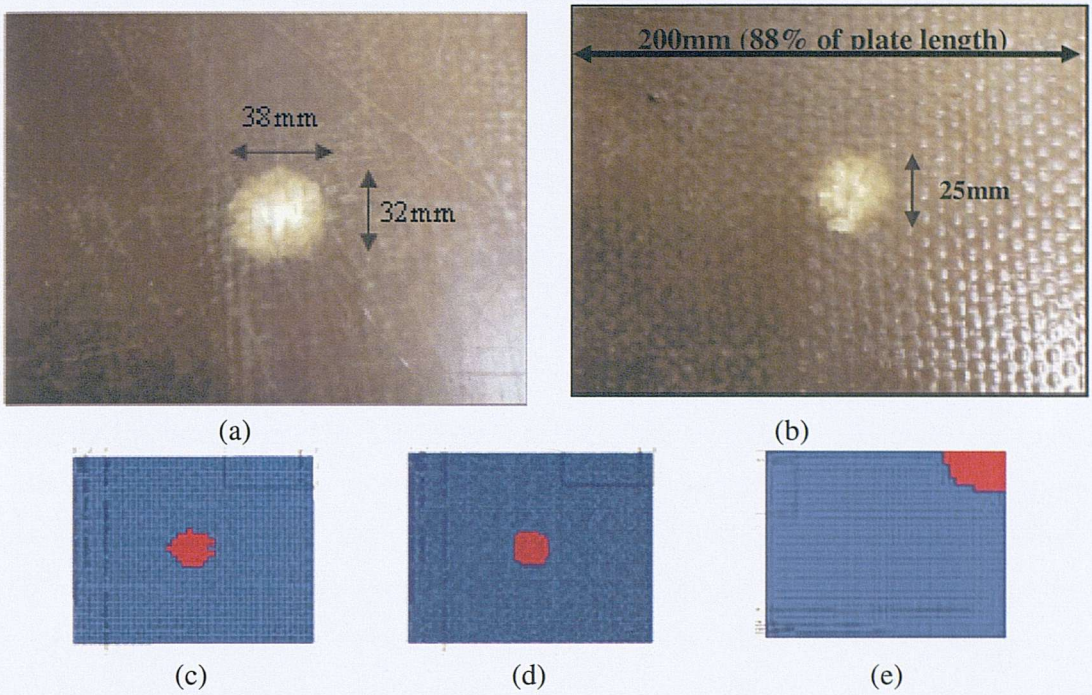


Figure 6-13. Delamination results for test 9M(195J), (a) bottom face, test and (b) top face, test, and FE predictions for the bottom face using analyses (c) coarse2 (34x44x2 elements), (d) fine2 (56x72x2 elements) and (e) fine9 (56x72x9 elements) a quarter-plate model.

6.2.4.3. In-plane and through-thickness mesh density effect on delamination

In test 9M(195J) delamination also developed at the top face, see Figure 6-13(b), with evidence of matrix crushing of the top surface at the centre of the whitened area. The largest SSAVG6 predictions were with fine9, as discussed above. The maximum compressive SSAVG6 values predicted in fine9 were about $75(10^6)N/m^2$ which is significantly less than the compressive strength values from quasi-static test data (which gave values of over $500(10^6)Nm^2$). They are also smaller than the $400(10^6)N/m^2$ strength values obtained from the $100s^{-1}$ strain rate compressive tests on the Corvette composite hull material. If we consider the FE model SSAVG predictions as a fair approximation of reality, then the delaminations nearest the top face of the plate must therefore be largely propagated by the transverse *shear* stresses as opposed to the *normal* transverse stresses.

The energy criterion for delamination obtained from the impact tests does not differentiate between compressive and tensile stresses and the through-thickness stresses are not considered where shell elements are concerned. However, the in-plane stress predictions used in the energy equation are affected by the number of elements through the thickness. The delamination for analyses fine2 and fine9 is shown in Figure 6-14 and Figure 6-15. For both analyses the area of delamination is shown to be greatest for the RR-layer at the bottom

of the plate. Analysis fine2 predicts delamination throughout the thickness, unlike fine9 showing damage on the top and bottom surfaces and two intact layers in the centre. Although the tests show delamination more extensively towards the top and particularly at the bottom of the plate, there is as yet no C-Scan data to assess the variation in the delamination seen in the FE results for a more accurate comparison. What is known is that the maximum test delamination area within the bottom half of the plate is more closely approximate by fine2 than fine9, whereas the opposite can be said about the maximum delamination within the top half of the plate. This does not mean that modelling with fewer elements through the thickness is better, it simply reflects upon the inconsistency obtained with the proposed energy model when it comes to meshing. The number of elements through-the-thickness will affect the position of the 8 RR-layers within the shell elements, thus outputting comparably varying in-plane stresses at the RR-layer integration points. Because the delamination model is one based on plane-stress, the amount of predicted delamination thus varies between models of varying through-thickness mesh densities. Table 6-2 shows a summary of test 9M(195J) results and the FE simulations of this test. In terms of the in-plane critical energy criterion used at the RR-layers, increasing the number of SC8R elements through the thickness does not benefit the accuracy of the delamination damage predictions with the proposed energy model, it simply provides a more conservative result for the largest delaminated areas but the locations may not be correct.

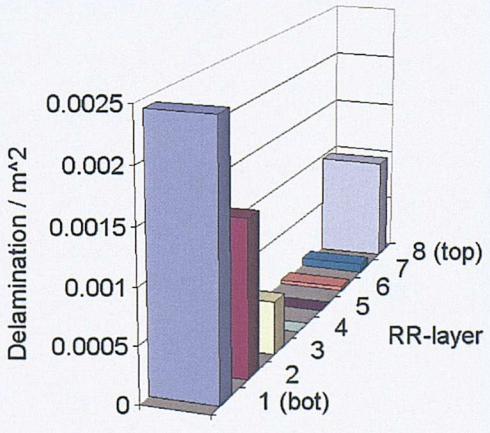


Figure 6-14. Delamination damage through the thickness for FE analysis 'fine9', test 9M(195J).

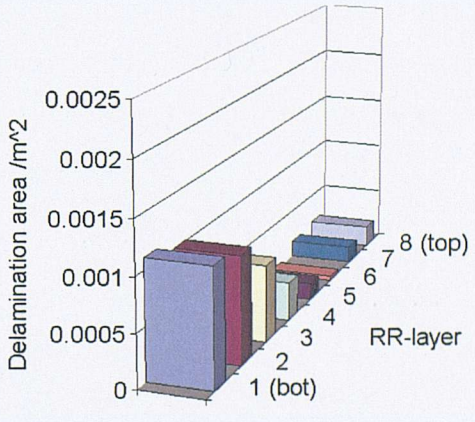


Figure 6-15. Delamination damage through the thickness for FE analysis 'fine2', test 9M(195J).

The in-plane density of the mesh has no significant effect on the delamination predictions through the thickness and the same delamination area is predicted at the bottom of the plate for coarse2 and fine2 analyses, see Figure 6-13(a) & (b). However, the maximum through-

thickness stresses are noticeably affected, as seen with 'fine2' and 'coarse2' in Figure 6-12. The delamination damage for the three different mesh analyses is shown for the RR-layer at the bottom face of the plate for test 9M(195J) with Figure 6-13 (a) to (c).

Analysis	Max o.o.p disp. (m)	Max. normal contact force (N)	Max. SSAVG6, ten. & comp. (10^6 N/m^2)	Delam. on bot. RR-layer (10^{-3} m^2)
Coarse2	17.2	30.2	19 - 94	1.11
Fine2	17.3	28.2	6 -15	1.11
Fine9	16.68	29.9	350 -75	2.41
Test	15.3	26	unknown	1.45

*Maximum always on centre element, lower face.
disp. = displacement; ten.=tension; com.=compression; delam.=delamination

Table 6-2. Summary of main test and FE results for test 9M(195J)

6.2.4.4. Impact energy effect on delamination

Test results of delamination damage at the top and bottom faces of the plates for tests 1S(91J), 2S(140J), 9M(195J) and 13L(284J) are shown in Table 6-3 together with their FE simulations carried out using 'fine2' mesh. Maximum delamination damage was captured relatively well, although slightly under-predicted again at the top of the plate. Matrix and fibre damage on the other hand was substantially over-predicted in the FE analyses, with top layers appearing to suffer corner damage also, propagating towards the centre at the top ply. Generally we can say that Hashin's 2D failure criterion did not work satisfactorily in these simulations, producing unpredictable and erroneous results.

Test	Test, delamination area, in m (in)	FE, delamination area, in m (in)	FE, matrix damage area, in m (in)+	FE, fibre damage area, in m (in)+
1(91J)	BOT: 0.0381x 0.0381 *(1.5 x 1.5)* TOP: 0.0381 x 0.0254 *(1.5 x1)*	0.0286 x 0.032 *(1.125 x 1.245)* TOP: zero	BOT: 0.04445 x 0.060325 *(1.7499 x 2.375)*	BOT: 0.05715 x 0.03175 *(2.25 x 1.25)*
2(140J)	BOT: 0.0381 x 0.0381 *(1.5 x 1.5)* TOP: 0.03175 x 0.0254 *(1.25 x 1)*	BOT: 0.03175 x 0.03175 *(1.25 x 1.25)* TOP: 0.0127 x 0.0127 *(0.5 x 0.5)*	BOT: 0.057 x 0.073 *(2.24 x 2.87)* TOP: 0.035 x 0.058 *(1.38 x 2)*	BOT: 0.057 x 0.0381 *(2.24 x 1.5)* TOP: : 0.0381 x 0.016 *(1.5 x 0.63)*
9(195J)	BOT: 0.0381x 0.03175 *(1.5 x 1.25)* TOP: 0.03175 x 0.0254 *(1.25 x 1)*	BOT: 0.03175 x 0.04445 *(1.249 x 1.748)* TOP: 0.0127 x 0.0159 *(0.5 x 0.63)*	BOT: 0.0635 x 0.0889 *(2.5 x 3.5)* TOP: large cross shape from corners.	BOT: 0.07 x 0.057 *(2.76 x 2.24)* TOP: 0.0381 x 0.019 *(1.5 x 0.75)*
13(284J)	BOT: 0.0381x 0.0381 *(1.5 x 1.5)* TOP: 0.05715 x 0.03175 *(2.25 x 1.25)*	BOT: 0.04445x0.04445 *(1.75 x1.75)* TOP: 0.015875 x 0.01905 *(0.625 x 0.75)*	BOT: 0.083 x 0.095 *(3.27 x 3.74)* TOP: large cross shape from corners.	BOT: 0.073 x 0.07 *(2.87 x 2.75)* TOP: 0.0381 x 0.019 *(1.5 x 0.75)*

+ Any corner damage is not included.

Top=top layer of plate; bot=bottom layer of plate

Table 6-3. Delamination test results for test 1S(91J), 2S(140J), 9M(195J) and 13L(284J) and FE damage predictions.

Even for larger mass differences, simply increasing the mass of the tup will not generally increase the delamination area, as shown with tests 1S(91J), 6S(190J) in Table 7-7 of Chapter7. Test 6S(190J) used a tup mass that was double that of test 1S(91J). The delamination areas were the same but the extra impact energy in test 6S(190J) was expended in penetrating the plate. This was also proven for test 13L(284J) and test 16L(665J). In order to increase the delamination damage to the plates and prevent penetration, both the diameter and mass of the tup should be increased in the same test, as demonstrated through tests 15(495J) and 16(665J).

Delamination on the top and bottom face is shown in Figure 6-16 for test 13L(284J) and its FE simulation, and the delamination through the thickness is believed to be relatively well captured in the FE model as shown with Figure 6-17.

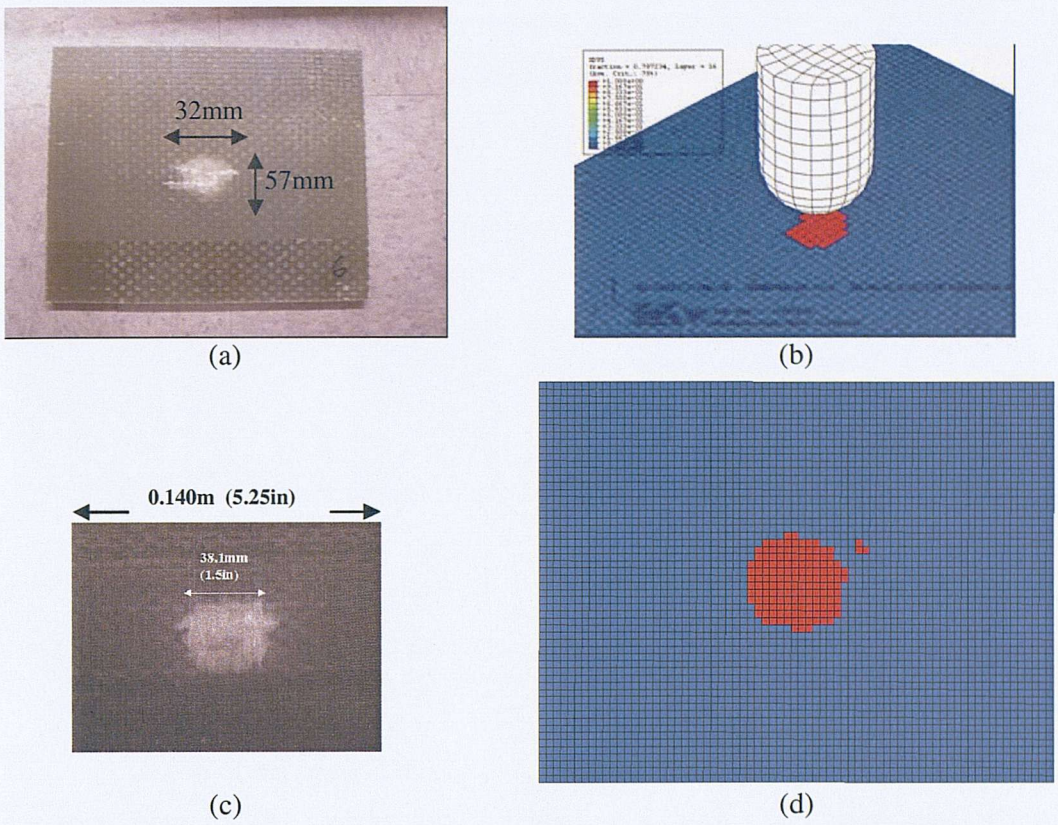


Figure 6-16. Delamination damage for test 13L(284J), shown to scale. (a) top face, test, (b) top face, FE, (c) bottom face, test, (d) bottom face, FE

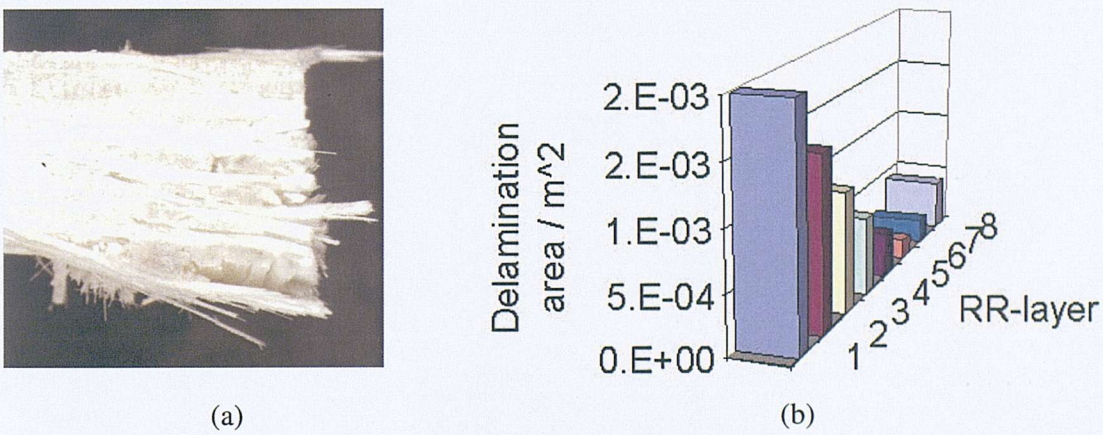


Figure 6-17. Delamination damage for (a) test 13L(284J) cross-section, (b) FE prediction through the thickness

The tup in test 13L(284J) did not penetrate the plate but there was substantial damage in the form of delamination and matrix cracking on the bottom of the plate, with fibre failure occurring for some of the fibres in one or two bundles at the bottom-centre of the plate. However, the extent of matrix and fibre damage predicted with Hashin's criteria is excessive, see Figure 6-18 for the lower and higher energy impact tests: test 1S(91J) and 13L(284J). Had the delaminated layers been physically modelled as separating, the FE o.o.p displacement would be larger and the contact force smaller. Also the transverse stiffness of

the plate remains intact through-out the analysis and the transverse strength is likely to have been more affected with the large tup than with the medium sized tup. This may be one reason why this test saw a proportionally larger over-prediction of the contact force and under-prediction of the o.o.p displacement compared to the smaller tup tests. Another reason is also the effectiveness of the contact between the tup and plate.

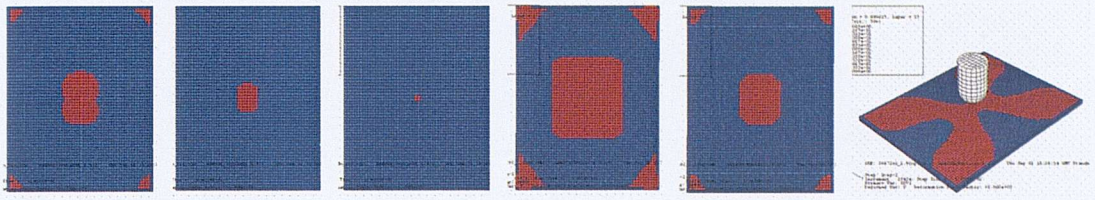


Figure 6-18. Matrix cracking predictions using 2d Hashin, for the bottom, middle and top layers, (a) test 1S(91J), (b)test 13(284J).

The cross-section of the plate in test 2S(140J) after impact testing, Figure 6-19, corroborates the large effect of the tensile normal transverse stresses. The plate shows significant delamination near the bottom face of the plate where the tensile transverse normal stresses are acting to pull the plies apart. The top of the plate saw matrix crushing and some surface indentation, a characteristic witnessed in all the impact tests.

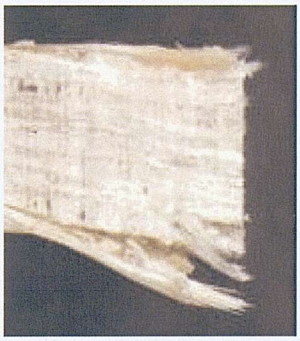


Figure 6-19. Cross-section of the plate, test 2S(140J), showing delamination.

6.2.4.5. Contact force and out-of-plane displacements for small and large tup impacts

The o.o.p displacements at the centre of the plates impacted with the smallest tup are slightly over-predicted through the FE analyses by about 1mm (0.04in), shown in Figure 6-21. In contrast, the large tup with a larger mass, test 13L(284J), produced a maximum o.o.p displacement of nearly 23mm, compared to the under-predicted 20mm in the FE analysis.

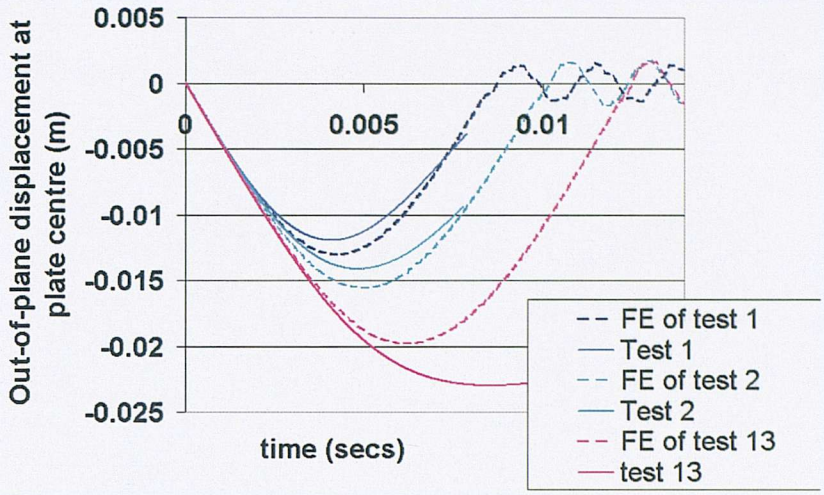


Figure 6-20. Max. o.o.p disp.-time history for tests 1S(91J), 2S(140J) and 13L(284J), test and FE.

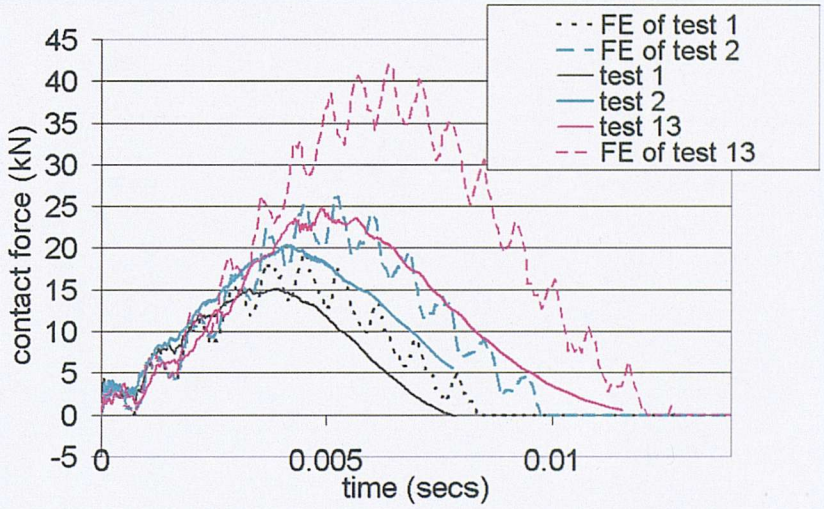


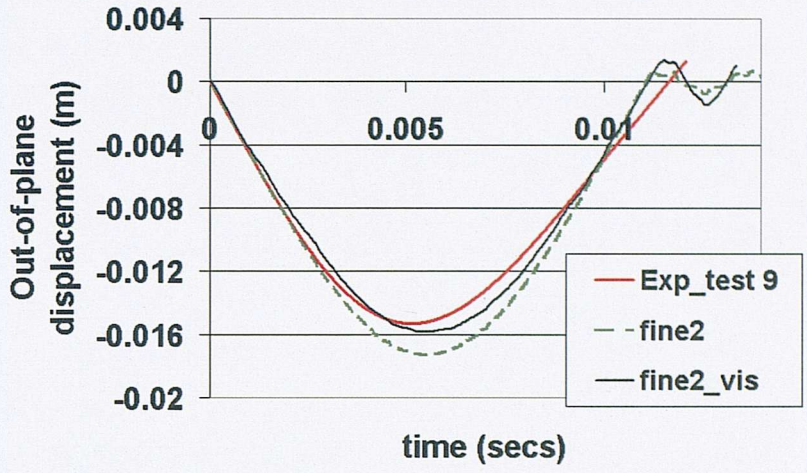
Figure 6-21. Contact force-time history for tests 1S(91J), 2S(140J) and 13L(284J), test and FE.

The largest difference between measured and predicted contact forces was for test 13L(284J); a 37% difference, see Figure 6-21. All the other finite element analyses predict contact forces that are up to 16% higher compared to experiment. However, the maximum contact force for the FE analyses are taken as the peaks of the contact force plots, which do see some pronounced oscillations.

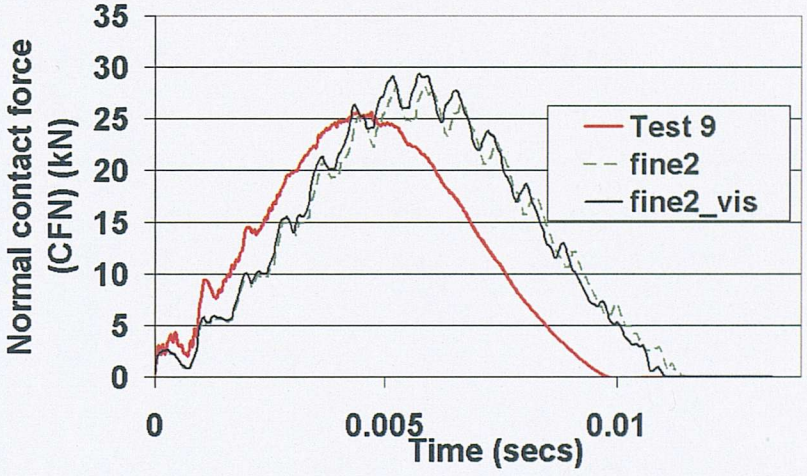
6.2.4.6. Implementation of a viscoplastic model at the RR-layers

The effect of modelling the resin rich layers as viscoplastic has a significant effect on the out-of-plane displacement results, shown with Figure 6-22(a) but a negligible effect on the contact force, see Figure 6-22(b). For a more significant influence, the rate-sensitive woven

layers, not just the resin-rich regions, should ideally be modelled with an orthotropic viscoplastic model. Consequently, this would require the application of a damage-lag model.



(a)



(b)

Figure 6-22. (a)Max. o.o.p disp. and (b) contact force-time histories, for RR-layer and energy for failure FE analyses with and without strain rate sensitivity, test 9M(195J).

6.2.5. Concluding remarks

The thick-shell and RR-layer model can be applied to any composite and relies on a failure criterion at the RR-layers to depict delamination failure between two plies. The simple energy criterion at the RR-layers provided better results over the two simple stress criteria tested. Here the energy value for failure requires the knowledge of the contact force; an empirical derivation chosen to minimize the errors in the assessment of the resin-rich layer and energy concept. The method for obtaining an expression for this energy that is independent of each test is outside the scope of this work. What we can surmise is that the

critical fracture energy value obtained from full scale impact tests was relatively successful in this model unlike the value obtained from mode I fracture tests.

The delamination predictions obtained from the impact test simulations were encouraging but ideally a 3d energy criterion is required. However, the main advantage of this 2d energy criterion for delamination is that it can be applied to shell elements and still obtain a reasonable prediction of the maximum delamination size. The criterion is also simple and quick to use and for the meshes tested is little affected by in-plane mesh density.

The number of stacked elements through the thickness is particularly influential on the through-thickness stress predictions and to a lesser extent on the in-plane stresses. For the meshes tested, the mesh density appeared to have a negligible effect on the contact force, provided that the relative mesh size between the tup and the mesh are adequate.

The fibre and matrix damage predictions were not so agreeable. Hashin's 2d stress criteria in the prediction of these two damage modes was not reasonable or consistent between tests. The matrix damage for the large plate (which had clamped boundary conditions), was possibly a little under-predicted yet the fibre damage did not occur as extensively as predicted. The smaller, simply supported plate simulations showed overly large areas of both damage modes.

The out-of-plane displacements obtained from the FE analyses on the small plates were all very conservative and this was improved with the strain rate model applied at the resin-rich layers.

The transverse shear stiffness has a substantial effect on the contact force predictions and it is important to use the correct value when modelling with shell elements and a user subroutine.

Although the continuum shells have their advantages over thick shell elements they have yet to be further developed and they are currently of limited practicality in failure modelling. The continuum shell elements are new to Abaqus; they can be stacked and appear to provide transverse stress predictions. Stacking the continuum shells produced a more detailed section transverse stress output through the thickness than using one element only and thus increased the maximum delamination predictions. However, the transverse force and stress estimates can be outputted but cannot be used in any subroutine, thus limiting the practicality of the SC8R element and preventing the implementation of a 3D failure criterion. In addition, only

the in-plane material properties can be degraded as there is no control over the through-thickness moduli. The contact force predictions were higher for the S4R elements and the SC8R are overall superior in their contact prediction over the standard shells.

6.3. 3d Damage at the woven plies with a cohesive zone model for delamination

6.3.1. Introduction

The present chapter implements the CDM model described in Chapter 4 and the linear cohesive zone model in Chapter 5 using Abaqus/Explicit and a VUMAT. The behaviour of the three plate sizes: small, large1 and large2 is examined through contact force and out-of-plane displacement-time histories and damage predictions, as well as the effect of several model variables.

Solid elements of the type C3D8R are used in all the models, with hourglass control, and a material property residual of 10% is retained on full failure of a material point.

6.3.2. Small-scale plate impact

The small, medium and large impactor tests described in tables 7-8, 7-9 and 7-10 in Chapter 7 are validated with the CDM model.

Unless otherwise specified, all except two of the analyses used the 3d equivalent strain criterion for global damage initiation, Equation (4-10) in Chapter 4 and the linear strain criterion for matrix damage propagation, Equation (4-22) in Chapter 4 and through-thickness damage at the woven plies was modelled using Equation (4-28) in Chapter 4.

A model exclusive of through-thickness damage is labelled as '2d'. The variation in the normal transverse modulus obtained from standard tensile tests was significant, with values ranging from 6.98 to 22.68kN/mm^2, and for simplicity the average value of this range was used in the subsequent analyses.

The sensitivity of the analyses to several model parameters independent of the test conditions is briefly examined. Some of these model variations will affect different analyses

to varying degrees and only a few of the impact tests were used as examples of possible trends.

In the following sections, a few of the modelling parameters were varied to see the effect on the results. These are namely: tup and plate mesh density; the number of cohesive layers; removing the transverse damage degradation at the woven plies; parameter dII (see Equation (4-25) of Chapter 4). The mesh labeling is defined in Table 6-4. The finer meshed models apply a finer mesh in the impact zone only. The plates are made-up of nine woven plies and the consequence of modelling half the cohesive layers, i.e. 4 , over the full number, which is 8, is discussed. All the mesh densities fall within the maximum cohesive length requirements as stated in Section 5.5.4 of chapter 5. Unless otherwise specified, the mesh density used in the analyses is 'p1t1'.

	Region mesh (for quarter-plate model)	Average element size in impact zone (mm)
Plate model		
P1	28x36 = 1008 surface elements	3.175
P2	1128 surface elements (finer, 144 elements in impact site)	1.6
P3	1128 surface elements (very fine, 380 elements in impact site)	0.8
Tup model		
T1		4.68
T2		1.8
T3		0.82

Table 6-4. Mesh densities studied

6.3.2.1. The effect of a delamination model

The significance of including a 3d damage model at the woven plies and delamination using cohesive elements in the impact analysis is demonstrated with Figure 6-23 for test 9M(195J). 'Solid 5', represents an analysis with 5 solid elements through the thickness and a 3d damage model but no cohesive elements, and 'co4' which also includes the cohesive layers. The contact force was about 25% larger for the analysis modelling no damage than for the other two damage models, and because the no-damage model is stiffer, it picks up the higher frequencies.

The use of cohesive layers not only reduced the peak contact force but also appeared to stabilise the shape of it. Inclusion of these cohesive layers not only had the effect of further reducing the stiffness of the plate but further decreased the detection of some of the higher frequency components. A likely reason for this is the extra energy absorption at these layers.

Without the cohesive layers, analysis 'solid 5', the excess energy that would normally go into delamination goes into more matrix and fibre damage, causing the elements to excessively deform.

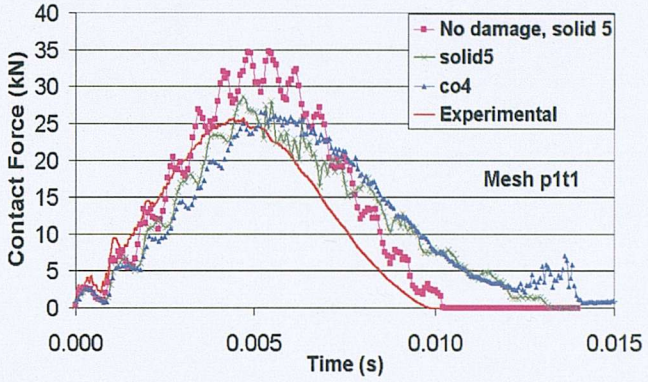


Figure 6-23. Contact force-time history, comparing a damage model exclusive of delamination with a no-damage and full damage model, test 9M(195J), mesh p1t1.

6.3.2.2. Excluding the transverse material degradation at the woven plies

Excluding the through-thickness material degradation at the woven plies for a model with half the number of inter-ply cohesive zones (i.e. 4) had the effect of increasing the contact force, as shown with 'co4_2d' compared to 'co4' in Figure 6-24 and for test 9(195J). Nevertheless, co4_2d was still an improvement over the no damage model. However, including the through-thickness damage in a full 8 cohesive layer model can sometimes cause an analysis to stop prematurely due to large distortion of the solid elements, see Figure 6-25 for test 7M(247J). The induced waviness in the plies is apparent in Figure 6-26 for 'co4_p2t2' but less obvious with 'co4_p2t2_2d' Figure 6-27.

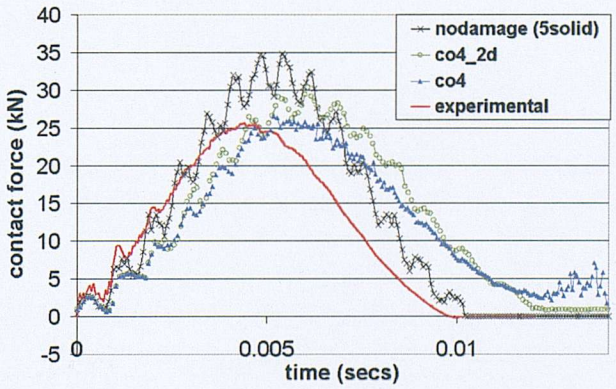


Figure 6-24. Contact force-time history, comparing a no-damage model with a 2d and 3d damage model at the woven plies, test 9M(195J), mesh p1t1.

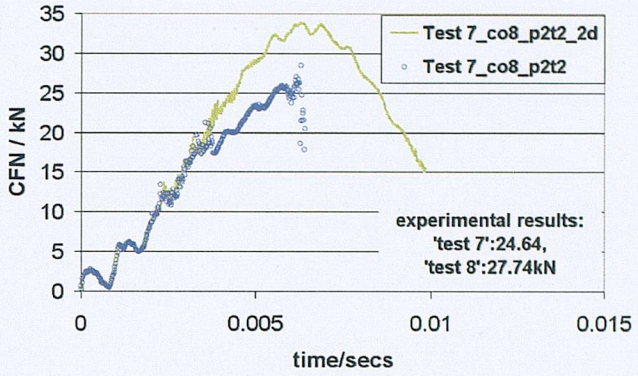


Figure 6-25. Contact force-time history, comparing a 2d and 3d damage model at woven plies, test 7M(247J).

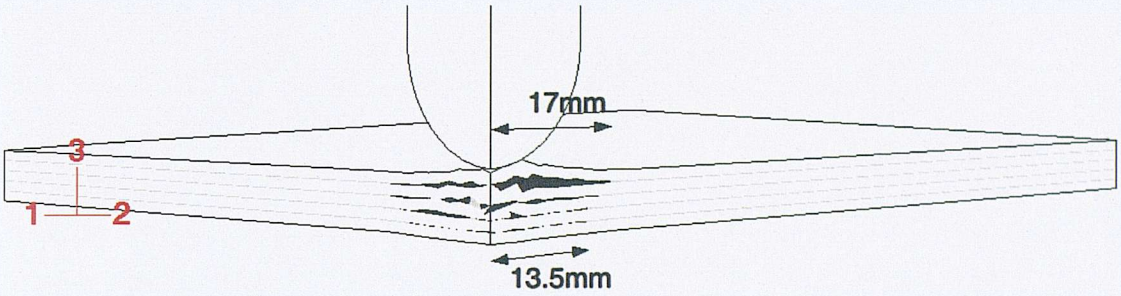


Figure 6-26. Delamination predictions for test 9M(195J), analysis 'co4_ p2t2'

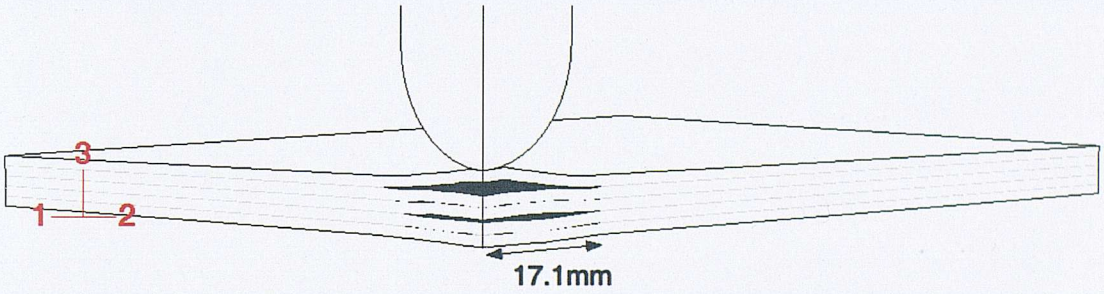


Figure 6-27. Delamination predictions for test 9M(195J), analysis 'Co4_p2t2_2d'

6.3.2.3. Strain rate effects

It is interesting to note that modelling in-plane damage alone causes a time delay in reaching the peak contact force compared to a no-damage analysis. The total time for the impact event for the no-damage analysis is well matched with the test and so is the first half of the contact force-time curve compared to the damage analysis. However, the no-damage analysis produces a symmetrical contact force-time curve and a higher peak contact force because of the lack of material property degradation. It is very likely that modelling the strain rate modelling at the plies will improve upon the lower contact force values during the impact phase. The strain rate model will have the effect of enhancing the strength and stiffness of the plate during this damage phase, creating a 'damage lag' effect.

6.3.2.4. Modelling half the number of cohesive layers

Modelling the full number of cohesive layers (i.e. 8) and applying a 2d degradation model at the woven plies still gave over-sized contact force predictions, shown in Figure 6-28. The number of cohesive layers appeared to make little difference in the 2d model.

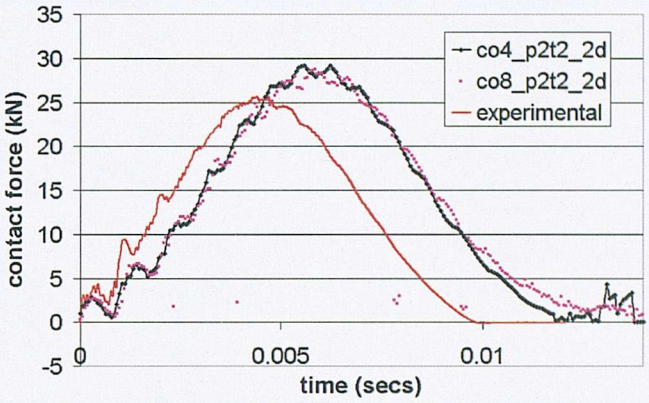


Figure 6-28. Contact force-time history for a 2d damage model at the woven plies, comparing 4 and 8 cohesive layers, test 9M(195J)

The effect of full through-thickness damage modelling (i.e. 8 cohesive layer modelling and transverse degradation at the woven plies) appeared to favour a higher energy analysis such as test 10M(217J), see Figure 6-29. Here, a coarse 4 layer model did not sufficiently reduce the contact force but an 8 cohesive layer model improved it dramatically. The effect was not observed for a larger tup analysis impacting with a similar size of energy such as test 11L(211J), see Figure 6-30. However, if the energy is increased further as with test 13L(284J), the number of cohesive layers was influential again, see Figure 6-31. Similarly for test 15L(496J), see Figure 6-32. The increase in contact force once the tup moves away is only a spurious effect and was not recorded as the peak contact force. Despite the significant transverse modulus degradation the peak contact force was still high for this simulation, possibly indicating other factors of influence other than the degree of material degradation.

The larger tup diameter impact analyses thus appear to benefit more significantly from the full-cohesive layer model. When the tup diameter is small compared to the plate size, the results can be over-conservative, i.e. low contact force predictions and large amounts of fibre damage.

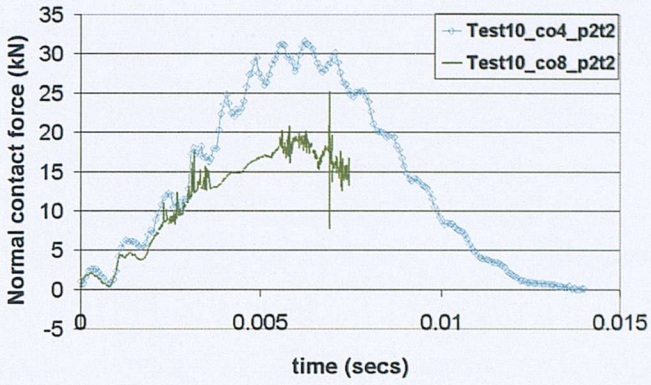


Figure 6-29. Contact force-time history for a 4 and 8 cohesive layer model, test 10M(217J).

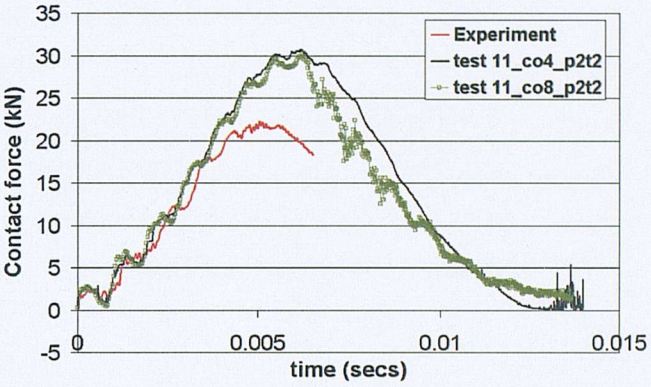


Figure 6-30. Contact force-time history for a 4 and 8 cohesive layer model, test 11L(211J).

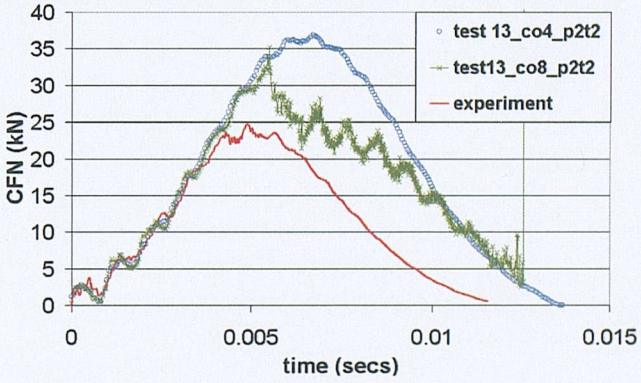


Figure 6-31. Contact force-time history for a 4 and 8 cohesive layer model, test 13L(284J),

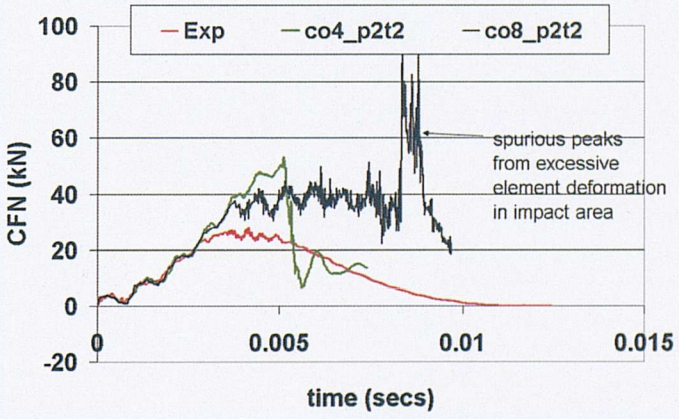


Figure 6-32. Contact force-time history for a 4 and 8 cohesive layer model, test 15L(496J).

6.3.2.5. Mesh density effects

By default, Abaqus/Explicit uses finite sliding for contact pairs and it is the more robust algorithm for this type of analysis. When using hard kinematic contact with the pure master-slave algorithm as in with the present models, the master surface (in this case the tup) may still penetrate the slave surface even after the acceleration corrections for the master and slave nodes have been made [1]. For lesser dependence on the mesh density the analysis should be run as finite sliding as opposed to the other option of small sliding.

The discretization of the tup should be fine enough to minimize any sharp corners and the tup elements should be slightly larger than the plate elements. When modelling delamination at every inter-ply, it is important that the plate mesh is relatively fine; this becomes less important with reduction in the number of cohesive layers. The effect of using small sliding versus finite sliding for the same mesh densities (coarse mesh) is shown in Figure 6-33 with 'co4_p1t1_finites' and'co4_p1t1_smalls'.

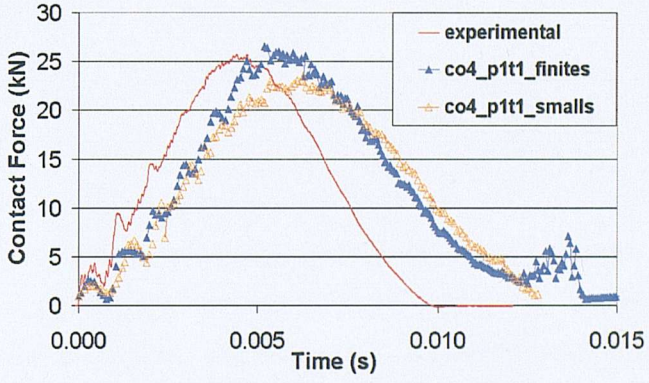


Figure 6-33. Contact force-time history for variations in contact definitions, test 9M(195J), mesh p1t1.

The effect of incorrect implementation of a small sliding analysis is prominent when there is a significant difference between the plate and tup mesh size, as seen with 'co8_p2t1_smalls' compared to 'co8_p2t2_smalls', in Figure 6-34. When finite sliding is instead, the tup mesh is less significant as shown with 'co8_p2t2' and 'co8_p2t1' in Figure 6-35.

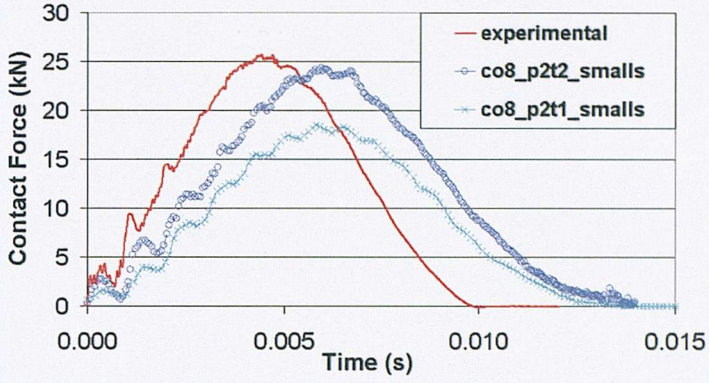


Figure 6-34. Contact force-time history for variations in mesh density using a small sliding analysis test 9M(195J)

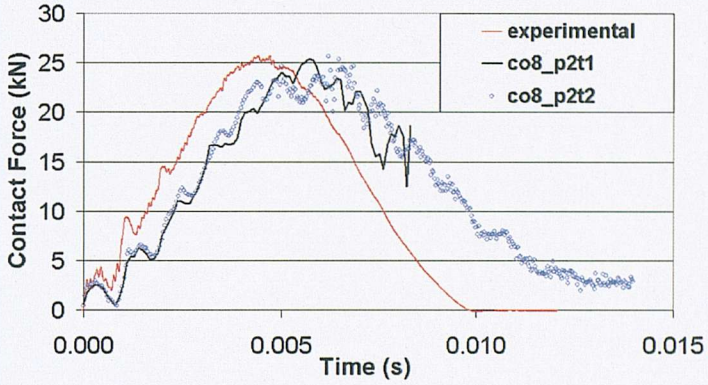


Figure 6-35. Contact force-time history for variations in mesh density using a finite sliding analysis test 9M(195J)

Maintaining the concept of a marginally larger tup element size relative to the impact region of the plate but increasing the mesh density had the effect of smoothing out the contact force-time curve, as shown with Figure 6-37 for test 10M(214J). The peak contact force was also visibly reduced with the finer meshed model. A similar assessment of test 13L(284J) , which had higher impact energy but a larger tup size than test 10M(217J), shows how the contact force was negligibly affected by the finer mesh density, see Figure 6-37.

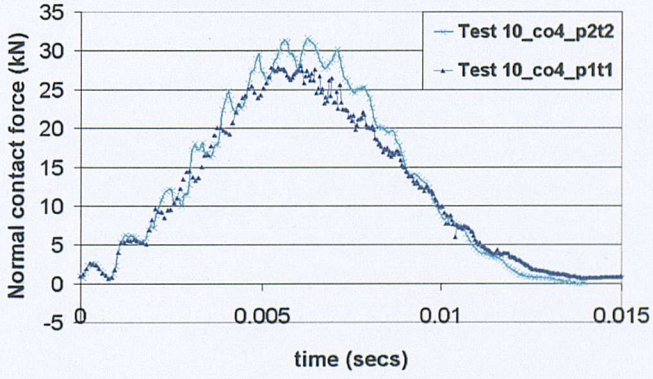


Figure 6-36. Contact force-time history for variations in the plate and tup mesh density, 4 cohesive layer model, test 10M(217J)

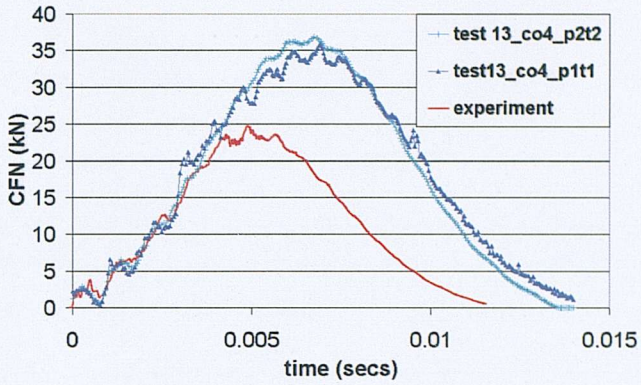


Figure 6-37. Contact force-time history for variations in plate and tup mesh, 4 cohesive layer model, test 13L(284J).

6.3.2.6. Varying the cyclic loading parameters

The reduction in modulus obtained from the tensile cyclic tests is 19.5% for matrix damage only, giving a value of 0.195 (~0.2) for the start of fibre damage parameter, dII. However, the damage parameters dI and dII differed slightly for compressive and tensile loading, as seen in Table 7-5 in Chapter 7. Differentiating between compressive and tensile in-plane strains in the FE model and implementing the relevant dI and dII values makes a small difference to the maximum o.o.p displacement and has the effect of increasing the maximum contact force by 3%, see Figure 6-38.

It was found that if dII is doubled for both tension and compression but all other parameters including the strain at the start of fibre damage, ε_f, are kept the same, the effect on the contact force was still very small. Increasing the rate of damage in the early part of the loading curve: from dI to dII, see Figure 6-39, but keeping all other parameters constant, brought about a decrease in the rate of damage after F=FII, when the strain value was larger than ε_f.

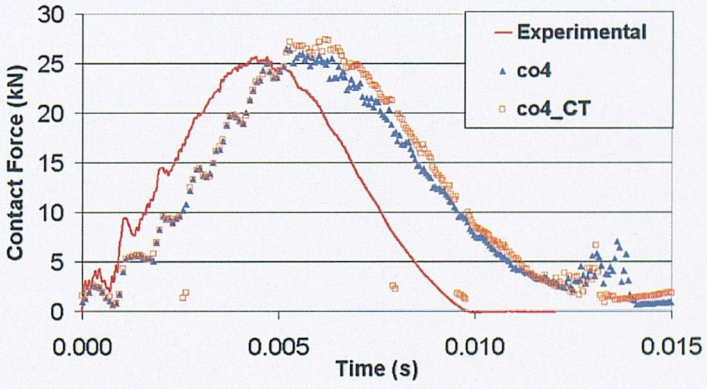


Figure 6-38. Contact force-time history, the effect of differentiating tensile and compressive cyclic loading parameters, test 9M(195J), mesh p1t1.

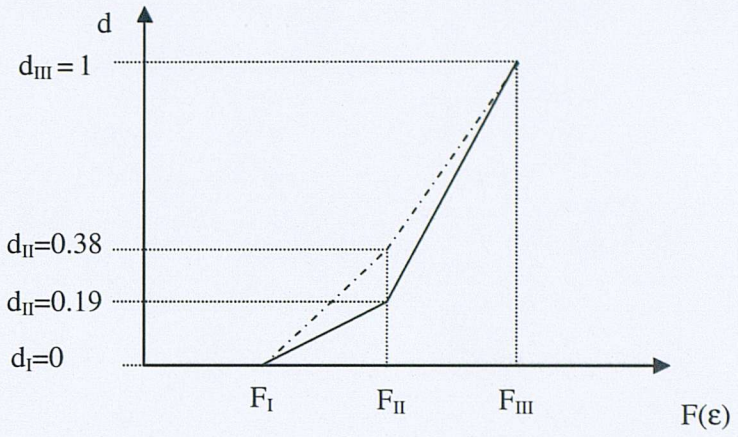


Figure 6-39. Damage vs the potential function and the effect of increasing d_{II}.

6.3.2.7. Damage propagation criterion – energy versus strain

The strain and energy based equations for matrix damage propagation, Equations (4-22) and (4-23) in Chapter 4 respectively, produced very similar results, as can be seen with the contact force-time history in Figure 6-40.

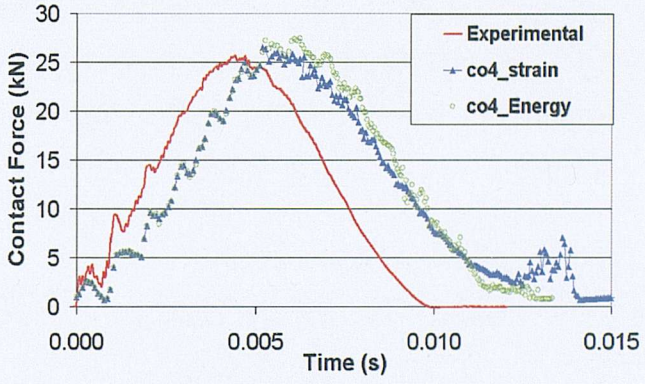


Figure 6-40. Contact force-time history, comparing the strain versus the energy approach for in-plane damage propagation, for test 9M(195J), mesh p1t1.

6.3.2.8. The influence of the initiation criterion on the translaminar degradation

In all the previous analyses, the equivalent strain criterion, Equation (4-10) in Chapter 4, was used to initiate damage on all planes. Here, the two separate damage initiation criteria for the translaminar degradation of the woven plies were assessed. Analysis 'co4_TT2' applied the maximum stress criterion, Equation (4-11) in Chapter 4, with a one-off degradation rule, and the equivalent strain criterion 1 for in-plane damage initiation only. Analysis 'co4_TT1'

applied the quadratic stress criterion instead, Equation (4-12) chapter 4. The contact force for these two analyses is presented in Figure 6-41.

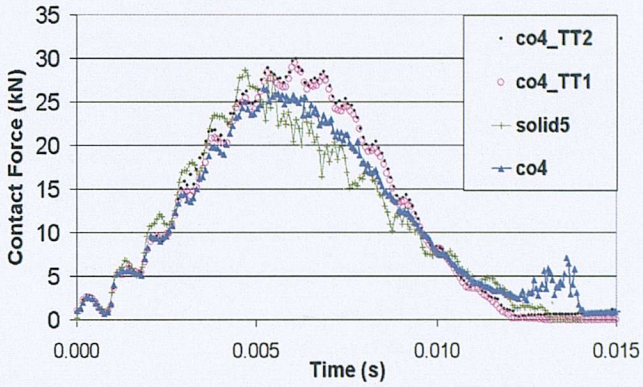


Figure 6-41. Contact force-time history for variation of the transverse damage initiation criteria, test 9(195J), mesh p1t1.

These separate transverse damage initiation criteria at the woven plies produced negligible transverse damage and the contact behaviour resembled that of the 2d damage model at the woven layers in Figure 6-24, ('co4_2d'). The contours for the degradation of the E33 modulus are minimal compared to the original 3d model using the global strain criterion for damage initiation on all planes, see Figure 6-42. This is probably because damage initiation for the current structure and loading is in the form of transverse cracks produced by in-plane stresses. These stresses must therefore be included in the function for damage initiation. The delamination predicted is shown in Figure 6-43.

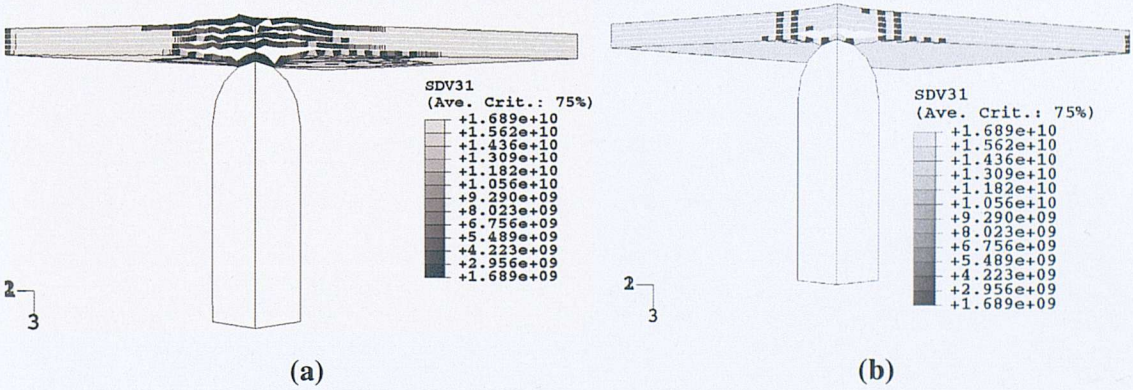


Figure 6-42. Degradation contours of the transverse modulus E_{33} in Pa, using analysis (a) Co4 and (b) Co4_TT2, for test 9M(195J), mesh p1t1

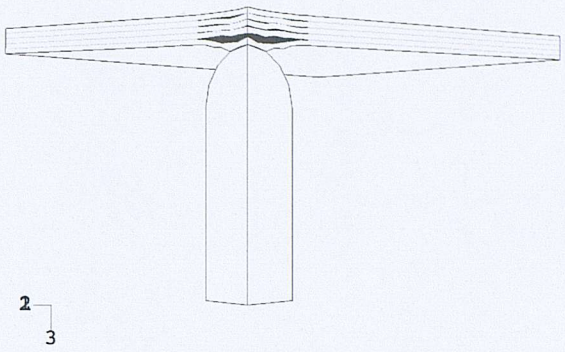
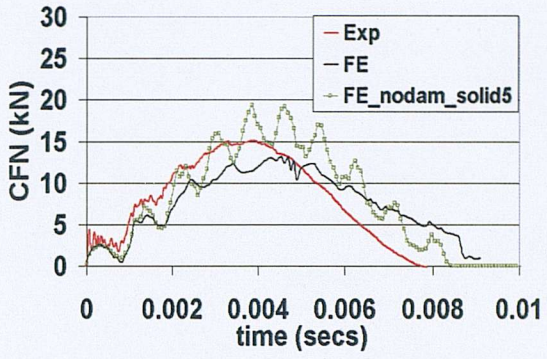


Figure 6-43. Delamination, test 9M(195J), 'co4_TT2' (mesh p1t1)

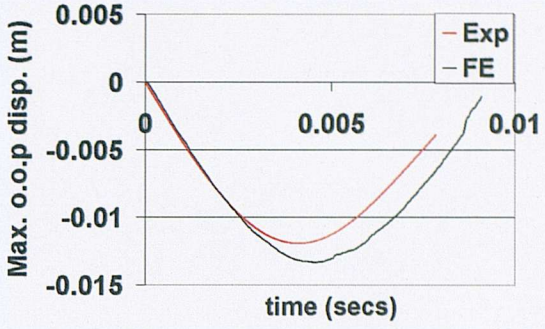
6.3.2.9. Contact force and displacement results for all the small plate tests

This section presents the contact force and the maximum out-of-plane displacements for all the plate impacts, see Figure 6-44, Figure 6-45 and Figure 6-46, shown in order of tup size and impact energy. A few of the graphs also show the results for a no damage model, labelled as 'nodam' and stating the number of solid elements used through the thickness. Unless specified, 8 cohesive elements and a fine mesh p2t2 was used in the analyses. Some of the contact force time histories show spurious high peaks after the plate has reached it's maximum o.o.p displacement and the tup is moving away, as an example see Figure 6-45(a). These peaks are ignored in the assessment of the maximum contact force predictions. The o.o.p displacement-time histories are taken at the bottom of the plate unless otherwise specified in the caption with 'top'. Often the readings are spiky towards the maximum displacement value and this is due to large deformation of the element at the bottom-centre of the plate, affecting the monitored bottom node. Figure 6-46(j) for test 15(495J) shows both node top and bottom node readings for comparison.

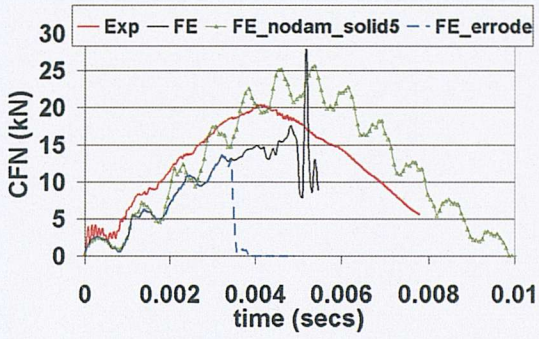
The majority of the small tup impact tests resulted in tup penetration, either full or partial and therefore the potential for element erosion was introduced in some of the analyses. Many of the tests were carried out with very similar impact energies, with only small deviations in impact velocity and mass. Such tests include 5S(195J), 6S(196J) for the small tup and 9M(195J), 21S(198J) for the medium tup tests. The peak contact force varies between each pair of analyses but not significantly.



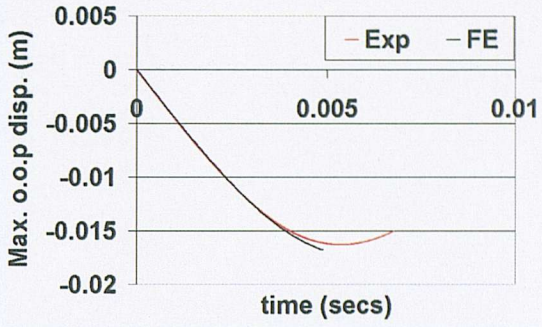
(a) Test 1S(91J)_co8_p2t2, CFN



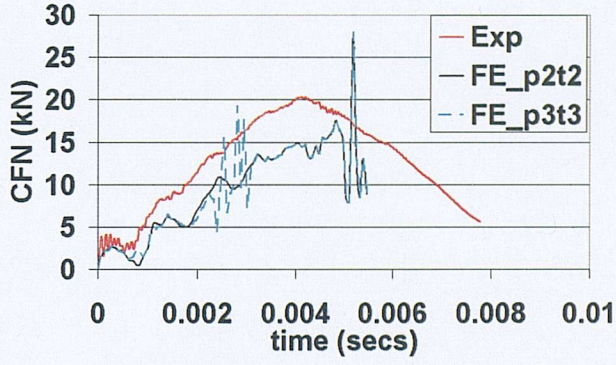
(b) Test 1S(91J)_co8_p2t2, max. o.o.p disp.



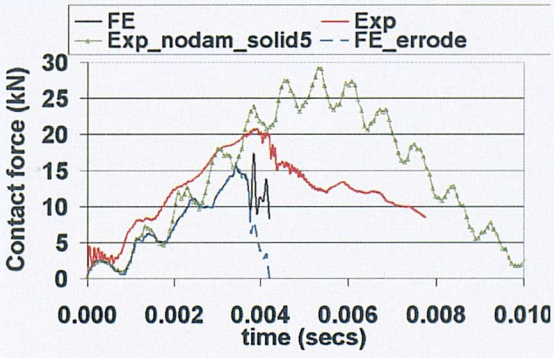
(c) Test 2S(140J)_co8_p2t2, CFN



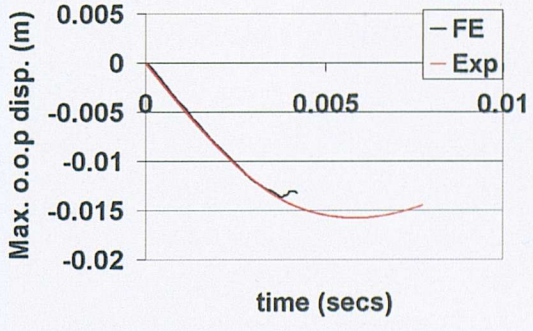
(d) Test 2S(140J)_co8_p2t2, max. o.o.p disp.



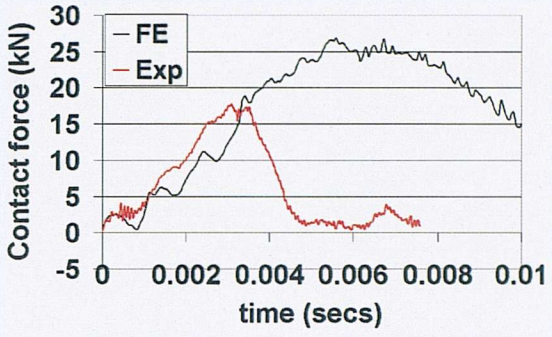
(e) Test 2S(140J)_co8_p3t3, CFN



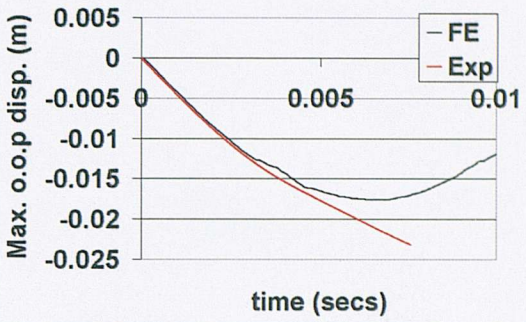
(f) Test 3S(166J), co8_p2t2, CFN



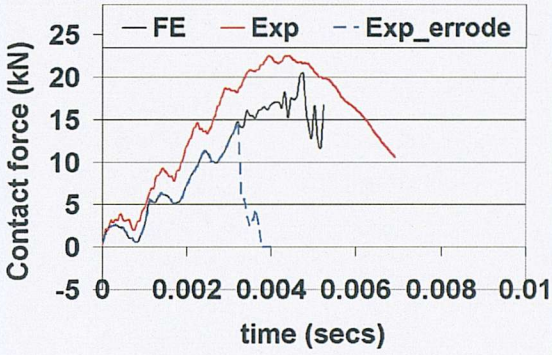
(g) Test 3S(166J), co8_p2t2, max. o.o.p disp.



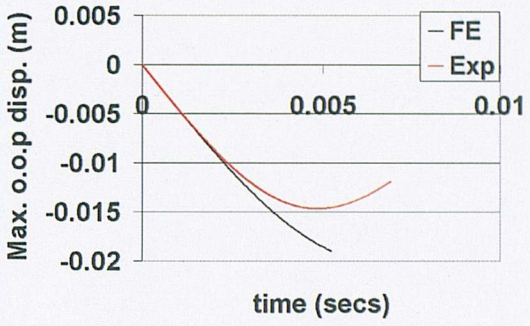
(h) Test 4S(193J) _co8_p2t2, CFN



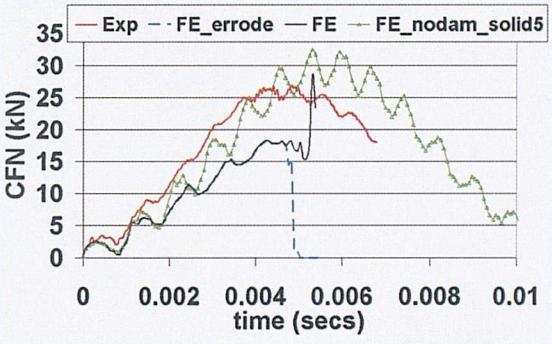
(i) Test 4S(193J) _co8_p2t2, max. o.o.p disp.



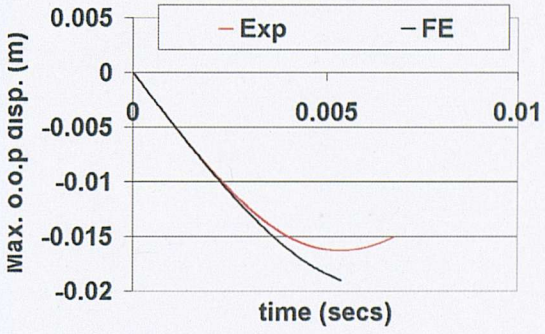
(j) Test 5S(195J)_co8_p2t2, CFN



(k) Test 5S(195J)_co8_p2t2, max. o.o.p disp,top

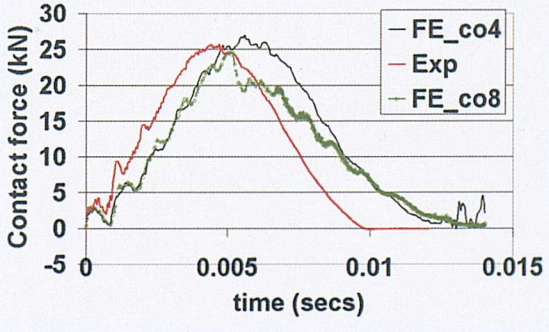


(l) Test 6S(196J)_co8_p2t2, CFN

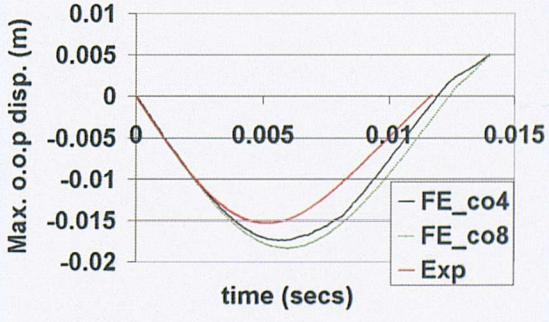


(m) Test 6S(196J)_co8_p2t2, max. o.o.p disp.top

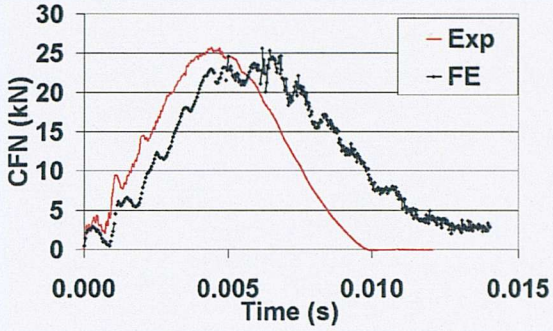
Figure 6-44. Contact force-time history and maximum o.o.p displacement predictions for the small tup impacts



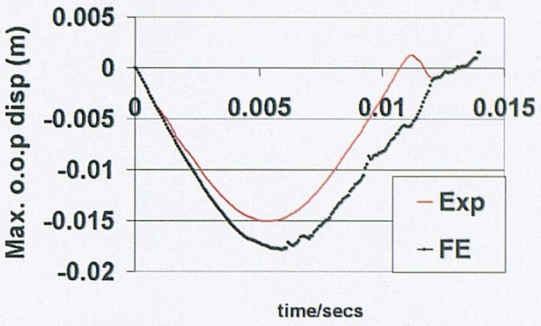
(a) Test 20M(180J), p2t2, CFN



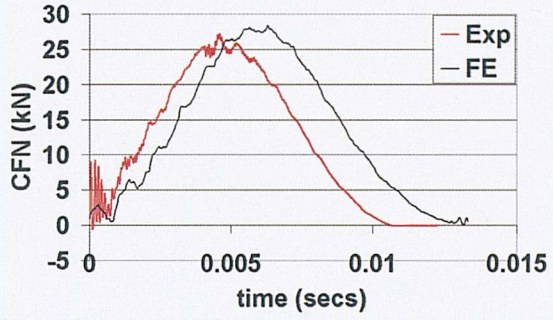
(b) Test 20M(180J), p2t2, max. o.o.p disp.



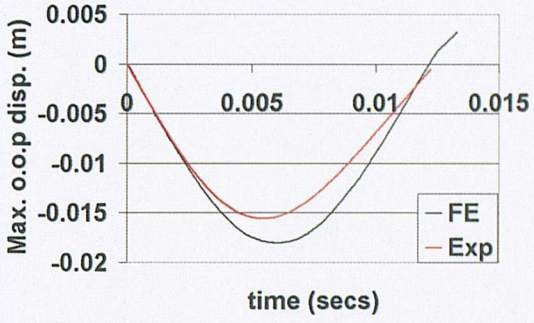
(c) Test 9M(195J), co8_p2t2, CFN



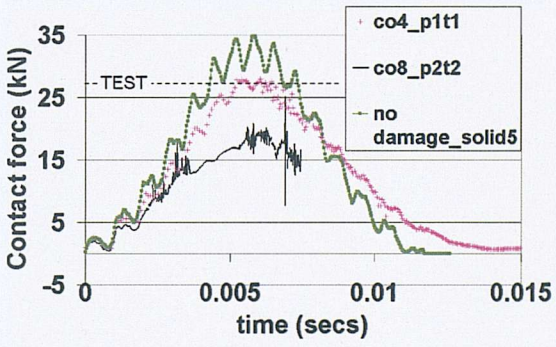
(d) Test 9M(195J), co8_p2t2, max. o.o.p disp.



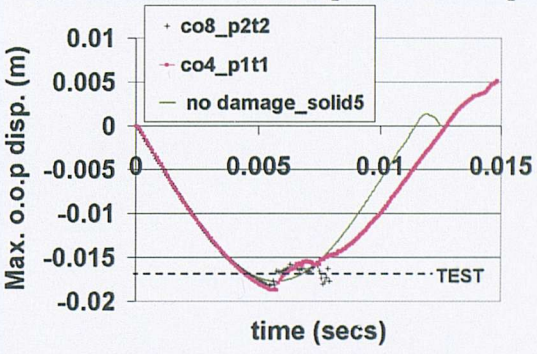
(e) Test 21M(197J), co4_p2t2, CFN



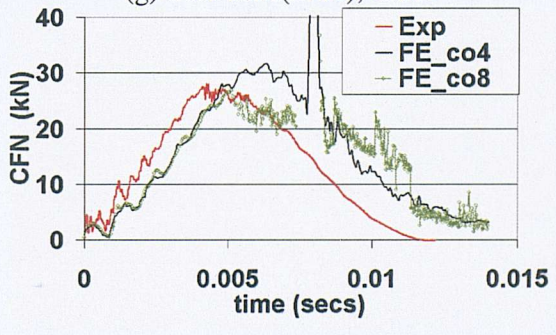
(f) Test 21M(197J), co4_p2t2, max. o.o.p



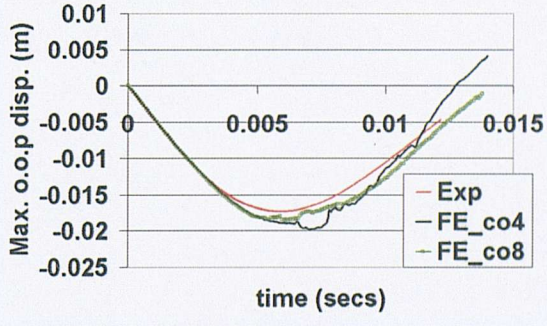
(g) Test 10M(271J), CFN



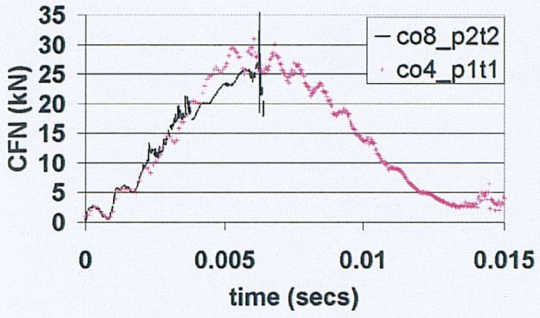
(h) Test 10M(271J), max. o.o.p. displacement



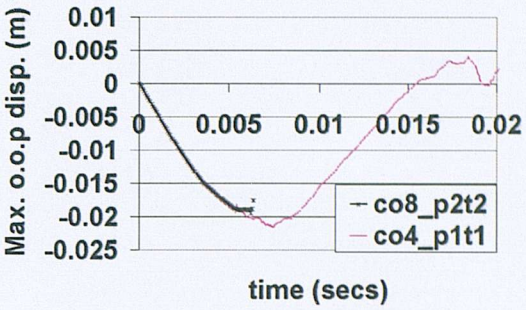
(i) Test 22M(228J), p2t2, CFN



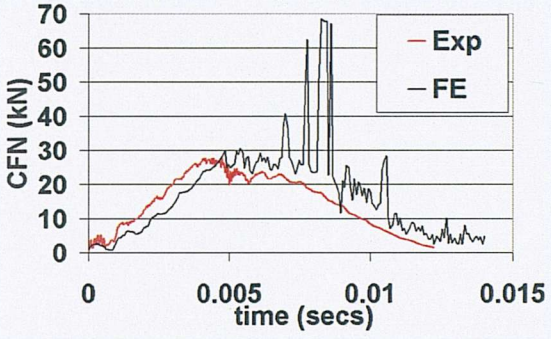
(j) Test 22M(228J), p2t2, max. o.o.p



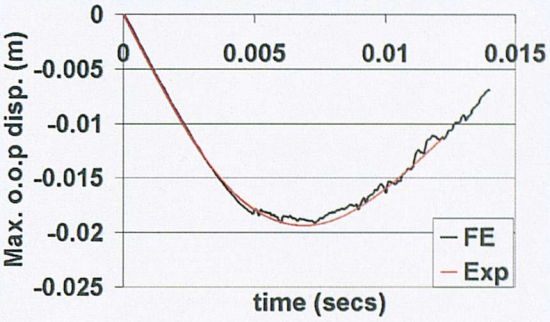
(k) Test 7M(247J), CFN



(l) Test 7M(247J), max. o.o.p disp.

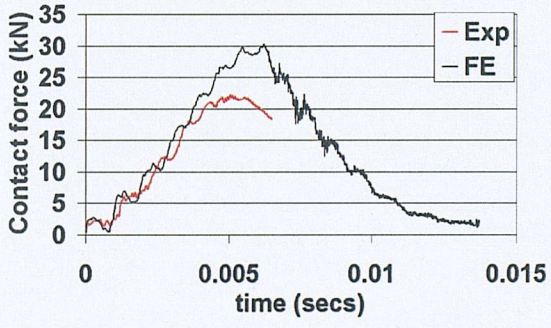


(m) Test 23M(270J), co4_p2t2, CFN

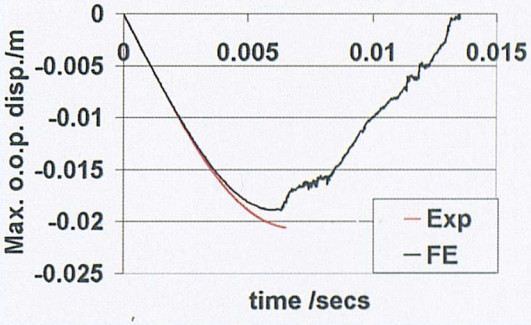


(n) Test 23M(270J), co4_p2t2, max. o.o.p

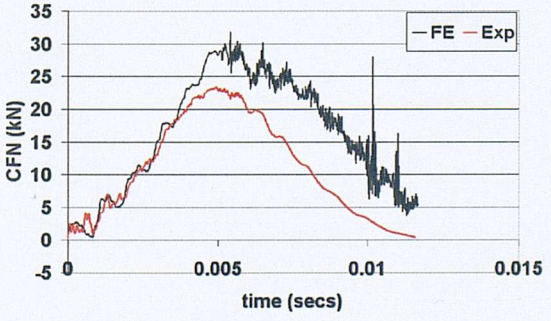
Figure 6-45. Contact force-time history and maximum o.o.p displacement predictions for the medium tup impacts



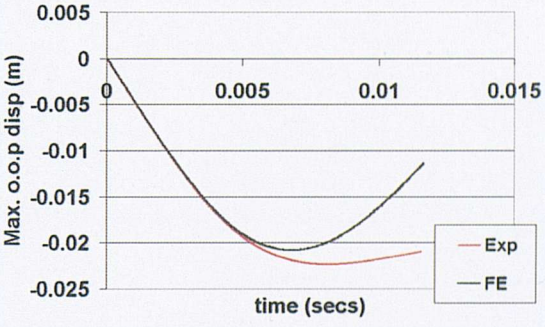
(a) Test 11L(211J)_co8_p2t2, CFN



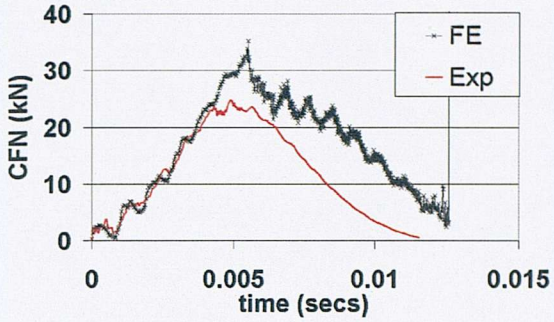
(b) Test 11L(211J)_co8_p2t2, max. o.o.p



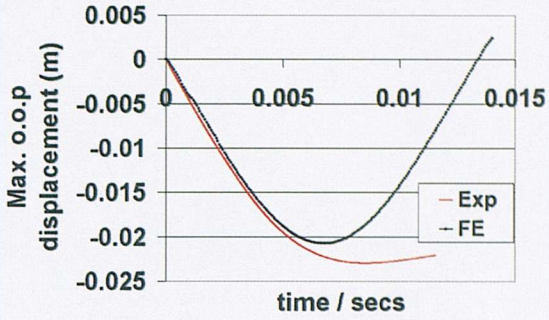
(c) Test 12L(263J)_co8_p2t2, CFN



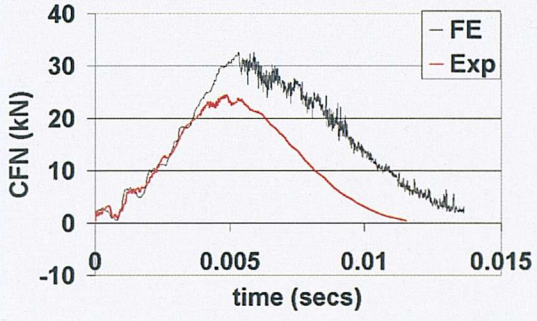
(d) Test 12L(263J)_co8_p2t2, max. o.o.p.top



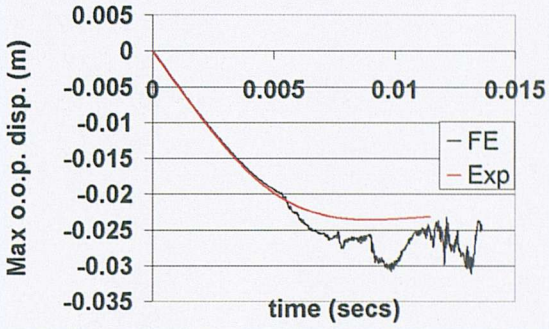
(e) Test 13L(284J)_co8_p2t2, CFN



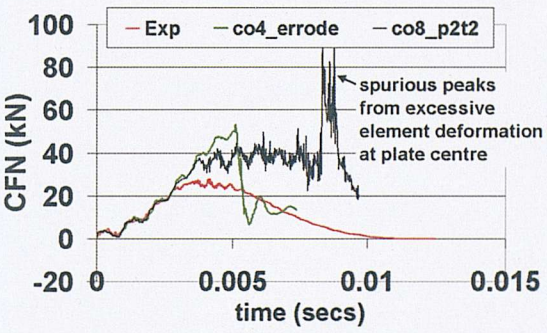
(f) Test 13L(284J)_co8_p2t2, o.o.p disp.



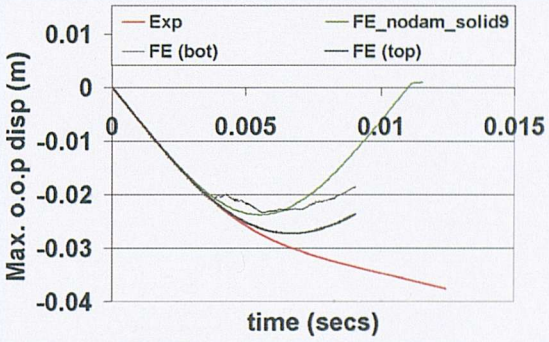
(g) Test 14L(294J)_co8_p2t2, CFN



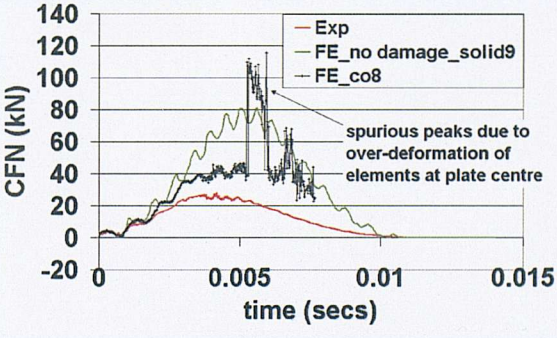
(h) Test 14L(294J)_co8_p2t2, o.o.p disp.



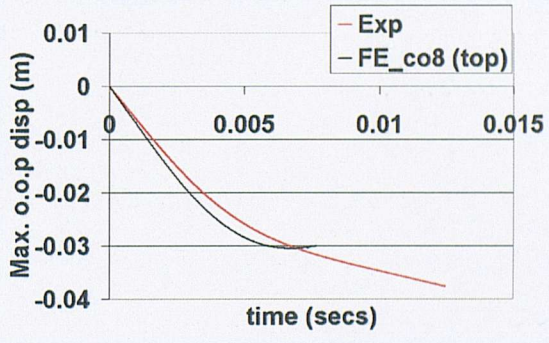
(i) Test 15L(496J)_co8_p2t2, CFN



(j) Test 15L(496J)_co8_p2t2, o.o.p disp



(k) Test 16L(665J)_co8_p2t2, CFN



(l) Test 16L(665J)_co8_p2t2, o.o.p disp.

Figure 6-46. Contact force-time history and maximum o.o.p displacement predictions for the large tup impacts

6.3.2.10. A quarter plate model and corner damage

Often, for significant impact energies, an analysis predicted damage at one of the symmetry corners in the transverse direction, see test 22M(228J) Figure 6-47. This is not observed, however, with the larger plates. The corner of symmetry in question is on the plate side undergoing the most rotation and the damage criterion is picking up the higher compressive transverse stresses that develop around this region during the compression phase. Figure 6-48 shows a full plate RR-layer model with contours average section normal transverse stresses, demonstrating the high stress concentration in red.

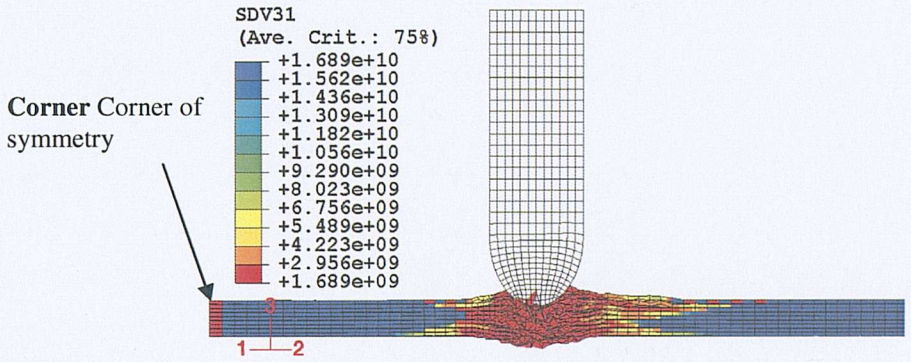


Figure 6-47. Showing damage at one corner of symmetry, for E_{33} contours test 22M(228J), in Pa.

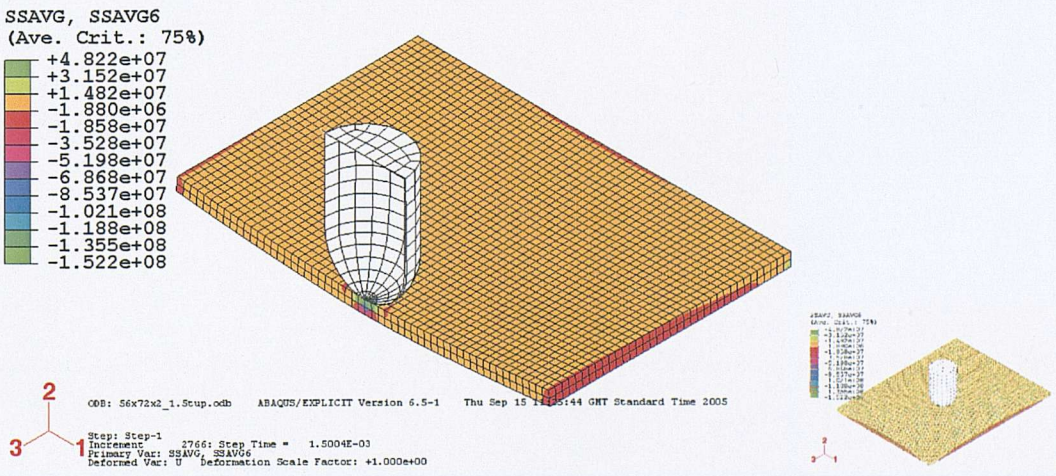


Figure 6-48. Full plate RR-layer model shown in half, showing section normal transverse stress SSAVG6 in Pa, using SC8R elements, test 9M(195J).

6.3.2.11. Element erosion

To effectively model tup penetration, the completely failed elements would need to be deleted/'eroded'. The proposed criterion for solid element erosion is described in Section 4.8

of Chapter 4. It was important to also test this element erosion capability for impact conditions that did not result in any tup penetration. Therefore the erosion criterion was also tested for two of the larger tup impact tests. The criterion worked well with the small impactor tests, predicting tup penetration for all the small impactor tests except test 1S(91J). See Figure 6-49, for test 6S(190J). Element erosion is predicted to begin at the bottom-centre elements followed by the 'puncturing' of the top surface elements, coinciding with fibre rupture (fibre spalling) occurring in the test resulting largely from the high tensile in-plane stresses. This is not uncommon as is later demonstrated with the larger plate tests, where fibre spall occured on the underside of the plate yet there was no tup penetration on the impact surface. This is in contrast with high velocity (ballistic) penetrative impact, where the material local to the impact point fails first, followed by bulging of the material on the underside of the plate (in the shape of a frustrum) [2].

However, where 'partial penetration' was recorded in the tests, the FE analysis indicated full penetration. Poor results were obtained with the larger tup (and larger energy) impact tests since the criterion predicted element erosion as shown in Figure 6-46(i) and (j) with 'co4_errode' where no tup penetration took place. A much finer element mesh of p3t3 in the impact region makes no difference to the contact force other than in the creation of a few extra frequencies, as shown in Figure 6-44(e) for test 2S(140J). The fault therefore lies with the erosion criterion, which is clearly far too conservative.

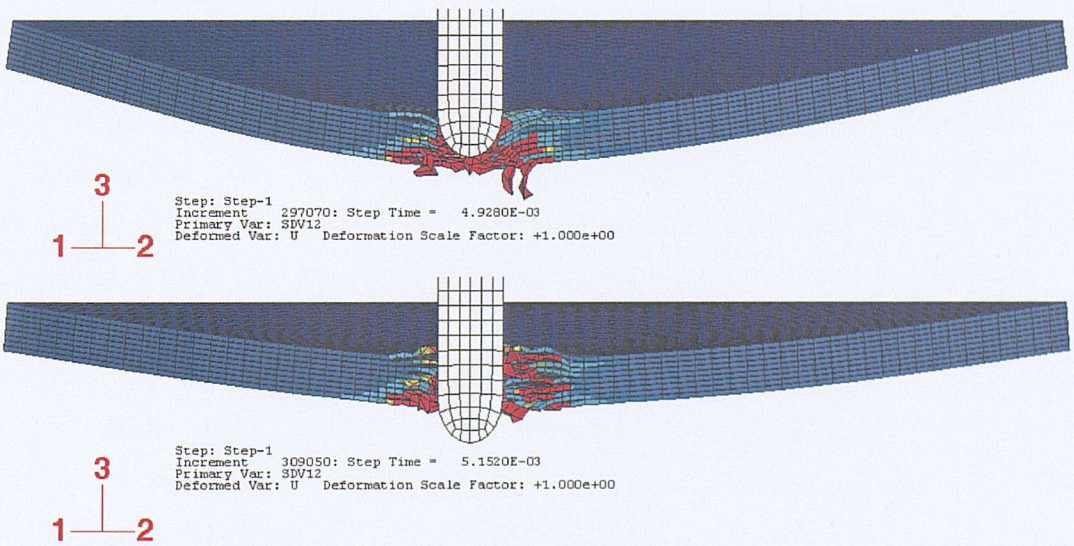


Figure 6-49. Damage with element erosion for test 6S(190J), co8_p2t2. Shown with the in-plane modulus E_{11} contours.

6.3.2.12. Energy versus contact force

As we have previously discussed, a full through-thickness damage model at the woven plies with in-plane damage has the effect of substantially reducing the contact force but sometimes de-stabilizing the analysis resulting from the transverse degradation of the plies. This instability is not only dependent on the degradation rules but also on the incident kinetic energy and the tup diameter. Instability is also intensified if, for a given tup diameter, the impact energy is increased, creating more damage which is represented with a reduction in modulus. Test 13L(284J) produced larger incident kinetic energies than any of the medium tup tests but did not show the same numerical instabilities when 8 cohesive layers were modelled. This is probably due to the larger tup diameter and the energy per unit area of the tup cross-section for the medium tups is 35.5% greater than for the large tup. A strain rate hardening model may help with regards to the excessive element damage developed at the plate centre with the smaller tup analyses.

There is a trend amongst all the analyses that shows an increase in the asymmetry of the contact force-time plots with increase in impact energy, which indicates an increase in damage [3]. However the exceptionally low contact force and asymmetry recorded for test 4S(193J) suggests dubious results. Test 4S(193J) was carried out under almost the same impact conditions as test 5S(195J) and 6S(196J) except for a slightly lower impact velocity, but the results indicate a predominantly shorter contact time and total impact time.

Significant fibre failure associated with high impact energies was often demonstrated with a sudden drop in contact force, which was predominant with test 22(270J) Figure 6-45. The FE model of this test became very unstable at this point of impact, and although it provided a good peak contact force, the unloading part of the curve contained many sporadic peaks that are reflection of the actual contact behaviour of the panel.

A plot of the contact force against impact energy is shown for all the tup diameter tests in Figure 6-50 to Figure 6-52. The contact force is always slightly under-predicted with the smaller diameter tups and over-predicted for the larger tups. It is found that the amount of in-plane and particularly transverse damage predicted with the larger tups is in proportion less than for the smaller tup tests. In summary however, the results obtained with the damage model are always an improvement over those without damage, as also demonstrated in the figures.

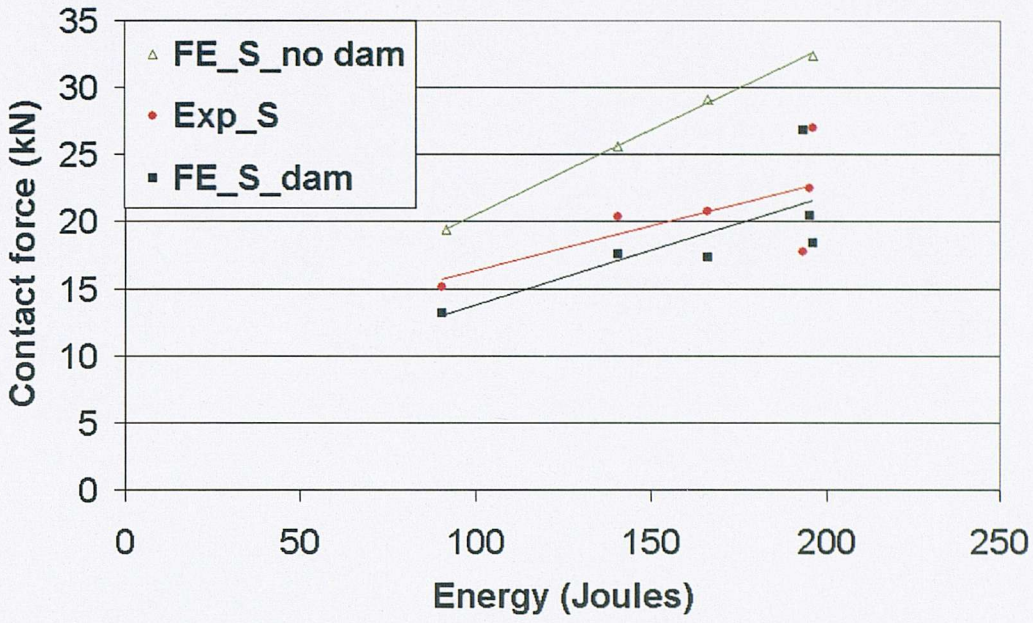


Figure 6-50. Contact force-energy relationship for the small tup tests

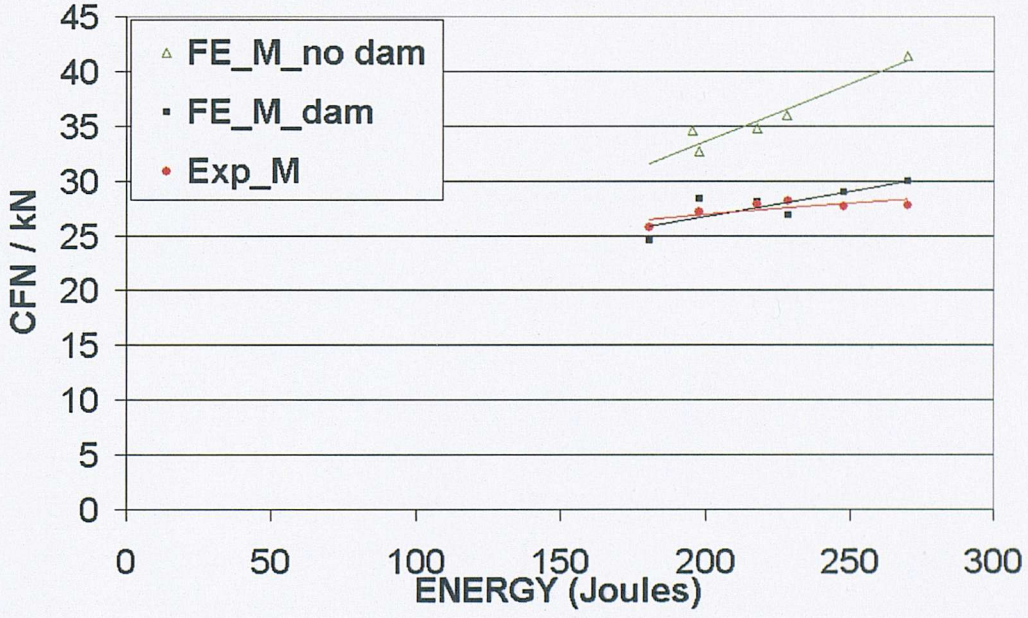


Figure 6-51. Contact force-energy relationship for the medium tup tests

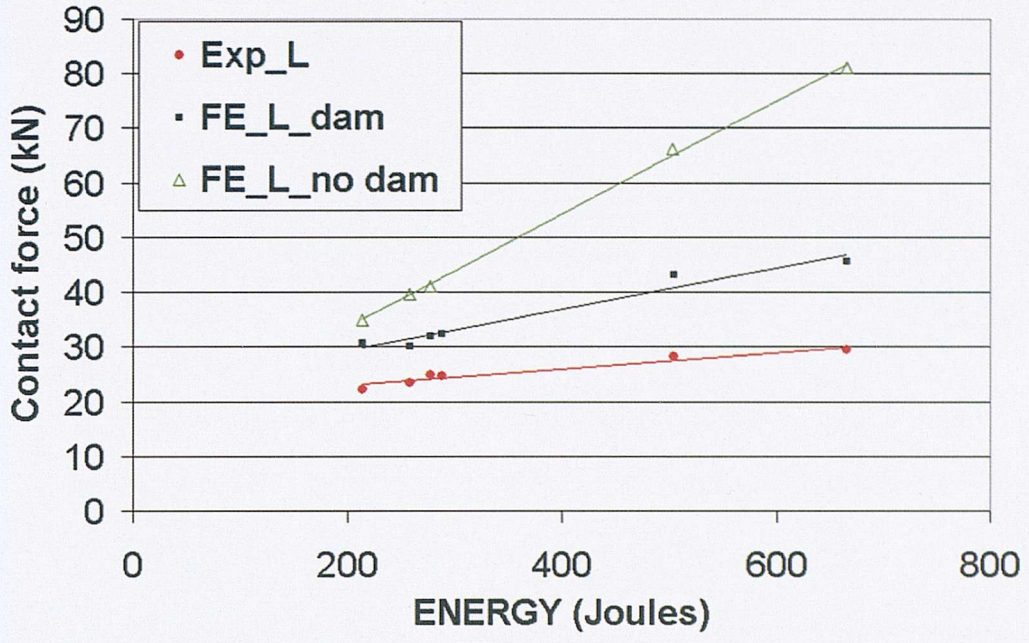


Figure 6-52. Contact force-energy relationship for the large tup tests

6.3.3. Damage predictions

The damage areas are detailed for a few of the tests in Table 6-5 to Table 6-7, shown both in metric and Imperial units. These were taken by measuring the largest discoloured areas seen from the top and bottom faces of the plates. These principal damage regions are not necessarily found on the surface of the plate and are presumed to lie within the half of the plate nearest the inspected face. It is reasonable to say that the only damage that can be seen with clarity with the naked eye is delamination damage and/or a heavily cracked region. The extent of matrix cracking has yet to be measured from experiment and could extend further than the delaminated areas. Similarly, the least damaged regions (forming the out-most damage contours) predicted by the FE model may represent these actual indistinct matrix regions. Therefore in these tables only the predicted delamination is shown underneath the test results. Only the largest delaminated areas predicted at the top and bottom halves of the plates are given. It must be noted that in all cases, the in-plane matrix damage predictions were always larger than the delamination predictions. The models used for these predictions had 8 cohesive layers and a mesh density p2t2. There appears to be a trend of over-predicting the delamination in the top half of the plate and under-predict in the bottom half (the opposite was true with the resin-rich layer model). It is interesting to note also that a small increase in impact energy does not always increase the largest delaminated areas, compare tests 3 and 4 and 4 and 5 for example. The same applies with the FE predictions,

particularly in the lower half of the plate. Impact energy and maximum delamination measured show little trend in these small plate tests as shown with Figure 6-53.

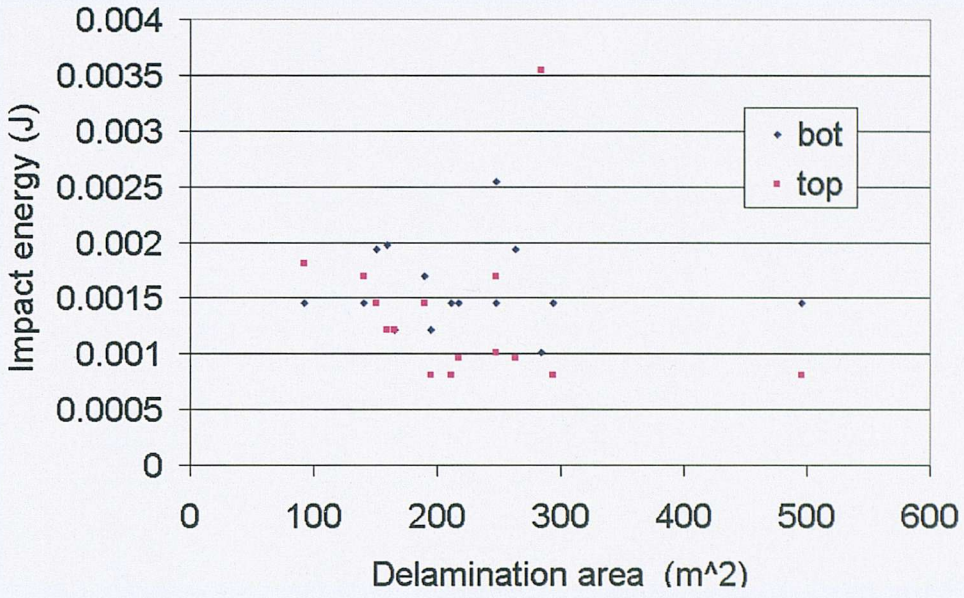


Figure 6-53. Delamination area versus impact energy for the small plate impact tests. 'Bot' and 'top' refer to the maximum delamination measured in the top and bottom half of the plates respectfully.

Energy Level in J (ft lbf)	**Test N°**	***Test approximate Damage Size (Top) in m (in)*** **[FE in m](cohesive layer 'c')***	***Test approximate Damage Size (Bottom) in m (in)*** **[FE in m] (cohesive layer 'c')***
91.5 (67.5)	1	*0.0381 x 0.0254* *(1.5 x1)* **[0.0253 x 0.016]**	*0.0381 x 0.0381* *(1.5 x 1.5)* **[0.0253 x 0.022]**
140.6 (103.68)	2	*0.03175 x 0.0254* *(1.25 x 1)* **[0.0492 x 0.035] (c1)**	*0.0381 x 0.0381* *(1.5 x 1.5)* **[0.0318 x 0.0286] (c8)**
150.6 (111.09)	3	0.0381 x 0.0254 (1.5 x1) **[0.0492 x 0.0438] (c6,8)**	0.0381 x 0.0508 (1.5 x 2) **[0.0552 x 0.0492](c1,2)**
159.3 (117.46)	4	0.03175 x 0.0254 (1.25 x 1) **[0.0492 x 0.035] (c7,8)**	0.0381 x 0.0381 (1.5 x 1.5) **[0.0192 x 0.0192] (c1-3)**
165.8 (122.3)	5	*0.03175 x 0.0254* *(1.25 x 1)* **[0.0436 x 0.022] (c8)**	*0.0381 x 0.0381* *(1.5 x 1.5)* **[0.022 x 0.0436] (c1,2)**
190.1 (140.2)	6	*0.0381 x 0.0254* *(1.5 x1)* **[0.0492 x 0.035] (c8)**	*0.0381 x 0.0381* *(1.5 x 1.5)* **[0.0318 x 0.0318) (c1,2)**

Table 6-5. Small tup (12.7mm dia.) test damage measurements against FE delamination results, using a co8_p2t2 mesh. Tests are in order of increasing impact energy.

Energy Level in J (ft lbf) [FE in J]	Tup size/ mm (inches)	Test No	*Test approximate Damage Size (Top) in m (in)* [FE in m](cohesive layer 'c')*	*Test approximate Damage Size (Bottom) in m (in)* [FE in m] (cohesive layer 'c')*
195.5 (144.2) [197.8]	'M' 25.4mm (1)	9	*0.03175 x 0.0254 (1.25 x 1)* [0.044x0.044] (c5)	*0.0381 x 0.03175 (1.5 x 1.25)* [0.038x0.038] (c3)
217.4 (160.35) [215.2]		10	*0.0381 x 0.03175 (1.5 x 1.25)* [0.052x0.038] (c7)	*0.0381 x 0.03175 (1.5 x 1.25)* [0.043x0.033] (c4)
247.6 (182.61) [250.64]		7_R	*0.03175 x 0.0381 (1.25 x 1.5)* [0.0478x0.043] (c7)	*0.04445 x 0.04445 (1.75 x 1.75)* [0.0382x0.033] (c2&4)

Table 6-6. Medium tup (24.5mm dia.) test damage measurements against FE delamination results, using a co8_p2t2 mesh. Tests are in order of increasing impact energy.

Energy Level in J (ft lbf)	Test No	*Test approximate Damage Size (Top) in m (in)* [FE in m](cohesive layer 'c')*	*Test approximate Damage Size (Bottom) in m (in)* [FE in m] (cohesive layer 'c')*
211.7 (156.15)	11	*0.04445 x 0.0381 (1.75 x 1.5)* [0.073 x 0.036](c8)	*0.0381 x 0.0381 (1.5 x 1.5)* [0.0437 x 0.0382](c1)
263.41 (194.28)	12	*0.04445 x 0.0381 (1.75 x 1.5)*	*0.0381 x 0.0381 (1.5 x 1.5)*
284.1 (209.5)	13	*0.05715 x 0.03175 (2.25 x 1.25)* [0.055x0.029] (c7,8)	*0.0381 x 0.0381 (1.5 x 1.5)* [0.0318 x 0.035] (c1-2)
294.2 (216.96)	14	*0.0381 x 0.0381 (1.5 x 1.5)* [0.068 x 0.036](c6-8)	*0.04445 x 0.0381 (1.75 x 1.5)* [0.055 x 0.0494](c1,2)
495.9 (365.72)	15	*0.03175 x 0.03175 (2.5 x 1.25)* [0.0976 x 0.1778](c8)	*0.05715 x 0.04445 (2.25 x 1.75)* [0.072 x 0.1778**](c1)
559.7 (412.8)	16	*0.06985 x 0.0508 (2.75 x 2)* [0.055 x 0.0318](c6-8)	*0.03175 x 0.03175 (2.5 x 2.5)* [0.0794 x 0.0492](c1)

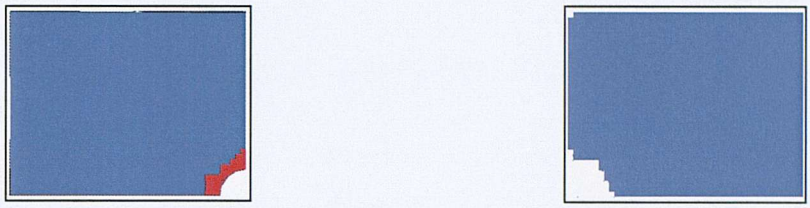
*** c1 refers to cohesive layer number one (8 cohesive layers, c1 to c8, from bottom to top of plate).**

Table 6-7. Large tup (38mm dia.) test damage measurements against FE delamination results, using a co8_p2t2 mesh. Tests are in order of increasing impact energy.

6.3.3.1. Delamination damage

The extent of predicted delamination for test 9M(195J) is shown in Figure 6-54(a) and (b) (noting it is a quarter plate model), giving good comparisons with the test results pictured photographically in Figure 6-13(a) and (b). We can see from these test figures that the

largest delaminated area that can be visually seen from the bottom face may be several locations above the bottom layer (the white, centre bit is at the surface ply).



(a) (b)

Figure 6-54. Damage results for test 9M(195J), (a) 1/5 from top of plate, (b) 1/5 from bottom of plate

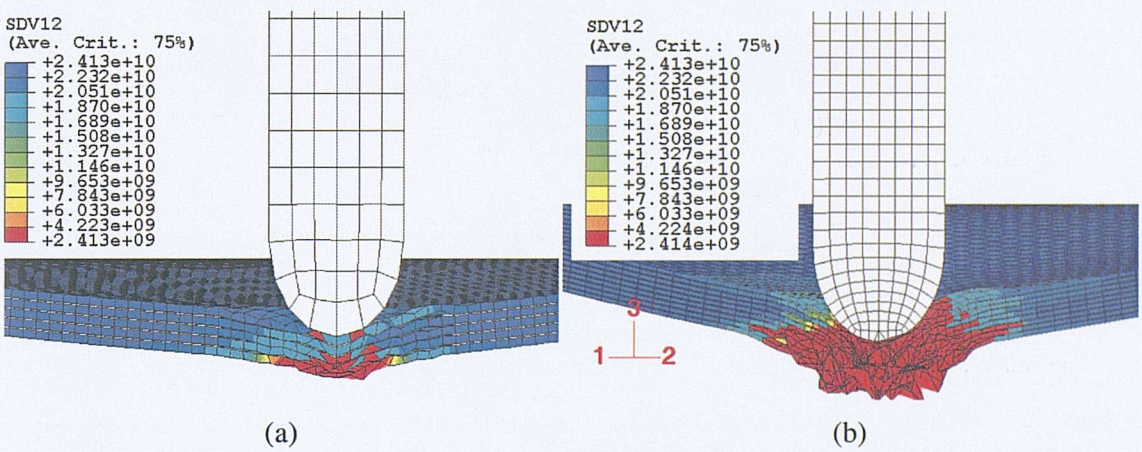
The delamination damage for one of the larger tup tests, 13L(284J), Figure 6-16. The cross-section shows a larger inter-ply separation at the bottom of the plate however the widest area of damage was recorded from the top face, indicating that the largest delaminated layer must be closer to the top than the bottom of the plate, however C-Scan images are needed to provide a clearer analysis. Cutting the plate in half released some of the residual stress created from the delamination process, particularly at the bottom of the plate where the transverse normal tension develops, thus the 'fanning out' of the bottom plies. The delamination was very marginally under-predicted with the finer co8_p2t2 FE model but the location of the delaminated plies is better modelled than with the RR-layers and 2d failure criteria.

With all the analyses, failure of the cohesive elements during the compression phase occurred only due to the shear stresses because the normal transverse stress contribution during the compression phase is excluded in the failure criteria. Therefore the effect of delamination on the peak contact force is often governed largely by the transverse shear stresses only. The extent of the shear stress contribution in the FE model is often dictated by the mesh density, as we saw in the previous Chapter 5. It is during the tensile phase (when the tup moves away), that some of these central cohesive elements begin to fail under normal transverse tension. Besides the extensive through-thickness delamination seen in most tests and their simulations, the maximum bending stresses are foremost responsible for large amounts of matrix and fibre damage formation at the top and bottom of the plate. This damage is accentuated at the bottom of the plate due to the low compressive or tensile normal transverse stresses at the bottom plies, whereas at the top of the plate the layers are closed-up under the large compressive force.

The in-plane and through-thickness damage predictions for all the analyses are shown in Appendix C, which unless otherwise specified are displayed for 8 cohesive elements and a mesh size p2t2, giving the most conservative results.

6.3.3.2. Stress resolution on matrix and fibre damage predictions

The in-plane damage prediction is shown in Figure 6-55, for test 9M(195J) analysis 'co4_p1t1' and 'co8_p2t2'. The proportions of pure matrix damage and combined matrix and fibre damage can be approximated from these modulus contours using Figure 4-7 in Chapter 4. The coarser meshed model with 4 cohesive layers appears to be a better representation of the actual damage. This model showed more in-plane damage at the bottom than at the top of the plate, correlating well with Mouritz's work [4] and a bit of fibre damage at the top and bottom of the plate. The finer meshed model with 8 cohesive layers exaggerated the damage to an unrealistic degree largely because of the higher stress resolution at the elements plus also the greater through-thickness damage modelling resulting from the increased number of cohesive layers. Therefore a full cohesive layer model with the proposed transverse degradation at the woven plies may be beneficial in reducing the contact force but does not always necessarily improve the damage prediction.



(a) (b)

Figure 6-55. Degradation contours of modulus E_{11} in Pa, (a) test 9M(195J), co4_ p1t1, (b) test 9M(195J), co8_p2t2.

6.3.3.3. Effect of impactor diameter on damage prediction

Compare test 10M(217J) and test 11L(212J), both of similar impact energies but different tup diameters, as previously compared above in Section 6.2.2.3. The impact energy per unit tup contact area is larger with the smaller tup diameter, therefore there is less damage concentration and a full damage model appears to work better with the larger diameter tups.

Figure 6-56(a) and (b) shows the through-thickness modulus, E_{33} contours for analyses carried out with 8 cohesive layers and a mesh density p2t2.

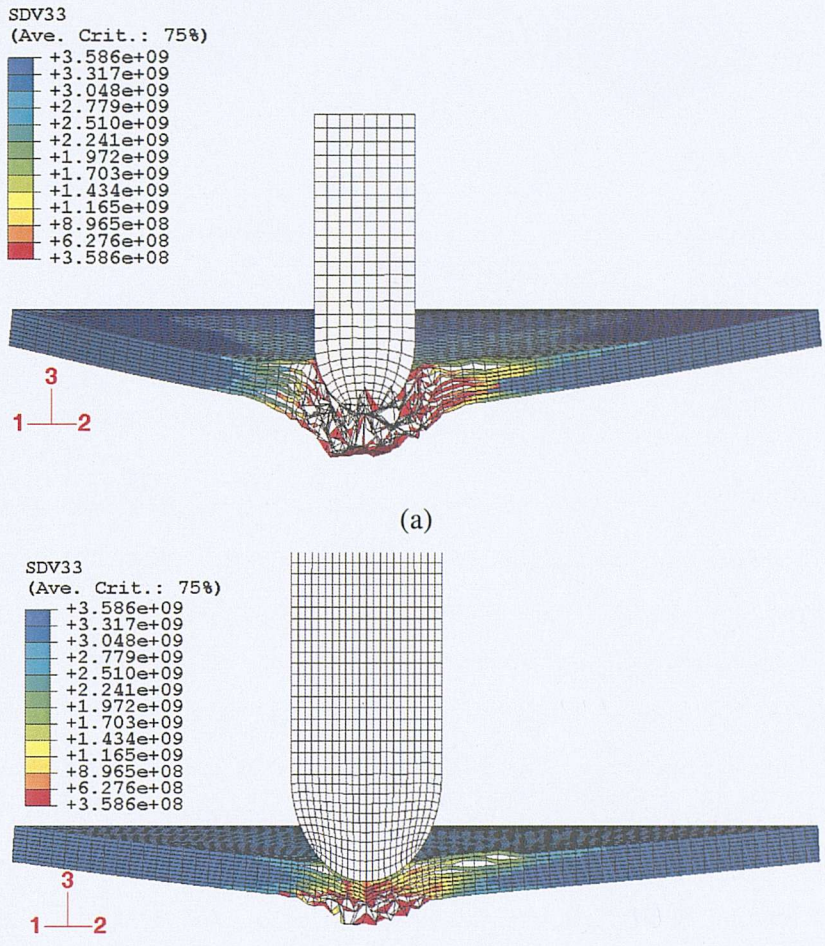
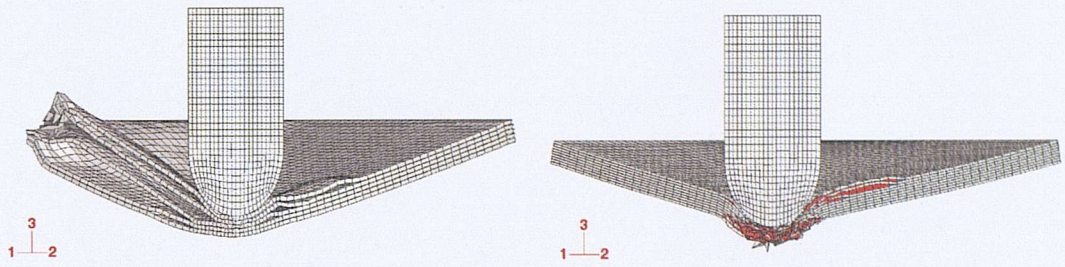


Figure 6-56. Normal transverse damage shown with E_{33} contours in Pa, co8_p2t2 type analyses, (a) test 10M(217J), (b) test 13L(211J)

The large tup impact tests are more likely to induce delamination damage than the smaller tup tests, however when the velocity is high, as with tests 15L(495J) and 16L(665J), the weaker inter-laminar regions have a tendency to fail more dramatically when few of these are modelled. This is demonstrated with test 15L(495J). The model with four cohesive layers delaminated extensively unlike the one with the full 8 cohesive layers, see Figure 6-57. The mesh size had in comparison no substantial effect on these results.



(a) (b)

Figure 6-57. Delamination predicted using (a) 4 cohesive layers and (b) 8 cohesive layers, for test 15L(495J)

6.3.3.4. Displacement-contact force history

A plot of displacement against contact force for several of the 1 inch tup tests (producing the low to intermediate impact energies), Figure 6-58, showed some important features during the loading event. The plate width-to-thickness ratio of these plates is large enough for membrane action to take effect and this is apparent with the increase in the stiffness of the plate from the start to the finish of loading. Some of the peaks and troughs present in all the experimental plots were replicated in the FE models, here demonstrated for test 21M(198J) and it's FE simulation prediction. One obvious difference between the test and FE results includes the lack of un-recoverable (irreversible) energy in the numerical analysis and its rotational shift relative to the test by over-predicted out-of-plane displacements and longer contact times. This observation was previously discussed in Section 4.12.3 of Chapter 4. At peak '1', the FE model predicts no damage, and the reduction in contact force may be attributed to the compression of the top element and the contact definition. Peak '2', coincides with the start of in-plane damage at the bottom of the plate, see Figure 6-59(a), and shear induced delamination, Figure 6-59(b). At peak '3' significant drops in the in-plane modulus took place for those elements at the centre of the plate, particularly at the bottom of the plate, as seen with Figure 6-60 for the elements in Figure 6-61 and some fibre damage was created. From this point onwards more elements in and around the impact site began to loose stiffness, see Figure 6-62 where we can see some of the bottom elements with strains of over 0.0248, greater than the strain for start of fibre damage ε_f and further significant delamination took place. At peak '4', full failure occurred and unloading began. The same Figure 6-60 showing the in-plane degradation with time history is repeated in Figure 6-63 with the added results of surrounding elements in the top half of the plate. It demonstrates graphically how throughout the loading history, the plate elements towards the top of the plate degraded less in comparison to the bottom of the plate.

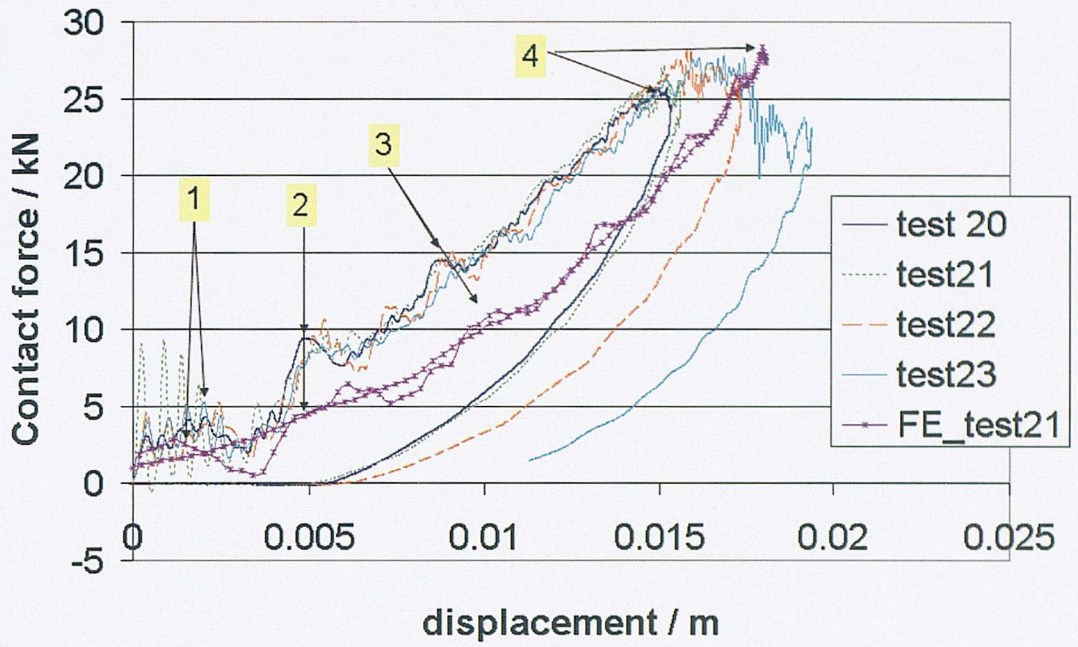
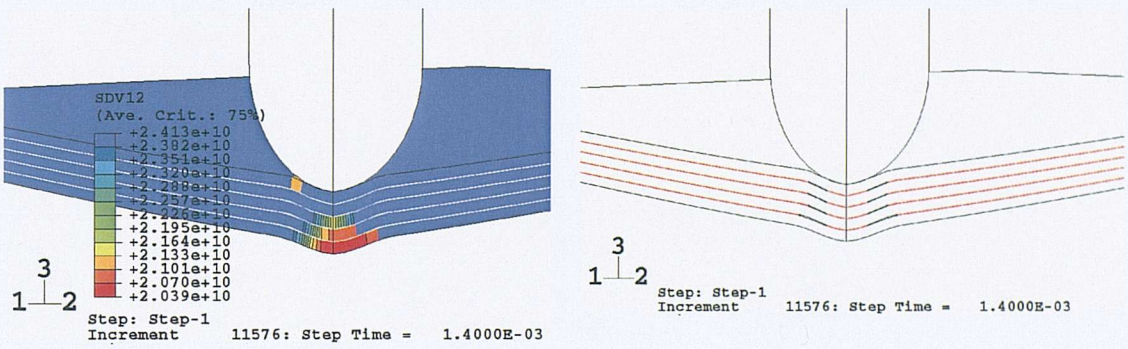


Figure 6-58. Contact force-disp. results for a few of the medium sized tup impact tests



(a) (b)

Figure 6-59. FE results, test 20M(180J), (a) Start of in-plane damage, (b) start of delamination damage (initiating at the bottom layers)

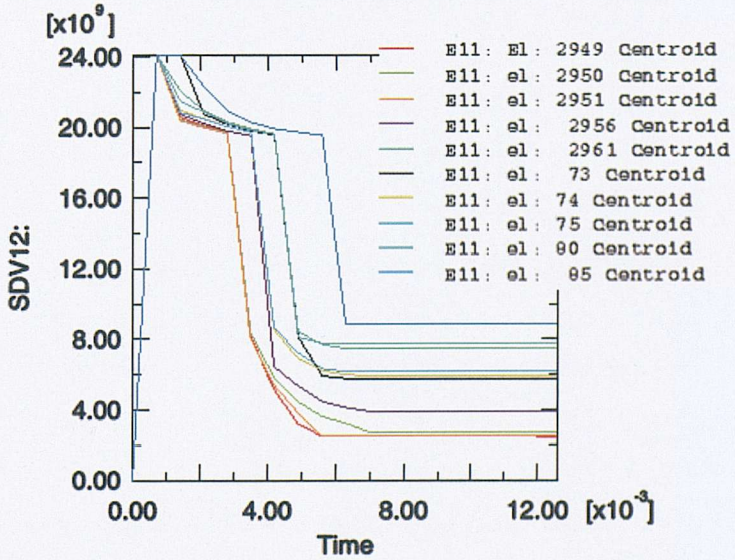


Figure 6-60. Modulus E_{11} (in Pa) vs time (in secs) for a few elements at the bottom centre of the plate shown in Figure 6-61

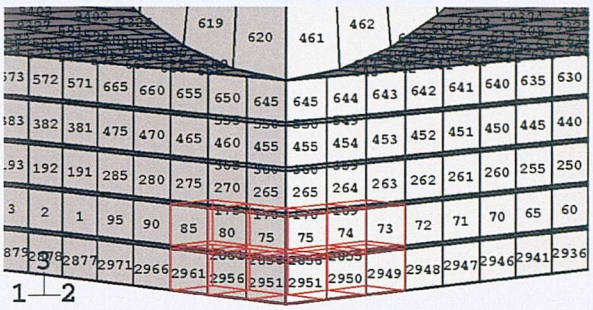


Figure 6-61. Elements selected at the bottom-centre of the plate for analysis

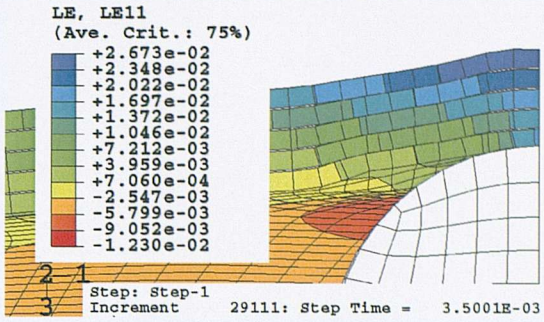


Figure 6-62. strain in the impact site at time 3.5E-3 approximately at 'peak 3'

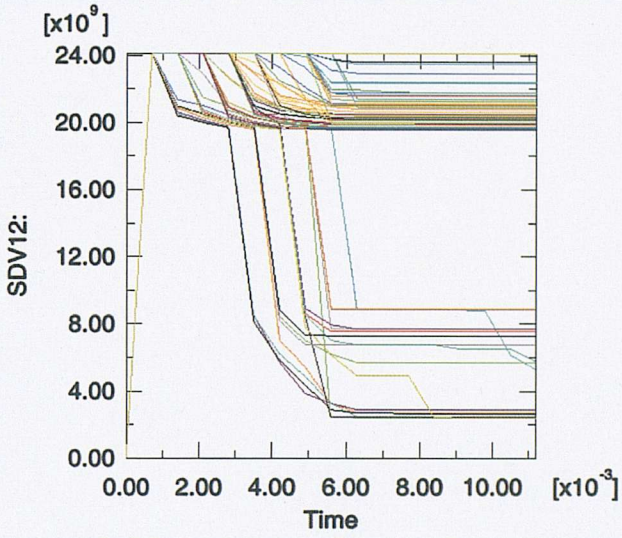


Figure 6-63. Modulus E_{11} (in Pa), vs time (in secs), for all the elements through-the thickness in the immediate impact site.

6.3.4. Large-scale plates 1

Plates of size 1.07315x0.76835x0.019m^3 (42.25x30.25x0.75in^3) were impacted with three different tup masses using the same tup diameter of 0.203m (8ins) at a velocity of 4.6ms^{-1}. The tests are labelled from A to D, as shown in Table 6-8..

A quarter-plate model was used in all the FE analyses with symmetry boundary conditions applied and the outside edges are treated as simply supported. Unlike Abaqus/Standard (implicit) Abaqus/Explicit does not allow composite layering within the solid elements. The composite has 29 plies and eight continuum elements (C3D8R) are used through the thickness in an attempt to model groups of plies. The smallest mesh size used for this plate was nearly four times the size of mesh used with the small plates, falling short of the scale difference between their longest plate lengths. This not only significantly reduced the

computational time, but prevented an unrealistic increase in stress resolution between the two scales.

6.3.4.1. Contact force and displacement results

The finite element results show that the contact force is slightly under predicted for the smaller mass impacts but good results are obtained with the largest mass 1503lbs tup used in tests C and D. The results for the no-damage model still show an under-prediction in the contact force for the lowest energy impact, test A, but for test B the peak contact force is close to the experimental value. This indicates that the damage model is not necessarily to blame but some other FE modelling parameters are responsible in some way. It is likely that the element type is a large contributor to the problem. In Chapter 5 it was found that the shells produced higher contact force predictions than the solid (continuum) elements for an analysis exclusive of damage. It is interesting to see the short impact time predicted with these large plate simulations compared to the experiment. This trend is contrary to that observed with the small plate impacts. As shown later, the damage predicted at the woven layers for the large plate simulations is relatively tame compared to the actual damage recorded in the tests. The small plate impact simulations predicted more severe damage in comparison.

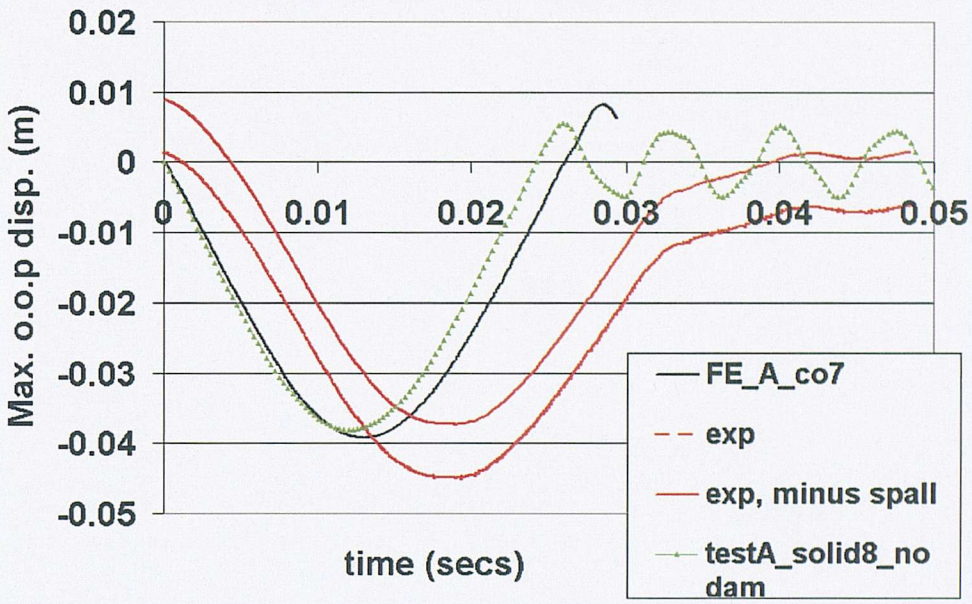
The o.o.p displacements were well predicted when compared to the test displacements minus the fibre spall, which was measured for all the tests, see Table 6-9.

Test	TEST Max contact force /kN (lbf)	FE Max contact force /kN (lbf)
A (340.2kg, 750 lbs)	296 (66543)	250 (56202)
B (454.5kg, 1002 lbs)	339 (76394)	295 (66318)
C/D (681.8kg, 1503 lbs)	382 (85878) 387 (87057)	428 (96218)

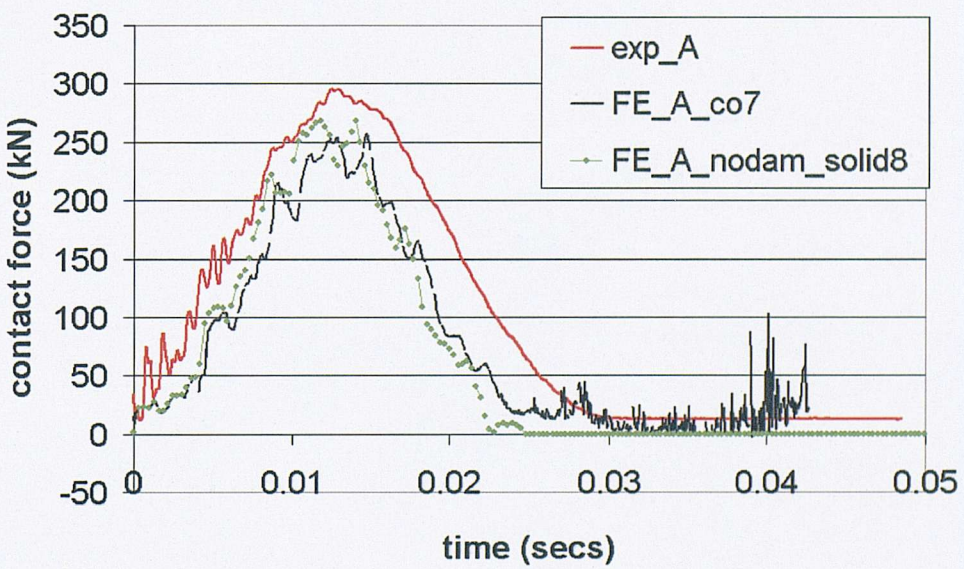
Table 6-8. Summary of 42x30x0.75in plate test and FE results

CFN from FE / lbs	Total oop disp LASER / m (in)	Depth of Damage MOUND (1)/m (in)	oop minus depth of damage NET DISP (1) /m (in)	oop from FE /m (in)
Test A	0.0449 (1.7677)	0.00762 (0.3)	0.0372 (1.4677)	0.03911 (1.54)
Test B	0.057 (2.2425)	0.0139 (0.55)	0.04298 (1.6925)	0.04368 (1.72)
Test C	0.074 (2.9123)	0.0279 (1.1)	0.04603 (1.8123)	0.0500 (1.97)
Test D	0.067 (2.6356)	0.0267 (1.05)	0.04027 (1.5856)	

Table 6-9. Summary of the max. o.o.p disp. from the tests and FE predictions

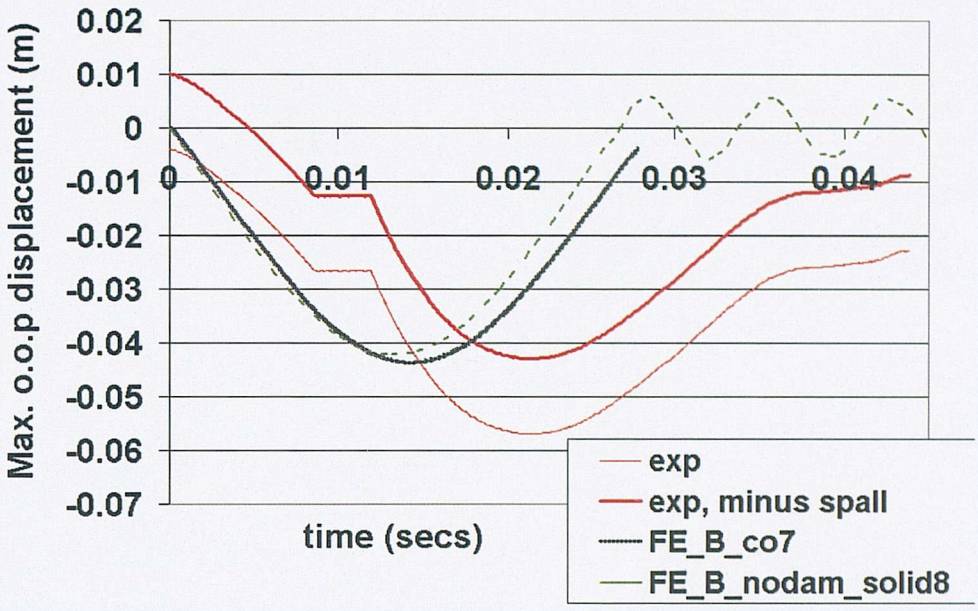


(a)

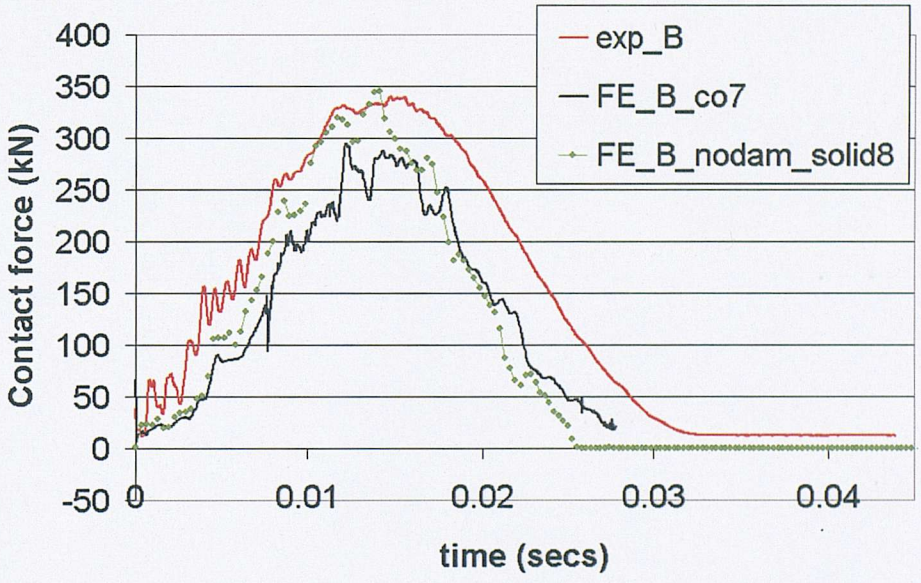


(b)

Figure 6-64. Test A, (a) o.o.p displacement-time, (b) contact force-time histories

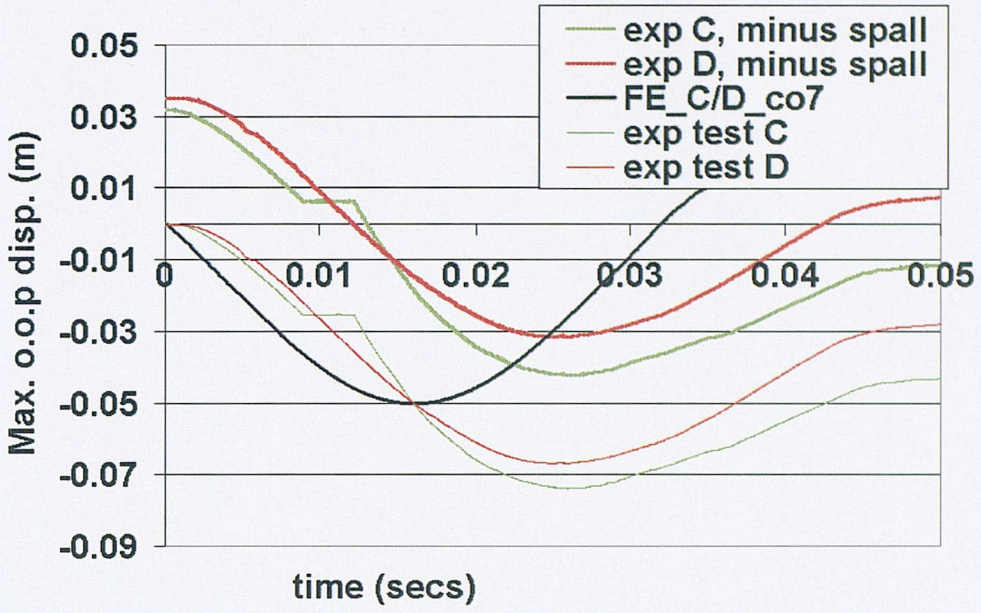


(a)

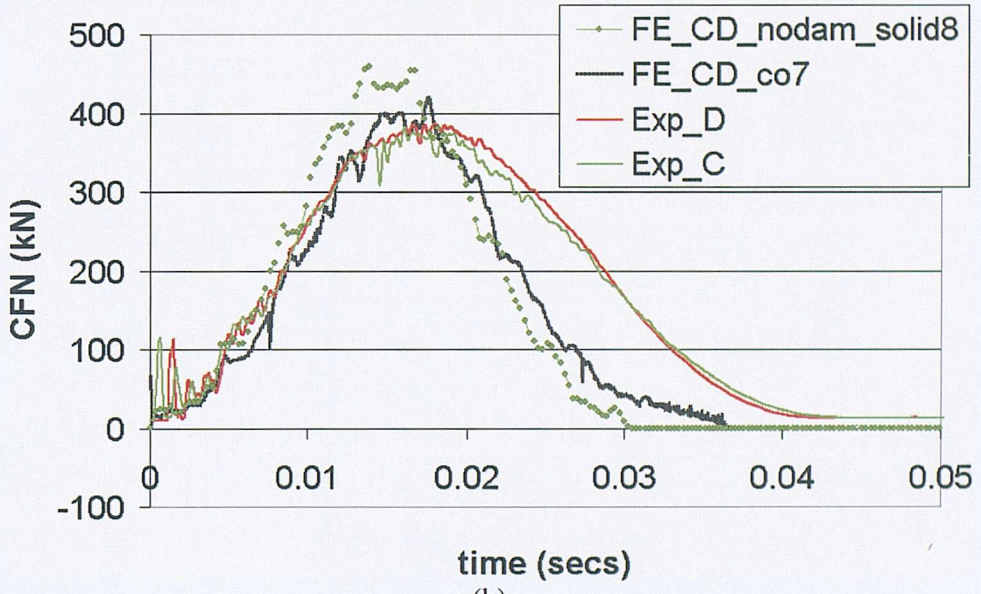


(b)

Figure 6-65. Test B, (a) max. o.o.p displacement-time (b) contact force-time histories



(a)



(b)

Figure 6-66. Test C and D, (a) max. o.o.p displacement-time, (b) contact force-time histories

6.3.4.2. Surface strains

Strain readings were taken at several locations on each side of the plates. The gauge locations are shown in Figure 6-67 for the top and bottom face of the plates. The FE strain predictions are reasonable, particularly near the impact site on the top of the plate at strain location '1'. Some strains recorded towards the end of the impact event reverse in sign and reflect poorly damped local elastic response, as exemplified with Figure 6-68.(i) and (l).

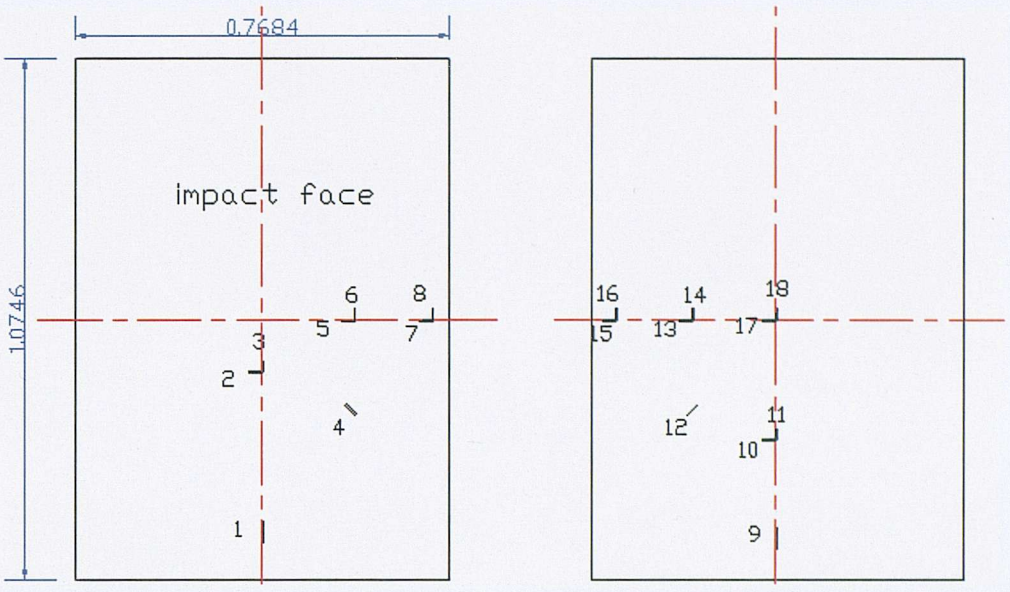
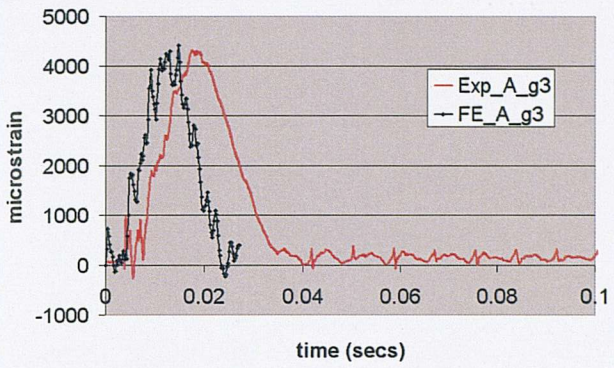


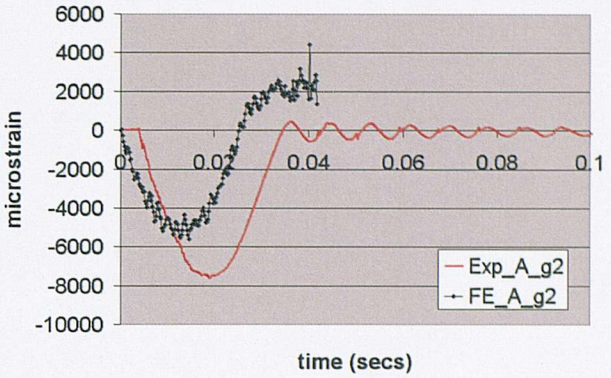
Figure 6-67. Gauge locations on the (a) top (impact) face of the plates with corresponding (b) bottom face gauge locations

Some of the strain gauges were damaged during the impact and a selected number of strain measurements, representative of the trend between numerical and experimental results, are shown in Figure 6-68 for test A and Figure 6-70 for tests C and D.

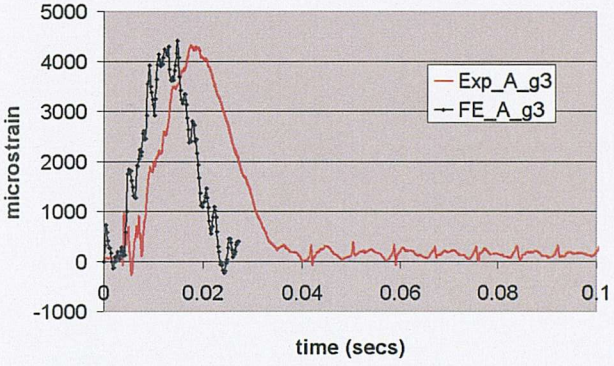
It was observed that the strain predictions for the plate impacted with the lowest energies, test A and B, compared quite well with the test results. However, on examination of the results for the largest mass impacts, test C and D, the strains were very often under-predicted. Although, it is important to note that the strain measurements obtained experimentally did vary between tests C and D, in fact quite significantly in the case of gauge 8, see Figure 6-70 (h). For this gauge location, the FE prediction lies almost half-way in between the reading for test C and D. The largest under-prediction of strain was for gauge 16 (bottom face) and this is consistent for the three analyses. Many gauges near the impact site failed, shown here for completion.



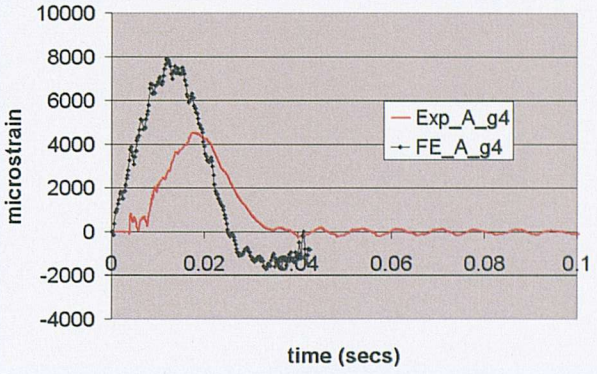
(a) g1



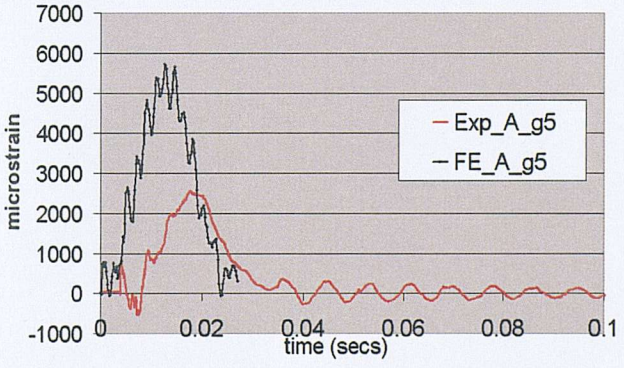
(b) g2



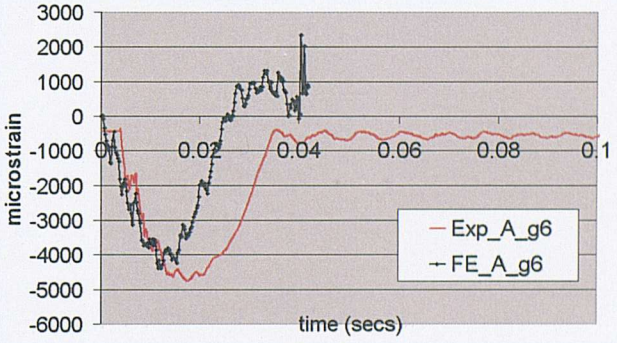
(c) g3



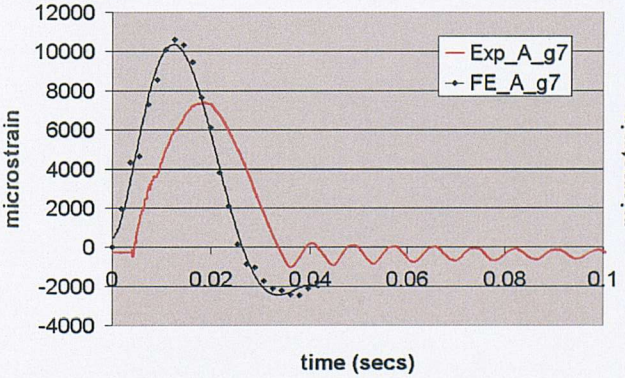
(d) g4



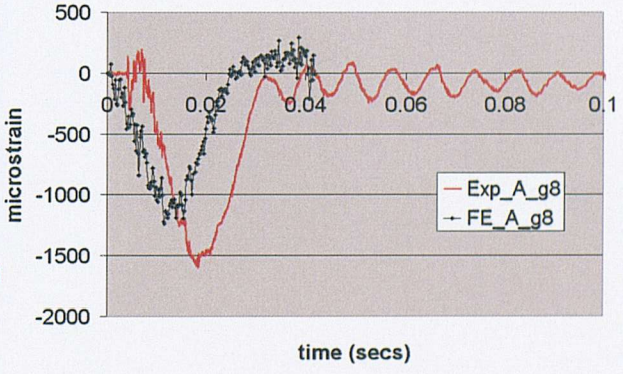
(e) g5



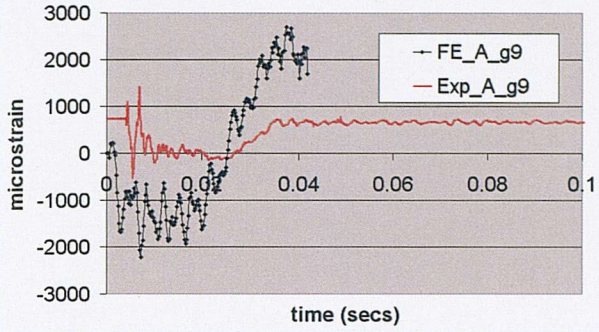
(f) g6



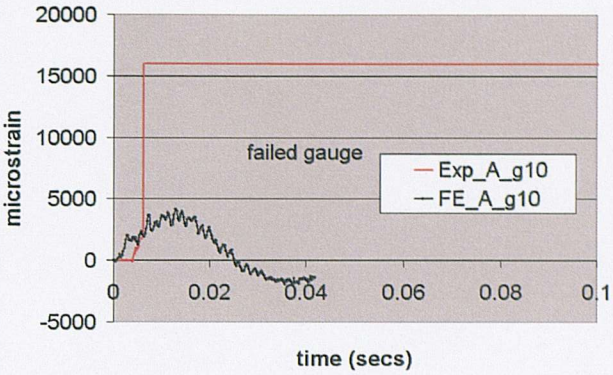
(g) g7



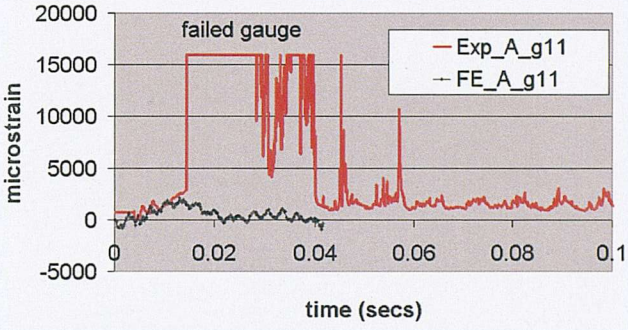
(h) g8



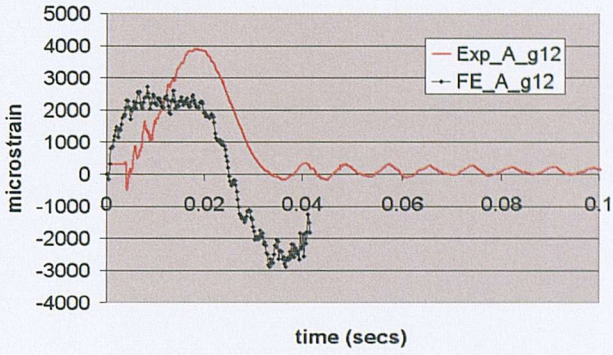
(i) g9



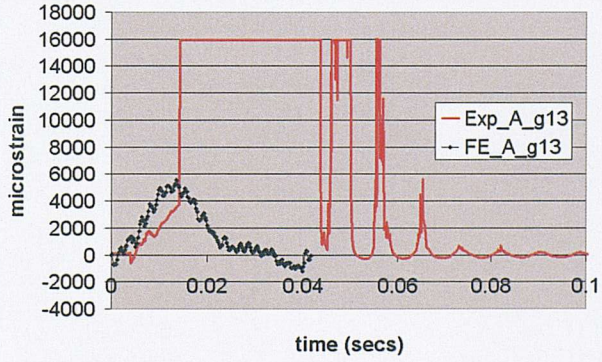
(j) g10



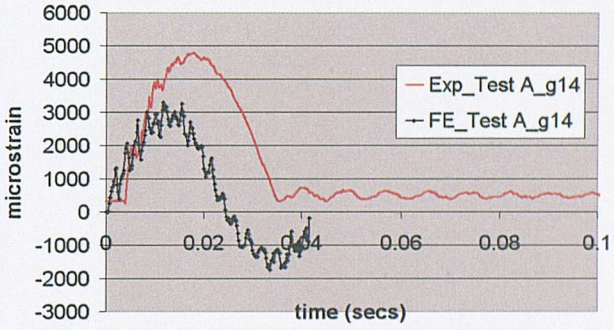
(k) g11



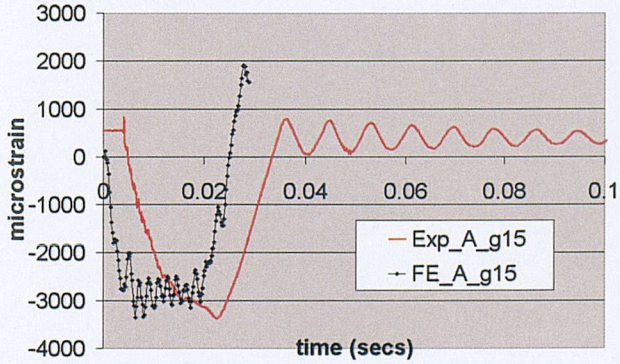
(l) g12



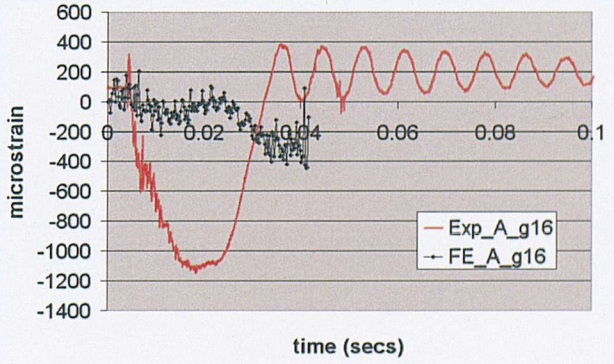
(m) g13



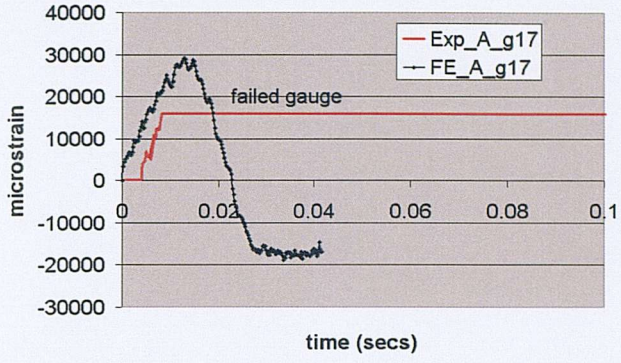
(n) g14



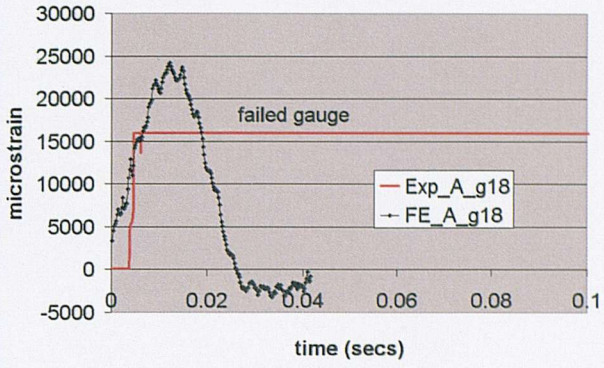
(o) g15



(p) g16

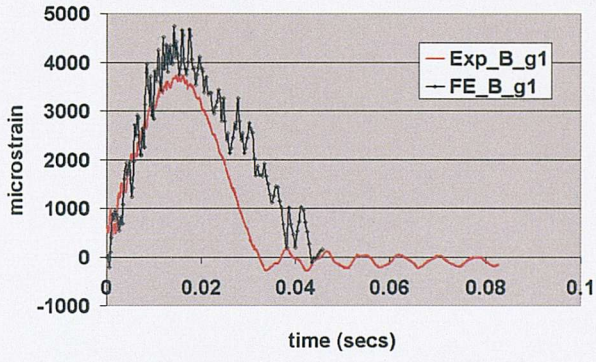


(q) g17

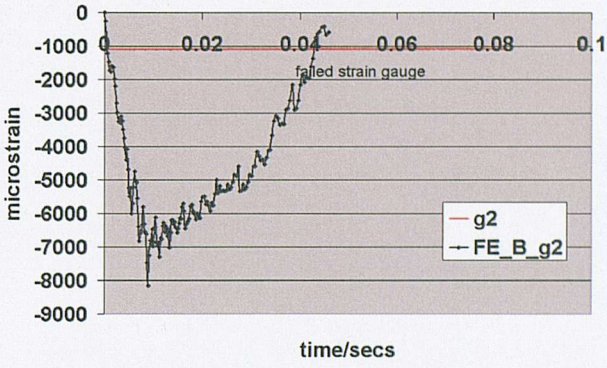


(r) g18

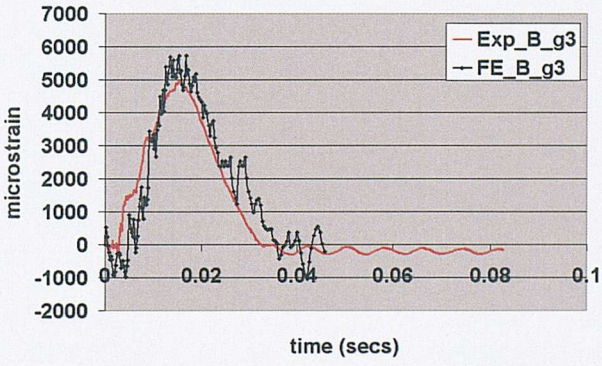
Figure 6-68. (a) to (r) Predicted and measured strains for test A, at gauge locations 1 to 18.



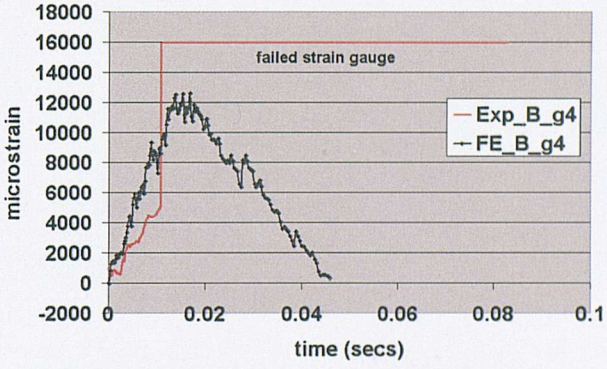
(a) g1



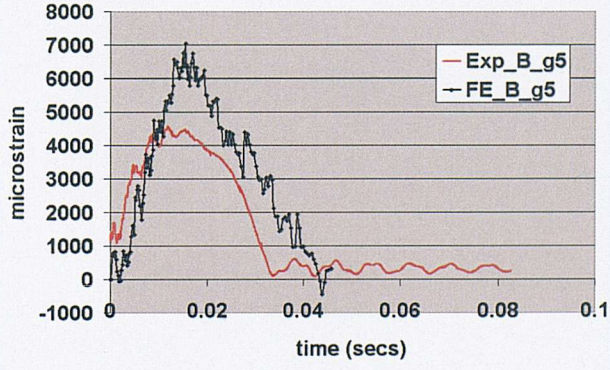
(b) g2



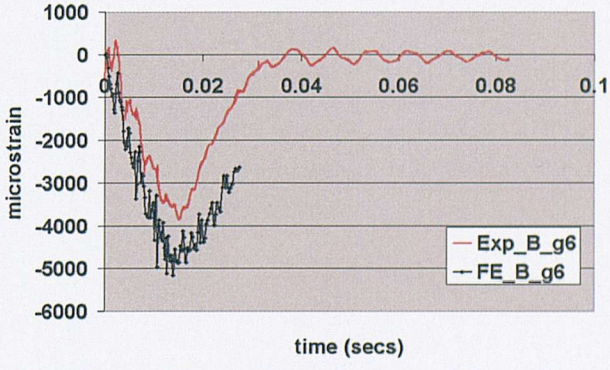
(c) g3



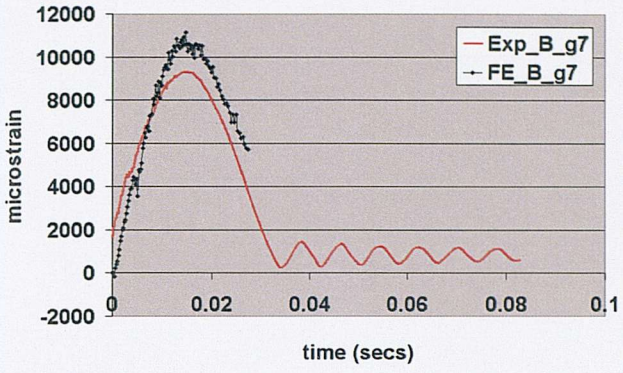
(d) g4



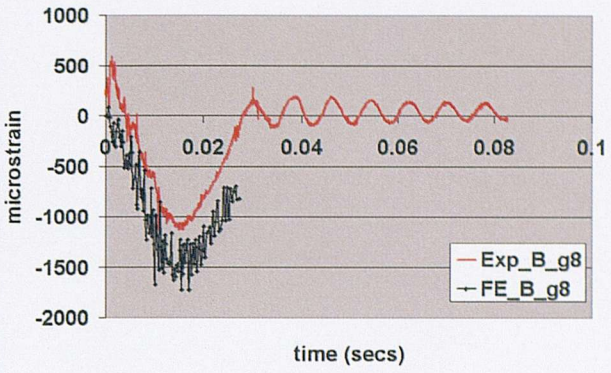
(e) g5



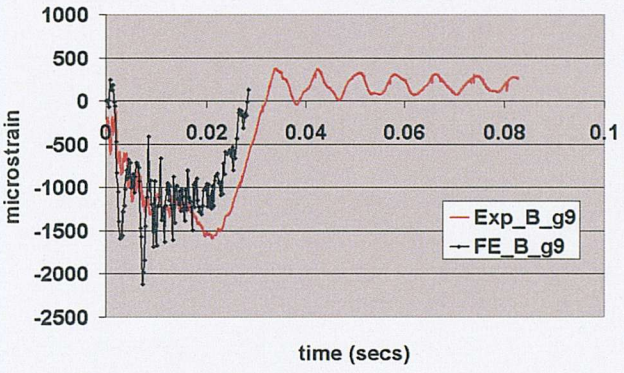
(f) g6



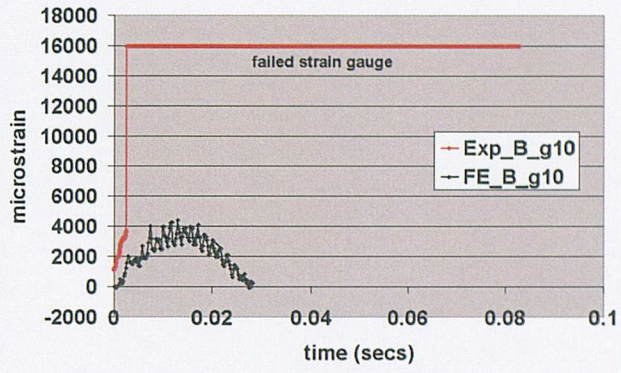
(g) g7



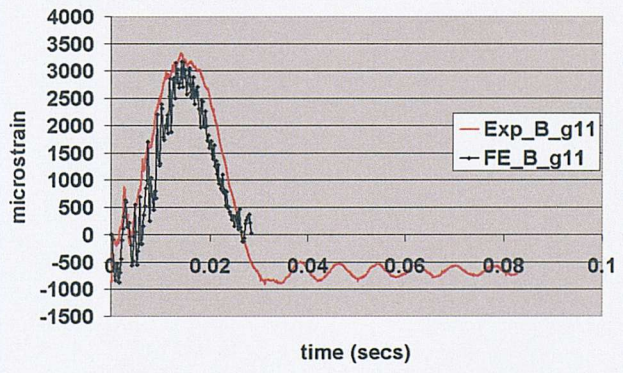
(h) g8



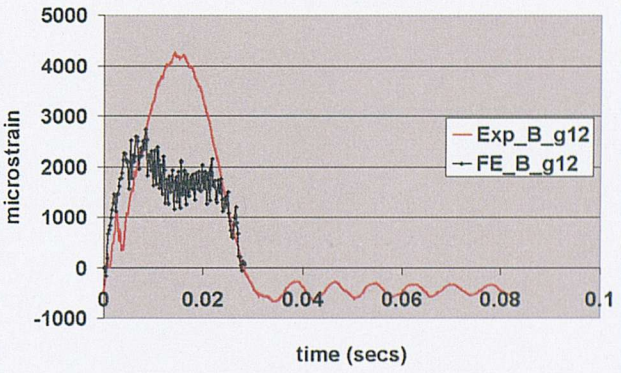
(i) g9



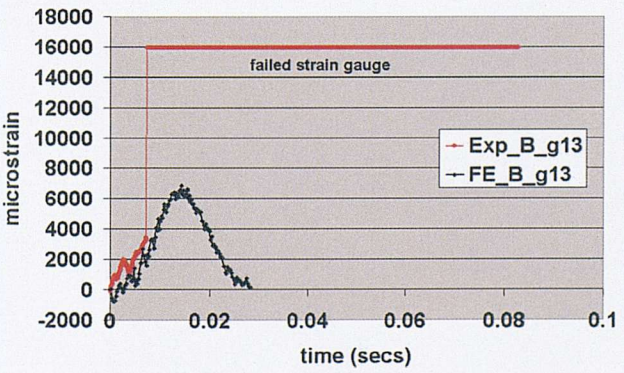
(j) g10



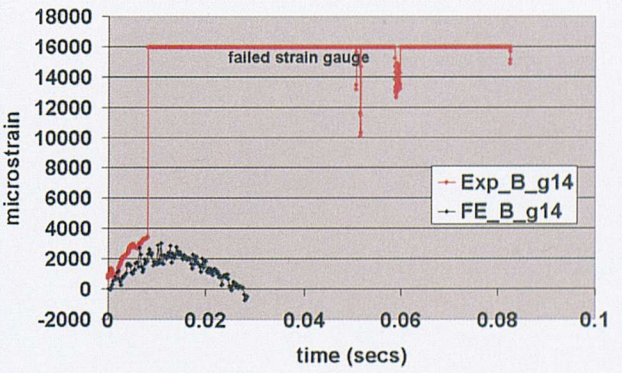
(k) g11



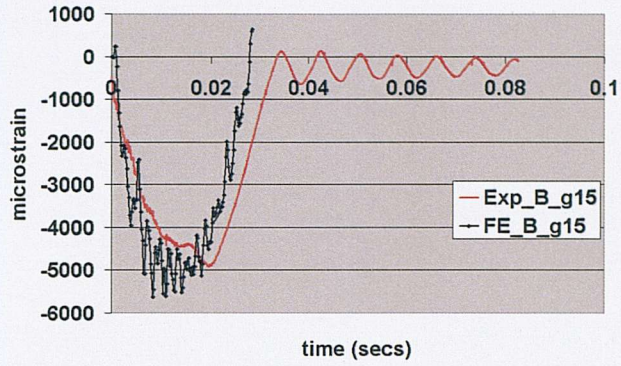
(l) g12



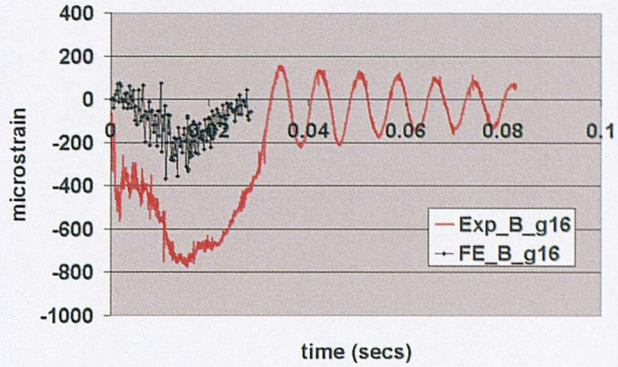
(m) g13



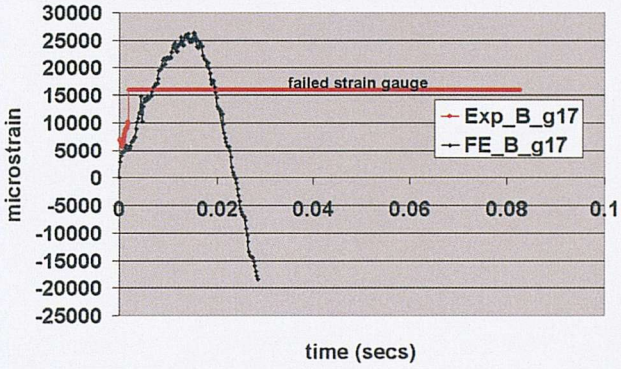
(n) g14



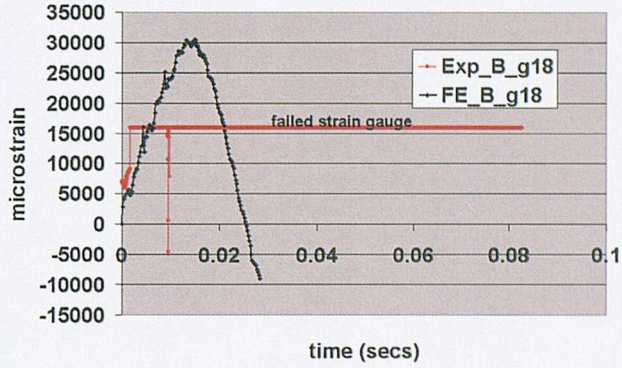
(o) g15



(p) g16

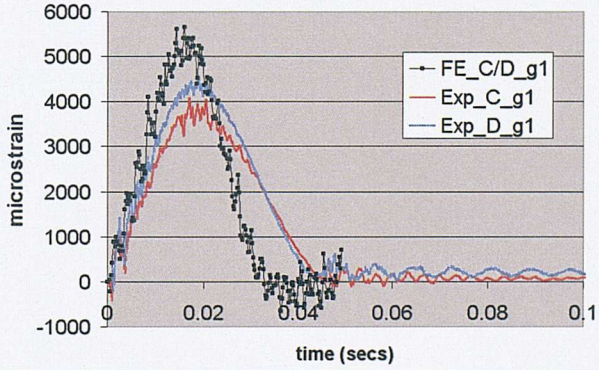


(q) g17

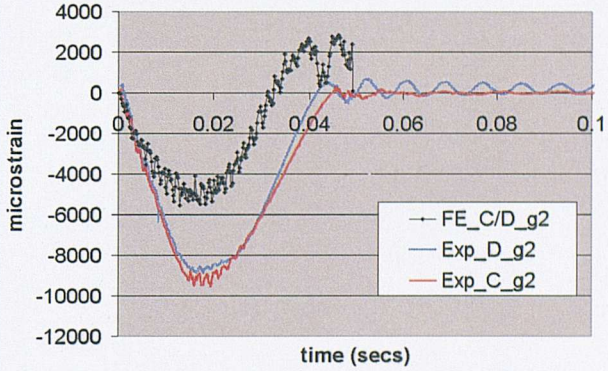


(r) g18

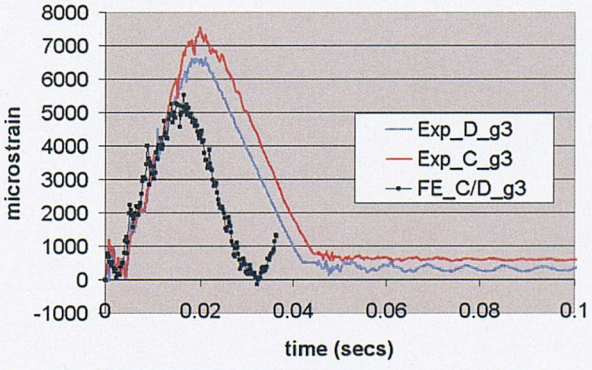
Figure 6-69. (a) to (r) Predicted and measured strains for test B, at gauge locations 1 to 18.



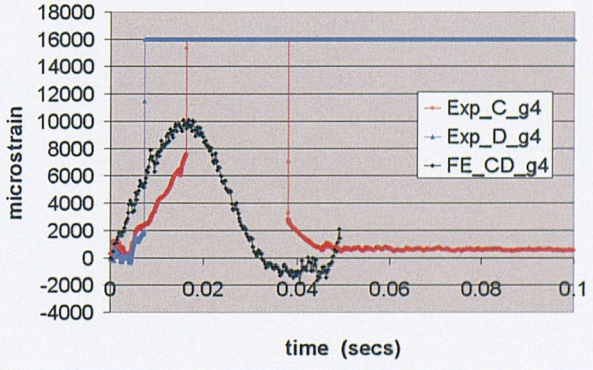
(a) g 1



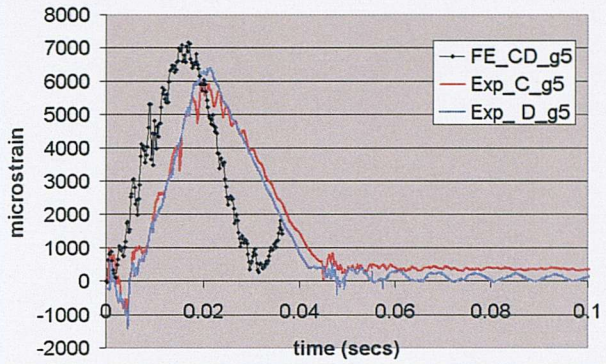
(b) g2



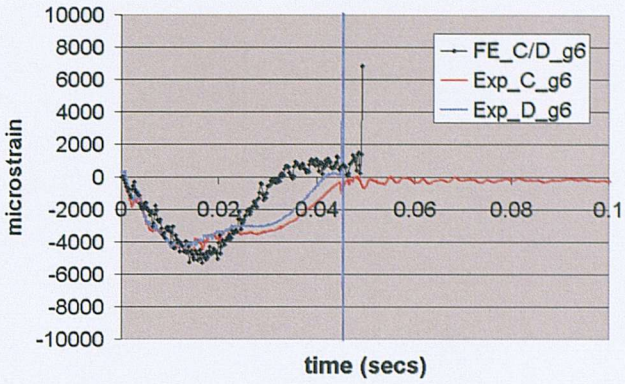
(c) g3



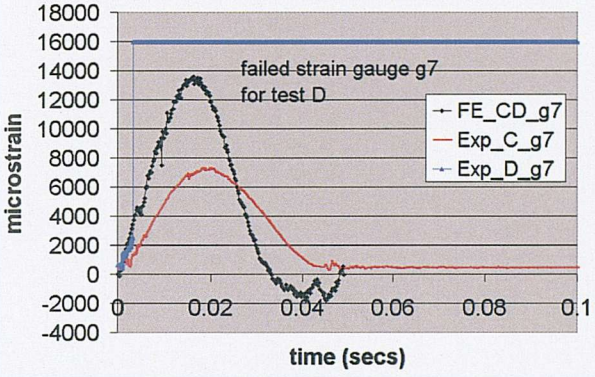
(d) g4



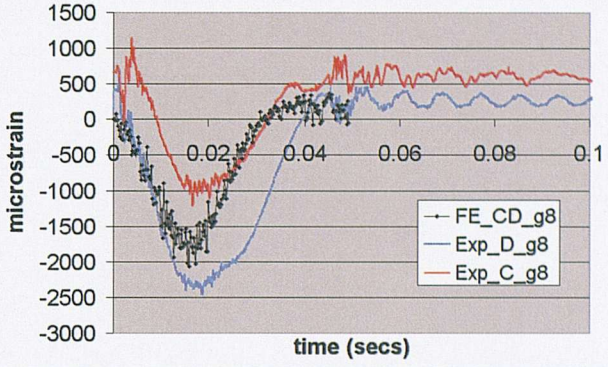
(e) g5



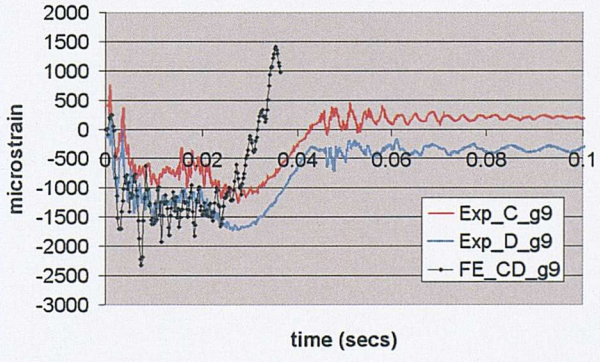
(f) g6



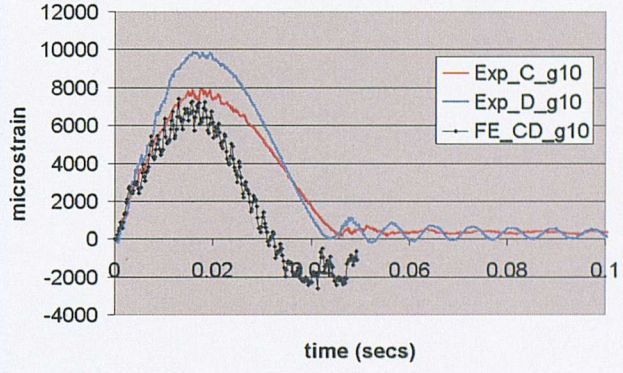
(g) g7



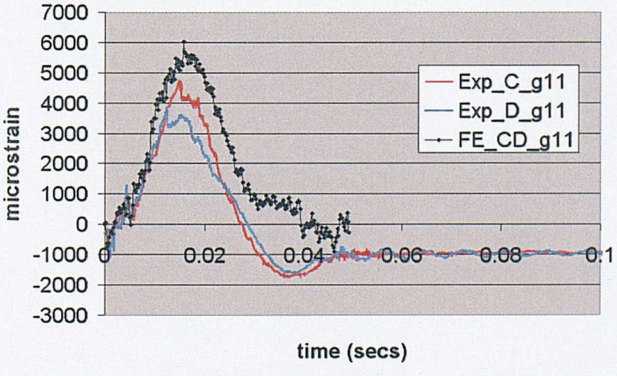
(h) g8



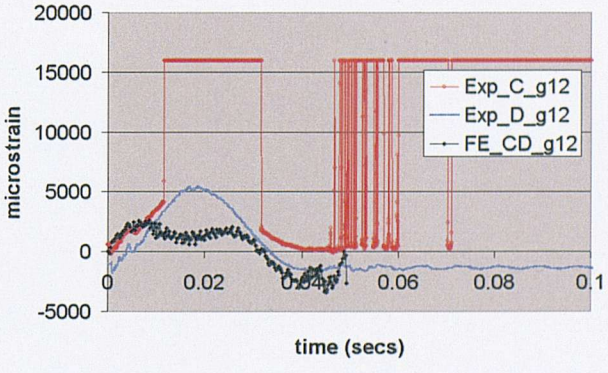
(i) g9



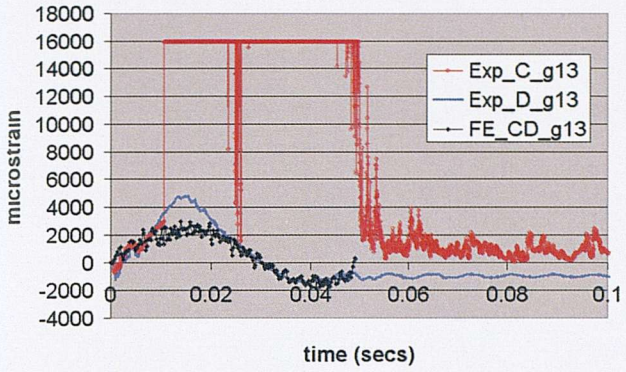
(j) g10



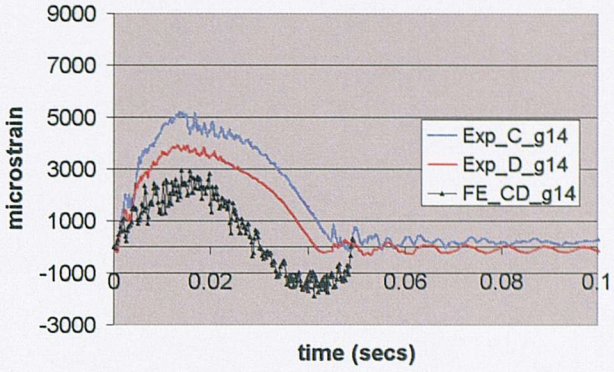
(k) g11



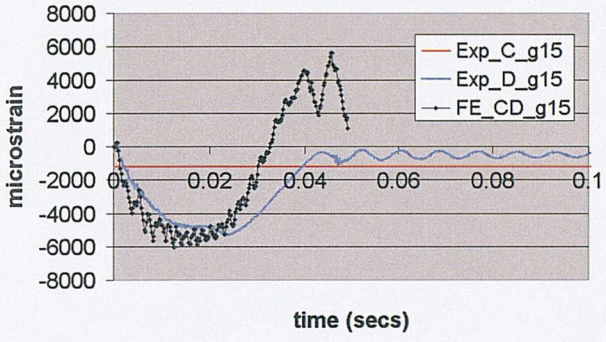
(l) g12



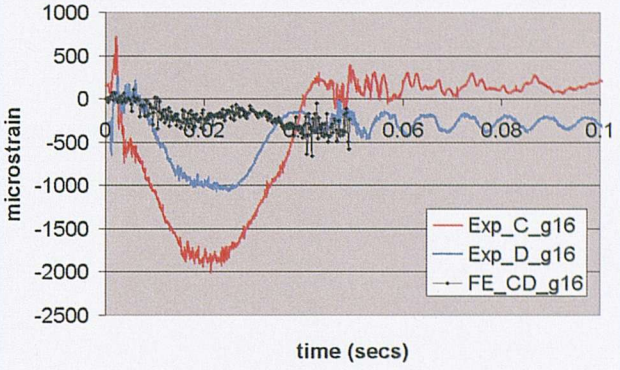
(m) g13



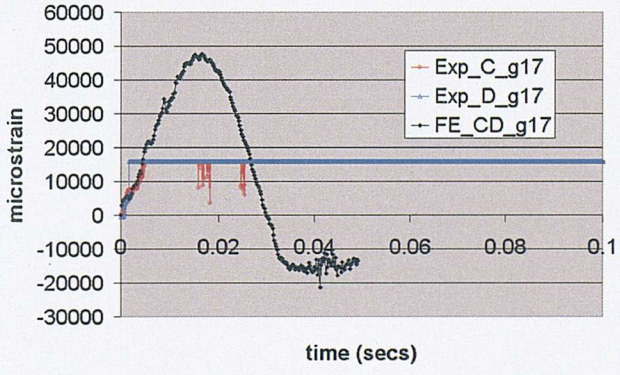
(n) g14



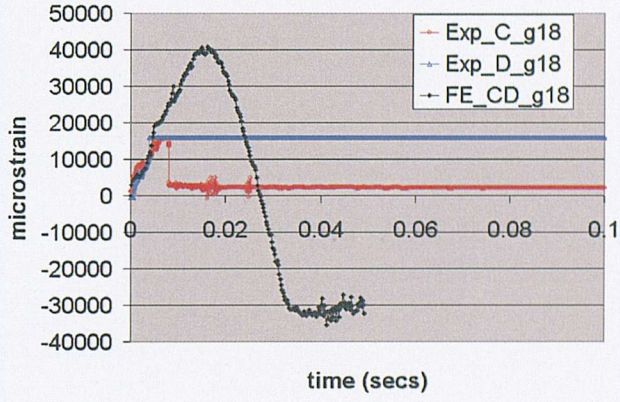
(o) g15



(p) g16



(q) g17



(r) g18

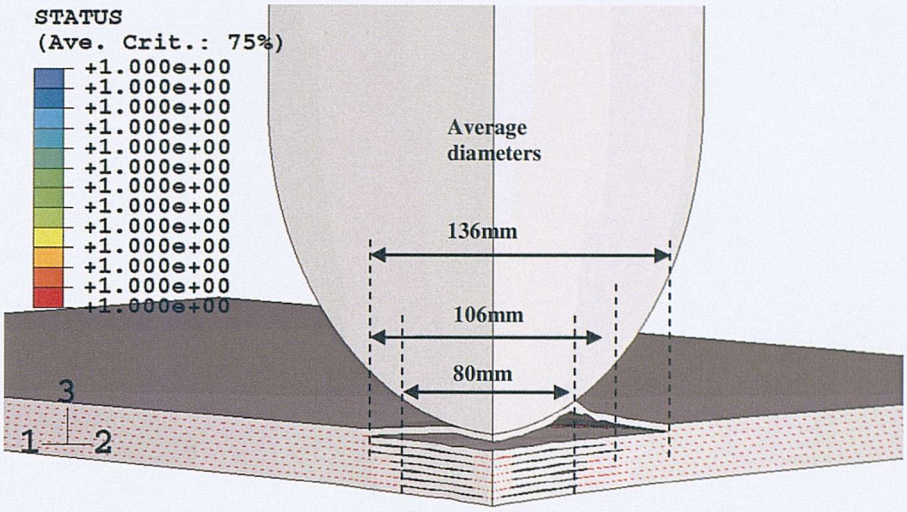
Figure 6-70. (a) to (r) Predicted and measured strains for tests C & D, at gauge locations 1 to 18.

6.3.4.3. Damage predictions

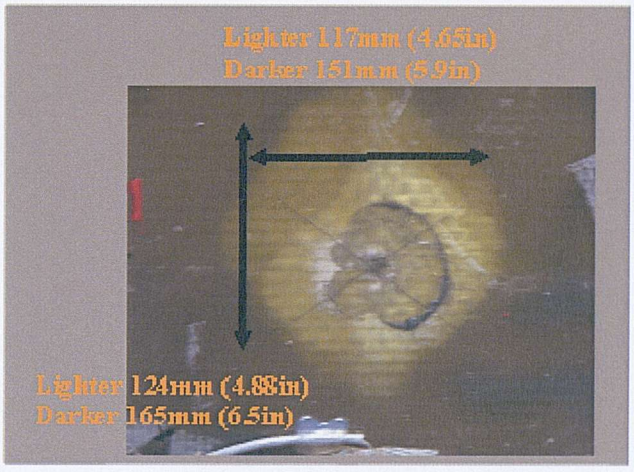
The largest delamination FE predictions were generally located just above the mid-thickness of the plates. Within the bottom half of the plate only, the largest delaminations were located on average about one quarter of the way from the bottom face.

The matrix/fibre and delamination damage predictions and test results for tests A, B and C are shown in Figure 6-71, Figure 6-72 and Figure 6-73 respectively. The contours of the damaged in-plane modulus for one of the fibre directions are shown in captions (c). Fibre

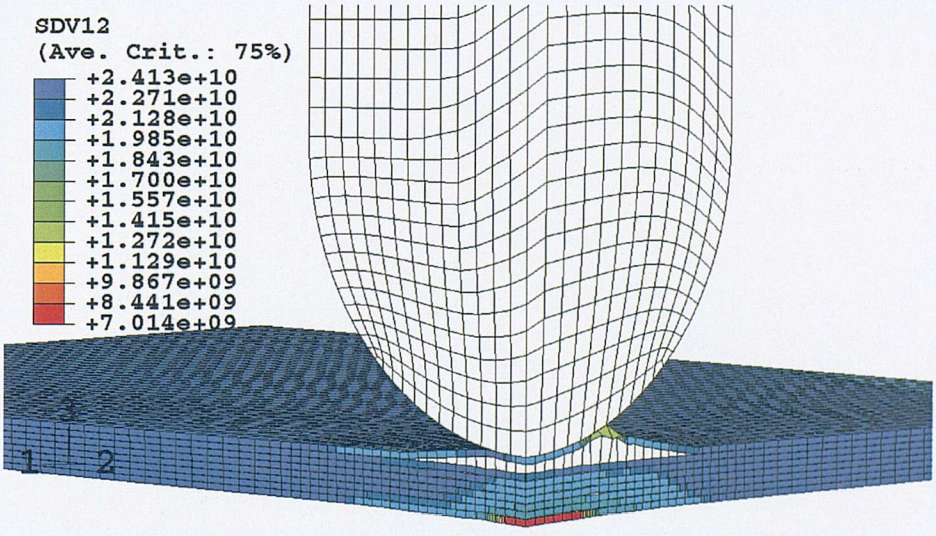
failure is represented with the red contours, which compares well with the actual fibre breakage observed at the bottom of the panels. Presenting the in-plane modulus contours individually does not give a full picture of the in-plane damage prediction and gives an illusion of unsymmetrical damage. Figure 6-74 shows an over-lay plot of line contours of moduli E_{11} and E_{22}, providing a better indication of the size of in-plane damage. Over all, the damage predictions are promising. The delamination areas visually measured in the tests from the top and bottom faces of the plate are shown in Table 6-10. The 'l' and 'w' measurements are the maximum 'length' and 'width' of the delamination (along the respective plate directions). The outer damage was measured as the lightest colored damage, closest to the outside face in question. The inner most damage was the darker discoloration, further form the outside face. The delamination predictions correlate quite well with the experimental trend: where the largest delaminations appear inside the plates, not at the surfaces. There were some small under-predictions, namely the largest delamination in the bottom half of the plate in test A, and some over-predictions such as the largest internal delamination area in test B. Figure 6-71(a) shows delamination whilst the tup is half way through it's rebound (tensile) phase, demonstrating the pending delamination for the plies just below the tup. These plies did not delaminate during the compression phase, indicating that the damage from shear alone was not large enough under compression to cause delamination. Recall that the normal transverse stress is not used in the traction-separation law damage initiation criterion when it is compressive. Although C-scan pictures would allow a more detailed comparison and quantification of the damage incurred, it is unlikely that the delamination predictions are accurate in their location. However, what the FE element predictions do predict reasonably well is the maximum delamination area, whether it lies internally or at a surface ply. Currently there is no experimental evidence relating to the through-thickness damage at the woven plies. However, for completion, the through-thickness contours for the three plates are illustrated in Appendix C.



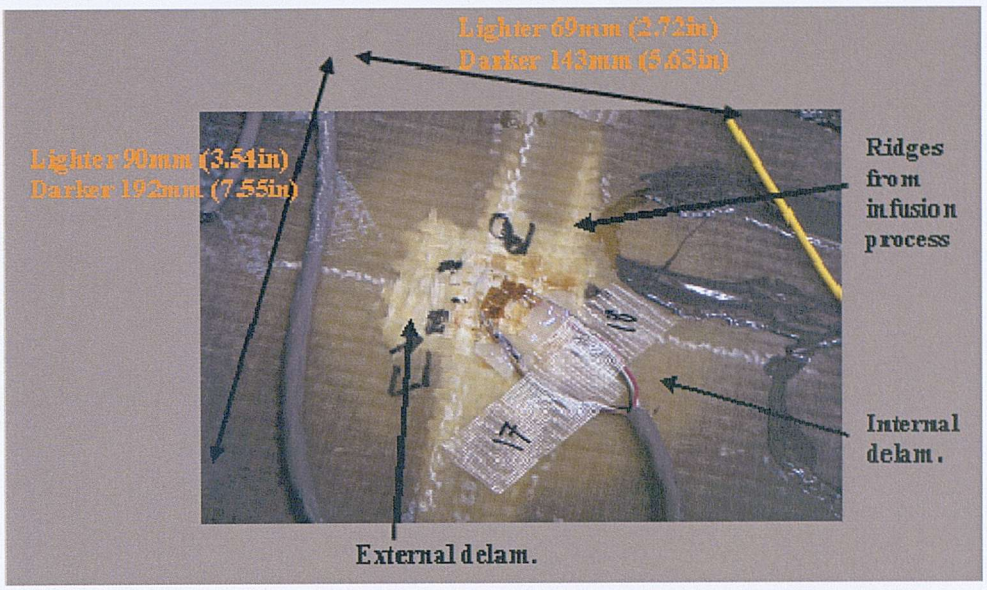
(a) Test A. Delamination prediction



(b) Test A. Damage seen at the centre of the panel from the top, impact face

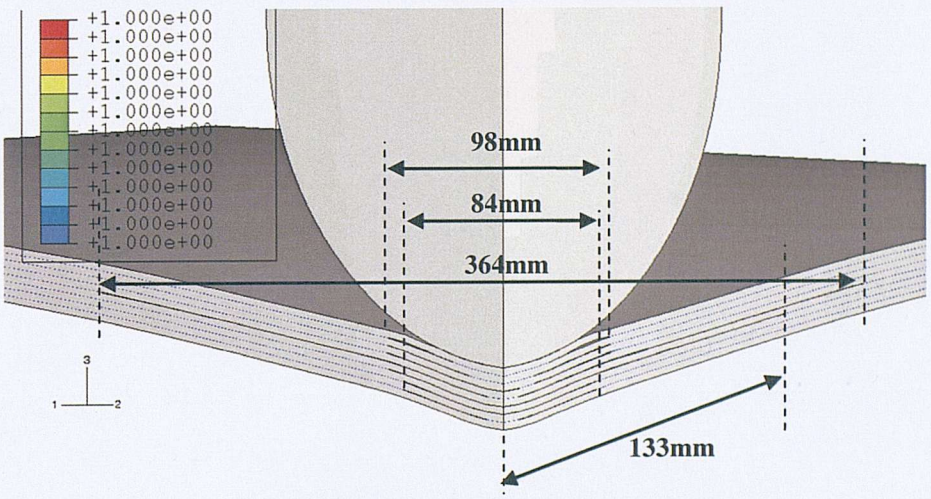


(c) Test A. In-plane damage, showing E11 modulus in Pa.

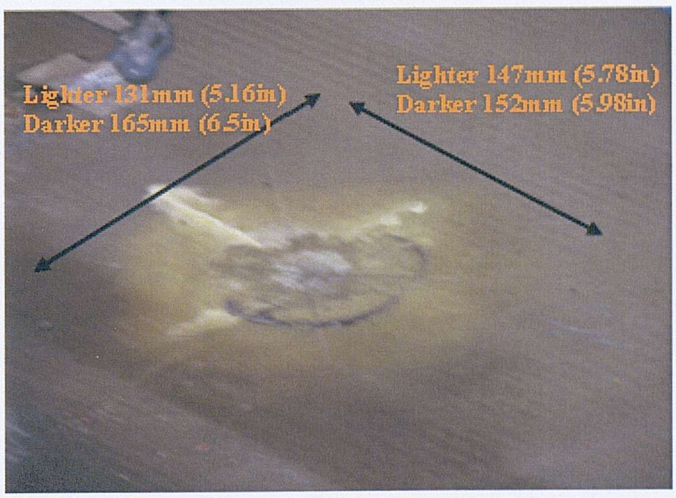


(d) Test A. Damage seen at the centre of the panel from the bottom face

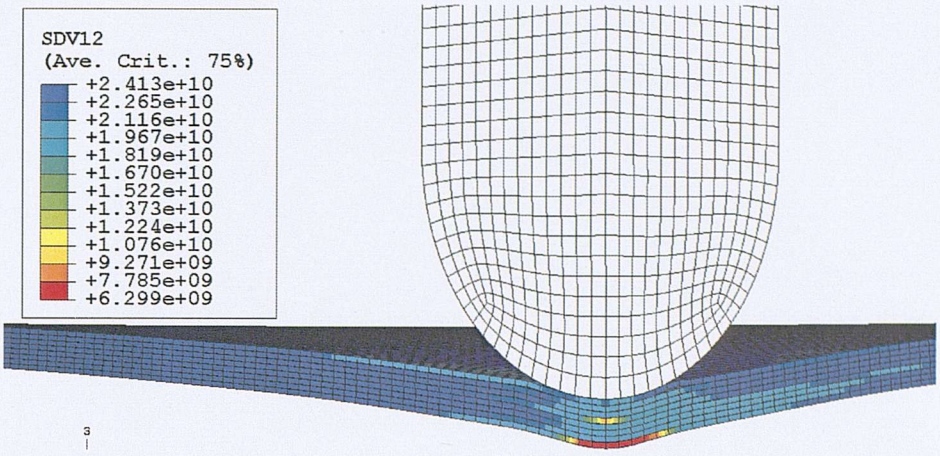
Figure 6-71. (a) to (d) Damage for test A – predicted and experimental



(a) Test B. Delamination prediction at t=0.0275secs.



(b) Test B. Damage seen from the top (impact face) of the plate

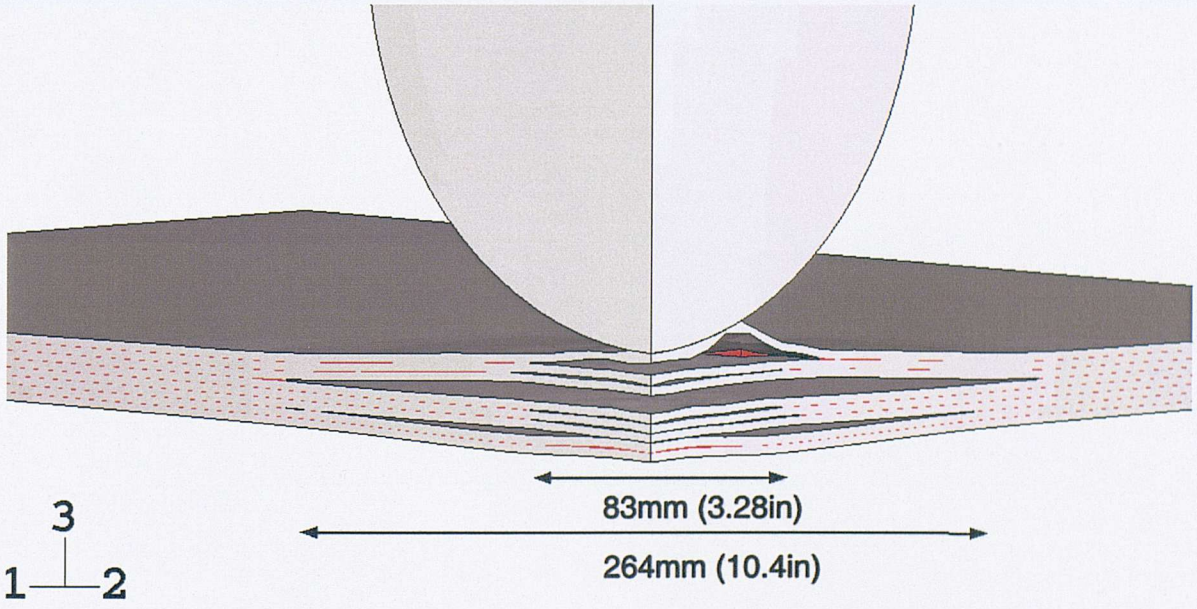


(c) Test B. In-plane damage – E_{11} modulus contours in Pa.

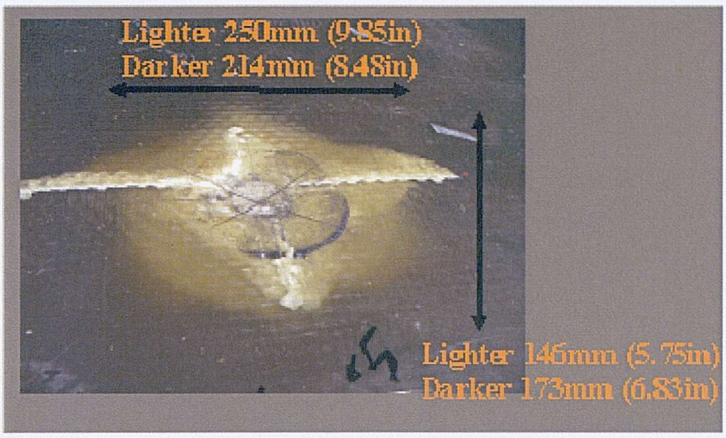


(d) Test B. Damage seen from the bottom of the plate

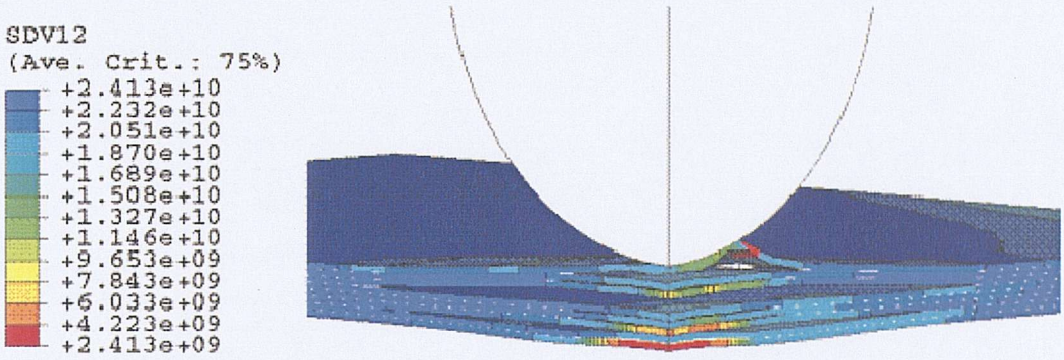
Figure 6-72. Damage for test B – predicted and experimental



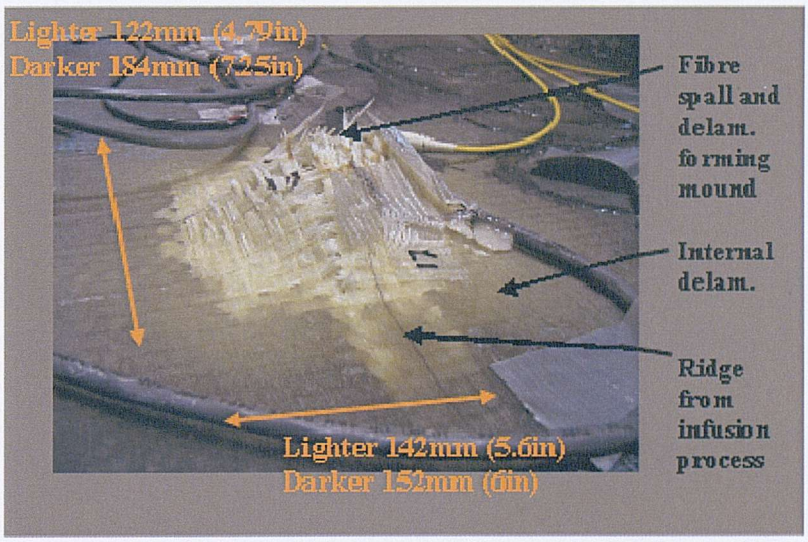
(a) Test C/D. Delamination prediction at t=0.0365secs



(b) Test D. Damage seen at the centre of the panel from the top face



(c) Test C/D. In-plane damage, showing E11 modulus in Pa.



(d) Test D. Damage seen at the centre of the panel from the bottom face

Figure 6-73. Experimental and predicted damage – test C/D

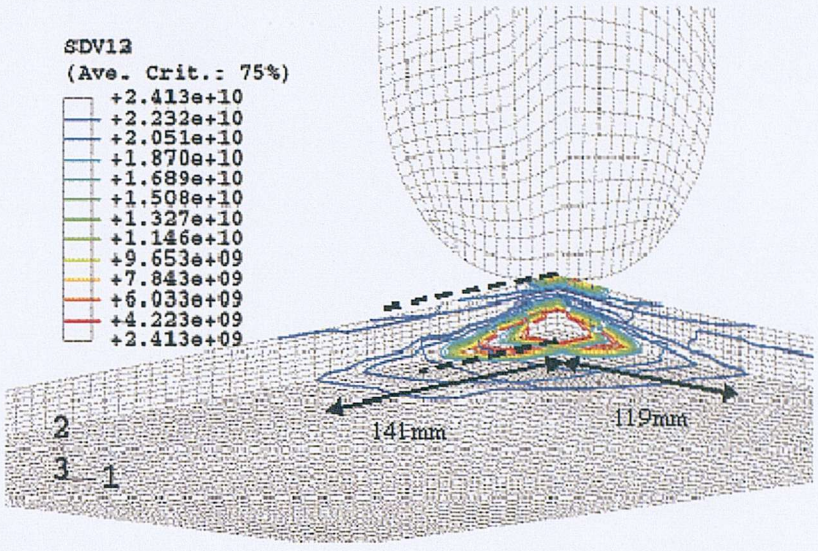


Figure 6-74. Finite element E_{11} and E_{22} modulus contours in Pa, for test C/D.

	TOP FACE (smooth)				BOTTOM FACE			
	lighter discoloration (lxw)/ mm		darker discoloration (l x w) / mm		lighter discoloration (l x w) /mm		darker discoloration (l x w) /mm	
	l	w	l	w	l	w	l	w
340kg, Test A	124	117	151	16	69	90	143	192
454.5kg, Test B	147	131	152	165	74	132	142	186
682kg, Test C	250	146	215	174	122	143	152	184
682kg, Test D	206	144	164	170	110	112	147	145

Table 6-10. Delamination areas measured for tests A, B, C and D

A closing comment must be to highlight the potential discrepancy in the finite element boundary conditions and those of the test. The plates were bolted down to the test fixture via holes drilled along the plate edges, see Figure 6-75. This boundary condition is not clamped but neither is it completely simply supported (as implemented in the FE model).

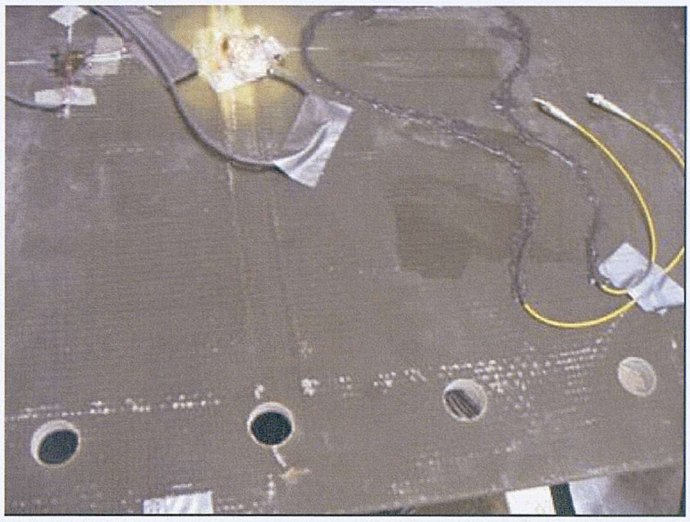


Figure 6-75. Holes along a large1 plate edge used to attach the plates to the test fixture

6.3.5. Large-scale plates 2

The large plate tests 'large2' were impacted with a 453kg tup of diameter 0.203m, as with large1, but the plate size is larger: 1.372x1.372x0.0381m (see Section 7.8.3.2 chapter 7). The effect of a full damage model and modelling 9 out of the total 57 cohesive layers is not as obvious as with the smaller plate tests. Figure 6-76 shows the contact-time history for a no-damage model with 6 solid elements through the thickness against a full damage model with 10 solid elements (thus the 9 cohesive layers). The peak contact force can often be misleading, as in this case, predicting a higher contact force for the full damage model. However, the latter produced more detailed frequency content. It is interesting to note the behaviour of the peaks between approximately $5(10^{-3})$sec when the damage begins, and $1.2(10^{-2})$sec by which point the bulk of the damage has been inflicted. The contact force appears to drop to zero just after $5(10^{-3})$sec which is when all except one of the layers delaminate underneath the impactor.

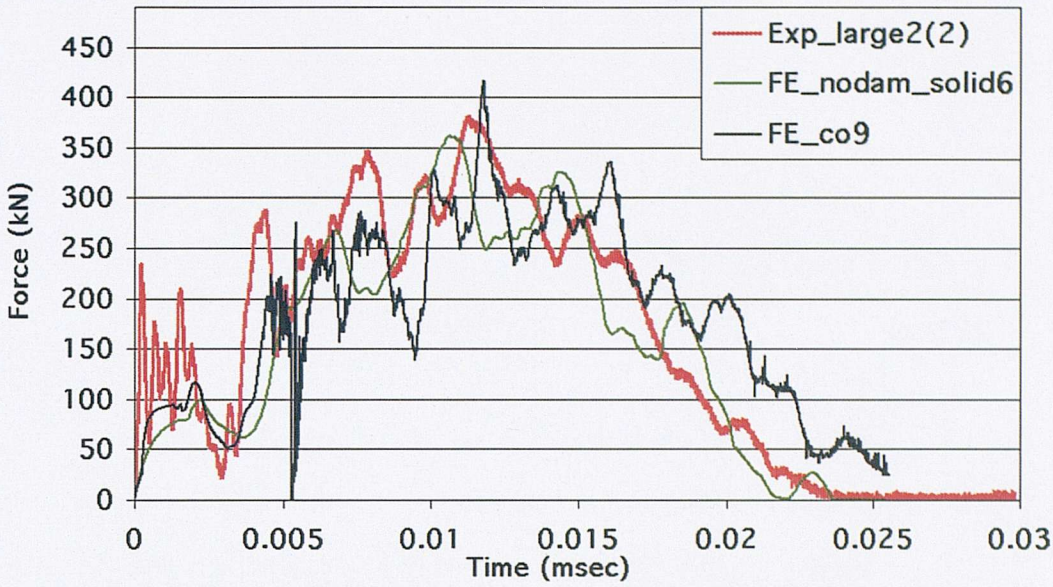


Figure 6-76. Contact force-time history for large2(2) and FE with 9 cohesive layers.

A better delamination prediction is achieved with this full damage model and 9 cohesive layers as opposed to the 5 cohesive layer delamination only model (see Chapter 5). Figure 6-77 shows delamination and E_{12} modulus contours. The maximum delamination size measured from the C-scan image (in Chapter 2) is larger than the largest measured for large1(B) impacted with almost exactly the same velocity and energy. Tests large1(C) and (D) produced a similar sized peak contact force yet the largest delaminations measured were smaller than compared to test large2(2). One of the significant energy absorbing mechanisms of the thinner plates was fibre breakage. The larger in-plane dimensions of the large2 plate must also been taken into account and the difference in boundary conditions because these latter observations are contrary to the those made by Zhou & Greaves [5]. They found that for identical impact forces the delamination areas of the thicker laminates were much smaller than those of the thin ones. Larger plate diameters will result in an increase in contribution of membrane stretching specially under clamped boundary conditions, Zhou & Greaves found it did not seem to affect the threshold forces corresponding to the onset of delamination.

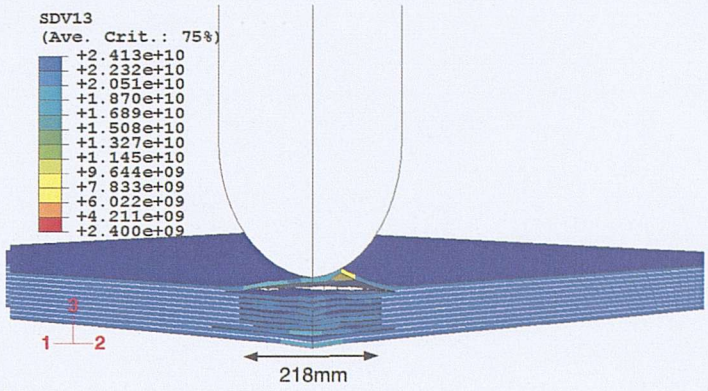


Figure 6-77. Delamination and E_{12} contours in Pa, for large2.

6.3.6. Energy versus contact force for the large plates

The kinetic energy for the four large plate tests (large1(A), (B), (C) and large2(2)) was plotted against the contact force using the experimental and predicted values (for the finer meshed models), see Figure 6-78. The contact force shows to increase with kinetic energy and more so when the plate is thicker. Large1(B) and large2 tests produced the same kinetic energy but the contact force was higher for the thicker large2 plate although the contact time was shorter. A broader range of large plate tests needs to be carried out to form a clearer relationship between the two variables.

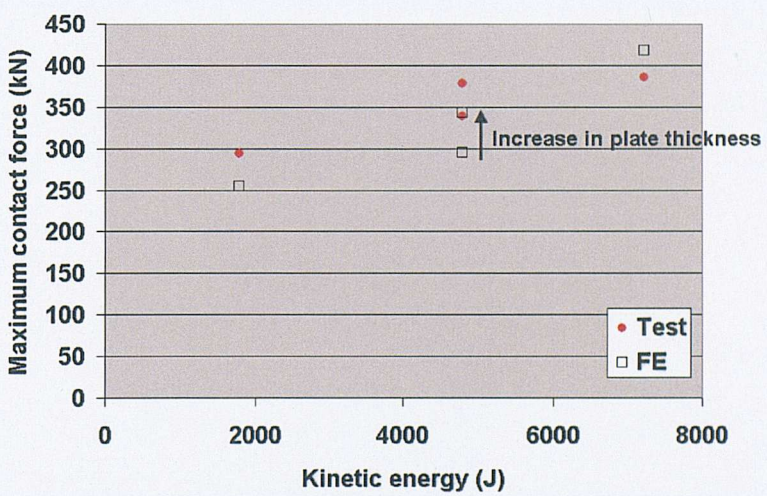


Figure 6-78. Relationship between kinetic energy and contact force for the large plates

6.3.7. Concluding remarks

There is limited literature on impact modelling of large-scale composite plates. This work shows how modelling in-plane and transverse damage is often necessary to effectively model the behaviour of thicker plates under transverse loading.

It was found that 3d damage model at the plies is the largest cause of reduction in contact force followed by the delamination model which also has the effect of stabilizing the contact behaviour through the absorption of some of the impact energy.

It was observed that modelling 3d damage at the ply level and delamination reduces the contact force by up to 36% compared to a no-damage model but increases the contact time and out-of-plane displacement compared to the experiment. An increase in cohesive layer modelling helps to reduce the contact force. However, thick plates with relatively few plies (in this case 9) simulated with cohesive layers at every inter-ply and a 2d damage model at the woven plies still gave a highly over-predicted contact force. To reduce this it was necessary to model through-thickness damage at the woven layers. However, inserting cohesive zones in between every ply may not be computationally reasonable for plates with many layers and modelling fewer cohesive layers can still provide satisfactory results as long as through-thickness damage is incorporated at the plies.

The relative tup and plate size affects the results and the larger tup diameter impacts benefit the most from the full cohesive layer model and transverse degradation of the woven plies. Smaller tup diameters produce a higher contact stress over the larger tups for the same impact energy and a rise in contact stress in the FE analyses predicts more damage which is turn exacerbated with increase in mesh density. The model predicts a higher element degradation in the impact zone with decrease in tup size than occurs in reality. The outcome is simply more conservative result.

There are limits to the maximum element size that should be used with the cohesive zone model, but for the scale of plates considered these element size requirements do not create a particularly fine mesh. The tup mesh and the relative mesh size between the tup and the plate has an effect on the contact force and delamination predictions however a coarser mesh generally predicts more conservative delamination results (the opposite of the matrix and fibre damage predictions at the woven layers). In order to have a coarser cohesive zone mesh relative to the solid element regions, requires applying tie constraints between the cohesive elements and the neighbouring solid elements. This has yet to be experimented with.

An in-plane orthotropic strain rate model at the woven plies would be beneficial in increasing the contact force predictions were localised damage is more prevalent i.e. with reduction in tup size, by creating a 'damage lag' effect. The ability to model the rate dependency of the material in the transverse direction may also make a substantial difference to the FE results with regard to the out-of-plane stress predictions.

Despite the limitations of the proposed 3d damage model, its application makes a substantial improvement to the contact force predictions and provides a good reflection of the size and severity of the damage incurred. The contact and mesh issues are not serious concerns with the range of plate scales considered, however it is an areas that must be addressed where a larger plate range is concerned.

6.4. Conclusion

Modelling delamination with resin-rich layers between laminated plies embedded within shell elements using the 2d energy for failure criterion, provides a reasonable, simple to use approximation of the behaviour of impacted plates. The maximum delamination areas are relatively well predicted however the sequence of delamination size through the thickness is not correctly modelled. The peak contact force although reduced compared to a no-damage model, is still generally notably higher than the test result. In contrast, Hashin's 2d failure criterion produced unpredictable and often erroneous matrix and fibre damage predictions.

Introducing a 3d gradually damaging model makes a substantial improvement to the damage size, shape, damage location predictions and contact force, giving relatively good correlations with experiment. The matrix and fibre damage modelling at the woven plies is carried out using simple damage mechanics concepts requiring cyclic tests for material data. Cohesive elements are a good method of modelling delamination and improve contact force predictions even if not all the cohesive regions are modelled as delaminating. However, these elements are not exempt from mesh density limitations.

Strain rate sensitivity is an issue that still needs addressing and its implementation may improve the contact force-time relationship during the impact phase of the tup, when the material is undergoing the most damage. This will have a knock on effect on the unloading phase of the impact event and improve the total time for impact prediction. One of the largest obstacles which must be over-come however, is the mesh sensitivity of the analyses which

prevents increasing the mesh size for the large plate analyses and results in long computational times. This is largely because of mesh constraints relating particularly to the mesh sensitivity of the cohesive zone model.

Large deformation of the elements appears to be generally reflective of rather harsh transverse damage criteria at the woven plies for a full cohesive layer model. However, there are some drawbacks with the C3D8R element. This brick element tends not to be stiff enough in bending, which shows in the lower contact force obtained over the S4R shell elements discussed earlier in Chapter 5. The stresses and strain outputs are most accurate at the integration points therefore the element size should be small in order to capture a stress concentration at the boundary of a structure. This will have an influence on the contact force calculations. The element has several spurious zero energy modes leading to a large amount of hourglassing: this means that the correct solution comes with unreasonably large displacements corresponding to the zero energy modes. This can only be improved but not eliminated by switching on the hourglass control.

Where less than the full number of cohesive regions is modelled, it is important to include a through-thickness damage model at the woven plies to effectively predict the contact force. Also, a poor contact definition can be very influential on the results (particularly on the contact force calculations), some of which is largely mesh dependent. There is some mesh dependency with both the damage models proposed. As long as tup penetration is not involved and for the range of plate sizes considered, an experienced user can mimimise this mesh dependency.

6.5. Reference List

1. Abaqus Users Manual. 6.5. 2005.

2. Wiedenman N, Dharan CKH. Ballistic penetration of compressively loaded composite plates. Journal of Composite Materials 2006; 40(12):1041-61.

3. Sutherland LS, Guedes Soares C. Impact characterisation of low fibre-volume glass reinforced polyester circular laminated plates. International Journal of Impact Engineering 2005; 31(1):1-23.

4. Mouritz AP. The damage to stitched GRP laminates by underwater explosion shock loading. Composites Science and Technology 1995; 55(4):365-74.

5. Zhou G, Greaves LJ. Damage resistance and tolerance of thick laminated woven roving GFRP plates subjected to low-velocity impact. In: Reid SR, Zhou G (eds.), Impact Behaviour of Fibre-reinforced Composite Materials and Structures. Woodhead Publishing Ltd, 2000: 133-83.

CHAPTER 7

Conclusion and Future Work

7.1 Conclusion

The marine industry has seen much growth in its research community and there is a growing demand for experimental data particularly on composite systems. There is also limited familiarity with the performance of finite element models and thick, large-scale composite plates, both under quasi-static in-plane loading and under shock loads. The current work presented an experimental and computational study on the buckling and post-buckling behaviour of thick woven roving large-scale composite plates. Furthermore, a validation study was carried out using existing plane stress damage criteria. Poor performance of these models under dynamic loading prompted the proposal of a simple damage mechanics model using an equivalent strain criterion for damage initiation. This model was tested on small and large-scale plates.

Prior to the current work, the in-plane strength of the 24oz WR E-glass/Derakane vinyl-ester panels was undocumented in the public domain and now a good appreciation of their strength has been derived experimentally. Moreover, an understanding has been acquired of the sensitivity of commercial FE software to different variables such as plate boundary conditions and imperfection size. The performance of a few of the most commonly used stress-based based criteria was also assessed under the in-plane loading conditions, pointing towards Hashin's 2d criterion as the better candidate. However, a modified version of Hashin's 2d failure criterion was proposed, proving to be the most successful in modeling the in-plane behaviour of the panel. Contrasting results were obtained under impact loading as Hashin's 2d stress criteria not only predicted excessive matrix and fibre damage but also in erroneous locations such as near the corners. Hashin's 3d matrix damage criterion was also inappropriate as a damage initiation criterion for impact loading using solid elements.

Most criteria are developed and tested on coupon-test scale specimens and although continuum damage mechanics approaches are now more prevalent, some of the models require complex test procedures and are limited to 2d damage modelling. The effect of full transverse material property degradation of thick large-scale composite plates has previously not been tested under impact. The proposal of the RR-layer model and the 3d damage model gave some indication of the importance of through-thickness modeling where thick plates are concerned.

Modelling delamination with resin-rich layers between laminated plies embedded within shell elements using 2d failure criteria, provides a reasonable, simple to use approximation of the behaviour of impacted plates. The maximum delamination areas were relatively well predicted however the sequence of delamination size through the thickness were not correctly modeled. The peak contact force although reduced compared to a no-damage model, was still generally notably higher than the test result. The analyses also re-confirmed that continuum shell elements are better for contact simulations than the standard S4R. The effect of an isotropic viscoplastic model at the resin-rich layers has a minimum effected on the contact force and damage predictions.

Despite the moderate success of the RR-layer method, introducing a 3d gradually damaging model made a substantial improvement to the damage size, damage location and contact force predictions, giving relatively good correlations with experiment and vast improvements compared to a no-damage model. The matrix and fibre damage modelling at the woven plies was carried out using simple damage mechanics concepts requiring cyclic tests for material data. A linear cohesive traction-separation law with high penalty stiffness, proved more successful than the computationally more expensive non-linear law. The cohesive elements are currently probably the most reliable method of modelling delamination and improve contact force predictions even if not all the cohesive regions are modelled as delaminating. However, these elements are not exempt from mesh density dependence. Also this method takes up a lot more computational time.

On the whole, good contact force, damage and strain predictions were obtained with the range of plate sizes considered. However there is a tendency to marginally over-predict the damage with the smaller plate and tup impacts and hence under-predict the size of the contact force with the lower energy large plate impacts. It is very important to note however, that a no-damage analysis also had the same affect and thus the problem may be partly due to the element choice. It was found that in an analysis modeling no damage, shell elements

(both the standard thick shell and continuum shell) predicted higher contact forces than the stacked solids used in these 3d damage models. The analyses may also benefit from an in-plane orthotropic viscoplastic model at the woven plies so that the damage rate is time dependent. This may help the stress and thus damage predictions predominantly in the central region of the impact site where much element distortion is seen.

The contact definition and the mesh density of the tup and plate collectively proved to be largely influential in the contact force predictions. The contact normals between the tup and the plate can be largely affected by mesh density and mesh density also affected the richness of the stress output which influenced the severity of damage predicted. An experienced user can minimise the influence of mesh density on the results over a certain range of plate sizes, however mesh-independency is important with even larger scales than those considered in this work. For the plate sizes considered, both models provided reasonable results using a sensible mesh size. Although there are some element size limitations with the cohesive zone model, greatly increasing the mesh density does not improve the contact force or damage predictions compared to the tests.

Where thick, large-scale plates are concerned and the model is discretised with solid elements, there are limitations regarding the number of cohesive layers that can be introduced, without over-reducing the element thickness or introducing an excessive amount of solid elements in the model. In order to model cohesive layers at every ply interface, forces the user to use shell elements, allowing element stacking if continuum shells are used but inevitably requiring plane stress damage criteria. Although this allows composite sub-layering, the computational time is likely to be far greater with increase in plate thickness and thus increase in the number of cohesive layers.

The continuum shells picked-up the contact frequencies more accurately than the solid elements but are of limited practicality in terms of transverse damage modelling. Up to now, they are can only provide section approximations of the transverse stresses, which are vastly affected by the number of elements stacked through the thickness. For composite applications, a shell element is typically composite sub-layered and each layer has one or more material integration points. The continuum shell elements are limited in their utility because the transverse stress approximations are not outputted at the material integration points and thus the values do not get fed into the user subroutine.

The in-plane RR-layer model with Hashin's 2d stress criterion over-predicted the contact force with the smaller tup impacts whereas the contrary is true with the 3d damage model. This corroborates the fact that transverse damage modelling is therefore very influential on the contact force predictions. It was observed that where less than the full number of cohesive regions is modelled, it is important to include through-thickness damage criteria at the woven plies to effectively predict the reduction in contact force over a no-damage model. This was particularly evident in contact simulations when the tup size is large relative to the plate size.

There are numerical limitations that prevent expansion of the damage model, the key being the inability to embed composite layers in solid elements in Abaqus/Explicit and the lack of knowledge of the element and integration point location within the user material subroutine. This prevents the use of applying any unit area or unit volume damage criteria. Despite this there are still controllable areas of the damage model which can undergo further development and these are outlined in *Further Developments*.

7.2 Future work

Some of the most important areas to undergo further development are listed below:

- Delamination

  - Failure in compression under the influence of both normal and shear stresses
  - Coupling of delamination and damage at woven layers
  - Scale-independence.
    - Mesh density issues when modelling large panels.

  This model would involve implementing a coupled (linear or non-linear) damage relationship between the transverse stresses. Moreover, this would allow failure of the cohesive element in compression to be influenced not only by the transverse shear stresses but also by the normal transverse stress. Scale-dependency is still an issue with cohesive zone modelling, particularly when it comes to larger plates than the ones considered in this report.

- 3d damage model

- Strain rate dependence
- Coupled continuum damage mechanics model (CDM)
  - Cyclic testing at various strain rates
- Scale-independence.
  - Coupon test data is currently used for large panels
  - Mesh density issues when modelling large panels.

So far, the strain rate sensitivity of the composite has not been included at the woven ply level in any of the models in this study. In order to implement a gradually degrading model (a CDM model) that is also strain rate sensitive requires cyclic testing to be carried out under the high strain rates. There is a limit to how this can be achieved with normal tensile/compressive loading machines before having to turn to more complicated tests involving the split-Hopkinson bar. In addition, the CDM model currently used in this study does not couple the in-plane and through-thickness damage criteria. This is another area of much scope. Scaling issues need also to be addressed with regards to the use of data from small-coupon tests for the modelling of very large plates. Also, mesh density is an important issue when modelling these plates. Keeping the same element size for all plate sizes is unrealistic for very large plates and does not resolve the material property scaling issue.

- Residual strength after impact

  - Damaged state after impact (Explicit/VUMAT
  - In-plane compression loading of damaged panel in Implicit/VUMAT

In order to obtain the residual strength of the panel after impact, the impacted panel must be loaded in-plane as with the intact panel, and thus strength values can be compared. Modelling this test implicitly requires the transfer of all the state dependent variables from the damaged model in Abaqus/Explicit into Abaqus/Standard.

- Full-scale modelling

The reason for seeking to develop a practical yet effective composite damage model is to eventually model the entire ship structure and enable the modelling of a structural component in more detail. This requires finer meshes and the mesh difference between the

detailed portion and the surrounding material will cause time step issues. How to deal with this is another important area to be examined.

APPENDIX A

A.1 Resin-rich layer model – viscoplasticity of resin-rich layers

$$\begin{Bmatrix} \dot{\varepsilon}^{p}_{11} \\ \dot{\varepsilon}^{p}_{22} \\ \dot{\varepsilon}^{p}_{12} \end{Bmatrix} = \begin{bmatrix} A_{11} \\ A_{22} \\ A_{12} \end{bmatrix} \alpha\dot{\sigma}_{kk} + \begin{bmatrix} A_{11}S_{11} \\ A_{22}S_{22} \\ 2A_{12}S_{12} \end{bmatrix} \frac{1}{\sqrt{S_{ij}S_{ij}}} \begin{Bmatrix} \dot{S}_{11} \\ \dot{S}_{22} \\ \dot{S}_{12} \end{Bmatrix}$$

Equation A.1. Plastic strain rate.

$$A_{11} = \frac{\sqrt{3}}{H^{p}} \left(\frac{S^{old}_{11}}{2\sqrt{\frac{1}{2}S^{old}_{ij}S^{old}_{ij}}} + \alpha\delta_{11} \right)$$

$$A_{22} = \frac{\sqrt{3}}{H^{p}} \left(\frac{S^{old}_{22}}{2\sqrt{\frac{1}{2}S^{old}_{ij}S^{old}_{ij}}} + \alpha\delta_{22} \right)$$

etc..

Equation A. 2. Coefficients in Equation A.1.

$$\{s_e\} = \frac{1}{E} \begin{bmatrix} 1 & -v & 0 \\ -v & 1 & 0 \\ 0 & 0 & 1+v \end{bmatrix}$$

Equation A. 3. Elastic compliance matrix.

$$\begin{Bmatrix} \dot{\varepsilon}_{11} \\ \dot{\varepsilon}_{22} \\ \dot{\varepsilon}_{12} \end{Bmatrix} = \frac{1}{E} \begin{bmatrix} 1+A_{11} & -v+A_{22} & 0 \\ -v+A_{11} & 1+A_{22} & 0 \\ 0 & 0 & 0 \end{bmatrix} \alpha\dot{\sigma}_{kk} + \frac{1}{E} \begin{bmatrix} (1+A_{11})S_{11} & (-v+A_{22})S_{22} & 0 \\ (-v+A_{11})S_{11} & (1+A_{22})S_{22} & 0 \\ 0 & 0 & (2(1+v)+A_{12})S_{12} \end{bmatrix} \begin{Bmatrix} \dot{S}_{11} \\ \dot{S}_{22} \\ \dot{S}_{12} \end{Bmatrix}$$

Equation A. 4. Total strain rate

$$d\sigma^{new}_{ij} = \begin{pmatrix} s_{11} & s_{12} & s_{16} \\ s_{21} & s_{22} & s_{26} \\ s_{61} & s_{62} & s_{66} \end{pmatrix} \begin{Bmatrix} d\varepsilon_{11} \\ d\varepsilon_{22} \\ d\varepsilon_{12} \end{Bmatrix} - \left\{ \frac{\begin{pmatrix} s_{11} & s_{12} & s_{16} \\ s_{21} & s_{22} & s_{26} \\ s_{61} & s_{62} & s_{66} \end{pmatrix} d\lambda \frac{\partial f}{\partial \sigma_{11}} \begin{Bmatrix} d\varepsilon_{11} \\ d\varepsilon_{22} \\ d\varepsilon_{12} \end{Bmatrix}}{d\sigma^{old}_{11} + \begin{pmatrix} s_{11} & s_{12} & s_{16} \\ s_{21} & s_{22} & s_{26} \\ s_{61} & s_{62} & s_{66} \end{pmatrix} d\lambda \frac{\partial f}{\partial \sigma_{11}}} \right\}$$

Equation A. 5. Increment in stress

APPENDIX B

B.1 Non-linear model

	Normal	Shear
Loading	$\frac{\partial \tau_n(u_n,\lambda)}{\partial u_n} = \frac{27}{4U_n^f}\tau_{max}(1-\lambda)^2$ $\frac{\partial \tau_n(u_n,\lambda)}{\partial \lambda} = \alpha\frac{u_n}{U_n^f}\frac{27}{2}\tau_{max}(\lambda-1)$ $\frac{\partial \lambda}{\partial u_n} = \frac{u_n}{U_n^{f2}}\frac{1}{\lambda}$	$\frac{\partial u_{ts}}{\partial u_t} = \frac{u_t}{u_{ts}}$ $\frac{\partial \tau_{ts}(u_{ts},\lambda)}{\partial u_{ts}} = \alpha\frac{1}{U_t^f}\frac{27}{4}\tau_{max}(1-\lambda)^2$ $\frac{\partial \tau_{ts}(u_{ts},\lambda)}{\partial \lambda} = \alpha\frac{u_{ts}}{U_t^f}\frac{27}{2}\tau_{max}(\lambda-1)$ $\frac{\partial \lambda}{\partial u_{ts}} = \frac{u_{ts}}{U_t^{f2}}\frac{1}{\lambda}$
Unloading	$\frac{\partial \tau_n}{\partial u_n} = \frac{\tau(\lambda_u)\lambda}{U_n^f\lambda_u}$ $\frac{\partial \tau_n}{\partial \lambda} = \frac{u_n\tau(\lambda_u)}{U_n^f\lambda_u}$	$\frac{\partial \tau_t}{\partial u_n} = \frac{\alpha\tau(\lambda_u)\lambda}{U_t^f\lambda_u}$ $\frac{\partial \tau_t}{\partial \lambda} = \alpha\frac{u_t}{U_t^f}\frac{\tau(\lambda_u)}{\lambda_u}$

Table B.1. Constituents of differential equations.

APPENDIX C

FE modulus degradation contours

C.1 Damage Results – 12.7mm tup tests

These FE results were carried out with the 3d damage model and cohesive elements (chapter 6) using the global strain criterion for prediction of damage initiation and the linear coupled traction-separation law.

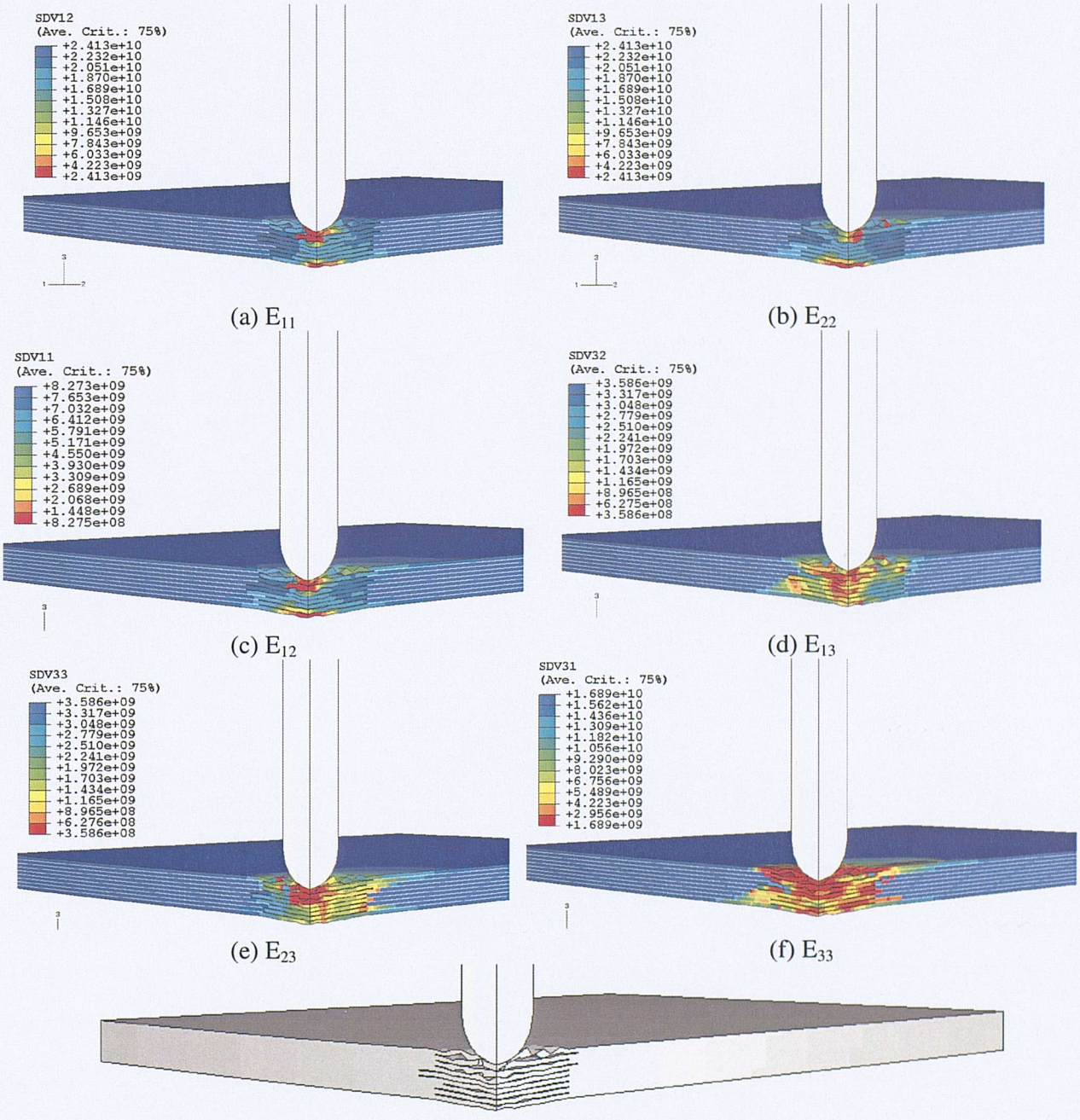


Figure 1. Test 1S(91J), FE modulus contours and delamination, exclusive of element erosion

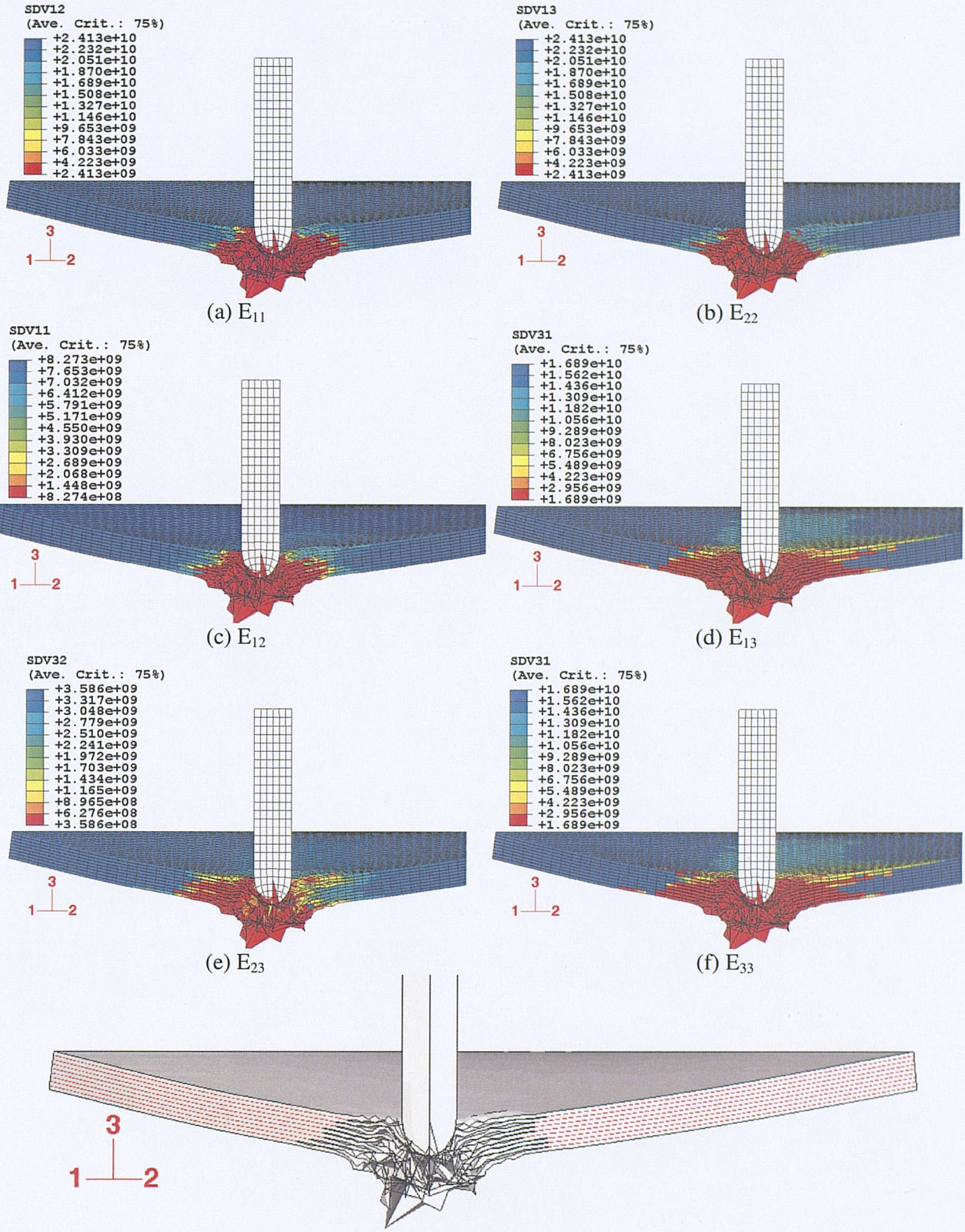
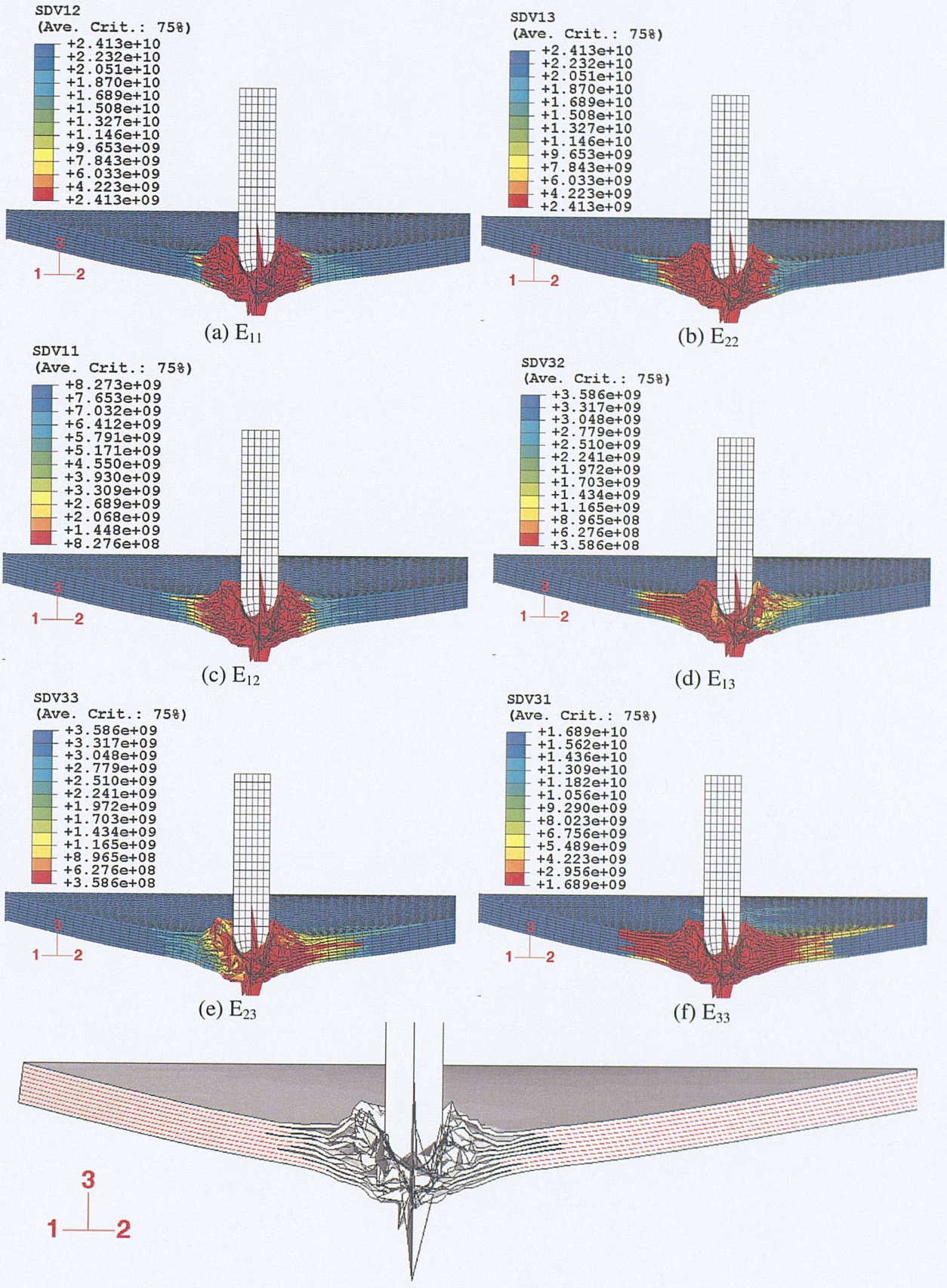


Figure 2. Test 2S(140J), FE modulus contours and delamination, exclusive of element erosion



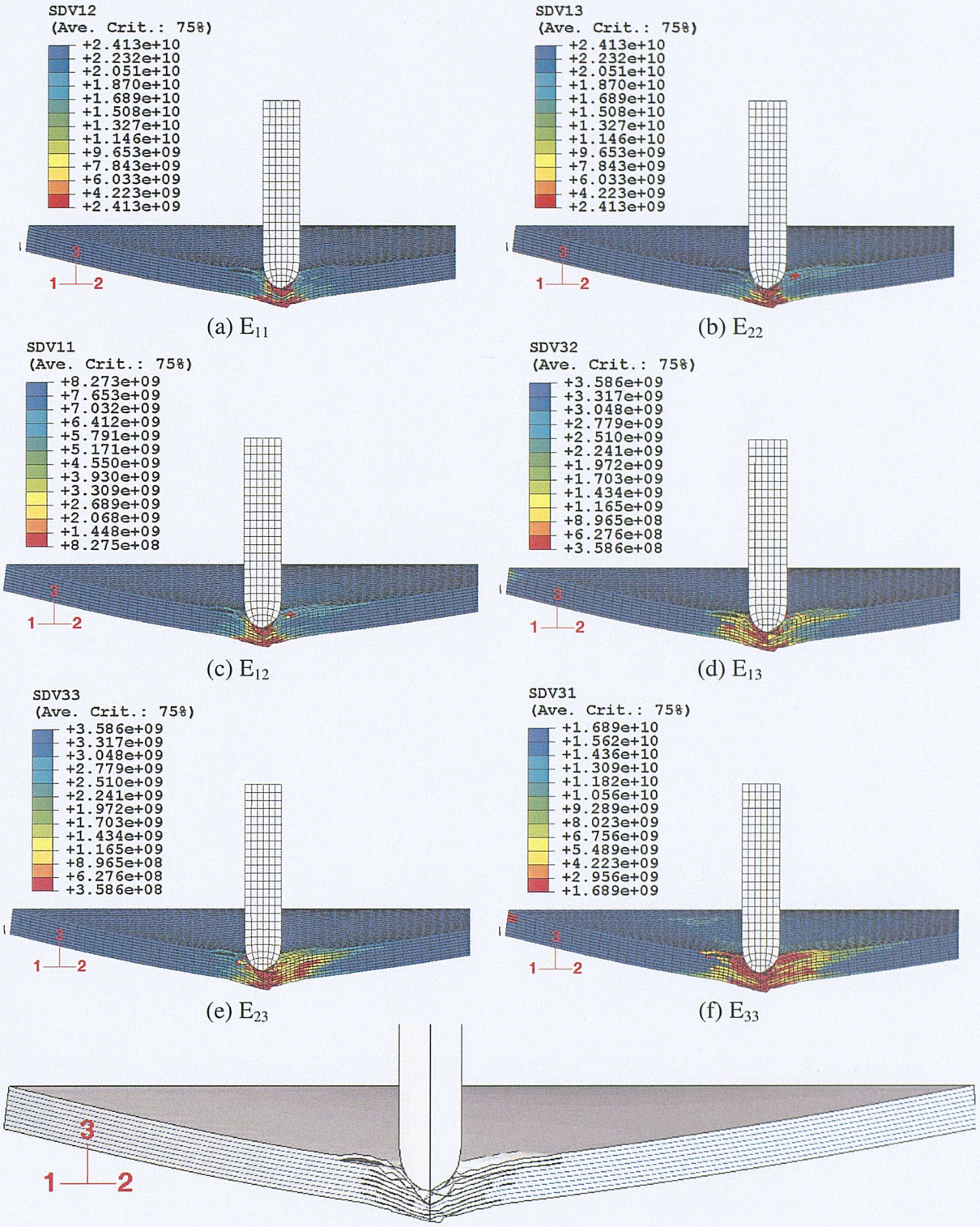
(a) E_{11} (b) E_{22}

(c) E_{12} (d) E_{13}

(e) E_{23} (f) E_{33}

(g) Delamination, (showing full plate)

Figure 3. Test 3S(166J), FE modulus contours and delamination, exclusive of element erosion



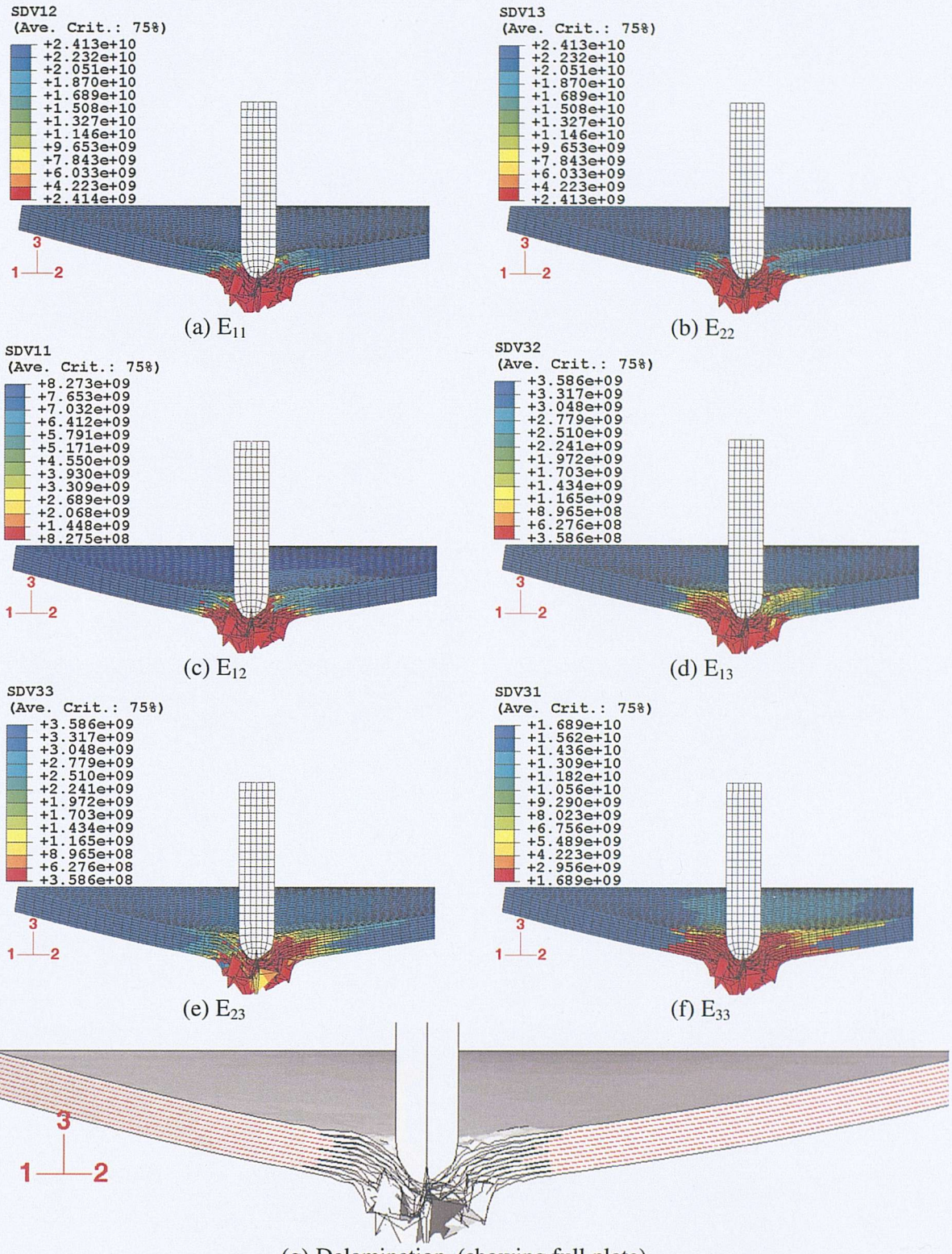
(a) E_{11} (b) E_{22}

(c) E_{12} (d) E_{13}

(e) E_{23} (f) E_{33}

(g) Delamination, (showing full plate)

Figure 4. Test 4(193J), FE modulus contours and delamination, exclusive of element erosion



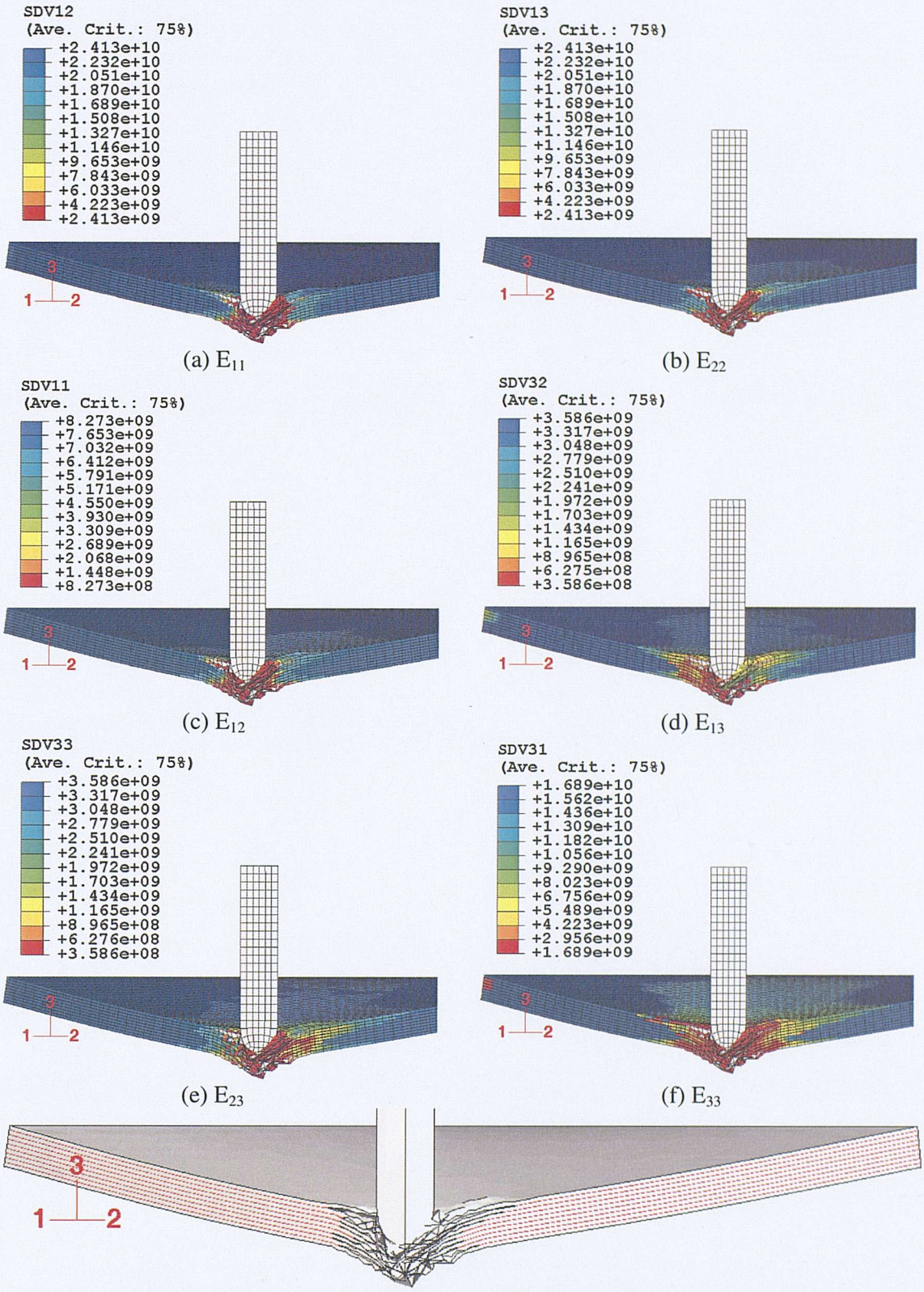
(a) E_{11} (b) E_{22}

(c) E_{12} (d) E_{13}

(e) E_{23} (f) E_{33}

(g) Delamination, (showing full plate)

Figure 5. Test 5S(195J) , FE modulus contours and delamination



(a) E_{11} (b) E_{22}

(c) E_{12} (d) E_{13}

(e) E_{23} (f) E_{33}

(g) Delamination, (showing full plate)

Figure 6. Test 6(196J), FE modulus contours and delamination

C.2 Damage Results – 25.4mm tup tests

These FE results were carried out with the 3d damage model and cohesive elements (see chapter 6) using the global strain criterion for prediction of damage initiation and the linear coupled traction-separation law.

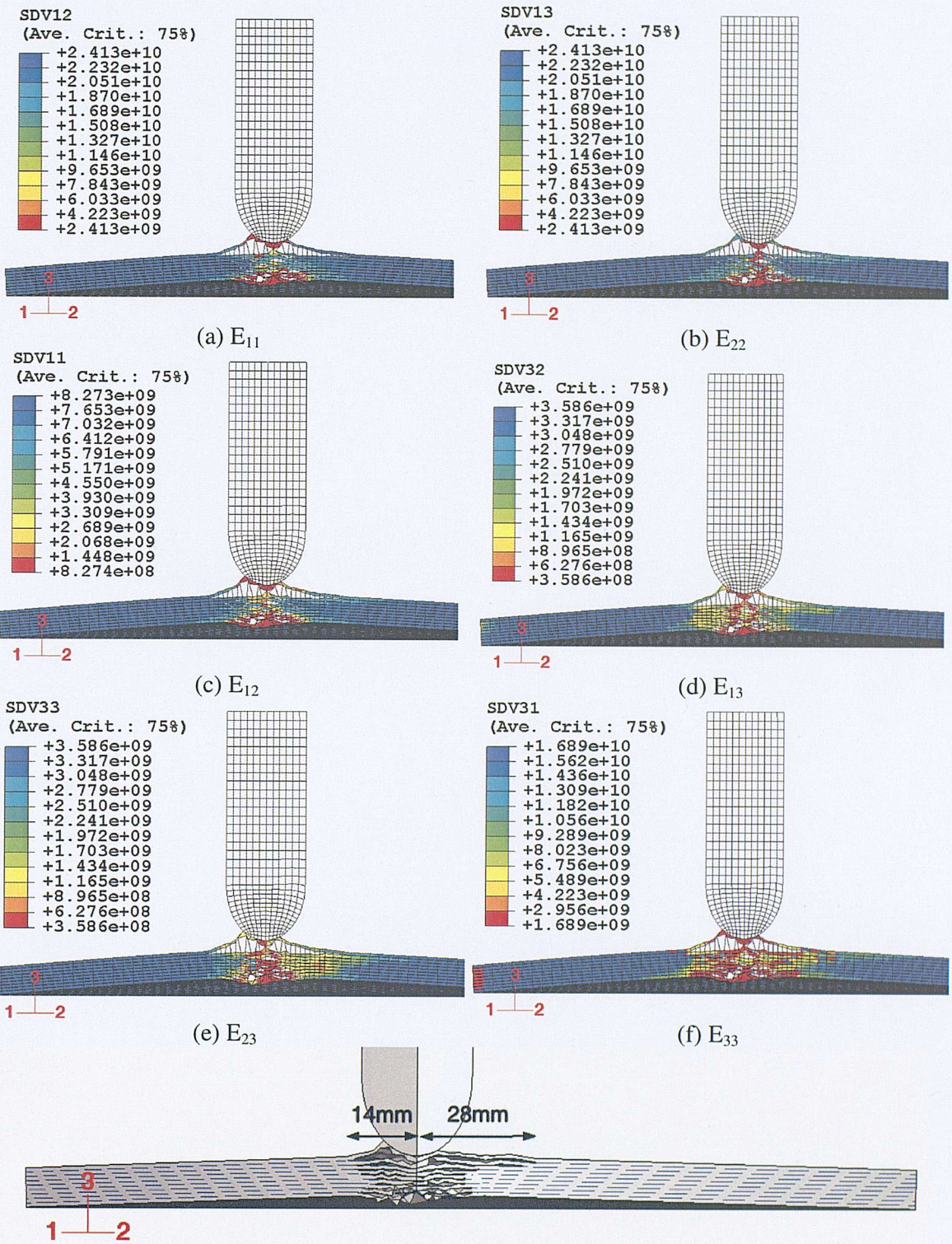


Figure 7. Test 20(J), FE modulus contours and delamination

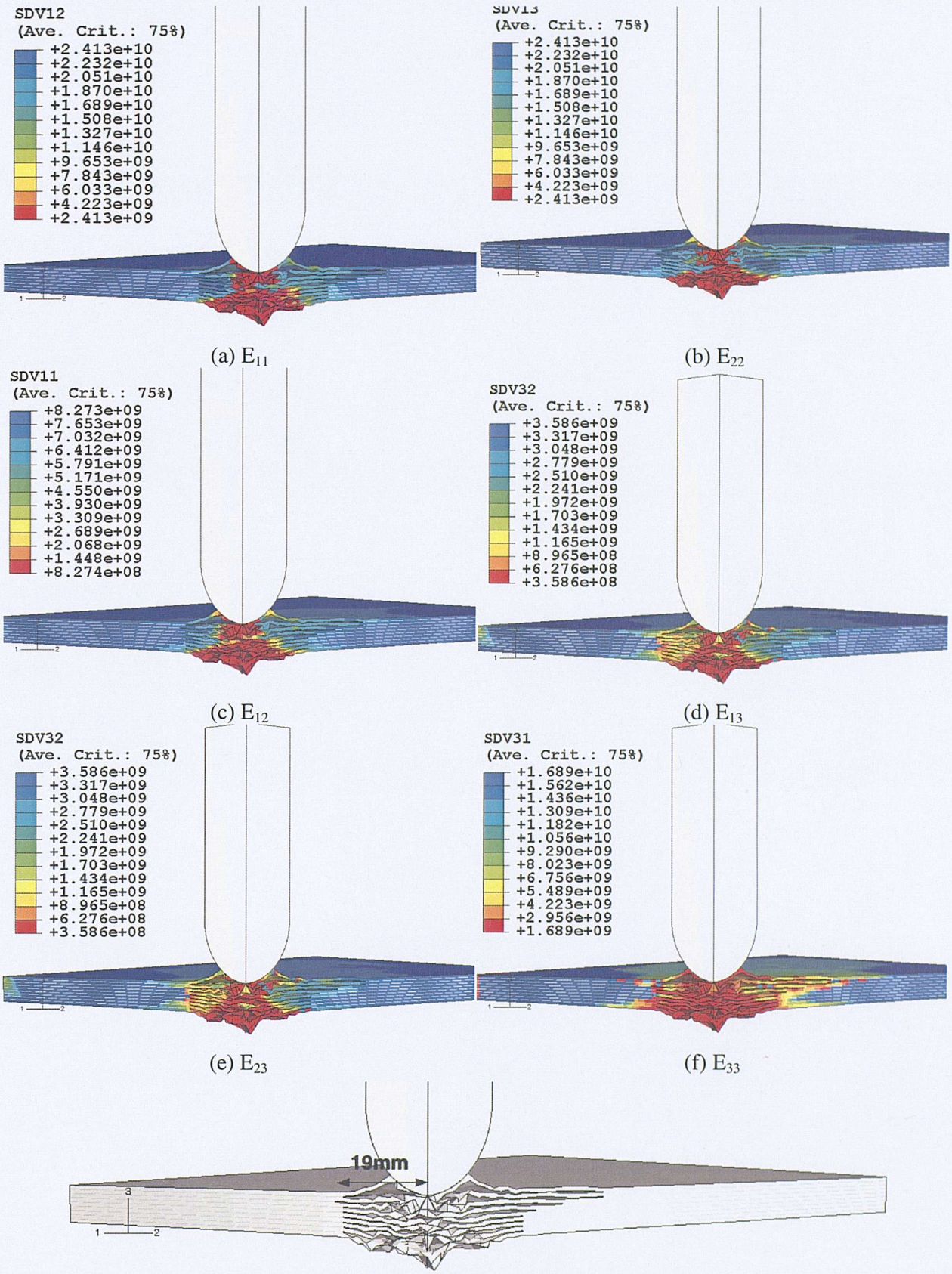


Figure 8. Test 9(195J), FE modulus contours and delamination

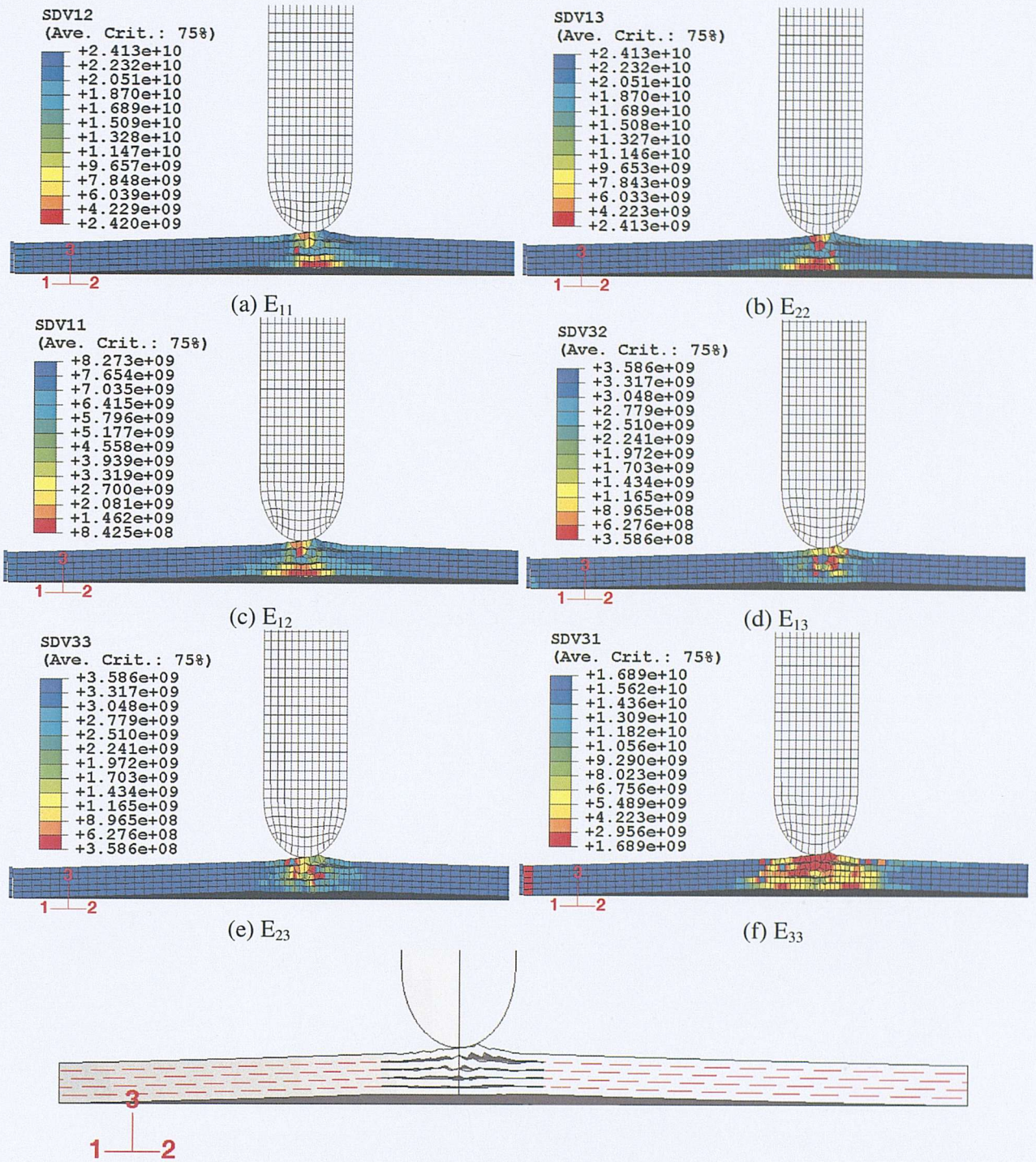
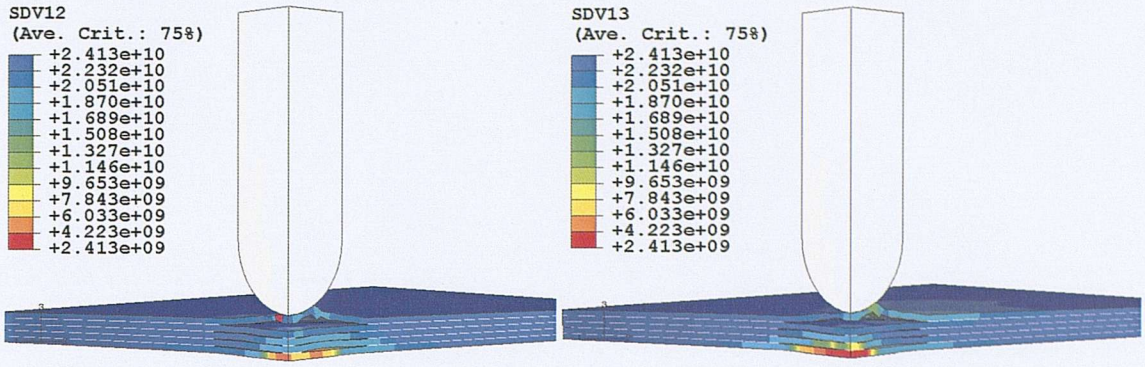
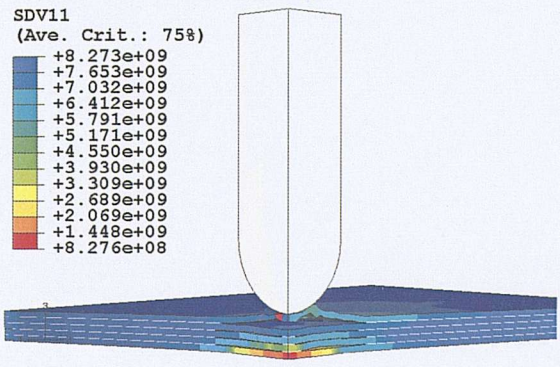


Figure 9. Test 21(198J) mesh co4_p2t2, FE modulus contours and delamination

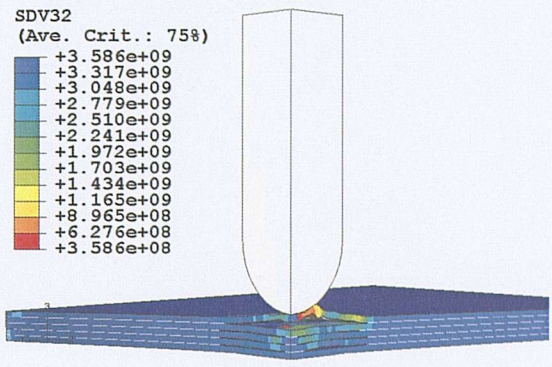


(a) E_{11}

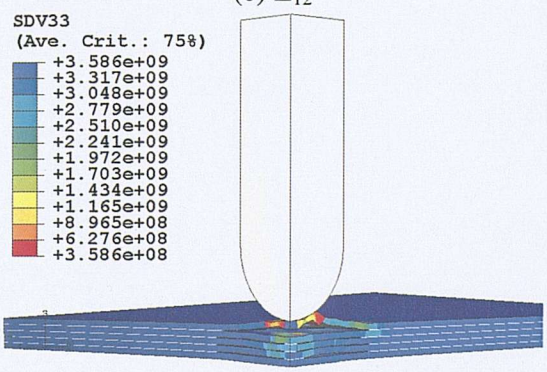
(b) E_{22}



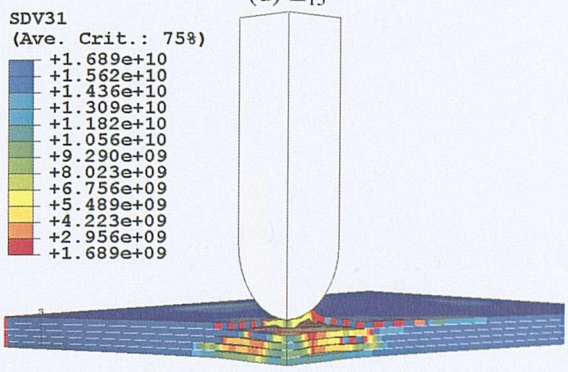
(c) E_{12}



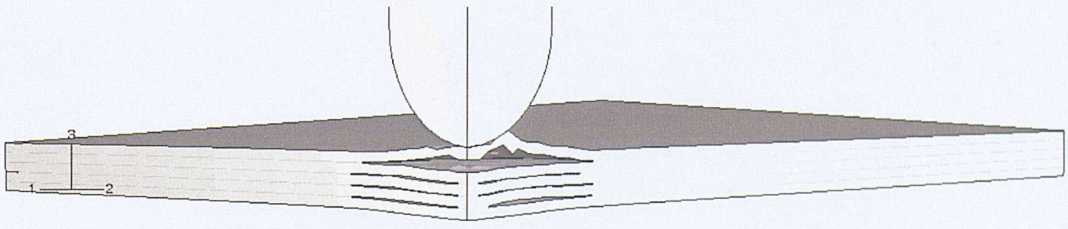
(d) E_{13}



(e) E_{23}

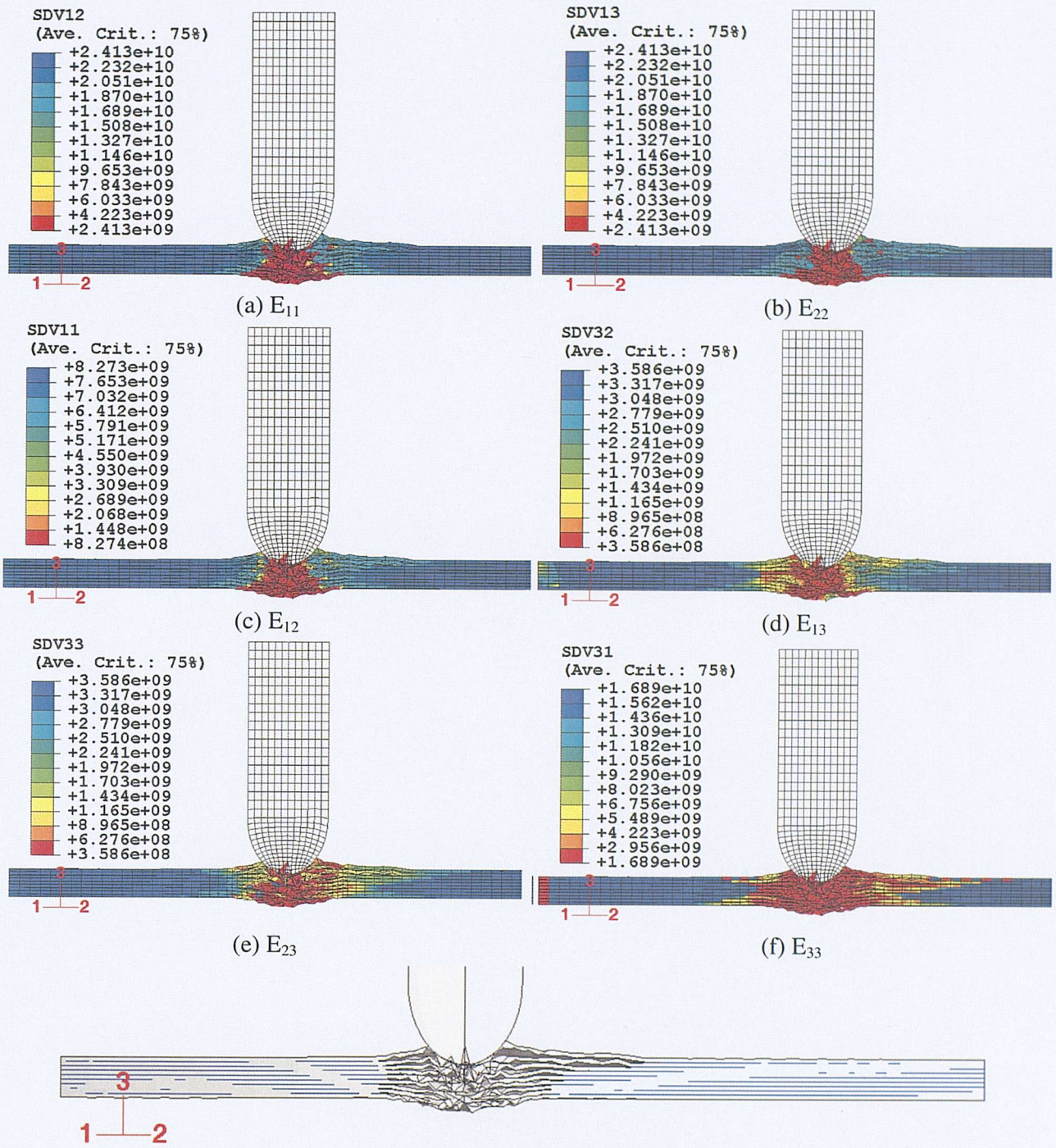


(f) E_{33}



(g) Delamination, (showing full plate)

Figure 10. Test 10(217J), mesh co4_p2t2, FE and delamination



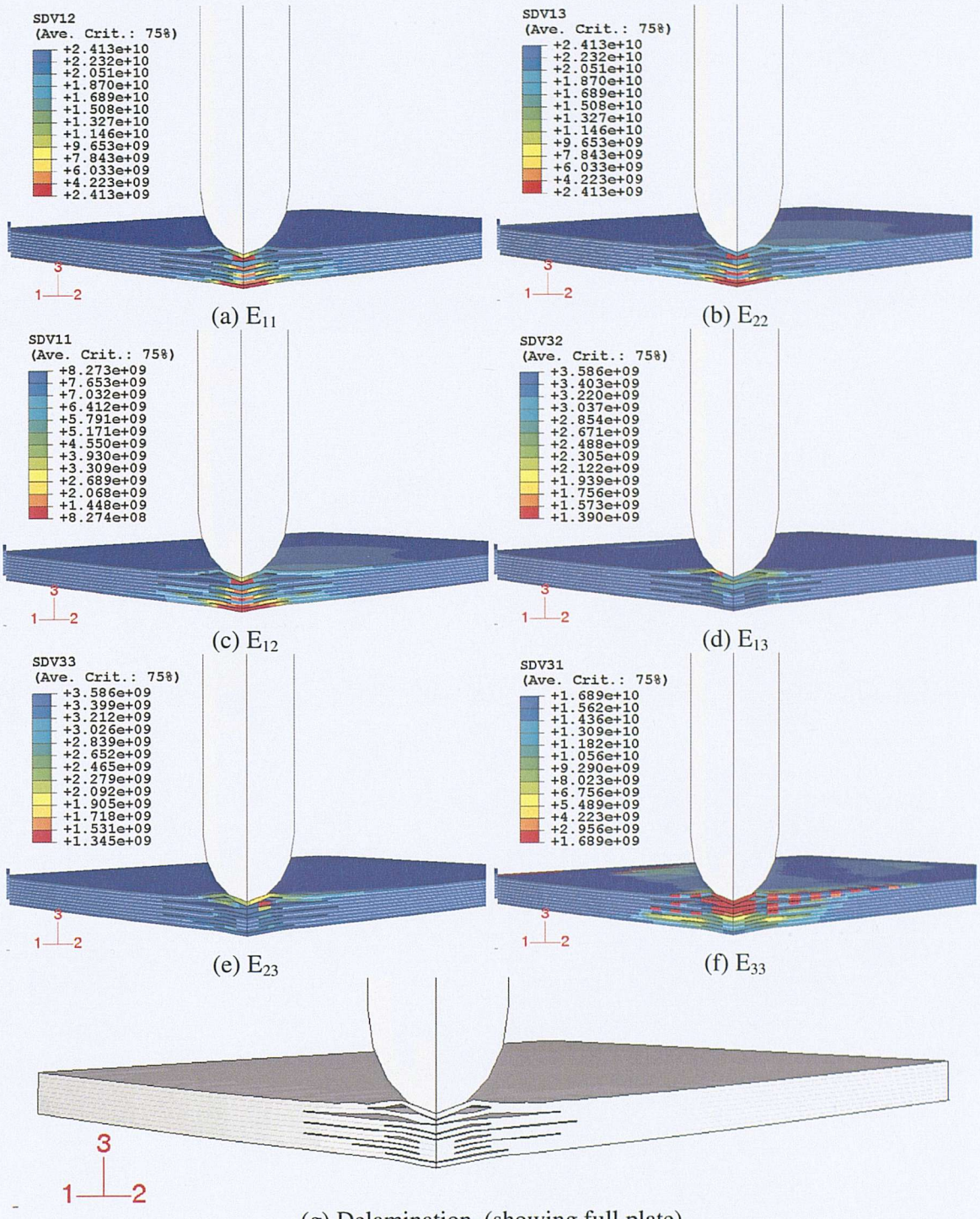
(a) E_{11} (b) E_{22}

(c) E_{12} (d) E_{13}

(e) E_{23} (f) E_{33}

(g) Delamination, (showing full plate)

Figure 11. Test 22(228J), FE and delamination



(a) E_{11} (b) E_{22}

(c) E_{12} (d) E_{13}

(e) E_{23} (f) E_{33}

(g) Delamination, (showing full plate)

Figure 12. Test 7(247J), FE and delamination

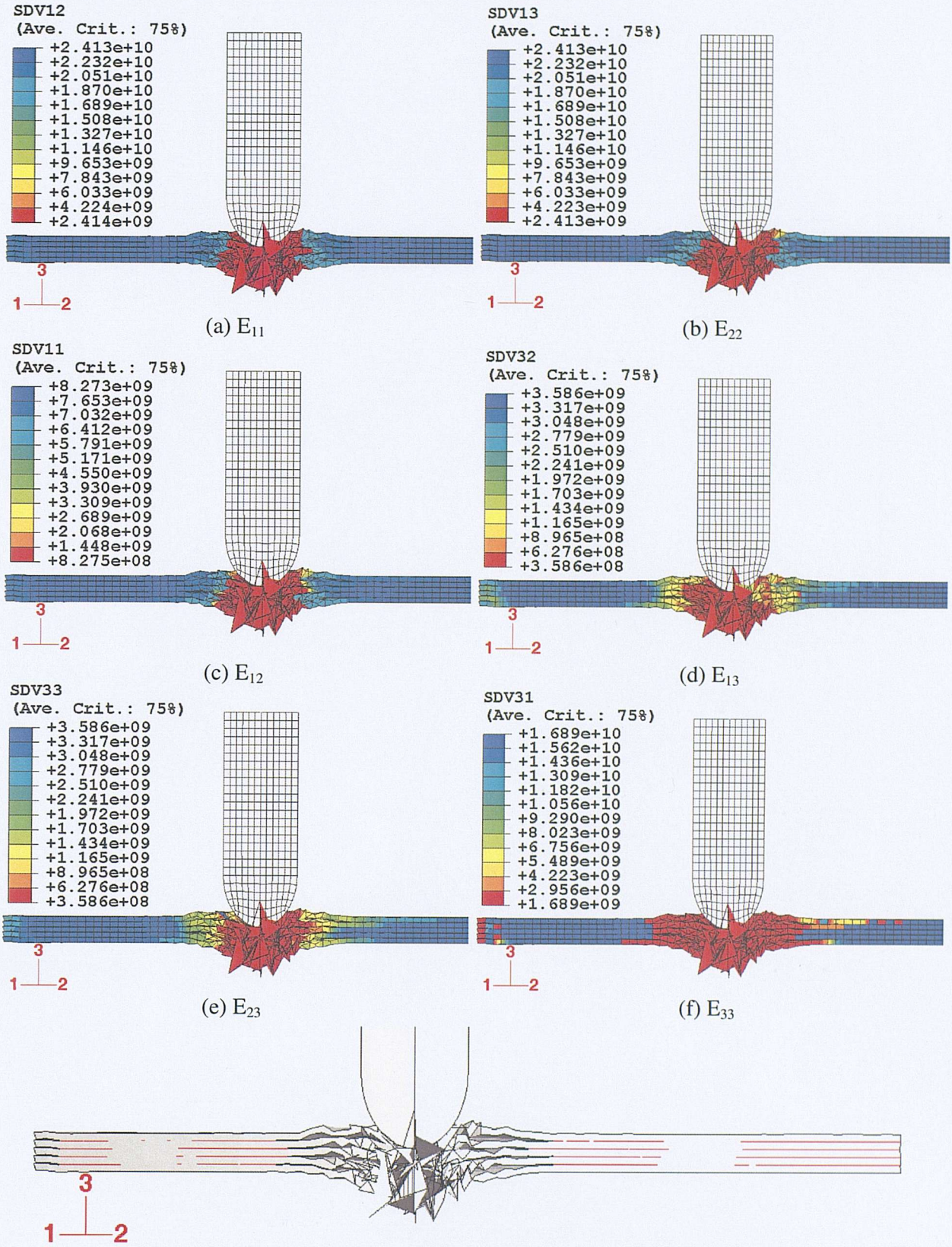
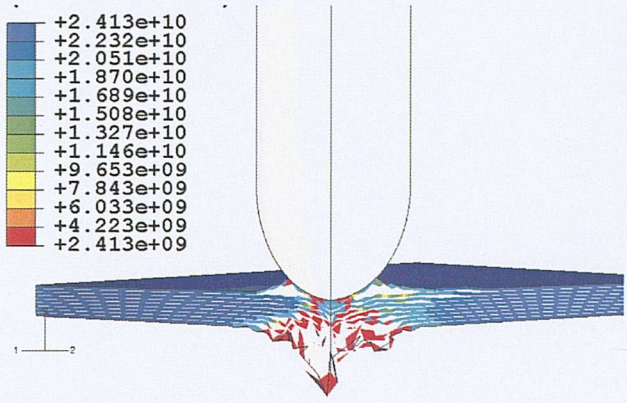
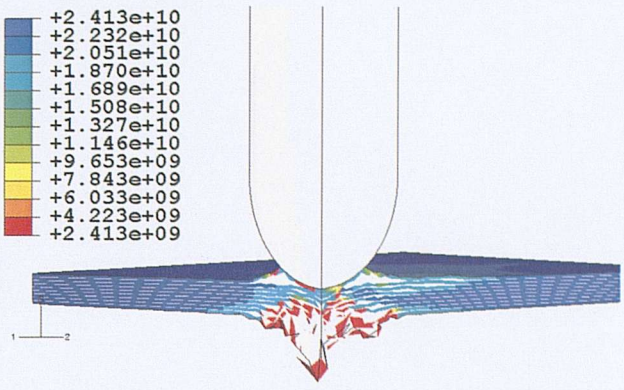


Figure 13. Test 23(269J), FE modulus contours and delamination

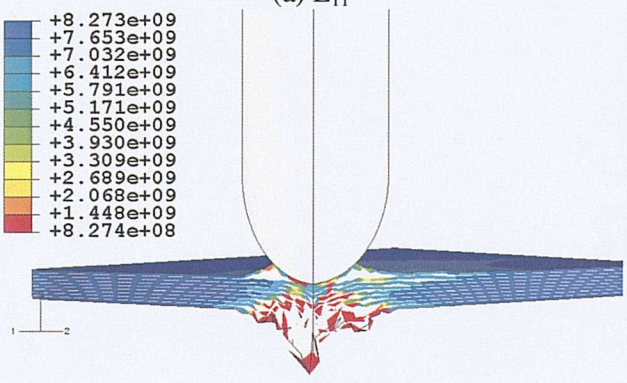
C.3 Damage Results – 38mm tup tests



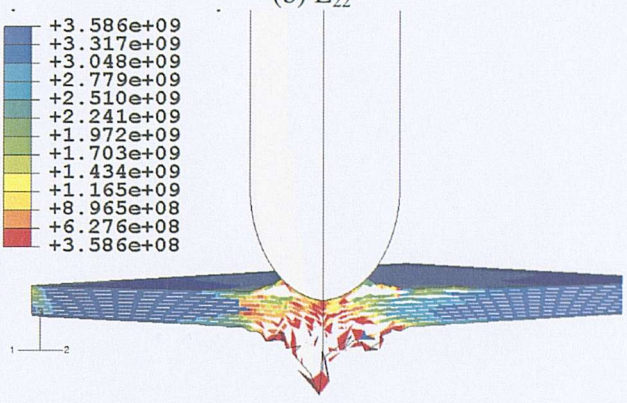
(a) E_{11}



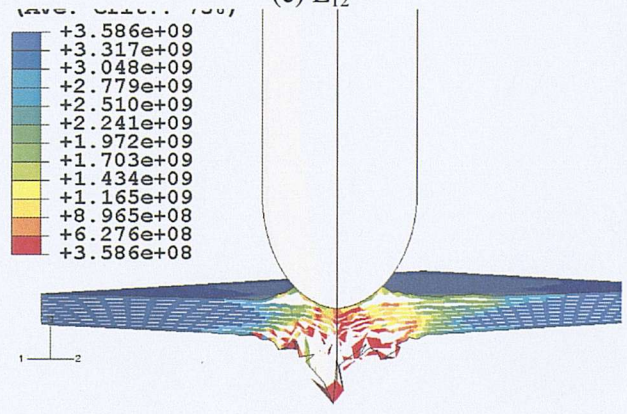
(b) E_{22}



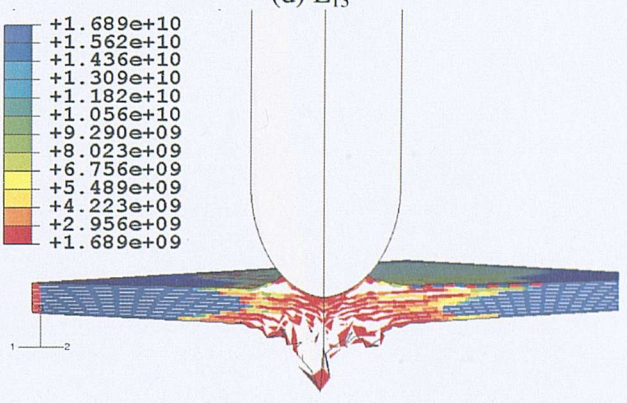
(c) E_{12}



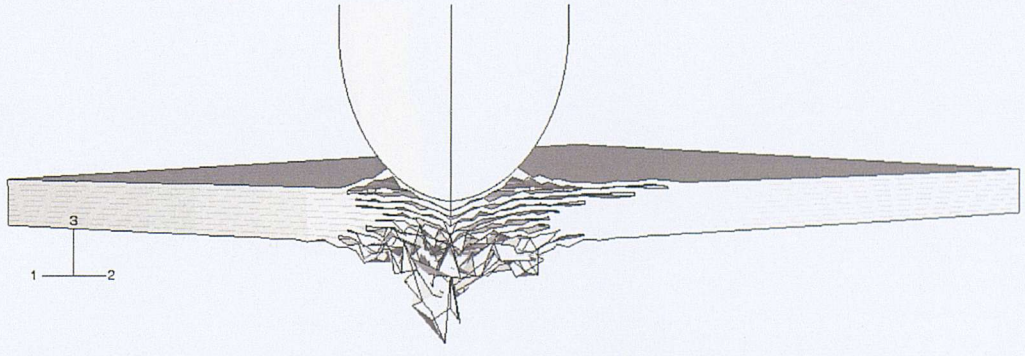
(d) E_{13}



(e) E_{23}

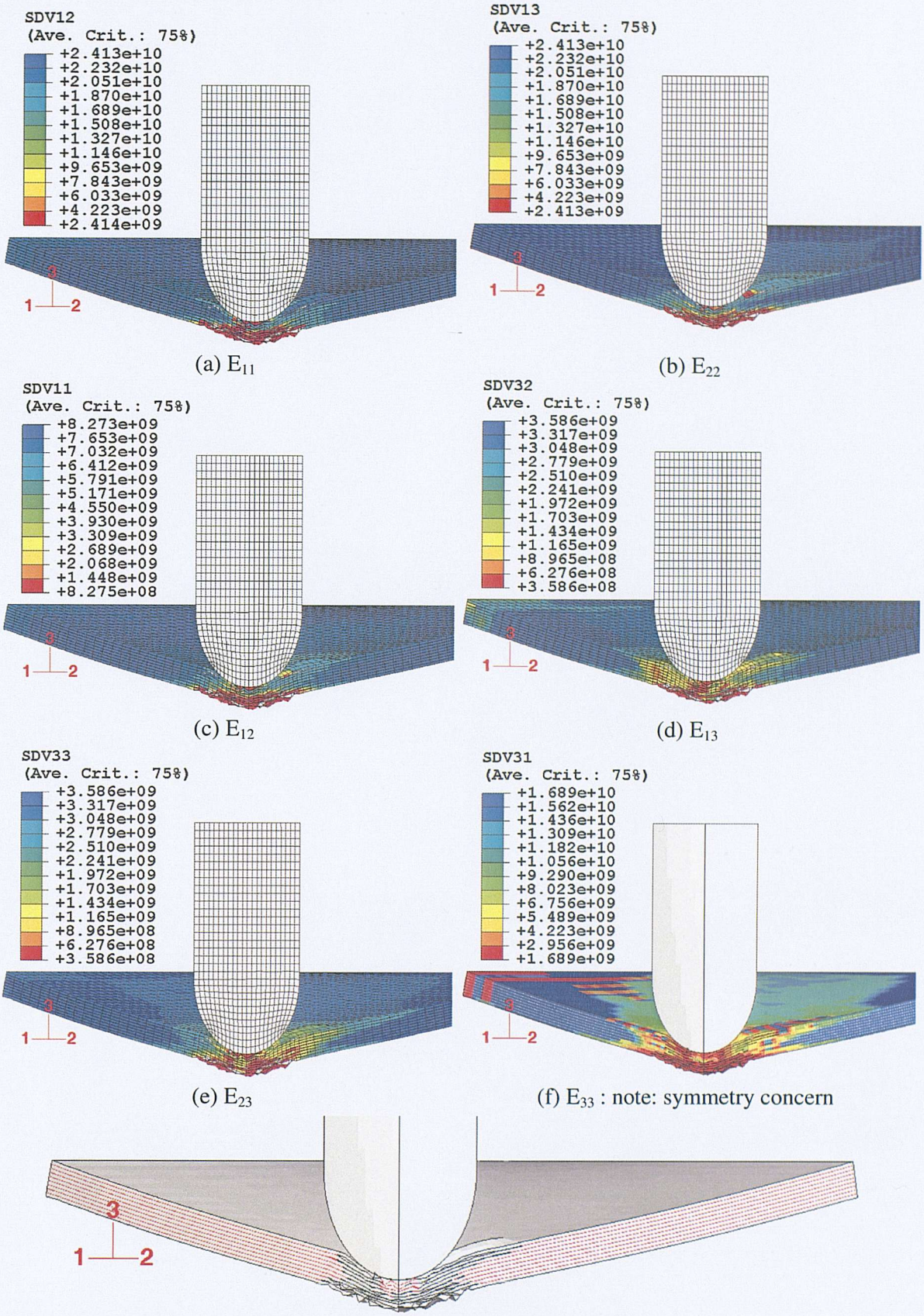


(f) E_{33}



(g) Delamination, (showing full plate)

Figure 14. Test 11(211J), FE modulus contours and delamination



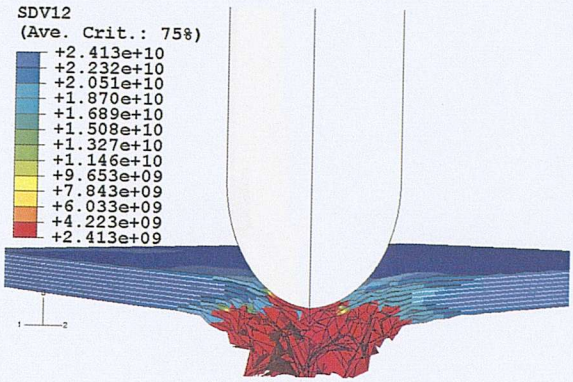
(a) E_{11} (b) E_{22}

(c) E_{12} (d) E_{13}

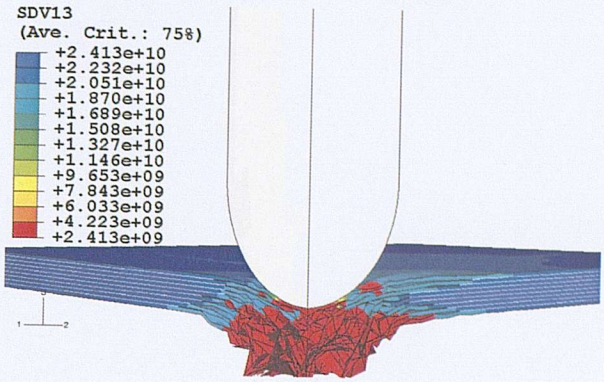
(e) E_{23} (f) E_{33} : note: symmetry concern

(g) Delamination, (showing full plate)

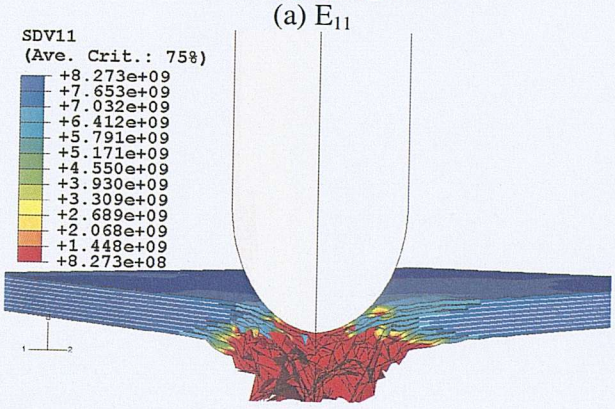
Figure 15. Test 13(284J), FE modulus contours and delamination *at maximum o.o.p displacement*



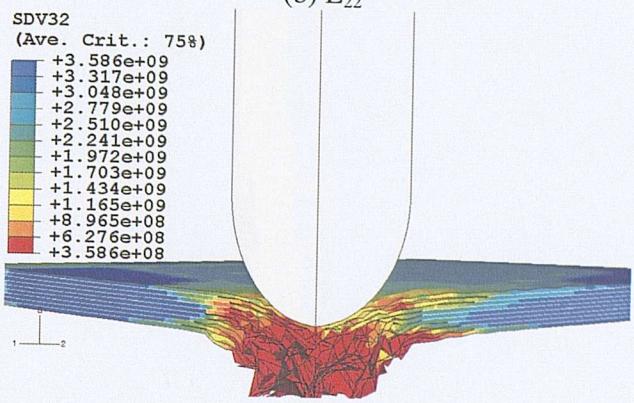
(a) E_{11}



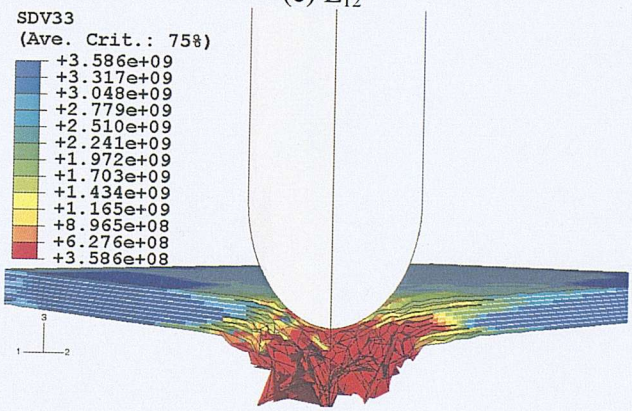
(b) E_{22}



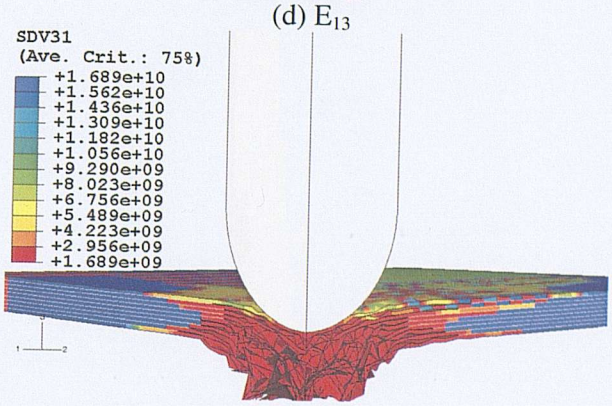
(c) E_{12}



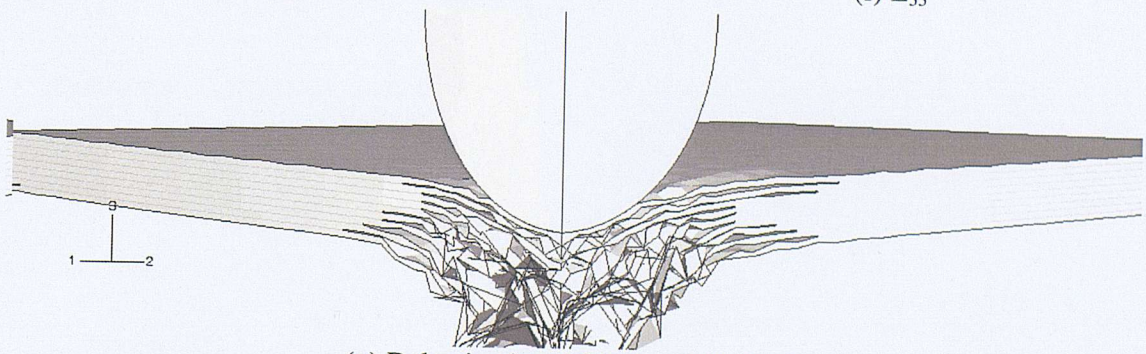
(d) E_{13}



(e) E_{23}

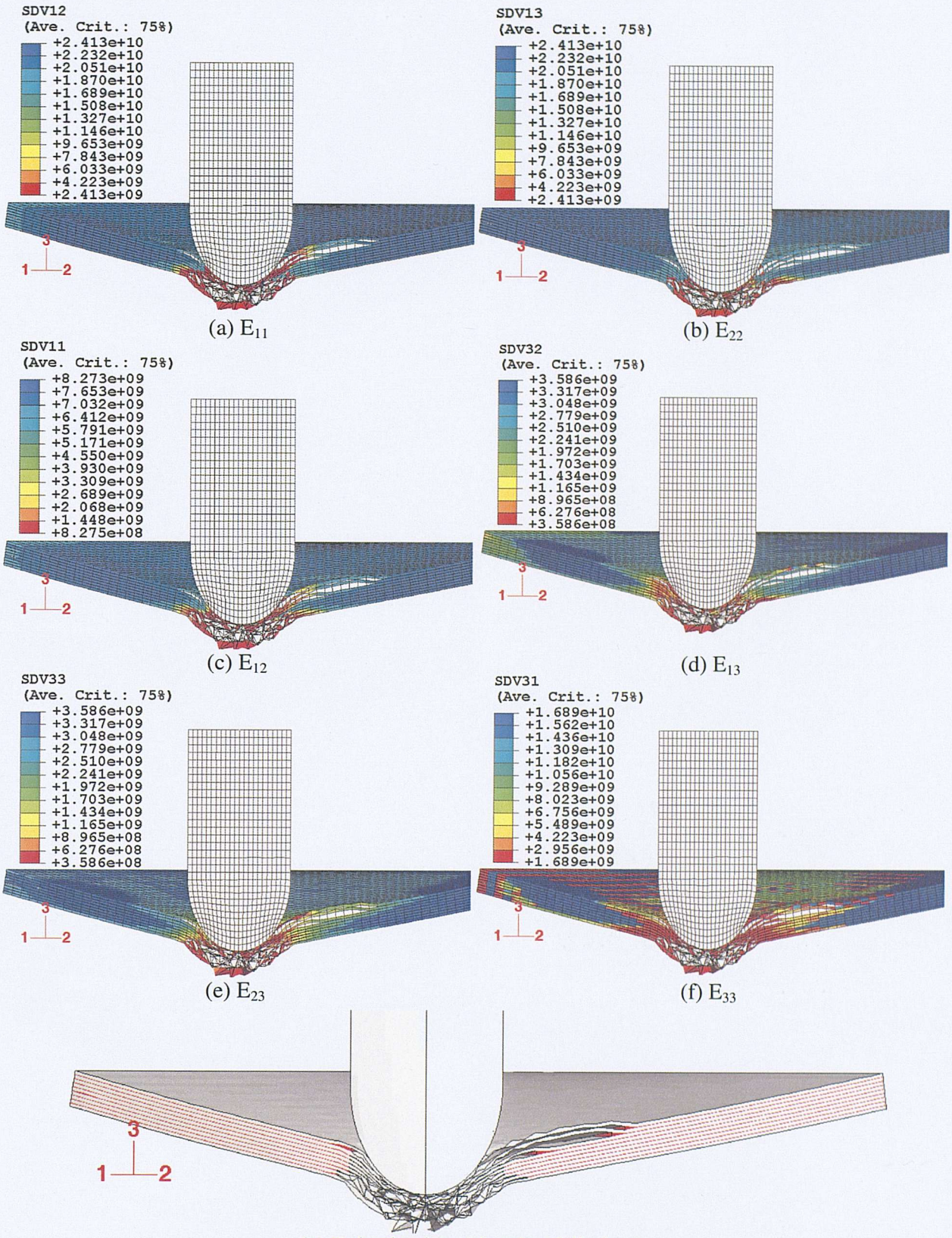


(f) E_{33}



(g) Delamination, (showing full plate)

Figure 16. Test 14(294J), FE modulus contours and delamination



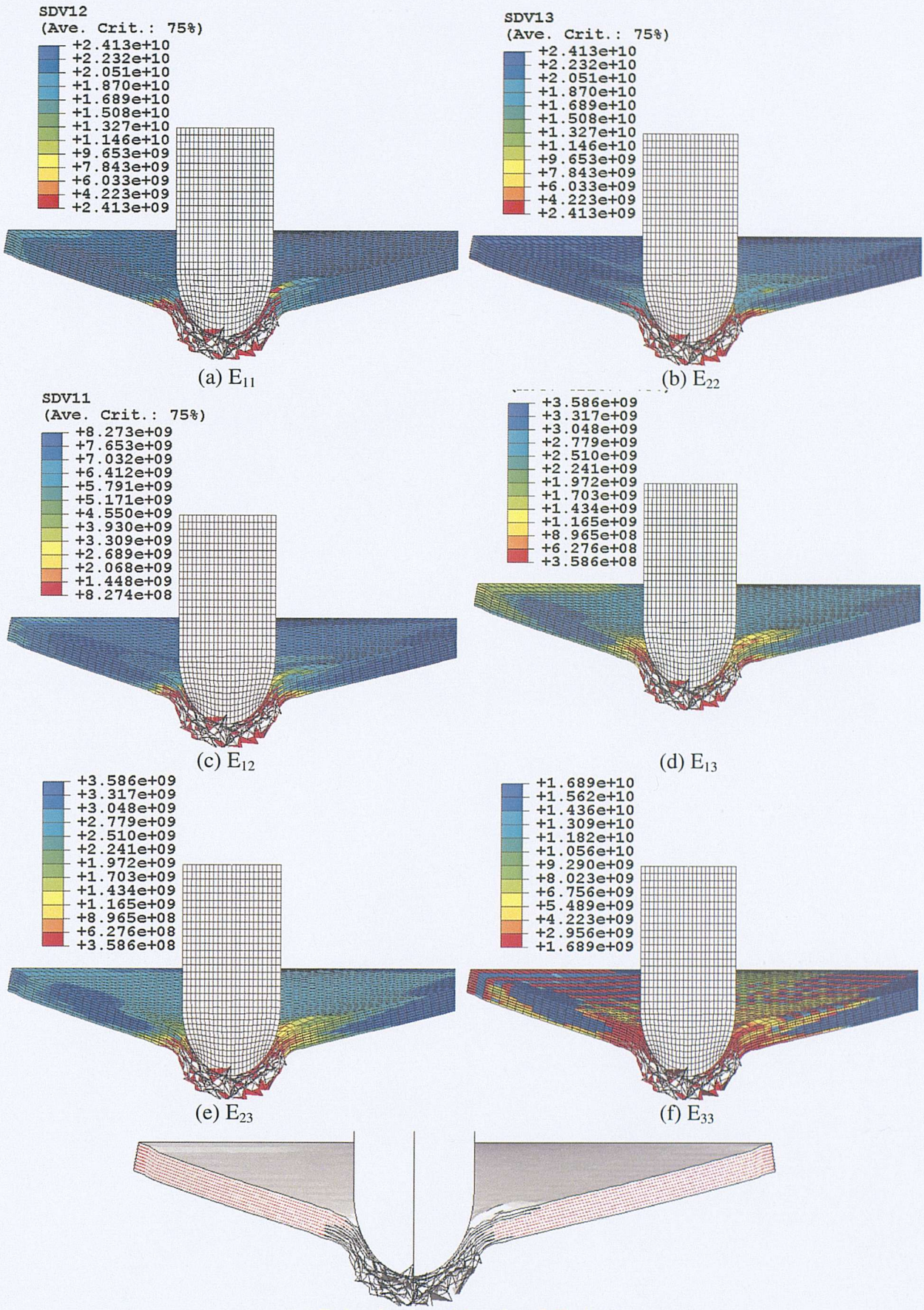
(a) E_{11} (b) E_{22}

(c) E_{12} (d) E_{13}

(e) E_{23} (f) E_{33}

(g) Delamination, (showing full plate)

Figure 17. Test 15(495J), mesh co4_p2t2, FE modulus contours and delamination



(a) E_{11} (b) E_{22}

(c) E_{12} (d) E_{13}

(e) E_{23} (f) E_{33}

(g) Delamination, (showing full plate)

Figure 18. Test 16(665J), mesh co8_p2t2, FE modulus contours and delamination

C.4 Damage Results – large1 (1.07315x0.76835x0.019m) plate

These FE results were carried out with the 3d damage model and cohesive elements (chapter 6) using the global strain criterion for prediction of damage initiation and the linear coupled traction-separation law.

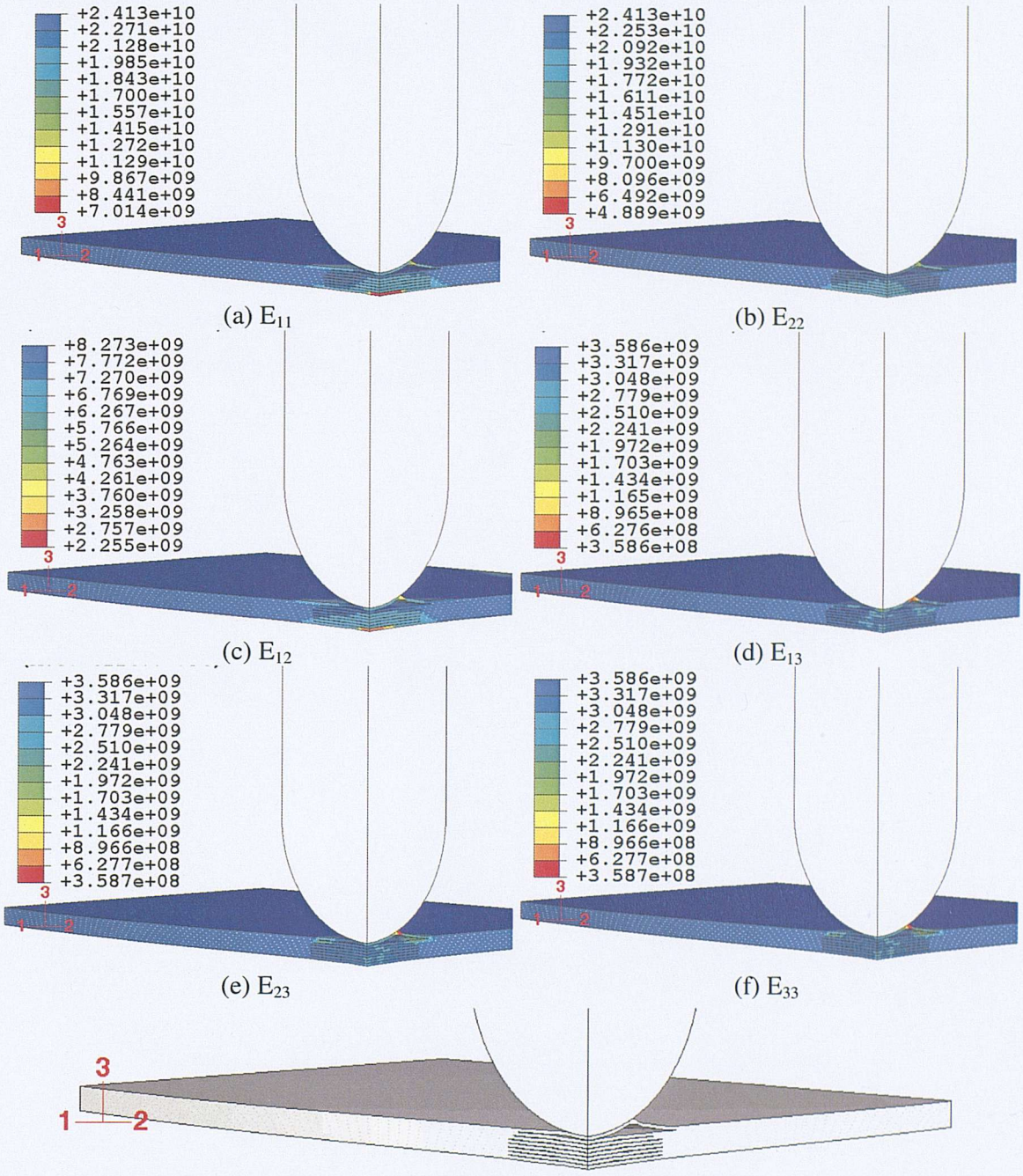


Figure 19. FE modulus contours and delamination for test A

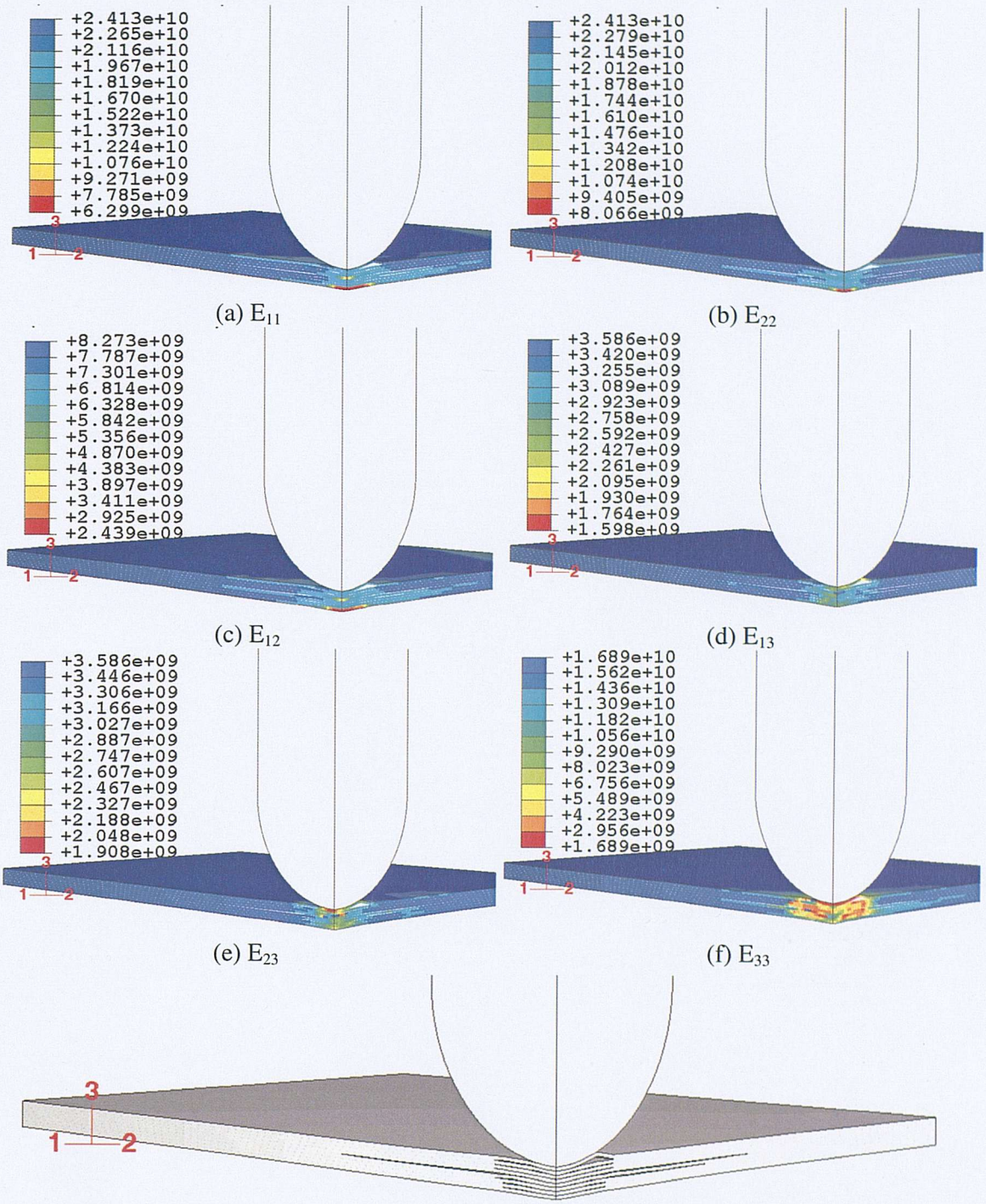


Figure 20. FE modulus contours and delamination for test B

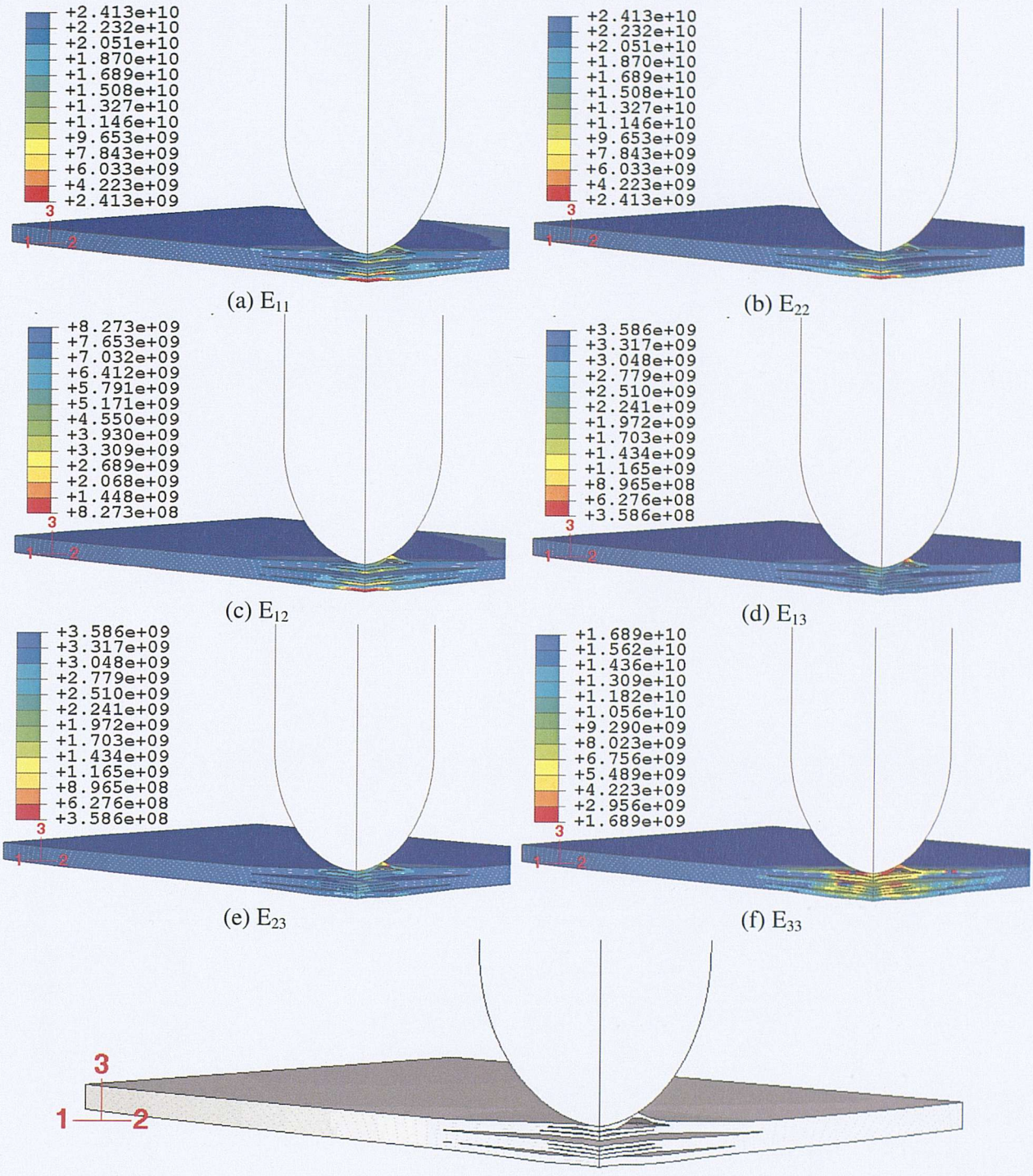
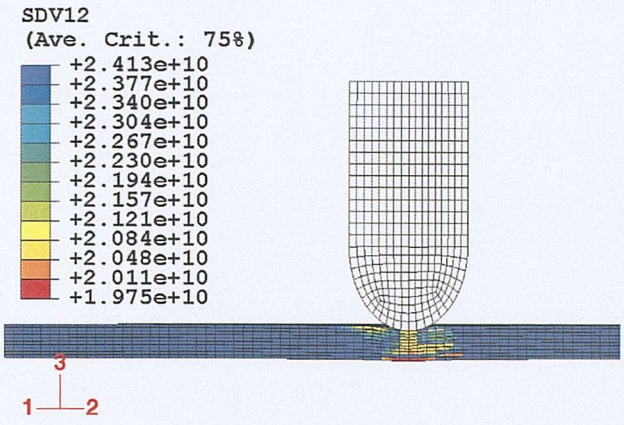
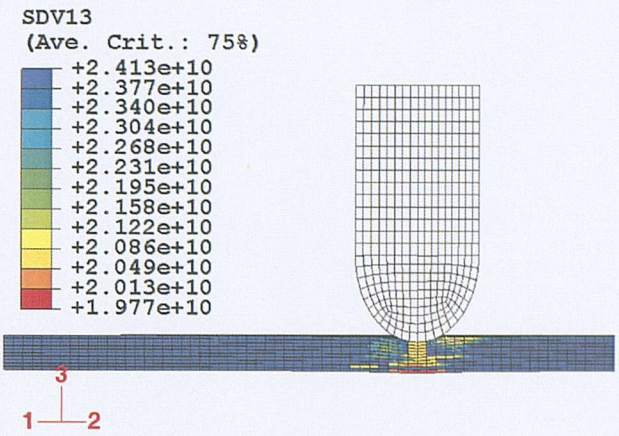


Figure 21. FE modulus contours and delamination for test C/D

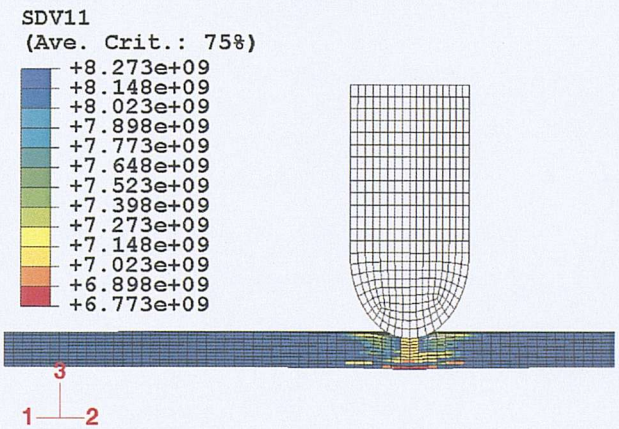
C.5 Damage Results – Large2 (1.372x1.372m) plate



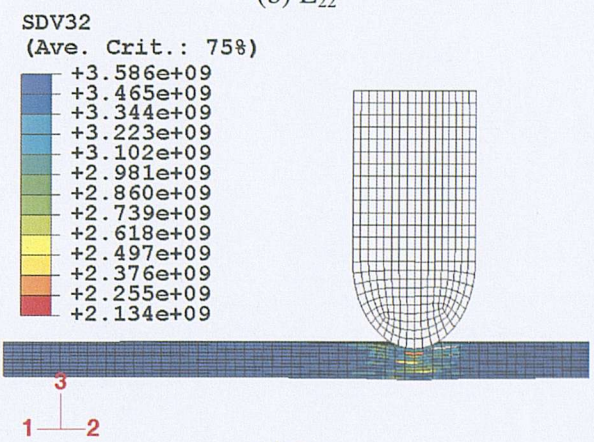
(a) E_{11}



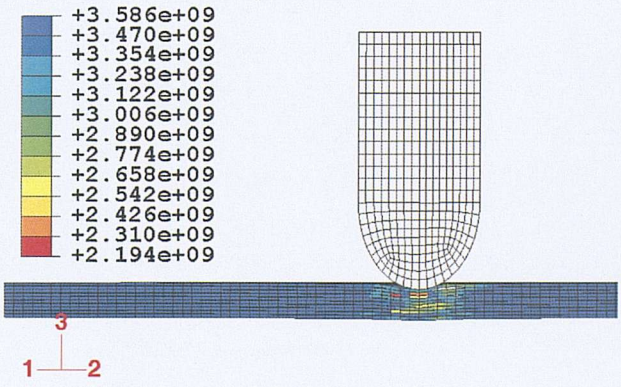
(b) E_{22}



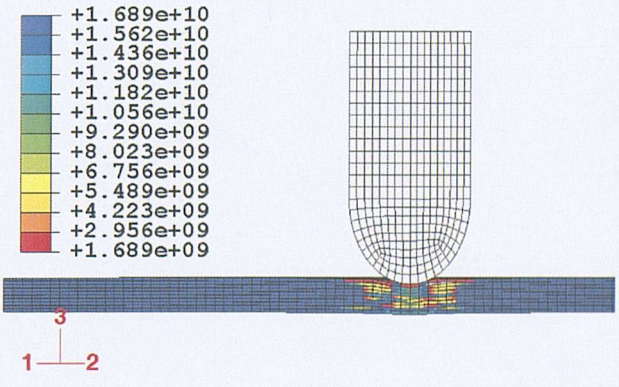
(c) E_{12}



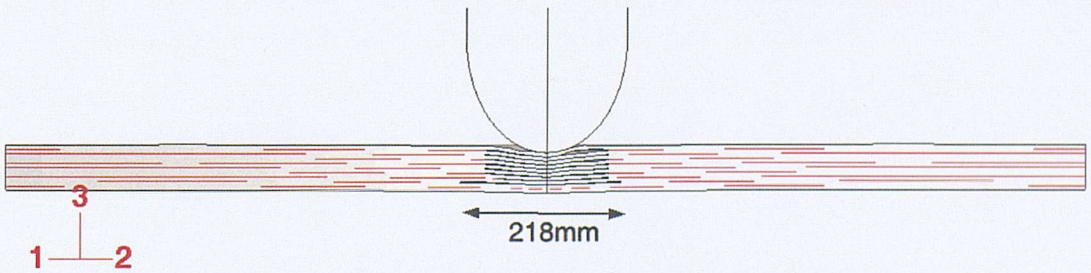
(d) E_{13}



(e) E_{23}



(f) E_{33}



(g) Delamination, (showing full plate)

Figure 22. FE modulus contours and delamination for test large2

PUBLICATIONS

1. Boh J.W. and Johnson H.E., Woven roving laminate beam subjected to shear, Industrial Affiliates Annual Review Meeting, The Composites Centre, Roderic Hill building, Imperial College London, 25 Sept. 2003
   Type: Poster

2. Johnson H.E., Residual strength and stiffness of shock damaged composite panels, Annual Review Meeting, The Composites Centre, Imperial College London, 30 Sept.2004
   Type: Presentation and poster.

3. Johnson H.E. and Louca L.A., Damage modelling of marine composites under static and shock loading conditions, Lloyds Register meeting, Department of Aeronautics, Imperical College London, 20 Jan.2005
   Type: Presentation

4. Johnson H.E., Behaviour and design of composite blast barriers, Impact research focus group, Department of Aeronautics, Imperial College London, 21 Sept.2005
   Type: Presentation

5. Johnson H.E., Mouring S.E., and Louca L.A., Large scale testing of composite panels subjected to in-plane compression, Proceedings of the New Horizons for Materials and Processing Technologies, SAMPE'05, Long Beach, California , May 2005

6. Johnson H.E., Current research into modelling of shock damage to large scale composite panels, Proceedings of the Advances in Multi-Scale Modelling of Composite Material Systems and Components, Monterey Bay, California , Sept 2005

7. Johnson H.E., Journal of Materials Science, Current research into modelling of shock damage to large scale composite panels, 41 (20) (2006): 6655-72.

8. Louca L.A. and Johnson H.E., Predictive modelling of damage in marine composite structures, Global Research Awards, The Royal Academy of Engineering, Sept. 2006
   Type: Poster

9. Johnson H.E., Louca L.A., Mouring S.E., International Journal of Impact Engineering, Modelling impact damage in marine composite panels (2006). *Pending review.*

10. Johnson H.E., Louca L.A., Mouring S.D., Large scale testing of thick composite panels subjected to in-plane compression. *Pending submission to Journal of Marine Structures.*

Plus several other miscellaneous presentations given and posters displayed within the Civil and Environmental Engineering Department, Imperial College London.